BEILSTEIN JOURNAL OF NANOTECHNOLOGY

Frontiers in pharmaceutical nanotechnology

Edited by Matthias G. Wacker

Imprint

Beilstein Journal of Nanotechnology
www.bjnano.org
ISSN 2190-4286
Email: journals-support@beilstein-institut.de

The *Beilstein Journal of Nanotechnology* is published by the Beilstein-Institut zur Förderung der Chemischen Wissenschaften.

Beilstein-Institut zur Förderung der Chemischen Wissenschaften
Trakehner Straße 7–9
60487 Frankfurt am Main
Germany
www.beilstein-institut.de

BEILSTEIN JOURNAL OF NANOTECHNOLOGY

Frontiers in pharmaceutical nanotechnology

Matthias G. Wacker

Editorial

Open Access

Address:
National University of Singapore, Faculty of Science, Department of Pharmacy, 6 Science Drive 2, 117546 Singapore

Email:
Matthias G. Wacker - phamgw@nus.edu.sg

Keywords:
drug delivery; nanocarriers; nanomedicines; nanotheranostics; pharmaceutical nanotechnology

Beilstein J. Nanotechnol. **2019,** *10,* 2538–2540.
doi:10.3762/bjnano.10.244

Received: 07 November 2019
Accepted: 29 November 2019
Published: 17 December 2019

This article is part of the thematic issue "Frontiers in pharmaceutical nanotechnology".

Editor-in-Chief: T. Schimmel

Today, pharmaceutical nanotechnology is a very dynamic and evolving research area that integrates a wide variety of disciplines such as chemical, biological and biomedical science. At the frontier of knowledge, nanoparticles, exosomes and even more advanced drug delivery systems [1] blur the line between drug discovery and formulation science. They have fundamentally changed our understanding of the way dosage forms can facilitate drug therapy.

Prof. Jörg Kreuter has been a pioneer in this research area and dedicated his life's work to nanoparticle research and the blood–brain barrier [2]. One of his most outstanding discoveries, the active transport of nanoparticles into the central nervous system using the low-density lipoprotein receptor family [3-6], provided an entry route for the cytostatic drug doxorubicin into the brain. The drug delivery system has been tested in a phase II clinical trial and hopefully will make its way into the market.

Although nanotechnology has gained significant attention in the scientific community, this is one of very few examples where targeted delivery was successfully developed to the stage of clinical translation. Today, a fierce competition between different technologies decides on commercial success, and consequently, the number of new therapies [7].

Nanotechnology comes in a thousand varieties and there is a rising number of "engineered nanomaterials" under development [1,8]. In this dedicated issue, we present some of the latest trends ranging from the synthesis of new materials [9] to the application of nanoparticles in our fight against drug resistance [10]. But what are the frontiers of tomorrow?

Recently, the Center for Drug Evaluation and Research within the United States Food and Drug Administration presented the progress in new drug applications and concluded that, although the use of nanomaterials has generally increased, the number of approved nanomedicines is still very limited when compared to the tremendous research activity in this area [1].

Because nothing is older than yesterday's newspaper, this editorial will take a look into the crystal ball.

Nanomedicine was proclaimed to revolutionize medicine, but what we are seeing at present is a slow transformation rather than a revolutionary overthrow. Now more than ever, the poten-

tial for clinical translation will be in the spotlight. In many areas, nanotechnology is already accepted, for example, in the production of nanocrystals. To date, the nanomilling platform of Elan Drug Technologies is widely used for the formulation of poorly soluble compounds [11]. Also, with regards to the topical administration route, nanometer-scale excipients have been rarely associated with safety issues and have been widely applied in the development of semisolids. But we still have much to learn.

Pharmaceutical science has indisputably become more complex with the discovery of nanocarrier-based delivery systems. Fueled by first successes in the 1990s, liposomes were at the forefront of cancer therapy [12,13]. The challenges associated with their characterization earned them the name "non-biological complex drugs" (NBCDs) [8].

Nowadays, there is broad acceptance for liposomal drugs as a niche product, but we still do not know much about the attributes that enable targeted delivery in humans [14]. In 2018, Alnylam announced the approval of a first-of-its-kind RNA interference (RNAi)-based drug, Onpattro™, which uses solid lipid nanoparticles to protect the sensitive compound from early degradation. Again, lipid materials rather than synthetic polymers have been used for drug delivery applications.

In pharmaceutical research, the economic success of drug products is closely related to product efficacy and safety. While lipids have a solid track record of clinical safety [7,12], there are few polymers generally used for the parenteral route of administration. Further, the procedure of drug approval usually does not provide market exclusivity or a general recommendation for the excipient but for the drug product only [7]. This together makes it more difficult to justify the time-consuming and expensive toxicological studies required to establish clinical safety of the excipient. Consequently, there is a trend towards materials with a long history of medical use [12].

Pharmaceutical nanotechnology is not limited to translational research but, after many years of trial and error, we have to accept that reliable pharmacological and toxicological effects are a key element of industrial formulation development. Understanding the intertwined processes involved in biodistribution of deposition of nanocarrier delivery will finally lead to a broader acceptance, and consequently, to successful translation from bench to bedside.

Matthias G. Wacker

Singapore, November 2019

Acknowledgements

The author acknowledges Prof. Jörg Kreuter and Prof. Jennifer Dressman for supporting his career over so many years. Further, he thanks the National University of Singapore, Office of the Deputy President Research and Technology (WBS no. R-148-000-282-133) as well as the Faculty of Science (Grant no. R-148-000-282-750) for financial contributions to his research group.

ORCID® iDs

Matthias G. Wacker - https://orcid.org/0000-0002-2789-6463

References

1. D'Mello, S. R.; Cruz, C. N.; Chen, M.-L.; Kapoor, M.; Lee, S. L.; Tyner, K. M. *Nat. Nanotechnol.* **2017,** *12,* 523–529. doi:10.1038/nnano.2017.67
2. Kreuter, J. *Adv. Drug Delivery Rev.* **2014,** *71,* 2–14. doi:10.1016/j.addr.2013.08.008
3. Wagner, S.; Zensi, A.; Wien, S. L.; Tschickardt, S. E.; Maier, W.; Vogel, T.; Worek, F.; Pietrzik, C. U.; Kreuter, J.; von Briesen, H. *PLoS One* **2012,** *7,* e32568. doi:10.1371/journal.pone.0032568
4. Zensi, A.; Begley, D.; Pontikis, C.; Legros, C.; Mihoreanu, L.; Büchel, C.; Kreuter, J. *J. Drug Targeting* **2010,** *18,* 842–848. doi:10.3109/1061186x.2010.513712
5. Zensi, A.; Begley, D.; Pontikis, C.; Legros, C.; Mihoreanu, L.; Wagner, S.; Büchel, C.; von Briesen, H.; Kreuter, J. *J. Controlled Release* **2009,** *137,* 78–86. doi:10.1016/j.jconrel.2009.03.002
6. Feczkó, T.; Piiper, A.; Ansar, S.; Blixt, F. W.; Ashtikar, M.; Schiffmann, S.; Ulshöfer, T.; Parnham, M. J.; Harel, Y.; Israel, L. L.; Lellouche, J.-P.; Wacker, M. G. *J. Controlled Release* **2019,** *293,* 63–72. doi:10.1016/j.jconrel.2018.11.017
7. Wacker, M. G. Nanomedicines–A Scientific Toy or an Emerging Market?. In *Polymer Nanoparticles for Nanomedicines: A Guide for their Design, Preparation and Development;* Vauthier, C.; Ponchel, G., Eds.; Springer International Publishing: Cham, Switzerland, 2016; pp 591–614. doi:10.1007/978-3-319-41421-8_18
8. Marques, M. R. C.; Choo, Q.; Ashtikar, M.; Rocha, T. C.; Bremer-Hoffmann, S.; Wacker, M. G. *Adv. Drug Delivery Rev.* **2019,** *151–152,* 23–43. doi:10.1016/j.addr.2019.06.003
9. Levin, T.; Sade, H.; Binyamini, R. B.-S.; Pour, M.; Nachman, I.; Lellouche, J.-P. *Beilstein J. Nanotechnol.* **2019,** *10,* 811–822. doi:10.3762/bjnano.10.81
10. Onafuye, H.; Pieper, S.; Mulac, D.; Cinatl, J. C., Jr.; Wass, M. N.; Langer, K.; Michaelis, M. *Beilstein J. Nanotechnol.* **2019,** *10,* 1707–1715. doi:10.3762/bjnano.10.166
11. Merisko-Liversidge, E.; Liversidge, G. G. *Adv. Drug Delivery Rev.* **2011,** *63,* 427–440. doi:10.1016/j.addr.2010.12.007
12. Wacker, M. *Int. J. Pharm.* **2013,** *457,* 50–62. doi:10.1016/j.ijpharm.2013.08.079
13. Barenholz, Y. *J. Controlled Release* **2012,** *160,* 117–134. doi:10.1016/j.jconrel.2012.03.020
14. Shen, J.; Burgess, D. J. *J. Controlled Release* **2015,** *219,* 644–651. doi:10.1016/j.jconrel.2015.09.052

BEILSTEIN JOURNAL OF NANOTECHNOLOGY

Tungsten disulfide-based nanocomposites for photothermal therapy

Tzuriel Levin[1], Hagit Sade[1], Rina Ben-Shabbat Binyamini[1], Maayan Pour[2], Iftach Nachman[2] and Jean-Paul Lellouche[*1]

Full Research Paper

Open Access

Address:
[1]Institute of Nanotechnology and Advanced Materials & Department of Chemistry, Faculty of Exact Sciences, Bar-Ilan University, Ramat Gan, 5290002, Israel and [2]Department of Biochemistry and Molecular Biology, George S. Wise Faculty of Life Sciences, Tel Aviv University, Tel Aviv, 6997801, Israel

Email:
Jean-Paul Lellouche* - Jean-Paul.M.Lellouche@biu.ac.il

* Corresponding author

Keywords:
cerium complex; magnetic nanoparticles; photothermal therapy; surface functionalization; WS_2 nanotubes

Beilstein J. Nanotechnol. **2019,** *10,* 811–822.
doi:10.3762/bjnano.10.81

Received: 27 November 2018
Accepted: 11 March 2019
Published: 02 April 2019

This article is part of the thematic issue "Frontiers in pharmaceutical nanotechnology".

Guest Editor: M. G. Wacker

Abstract

Nanostructures of transition-metal dichalcogenides (TMDC) have raised scientific interest in the last few decades. Tungsten disulfide (WS_2) nanotubes and nanoparticles are among the most extensively studied members in this group, and are used for, e.g., polymer reinforcement, lubrication and electronic devices. Their biocompatibility and low toxicity make them suitable for medical and biological applications. One potential application is photothermal therapy (PTT), a method for the targeted treatment of cancer, in which a light-responsive material is irradiated with a laser in the near-infrared range. In the current article we present WS_2 nanotubes functionalized with previously reported ceric ammonium nitrate–maghemite (CAN-mag) nanoparticles, used for PTT. Functionalization of the nanotubes with CAN-mag nanoparticles resulted in a magnetic nanocomposite. When tested in vitro with two types of cancer cells, the functionalized nanotubes showed a better PTT activity compared to non-functionalized nanotubes, as well as reduced aggregation and the ability to add a second-step functionality. This ability is demonstrated here with two polymers grafted onto the nanocomposite surface, and other functionalities could be additional cancer therapy agents for achieving increased therapeutic activity.

Introduction

In 1992, Prof. Reshef Tenne reported the synthesis of cylindrical and polyhedral nanostructures of tungsten disulfide (WS_2) [1]. These nanostructures are composed of triple-layer units, where a hexagonal layer of tungsten atoms is sandwiched between two hexagonal sulfur layers. WS_2 belongs to a family of compounds called transition-metal dichalcogenides (TMDCs), with a general formula of MX_2 (M = W, Mo and X = S, Se, Te) and a similar structure based on triple-layers.

Good mechanical properties of WS_2 inorganic nanotubes (INTs; up to 15 μm length, 100 nm diameter) and inorganic fullerene-like nanoparticles (IFs) were reported in multiple literature sources [2-8], making them an excellent alternative to carbon nanotubes as additives for the mechanical enforcement of polymeric matrices [9-17].

An important advantage of WS_2 (and of other TMDCs) nanostructures over their carbon equivalents is the low toxicity and biocompatibility, enabling their use for medical applications. Preliminary studies on rats with WS_2 INTs and IFs showed no apparent toxic reaction after oral administration [18], inhalation [19], or dermal application [20]. More recent studies conducted on rhenium-doped MoS_2 nanoparticles showed no acute toxic risk, neither by oral administration nor by dermal application [21,22]. A few years ago, Teo et al. compared the cytotoxicity of exfoliated MoS_2, WS_2, and WSe_2 to that of their carbon equivalent and found the toxicity of the former to be lower [23]. Wu et al. produced biocompatible MoS_2 nanoparticles by a pulsed laser ablation technique [24]. Examples of medical applications with TMDC nanostructures are their addition as reinforcing agents to polymers for bone-tissue engineering, and their incorporation in dental devices [25-32]. Another important medical application for nanostructures in general, and for TMDC nanostructures in particular, is targeted cancer treatment through photothermal therapy (PTT). In this method, light-responsive materials accumulate on the tumor area, absorb light, and release it as heat, killing the cancerous cells. The light is generated by a laser, in a near-infrared (NIR) wavelength range (750–1000 nm). NIR irradiation has low off-target interaction and a high penetration depth of ca. 1–2 cm in the human body. PTT mediated by nanomaterials is less invasive than laser irradiation alone, requires lower radiation intensity, and its selectivity towards the tumor can be adjusted by carefully engineering the light-responsive nanostructure. In general, nanomaterials in the size range of 100–200 nm should give the maximum accumulation effect, but parameters such as nanostructure shape and surface charge are extremely important [33].

A wide range of nanomaterials has been studied for cancer PTT to now, from organic conjugated polymers [34,35], through carbon-based nanomaterials [36,37], to inorganic nanostructures. Within the latter group, nanostructures of metals [38], metal oxides (including iron oxides) [39], and metal chalcogenides [40,41] were studied. Tungsten oxides [42] and molybdenum oxides [43] were studied, as well as their disulfides. The disulfides were tested mainly in the forms of nanosheets [44], nanoflakes [45], nanodots [40] and hollow spheres [46]. Recently, WS_2 nanotubes functionalized with C-dots showed promising results for PTT and cell imaging [47]. We selected nanotubes for their mechanical properties and the possibility of coordinate bonds with sulfur atoms, which enables bonding with CAN-mag, thereby offering the possibility of bonding of additional biologically active agents. The properties of the CAN-mag also enabled magnetism-based targeting.

In order to maximize the benefit from TMDC nanostructures in different applications, their surface functionalization is important. The relative chemical inertness of the outer chalcogen layer makes TMDC nanostructures very hard to disperse in many solvents, especially in water. This is a significant limitation when attempting to use these nanostructures for biological applications. Functionalization, especially the attachment of organic moieties to the walls of TMDC nanostructures is a challenging task. Coordinative chemistry is one approach used to face this challenge.

The Tremel group has been successfully developing coordination-chemistry-based strategies for the functionalization of TMDC nanostructures for more than a decade. In 2006, they reported a method based on a nickel–nitrotriacetic acid (Ni-NTA) complex as an anchoring group for different chemical functionalities [48-50]. Another study of the Tremel group involves terpyridine (TerPy) ligands [51]. NTA and TerPy are multidentate ligands, forming complexes with chalcophylic metal ions (nickel, iron, ruthenium) and leaving parts of the ion coordination sites free for docking to the chalcogen layer. The molecular structure of both NTA and TerPy enables performing versatile chemistry on the ligand.

Cerium is a metal of the lanthanide series with versatile coordinative chemistry, thanks to an available valence electron in its 4f orbital. In our group, cerium was utilized in the complex form of ceric ammonium nitrate [$(NH_4)_2Ce(IV)(NO_3)_6$, or CAN]. In CAN the cerium ion is coordinated with six nitrate ligands through their oxygen atoms. CAN is a strong oxidizer, turning magnetite nanoparticles into γ-maghemite (mag) nanoparticles. The cerium ion attaches to the nanoparticle, producing surface defects (an Fe–O–[CeL_n] bond is formed). The cerium-doped maghemite nanoparticles are more stable than the non-doped ones, which tend to aggregate. In addition to the stabilization effect, other ligands on the cerium ion can be replaced by different polymers and linkers. The resulting nanocomposites can be used for biomedical applications, such as gene silencing [52], magnetic imaging, and drug delivery.

Here we present a new and simple-to-fabricate WS_2-NT-CAN-mag (WS_2-NT-CM) nanocomposite. The composite is magnetic and forms a stable dispersion in water. It was characterized to verify the CAN-mag attachment to the nanotubes, and tested for PTT. Preliminary in-vitro PTT tests show that the WS_2-CAN-

mag nanocomposite successfully eliminated two types of cancerous cells: HeLa cells (cervical cancer) and MCF7 cells (breast cancer), in higher percentages compared to non-functionalized nanotubes. In addition, WS_2-CAN-mag nanocomposites with two types of organic polymers were successfully prepared and characterized. Indeed, functionalization with CAN-mag gives WS_2 nanotubes the added values of reduced aggregation, which leads to better targeting, and the possibility for attachments of additional cancer therapy agents.

Experimental

A schematic description of the experimental pathway leading to CAN-mag functionalized WS_2 nanotubes is given in Figure 1, followed by fully detailed preparation procedures.

Preparation of CAN-mag nanoparticles

A solution of $FeCl_3{\cdot}H_2O$ (240.0 mg, 0.9 mmol) in degassed, ddH_2O water (4.5 mL) was mixed with an aqueous solution of $FeCl_2{\cdot}4H_2O$ (97.5 mg, 0.45 mmol, 4.5 mL H_2O). The mixture was kept under nitrogen and ultra-sonicated for 1 min at room temperature. Then, a concentrated (24 wt %) NH_4OH solution (750 µL) was added, resulting in the immediate formation of a black precipitate of magnetite (Fe_3O_4) nanoparticles. Sonication was continued for an additional 10 min. The liquid was decanted with the help of magnetic separation, using a 0.5 T magnet. The nanoparticles were washed with three portions of ddH_2O (40 mL each) to neutrality. Then, ddH_2O (30 mL) was added, and the maghemite NPs suspension was set aside for a minimum of 1.5 h at ambient temperature for aging, before any further use.

A solution of CAN (500.0 mg, 0.912 mmol) in acetone (6.0 mL) was added to the decanted magnetite NPs, followed by the addition of degassed purified water (18 mL). The resulting mixture was ultrasonicated for 30 min under nitrogen using a high-power sonicator, then transferred into 50 mL Amicon® Ultra-15 centrifugal filter tubes (100KD, Millipore, Cork, Ireland). The contents were washed with three portions of ddH_2O (10 mL each), and centrifuged at 4000 rpm for 10 min at 18 °C each time. The washed nanocomposite was dispersed in

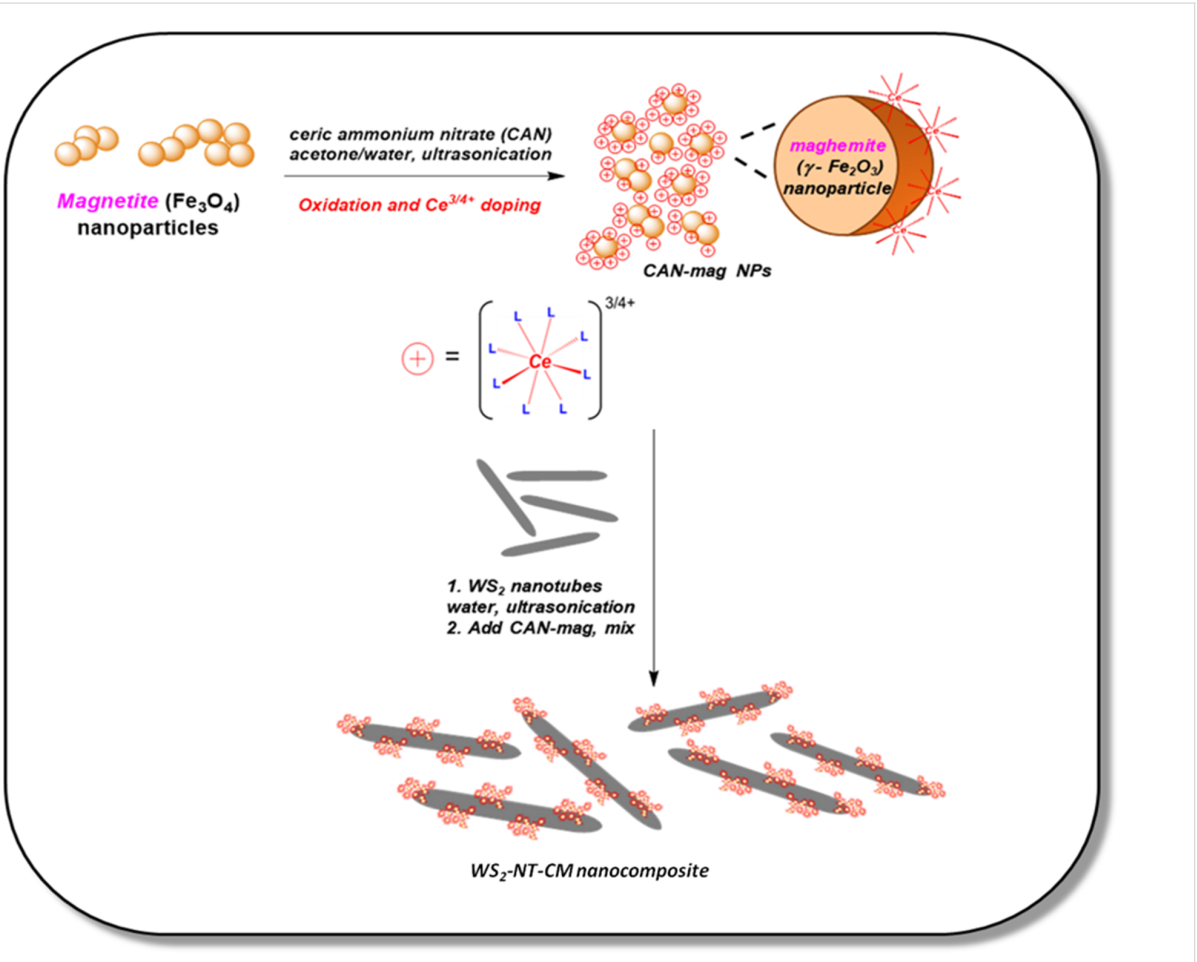

Figure 1: Schematic description for WS_2-NT-CM nanocomposite preparation.

ddH_2O (25 mL). The iron concentration in the dispersion was determined by the inductively coupled plasma (ICP) method to be 2.7 mg/mL.

Preparation of WS_2-NT-CM nanocomposite

WS_2-NTs (15 mg, NanoMaterials Ltd., Yavne, Israel; Lot number: TWPO-MA018) were dispersed in ddH_2O (15 mL) using an ultrasonic probe (set to reach 3.7 KJ, with 20% amplitude) for 7 min at room temperature. Then, the aqueous CAN-mag dispersion (550 µL) was added (this volume gives a 1:10 weight ratio between the iron and the WS_2-INTs). The mixture was shaken for 24 h at ambient temperature. WS_2-NT-CM was separated from the solution using a 0.5 T magnet, washed with three portions of ddH_2O (20 mL each, no centrifugation), and dried by using a lyophilizer.

Preparation of polymer-functionalized WS_2-NT-CM nanocomposites

WS_2-NT-CM (20 mg) was dispersed in ddH_2O (75 mL) using an ultrasonic bath. Then, polyethylenimine (11.5 mg, branched PEI, $M_w \approx 25000$, Sigma-Aldrich, St. Louis, MO, US) dissolved in ddH_2O (1 mL) was added. The mixture was shaken at 15 °C for 48 h (220 RPM). The WS_2-NT-CM-PEI was washed with 3 portions ddH_2O (50 mL each, 5000 RPM, 5 °C, 10 min) and dried by using a lyophilizer. Alternatively, polyacrylic acid (25 mg, PAA, sodium salt, $M_w \approx 8000$, 45% aq. Sol., Sigma-Aldrich, St. Louis, MO, US) dissolved in ddH_2O (1 mL) was added, and the mixture was shaken at 10 °C for 72 h.

Characterizations

ATR-FTIR spectra were obtained on a Nicolet iS5 FT-IR spectrometer (Thermo Scientific, Waltham, MA, US) equipped with an iD5 ATR accessory featuring a laminated diamond crystal. Samples were analyzed without further preparation. The data processing was performed using OMNIC 9 spectra software (Thermo Scientific, Waltham, MA, US).

Thermogravimetric analysis (TGA) was performed by employing a TGA/DSC1 analyzer (Mettler-Toledo, Greifensee, Switzerland). All thermograms were recorded in a nitrogen (50 mL/min) environment at a heating rate of 10 °C·min^{-1} over the temperature range of 30–800 °C. Weight change and heat flow were measured simultaneously during the analysis. The results were processed using STARe evaluation software (Mettler-Toledo, Greifensee, Switzerland).

Transmission electron microscopy (TEM) images were acquired by a Tecnai Spirit Bio-Twin microscope (FEI, Hillsboro, OR, US) equipped with a 1k × 1k CCD camera (Gatan, Pleasanton, CA, US). Samples for TEM analysis were dispersed in water. A drop of the dispersion was placed on a formvar/carbon film on a 400-mesh copper TEM grid (FCF400-Cu, Electron Microscopy Sciences, Hatfield, PA, US) and then dried at ambient temperature for 24 h.

High-resolution transmission electron microscopy (HRTEM) images were acquired using a high-resolution transmission electron microscope (JEM 2100, JEOL Inc., Peabody, MA, US) equipped with a 4k × 4k CCD camera (Gatan, Pleasanton, CA, US). Samples were prepared using the same procedure as for TEM analysis.

High-resolution scanning electron microscopy (HRSEM) images were acquired using a Magellan 400L high-resolution scanning electron microscope (FEI). Samples for HRSEM were prepared by placing a few drops of the aqueous dispersion of the dried sample on a square piece of a clean silicon wafer and drying overnight at ambient temperature.

Zeta potential measurements were performed using a Zetasizer Nano-ZS device (Malvern Instruments Ltd., Worcestershire, UK). Samples for zeta potential measurements were dispersed in water (ca. 0.5 mg/mL).

Inductively coupled plasma (ICP) was used to determine the concentration of cerium and iron (Ultima-2 instrument, Horiba [Jobin-Yvon division], Kyoto, Japan). For cerium analysis, lyophilized nanocomposite sample (2–5 mg) was dissolved in concentrated hydrochloric acid (350 µL, DaeJung, Busan, Korea), diluted to 10 mL with dd water, and set aside overnight for decomposition. The solution was then filtered through a 0.22 µm PTFE syringe filter (Millipore, Darmstadt, Germany). For iron analysis, 1 mL of the filtered solution was diluted to 10 mL with dd water.

Superconducting quantum interference device (SQUID) measurements were performed (MPMS-5XL magnetometer, Quantum Design, San Diego, CA, US). For analysis, dried samples were placed in a plastic capsule. The measurements were run at a temperature of 100 K.

Photothermal therapy activity

For photothermal therapy experiments, we tested two different human cancer cells – HeLa (cervical cancer) and MCF7 (breast cancer). The cells were cultured on 24-well plates. When the cells reached 80% confluence, freshly prepared aqueous dispersions of WS_2-NT or WS_2-NT-CM (45 µL, 1 mg/mL) were added to two of the plates, and a third plate, with no additives, was used for control. After 10 min of incubation, the cells were washed three times with PBS buffer and a fresh DMEM medium was added. For each condition, four representative frames were imaged under a Zeiss LSM7 inverted two-photon micro-

scope at 10× magnification in phase-contrast. Next, a square region of 157 µm × 157 µm in the middle of each frame was irradiated with a 700 nm laser (Chameleon Vision II) at 123 mW for 1 min. The same frames were then imaged again. A dye exclusion test of cell viability was performed, using Trypan Blue for staining. A mixture of 0.5 wt % trypan blue solution and PBS (1:1 v/v) was added to all wells after the laser irradiation. After 5 min, the cells were washed with PBS buffer and the same frames were imaged.

Results and Discussion

This section will include all the chemical and biological results. The preparation procedures of the composites included sonication steps that might cause massive breakage or exfoliation of the nanotubes. For this reason, we aimed for preparation conditions that would allow composite formation without damaging the nanotubes. Electron microscopy images (Figure 2) show that WS_2 nanotubes maintained their general shape after conjugation of CAN-mag nanoparticles, and later on, of the polymers. At the same time, attachment of CAN-mag to the nanotubes is clearly visible (Figure 2d–f). Rather than conformally coating the nanotubes, CAN-mag nanoparticles seem to attach to the surface of the nanotubes in small clusters, appearing dark in TEM, and bright in SEM. A possible reason for this is that CAN-mag composite has a strong positive surface charge (see zeta potential results below in Figure 7), causing electrostatic

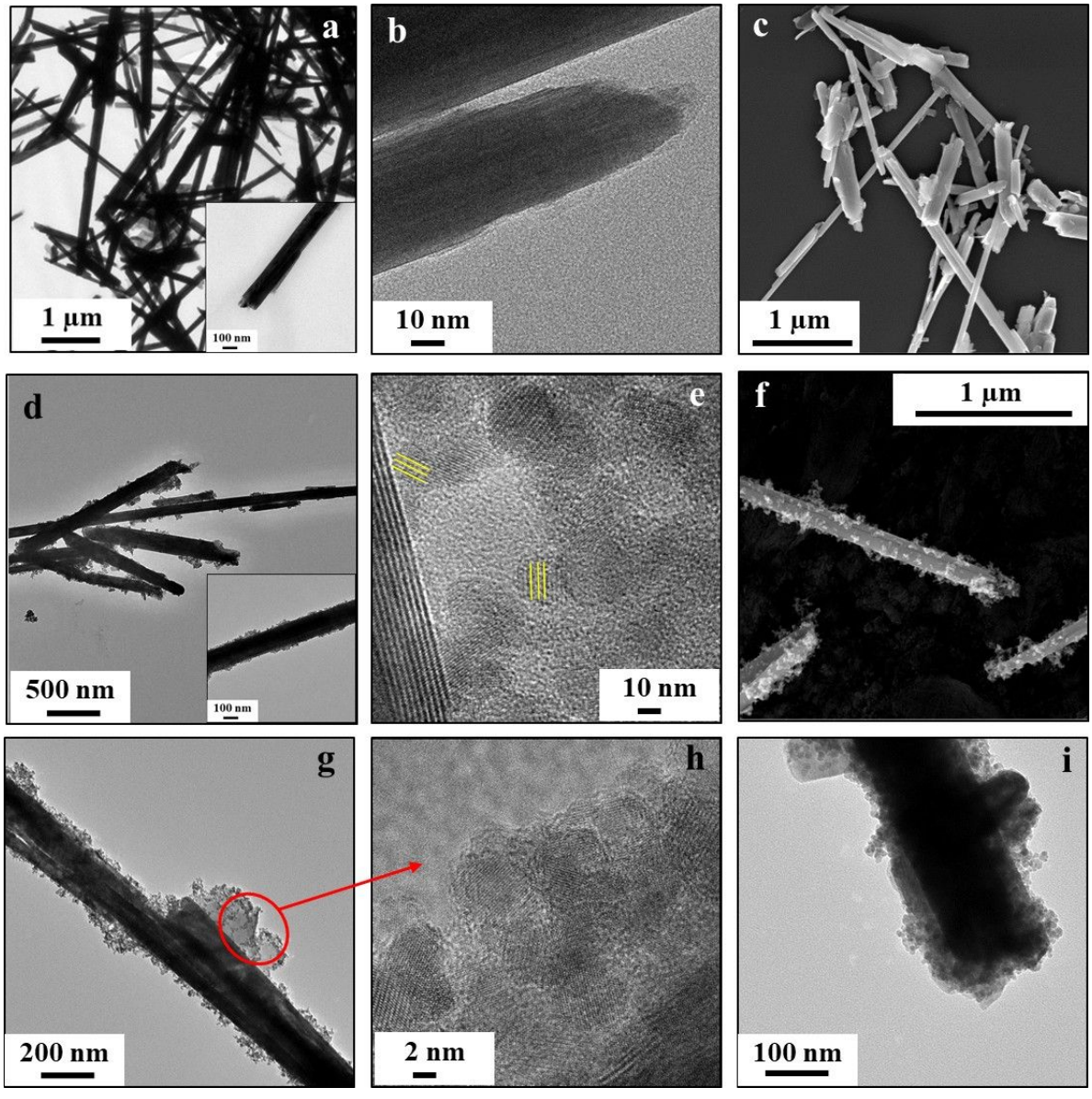

Figure 2: TEM, HRTEM, and SEM images of (a–c) WS_2-NT; (d–f) WS_2-NT-CM; (g,h) WS_2-NT-CM-PEI and (i) WS_2-NT-CM-PAA.

repulsion forces that prevent a denser coverage. Another point that the electron microscope images show (see Figure 2a and Figure 2c; cf. Figure 2d and Figure 2f), is that WS_2-NT-CM is significantly less aggregated in aqueous dispersion compared to WS_2-NT. Here, too, the electrostatic repulsion provided by CAN-mag is probably the reason. In the HRTEM image of WS_2-NT-CM (Figure 2e), the crystalline nanoparticles of maghemite are easily observed, including visible lattice fringes (marked in yellow). TEM images of WS_2-NT-CM-PEI (Figure 2g) and WS_2-NT-CM-PAA (Figure 2i) show that the dark CAN-mag composite is surrounded by a lighter substance, namely the organic polymer (PEI or PAA). A closer look by HRTEM into WS_2-NT-CM-PEI (Figure 2h) shows that the wavy-looking matrix surrounding the crystalline maghemite is amorphous.

Table 1 shows the results of ICP analysis of CAN-mag nanoparticles and WS_2-NT-CM composite. The ratios between iron and cerium are very close when comparing the nanoparticles and the composites. This means that there was almost no detachment of CAN during the composite preparation, which is a possibility when using probe sonication. The numbers show a small quantity of cerium in CAN-mag, which is even smaller within the composite, yet the presence of cerium still allows coordinative attachment of polymers to the composite.

Figure 3 shows the FTIR absorbance spectra of WS_2-NT and its composites. The absorption of the WS_2-NTs was so weak that we are not sure that anything can be learned from such absorption. In the spectrum of WS_2-NT-CM (and of its two composites), the strong peak at 570 cm^{-1} is characteristic of iron oxides, and represents the stretching vibration of Fe–O bond [53,54]. The peaks at 1640 cm^{-1} and 3400 cm^{-1} originate from interlayer water: the former is assigned H–O–H bending vibrations, and the latter to O–H stretching vibrations [53,54]. The peak at around 820 cm^{-1} might be assigned to Ce–O stretching vibrations [55]. In the spectrum of WS_2-NT-CM-PEI, the peaks at 1050 cm^{-1} and 1640 cm^{-1} are a bit more accentuated compared to the WS_2-NT-CM spectrum. These bands may be assigned to the C–N stretching vibrations and N–H stretching vibrations, respectively, of the PEI chains. The peak at 2350 cm^{-1} is typical to CO_2, most likely captured by PEI [56]. In the spectrum of WS_2-NT-CM-PAA, the peaks originating from the polyacrylic acid are dominant. The peak at 800 cm^{-1} is assigned to C–H bending vibrations in the PAA chain. The peaks in the range of 1000–1260 cm^{-1} may be assigned to C–O stretching vibrations. The peaks at around 1400 cm^{-1} and 1540 cm^{-1} are assigned to symmetric and asymmetric stretching vibrations of carboxylate $[O–C–O]^-$ ions. The positions of the peaks indicate attachment of the polymer ligand to the surface of the maghemite nanoparticles through carboxylate groups. In the species –COO–Fe, these are shifted to slightly higher energies compared to non-attached carboxylates [57,58]. The peaks at 2850 cm^{-1}, 2920 cm^{-1}, and 2960 cm^{-1} are assigned to C–H stretching vibrations in the PAA chain. The broad peak at 3400 cm^{-1} is stronger compared to the other spectra. PAA is a very hygroscopic polymer, and the absorbed water contributes to the intensity of the OH band.

Figure 4 shows the thermogravimetric analysis (conducted under nitrogen) results for WS_2-NT and its composites. WS_2-NTs (blue line) show almost no weight loss, as expected under these conditions. The nanotubes with CAN-mag functionalization (red line) show a small and gradual weight loss, at a relatively low temperature range, assigned to the organic ammonium and nitrate components of CAN (cerium and iron oxide are not expected to be affected under nitrogen). WS_2-NT-CM-PAA (yellow line) starts with a relatively steep weight loss step, most probably due to adsorbed water molecules (as mentioned, PAA is highly hygroscopic). A more significant weight loss reaches its plateau around 500 °C, typical for PAA [59,60]. For WS_2-NT-CM-PEI (green line), there seem to be two sequential weight-loss steps overlapping at approximately 400 °C. The first and major one is typical to PEI [61,62], and the second one, at higher temperatures, originates from a mixed PEI-organic matter polyCOOH/$[Ce^{3/4+}L_n]$ complex adlayer phase [63].

Figure 5 and Figure 6 demonstrate the application of WS_2-NT-CM composite as a photothermal therapy agent. Figure 5 shows optical microscope images taken from a cell viability test of HeLa cells incubated for 10 min with WS_2-NTs (d–f), with WS_2-NT-CM (g–i), and without any addition (a–c) for reference. Figure 6 shows the percentage of alive, dead, and de-

Table 1: ICP results for CAN-maghemite nanoparticles before and after conjugation to WS_2 nanotubes. CAN/maghemite molar ratio calculation is based on two moles of iron in each mole of maghemite.

	element in composite [wt %]		Fe/Ce	mag/CAN
	iron	cerium	weight ratio	molar ratio
CAN-mag NPs	71.1 ± 0.1	1.84 ± 0.01	39	48
WS_2-NT-CM	8.6 ± 0.1	0.21 ± 0.01	41	51

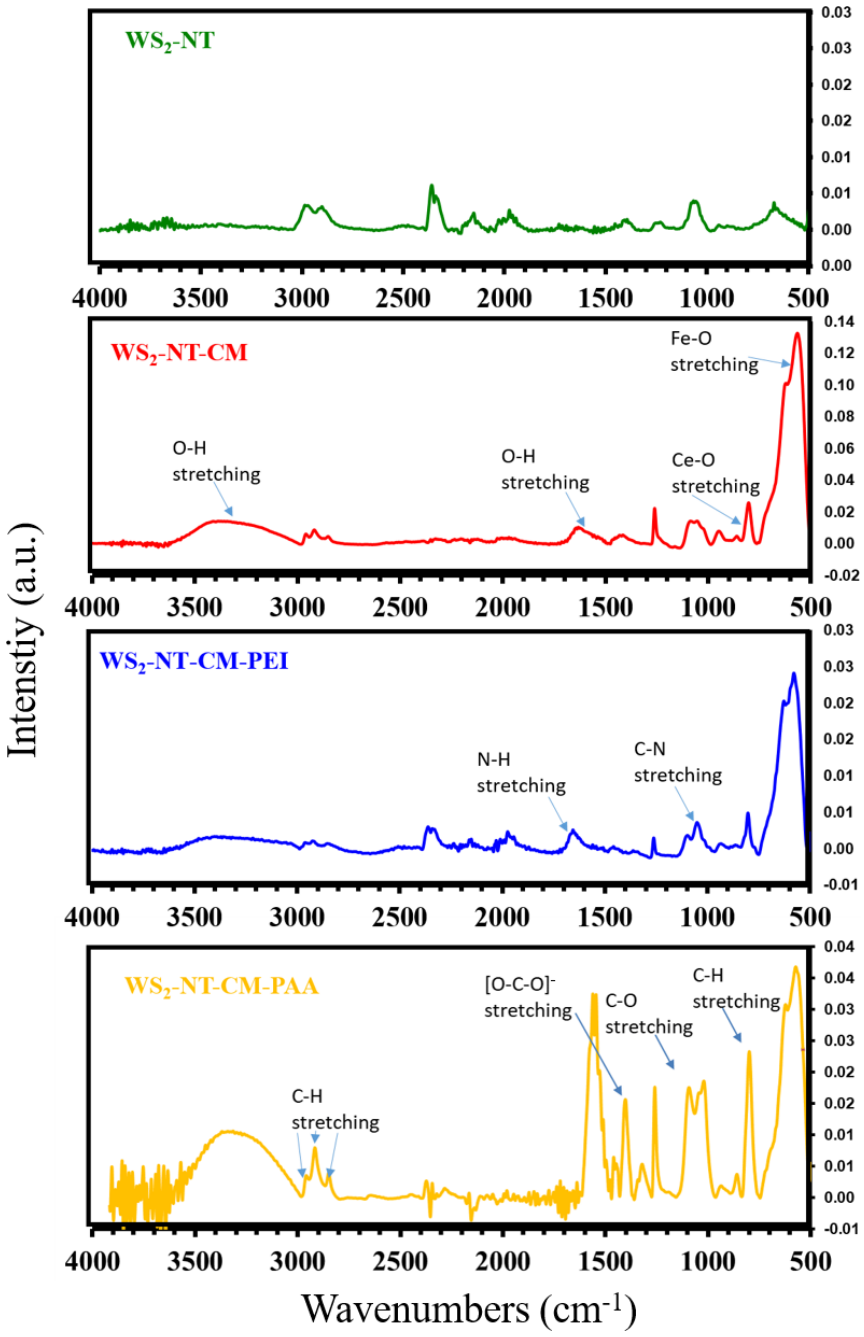

Figure 3: FTIR absorbance spectra of WS_2-NT and its nanocomposite samples.

tached HeLa (A) cells and MCF7 (B) cells after incubation and irradiation (percentages are averaged from three repetitions for each viability test; for the images of the viability test with MCF7 cells, see Supporting Information File 1). The incubated cells were irradiated with a 700 nm NIR laser for 1 min. The irradiated area in each image within Figure 5 is represented by a white square. In the left column are the incubated cells before irradiation, in the middle column after irradiation, and in the right column after irradiation and application of trypan blue. Notice that the entire area in the images was stained, but only the squared area was irradiated. Only dead cells are dyed by trypan blue, and in the images they appear gray and blurry due to the collapse of the cell membrane and the penetration of the dye. The images show cell death only in the squared area, for only the cells incubated with the nanomaterials. This means that the cell death was not caused by irradiation alone or by the addition of the nanomaterials alone, but by the combination of both, proving a photothermal activity. Looking at Figure 5f and

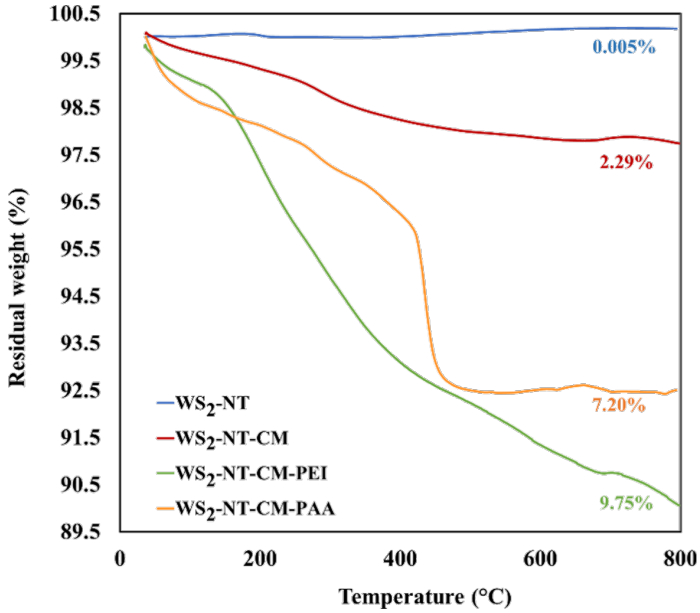

Figure 4: TGA analysis data of WS_2-NTs and its nanocomposites. The analysis was conducted under nitrogen. Weight loss percentages appear near each thermogram.

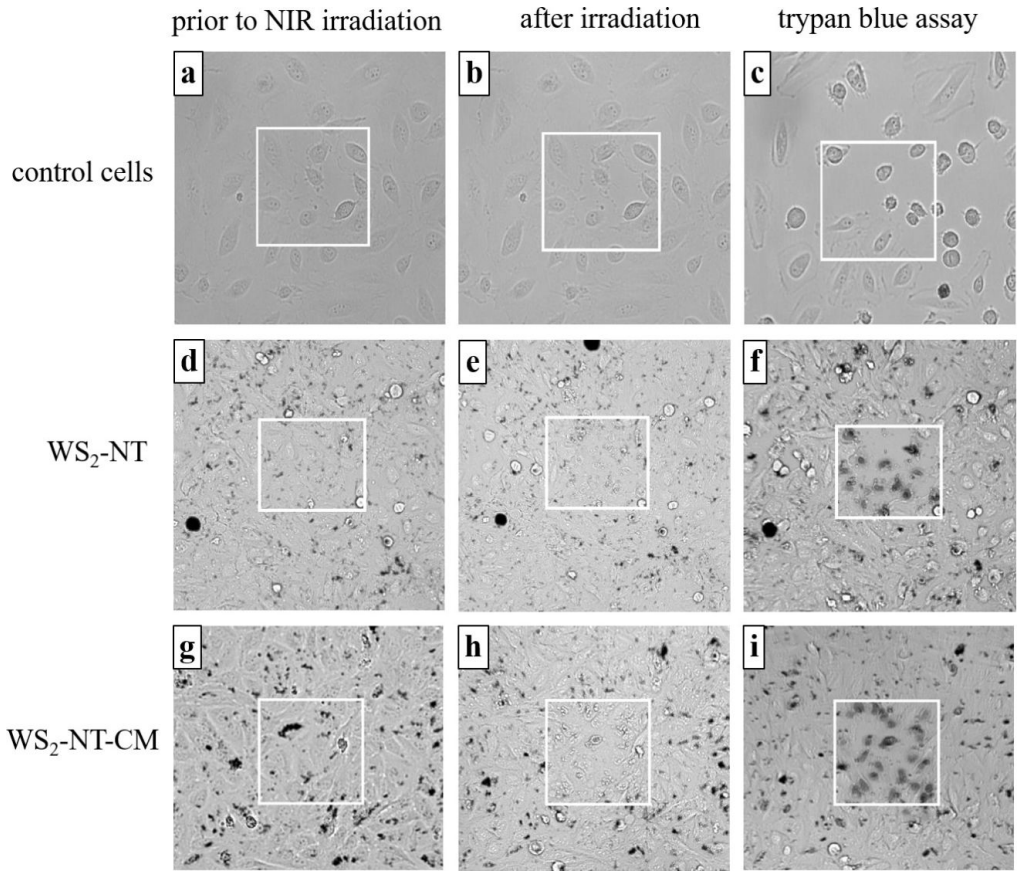

Figure 5: Phase-contrast microscopy images of HeLa cells. The white squares indicate 157 µm × 157 µm areas irradiated with an NIR (700 nm) laser. Left column: cells prior to NIR irradiation; middle column: after irradiation for 1 minute; right column: after irradiation for 1 minute and application of trypan blue assay: (a–c) control (untreated) cells; (d–f) cells pre-incubated with WS_2-NT; (g–i) cells pre-incubated with WS_2-NT-CM.

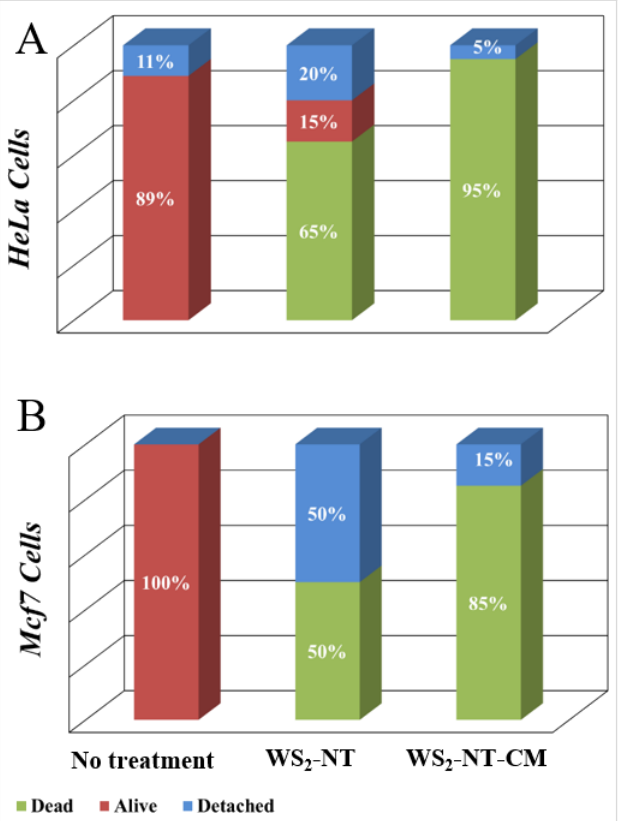

Figure 6: PTT results histograms for WS_2 nanotubes and WS_2-NT-CM nanocomposite, tested with HeLa(A) and MCF7(B) cancer cells. Percentages of dead, alive and detached cells are shown for each test.

Figure 5i, cell death is observed both when incubated with bare WS_2-NTs and with WS_2-NT-CM. However, cell death is more accentuated after addition of the latter (Figure 5i). This is also expressed in higher percentages of dead HeLa cells. For MCF7 cells, the cell viability results are less conclusive compared to HeLa cell results (see Supporting Information File 1). While a comparison between Figure S2f and Figure S2i shows more dead cells in the latter, half of the cells tested with WS_2-NTs were detached during the viability test. Those cells were most likely dead as well, meaning that the advantage of WS_2-NT-CM over WS_2-NT in the elimination of MCF7 cells is not distinct.

There is another advantage of the composites over their components alone. WS_2-NTs tend to aggregate, and the addition of CAN-mag reduces aggregation. Aqueous dispersions of the functionalized nanotubes stay stable for hours, while bare nanotubes in water sink almost instantly. Also, when comparing the images in the bottom and middle rows for both cell types, we see that the WS_2-NT-CM composite tends to preferably accumulate in and near the cells, while the bare WS_2-NTs are distributed all around in the imaged area, at times in large aggregates. For targeted PTT purposes, the use of bare nanotubes is not practical, because they will aggregate on the walls of the blood vessels and not reach the tumor area. The use of CAN-mag alone, on the other hand, is not good either, as it will undergo filtration by the liver [64]. So overall, there is a double advantage of WS_2-NTs functionalized with CAN-Mag, namely increased cancerous-cell death and better targeting.

Figure 7 shows zeta potential averages and distribution curves for WS_2-NTs, CAN-mag, and their composites. The values for WS_2-NT and CAN-mag are consistent with previous works [52,65,66]. For each composite, the zeta values reflect the contributions of the components. The presence of the positively charged CAN-mag on the surface of WS_2-NTs shifts their value from −21.4 mV to −9.90 mV. The fact that the zeta potential

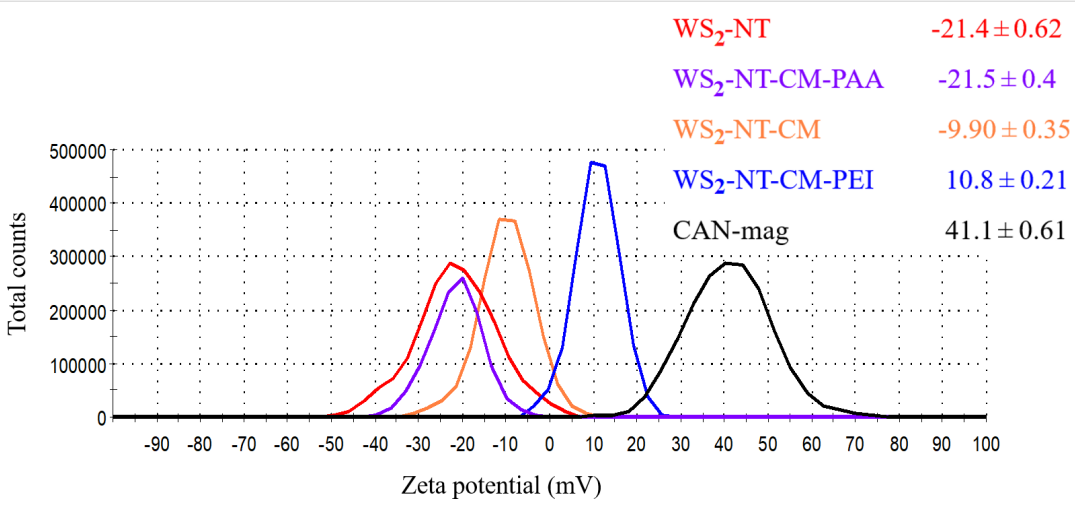

Figure 7: Zeta potential values and distribution curves for samples WS_2-NT-CM-PEI (blue), WS_2-NT (red), WS_2-NT-CM (Orange), WS_2-NT-CM-PAA (purple), and CAN-mag (Black). For each sample, three measurements were taken, and the values given include the average result and the standard deviation.

value of WS_2-NT-CM is not positive is another indication of the inhomogeneity of the coating, as seen in the TEM and SEM images (Figure 2). The addition of polymers to WS_2-NT-CM has a stronger influence on the zeta potential of the resulting composites. The value shifts more towards the zeta potential of the polymer, because the polymer constitutes the surface. PEI is highly positively charged in water because of the many protonated amine groups, and the WS_2-NT-CM-PEI composite becomes positively charged. PAA is negatively charged (carboxylate groups), shifting the composite from −9.90 mV to −21.4 mV.

Figure 8 shows the magnetization spectra of WS_2-NT, CAN-mag, and WS_2-NT-CM nanocomposites, all taken at a temperature of 10 K. For WS_2-NTs (red spectrum, inset image), the external magnetic field induces a very weak magnetic field in the opposite direction. This means that WS2-NTs are diamagnetic. The CAN-mag curve (green) demonstrates superparamagnetic behavior, where the magnetization increases with the strength of the magnetic field until it approaches saturation, and there is no hysteresis loop. Superparamagnetism is typical for iron-oxide nanoparticles [67]. The nanocomposite WS_2-NT-CM (blue curve) maintains superparamagnetism, with a saturation value of about ±13 emu/g, which is a sixth of the saturation value for CAN-mag alone. The latter reaches a saturation value of ±78 emu/g, which is consistent with a previous publication [52]. These results are understandable when evaluating the part of CAN-mag in the WS_2-NT-CM composite. A calculation based on the weight percentages of iron and cerium in the nanocomposite from ICP (Table 1), and the molecular weights of CAN and maghemite, results in 13.2% weight of CAN-mag of the whole composite weight. Taking into account this percentage and the fact that diamagnetism is a weak effect that is always dominated by ferromagnetism (hence, by superparamagnetism), the curve shape and saturation values for WS_2-NT-CM are to be expected.

When bringing dispersions of CAN-mag nanoparticles and WS_2-NT-CM close to a magnet, however, it is only the latter that is visibly attracted. The video (Supporting Information File 2) shows the liquid of a WS_2-NT-CM dispersion gradually clearing up when brought near a magnet, and the composite particles moving towards the magnet. Despite the fact that the magnetization intensity of CAN-mag nanoparticles is higher compared to WS_2-NT-CM, only the latter is drawn to the magnet, and very slowly, over the course of days. The reason is that CAN-mag nanoparticles are more stable in water than WS_2-NT-CM (see also the zeta potential results), meaning there are strong electrostatic interactions successfully competing with the magnetic force.

Conclusion

To summarize, we prepared a nanocomposite of WS_2-NTs functionalized with CAN-maghemite nanoparticles. The preparation procedures are facile and make use of readily available reagents and equipment. Electron microscopy, FTIR, zeta

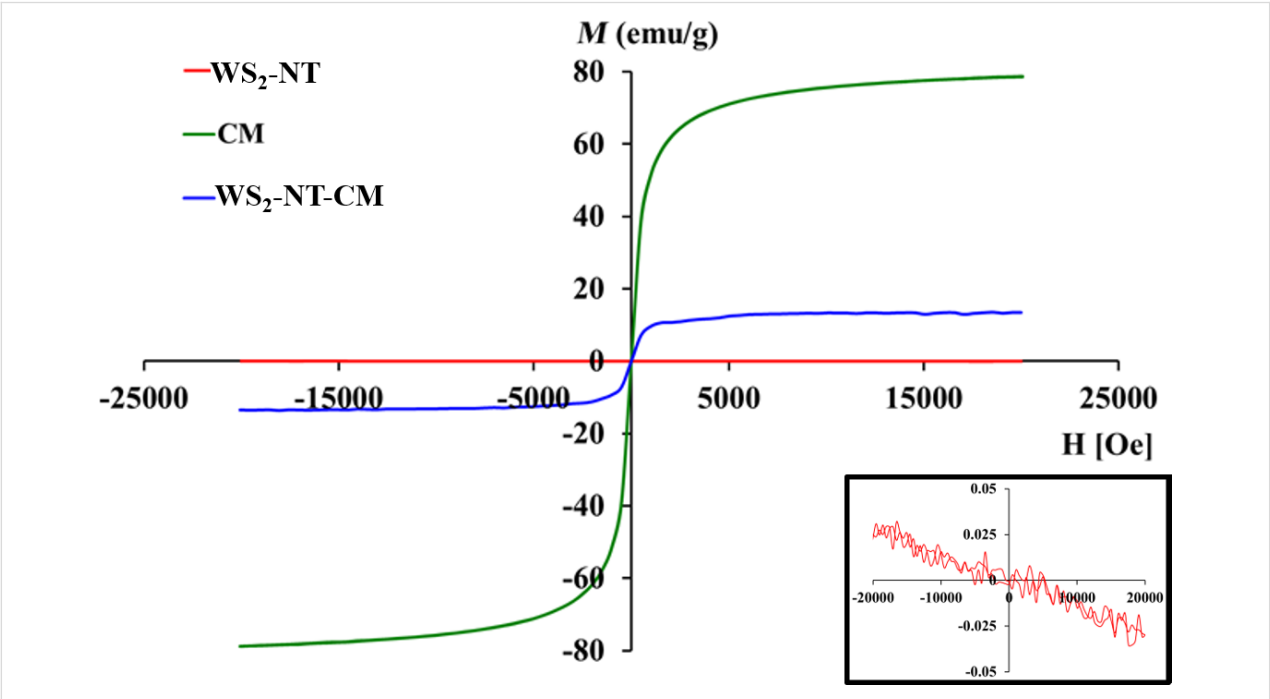

Figure 8: Magnetization spectra of WS_2-NTs, CAN-mag, and WS_2-NT-CM, taken at 10 K. Inset is the magnetization spectra of WS_2-NTs.

potential, TGA, and ICP analyses demonstrated the attachment of CAN-mag nanoparticles to the nanotubes. CAN-mag attachment around the nanotubes was not conformal, and in small percentages. Yet, the composite maintained the magnetic character of the nanoparticles. Moreover, the functionalized nanotubes proved to have a higher activity as PTT agents compared to bare WS_2-NTs in in vitro tests done with HeLa and MCF7 cancer cells.

In addition, functionalization with CAN-mag enabled the attachment of PEI and PAA onto the nanocomposite, as shown by TEM, FTIR, TGA, and zeta potential. The ability for further attachment of polymers and other molecules can be utilized to enhance the therapeutic activity. One way is the attachment of a second PTT agent, such as a polypyrrole, and irradiation in two wavelengths. Another way is the attachment of a photodynamic therapy (PDT) agent. In this preliminary work, we used WS_2-NTs with a wide size distribution range. A very important step for future research, required prior to in vivo trials, is to use nanotubes in a narrower size range, suitable for targeted PTT.

Supporting Information

Supporting Information File 1

Selected FTIR characterisation data and viability tests using MCF7 cells.
[https://www.beilstein-journals.org/bjnano/content/supplementary/2190-4286-10-81-S1.pdf]

Supporting Information File 2

A video of a WS_2-NT-CM dispersion brought near a magnet.
[https://www.beilstein-journals.org/bjnano/content/supplementary/2190-4286-10-81-S2.mov]

ORCID® iDs

Hagit Sade - https://orcid.org/0000-0001-6128-4746

References

1. Tenne, R.; Margulis, L.; Genut, M.; Hodes, G. *Nature* **1992,** *360,* 444–446. doi:10.1038/360444a0
2. Kaplan-Ashiri, I.; Cohen, S. R.; Gartsman, K.; Ivanovskaya, V.; Heine, T.; Seifert, G.; Wiesel, I.; Wagner, H. D.; Tenne, R. *Proc. Natl. Acad. Sci. U. S. A.* **2006,** *103,* 523–528. doi:10.1073/pnas.0505640103
3. Kaplan-Ashiri, I.; Cohen, S. R.; Gartsman, K.; Rosentsveig, R.; Seifert, G.; Tenne, R. *J. Mater. Res.* **2004,** *19,* 454–459. doi:10.1557/jmr.2004.19.2.454
4. Kaplan-Ashiri, I.; Tenne, R. *J. Cluster Sci.* **2007,** *18,* 549–563. doi:10.1007/s10876-007-0118-9
5. Joly-Pottuz, L.; Martin, J. M.; Dassenoy, F.; Belin, M.; Montagnac, G.; Reynard, B.; Fleischer, N. *J. Appl. Phys.* **2006,** *99,* 023524. doi:10.1063/1.2165404
6. Tevet, O.; Von-Huth, P.; Popovitz-Biro, R.; Rosentsveig, R.; Wagner, H. D.; Tenne, R. *Proc. Natl. Acad. Sci. U. S. A.* **2011,** *108,* 19901–19906. doi:10.1073/pnas.1106553108
7. Lahouij, I.; Dassenoy, F.; Vacher, B.; Martin, J.-M. *Tribol. Lett.* **2012,** *45,* 131–141. doi:10.1007/s11249-011-9873-8
8. Kaplan-Ashiri, I.; Tenne, R. *JOM* **2016,** *68,* 151–167. doi:10.1007/s11837-015-1659-2
9. Naffakh, M.; Martín, Z.; Fanegas, N.; Marco, C.; Gómez, M. A.; Jiménez, I. *J. Polym. Sci., Part B: Polym. Phys.* **2007,** *45,* 2309–2321. doi:10.1002/polb.21231
10. Naffakh, M.; Díez-Pascual, A. M.; Marco, C.; Ellis, G. J.; Gómez-Fatou, M. A. *Prog. Polym. Sci.* **2013,** *38,* 1163–1231. doi:10.1016/j.progpolymsci.2013.04.001
11. Flores, A.; Naffakh, M.; Díez-Pascual, A. M.; Ania, F.; Gómez-Fatou, M. A. *J. Phys. Chem. C* **2013,** *117,* 20936–20943. doi:10.1021/jp406513y
12. Díez-Pascual, A. M.; Naffakh, M.; Marco, C.; Ellis, G. *J. Phys. Chem. B* **2012,** *116,* 7959–7969. doi:10.1021/jp3035314
13. Díez-Pascual, A. M.; Naffakh, M.; Marco, C.; Ellis, G. *Composites, Part A* **2012,** *43,* 603–612. doi:10.1016/j.compositesa.2011.12.026
14. Naffakh, M.; Marco, C.; Gómez, M. A.; Jiménez, I. *J. Phys. Chem. B* **2008,** *112,* 14819–14828. doi:10.1021/jp8063245
15. Naffakh, M.; Díez-Pascual, A. M.; Marco, C.; Gómez, M. A.; Jiménez, I. *J. Phys. Chem. B* **2010,** *114,* 11444–11453. doi:10.1021/jp105340g
16. Zhang, W.; Ge, S.; Wang, Y.; Rafailovich, M. H.; Dhez, O.; Winesett, D. A.; Ade, H.; Shafi, K. V. P. M.; Ulman, A.; Popovitz-Biro, R.; Tenne, R.; Sokolov, J. *Polymer* **2003,** *44,* 2109–2115. doi:10.1016/s0032-3861(03)00053-3
17. Reddy, C. S.; Zak, A.; Zussman, E. *J. Mater. Chem.* **2011,** *21,* 16086–16093. doi:10.1039/c1jm12700d
18. Tsabari, H. *Final report. Batch No. HP6, Harlan Biotech, Isr.* 2005.
19. Moore, G. E. *Acute Inhalation Toxicity Study in Rats – Limit Test. Product Safety Laboratories, study no.18503;* Dayton, NJ, U.S.A, 2006.
20. Haist, I. Project no. 052052, BSL, 2005.
21. Nachshon, B. In *Batch No. 200910-2*; Harlan Biotech, Israel, 2011.
22. Nachshon, B. In *Batch No. 241111-1*; Harlan Biotech, Israel, 2012.
23. Teo, W. Z.; Chng, E. L. K.; Sofer, Z.; Pumera, M. *Chem. – Eur. J.* **2014,** *20,* 9627–9632. doi:10.1002/chem.201402680
24. Wu, H.; Yang, R.; Song, B.; Han, Q.; Li, J.; Zhang, Y.; Fang, Y.; Tenne, R.; Wang, C. *ACS Nano* **2011,** *5,* 1276–1281. doi:10.1021/nn102941b
25. Place, E. S.; George, J. H.; Williams, C. K.; Stevens, M. M. *Chem. Soc. Rev.* **2009,** *38,* 1139–1151. doi:10.1039/b811392k
26. Liu, X.; Ma, P. X. *Ann. Biomed. Eng.* **2004,** *32,* 477–486. doi:10.1023/b:abme.0000017544.36001.8e
27. Rezwan, K.; Chen, Q. Z.; Blaker, J. J.; Boccaccini, A. R. *Biomaterials* **2006,** *27,* 3413–3431. doi:10.1016/j.biomaterials.2006.01.039
28. Lalwani, G.; Henslee, A. M.; Farshid, B.; Parmar, P.; Lin, L.; Qin, Y.-X.; Kasper, F. K.; Mikos, A. G.; Sitharaman, B. *Acta Biomater.* **2013,** *9,* 8365–8373. doi:10.1016/j.actbio.2013.05.018
29. Adini, A. R.; Feldman, Y.; Cohen, S. R.; Rapoport, L.; Moshkovich, A.; Redlich, M.; Moshonov, J.; Shay, B.; Tenne, R. *J. Mater. Res.* **2011,** *26,* 1234–1242. doi:10.1557/jmr.2011.52
30. Katz, A.; Redlich, M.; Rapoport, L.; Wagner, H. D.; Tenne, R. *Tribol. Lett.* **2006,** *21,* 135–139. doi:10.1007/s11249-006-9029-4

31. Redlich, M.; Katz, A.; Rapoport, L.; Wagner, H. D.; Feldman, Y.; Tenne, R. *Dent. Mater.* **2008,** *24,* 1640–1646. doi:10.1016/j.dental.2008.03.030
32. Naveh, G. R. S.; Redlich, M.; Katz, A.; Adini, A. R.; Gorodnev, A.; Rapoport, L.; Moshkovich, A.; Cohen, S. R.; Rosentsveig, R.; Moshonov, J.; Shay, B.; Tenne, R. *Int. J. Nano Biomater.* **2010,** *3,* 140–152. doi:10.1504/ijnbm.2010.037802
33. de Melo-Diogo, D.; Pais-Silva, C.; Dias, D. R.; Moreira, A. F.; Correia, I. J. *Adv. Healthcare Mater.* **2017,** *6,* 1700073. doi:10.1002/adhm.201700073
34. Cheng, L.; Yang, K.; Chen, Q.; Liu, Z. *ACS Nano* **2012,** *6,* 5605–5613. doi:10.1021/nn301539m
35. Jaemoon, Y.; Jihye, C.; Doyeon, B.; Eunjung, K.; Eun-Kyung, L.; Huiyul, P.; Jin-Suck, S.; Kwangyeol, L.; Kyung-Hwa, Y.; Eun-Kyung, K.; Yong-Min, H.; Seungjoo, H. *Angew. Chem., Int. Ed.* **2011,** *50,* 441–444. doi:10.1002/anie.201005075
36. Yang, K.; Zhang, S.; Zhang, G.; Sun, X.; Lee, S.-T.; Liu, Z. *Nano Lett.* **2010,** *10,* 3318–3323. doi:10.1021/nl100996u
37. Liu, X.; Tao, H.; Yang, K.; Zhang, S.; Lee, S.-T.; Liu, Z. *Biomaterials* **2011,** *32,* 144–151. doi:10.1016/j.biomaterials.2010.08.096
38. Xiao, J.-W.; Fan, S.-X.; Wang, F.; Sun, L.-D.; Zheng, X.-Y.; Yan, C.-H. *Nanoscale* **2014,** *6,* 4345–4351. doi:10.1039/c3nr06843a
39. Haibao, P.; Shiwei, T.; Ye, T.; Rui, Z.; Lei, Z.; Wuli, Y. *Part. Part. Syst. Charact.* **2016,** *33,* 332–340. doi:10.1002/ppsc.201600071
40. Yuwen, L.; Zhou, J.; Zhang, Y.; Zhang, Q.; Shan, J.; Luo, Z.; Weng, L.; Teng, Z.; Wang, L. *Nanoscale* **2016,** *8,* 2720–2726. doi:10.1039/c5nr08166a
41. Lei, Z.; Zhu, W.; Xu, S.; Ding, J.; Wan, J.; Wu, P. *ACS Appl. Mater. Interfaces* **2016,** *8,* 20900–20908. doi:10.1021/acsami.6b07326
42. Sharker, S. M.; Kim, S. M.; Lee, J. E.; Choi, K. H.; Shin, G.; Lee, S.; Lee, K. D.; Jeong, J. H.; Lee, H.; Park, S. Y. *J. Controlled Release* **2015,** *217,* 211–220. doi:10.1016/j.jconrel.2015.09.010
43. Bao, T.; Yin, W.; Zheng, X.; Zhang, X.; Yu, J.; Dong, X.; Yong, Y.; Gao, F.; Yan, L.; Gu, Z.; Zhao, Y. *Biomaterials* **2016,** *76,* 11–24. doi:10.1016/j.biomaterials.2015.10.048
44. Karakoti, A. S.; Singh, S.; Kumar, A.; Malinska, M.; Kuchibhatla, S. V. N. T.; Wozniak, K.; Self, W. T.; Seal, S. *J. Am. Chem. Soc.* **2009,** *131,* 14144–14145. doi:10.1021/ja9051087
45. Yu, C.; Guanglin, W.; Chao, L.; Xuan, Y.; Xiaoyan, Z.; Jingjing, L.; Min, G.; Kai, Y.; Liang, C.; Zhuang, L. *Small* **2016,** *12,* 3967–3975. doi:10.1002/smll.201601375
46. Longfei, T.; Shengping, W.; Ke, X.; Tianlong, L.; Ping, L.; Meng, N.; Changhui, F.; Haibo, S.; Jie, Y.; Tengchuang, M.; Xiangling, R.; Hong, L.; Jianping, D.; Jun, R.; Xianwei, M. *Small* **2016,** *12,* 2046–2055. doi:10.1002/smll.201600191
47. Nandi, S.; Bhunia, S. K.; Zeiri, L.; Pour, M.; Nachman, I.; Raichman, D.; Lellouche, J.-P. M.; Jelinek, R. *Chem. – Eur. J.* **2017,** *23,* 963–969. doi:10.1002/chem.201604787
48. Tahir, M. N.; Zink, N.; Eberhardt, M.; Therese, H. A.; Kolb, U.; Theato, P.; Tremel, W. *Angew. Chem., Int. Ed.* **2006,** *45,* 4809–4815. doi:10.1002/anie.200504211
49. Tahir, M. N.; Zink, N.; Eberhardt, M.; Therese, H. A.; Faiss, S.; Janshoff, A.; Kolb, U.; Theato, P.; Tremel, W. *Small* **2007,** *3,* 829–834. doi:10.1002/smll.200600663
50. Tahir, M. N.; Yella, A.; Sahoo, J. K.; Natalio, F.; Kolb, U.; Jochum, F.; Theato, P.; Tremel, W. *Isr. J. Chem.* **2010,** *50,* 500–505. doi:10.1002/ijch.201000053
51. Sahoo, J. K.; Tahir, M. N.; Yella, A.; Branscheid, R.; Kolb, U.; Tremel, W. *Langmuir* **2011,** *27,* 385–391. doi:10.1021/la103687y
52. Israel, L. L.; Lellouche, E.; Kenett, R. S.; Green, O.; Michaeli, S.; Lellouche, J.-P. *J. Mater. Chem. B* **2014,** *2,* 6215–6225. doi:10.1039/c4tb00634h
53. Ismail, R. A.; Sulaiman, G. M.; Abdulrahman, S. A.; Marzoog, T. R. *Mater. Sci. Eng., C* **2015,** *53,* 286–297. doi:10.1016/j.msec.2015.04.047
54. Li, N.; Chen, J.; Shi, Y.-P. *Anal. Chim. Acta* **2017,** *949,* 23–34. doi:10.1016/j.aca.2016.11.016
55. Sharma, A.; Kumar, P. S. *Nano Sci. Nano Technol.* **2012,** *2,* 82–85. doi:10.5923/j.nn.20120203.07
56. Liu, Q.; Shi, J.; Wang, Q.; Tao, M.; He, Y.; Shi, Y. *Ind. Eng. Chem. Res.* **2014,** *53,* 17468–17475. doi:10.1021/ie503118j
57. Majeed, M.; Guo, J.; Yan, W.; Tan, B. *Polymers (Basel, Switz.)* **2016,** *8,* 392. doi:10.3390/polym8110392
58. Rui, Y.-P.; Liang, B.; Hu, F.; Xu, J.; Peng, Y.-F.; Yin, P.-H.; Duan, Y.; Zhang, C.; Gu, H. *RSC Adv.* **2016,** *6,* 22575–22585. doi:10.1039/c6ra00347h
59. Moharram, M. A.; Khafagi, M. G. *J. Appl. Polym. Sci.* **2006,** *102,* 4049–4057. doi:10.1002/app.24367
60. Solhi, L.; Atai, M.; Nodehi, A.; Imani, M.; Ghaemi, A.; Khosravi, K. *Dent. Mater.* **2012,** *28,* 369–377. doi:10.1016/j.dental.2011.11.010
61. Huang, T.; Zhang, L.; Chen, H.; Gao, C. *J. Mater. Chem. A* **2015,** *3,* 19517–19524. doi:10.1039/c5ta04471e
62. Roy, S.; Tang, X.; Das, T.; Zhang, L.; Li, Y.; Ting, S.; Hu, X.; Yue, C. Y. *ACS Appl. Mater. Interfaces* **2015,** *7,* 3142–3151. doi:10.1021/am5074408
63. Lellouche, J.-P.; Michaeli, S.; Liron, L.; Lellouche, E.; Kapilov-Buchman, Y. Magnetic Inorganic Iron-Based Nanoparticles. WO2014147608A1, Sept 29, 2016.
64. Blanco, E.; Shen, H.; Ferrari, M. *Nat. Biotechnol.* **2015,** *33,* 941–951. doi:10.1038/nbt.3330
65. Haviv, A. H.; Grenèche, J.-M.; Lellouche, J.-P. *J. Am. Chem. Soc.* **2010,** *132,* 12519–12521. doi:10.1021/ja103283e
66. Raichman, D.; Strawser, D. A.; Lellouche, J.-P. *Nano Res.* **2015,** *8,* 1454–1463. doi:10.1007/s12274-014-0630-9
67. Teja, A. S.; Koh, P.-Y. *Prog. Cryst. Growth Charact. Mater.* **2009,** *55,* 22–45. doi:10.1016/j.pcrysgrow.2008.08.003

License and Terms

BEILSTEIN JOURNAL OF NANOTECHNOLOGY

Serum type and concentration both affect the protein-corona composition of PLGA nanoparticles

Katrin Partikel[1], Robin Korte[2], Dennis Mulac[1], Hans-Ulrich Humpf[2] and Klaus Langer[*1,§]

Full Research Paper

Open Access

Address:
[1]Institute of Pharmaceutical Technology and Biopharmacy, University of Muenster, Corrensstraße 48, 48149 Muenster, Germany and
[2]Institute of Food Chemistry, University of Muenster, Corrensstraße 45, 48149 Muenster, Germany

Email:
Klaus Langer[*] - k.langer@uni-muenster.de

* Corresponding author
§ Phone:+49 251 8339860; Fax: +49 251 8339308

Keywords:
human serum; nanoparticles; poly(lactide-*co*-glycolic acid); protein corona; proteomics

Beilstein J. Nanotechnol. **2019,** *10,* 1002–1015.
doi:10.3762/bjnano.10.101

Received: 12 February 2019
Accepted: 26 April 2019
Published: 06 May 2019

This article is part of the thematic issue "Frontiers in pharmaceutical nanotechnology".

Guest Editor: M. G. Wacker

Abstract

Background: When nanoparticles (NPs) are applied into a biological fluid, such as blood, proteins bind rapidly to their surface forming a so-called “protein corona”. These proteins are strongly attached to the NP surface and confers them a new biological identity that is crucial for the biological response in terms of body biodistribution, cellular uptake, and toxicity. The corona is dynamic in nature and it is well known that the composition varies in dependence of the physicochemical properties of the NPs. In the present study we investigated the protein corona that forms around poly(lactide-*co*-glycolide) (PLGA) NPs at different serum concentrations using two substantially different serum types, namely fetal bovine serum (FBS) and human serum. The corona was characterized by means of sodium dodecylsulfate polyacrylamide gel electrophoresis (SDS-PAGE), Bradford protein assay, zeta potential measurements, and liquid chromatography–mass spectrometry/mass spectrometry (LC–MS/MS). Additionally, the time-dependent cell interaction of PLGA NPs in the absence or presence of a preformed protein corona was assessed by in vitro incubation experiments with the human liver cancer cell line HepG2.

Results: Our data revealed that the physiological environment critically affects the protein adsorption on PLGA NPs with significant impact on the NP–cell interaction. Under comparable conditions the protein amount forming the protein corona depends on the serum type used and the serum concentration. On PLGA NPs incubated with either FBS or human serum a clear difference in qualitative corona protein composition was identified by SDS-PAGE and LC–MS/MS in combination with bioinformatic protein classification. In the case of human serum a considerable change in corona composition was observed leading to a concentration-dependent desorption of abundant proteins in conjunction with an adsorption of high-affinity proteins with lower abundance. Cell incubation experiments revealed that the respective corona composition showed significant influence on the resulting nanoparticle–cell interaction.

Conclusion: Controlling protein corona formation is still a challenging task and our data highlight the need for a rational future experimental design in order to enable a prediction of the corona formation on nanoparticle surfaces and, therefore, the resulting biodistribution in the body.

Introduction

Nanoparticle (NP)-based drug carrier systems offer outstanding opportunities in the treatment of many serious diseases. The unique physicochemical properties and the ability to bind a library of ligands make them advantageous for targeted drug delivery while minimizing side effects [1]. Among the different materials used to synthesize NPs, the biodegradable polymer poly(DL-lactide-*co*-glycolide) (PLGA) has attracted consideration due to its minimal systemic toxicity, favorable degradation characteristics, and sustained release properties. Furthermore, approval by the US Food and Drug Administration and the European Medicines Agency turned PLGA into a promising candidate as carrier material for NPs in future clinical applications [2]. However, despite intensive preclinical and clinical research only a few NPs have made it to clinical trials or market maturity [2,3]. One possible reason is the limited understanding of the interaction occurring at the interface between NPs and the physiological surrounding [3]. Once in contact with biological fluids, such as blood, proteins adsorb onto the surface of NPs forming a protein corona [4]. Consequently, the synthetic identity of the NPs is replaced by a new biological identity that determines their physiological response including biodistribution, cellular uptake, trafficking, and toxicity [5]. Corona formation is a very dynamic process in nature, and it has been extensively investigated and comprehensively reviewed that the corona composition varies in dependence of the physicochemical properties of the NPs [5,6]. However, it is emerging that the characteristics of the biological environment, e.g., protein concentration [7-9], protein source [10-12], temperature [13], incubation time [14], and flow status [15], also play a determinant role in the formation of the protein corona. NPs can be administered via different routes, such as intravenous, intradermal, oral administration or via inhalation. During their journey through the body, NPs are exposed to changing biological microenvironments containing different protein compositions and concentrations affecting the corona formation with possible deep implications on the physiological response [3,16]. This emphasizes the great importance of examining the effects provoked by these environmental factors in order to successfully introduce and firmly establish new nanoparticulate dosage forms onto the market, thus offering further options to prevent and treat many major illnesses.

The main objective of the present study was to investigate the compositional evolution of the NP protein corona as a function of increasing serum concentration. Therefore, we produced NPs composed of the biodegradable polymer PLGA stabilized with poly(vinyl alcohol) (PVA) and subsequently incubated them with increasing amounts of either fetal bovine serum (FBS) or human serum to induce the formation of a protein corona. The use of two substantially different serum types further allowed us to assess the effect of the source origin on the protein adsorption. FBS is a common additive in standard cell culture media for many human cell lines and is frequently used as protein source in corona studies probably for economic reasons [14,17,18]. As human serum better mimics the in vivo conditions, we attempt to evaluate the difference of the protein source in order to contribute to a more rational design in future experimental studies.

Following corona formation and separation of the resulting NP–corona complexes from excess serum proteins we used sodium dodecylsulfate polyacrylamide gel electrophoresis (SDS-PAGE), zeta potential measurements, and liquid chromatography–mass spectrometry/mass spectrometry (LC–MS/MS) to study the composition of adsorbed proteins in detail. A quantitative analysis of corona proteins was conducted by Bradford assay after alkaline hydrolysis of PLGA–NPs. Finally, the consequences of corona formation on the interaction between NPs and cells were examined by in vitro incubation experiments with the human liver cancer cell line HepG2.

Results and Discussion

Compositional evolution of the protein corona with increasing serum concentration

Nanoparticles (NPs) of the present study are based on the biodegradable polymer PLGA stabilized with poly(vinyl alcohol) (PVA) and were prepared by an emulsion diffusion method [19]. Incorporation of Lumogen® Red led to fluorescent labeled NPs easily trackable in cell culture experiments. Prior to NP incubation with increasing amounts of serum (FBS, human serum) and protein corona analysis the NPs were characterized accurately by PCS and zeta potential measurements. The obtained NPs showed a diameter of approximately 200 nm and a monodisperse size distribution with a PDI below 0.1 (see Table 1). The zeta potential of about −40 mV indicated colloidal stability due to electrostatic particle repulsion [14].

In our experimental setup we always referred to a constant surface area of NPs incubated with varying concentrations of serum. Surface asperities could lead to a higher surface area that

Table 1: Physicochemical characteristics of PLGA NPs (mean ± SD; $n \geq 3$).

nanoparticle system	hydrodynamic diameter [nm]	polydispersity index	zeta potential [mV]	drug load [µg Lumogen® Red/mg NPs]
PLGA NPs	214.6 ± 13.2	0.06 ± 0.02	−41.2 ± 8.1	—
PLGA NPs (Lumogen® Red loaded)	221.0 ± 16.4	0.03 ± 0.02	−45.9 ± 1.5	8.14 ± 1.29

would enhance the protein adsorption [20]. Therefore, we confirmed the spherical shape of the NPs and the smoothness of the surface by SEM (Figure 1). This allowed for a reliable examination of protein adsorption that will not be biased by effects of NP surface anomalies.

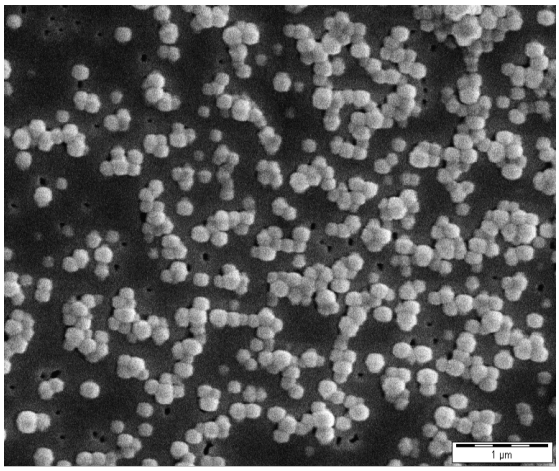

Figure 1: SEM confirmed the spherical shape of the PLGA NPs and the smoothness of the surface.

To focus on the evolution of the protein corona formed around PLGA NPs upon exposure to increasing amounts of serum, we applied the Bradford assay as a quantitative colorimetric approach to determine the total amount of proteins bound on PLGA NPs (Figure 2). NPs were incubated with either 50–1600 µL FBS or 1–1000 µL human serum for 30 min at 37 °C and subsequently purified in order to separate the NPs from unbound serum proteins. As can be seen from Figure 2A, the amount of NP-bound proteins at the lowest serum concentration level is 23.2 µg/0.08 m^2 for FBS and 49.6 µg/0.08 m^2 for human serum incubation. The amount of bound proteins steadily rises with increasing serum concentration until a plateau is reached. The plateau after incubation with human serum is twice as high as that after FBS incubation. The total amount of protein in serum prior to incubation was determined and was 47.7 mg/mL and 86.6 mg/mL for FBS and human serum, respectively. Afterwards, the equilibrium free fraction of protein in the incubation samples for each data point was calculated and the amount of protein adsorbed onto the surface of

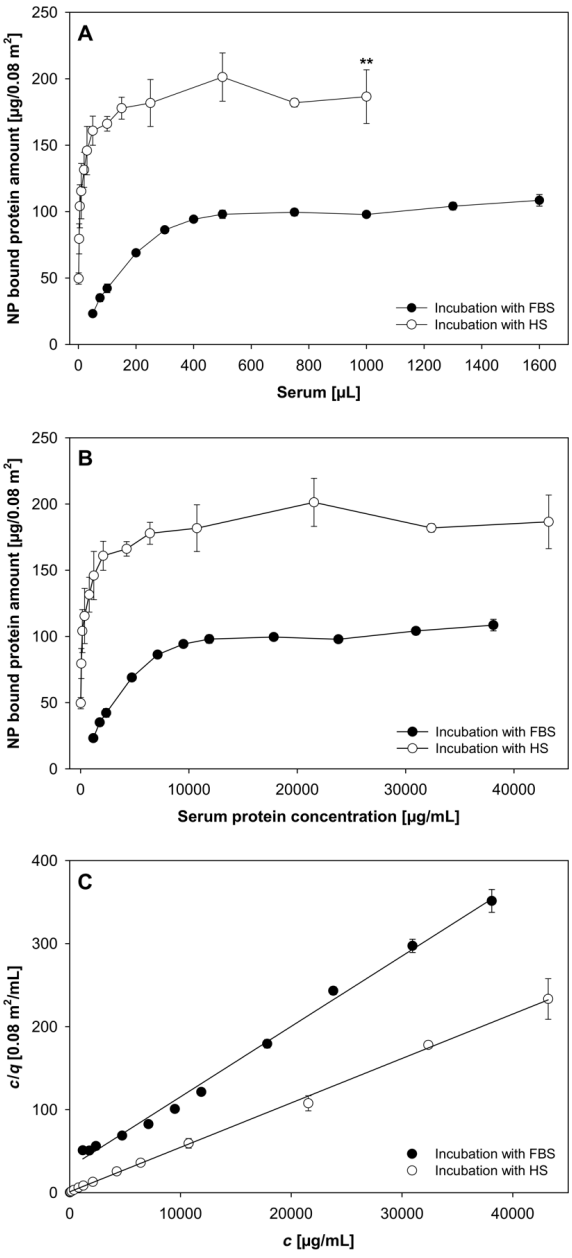

Figure 2: Adsorption of serum proteins on PLGA NPs ($n \geq 3$; mean ± SD). (A) Quantification of the total amount of proteins adsorbed on NPs after incubation with different amounts of serum for 30 min at 37 °C and subsequent purification. (B) Langmuir adsorption isotherm. (C) Adsorption of FBS and human serum by PLGA NPs plotted according to Equation 2 using the data from (B). Abbreviations: fetal bovine serum (FBS), human serum (HS).

PLGA NPs was plotted as a function of protein that is free in solution (Figure 2B). The results exhibit the characteristic shape of a Langmuir adsorption isotherm for a multicomponent fluid indicating that equilibrium conditions could be achieved with increasing contents of serum in the incubation medium.

The Langmuir equation was arranged into the linear form and the adsorptive capacity (q_{max}) of PLGA NPs for the different serum types was determined from the slope of c/q as a function of the concentration as shown in Figure 2C. The maximum amount of protein adsorbed after FBS incubation was 117.9 µg/0.08 m^2 and for human serum incubation 186.9 µg/0.08 m^2.

In order to visualize the corona proteins after exposure of the NPs to increasing serum concentrations and to get more detailed information about the molecular composition, one-dimensional SDS-PAGE analysis was performed (Figure 3).

The results illustrate a clear difference in corona protein identity and evolution trend for the two biological incubation fluids. The electrophoresis was carried out in triplicate. The protein pattern was reproducible and one gel for the incubation of PLGA NPs with increasing amounts of FBS is presented exemplarily in Figure 3A. The positive control is dominated by one major band corresponding to the molecular weight of serum albumin (67 kDa). In contrast, protein adsorption led to a highly selective enrichment of serum proteins on the surface of PLGA NPs [21], even at the lowest incubation concentration. The NPs are characterized by a protein pattern consisting of numerous protein bands ranging from 29 to 212 kDa. An accumulation of protein bands occurs between 43 and 118 kDa and a sharply defined band is located at the top of the gel above 118 kDa. Besides, three distinctive bands appear around 29 kDa. Figure 3A clearly shows that the composition of the hard corona remains stable over a wide range of FBS concentrations, while only the intensity of protein bands evolves until no further increase in staining intensity is visible. These findings reinforce the previously described assertion that the surface of PLGA NPs is more or less fully covered by proteins and a saturation effect occurred for FBS concentrations above a defined limit. Moreover, zeta potential measurements also provide evidence that the identity of corona proteins is quite stable when passing from low to high serum concentrations (Figure 4). In general, serum protein adsorption on negatively charged NPs leads to a decrease in zeta potential in dependence of amount and identity of the bound proteins [9,22]. The bare NPs display a zeta potential of −42.3 mV. Following incubation with 50 µL FBS it is significantly decreased to −32.5 mV suggesting that even for low serum concentrations a relatively complete protein layer was formed. With increasing amounts of FBS the zeta potential does not change considerably, which indicates that the qualitative composition of corona proteins remains constant. In order to address the effect of a higher ionic background the zeta potential of bare PLGA NPs as well as NPs incubated with 500 µL serum was measured in pure water and 0.2 mM NaCl, respectively. After water dilution PLGA NPs and NPs incubated with 500 µL FBS or human serum show zeta potentials of

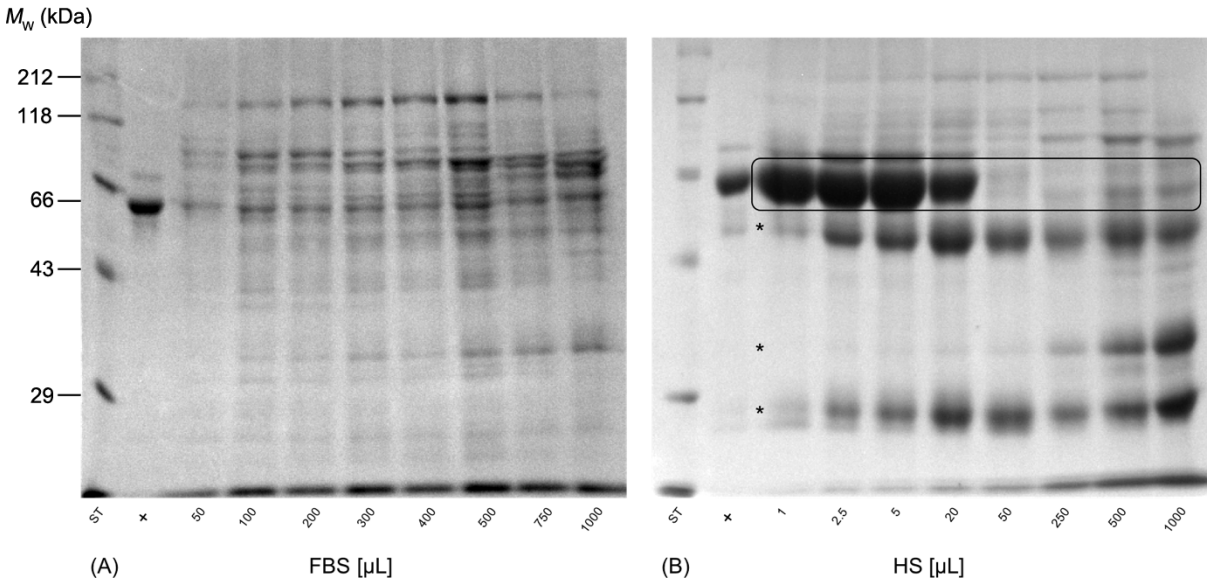

Figure 3: One-dimensional SDS-PAGE of adsorbed serum proteins obtained from the corona of PLGA NPs following incubation with increasing amounts of (A) FBS and (B) human serum. The molecular weights (M_W) of the proteins in the marker lane on the left are reported for reference and positive controls (+) derived from pure serum diluted with purified water. Abbreviations: fetal bovine serum (FBS), human serum (HS).

−43.2 mV, −34.0 mV and −21.4 mV, respectively. As could be expected the higher ionic background of 0.2 mM NaCl leads to a moderate reduction of the zeta potential to −33.0 mV, −30.5 mV, and −19.4 mV, respectively, but the graduation of the zeta potential values between the different samples remains the same. In brief, the incubation of PLGA NPs with increasing concentrations of FBS enabled us to modulate the amount of bound protein and to create a saturated surface while the identity of corona proteins was quite unchanged. These findings are consistent with former reports [7-9] in which Gräfe and collaborators revealed a saturation effect for the incubation of magnetic NPs at fetal calf serum concentrations above 75% (v/v) [8].

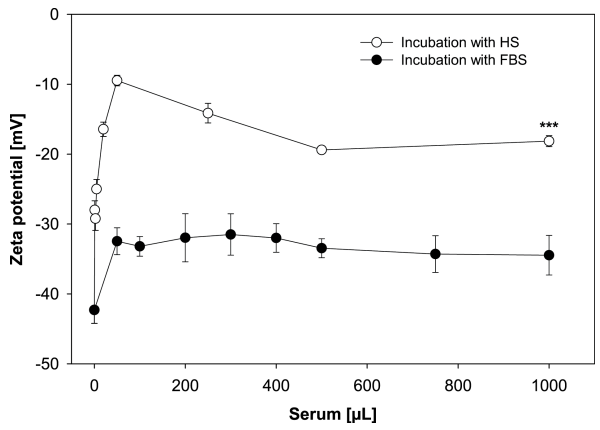

Figure 4: Surface charge evolution of PLGA NPs after exposure to different amounts of serum in the incubation solution. The differences in the mean values (mean ± SD; $n \geq 3$) were statistically significant at the highest serum concentration indicating an enrichment of cationic proteins in the corona after exposure to human serum. Abbreviations: fetal bovine serum (FBS), human serum (HS).

Nonetheless, the most intriguing observation of the present study is that the qualitative composition of the protein corona changed considerably with increasing human serum concentration in contrast to the incubation with FBS (Figure 3) even though the quantification of total amount of proteins bound to NPs reveals the same characteristic shape of an adsorption isotherm as for FBS incubation (Figure 2). Furthermore, it is noteworthy how selective and reproducible the adsorptive processes take place at the interface between particle surface and serum, considering that the serum is composed of more than 3700 different proteins [23].

In the case of human serum the SDS-PAGE results (Figure 3B) illustrate that the protein signature is dominated by one intense protein band corresponding to a molecular weight of 66 kDa following incubation with 1 µL human serum. Below, three faintly visible bands emerged (marked with asterisks) of which the intensity increases with higher serum content during incubation. However, the most striking shift in corona composition occurs from 20 to 50 µL addition of human serum. The predominant protein band (66 kDa) vanishes almost entirely and the overall profile is more complex. This observation was confirmed by a semiquantitative densitometry analysis of the eight highlighted protein bands at 66 kDa (Figure 5). The first band was used as standard and then, the relative density was calculated by dividing the density of each band by the density of the standard band. As can be seen, the relative protein band density significantly drops from 94.0% to 41.1% when increasing the content of human serum in the incubation medium to 50 µL.

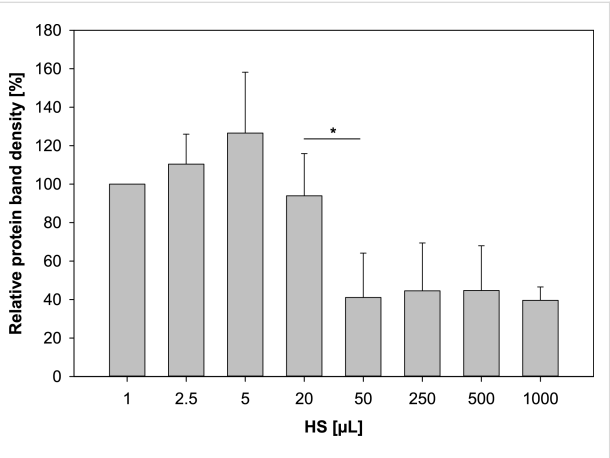

Figure 5: Semiquantitative densitometry analysis of the eight highlighted protein bands from Figure 3B (mean ± SD; $n = 3$). The first lane has been selected as standard and the density of the other bands is given relative to this selected band. Abbreviations: human serum (HS).

In addition, zeta potential measurements also affirmed the variation in corona composition with increasing human serum concentration (Figure 4). At low concentrations, the zeta potential decreases continuously until the minimum value of −9.5 mV is reached after the addition of 50 µL human serum. After that, the potential rises again slowly to a value of about −19 mV. However, a further increase in human serum concentration does not lead to further changes of the zeta potential. This is in good agreement with the results illustrated in Figure 2 and Figure 3B and demonstrates that the amount and the molecular composition of the protein corona formed around PLGA NPs after exposure to human serum evolves quite significantly at low concentration levels but becomes constant when passing to higher serum concentrations.

Corona formation is a very dynamic, competitive and time-dependent process. In the early stage, low-affinity proteins with high abundance in serum, for instance, human serum albumin (HSA), adsorb onto the surface and are immediately replaced by high-affinity proteins with lower abundance and slower kinetics, such as apolipoproteins and immunoglobulins [4,24].

According to the predominant protein band at M_W = 66 kDa, we suggest an enrichment of HSA in the corona of the PLGA NPs following incubation with 1–20 µL human serum (Figure 3B). At low incubation concentrations highly abundant proteins tend to attach strongly onto the NP surface and form the hard corona although they exhibit a low affinity. With increasing human serum concentration in the samples, the total content of high-affinity proteins in the incubation medium increases. This enables them to act as competitive binders and enhances the desorption of proteins with lower binding affinity [4,7,9]. Hence, the formation of the protein corona in dependence on the human serum concentration may have deep implications for the prediction of the biological response and the pharmacokinetic behavior of colloidal drug carrier systems in the body. For instance, the coating of polystyrene NPs with HSA enhances their circulating lifetime in blood and reduces hepatic uptake clearance after intravenous injection into rats [25]. In contrast, some high-affinity proteins, for example immunoglobulins, facilitate phagocytosis by cells of the mononuclear phagocyte system (MPS) [26]. Furthermore, one has to consider that the ratio between NP surface and protein concentration is closely related to the administration route and dose [27]. As a result, controlling the protein-corona formation is still a challenging task and our study emphasizes the need of a careful control in future experimental designs in order to ensure predictability of NP biodistribution.

The characteristics of the protein corona depending on serum type

One major goal of the present study was to compare the protein corona of PLGA NPs that were exposed to 1000 µL of either FBS or human serum in order to explore the effect of the origin of the protein source on the amount, surface charge, and identity of the adsorbed protein layer. As already discussed above, 1000 µL serum in the incubation medium create a saturated NP surface for both biological fluids and a further increase in serum content does not lead to changes in the corona formation. Accordingly, this allowed us to reliably address the aforementioned research topic without considering the variabilities caused by phenomena depending on the serum concentration.

The quantification of corona proteins was performed by Bradford assay and revealed a significant higher protein content after incubation with human serum (Figure 2). Nevertheless, this result did not only reflect the higher total concentration of proteins in pure human serum, which was determined right before incubation and was about twice as high as that of FBS. For instance, the protein amount bound to NPs following the addition of 50 µL serum is 160.91 µg/0.08 m^2 for human serum and 23.18 µg/0.08 m^2 for FBS. This provides first evidence that the different adsorptive capacities of PLGA NPs for the two serum types were due to a higher affinity of several human proteins to the NP surface. Furthermore, the protein patterns on SDS-PAGE gels confirm differences in the qualitative corona composition, and the significant lower zeta potential values after exposure to human serum indicate a higher level of cationic proteins in the corona (Figure 3 and Figure 4) [28]. Additionally, the hard-corona proteins were identified by a shotgun proteomics-based approach. The adsorbed proteins were tryptically digested and the resulting peptides were analyzed by LC–MS/MS and subsequently bioinformatically interpreted. In three independent replicates, we detected numerous individual proteins on the PLGA NPs surface in dependence of the origin of the incubation solution. The complete list of identified proteins including their physiological function in blood, M_W values, as well as their isoelectric point (pI) is shown in Table S1 and Table S2 (Supporting Information File 1). A total number of 53 to 59 different proteins was detected in the corona after incubation with human serum. In contrast, the corona of PLGA NPs exposed to FBS was found to be less enriched with a total number of 22 to 36 identified proteins. Towards a better understanding of protein adsorption processes in dependence of the local biological environment and its consequences for the fate of the NPs in vivo, we divided the identified proteins roughly into seven groups according to their physiological function in the body (Figure 6). A substantial part of the coronas consist of apolipoproteins. They are important components of lipoproteins that facilitate the transport of cholesterol, triglycerides, and phospholipids between plasma and cells [29]. Due to their lipid-binding domains, they are even more attracted to NPs composed of hydrophobic core materials [30,31] resulting in a prolonged circulation time in blood [18]. Moreover, covalent attachment of apolipoprotein A–I and apolipoprotein E to the NP surface enables drug transport across the blood–brain barrier [32]. Here, both proteins were identified as constituents of the corona of PLGA NPs underlining the involvement in cellular transport mechanisms and biodistribution.

It is noteworthy that, in particular, the number of identified opsonins depends on the choice of protein source. This is important because the presence of opsonins on the NP surface could shorten their circulation lifetime and increase their uptake by immune cells [10,26]. In particular, the number of proteins that are involved in immune response is considerably increased in the corona formed during human serum incubation (Figure 6). In Table S2 (Supporting Information File 1) many immunoglobulin (Ig) fractions are listed that have been exclusively identified in the hard corona after human serum exposure, for instance IgG L chain, immunoglobulin kappa variable 3-20 and immunoglobulin J chain. This is readily conceivable since fetal serum does not contain antibodies [17]. IgG is a major effector molecule of the humoral immune response and

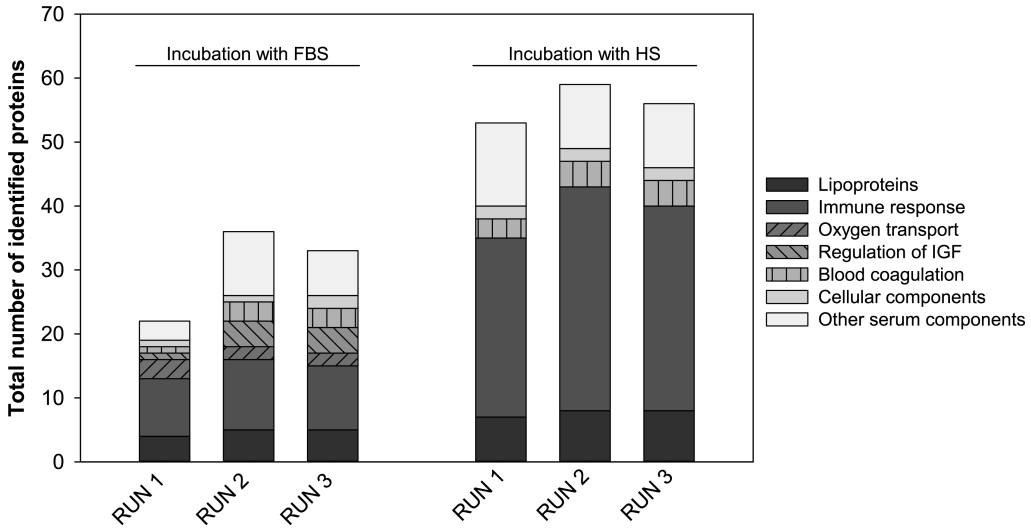

Figure 6: Bioinformatic classification of proteins identified in the corona of PLGA NPs after exposure to FBS or human serum. Proteins were analyzed by LC–MS/MS in three independent measurements (RUN 1–3) and grouped according to their function in blood. Abbreviations: fetal bovine serum (FBS), human serum (HS), insulin-like growth factor (IGF).

takes part in the general process of opsonization for presentation to macrophages [26]. Besides, it activates the classical pathway of the complement system. Immediately after binding of IgG to foreign materials it forms a complex with complement component C1. We detected subcomponents of the proteases C1r and C1s in the HS corona, which are part of the C1 complex and ensure complement amplification (Table S2, Supporting Information File 1) [33]. In a current study, Chen et al. emphasized the role of the complement system in blood clearance mechanisms of nanospheres [34]. However, one has to keep in mind that this is probably not the sole mechanism of elimination. For instance, Hu and co-workers supposed that adsorption of platelet factor 4 also promotes rapid clearance from the bloodstream (Table S2, Supporting Information File 1) [35]. In contrast, we identified hemoglobin subunits exclusively in the corona derived from incubation with FBS (Figure 6 and Table S1, Supporting Information File 1). Systemically administered NPs can interact with circulating blood cells resulting in an erythrocyte aggregation that is in many cases accompanied by hemoglobin release. Hemoglobin adsorbs to NP surfaces and therefore facilitates phagocytosis by macrophages [36].

The LC–MS/MS results are consistent with the data presented in Figures 2–4, leading us to the assumption that the origin of the protein source plays a crucial role in defining the biological identity of nanocarriers. Therefore, the results obtained in animal models are not directly applicable to humans. For example, due to the higher number of opsonins in the corona after NP incubation with human serum, one may expect a reduced circulation time in human patients [11]. Nevertheless, FBS is still widely used as protein source for the investigation of the reaction at the interface between NPs and biomolecules [14,18]. Consequently, we propose to examine the protein corona formation in the respective medium of the desired species (e.g., murine or human) for a better prediction of the NP biodistribution in vivo.

Protein corona alters nanoparticle-cell interaction

It is now clearly emerging that the primary defining element of NPs in biological media is their protein corona, which is the entity actually seen by target cells [7]. In the present study we convincingly demonstrated that the composition of the protein corona formed around PLGA NPs strongly depends on the concentration and the species origin of the incubation solution. In order to investigate the biological consequences of varying protein corona characteristics on the interaction of PLGA NPs and cells, the human liver cancer cell line HepG2 was used for in vitro incubation experiments.

For an easy tracking of NPs in cell culture experiments, the fluorescent dye Lumogen® Red was incorporated into the hydrophobic particle matrix. Due to the lipophilic properties of the dye molecule an average of 8.14 µg Lumogen® Red/mg NPs was entrapped, which corresponds to a high embedding efficiency of 81.4% of the initially used substance (Table 1). Furthermore, Raudszus and colleagues showed that only a very slight Lumogen® Red amount of less than 0.1% was released when polymeric NPs were incubated in serum-containing medium [37]. Therefore, we assumed a stable entrapment of the model drug even in the presence of proteins. Consequently, the

Lumogen® Red fluorescence measured in cell culture experiments could be directly associated with the interaction between NPs and cells and is not distorted by effects of dye leakage.

The strategy used for this investigation was to preform coronas around PLGA NPs before exposure to cells, by incubating the NPs with 500 µL FBS (PLGA-500-FBS-NP), 500 µL human serum (PLGA-500-HS-NP) or 5 µL human serum (PLGA-5-HS-NP). Additionally, one sample was prepared by incubating the NPs with water instead of serum (PLGA NPs). We then added the NPs as well as the free dye Lumogen® Red to the cells and monitored the cell interaction under serum-free conditions over a time period of 24 h by live-cell imaging (Figure 7). The results revealed that the interaction between the unformulated Lumogen® Red and cells was neglectable. In contrast, all NP formulations showed an increasing cell interaction over time resulting in a plateau after approximately 18 h. The presence of proteins on the PLGA NP surface facilitates the adhesion to HepG2 cells compared to the bare particles. The significant lower zeta potential after exposure to serum indicated higher levels of cationic proteins in the corona (Figure 4) [28]. Therefore, we suppose a higher electrostatic attraction between the negatively charged cell membrane and the preincubated PLGA NPs [38]. Moreover, it became apparent that not only the mere presence of a protein corona but also the amount and type of protein adsorbed onto the surface determines the NP-cell interaction (Figure 7).

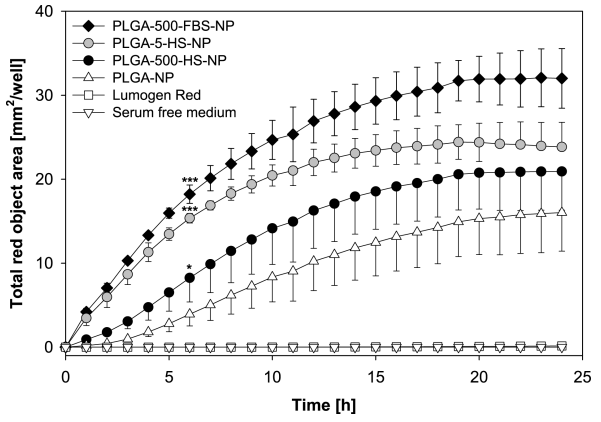

Figure 7: Time-dependent cell interaction of PLGA NPs with HepG2 cells in the absence or presence of a preformed protein corona (mean ± SD; n = 3). Statistical significances after 6 h versus PLGA NPs are marked with asterisks. Nanoparticles were loaded with Lumogen® Red to visualize the nanoparticle-cell-interaction. Abbreviations: fetal bovine serum (FBS), human serum (HS).

For instance, the interaction between cells and NPs after 6 h is about two- and about fourfold higher for PLGA-500-HS-NP and PLGA-5-HS-NP, respectively, when compared to the bare NPs. PLGA NPs preincubated with 500 µL FBS lead to the highest total red object area of 18.22 mm^2/well. The results are consistent with the fluorescence microscopy images which were taken after an incubation time of 6 h (Figure 8). Furthermore, the images clearly demonstrate that all NP formulations are strongly attached to the cell membranes because they could not be removed by repetitive washings steps during sample processing. As can be seen in Figure 8F, lots of red dots are precisely located in the cell membrane indicating that treatment with PLGA NPs leads to an enrichment in the membrane. This step is usually considered as a prerequisite for a successive internalization by cells [38]. Besides, some of the proteins in the corona could mediate the interaction with cells by the recognition of specific receptor binding sites localized on the cell surface and thus induce different cellular behavior [17,38].

In summary, even in the case of NPs with the same chemical and physical properties, it is difficult to assess the biological response as long as the reaction at the nano–biointerface is not sufficiently understood. Therefore, the results of this study confirm the need to carefully evaluate the data acquired so far from in vitro studies in order to develop safe biomedical applications.

Conclusion

We investigated the importance of selecting a proper physiological medium used for in vitro protein corona analysis. Therefore, we employed several analytical approaches to examine the protein corona that forms around PLGA NPs at different serum concentrations using two substantially different serum types. Our results showed that the amount of proteins bound to NPs increased when passing from low to high FBS concentrations while the identity of adsorbed proteins remained constant. In contrast, the corona composition of PLGA NPs incubated with human serum evolved considerably. Interestingly, the fraction of proteins displaying a M_W of about 66 kDa vanished almost entirely at higher concentrations. To further evaluate the effect of source origin on the corona formation we analyzed the proteins that bound under equilibrium conditions onto the NP surface in order to ensure comparability between the obtained results. Incubation with human serum led to a significantly higher amount of bound protein and the number of proteins involved in immune response was considerably increased indicating that circulation times in human patients may be different than that observed in animal models. However, one has to keep in mind that variations in analytical methods as well as measurement interpretation based on different databases can make direct comparisons of individual studies challenging.

Additionally, our data revealed that the characteristics of the protein corona altered the interaction between NPs and HepG2

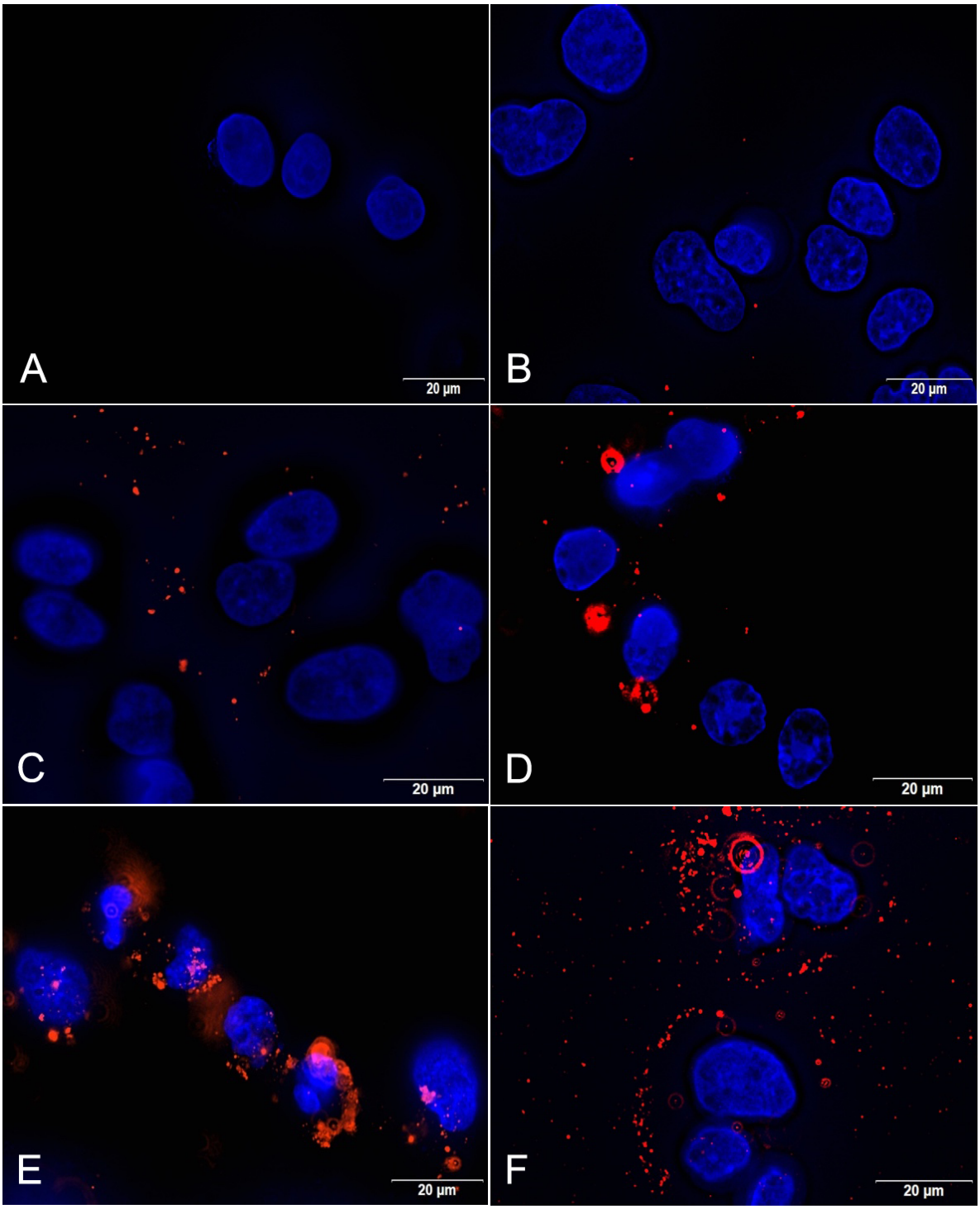

Figure 8: Visualization of the cell interaction of PLGA NPs after 6 h with HepG2 cells in the absence (C) or presence (D–F) of a preformed protein corona. Cell nuclei were stained with DAPI (blue) and Lumogen® Red was detected through its autofluorescence (red). A: untreated cells; B: unformulated Lumogen® Red; C: PLGA NPs; D: PLGA-500-HS-NP; E: PLGA-5-HS-NP; F: PLGA-500-FBS-NP. Abbreviations: fetal bovine serum (FBS), human serum (HS).

cells underlining the importance of a careful control of experimental parameters in order to improve the interpretation and extrapolation of in vitro based studies. Consequently, our study represents a fundamental step towards establishing detailed relations between the interaction of PLGA NPs and the environmental surrounding, thus offering advances for accelerating the

translation of new nanoparticulate dosage forms into the clinical practice.

Experimental

Reagents

The biodegradable polymer poly(DL-lactide-*co*-glycolide) (PLGA, Resomer® RG 502 H), which was used as NP matrix, was obtained from Evonik Industries (Darmstadt, Germany). The steric NP stabilizer poly(vinyl alcohol) (PVA; Emprove® exp 8-88, molecular weight approx. 67,000 g/mol, degree of hydrolysis 85–89%) was purchased from Merck KGaA (Darmstadt, Germany). The fluorescent dye Lumogen® F Red 305 was kindly provided by BASF SE (Ludwigshafen, Germany). Fetal bovine serum (FBS) superior for NP incubation and cell cultivation was received from Biochrom AG (Berlin, Germany). Human serum was obtained from in.vent Diagnostica GmbH (Henningsdorf, Germany), donors informed consent documents and ethic votes are available. Roti-Load®1, Roti®-Mark STANDARD and all other chemicals used for sodium dodecyl sulfate polyacrylamide gel electrophoresis (SDS-PAGE) were delivered by Carl Roth GmbH & Co. KG (Karlsruhe, Germany). The dye Coomassie Brilliant Blue G-250 was purchased from VWR Life science AMRESCO (Solon, Ohio). Bovine serum albumin (BSA), DL-dithiothreitol (DTT), and iodoacetamide (IAA) were obtained from Sigma-Aldrich (Steinheim, Germany). Trypsin (sequencing grade) for protein digestion was obtained from Promega Corporation (Madison, USA). Urea was purchased from Acros Organics (New Jersey, USA).

Human liver cancer cells (HepG2) were kindly provided by the Institute of Food Chemistry of the University of Muenster, Germany. Phosphate-buffered saline (PBS), Dulbecco's modified Eagle's medium (DMEM) and all used supplements were received from Biochrom AG. Vectashield® Mounting medium with DAPI was purchased from Vector Laboratories Inc. (Burlingname, USA) and wheat germ agglutinin (WGA) AlexaFluor® 350 from Life Technologies (Carlsbad, USA). All other chemicals and organic solvents were delivered in the highest grade available.

Nanoparticle preparation

The NPs were prepared by an previously described emulsification–diffusion method [19]. Briefly, 100 mg PLGA was dissolved in 2 mL ethyl acetate and subsequently added to 4 mL of an aqueous solution containing PVA (2%, w/w). The mixture was emulsified using a high-speed homogenizer (Ultra-Turrax®, S25NK-10G, IKA, Staufen, Germany) at 21,000 rpm for 30 min. The resulting pre-emulsion was poured into 6 mL of PVA solution (2%, w/w) and stirred overnight at room temperature to remove the organic phase. Finally, the NPs were purified by three steps of centrifugation (10 min, 16,000*g*) and following resuspension into ultrapure water. The NPs were referred to as PLGA NPs.

In order to visualize the NPs during cell culture experiments a fluorescent dye was embedded into the polymer matrix. Therefore, 100 mg PLGA and 1 mg Lumogen® Red were dissolved in 2 mL ethyl acetate. All other preparation steps were conducted as described above.

Nanoparticle diameter, size distribution and zeta potential

The hydrodynamic NP diameter and polydispersity index (PDI) were determined by photon correlation spectroscopy (PCS) using a Malvern Zetasizer Nano ZS system (Malvern Instruments Ltd., Malvern, United Kingdom). An appropriate volume of the different NP formulations was diluted in 2 mL ultrapure water in a disposable cuvette right before use and measured at a temperature of 22 °C using a backscattering angle of 173°.

The zeta potential was measured in the same instrument by laser Doppler microelectrophoresis to provide information about the surface charge of the NPs. The NP dilutions described above were transferred into a folded capillary cell and the determination was conducted at 22 °C.

Morphological analysis of nanoparticles by SEM

A quantity of 3 µL diluted PLGA NP suspension (0.2 mg/mL) was applied on a 0.1 µm membrane filter (Isopore™ membrane filter, Merck Millipore, Darmstadt, Germany) and dried overnight in a desiccator. Afterwards, the membrane filter was sputtered with gold (Sputter SCD 040, BALTEC, Liechtenstein) under argon atmosphere. SEM was performed on a CamScan CS4 microscope (Cambridge Scanning Company, Cambridge, United Kingdom) and the sample was visualized with an accelerating voltage of 10 kV, a working distance of 10 mm, and 20,000× magnification.

Determination of Lumogen® Red loading

The amount of embedded Lumogen® Red was analyzed by HPLC using a fluorescence detector (Agilent Technologies 1200 Series, Agilent Technologies GmbH, Böblingen, Germany) [37]. Therefore, an aliquot of NP suspension corresponding to 1 mg of PLGA NPs was centrifuged for 30 min at 30,000*g*. Following this, the supernatant was discarded and the pellet was extracted with 1 mL acetonitrile for 2 h under slight shaking. Prior to HPLC analysis, the sample was centrifuged again (30 min, 30,000*g*) and 10.0 µL of the supernatant was injected onto a reversed-phase column (LiChroCart, Lichrosphere RP-18, 5 µm, 100 Å, 125 × 4 mm, Merck Millipore, Darmstadt, Germany). The elution was performed with pure

acetonitrile as mobile phase at a constant flow rate of 1 mL/min and Lumogen® Red was detected using a fluorescence detector at an excitation wavelength of 575 nm and an emission wavelength of 610 nm. Quantification was carried out using a calibration curve ranging from 0.1–10 µg/mL.

Serum protein adsorption on nanoparticles

Serum protein adsorption on NPs was carried out according to a modified method described by Gossmann and co-workers [18]. Therefore, increasing amounts of either FBS (50–1600 µL) or human serum (1–1000 µL) were added to an aliquot of PLGA NP suspension corresponding to a total surface area ($A = 4\pi r^2$) of 0.08 m^2. Afterwards, samples were filled up to a total volume of 2 mL with ultrapure water and were incubated for 30 min at 37 °C under gentle shaking (1200 rpm). Finally, the samples were purified by at least two cycles of centrifugation (10 min, 16,000*g*) and redispersion into ultrapure water in order to remove unbound serum proteins. For the purpose of cell culture experiments, the Lumogen® Red-loaded PLGA NPs were incubated likewise and resuspended after the last centrifugation step in DMEM supplemented with 1% (v/v) non-essential amino acids (NEA), 1% (v/v) L-alanyl-L-glutamine (200 mM), and 1% (v/v) penicillin/streptomycin (100 U/mL) (serum-free medium).

For the identification of corona proteins by LC–MS/MS analysis a larger particle surface area was required. Thus, 1000 µL of either FBS or human serum were added to an aliquot of PLGA NP suspension corresponding to a total surface area of 0.24 m^2 and subsequently filled up to a total volume of 4 mL with ultrapure water. The further experimental procedure was conducted as described above.

Quantification of total nanoparticle bound protein amount

For the quantification of the proteins in the corona, a photometric method based on a protein determination protocol by Bradford et al. [39] was used. The dye Coomassie Brilliant Blue G-250 binds to the proteins and causes a shift in the absorption maximum from 465 to 595 nm, which was monitored in a spectrophotometer Typ U-2900 (Hitachi High Technologies Corporation, Tokyo, Japan).

The previously obtained NP pellet was hydrolyzed with 100 µL NaOH 1 M and 400 µL purified water (15 min, 60 °C, 1200 rpm). Afterwards, 1.9 mL Bradford reagent was added to 100 µL of the hydrolyzed sample. Incubation for 10 min at 1200 rpm led to a stable protein–dye complex that was read at 595 nm. The amount of proteins bound to the NPs was quantified using a BSA calibration curve (0.05–0.5 mg/mL) with addition of 1 M NaOH.

In addition, the total protein amount in serum (FBS and human serum) was determined. Consequently, the free fraction of protein in serum for the different incubation conditions could be calculated by subtraction of the total amount of NP-bound proteins. This relation was represented as Langmuir adsorption isotherm for a multicomponent fluid applying the following equation:

$$q = \frac{K_L \cdot q_{max} \cdot c}{1 + K_L \cdot c}, \quad (1)$$

where q is the amount of solute (serum protein) adsorbed per weight of adsorbent (PLGA NPs), c is the serum protein concentration at equilibrium, K_L is a constant related to the enthalpy of adsorption and q_{max} is related to the surface area of the solid. This equation was arranged into the linear form

$$\frac{c}{q} = \frac{c}{q_{max}} + \frac{1}{K_L \cdot q_{max}}. \quad (2)$$

The value of q_{max} is a measure of the adsorptive capacity of the adsorbent for the adsorbate under examination and was calculated for the adsorption of serum proteins on PLGA NPs.

SDS-PAGE analysis of corona proteins

After protein adsorption and the last centrifugation step the pellet was resuspended under shaking (1200 rpm, 22 °C) in 30 µL reducing loading buffer (Roti-Load®1) overnight to desorb the proteins from the NP surface. Hereafter, the samples were centrifuged again (45 min, 30,000*g*) and the supernatant containing the proteins was transferred into a new reaction vessel and boiled for 5 min at 95 °C to denature the proteins. Subsequently, a 10% polyacrylamide gel was prepared and the samples as well as the protein standard (Roti®-Mark STANDARD) and serum positive controls were applied on the gel. For positive controls, serum was diluted 1:100 with ultrapure water. The SDS-PAGE was carried out at a constant voltage of 200 V for 1 h on an OmniPAGE mini system (Omnilab-Laborzentrum GmbH & Co. KG, Bremen, Germany). The resulting gel was fixed (79% water, 1% orthophosphoric acid, 20% methanol), stained with a colloidal Coomassie Brilliant Blue G-250 solution overnight and destained in methanol/water (1:3, v/v). Finally, Gel ix Imager (INTAS Science Imaging Instruments GmbH) was used for imaging.

In order to compare the density of protein bands after the visualization step a densitometric analysis was performed by using ImageJ software (Vers. 1.52s, https://imagej.nih.gov/ij/down-

load.html). For data analysis, the density of the bands was expressed relative to the density of a selected standard band.

Determination of zeta potential after serum protein adsorption

Following protein adsorption and the final centrifugation step the NP pellet was resuspended into 1 mL ultrapure water. 10 µL of the NP dispersion was diluted with 2 mL ultrapure water. Subsequently, the sample was transferred into a folded capillary cell and the zeta potential of the NP–protein complex was determined as described above.

Identification of corona proteins by LC–MS/MS

Corona proteins were identified using a shotgun proteomics-based approach that has become the standard technique for the investigation of complex protein mixtures in recent years. Following tryptic digestion of the proteins, peptides were identified using LC–MS/MS on an orbitrap-based mass spectrometer and software-based data evaluation to interpret the peptide fragmentation data. In this study we referred to a protocol of Gossmann and co-workers [18].

In-solution digestion of corona proteins

After washing and collecting the NPs with protein corona by centrifugation, the resulting pellet was resuspended in 100 µL TRIS buffer containing 6 M urea overnight at room temperature to desorb the proteins from the surface. Following this, the samples were centrifuged again (45 min, 30,000*g*) in order to isolate the desorbed proteins from the NPs. The supernatant consisting of corona proteins was mixed with 5 µL of 200 mM dithiothreitol for 1 h at room temperature to reduce the disulfide bonds. Subsequently, 20 µL of 200 mM iodoacetamide was added to the solution in order to alkylate cysteines. The reaction was conducted for 1 h in the dark. After that, the excess iodoacetamide was inactivated by another addition of dithiothreitol (20 µL, 200 mM) to the solution (1 h, 1200 rpm, 22 °C). To prepare tryptic in-solution digestion of proteins, the samples were diluted to a total volume of 1000 µL with ultrapure water to a final concentration of 0.6 M urea to maintain the activity of trypsin. Next, 10 µL of ice-cooled trypsin solution (200 ng/µL) was added to the diluted samples and digestion was carried out overnight under slight shaking (37 °C, 900 rpm). Finally, the reaction was stopped by adjusting the pH to below 6 with glacial acetic acid and the samples were filled up to a total volume of 2 mL with ultrapure water for the further experimental procedure.

Sample preparation for mass spectrometry

To prepare for a successful mass spectrometric analysis of the peptides the samples were purified by solid-phase extraction in order to remove salts and undesired impurities. Briefly, Strata^{TM}-X 33u RP 30 mg/1 mL columns (Phenomenex, Aschaffenburg, Germany) were sequentially activated and equilibrated with 1 mL methanol and 1 mL 1% formic acid before the digestion solutions were applied onto the columns in aliquots of 1 mL. Thereafter, the samples were desalted by washing with 1 mL of purified water. Then, the stationary phase including the peptides was rinsed with 600 µL of Eluent I (MeOH/H_2O + 1% FA (5:5)) followed by 400 µL of Eluent II (MeOH/H_2O + 1% FA (7:3)). The eluents were collected and evaporated nearly to dryness in a Thermomixer® comfort (40 °C, 300 rpm) under nitrogen atmosphere. Finally, the residue was redissolved in a mixture of 100 µL acetonitrile, formic acid, and purified water (3:1:96, v/v) and the samples were stored at −20 °C until LC–MS/MS analysis.

Mass spectrometric detection of peptides

Data were acquired on an LTQ Orbitrap XL hybrid ion trap-orbitrap mass spectrometer coupled to an Accela HPLC system (both Thermo Scientific, Dreieich, Germany). The injection volume was 20.0 µL and LC separation of enzymatic digests was carried out on an 2.1 × 150 mm, 2.6 µm Accurore C18 column (Thermo Scientific) at a constant flow rate of 250 µL/min employing the following gradient of ACN + 1% formic acid (A) and H_2O + 1% formic acid (B): 3% A for 6 min, 3 to 12% A in 6 min, 12 to 35% A in 79 min, 35 to 60% A in 9 min, holding 60% A for 8 min, 60 to 3% A in 2 min and reequilibration at 3% A in 10 min. The mass spectrometer was operated in positive full scan and data-dependent mode (DDMS). Survey full-scan mass spectra (m/z 300–1500) were acquired in the Orbitrap (r = 30,000) and the two most intense ions were sequentially isolated, fragmented, and analyzed in the linear ion trap, using collision-induced dissociation (CID, normalized collision energy of 30% and an activation time of 30 ms). No charge states were rejected from fragmentation and target ions were dynamically excluded from repeated fragmentation for 45 s. Conditions for electrospray ionization (ESI) were: capillary temperature 225 °C; vaporizer temperature 350 °C; sheath gas flow 40 (arbitrary units); auxiliary gas flow 20 (arbitrary units); sweep gas flow 5 (arbitrary units); source voltage 3.5 kV; and tube lens 135 V.

Data analysis for protein identification

For protein identification a database search was performed with PEAKS 7 (Bioinformatics Solutions, Waterloo, Canada) against the UniProt KB databases (*Bos taurus*, created 2016-04-25, 43803 entries; *Homo sapiens*, created 2016-03-12, 1073900 entries) using the PEAKS de novo algorithm and the enhanced target-decoy method ("decoy fusion") for false discovery rate (FDR) estimation and result validation [40,41]. Search parameters were: (a) trypsin as specific enzyme, three missed cleavage

allowed; (b) fixed modification: carbamidomethylation of cysteine and variable modification: oxidation of methionine, allowing for three variable PTM per peptide; (c) precursor mass error tolerance of 5 ppm; (d) fragment mass error tolerance of 1 Da. Proteins with a −log *P* value > 80 were considered to be reliable.

Cell culture

HepG2 cells were cultivated in 75 cm^2 flasks with DMEM supplemented with 10% (v/v) FBS, 1% (v/v) non-essential amino acids (NEA), 1% (v/v) L-alanyl-L-glutamine (200 mM), 1% (v/v) penicillin/streptomycin (100 U/mL) at 37 °C, 100% humidity in a 10% CO_2 atmosphere. Cells were subcultivated twice a week at a ratio of approximately 1:5 after reaching 80–90% confluence or were used for cell culture experiments.

Determination of nanoparticle–cell interaction by live-cell imaging

In order to investigate the interaction between PLGA NPs displaying a protein corona of different characteristics and HepG2 cells an IncuCyte®S3 Live-Cell Analysis Imaging System (Essen Bioscience, Inc., Michigan, USA) was used. Therefore, 1×10^5 cells/well were seeded into a collagen coated 24-well plate and cultivated under serum-containing conditions as described above. After four days, the medium was replaced by 500 µL serum-free medium containing Lumogen® Red-loaded PLGA NPs in a concentration corresponding to 0.2 nM Lumogen® Red. Furthermore, unformulated Lumogen® Red dissolved in serum-free medium with addition of 1% DMSO and serum-free medium without NPs were applied onto the cells as control. Subsequently, the cell interaction was monitored over a time period of one day taking nine images of each well every hour. Image channel red (excitation: 565–605 nm/emission: 625–705 nm) was used to determine Lumogen® Red. Data evaluation was performed by calculation of the total red object area using the system software.

Visualization of nanoparticle–cell interaction by fluorescence microscopy

For fluorescence microscopy, HepG2 cells were seeded at a density of 3×10^4 cells/chamber on Millicell® EZ slides (Merck KGaA, Darmstadt, Germany) and cultivated overnight. Afterwards, the serum-containing medium was removed and cells were incubated with Lumogen® Red-loaded PLGA NPs, free Lumogen® Red or serum-free medium as previously described. After 6 h, the cells were washed twice with phosphate-buffered saline (PBS^{++}, containing Ca^{2+} and Mg^{2+}) and fixed for 15 min with 4% paraformaldehyde at room temperature. After an additional washing step, the cells were covered with Vectashield® Mounting medium with DAPI (Vector Laboratories Inc., Burlingname, USA) for nuclear staining.

All images were taken using a IX81 fluorescence microscope (Olympus, Hamburg, Germany) with filter systems including excitation at 360–370 nm, dichroic mirror at 400 nm, emission at 426–446 nm for DAPI and Alexa Fluor® 350 and excitation at 535–555 nm, dichroic mirror at 565 nm, emission at 570–650 nm for Lumogen® Red. All images were taken as multi-layer image stacks with a minimum of 15 images. To reduce out of focus fluorescence the stacks were processed by deconvolution (Wiener filter) using cellSens Dimensions Software 1.8.1.

Statistical methods

All experiments were performed at least three times. The results are shown as average value with standard deviation. Significance tests were conducted with Sigma Plot 12.5 (Systat Software GmbH, Erkrath, Germany), using a one-way ANOVA test with the Holm–Sidak post test. Significance levels were depicted as * for $p \leq 0.05$, ** for $p \leq 0.01$, and *** for $p \leq 0.001$.

Supporting Information

Supporting Information File 1

Proteins identified on NP surfaces.
[https://www.beilstein-journals.org/bjnano/content/supplementary/2190-4286-10-101-S1.pdf]

ORCID® iDs

Klaus Langer - https://orcid.org/0000-0002-0203-7478

References

1. Yohan, D.; Chithrani, B. D. *J. Biomed. Nanotechnol.* **2014,** *10,* 2371–2392. doi:10.1166/jbn.2014.2015
2. Danhier, F.; Ansorena, E.; Silva, J. M.; Coco, R.; Le Breton, A.; Préat, V. *J. Controlled Release* **2012,** *161,* 505–522. doi:10.1016/j.jconrel.2012.01.043
3. Caracciolo, G.; Farokhzad, O. C.; Mahmoudi, M. *Trends Biotechnol.* **2017,** *35,* 257–264. doi:10.1016/j.tibtech.2016.08.011
4. Cedervall, T.; Lynch, I.; Lindman, S.; Berggard, T.; Thulin, E.; Nilsson, H.; Dawson, K. A.; Linse, S. *Proc. Natl. Acad. Sci. U. S. A.* **2007,** *104,* 2050–2055. doi:10.1073/pnas.0608582104
5. Docter, D.; Westmeier, D.; Markiewicz, M.; Stolte, S.; Knauer, S. K.; Stauber, R. H. *Chem. Soc. Rev.* **2015,** *44,* 6094–6121. doi:10.1039/c5cs00217f
6. Nguyen, V. H.; Lee, B.-J. *Int. J. Nanomed.* **2017,** *12,* 3137–3151. doi:10.2147/ijn.s129300
7. Caracciolo, G.; Pozzi, D.; Capriotti, A. L.; Cavaliere, C.; Foglia, P.; Amenitsch, H.; Laganà, A. *Langmuir* **2011,** *27,* 15048–15053. doi:10.1021/la202912f
8. Gräfe, C.; Weidner, A.; Lühe, M. v. d.; Bergemann, C.; Schacher, F. H.; Clement, J. H.; Dutz, S. *Int. J. Biochem. Cell Biol.* **2016,** *75,* 196–202. doi:10.1016/j.biocel.2015.11.005

9. Monopoli, M. P.; Walczyk, D.; Campbell, A.; Elia, G.; Lynch, I.; Baldelli Bombelli, F.; Dawson, K. A. *J. Am. Chem. Soc.* **2011,** *133,* 2525–2534. doi:10.1021/ja107583h
10. Mirshafiee, V.; Kim, R.; Mahmoudi, M.; Kraft, M. L. *Int. J. Biochem. Cell Biol.* **2016,** *75,* 188–195. doi:10.1016/j.biocel.2015.11.019
11. Pozzi, D.; Caracciolo, G.; Capriotti, A. L.; Cavaliere, C.; La Barbera, G.; Anchordoquy, T. J.; Laganà, A. *J. Proteomics* **2015,** *119,* 209–217. doi:10.1016/j.jprot.2015.02.009
12. Schöttler, S.; Klein, K.; Landfester, K.; Mailänder, V. *Nanoscale* **2016,** *8,* 5526–5536. doi:10.1039/c5nr08196c
13. Mahmoudi, M.; Abdelmonem, A. M.; Behzadi, S.; Clement, J. H.; Dutz, S.; Ejtehadi, M. R.; Hartmann, R.; Kantner, K.; Linne, U.; Maffre, P.; Metzler, S.; Moghadam, M. K.; Pfeiffer, C.; Rezaei, M.; Ruiz-Lozano, P.; Serpooshan, V.; Shokrgozar, M. A.; Nienhaus, G. U.; Parak, W. J. *ACS Nano* **2013,** *7,* 6555–6562. doi:10.1021/nn305337c
14. Casals, E.; Pfaller, T.; Duschl, A.; Oostingh, G. J.; Puntes, V. *ACS Nano* **2010,** *4,* 3623–3632. doi:10.1021/nn901372t
15. Pozzi, D.; Caracciolo, G.; Digiacomo, L.; Colapicchioni, V.; Palchetti, S.; Capriotti, A. L.; Cavaliere, C.; Zenezini Chiozzi, R.; Puglisi, A.; Laganà, A. *Nanoscale* **2015,** *7,* 13958–13966. doi:10.1039/c5nr03701h
16. Ghavami, M.; Saffar, S.; Abd Emamy, B.; Peirovi, A.; Shokrgozar, M. A.; Serpooshan, V.; Mahmoudi, M. *RSC Adv.* **2013,** *3,* 1119–1126. doi:10.1039/c2ra22093h
17. Pisani, C.; Rascol, E.; Dorandeu, C.; Gaillard, J.-C.; Charnay, C.; Guari, Y.; Chopineau, J.; Armengaud, J.; Devoisselle, J.-M.; Prat, O. *PLoS One* **2017,** *12,* e0182906. doi:10.1371/journal.pone.0182906
18. Gossmann, R.; Fahrländer, E.; Hummel, M.; Mulac, D.; Brockmeyer, J.; Langer, K. *Eur. J. Pharm. Biopharm.* **2015,** *93,* 80–87. doi:10.1016/j.ejpb.2015.03.021
19. Spek, S.; Häuser, M.; Schäfer, M. M.; Langer, K. *Appl. Surf. Sci.* **2015,** *347,* 378–385. doi:10.1016/j.apsusc.2015.04.071
20. García-Álvarez, R.; Hadjidemetriou, M.; Sánchez-Iglesias, A.; Liz-Marzán, L. M.; Kostarelos, K. *Nanoscale* **2018,** *10,* 1256–1264. doi:10.1039/c7nr08322j
21. Tenzer, S.; Docter, D.; Rosfa, S.; Wlodarski, A.; Kuharev, J.; Rekik, A.; Knauer, S. K.; Bantz, C.; Nawroth, T.; Bier, C.; Sirirattanapan, J.; Mann, W.; Treuel, L.; Zellner, R.; Maskos, M.; Schild, H.; Stauber, R. H. *ACS Nano* **2011,** *5,* 7155–7167. doi:10.1021/nn201950e
22. Schäffler, M.; Semmler-Behnke, M.; Sarioglu, H.; Takenaka, S.; Wenk, A.; Schleh, C.; Hauck, S. M.; Johnston, B. D.; Kreyling, W. G. *Nanotechnology* **2013,** *24,* 265103–265111. doi:10.1088/0957-4484/24/26/265103
23. Walkey, C. D.; Chan, W. C. W. *Chem. Soc. Rev.* **2012,** *41,* 2780–2799. doi:10.1039/c1cs15233e
24. Vroman, L.; Adams, A. L.; Fischer, G. C.; Munoz, P. C. *Blood* **1980,** *55,* 156–159.
25. Ogawara, K.-i.; Furumoto, K.; Nagayama, S.; Minato, K.; Higaki, K.; Kai, T.; Kimura, T. *J. Controlled Release* **2004,** *100,* 451–455. doi:10.1016/j.jconrel.2004.07.028
26. Owens, D. E.; Peppas, N. A. *Int. J. Pharm.* **2006,** *307,* 93–102. doi:10.1016/j.ijpharm.2005.10.010
27. Zhang, T.-X.; Zhu, G.-Y.; Lu, B.-Y.; Zhang, C.-L.; Peng, Q. *Nanomedicine (London, U. K.)* **2017,** *12,* 2757–2769. doi:10.2217/nnm-2017-0238
28. Colapicchioni, V.; Tilio, M.; Digiacomo, L.; Gambini, V.; Palchetti, S.; Marchini, C.; Pozzi, D.; Occhipinti, S.; Amici, A.; Caracciolo, G. *Int. J. Biochem. Cell Biol.* **2016,** *75,* 180–187. doi:10.1016/j.biocel.2015.09.002
29. Yao, X.; Gordon, E. M.; Figueroa, D. M.; Barochia, A. V.; Levine, S. J. *Am. J. Respir. Cell Mol. Biol.* **2016,** *55,* 159–169. doi:10.1165/rcmb.2016-0060tr
30. Schöttler, S.; Becker, G.; Winzen, S.; Steinbach, T.; Mohr, K.; Landfester, K.; Mailänder, V.; Wurm, F. R. *Nat. Nanotechnol.* **2016,** *11,* 372–377. doi:10.1038/nnano.2015.330
31. Gessner, A.; Waicz, R.; Lieske, A.; Paulke, B.-R.; Mäder, K.; Müller, R. H. *Int. J. Pharm.* **2000,** *196,* 245–249. doi:10.1016/s0378-5173(99)00432-9
32. Kreuter, J.; Hekmatara, T.; Dreis, S.; Vogel, T.; Gelperina, S.; Langer, K. *J. Controlled Release* **2007,** *118,* 54–58. doi:10.1016/j.jconrel.2006.12.012
33. Ricklin, D.; Hajishengallis, G.; Yang, K.; Lambris, J. D. *Nat. Immunol.* **2010,** *11,* 785–797. doi:10.1038/ni.1923
34. Chen, F.; Wang, G.; Griffin, J. I.; Brenneman, B.; Banda, N. K.; Holers, V. M.; Backos, D. S.; Wu, L.; Moghimi, S. M.; Simberg, D. *Nat. Nanotechnol.* **2017,** *12,* 387–393. doi:10.1038/nnano.2016.269
35. Hu, Z.; Zhang, H.; Zhang, Y.; Wu, R.; Zou, H. *Colloids Surf., B* **2014,** *121,* 354–361. doi:10.1016/j.colsurfb.2014.06.016
36. Suk, J. S.; Xu, Q.; Kim, N.; Hanes, J.; Ensign, L. M. *Adv. Drug Delivery Rev.* **2016,** *99,* 28–51. doi:10.1016/j.addr.2015.09.012
37. Raudszus, B.; Mulac, D.; Langer, K. *Int. J. Pharm.* **2018,** *536,* 211–221. doi:10.1016/j.ijpharm.2017.11.047
38. Calatayud, M. P.; Sanz, B.; Raffa, V.; Riggio, C.; Ibarra, M. R.; Goya, G. F. *Biomaterials* **2014,** *35,* 6389–6399. doi:10.1016/j.biomaterials.2014.04.009
39. Bradford, M. M. *Anal. Biochem.* **1976,** *72,* 248–254. doi:10.1006/abio.1976.9999
40. Ma, B.; Zhang, K.; Hendrie, C.; Liang, C.; Li, M.; Doherty-Kirby, A.; Lajoie, G. *Rapid Commun. Mass Spectrom.* **2003,** *17,* 2337–2342. doi:10.1002/rcm.1196
41. Zhang, J.; Xin, L.; Shan, B.; Chen, W.; Xie, M.; Yuen, D.; Zhang, W.; Zhang, Z.; Lajoie, G. A.; Ma, B. *Mol. Cell. Proteomics* **2012,** *11,* M111.010587. doi:10.1074/mcp.m111.010587

License and Terms

BEILSTEIN JOURNAL OF NANOTECHNOLOGY

Nanoporous smartPearls for dermal application – Identification of optimal silica types and a scalable production process as prerequisites for marketed products

David Hespeler[1], Sanaa El Nomeiri[2], Jonas Kaltenbach[3] and Rainer H. Müller[*1]

Full Research Paper

Open Access

Address:
[1]Pharmaceutical Technology, Institute of Pharmacy, Freie Universität Berlin, Kelchstraße 31, 12169 Berlin, Germany, [2]Department for Mathematics, Physics and Chemistry, Beuth Hochschule für Technik Berlin, Luxemburger Straße 10, 13353 Berlin, Germany and [3]Institute of Functional Interfaces, Karlsruher Institute of Technology, Hermann-von-Helmholtz-Platz 1, 76344 Eggenstein-Leopoldshafen, Germany

Email:
Rainer H. Müller[*] - nanoteam@gmx.com

* Corresponding author

Keywords:
amorphous dispersion; bioavailability enhancement; dermal delivery system; rutin; smartPearls; solubility enhancement

Beilstein J. Nanotechnol. **2019,** *10,* 1666–1678.
doi:10.3762/bjnano.10.162

Received: 05 April 2019
Accepted: 16 July 2019
Published: 08 August 2019

This article is part of the thematic issue "Frontiers in pharmaceutical nanotechnology".

Guest Editor: M. G. Wacker

Abstract

smartPearls are a dermal delivery system for poorly soluble active agents, consisting of nanoporous silica particles loaded with a long-term stable, amorphous active agent in its mesopores (2–50 nm). The amorphous state of the active agent is known to increase dermal bioavailability. For use in marketed products, optimal silica types were identified from commercially available, regulatory accepted silica. In addition, a scalable production process was demonstrated. The loading of the particles was performed by applying the immersion–evaporation method. The antioxidant rutin was used as a model active agent and ethanol was applied as the solvent. Various silica particles (Syloid®, Davisil®) differing in particle size (7–50 µm), pore diameter (3–25 nm) and pore volume (0.4–1.75 mL/g) were investigated regarding their ease of processing. The evaporation from the silica–ethanol suspensions was performed in a rotary evaporator. The finest powders were obtained with larger-sized silica. The maximum loading staying amorphous was achieved between 10% and 25% (w/w), depending on the silica type. A loading mechanism was also proposed. The most suitable processing occurred with the large-sized Syloid® XDP 3050 silica with a 50 µm particle size and a pore diameter of 25 nm, resulting in 18% (w/w) maximum loading. Based on a 10% (w/w) loading and the amorphous solubility of the active agent, for a 100 kg dermal formulation, about 500 g of loaded particles were required. This corresponds to production of 5 kg of loaded smartPearls for a formulation batch size of a ton. The production of 5 kg (i.e., about 25 L of solvent removal) can be industrially realized in a commercial 50 L rotary evaporator.

Introduction

Many interesting active agents in pharma and cosmetics are poorly soluble. Active agents that are poorly soluble in water but soluble in lipophilic media can easily be formulated as creams or gels (e.g., the popular coenzyme Q10). The problems start when the active agents are poorly soluble both in aqueous and lipophilic/organic media. Classical examples are antioxidants (e.g., rutin, hesperidin), which are presently en vogue in cosmetics for antipollution products (e.g., the "molecular barrier" against reactive oxygen species (ROS), infrared (IR) radiation and blue light from computers) [1,2]. For the delivery of such molecules, efficient delivery systems are the only solution, because the application of simple suspensions to the skin normally does not provide a sufficient dermal bioavailability.

Classic delivery systems such as liposomes [3] or solid lipid nanoparticles (SLNs) [4,5] do not work because the active agents do not dissolve in the lipidic phase of these systems. A simple but very effective approach is to increase the saturation solubility of these active agents. This leads to an increased concentration gradient between the formulation and skin, C_s–C_{skin}, and thus to an increased diffusional flux into the skin. Moreover, using complexes with polymers or cyclodextrins, for example, can be of limited effect because of insufficient release of the molecules from such complexes (i.e., too high binding constants) [6,7]. Additionally, many molecules are not able to form such complexes. A highly effective solution is the dermal administration of nanocrystals (trade name smartCrystals®) [8-10]. These materials have been on the market as commercial dermal cosmetic products since 2007 (e.g., hesperidin, la prairie Switzerland) [11,12]. They can be considered as the current "gold standard".

The trick with nanocrystals is that the physicochemical properties on the micrometer scale differ from those on the nanometer scale, and this results in distinct changes (e.g., the saturation solubility distinctly increases) [13]. In general, amorphous materials have an even higher C_s than nanocrystalline materials [14]. Thus, it would be more effective to use active agents in the amorphous state. However, the amorphous state is physically unstable. Because of their high free energy, amorphous phase materials tend to recrystallize [15], especially in the presence of liquids [16]. This has hindered the broad application of amorphous active agents in dermal formulations. The company Capsulution (Berlin, Germany) incorporated active agents in the amorphous state inside the pores of silica particles with mesopores (2–50 nm) [17] using the technology from CapsMorph for oral administration [18]. With this, the amorphous state could be stabilized over the course of years [19]. Porous silica particles are commercially available, for example, from Grace, Merck Millipore and Formac [20]. They are considered nanoporous materials because their pore diameter is on the nanometer scale [21]. The silica they used had so-called "mesopores", i.e., pores with dimensions in the range of 2–50 nm. In 2006 this delivery technology was transferred from the oral to the dermal administration route [22] by applying a technology called smartPearls [23]. The name was changed to smartPearls to clearly differentiate them from silica used for oral administration.

smartCrystals are found in products on the cosmetic market, because industrial large-scale production is possible and an industrial supplier is available (Dr. Rimpler GmbH, Germany) for manufacturers of cosmetics. smartCrystals are crystals of nanometer dimension, typically 200–400 nm, which can be produced on a large scale by bead milling or high-pressure homogenization. Skin penetration studies showed that the smartPearls were actually superior to the nanocrystals [8,24,25]. However, the market introduction in final cosmetic products was blocked due to the lack of an industrial supplier of active agent-loaded smartPearls. To establish an industrial supply, an industrially feasible production method is required, which is the focus of this work.

Silica particles can be loaded by co-milling [26,27], however, with this technique, a large portion of the active agents are not incorporated into the pores. Loading can be performed by supercritical carbon dioxide processing [28], but it is expensive. Loading is also possible by the impregnation–evaporation method [29], but this is less suitable for large-scale production. In this study, the immersion–evaporation method [30] was applied and systematically investigated to define large-scale production parameters for an industry friendly one-step production process. Rutin was used as the model active agent because it has high application potential in cosmetic products as well as in dermal pharmaceutical products [31]. A loading mechanism for this industrial process is proposed in this work. In addition, the concentration of smartPearls in the final dermal products are estimated based on the achieved loadings and on the solubility data. This work could serve as a guideline for manufacturers of dermal products. Different types of silica were investigated having various parameters (e.g., particle size, pore diameter, pore volume) in order to identify particles which are most easy to process.

Materials and Methods

Materials

Rutin with a purity of 95% was purchased from Denk Ingredients (Munich, Germany). Various mesoporous silica particles (Table 1) with pore diameter of 3 nm (Syloid® AL-1 FP), 6 nm

Table 1: Silica particles used in this work and their properties according the certificate of analysis (manufacturer: W. R. Grace & Co., USA).

Product code	Pore diameter [nm]	Specific surface area [m^2/g]	Pore volume [mL/g]	Particle size [µm]
Syloid® XDP 3050	25	300	1.8	50
Syloid® 244 FP	17	380	1.6	3
Syloid® 72 FP	10	370	1.2	5
Davisil® SP53D	6	550	0.9	12
Syloid® AL-1 FP	3	740	0.4	7

(Davisil® LC 60 Å 12 µm), 10 nm (Syloid® 72 FP), 17 nm (Syloid® 244 FP), and 25 nm (Syloid® XDP 3050) were kindly provided by Grace GmbH & Co. KG (Worms, Germany). Ethanol, isopropanol, butanol, acetone, ethyl acetate, acetonitrile and dimethyl sulfoxide (DMSO) in gradient grade were purchased from VWR (Darmstadt, Germany), and purified water produced by a Milli-Q system from Merck Millipore (Darmstadt, Germany) was used.

Methods

Solubility investigation of rutin

To assess the maximum solubility of rutin, rutin suspensions were prepared with different solvents (dimethyl sulfoxide (DMSO), ethanol, isopropanol, butanol, acetone, ethyl acetate, acetonitrile, and water) (n = 1). The suspensions with 20% (w/w) rutin were shaken overnight at room temperature, centrifuged, filtered and the rutin concentration in the filtrate was analyzed after dilution in ethanol (by a factor of 100–1000) by UV spectrophotometry (UV-1700 PharmaSpec, Shimadzu, China) at 360 nm. The evaluation was conducted by the provided "UVprobe" software (version 2.21). The concentration was calculated based on the calibration curves determined in ethanol.

Particle loading

Prior to loading, the silica particles were dried in an oven at 120 °C for at least 2 h. The saturated rutin solution was produced by preparing a 2% (w/w) rutin suspension in ethanol (96 vol %), heating it under agitation to 60 °C for 1 h and subsequent filtration. After cooling, it was checked that no rutin crystals precipitated out. The rutin content was determined prior using the rutin solution for loading. For loading, 3 g of silica particles were dispersed in a respective volume of rutin ethanol solution. The volume used depended on how much rutin should be loaded into the silica particles (increasing amounts of solution with increased percent of loading). The suspension was stirred for 5 min to achieve a fine dispersion of the particles. Then the suspension was placed into a rotary evaporator (Büchi, Germany). The solvent evaporation took place at 40 ± 2 °C and 150 ± 10 mbar, until a film was formed on the wall of the evaporation flask. The evaporation time depends on the amount of solvent used (i.e., increased evaporation time with an increase of loading percentage). For removal/minimization of solvent residues, a secondary drying phase at 40 ± 2 °C and 20 mbar was performed for 30 min. All fractions presented are weight fractions unless otherwise stated. Each loading for each type of silica was performed once.

Differential scanning calorimetry (DSC)

The physical state of the silica particles, the rutin raw active agent powder and the rutin smartPearls was investigated by differential scanning calorimetry (DSC, Mettler Toledo GmbH, Germany) and calculated by the provided STARe software (version 12.10b). Exact amounts between 1–5 mg of rutin-loaded silica based on the respective mass of rutin (with a target of 0.5–1 mg) were weighed in a punctured 40 µL aluminum pan and sealed (n = 1). The measurements were performed at a heating rate of 20 K/min between 25 and 300 °C under 80 mL/min nitrogen purge.

X-ray diffraction (XRD)

To determine the amorphous state and possible residual crystal fractions of rutin in smartPearls, XRD was performed using a Bruker D8 (Bruker, USA) instrument (n = 1). A scan rate of 0.02°/s (2θ = 2–60°) was applied and the goniometer was equipped with a Cu anode (Cu Kα, λ= 0.15406 nm) at a voltage of 40 kV and current of 35 mA.

Light microscopy (LM) and scanning electron microscopy (SEM)

Light microscope imaging was performed using a Motic microscope (BA210, Motic Deutschland GmbH, Germany) with a Moticam camera and the software Motic Images Plus at 100, 400, and 1,000-fold magnification. SEM was performed at 10,000-fold magnification using a Zeiss DSM950 (Carl Zeiss AG, Germany) instrument. The samples were sputter-coated with gold–palladium in an argon atmosphere at 15–20 kV at 0.05 mbar for four minutes.

Determination of recovery rate

For photometric analysis, a precisely weighed amount of rutin-loaded silica particles (around 25 mg) was dispersed in 5 mL of

DMSO. DMSO was used because of the high rutin solubility in this solvent. After 10 min of shaking and 10 min of ultrasonication the suspension was centrifuged at 10,000 rpm for 10 min and an aliquot of the supernatant was diluted in ethanol by a factor of 100. Absorption spectroscopy was performed at 360 nm on a PharmaSpec UV-1700 instrument (Shimadzu, China). The peaks were evaluated using the PharmSpec software "UVprobe" (version 2.21).

High-performance liquid chromatography (HPLC) measurements of the same samples were performed at 25 °C using a Kontron 400 system (Kontron Instruments GmbH, Germany) equipped with a 20 µL loop and a Eurosper 100-5 C18 column (250 × 4 mm, 5 µm particle size) column. Determination was performed at 360 nm with 20:80 acetonitrile/acetate buffer (pH 4.8, 0.1 mol/L) as a mobile phase and at a flow rate of 1.25 mL/min. The peaks were evaluated with the provided software, KromaSystem 2000 (version 1.82).

Solubility determination of rutin dissolved from smartPearls

The solubility of the raw rutin active agent powder and the rutin smartPearls was monitored over one hour in 0.15 molar NaCl solution using in situ UV–vis measurements (Sirius inForm®, UK) with a fiber optic collector and a path length of 5 mm. The 0.15 molar NaCl solution was placed in a beaker and the aqueous phase was tempered to 25 °C. After calibration of the pH electrode and the UV–vis fiber optic, the sample was manually added immediately after and the UV–vis measurement with the fiber optic was started. The spectra were corrected using the Tyndall Rayleigh correction function. The different concentrations of raw active agent powder and rutin smartPearls were investigated, limited by a maximum overall absorption up to 2.5. The pH was determined over the whole measurement period.

Results and Discussion

Considerations for selection of the production method/variables

The production method should yield a high loading in the pores and complete transformation of the active agent into the amorphous state, thus co-grinding was excluded as a potential production method. Also excluded was supercritical CO_2 processing, due to production cost reasons, complexity of the process and cost of a production unit. Ideally, the processing method should be a one-step method. This excludes the impregnation–evaporation process, because in many cases one impregnation step is not sufficient to reach the anticipated loading. Thus, the immersion–evaporation process was selected.

The evaporation time of the solvent removal step ranged from 75 to 180 min, depending on the solvent volume. After the second drying step, the obtained free flowing, dry powder was removed. When a film was formed on the glass wall, the film was removed from the wall using a spatula. Potential aggregates were deaggregated by stirring the powder, whereby the aggregates were easily dispersed. The results from the processing steps are shown in Figure 1.

The principle of the procedure was to suspend the particles in an amount of solvent containing the total amount of active agent to be loaded into the pores of the particles. During the evaporation process, the concentration of the active agent increases, precipitation takes place, and continues until complete removal of the solvent. It was expected that precipitation takes place preferentially in the pores because of the largest available surface area. Minor precipitation on the outer shell of the particles as a thin layer represents no problem as long as the active agent on the surface remains amorphous. It is obvious that in addition to the inner surface in the pores, localization on the surface of silica particles also takes place. It is important to

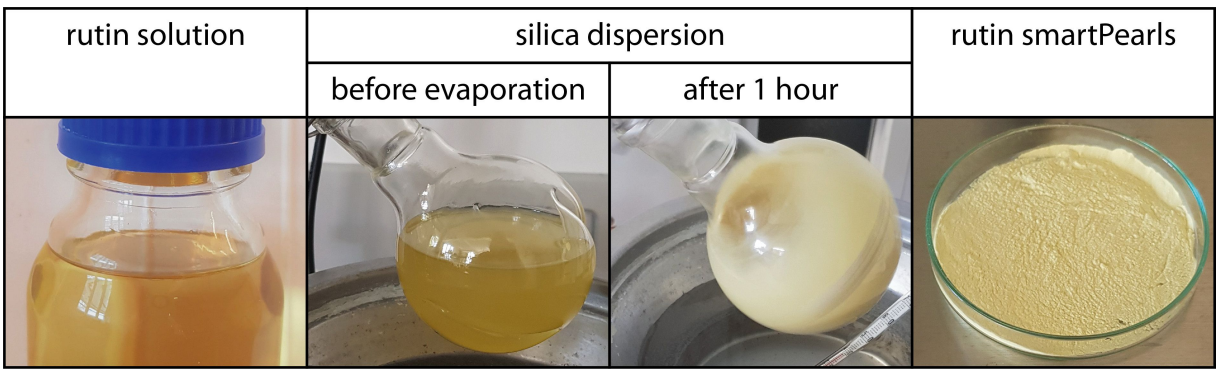

Figure 1: From left to right: rutin/ethanol solution, silica dispersed in rutin solution attached to the rotary evaporator, result after the first hour of solvent evaporation, and the obtained rutin-loaded silica powder, SP53D (right).

avoid the formation of crystals of the active agent on the shell of the particles. This was checked by light microscopy and scanning electron microscopy.

To study the suitability of the process, silica particles differing in particle size, pore diameter and pore volume were selected (Table 1). The investigation should also provide evidence as to which particle type is optimal to achieve maximum loading.

Solubility of rutin in solvents

A compromise had to be made between the highest possible solubility of rutin and the tolerability of the solvent by the skin. Furthermore, processing parameters such as evaporation temperature were crucial. DMSO was used in previous studies with the impregnation–evaporation method [24] because it has a high solubility and thus reduces the number of loading steps. The disadvantage was the long time required for solvent removal at high temperatures (>80 °C), which can cause degradation of the active agent. In addition, it is tedious to remove DMSO efficiently by rotary evaporation. Although DMSO can be found in products applied to the skin, it is less skin friendly. The efficient removal of critical solvents below the ppm specification is also a cost factor in the production process. Thus, a different, more skin-tolerable solvent was desirable.

Table 2 shows the obtained solubility of rutin in the various tested solvents. Rutin has the highest solubility in DMSO (17%), as expected, but it was decided to select ethanol as a compromise. With a maximum of 2%, the rutin solubility is substantial lower in ethanol than in DMSO, but distinctly higher than in acetone (0.8%) and the other organic solvents. The rutin/ethanol solution had a clear, yellowish appearance.

Table 2: Solubility of rutin at room temperature in various solvents (w/w %) and the macroscopic appearance of the solutions.

Solvent	Solubility [% (w/w)]	Appearance
DMSO	17.05	brown
ethanol	2.09	clear, bright yellow
n-butanol	2.07	clear, bright yellow
isopropanol	1.85	clear, bright yellow
acetone	0.83	pale yellow
ethyl acetate	0.42	mildly cloudy
acetonitrile	0.22	mildly cloudy
water	0.03	cloudy, slight yellow

Loading of silica particles

Different silica materials (Table 1) were loaded with rutin by dispersing them in a saturated rutin/ethanol solution and evaporating the solvent in a rotary evaporator, resulting in dry powders. Nitrogen adsorption/desorption studies were performed, showing little decrease in the pore diameter, but a reduction of the pore volume, supporting the bottom-to-top filling hypothesis of the pores [32,33]. Depending on the particle size and the pore diameter, the powders showed different macroscopic appearances (Figure 2). The silica AL-1 FP tended to form aggregates, and possessed particle diameter of 7 µm. The silica materials with the smallest pore diameter, 244 FP and 72 FP (particle diameter 3 and 5 µm; pore diameter 10 and 17 nm, respectively), showed slight agglomeration. SP53D,

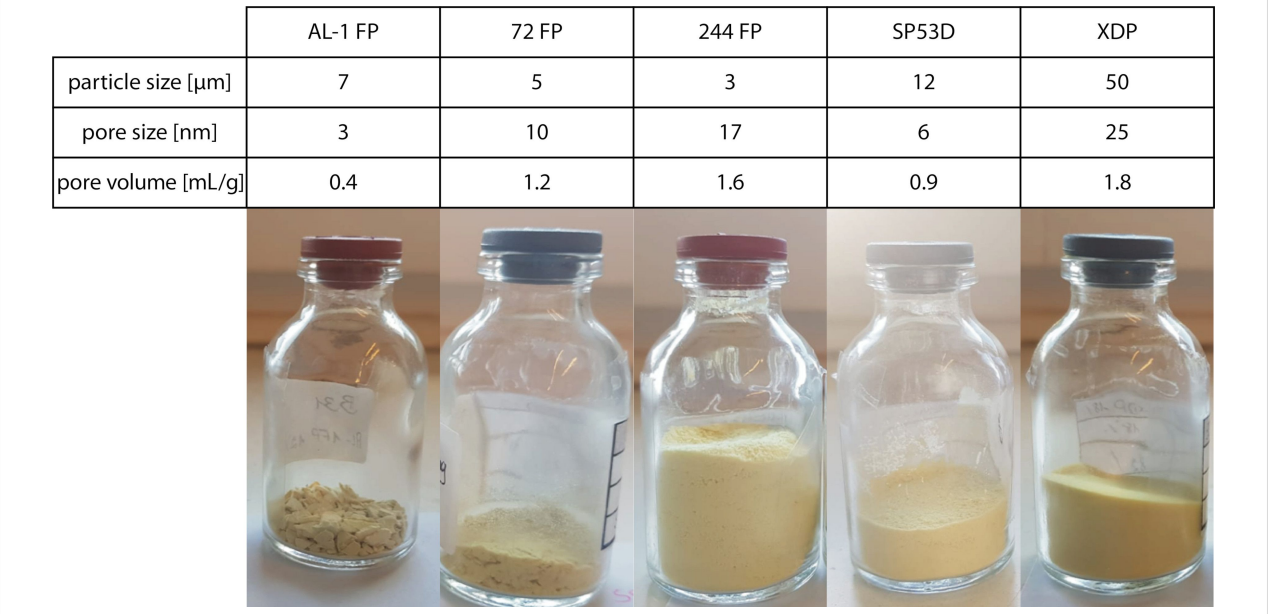

Figure 2: Macroscopic appearance of rutin-loaded silica powders, with decreasing agglomeration tendency from left to right (see text for details).

having a medium-sized particle size of 12 µm, showed almost no agglomeration, and at a higher loading of 28% and 30%, a film formed on the wall of the evaporator glass. The XDP 3050 particles, having the largest diameter of 50 µm (pore diameter of 25 nm), showed neither agglomeration nor film formation.

It is known that silica particles become more adhesive with decreasing size, which is easily explainable by powder technology. With decreasing particle size, the surface and contact area increase, thus promoting particle–particle interaction. Additionally, with increasing pore diameter, the agglomeration tendency decreases. The particles with a strong agglomeration tendency (AL-1 FP) have the smallest pore diameter of 3 nm, and additionally, the smallest pore volume. It is assumed that the pore parameters only play a significant role in agglomeration tendency when the pore volume is completely filled with active agent or when the pores are too small; this implies that an overloading takes place and the precipitating active agent acts as a kind of glue between the silica particles. This was assumed for the AL-1 FP samples since rutin with a molar weight of 610.5 g/mol and a minimum projection area of 9.2 nm^2 was assumed to be too large to efficiently diffuse into the pores prior to precipitation. Thus, such small pores promote agglomeration on the outside of the pores. Based on the behavior observed, silica particles with a larger size, larger pores and larger pore volume are easier to process on a large scale.

Determination of amorphous-phase content

The degree of amorphous phase of the loading was determined by performing DSC and XRD. An amount of 5% rutin in the physical mixture with amorphous unloaded silica was detectable by DSC. The analysis of the physical mixture of silica with crystalline rutin powder showed that an amount of only 3% crystalline rutin was clearly detectable by XRD, while 1.5% was hardly detectable (XRD not shown).

Figure 3 shows the DSC thermograms for the maximum-loaded silica, SP53D, which was loaded using different solvents and compared to unloaded silica, rutin and their physical mixture. In the physical mixture, 5% rutin was clearly detectable. No rutin peak was detectable for loadings up to 25% with ethanol, 28% with butanol and 35% with DMSO. Crystalline rutin was clearly detectable for a 28% loading with ethanol (detectable in temperature range 175–190 °C). It was thus concluded that the limit of loading in the amorphous state was 25% using ethanol as the solvent. As reported by Jin [24], loadings of 32% are achievable with DMSO using the impregnation–evaporation method. The same loading, or even higher, can be achieved using the immersion–evaporation method. However, the immersion–evaporation method is scalable and thus of more practical relevance. Since DMSO is a difficult to process solvent and more expensive than ethanol, a loading of 25% using ethanol is considered favorable.

Figure 4 shows XRD patterns of rutin in comparison to unloaded amorphous silica, crystalline rutin and their physical mixture. The respective XRD patterns of rutin-loaded SP53D silica with ethanol (25% loading), butanol (28% loading) and DMSO (35% loading) as solvents revealed the amorphous nature of these samples. A rutin peak was detectable in the physical mixture with 3% rutin. The crystalline rutin peaks

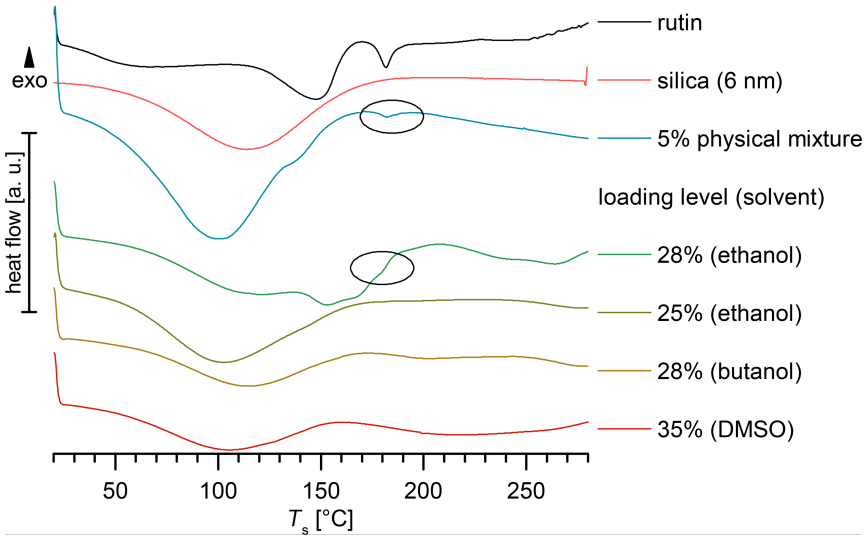

Figure 3: DSC thermograms of crystalline rutin, unloaded silica, a physical mixture of 5% rutin, to be compared to rutin-loaded SP53D processed with ethanol (28% and 25%), butanol (28%) and DMSO (35%).

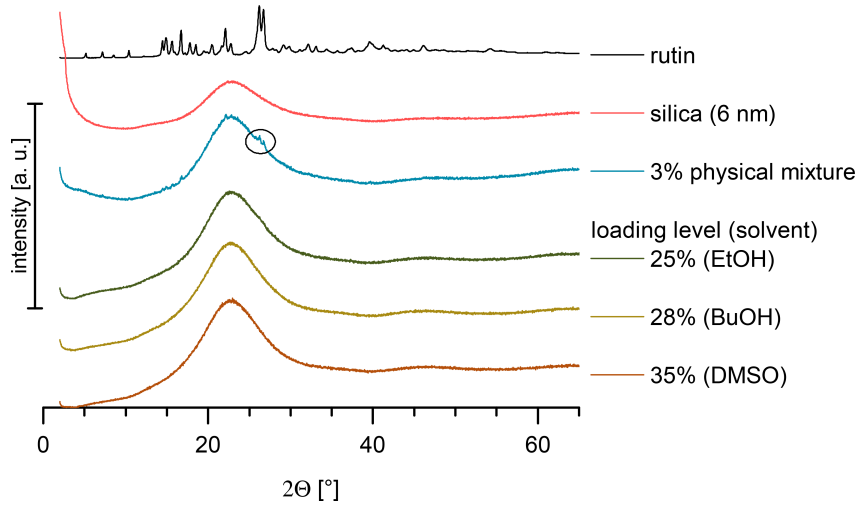

Figure 4: XRD of rutin, unloaded silica (SP53D), and a physical mixture (3% rutin) in comparison to the maximum loading with rutin-loaded silica SP53D using different solvents (ethanol, butanol, DMSO).

were only detectable for SP53D loaded with 28% rutin using ethanol as a solvent, which is in agreement with the DSC data. Even the silica with a high loading of up to 35% (loaded with DMSO) was a stable, amorphous material. As mentioned, the industrial feasibility is more important maximizing the achievable loading. To be on the safe side, 20% loadings produced with ethanol were used for determination of the saturation solubility, and this is recommended as the maximum loading for commercial use.

Figure 5 shows a comparison between all investigated silica samples, where the DSC curves (left) and XRD patterns (right) are plotted with the highest achievable loading of amorphous material for each silica type, showing no peaks for appropriately loaded silica samples. Only for 72 FP (the curve with no peaks (20% loading), and the curve with peaks are plotted (system overloaded, 25%). For AL-1 FP samples (the silica with the smallest pore size of 3 nm) only the overloaded curves are shown (12% and 15%). The comparison between DSC and XRD reveals that XRD was more sensitive to detecting crystallinity. In all overloaded systems, where peaks could be detected by XRD, no peaks could be seen in DSC. Thus, applying both methods in parallel was necessary. In conclusion, silica with a very small pore size of 3 nm are deemed to be less

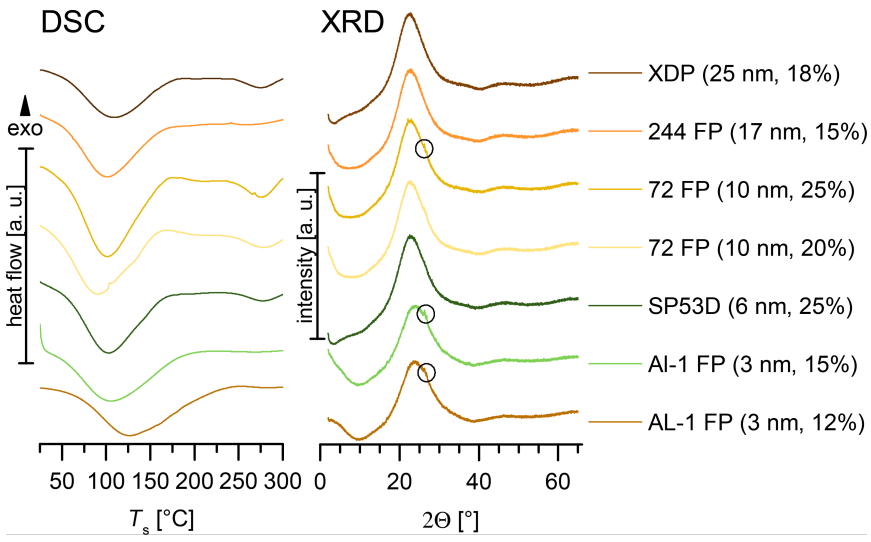

Figure 5: DSC thermograms (left) and XRD diffractograms (right) for selected silica nanoparticles, all loaded using ethanol as the solvent for rutin, showing curves with highest amorphous loading. For 72 FP (10 nm pores) the curves obtained with the overloaded system (25%) are also shown, and for AL-1 FP, only overloaded curves are presented (pore size 3 nm, 12% and 15% loading).

suitable. The loading of the other silica materials was generally between 15% and 25%.

Light microscopy and scanning electron microcopy

Light microscopy is readily accessible and fast to perform; thus, it was also used to follow the loading process. Light microscopy provides a general overview with one glance. When rutin crystals are present outside of the silica particles, they should be easily detectable. Also, it was expected to see changes on the surface of the silica, i.e., evidence of deposition of rutin. Figure 6 (upper row) shows exemplarily images of XDP 3050 particles. When unloaded, the silica particles appear translucent (upper left); loading rutin into the pores results in the coloring of the particles (upper middle). It is apparent that after loading some particles are still relatively translucent, while other particles become light to medium colored, although very dark colored particles can also be seen. That means that not all particles are loaded to the same degree, and thus there is a wide loading distribution among the particles. This is important for understanding the process. When adding more rutin solution, the heavily loaded particles will first show a crystalline fraction (due to rutin crystallizing on the surface). The overloaded system with 20% rutin (upper right) shows a majority of dark colored particles.

In Figure 6 (lower low), the SEM of unloaded silica (lower left) shows a smooth surface, almost free of fine particulate material. The maximum loaded particles (lower row, middle) show some fine particulate material on the surface. From light microscopy it can be concluded that there is a distribution in the degree of particle loading. Thus, the problem in SEM analysis is to distinguish to which particles the microscope is focusing on. In the sample XDP 3050 with overloaded silica (20% loading, lower right), the particles can be found with pronounced fine particulate material on the surface of some of the 50 µm silica particles.

In conclusion, light microscopy is a suitable complementary tool for evaluating the loading process, while SEM provides additional insight into the mechanism behind the loading process, but is not essential for batch monitoring during an industrial production process.

Based on this analysis, a loading mechanism is proposed (Figure 7) using the example of a silica material with a pore volume of 1.8 mL/g. At the beginning (before loading), all pores are empty (0 mL/g, see the upper graph in Figure 7). As seen from the light microscopy pictures (after the loading process), obviously some of the particles remain unfilled (light/transparent particles), some are partially filled, and some are heavily filled (very dark particles). This is represented in Figure 7 in the middle graph. The degree of solvent penetration into different particles varies, leading to particles remaining unfilled (at 0 mL/g filling) or particles that are partially or medium filled (0–0.4 and 0.4–0.8 mL/g, respectively). There are

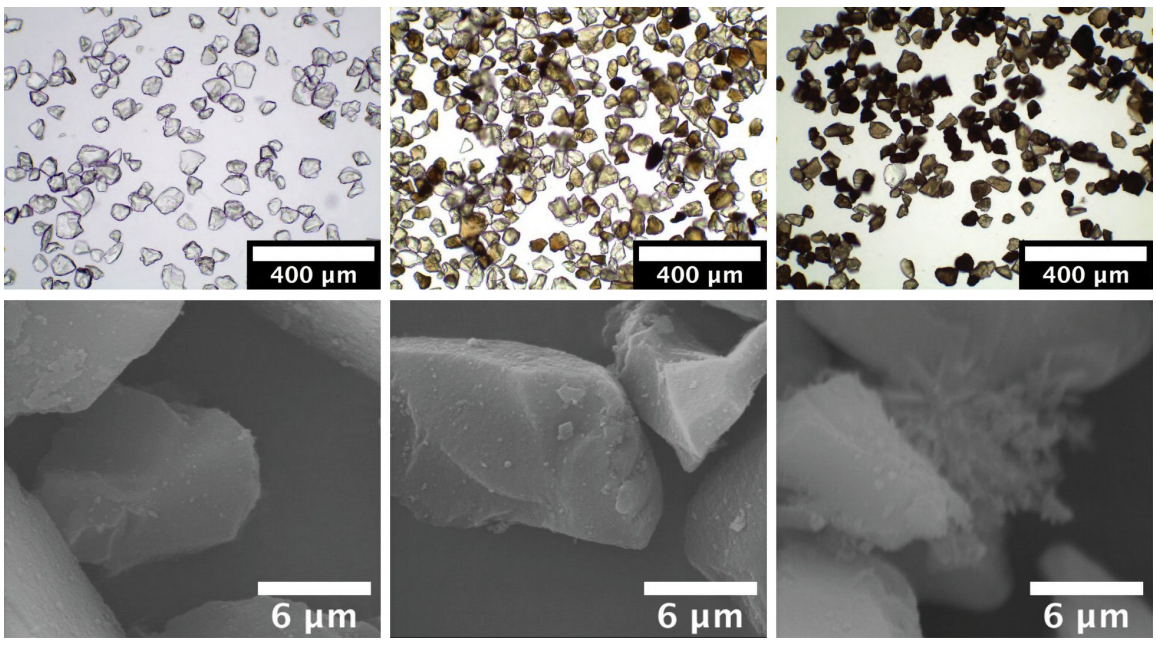

Figure 6: Upper row: light microscopy pictures of silica XDP 3050 unloaded (left), loaded with the maximum amorphous fraction of 18% (middle) and overloaded silica (20% rutin, right). Lower row: corresponding SEM pictures (from left to right).

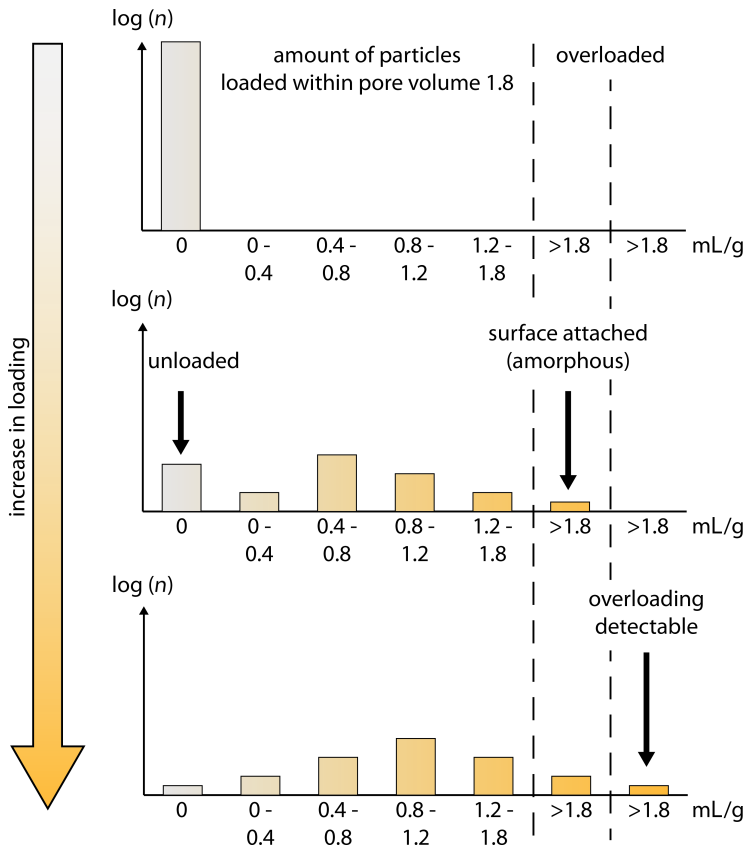

Figure 7: Description of the silica particle loading mechanism showing the distribution of differently filled particles as a function of loading. Upper plot: in the unloaded state, all particles fall within the 0 mL/g fraction. Middle plot: maximum loading condition where no crystallinity was detectable by XRD; the particles are filled to various extents, possibly with some being overloaded (>1.8 mL/g). Lower plot: some particles are obviously overloaded; the population contains a particle fraction in which detectable crystallization occurred.

also particles with higher pore volume filling (0.8–1.2 and 1.2–1.8 mL/g) and also particles with completely filled pores (filled volume 1.8 mL), which additionally have rutin on the surface. This implies that the rutin volume per gram of particles for these samples is >1.8 mL/g (Figure 7, middle). This surface material is amorphous, since no evidence of crystallinity was detected.

If too much rutin solution is used and evaporation continues, rutin continues to precipitate on the surface of completely loaded particles. When rutin deposits as a thin layer on the surface, the rutin stays amorphous; when the layer thickness increases above a critical threshold, crystallization occurs which can be detected by DSC/XRD (Figure 7, lower plot). For the use of the particles on the skin one could even argue that overloaded systems can be used, because the vast majority of the particles contain the amorphous phase active agent.

Loading efficiency – recovery rate

It was also investigated whether the initial content of rutin in the different particle types could be recovered. The rutin was extracted with a solvent, and the amount was determined by spectrophotometry and HPLC. The coefficient of determination was 0.9943 for HPLC and 0.9921 for UV spectrophotometric measurements. Figure 8 shows the amount recovered for two

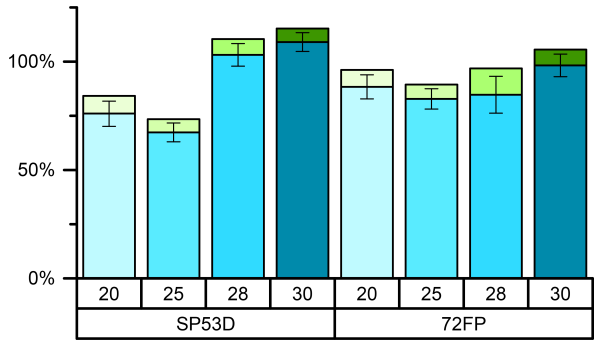

Figure 8: Recovered fraction of rutin after extraction from silica SP53D (left) and 72 FP (right) with rutin loadings of 20%, 25%, 28% and 30%, as measured with HPLC (blue) and spectrophotometry (green). The standard deviation is shown as the mean of all measurements (HPLC $n = 2$, UV $n = 1$).

silica samples, SP53D and 72 FP, with loadings from 20% to 30%. The SP53D and 72 FP silica are shown because of their high loading (>20%) and suitability for amorphous rutin stabilization.

At lower loadings (i.e., 20%, 25%) a minor fraction could not be recovered. It is reported in the literature that, due to the large surface area, a delayed release takes place, where some active agent is quite firmly bound to the surface and is thus not released [34]. Thus, the absolute retrieved amount increases with increasing loading. Additionally, the higher recovery rates for samples with a certain crystallinity is remarkable. This could explain the higher recovery rate at higher loadings of 28–30%. The silica sample with the smaller pores (3 nm, AL-1 FP) showed at low maximum loading (12%) and a recovery rate of only about 35%. The recovery rate was also analyzed by HPLC, and the recovery fractions are all slightly below, but in agreement with, the values obtained using spectrophotometry, as shown in Figure 8.

The difference in the results obtained from UV spectrophotometry and HPLC analysis can be explained by the extraction times applied for HPLC and UV spectrophotometry samples. In general, a higher recovery rate was found in the spectrophotometry analysis due to the longer extraction time (about 30 min for HPLC analysis versus 2 h for spectrophotometry). The incomplete release of the material from the small pores and the influence of extraction time is relevant for the in vivo situation. Dermal formulations are often applied for 10–12 h (e.g., morning application to the face, followed by face washing in the evening). To have a release as complete as possible, larger pores are thus favorable for dermal products. Apart from the consequence for dermal delivery, the data show that for better reproducibility, the extraction procedures need to be exactly identical.

Solubility determination of rutin dissolved from smartPearls

The saturation solubility, as reported by Mauludin et al., for rutin nanocrystals and rutin raw material is about 130 µg/mL [35]. Thus, the solubility of the raw active agent powder is attributed to the presence of nanometer-sized rutin particles in the raw material. Measuring the solubility of the rutin raw powder with the setup used in this study at 25 °C yielded a saturation solubility from 30 to 70 µg/mL at pH 5.5 ± 0.5 (Figure 9, lower curves). Apart from the nanometer-sized material, the general high values reported in the literature can be attributed to dissolution in a higher pH (6.8) and at a higher temperature (37 °C) than that used in this study (pH 5.5 for skin products and 25 °C). Additionally, the in situ measurement with baseline correction and the 0.15 molar NaCl solution used in this study also led to differences from the values reported in the literature. The assumption that nanometer-sized rutin particles are present in the raw material is supported by the fact that the measured C_s value increased from 30 to 70 µg/mL with increasing amount of rutin powder (from 0.28 mg/mL to 2.03 mg/mL) added to the solvent (i.e., more nanometer-sized rutin was added which dissolved and led to this increase in the measured solubility).

In contrast to the rutin powder, in this study, an increased C_s of about 160 µg/mL was obtained with amorphous rutin dissolved from smartPearls. This implies an increase by about a factor of two higher than the respective raw active agent powder. This higher C_s value leads to an increased concentration gradient between the dermal formulation and skin and thus to an increased flux of rutin into the skin.

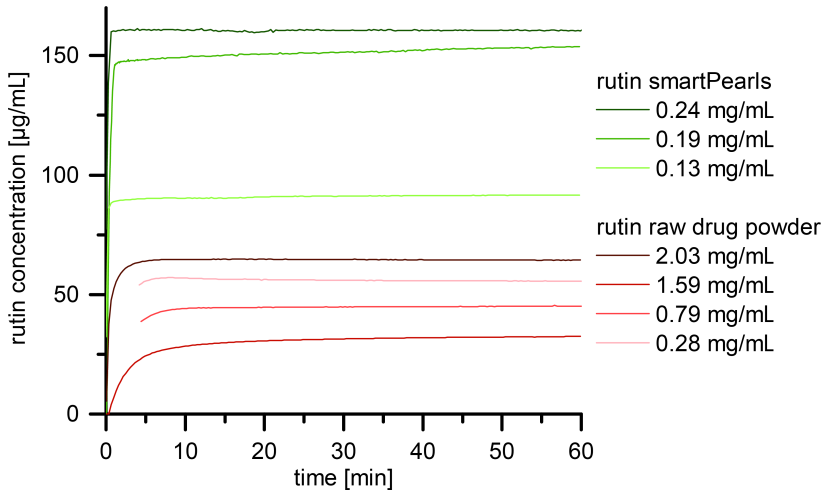

Figure 9: In situ determined saturation solubility of rutin raw active agent powder (lower curves, red) and amorphous rutin loaded into silica as smartPearls (upper curves, green) with various rutin concentrations.

The dissolution kinetics of rutin from the smartPearls is much faster than from the raw rutin powder. With smartPearls, the solubility saturation is reached after almost 1 min, for the raw rutin powder, it takes 5–10 min. For the dermal formulation the kinetics is not relevant, only the saturation solubility, C_s. The smartPearls are added in the preparation of the dermal formulation, and a saturated state will occur in the formulation. When applied to the skin, it can be predicted that the rate limiting step is the slow diffusion of dissolved rutin into the skin. There will be no difference if the diffused rutin molecules are replaced in the dermal formulation by faster or slower dissolution.

In vitro skin penetration studies showed an even higher increase in penetration when a gel with smartPearls was compared to a gel with rutin powder (pig skin penetration test, tape stripping [24]). Especially in the deeper skin layers, an increase by a factor of about four was observed.

Concentration of smartPearls in final market products

When adding smartPearls to the water phase of a dermal product, some portion of the rutin in the pores will dissolve, forming a supersaturated solution. Some portion must remain undissolved in the pores in order to provide a rutin source. When rutin dissolved in the water phase has penetrated into the skin, it should be replaced by new rutin molecules dissolving from the pores. With this scheme, a constant supersaturated state will be maintained. Based on this, the rutin concentration required for a dermal product can be calculated.

The measured saturation solubility of rutin from smartPearls is 150 µg/mL (i.e., 0.15 mg/mL). This will be the amount of rutin that dissolves when adding the smartPearls to the formulation. In addition, one needs a rutin loading in the pores. Thus, it is recommended to use about two times the amount dissolved. For highly penetrating active agents, the required amount stored in the pores might even be higher. Based on this, a minimum of about 0.5 mg/mL in the final product is required. Assuming a low loading of the smartPearls of 10% (w/w), a total of 5 mg of loaded smartPearls need to be added per mL (g) of product (i.e., 5 g/1 kg product).

Definition of large-scale production parameters

Based on this, producing a 100 kg batch requires 500 g of smartPearls; assuming only 10% loading, this corresponds to 50 g of rutin powder. In the production process, this 50 g of rutin has to be dissolved in ethanol. Based on an ethanol solubility of 2%, 2.5 kg of ethanol are required. In this rutin solution, 450 g of unloaded silica particles are dispersed. For evaporation, a rotary evaporator with about 2.5 L solvent evaporation capacity is required, i.e., a rotary evaporator with a volume of about 20 L.

Large rotary evaporators are available up to volumes of 200 L (e.g., from GlasKeller AG, Basel, Switzerland). That means that in one loading process, 5 kg of smartPearls are sufficient to produce 1000 kg of final product. This proposed production scheme indicates that the industrial production of smartPearls is feasible.

Conclusion

For monitoring and understanding the mechanism behind the loading process, a combination of DSC and XRD techniques is most suitable. In this study, XRD was found to be more sensitive to understanding the material crystallinity than DSC.

The particles demonstrated a maximum loading of amorphous-phase rutin of 25% when loaded using ethanol as the solvent. With DMSO as the solvent, a loading of up to 35% was possibly. However, DMSO is difficult to remove because of its high boiling point, and finally, ethanol is preferable because of its better skin tolerability, price and ease of processing.

To ensure complete amorphization a loading of 20% rutin is recommended given that recrystallization of excess rutin was first detected at loadings ≥28%. The saturation solubility of the loaded material was found to increase by a factor of two with just one tenth the amount of amorphous rutin compared to raw active agent powder.

Light microscopy contributed to the understanding of the loading process. It efficiently revealed that the pore filling follows a distribution in the degree of filling (ranging from unloaded to highly loaded). Only a portion of the particles achieve complete loading, and these are the particles that tend to show the first crystalline fractions.

Regarding the ease of processability, as predicted, the smaller particles (such as AL-1 FP, 7 µm diameter) have a higher tendency to agglomerate, and in combination with their small pore size of 3 nm, the maximum loading is low (<12%). Better processability was observed for larger particles with larger pores and pore volume, where the best results among the silica materials studied was found with Syloid® XDP 3050.

Due to the solubility properties, the amount of 5 kg loaded smartPearls required for one ton of final product is relatively low. However, with an established process, large-scale production should be possible using commercially available industrial-sized 50 L evaporators (i.e., the process is scalable). To reproduce the small-scale laboratory results on a large scale, only the

temperature and vacuum parameters need to be set so that the same amount of solvent evaporates in a given time (i.e., the Ostwald–Miers range is satisfied).

Acknowledgements

David Hespeler would like to thank the Hans-Böckler-Foundation for financial support of his doctoral studies.

ORCID® iDs

David Hespeler - https://orcid.org/0000-0003-3881-2664

References

1. Krutmann, J.; Liu, W.; Li, L.; Pan, X.; Crawford, M.; Sore, G.; Seite, S. *J. Dermatol. Sci.* **2014,** *76,* 163–168. doi:10.1016/j.jdermsci.2014.08.008
2. Jin, S.-P.; Li, Z.; Choi, E. K.; Lee, S.; Kim, Y. K.; Seo, E. Y.; Chung, J. H.; Cho, S. *J. Dermatol. Sci.* **2018,** *91,* 175–183. doi:10.1016/j.jdermsci.2018.04.015
3. Sharma, D.; Ali, A. A. E.; Trivedi, L. R. *PharmaTutor* **2018,** *6,* 50–62. doi:10.29161/pt.v6.i2.2018.50
4. Müller, R. H.; Shegokar, R.; Keck, C. M. *Curr. Drug Discovery Technol.* **2011,** *8,* 207–227. doi:10.2174/157016311796799062
5. Joseph, S.; Bunjes, H. Solid Lipid Nanoparticles for Drug Delivery. In *Drug Delivery Strategies for Poorly Water-Soluble Drugs;* Douroumis, D.; Fahr, A., Eds.; John Wiley & Sons Ltd.: New York, NY, U.S.A., 2013; pp 103–149. doi:10.1002/9781118444726.ch4
6. Loftsson, T.; Brewster, M. E. Drug Solubilization and Stabilization by Cyclodextrin Drug Carriers. *Drug Delivery Strategies for Poorly Water-Soluble Drugs;* John Wiley & Sons Ltd.: New York, NY, U.S.A., 2013; pp 67–101. doi:10.1002/9781118444726.ch3
7. Jambhekar, S. S.; Breen, P. *Drug Discovery Today* **2016,** *21,* 363–368. doi:10.1016/j.drudis.2015.11.016
8. Petersen, R. Nanocrystals for use in topical cosmetic formulations and method of production thereof. European Union Patent EP 2 099 420 B8, Nov 19, 2007.
9. Petersen, R. Nanocrystals for use in topical cosmetic formulations and method of production thereof. U.S. Patent US 9,114,077, Nov 19, 2007.
10. Müller, R. H.; Keck, C. M. *Eur. J. Pharm. Biopharm.* **2012,** *80,* 1–3. doi:10.1016/j.ejpb.2011.09.012
11. Romero, G. B.; Chen, R.; Keck, C. M.; Müller, R. H. *Int. J. Pharm.* **2015,** *482,* 54–60. doi:10.1016/j.ijpharm.2014.11.039
12. Müller, R. H.; Hespeler, D.; Keck, C. M. *Eurocosmetics* **2018,** *26,* 20–23.
13. Müller, R. H.; Shegokar, R.; Gohla, S.; Keck, C. M. Nanocrystals: production, cellular drug delivery, current and future products. In *Intracellular Delivery;* Prokop, A., Ed.; Springer: Berlin, Germany, 2011; pp 411–432. doi:10.1007/978-94-007-1248-5_15
14. Hancock, B. C.; Parks, M. *Pharm. Res.* **2000,** *17,* 397–404. doi:10.1023/a:1007516718048
15. Qian, K. K.; Bogner, R. H. *J. Pharm. Sci.* **2012,** *101,* 444–463. doi:10.1002/jps.22779
16. Murdande, S. B.; Pikal, M. J.; Shanker, R. M.; Bogner, R. H. *Pharm. Dev. Technol.* **2011,** *16,* 187–200. doi:10.3109/10837451003774377
17. Cremer, K.; Kröhne, L.; Mayer, J. Schnellfreisetztende, feste Darreichungsform zur oralen Applikation schwerlöslicher Wirkstoffe. International patent WO 2004030648A1, Sept 24, 2003.
18. Grabo, M.; Dunmann, C.; Müller, R. H.; Keck, C. M. CapsMorph technology for generation of amorphous oral formulations. AAPS Annual Meeting, Washington, DC, U.S.A., Oct 23–27, 2011; W4131.
19. Wei, Q.; Keck, C. M.; Müller, R. H. *Int. J. Pharm.* **2015,** *482,* 11–20. doi:10.1016/j.ijpharm.2014.10.068
20. Choudhari, Y.; Hoefer, H.; Libanati, C.; Monsuur, F.; McCarthy, W. Mesoporous Silica Drug Delivery Systems. In *Amorphous Solid Dispersions;* Shah, N.; Sandhu, H.; Choi, D.; Chokshi, H.; Malick, A., Eds.; Springer New York: New York, NY, U.S.A., 2014; pp 665–693. doi:10.1007/978-1-4939-1598-9_23
21. Fan, H.; Van Swol, F.; Lu, Y.; Brinker, C. J. *J. Non-Cryst. Solids* **2001,** *285,* 71–78. doi:10.1016/s0022-3093(01)00434-3
22. Monsuur, F. H.; Hoefer, H. H.; Keck, C. M. Active-loaded particulate materials for topical administration. WIPO Patent WO 2016/041992 A1, Sept 15, 2014.
23. Müller, R. H.; Hespeler, D.; Jin, N.; Pyo, S. M. *Int. J. Pharm.* **2019,** *555,* 314–321. doi:10.1016/j.ijpharm.2018.11.018
24. Jin, N. Nanocrystals & loaded porous silica for increased dermal bioavailability. Ph.D. Thesis, Freie Universität Berlin, Berlin, Germany, 2017. urn:nbn:de:kobv:188-fudissthesis000000105191-3.
25. Jermain, S. V.; Brough, C.; Williams, R. O., III. *Int. J. Pharm.* **2018,** *535,* 379–392. doi:10.1016/j.ijpharm.2017.10.051
26. Stein, J.; Fuchs, T.; Mattern, C. *Chem. Eng. Technol.* **2010,** *33,* 1464–1470. doi:10.1002/ceat.200900590
27. Watanabe, T.; Wakiyama, N.; Usui, F.; Ikeda, M.; Isobe, T.; Senna, M. *Int. J. Pharm.* **2001,** *226,* 81–91. doi:10.1016/s0378-5173(01)00776-1
28. Smirnova, I.; Mamic, J.; Arlt, W. *Langmuir* **2003,** *19,* 8521–8525. doi:10.1021/la0345587
29. Ahern, R. J.; Hanrahan, J. P.; Tobin, J. M.; Ryan, K. B.; Crean, A. M. *Eur. J. Pharm. Sci.* **2013,** *50,* 400–409. doi:10.1016/j.ejps.2013.08.026
30. Hespeler, D.; Kaltenbach, J.; Pyo, S. M. *Int. J. Pharm.* **2019,** *561,* 228–235. doi:10.1016/j.ijpharm.2019.02.028
31. Narayana, K. R.; Reddy, M. S.; Chaluvadi, M. R.; Krishna, D. R. *Indian J. Pharmacol.* **2001,** *33,* 2–16.
32. El Moneiri, S. Entwicklung und Charakterisierung von amorphen Rutin-Carriern zur dermalen Applikation, Master thesis, Beuth University of Applied Science, Berlin, 2019.
33. Hespeler, D.; Pyo, S. M. *Int. J. Pharm.* **2019**. To be submitted.
34. Wei, Q.; Keck, C. M.; Müller, R. H. *Eur. J. Pharm. Biopharm.* **2017,** *113,* 97–107. doi:10.1016/j.ejpb.2016.11.009
35. Mauludin, R.; Müller, R. H.; Keck, C. M. *Eur. J. Pharm. Sci.* **2009,** *36,* 502–510. doi:10.1016/j.ejps.2008.12.002

BEILSTEIN JOURNAL OF NANOTECHNOLOGY

Doxorubicin-loaded human serum albumin nanoparticles overcome transporter-mediated drug resistance in drug-adapted cancer cells

Hannah Onafuye[‡1], Sebastian Pieper[‡2], Dennis Mulac[2], Jindrich Cinatl Jr.[3], Mark N. Wass[1], Klaus Langer[*2,§] and Martin Michaelis[*1,¶]

Full Research Paper

Open Access

Address:
[1]Industrial Biotechnology Centre and School of Biosciences, University of Kent, Canterbury CT2 7NJ, United Kingdom, [2]Institute of Pharmaceutical Technology and Biopharmacy, University of Münster, Corrensstr. 48, 48149 Münster, Germany and [3]Institute for Medical Virology, University Hospital, Goethe-University, Paul Ehrlich-Straße 40, 60596 Frankfurt am Main, Germany

Email:
Klaus Langer[*] - k.langer@uni-muenster.de; Martin Michaelis[*] - m.michaelis@kent.ac.uk

* Corresponding author ‡ Equal contributors
§ phone: 0049 (0)251 / 83-39860
¶ phone: 0044 (0)1227 / 82-7804

Keywords:
ABCB1; cancer; doxorubicin; drug resistance; human serum albumin; nanoparticles; transporter

Beilstein J. Nanotechnol. **2019,** *10,* 1707–1715.
doi:10.3762/bjnano.10.166

Received: 30 May 2019
Accepted: 29 July 2019
Published: 14 August 2019

This article is part of the thematic issue "Frontiers in pharmaceutical nanotechnology".

Guest Editor: M. G. Wacker

Abstract

Resistance to systemic drug therapy is a major reason for the failure of anticancer therapies. Here, we tested doxorubicin-loaded human serum albumin (HSA) nanoparticles in the neuroblastoma cell line UKF-NB-3 and its ABCB1-expressing sublines adapted to vincristine (UKF-NB-3^{r}VCR^{1}) and doxorubicin (UKF-NB-3^{r}DOX^{20}). Doxorubicin-loaded nanoparticles displayed increased anticancer activity in UKF-NB-3^{r}VCR^{1} and UKF-NB-3^{r}DOX^{20} cells relative to doxorubicin solution, but not in UKF-NB-3 cells. UKF-NB-3^{r}VCR^{1} cells were re-sensitised by nanoparticle-encapsulated doxorubicin to the level of UKF-NB-3 cells. UKF-NB-3^{r}DOX^{20} cells displayed a more pronounced resistance phenotype than UKF-NB-3^{r}VCR^{1} cells and were not re-sensitised by doxorubicin-loaded nanoparticles to the level of parental cells. ABCB1 inhibition using zosuquidar resulted in similar effects like nanoparticle incorporation, indicating that doxorubicin-loaded nanoparticles successfully circumvent ABCB1-mediated drug efflux. The limited re-sensitisation of UKF-NB-3^{r}DOX^{20} cells to doxorubicin by circumvention of ABCB1-mediated efflux is probably due to the presence of multiple doxorubicin resistance mechanisms. So far, ABCB1 inhibitors have failed in clinical trials probably because systemic ABCB1 inhibition results in a modified body distribution of its many substrates including drugs, xenobiotics, and other molecules. HSA nanoparticles may provide an alternative, more specific way to overcome transporter-mediated resistance.

Introduction

According to Globocan there "were 14.1 million new cancer cases, 8.2 million cancer deaths and 32.6 million people living with cancer (within 5 years of diagnosis) in 2012 worldwide" [1]. Despite substantial improvements over recent decades, the prognosis for many cancer patients remains unacceptably poor. The outlook is particularly grim for patients that are diagnosed with disseminated (metastatic) disease who cannot be successfully treated by local treatment (surgery, radiotherapy) and depend on systemic drug therapy, because the success of systemic therapies is typically limited by therapy resistance [2-4].

Drug efflux mediated by transporters including adenosine triphosphate (ATP)-binding cassette (ABC) transporters has been shown to play a crucial role in cancer cell drug resistance [2,5]. ABCB1 (also known as P-glycoprotein or MDR1) seems to play a particularly important role in cancer cell drug resistance as a highly promiscuous transporter that mediates the cellular efflux of a wide range of structurally different substrates including many anticancer drugs. Different studies have reported that nanometer-sized drug carrier systems can bypass efflux-mediated drug resistance [6]. This includes various nanoparticle and liposome formulations of the ABCB1 substrate doxorubicin [7-12].

Here, we here investigated the effects of doxorubicin-loaded human serum albumin (HSA) nanoparticles in ABCB1-expressing neuroblastoma cells. HSA nanoparticles are easy to produce [13-17], and HSA is a well-tolerated material. It is the most abundant protein in human blood plasma and used in many pharmaceutical formulations, in particular as part of critical care treatment [18].

Results

Nanoparticle size, polydispersity and drug load

HSA nanoparticles were prepared by desolvation as previously described [13-17]. The nanoparticles were stabilised by the cross-linking of free amino groups present in albumin. Three different nanoparticle preparations were produced using glutaraldehyde at amounts that corresponded to a theoretical cross-linking of 40% (HSA 40% nanoparticles), 100% (HSA 100% nanoparticles), or 200% (HSA 200% nanoparticles) of the amino groups that are available in the HSA molecules. A nonstabilised (0% cross-linking) formulation was used as a control. The resulting particle sizes and polydispersity indices are shown in Table 1. HSA (0%) nanoparticles displayed a large particle size of almost 1 µm and a high polydispersity of 0.5, confirming that no stable nanoparticles had formed (Table 1). The three HSA nanoparticle preparations stabilised by the different glutaraldehyde concentrations displayed similar diameters between 460 and 500 nm and polydispersity indices in the range of 0.153 and 0.213, indicating a narrow but not monodisperse size distribution (Table 1).

The spherical shape and narrow size distribution of HSA nanoparticles was confirmed by scanning electron microscopy (SEM) as depicted for nanoparticles stabilised by a 100% cross-linking degree (Figure 1). For these nanoparticles a zeta potential of −12.5 ± 1.8 mV (n = 6) was detected, indicating only a moderate stabilisation by electrostatic repulsion.

While HSA (40%), HSA (100%), and HSA (200%) nanoparticles displayed similar drug loads between 152 and 191 µg doxorubicin/mg nanoparticle, HSA (0%) nanoparticles had bound 371 µg doxorubicin/mg HSA (Table 1). This probably reflected the higher accessibility of doxorubicin binding sites, which are known to be available on HSA [19], in HSA molecules in solution compared to the accessible binding sites available in HSA nanoparticles.

Doxorubicin sensitivity of the used neuroblastoma cell lines

The parental neuroblastoma cell line UKF-NB-3 and its doxorubicin- (UKF-NB-3^{r}DOX^{20}) and vincristine-adapted (UKF-NB-3^{r}VCR^{1}) sub-lines substantially differed in their doxorubicin sensitivity (Figure 2). UKF-NB-3 displayed the lowest doxorubicin IC_{50} (3.8 ng/mL). UKF-NB-3^{r}VCR^{1} was 4-fold more resistant to doxorubicin than UKF-NB-3 (doxorubicin IC_{50}: 15.5 ng/mL). UKF-NB-3^{r}DOX^{20} showed the highest doxorubicin IC_{50} (89.0 ng/mL), resulting in a 23-fold increase in doxorubicin resistance compared to UKF-NB-3 (Figure 2, Supporting Information File 1, Table S1).

Table 1: Nanoparticle diameter, polydispersity, and drug load.

Nanoparticle formulations	Diameter (nm)	Polydispersity	Drug load (µg doxorubicin/mg nanoparticle)
HSA (0%)	848.7	0.500	370.9
HSA (40%)	485.8	0.189	151.9
HSA (100%)	496.4	0.213	190.5
HSA (200%)	463.4	0.153	164.8

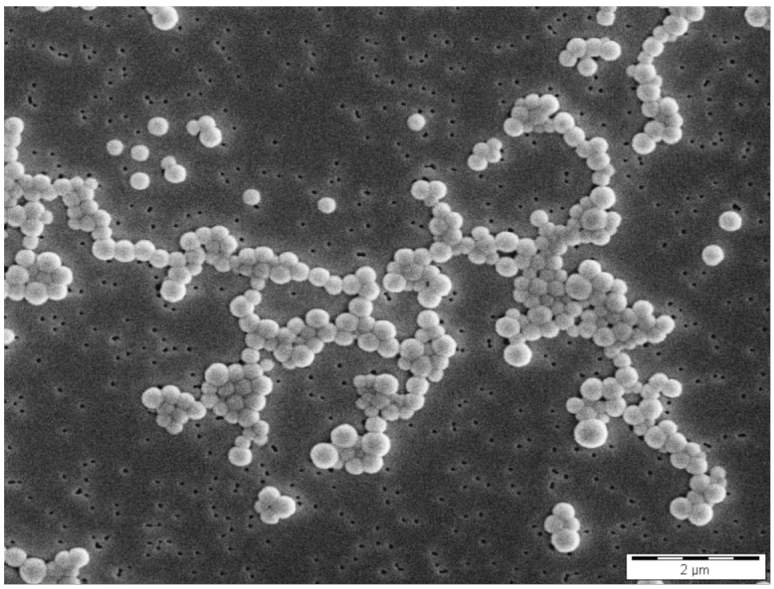

Figure 1: SEM confirmed the spherical shape and narrow size distribution of doxorubicin-loaded HSA (100%) nanoparticles.

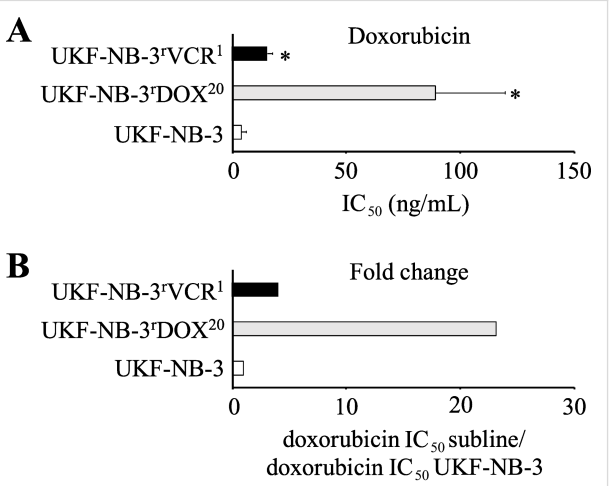

Figure 2: Doxorubicin sensitivity of UKF-NB-3, its doxorubicin-adapted sub-line UKF-NB-3^{r}DOX^{20} and its vincristine-adapted sub-line UKF-NB-3^{r}VCR^{1}. A) Doxorubicin concentrations that reduce cell viability by 50% (IC_{50}) as indicated by MTT assay after 120 h of incubation. B) Fold change in doxorubicin sensitivity (doxorubicin IC_{50} UKF-NB-3 sub-line/doxorubicin IC_{50} UKF-NB-3). Numerical values are presented in Supporting Information File 1, Table S1. *P < 0.05 relative to UKF-NB-3.

Effects of doxorubicin-loaded nanoparticles on neuroblastoma cells

The effects of doxorubicin applied in solution or incorporated into HSA (0%), HSA (40%), HSA (100%), or HSA (200%) nanoparticles on neuroblastoma cell viability are shown in Figure 3. The numerical values are presented in Supporting Information File 1, Table S1. Empty control nanoparticles did not affect cell viability in the investigated concentrations.

In the neuroblastoma cell line UKF-NB-3, the nanoparticle preparations displayed similar activity as doxorubicin solution, with doxorubicin-loaded HSA (40%), HSA (100%), and HSA (200%) nanoparticles potentially showing a trend towards a slightly increased activity (Figure 3). However, the differences did not reach statistical significance. Similar results were obtained in the doxorubicin-adapted UKF-NB-3 sub-line UKF-NB-3^{r}DOX^{20}, although the difference between doxorubicin-loaded HSA (200%) nanoparticles and doxorubicin solution reached statistical significance (Figure 3). Notably, non-stabilised doxorubicin-bound HSA (0%) nanoparticles differed in their relative activity and did not reduce UKF-NB-3^{r}DOX^{20} viability by 50% within the observed concentration range up to 200 ng/mL.

The vincristine-adapted UKF-NB-3 sub-line UKF-NB-3rVCR1 displayed decreased doxorubicin sensitivity. However, doxorubicin-loaded HSA (40%), HSA (100%), and HSA (200%) nanoparticles displayed a higher relative potency compared to doxorubicin solution in UKF-NB-3^{r}VCR^{1} (Figure 3, Figure 4). The fold sensitisation doxorubicin IC_{50} doxorubicin solution/ doxorubicin IC_{50} nanoparticle-bound doxorubicin for HSA (40%), HSA (100%), and HSA (200%) nanoparticles (3.6–4.5-fold) was higher than for UKF-NB-3 (1.9–2.5-fold), and UKF-NB-3^{r}DOX^{20} (2.1–2.9-fold). The differences between doxorubicin-loaded HSA (40%) nanoparticles, HSA (100%) nanoparticles, and HSA (200%) nanoparticles and doxorubicin solution reached statistical significance (P < 0.05) (Figure 3). Doxorubicin encapsulation into HSA (40%), HSA (100%), or HSA (200%) nanoparticles reduced the doxorubicin

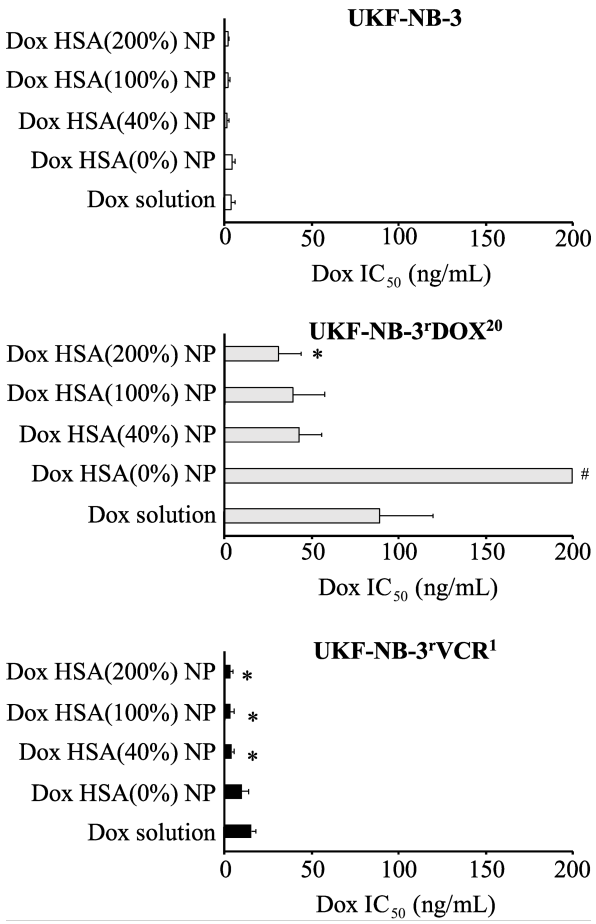

Figure 3: Effects of doxorubicin (Dox) applied as a solution or incorporated into human serum albumin (HSA) nanoparticles on neuroblastoma cell viability. The investigated nanoparticles differed in the amount of the cross-linker glutaraldehyde that was used for nanoparticle stabilisation. The amount of glutaraldehyde corresponded to 40% (Dox HSA (40%) NP), 100% (Dox HSA (100%) NP), or 200% (Dox HSA (200%) NP) theoretical cross-linking of the available amino groups present on HSA. Preparations prepared without glutaraldehyde served as a control (Dox HSA (0%) NP). Values are expressed as concentrations that reduce cell viability by 50% (IC_{50}) as determined by MTT assay after 120 h of incubation. Numerical values are presented in Supporting Information File 1, Table S1. Empty nanoparticles did not affect cell viability in the investigated concentrations. *$P < 0.05$ relative to doxorubicin solution; # IC_{50} > 200 ng/mL.

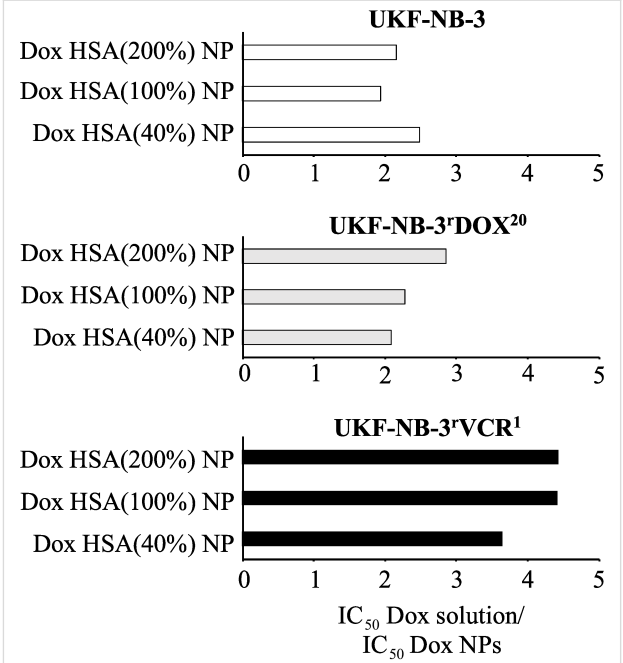

Figure 4: Fold sensitisation to doxorubicin by doxorubicin-bound nanoparticles (NPs). Values are expressed as fold changes doxorubicin (Dox) IC_{50} of doxorubicin solution/doxorubicin IC_{50} of doxorubicin-bound NPs. Human serum albumin (HSA) nanoparticles were stabilised by glutaraldehyde concentrations corresponding to 40% (Dox HSA (40%) NP), 100% (Dox HSA (100%) NP), or 200% (Dox HSA (200%) NP) theoretical cross-linking of the available amino groups present on HSA.

IC_{50} in UKF-NB-3^{r}VCR^{1} cells to the levels of doxorubicin solution in parental UKF-NB-3 cells (Figure 3, Supporting Information File 1, Table S1). In contrast, the doxorubicin IC_{50} of doxorubicin-loaded HSA nanoparticles remained clearly (8–11-fold) higher in UKF-NB-3^{r}DOX^{20} cells than the doxorubicin IC_{50} of doxorubicin solution in parental UKF-NB-3 cells.

Effects of the ABCB1 inhibitor zosuquidar on the efficacy of nanoparticle-bound doxorubicin in UKF-NB-3^{r}DOX^{20} cells

Doxorubicin is an ABCB1 substrate, and UKF-NB-3^{r}DOX^{20} cells are characterised by high ABCB1 expression [20,21]. Vincristine is also an ABCB1 substrate, and vincristine-adapted cancer cell lines often display enhanced ABCB1 levels [20,22,23]. Accordingly, UKF-NB-3^{r}VCR^{1} cells are sensitised by the ABCB1 inhibitor zosuquidar [2-6] to doxorubicin to the level of parental UKF-NB-3 cells (Supporting Information File 1, Figure S1), which indicates that ABCB1 expression contributes to the resistance phenotype observed in UKF-NB-3^{r}VCR^{1} cells.

Doxorubicin bound to nanometer-sized drug carrier systems has been shown to bypass ABCB1-mediated drug efflux [7-12]. In UKF-NB-3^{r}VCR^{1} cells, combining both doxorubicin with zosuquidar and doxorubicin encapsulation into HSA nanoparticles reduced the doxorubicin IC_{50} to the level of parental UKF-NB-3 cells (Figure 3, Supporting Information File 1, Figure S1, Table S1), which do not display detectable ABCB1 activity [20,22,23]. Hence, the increased activity of nanoparticle-bound doxorubicin that we observed in UKF-NB-3^{r}VCR^{10} cells is likely to be attributed to the circumvention of ABCB1-mediated doxorubicin efflux.

In UKF-NB-3^{r}DOX^{20} cells, however, the differences between doxorubicin solution and doxorubicin nanoparticles only reached statistical significance for doxorubicin-loaded HSA

(200%) nanoparticles (Figure 3). The reasons for this may include that nanoparticle-incorporated doxorubicin does not completely avoid ABCB1-mediated efflux from UKF-NB-3^{r}DOX^{20} cells and/or that doxorubicin resistance is caused by multiple resistance mechanisms and that avoidance of ABCB1-mediated transport is not sufficient to re-sensitise UKF-NB-3^{r}DOX^{20} cells to doxorubicin to the level of UKF-NB-3 cells.

To further study the role of ABCB1 as a doxorubicin resistance mechanism in UKF-NB-3^{r}DOX^{20} cells, we performed additional experiments in which we combined the ABCB1 inhibitor zosuquidar and doxorubicin applied as a solution or nanoparticle preparations in UKF-NB-3^{r}DOX^{20} and UKF-NB-3 cells. Zosuquidar (1 μM) did not affect the efficacy of doxorubicin solution or nanoparticle-bound doxorubicin in parental UKF-NB-3 cells (Figure 5), which do not display noticeable ABCB1 activity [20,22,23]. These experiments also confirmed that there is no significant difference in the anticancer activity between doxorubicin solution and doxorubicin nanoparticles in UKF-NB-3 cells, despite an apparent trend in the first set of experiments (Figure 3).

In UKF-NB-3^{r}DOX^{20} cells, the addition of zosuquidar resulted in an increased sensitivity to free doxorubicin (Figure 5). The doxorubicin IC_{50} decreased by 2.5-fold from 91 ng/mL in the absence of zosuquidar to 37 ng/mL in the presence of zosuquidar, but not to the level of UKF-NB-3 cells (4.6 ng/mL) (Supporting Information File 1, Table S2). This confirmed that ABCB1 is one among multiple resistance mechanisms that contribute to the doxorubicin resistance phenotype observed in UKF-NB-3^{r}DOX^{20}.

In this set of experiments, doxorubicin-loaded nanoparticles displayed a significantly increased activity compared to doxorubicin solution in UKF-NB-3^{r}DOX^{20} cells (Figure 5). This finding together with the non-significant trend observed in the first set of experiments (Figure 3) suggests that doxorubicin-loaded nanoparticles do indeed exert stronger effects against UKF-NB-3^{r}DOX^{20} cells than doxorubicin solution. Zosuquidar only moderately increased the efficacy of doxorubicin nanoparticles further (1.1–1.8-fold) in UKF-NB-3^{r}DOX^{20} cells (Figure 5, Supporting Information File 1, Table S2). In particular, the anticancer effects of doxorubicin-loaded HSA (200%) nanoparticles, the most active nanoparticle preparation in UKF-NB-3^{r}DOX^{20} cells, displayed a doxorubicin IC_{50} of 20 ng/mL, which was not further reduced by addition of zosuquidar (doxorubicin IC_{50}: 18 ng/mL) (Figure 5, Table S2). Hence, the increased anticancer activity of doxorubicin incorporated into HSA nanoparticles appears to be primarily caused by circumventing the ABCB1-mediated doxorubicin efflux in UKF-NB-3^{r}DOX^{20} cells.

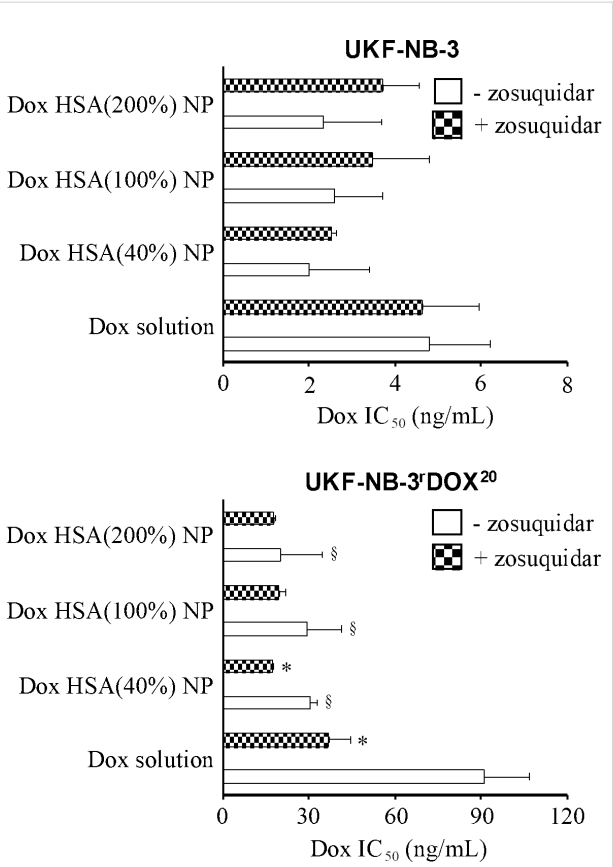

Figure 5: Doxorubicin (Dox) concentrations that reduce neuroblastoma cell viability by 50% (IC_{50}) in the presence or absence of the ABCB1 inhibitor zosuquidar (1 μM) as determined by MTT assay after 120 h incubation. Doxorubicin was either applied as a solution or incorporated into human serum albumin (HSA) nanoparticles which had been stabilised by addition of glutaraldehyde concentrations corresponding to 40% (Dox HSA (40%) NP), 100% (Dox HSA (100%) NP), or 200% (Dox HSA (200%) NP) theoretical cross-linking of the available amino groups present on HSA. Zosuquidar (1 μM) did not affect cell viability on its own. Numerical data are presented in Supporting Information File 1, Table S2. *P < 0.05 relative to the doxorubicin IC_{50} in the absence of zosuquidar; §P < 0.05 relative to doxorubicin solution.

Discussion

The occurrence of drug resistance is the major reason for the failure of systemic anticancer therapies [2]. Here, we investigated the effects of doxorubicin-loaded HSA nanoparticles on the viability of the neuroblastoma cell line UKF-NB-3 and its sublines adapted to doxorubicin (UKF-NB-3^{r}DOX^{20}) and vincristine (UKF-NB-3^{r}VCR^{1}), which both display ABCB1 activity and resistance to doxorubicin. The HSA nanoparticles were prepared by desolvation and stabilised by glutaraldehyde, which crosslinks amino groups present in albumin molecules [13-17]. Glutaraldehyde was used at molar concentrations that corresponded to 40% (Dox HSA (40%) nanoparticles), 100% (Dox HSA (100%) nanoparticles), or 200% (Dox HSA (200%) nanoparticles) theoretical cross-linking of the 59 amino groups

available per HSA molecule [24]. The resulting nanoparticles ranged from 463 to 486 nm in diameter and had a low polydispersity index in the range of 0.2.

Doxorubicin-loaded nanoparticles displayed similar activity as doxorubicin solution in the parental UKF-NB-3 cell line, but exerted stronger effects than doxorubicin solution in the ABCB1-expressing UKF-NB-3 sub-lines. The UKF-NB-$3^{r}VCR^{1}$ cells were similarly sensitive to doxorubicin-loaded nanoparticles as parental UKF-NB-3 cells to doxorubicin solution (and doxorubicin-loaded nanoparticles). This suggests that the doxorubicin resistance of UKF-NB-$3^{r}VCR^{1}$ cells exclusively depends on ABCB1 expression. In concordance, the ABCB1 inhibitor zosuquidar re-sensitised UKF-NB-$3^{r}VCR^{1}$ cells to the level of parental UKF-NB-3 cells.

The UKF-NB-$3^{r}DOX^{20}$ cells displayed a more pronounced doxorubicin resistance phenotype than UKF-NB-$3^{r}VCR^{1}$ cells and were neither re-sensitised by nanoparticle-encapsulated doxorubicin nor by zosuquidar to the level of UKF-NB-3 cells. This suggests that UKF-NB-$3^{r}DOX^{20}$ cells have developed multiple doxorubicin resistance mechanisms. In contrast, adaptation of UKF-NB-$3^{r}VCR^{1}$ cells to vincristine, a tubulin-binding agent with an anticancer mechanism of action that is not related to that of the topoisomerase II inhibitor doxorubicin [2,20,25,26], did not result in the acquisition of changes that confer doxorubicin resistance beyond ABCB1 expression.

Furthermore, zosuquidar did not increase the efficacy of doxorubicin-loaded HSA (100%) and HSA (200%) nanoparticles and only modestly enhanced the efficacy of doxorubicin-loaded HSA (40%) nanoparticles. Together, these data confirm that administration of doxorubicin as HSA nanoparticles resulted in the circumvention of ABCB1-mediated drug efflux. The difference between HSA (40%) nanoparticles and the other two preparations may be explained by elevated drug release due to the lower degree of cross-linking.

Interestingly, high concentrations of the cross-linker glutaraldehyde did not affect the efficacy of the resulting doxorubicin-loaded nanoparticles although high glutaraldehyde concentrations might have been expected to affect drug release and/or to covalently bind to doxorubicin via its amino group.

Notably, the results differ from a recent similar study in which nanoparticles prepared from poly(lactic-co-glycolic acid) (PLGA) or polylactic acid (PLA), two other biodegradable materials approved by the FDA and EMA for human use [27,28], did not bypass ABCB1-mediated drug efflux [29]. Differences in the mode of uptake and cellular distribution of the nanoparticles from different materials may be responsible for these discrepancies. HSA nanoparticles may be internalised upon interaction with cellular albumin receptors [30,31]. Notably, nab-paclitaxel, an HSA nanoparticle-based preparation of paclitaxel (another ABCB1 substrate [21]), which is approved for the treatment of different forms of cancer [32], had previously been shown not to avoid ABCB1-mediated drug efflux [33]. However, nab-paclitaxel is not produced by the use of cross-linkers, and the interaction of paclitaxel with albumin may differ from that of doxorubicin. Hence, variations in drug binding and drug release kinetics may be responsible for this difference.

Despite the prominent role of ABCB1 as a drug resistance mechanism, attempts to exploit it as drug target have failed so far, despite the development of highly specific allosteric ABCB1 inhibitors (of which zosuquidar is one) [5,21]. One reason for this is that ABCB1 is expressed at various physiological borders and involved in the control of the body distribution of its many endogenous and exogenous substrates. Systemic ABCB1 inhibition can therefore result in toxicity as a consequence of a modified body distribution of anticancer drugs (and other drugs that are co-administered for conditions other than cancer), xenobiotics, and other molecules. Hence, the use of drug carrier systems to bypass ABC transporter-mediated drug efflux is conceptually very attractive because it can (in contrast to inhibitors of ABCB1 or other transporters) overcome resistance mediated by multiple transporters and does not result in the systemic inhibition of transporter function at physiological barriers. However, cancer cells may be characterised by multiple further resistance mechanisms and just bypassing transporter-mediated efflux may not be sufficient to achieve therapeutic response (as illustrated by our current finding that UKF-NB-$3^{r}DOX^{20}$ cells cannot be fully re-sensitised to doxorubicin by zosuquidar) [2,5,21]. Hence, our results demonstrate that more sophisticated, personalised therapies will need to be developed. Such therapies will depend on an improved understanding of the resistance status of cancer cells to a certain drug beyond its transporter status. If biomarkers become available that predict cancer cell response to a certain drug more reliably, nanoparticles can be used to transport drugs under circumvention of transporter-mediated efflux into cancer cells that are likely to respond to them.

In conclusion, doxorubicin-loaded HSA nanoparticles produced by desolvation and cross-linking using glutaraldehyde overcome (in contrast to other nanoparticle systems) transporter-mediated drug resistance in drug-adapted neuroblastoma cells. However, our data also show that bypassing of transporter-mediated drug efflux may not be sufficient to sensitise cancer cells, which have developed multiple resistance mechanisms, to the level of sensitive parental cells.

Experimental

Reagents and chemicals

HSA and glutaraldehyde were obtained from Sigma-Aldrich Chemie GmbH (Karlsruhe, Germany). Dulbecco's phosphate buffered saline (PBS) was purchased from Biochrom GmbH (Berlin, Germany). Doxorubicin was obtained from LGC Standards GmbH (Wesel, Germany). All chemicals were of analytical grade and used as received.

Human serum albumin (HSA) nanoparticle preparation by desolvation

HSA nanoparticles were prepared by desolvation as previously described [13-17]. 100 µL of a 1% (w/v) aqueous doxorubicin solution was added to 500 µL of a 40 mg/mL (w/v) HSA solution and incubated for 2 h at room temperature under stirring (550 rpm, Cimaric i Multipoint Stirrer, ThermoFisher Scientific, Langenselbold, Germany). 4 mL of ethanol 96% was added at room temperature under stirring using a peristaltic pump (Ismatec ecoline, Ismatec, Wertheim-Mondfeld, Germany) at a flow rate of 1 mL/min. After the desolvation process, the resulting nanoparticles were stabilised/cross-linked using different amounts of glutaraldehyde that corresponded to different percentages of the theoretical amount that is necessary for the quantitative cross-linking of the 60 primary amino groups present in the HSA molecules of the particle matrix. The addition of 4.7 µL 8% (w/v) aqueous glutaraldehyde solution resulted in a theoretical cross-linking of 40% of the HSA amino groups, the addition of 11.8 µL 8% (w/v) aqueous glutaraldehyde solution in 100% cross-linking, and the addition of 23.6 µL 8% (w/v) aqueous glutaraldehyde solution in 200% cross-linking. The suspension was then stirred for 12 h at 550 rpm. The particles were purified by centrifugation (at 16,000*g* for 12 min) and resuspension steps performed three times in purified water. During the particle purification the supernatants were collected and the drug content was measured by high-performance liquid chromatography (HPLC) as described below. The loading efficiency of doxorubicin in the nanoparticles was calculated based on the difference between the doxorubicin amount used for nanoparticle preparation and the unbound amount detected in the collected supernatants.

Determination of particle size distribution

The average particle size and the polydispersity were measured by photon correlation spectroscopy (PCS) using a Malvern zetasizer nano instrument (Malvern Instruments, Herrenberg, Germany). The resulting particle suspensions were diluted 1:100 with purified water and measured at a temperature of 22 °C using a backscattering angle of 173°.

The zeta potential was measured in the same instrument by laser Doppler microelectrophoresis to provide information about the surface charge of the nanoparticles. Thus, the nanoparticle dilutions described above were transferred into a folded capillary cell and the experiment was conducted at 22 °C.

Morphological analysis of nanoparticles by scanning electron microscopy (SEM)

3 µL of diluted HAS nanoparticle suspension (0.25 mg/mL) was applied on a 0.1 µm membrane filter (Isopore™ membrane filter, Merck Millipore, Darmstadt, Germany) and dried overnight in a desiccator. Afterwards, the membrane filter was sputtered with gold (Sputter SCD 040, BALTEC, Liechtenstein) under argon atmosphere. SEM was performed on a CamScan CS4 microscope (Cambridge Scanning Company, Cambridge, United Kingdom) and the sample was visualised with an accelerating voltage of 10 kV, a working distance of 10 mm, and 10,000-fold magnification.

Doxorubicin quantification via HPLC-UV

The amount of doxorubicin that was incorporated into the nanoparticles was determined by HPLC-UV (HPLC 1200 series, Agilent Technologies GmbH, Böblingen, Germany) using a LiChroCART 250 × 4 mm LiChrospher 100 RP 18 column (Merck KGaA, Darmstadt, Germany). The mobile phase was a mixture of water and acetonitrile (70:30) containing 0.1% trifluoroacetic acid [16]. In order to obtain symmetric peaks a gradient was used. In the first 6 min the percentage of A was reduced from 70% to 50%. Subsequently within 2 min the amount of A was further decreased to 20% and then within another 2 min increased again to 70%. These conditions were held for a final 5 min, resulting in a total runtime of 15 min. While using a flow rate of 0.8 mL/min, an elution time for doxorubicin of t = 7.5 min was achieved. The detection of doxorubicin was performed at a wavelength of 485 nm [34].

Cell culture

The neuroblastoma cell line UKF-NB-3, which harbours a MYCN amplification (a major indicator of high-risk disease and poor prognosis [35]), was established from a stage 4 neuroblastoma patient [20]. The UKF-NB-3 sub-lines adapted to growth in the presence of doxorubicin 20 ng/mL (UKF-NB-3^{r}DOX^{20}) [20] or vincristine 1 ng/mL (UKF-NB-3^{r}VCR^{1}) were established by continuous exposure to step-wise increasing drug concentrations as previously described [20,36] and derived from the resistant cancer cell line (RCCL) collection [37].

All cells were propagated in Iscove's modified Dulbecco's medium (IMDM) supplemented with 10% foetal calf serum, 100 IU/mL penicillin and 100 µg/mL streptomycin at 37 °C. The drug-adapted sub-lines were continuously cultured in the presence of the indicated drug concentrations. The cells were

routinely tested for mycoplasma contamination and authenticated by short tandem repeat profiling.

Cell viability assay

Cell viability was determined by 3-(4,5-dimethylthiazol-2-yl)-2,5-diphenyltetrazolium bromide (MTT) assay modified after Mosman [38], as previously described [39]. 2×10^4 cells suspended in 100 µL of cell culture medium were plated per well in 96-well plates and incubated in the presence of various doxorubicin concentrations (free or nanoparticle-encapsulated) for 120 h. Where indicated, free or nanoparticle-encapsulated doxorubicin was combined with a fixed concentration of 1 µM of the ABCB1 inhibitor zosuquidar. Then, 25 µL of MTT solution (2 mg/mL (w/v) in PBS) was added per well, and the plates were incubated at 37 °C for an additional 4 h. After this, the cells were lysed using 200 µL of a buffer containing 20% (w/v) sodium dodecylsulfate and 50% (v/v) *N*,*N*-dimethylformamide with the pH adjusted to 4.7 at 37 °C for 4 h. The absorbance was determined at 570 nm for each well using a 96-well multiscanner. After subtracting of the background absorption, the results are expressed as percentage viability relative to control cultures which received no drug. The drug concentrations that inhibited cell viability by 50% (IC_{50}) were determined using CalcuSyn (Biosoft, Cambridge, UK).

Statistical testing

The results are expressed as the mean ± standard deviation of at least three experiments. The Student's *t*-test was used for comparing two groups. Three and more groups were compared by ANOVA followed by the Student–Newman–Keuls test. *P*-values lower than 0.05 were considered to be significant.

Supporting Information

Doxorubicin IC_{50}s in neuroblastoma cells in the absence or presence of the ABCB1 inhibitor zosuquidar. Effects of doxorubicin applied as solution or incorporated into HSA nanoparticles on neuroblastoma cell viability. Effects of doxorubicin solution or doxorubicin HSA nanoparticles on neuroblastoma cells with or without zosuquidar.

Supporting Information File 1

Additional experimental details.
[https://www.beilstein-journals.org/bjnano/content/supplementary/2190-4286-10-166-S1.pdf]

Acknowledgements

This work was supported by the Kent Cancer Trust, the Hilfe für krebskranke Kinder Frankfurt e.V., and the Frankfurter Stiftung für krebskranke Kinder.

ORCID® iDs

Mark N. Wass - https://orcid.org/0000-0001-5428-6479
Klaus Langer - https://orcid.org/0000-0002-0203-7478
Martin Michaelis - https://orcid.org/0000-0002-5710-5888

Preprint

A non-peer-reviewed version of this article has been previously published as a preprint doi:10.1101/655662

References

1. International Agency for Research on Cancer. Cancer Fact Sheets. http://globocan.iarc.fr/Pages/fact_sheets_cancer.aspx (accessed Sept 10, 2018).
2. Holohan, C.; Van Schaeybroeck, S.; Longley, D. B.; Johnston, P. G. *Nat. Rev. Cancer* **2013,** *13,* 714–726. doi:10.1038/nrc3599
3. Steeg, P. S. *Nat. Rev. Cancer* **2016,** *16,* 201–218. doi:10.1038/nrc.2016.25
4. Siegel, R. L.; Miller, K. D.; Jemal, A. *Ca-Cancer J. Clin.* **2018,** *68,* 7–30. doi:10.3322/caac.21442
5. Robey, R. W.; Pluchino, K. M.; Hall, M. D.; Fojo, A. T.; Bates, S. E.; Gottesman, M. M. *Nat. Rev. Cancer* **2018,** *18,* 452–464. doi:10.1038/s41568-018-0005-8
6. Bar-Zeev, M.; Livney, Y. D.; Assaraf, Y. G. *Drug Resist. Updates* **2017,** *31,* 15–30. doi:10.1016/j.drup.2017.05.002
7. Thierry, A. R.; Vigé, D.; Coughlin, S. S.; Belli, J. A.; Dritschilo, A.; Rahman, A. *FASEB J.* **1993,** *7,* 572–579. doi:10.1096/fasebj.7.6.8097173
8. Bennis, S.; Chapey, C.; Robert, J.; Couvreur, P. *Eur. J. Cancer* **1994,** *30,* 89–93. doi:10.1016/s0959-8049(05)80025-5
9. Wong, H. L.; Bendayan, R.; Rauth, A. M.; Xue, H. Y.; Babakhanian, K.; Wu, X. Y. *J. Pharmacol. Exp. Ther.* **2006,** *317,* 1372–1381. doi:10.1124/jpet.106.101154
10. Prados, J.; Melguizo, C.; Ortiz, R.; Velez, C.; Alvarez, P. J.; Arias, J. L.; Ruiz, M. A.; Gallardo, V.; Aranega, A. *Anti-Cancer Agents Med. Chem.* **2012,** *12,* 1058–1070. doi:10.2174/187152012803529646
11. Oliveira, M. S.; Aryasomayajula, B.; Pattni, B.; Mussi, S. V.; Ferreira, L. A. M.; Torchilin, V. P. *Int. J. Pharm.* **2016,** *512,* 292–300. doi:10.1016/j.ijpharm.2016.08.049
12. Maiti, C.; Parida, S.; Kayal, S.; Maiti, S.; Mandal, M.; Dhara, D. *ACS Appl. Mater. Interfaces* **2018,** *10,* 5318–5330. doi:10.1021/acsami.7b18245
13. Weber, C.; Kreuter, J.; Langer, K. *Int. J. Pharm.* **2000,** *196,* 197–200. doi:10.1016/s0378-5173(99)00420-2
14. Langer, K.; Balthasar, S.; Vogel, V.; Dinauer, N.; von Briesen, H.; Schubert, D. *Int. J. Pharm.* **2003,** *257,* 169–180. doi:10.1016/s0378-5173(03)00134-0
15. Langer, K.; Anhorn, M. G.; Steinhauser, I.; Dreis, S.; Celebi, D.; Schrickel, N.; Faust, S.; Vogel, V. *Int. J. Pharm.* **2008,** *347,* 109–117. doi:10.1016/j.ijpharm.2007.06.028
16. Dreis, S.; Rothweiler, F.; Michaelis, M.; Cinatl, J., Jr.; Kreuter, J.; Langer, K. *Int. J. Pharm.* **2007,** *341,* 207–214. doi:10.1016/j.ijpharm.2007.03.036
17. von Storp, B.; Engel, A.; Boeker, A.; Ploeger, M.; Langer, K. *J. Microencapsulation* **2012,** *29,* 138–146. doi:10.3109/02652048.2011.635218

18. Ferrer, R.; Mateu, X.; Maseda, E.; Yébenes, J. C.; Aldecoa, C.; De Haro, C.; Ruiz-Rodriguez, J. C.; Garnacho-Montero, J. *Expert Rev. Clin. Pharmacol.* **2018,** *11,* 125–137. doi:10.1080/17512433.2018.1412827
19. Elzoghby, A. O.; Samy, W. M.; Elgindy, N. A. *J. Controlled Release* **2012,** *157,* 168–182. doi:10.1016/j.jconrel.2011.07.031
20. Kotchetkov, R.; Driever, P.; Cinatl, J.; Michaelis, M.; Karaskova, J.; Blaheta, R.; Squire, J.; Von Deimling, A.; Moog, J.; Cinatl, J., Jr. *Int. J. Oncol.* **2005,** *27,* 1029–1037. doi:10.3892/ijo.27.4.1029
21. Szakács, G.; Paterson, J. K.; Ludwig, J. A.; Booth-Genthe, C.; Gottesman, M. M. *Nat. Rev. Drug Discovery* **2006,** *5,* 219–234. doi:10.1038/nrd1984
22. Michaelis, M.; Rothweiler, F.; Klassert, D.; von Deimling, A.; Weber, K.; Fehse, B.; Kammerer, B.; Doerr, H. W.; Cinatl, J., Jr. *Cancer Res.* **2009,** *69,* 416–421. doi:10.1158/0008-5472.can-08-1856
23. Michaelis, M.; Rothweiler, F.; Löschmann, N.; Sharifi, M.; Ghafourian, T.; Cinatl, J., Jr. *Oncotarget* **2015,** *6,* 17605–17620. doi:10.18632/oncotarget.2889
24. Carter, D. C.; Ho, J. X. *Adv. Protein Chem.* **1994,** *45,* 153–203. doi:10.1016/s0065-3233(08)60640-3
25. Kavallaris, M. *Nat. Rev. Cancer* **2010,** *10,* 194–204. doi:10.1038/nrc2803
26. Wijdeven, R. H.; Pang, B.; Assaraf, Y. G.; Neefjes, J. *Drug Resist. Updates* **2016,** *28,* 65–81. doi:10.1016/j.drup.2016.07.001
27. Wischke, C.; Schwendeman, S. P. *Int. J. Pharm.* **2008,** *364,* 298–327. doi:10.1016/j.ijpharm.2008.04.042
28. Tyler, B.; Gullotti, D.; Mangraviti, A.; Utsuki, T.; Brem, H. *Adv. Drug Delivery Rev.* **2016,** *107,* 163–175. doi:10.1016/j.addr.2016.06.018
29. Pieper, S.; Onafuye, H.; Mulac, D.; Cinatl, J., Jr.; Wass, M. N.; Michaelis, M.; Langer, K. *bioRxiv, Pharmacol. Toxicol.* **2018**. doi:10.1101/403923
30. Merlot, A. M.; Kalinowski, D. S.; Richardson, D. R. *Front. Physiol.* **2014,** *5,* 299. doi:10.3389/fphys.2014.00299
31. Hyun, H.; Park, J.; Willis, K.; Park, J. E.; Lyle, L. T.; Lee, W.; Yeo, Y. *Biomaterials* **2018,** *180,* 206–224. doi:10.1016/j.biomaterials.2018.07.024
32. Brufsky, A. *Exp. Hematol. Oncol.* **2017,** *6,* 7. doi:10.1186/s40164-017-0066-5
33. Vallo, S.; Köpp, R.; Michaelis, M.; Rothweiler, F.; Bartsch, G.; Brandt, M. P.; Gust, K. M.; Wezel, F.; Blaheta, R. A.; Haferkamp, A.; Cinatl, J., Jr. *Oncol. Lett.* **2017,** *13,* 4085–4092. doi:10.3892/ol.2017.5986
34. Sanson, C.; Schatz, C.; Le Meins, J.-F.; Soum, A.; Thévenot, J.; Garanger, E.; Lecommandoux, S. *J. Controlled Release* **2010,** *147,* 428–435. doi:10.1016/j.jconrel.2010.07.123
35. Fletcher, J. I.; Ziegler, D. S.; Trahair, T. N.; Marshall, G. M.; Haber, M.; Norris, M. D. *Nat. Rev. Cancer* **2018,** *18,* 389–400. doi:10.1038/s41568-018-0003-x
36. Michaelis, M.; Rothweiler, F.; Barth, S.; Cinatl, J.; van Rikxoort, M.; Löschmann, N.; Voges, Y.; Breitling, R.; von Deimling, A.; Rödel, F.; Weber, K.; Fehse, B.; Mack, E.; Stiewe, T.; Doerr, H. W.; Speidel, D.; Cinatl, J., Jr. *Cell Death Dis.* **2011,** *2,* e243. doi:10.1038/cddis.2011.129
37. University of Kent. The Resistant Cancer Cell Line (RCCL) collection. https://research.kent.ac.uk/industrial-biotechnology-centre/the-resistant-cancer-cell-line-rccl-collection/ (accessed Oct 19, 2018).
38. Mosmann, T. *J. Immunol. Methods* **1983,** *65,* 55–63. doi:10.1016/0022-1759(83)90303-4
39. Michaelis, M.; Matousek, J.; Vogel, J.-U.; Slavik, T.; Langer, K.; Cinatl, J.; Kreuter, J.; Schwabe, D.; Cinatl, J., Jr. *Anti-Cancer Drugs* **2000,** *11,* 369–376. doi:10.1097/00001813-200006000-00007

License and Terms

The definitive version of this article is the electronic one which can be found at:
doi:10.3762/bjnano.10.166

BEILSTEIN JOURNAL OF NANOTECHNOLOGY

Lipid nanostructures for antioxidant delivery: a comparative preformulation study

Elisabetta Esposito[*1], Maddalena Sguizzato[1], Markus Drechsler[2], Paolo Mariani[3], Federica Carducci[3], Claudio Nastruzzi[1], Giuseppe Valacchi[4,5,6] and Rita Cortesi[*1]

Full Research Paper

Open Access

Address:
[1]Department of Chemistry and Pharmaceutical Sciences, University of Ferrara, I-44121 Ferrara, Italy, [2]Bavarian Polymerinstitute "Electron and Optical Microscopy" University of Bayreuth, Germany, [3]Dipartmento di Scienze della Vita e dell'Ambiente, Università Politecnica delle Marche, I-60131 Ancona, Italy, [4]NC State University, Plants for Human Health Institute, Animal Science Dept. NC Research Campus, Kannapolis, NC 28081, USA, [5]Department of Biomedical and Specialist Surgical Sciences, University of Ferrara, I-44121 Ferrara, Italy and [6]Department of Food and Nutrition, Kyung Hee University, Seoul, Korea

Email:
Elisabetta Esposito[*] - ese@unife.it; Rita Cortesi[*] - crt@unife.it

* Corresponding author

Keywords:
α-tocopherol; cryogenic transmission electron microscopy (cryo-TEM); dermocosmetics; HO-1; nanostructured lipid carriers (NLCs); retinoic acid; skin pollution; solid lipid nanoparticles (SLNs)

Beilstein J. Nanotechnol. **2019,** *10,* 1789–1801.
doi:10.3762/bjnano.10.174

Received: 31 May 2019
Accepted: 07 August 2019
Published: 29 August 2019

This article is part of the thematic issue "Frontiers in pharmaceutical nanotechnology".

Guest Editor: M. G. Wacker

Abstract

This investigation is a study of new lipid nanoparticles for cutaneous antioxidant delivery. Several molecules, such as α-tocopherol and retinoic acid, have been shown to improve skin condition and even counteract the effects of exogenous stress factors such as smoking on skin aging. This work describes the design and development of lipid nanoparticles containing antioxidant agents (α-tocopherol or retinoic acid) to protect human skin against pollutants. Namely, solid lipid nanoparticles and nanostructured lipid carriers were prepared using different lipids (tristearin, compritol, precirol or suppocire) in the presence or absence of caprylic/capric triglycerides. The formulations were characterized by particle size analysis, cryogenic transmission electron microscopy, small-angle X-ray diffraction, encapsulation efficiency, preliminary stability, in vitro cytotoxicity and protection against cigarette smoke. Nanostructured lipid carriers were found to reduce agglomerate formation and provided better dimensional stability, as compared to solid lipid nanoparticles, suggesting their suitability for antioxidant loading. Based on the preformulation study, tristearin-based nanostructured lipid carriers loaded with α-tocopherol were selected for ex vivo studies since they displayed superior physico-chemical properties as compared to the other nanostructured lipid carriers compositions. Human skin explants were treated with α-tocopherol-loaded nanostructured lipid carriers and then exposed to cigarette smoke, and the protein levels of the stress-induced enzyme heme oxygenase were analyzed in skin homogenates. Interestingly, it was found that pretreatment with the nanofor-

mulation resulted in significantly reduced heme oxygenase upregulation as compared to control samples, suggesting a protective effect provided by the nanoparticles.

Introduction

Air pollution increasingly affects industrialized urban areas in a negative manner with dramatic consequences for the environment and human health. This problem also affects rural areas, worsening the air quality all over the world. Besides being the primary cause of many respiratory diseases (e.g., chronic obstructive pulmonary disease, asthma and lung cancer), pollution is also responsible for cutaneous pathologies, spanning from skin aging, inflammation and allergy to skin cancer [1].

Cigarette smoke (CS) is one of the major toxic pollutants, exerting an important role in the onset of many serious and fatal diseases. Indeed, it is well known that CS can provoke various pathologies especially related to the lungs (e.g., cancer, emphysema, bronchitis) as well as the cardiovascular apparatus [2,3]. In the last two decades, the noxious effect of CS on skin has been well demonstrated [4-6]. For instance, the chronic exposure of skin to CS induces premature skin ageing, delayed wound healing, psoriasis and inflammatory skin diseases [3]. CS increases the risk of squamous cell carcinoma, with respect to non-smokers, as well as oral leukoplakia and oral cancers, such as lip cancer. Indeed, tobacco smoke is constituted of thousands of toxic compounds, including benzene, formaldehyde, hydrogen cyanide, carbon monoxide, arsenic and radioactive components, producing free radicals that cause oxidative stress [7]. The release of reactive oxygen species from tobacco smoke provokes a series of systemic immunomodulatory effects that leads to a compromised inflammatory response. These destructive mechanisms also affect collagen synthesis and the skin cellular reparative effects [8,9]. It has been found that antioxidants play a key role in the regulation of the deleterious activity exerted by CS in humans, nevertheless CS alters the requirements of antioxidants, such as vitamins E and A [9-14]. In this respect, quitting smoking does not always resolve the issue, since even more toxic effects have been shown from exposure to second-hand smoke.

Recently many cosmetic producers have focused their efforts towards antipollution dermocosmetics that are able to defend the skin against prolonged and repetitive daily exposure to pollutants; for instance, film-formers or skin rejuvenating excipients have been developed. Nevertheless, these strategies offer merely a short-term improvement of skin barrier function. Thus, in this respect, there is an unmet need for an effective product that endows skin protection from pollutants from long-term exposure, as well as for antipollution test methods suitable for assessing product efficacy and safety [15].

Vitamin E is a potent antioxidant, able to counteract the reactive oxygen species production during fat oxidation and free radical propagation – indeed it can protect the cell membranes from free radical attack, acting against lipid peroxidation. Vitamin E exists in 8 different forms, 4 tocopherols and 4 tocotrienols [16]. Among them α-tocopherol (TOC) can be mostly adsorbed and accumulated, thus it is largely employed as an antioxidant for edible oils and in anti-aging products. Notably, TOC has been proposed for the treatment of cancer and skin barrier improvement [17-19].

Vitamin A is defined as a group of lipophilic retinoids, including retinoic acid (RA), derived from food and stored in the liver. Due to its antioxidant action, RA plays a role in cancer chemoprevention and differentiation [20]. Particularly, RA has been proposed in the treatment of breast, lung and liver cancers [21,22]. Notably, it has been demonstrated that CS induces RA deficiency [23].

Despite the enormous potential of TOC and RA, some drawbacks are associated to their topical use, such as photodegradation, poor water solubility and irritative skin effects when employed in high dosage [24,25]. Thus, TOC and RA need to be loaded in specialized formulations suitable for skin application and able to adequately protect them from degradation. In this respect, recently different lipid nanoparticles have been proposed, including solid lipid nanoparticles (SLNs) and nanostructured lipid carriers (NLCs) [26-28]. SLNs possess several advantages over conventional lipid formulations being able to carry drugs in a biocompatible solid nanometric matrix, thus achieving

1. improvement of solubility,
2. stability of the loaded active molecule and
3. suitability of administration through different routes [29,30].

NLCs represent a smart generation of lipid nanoparticles, being based on a blend of solid and liquid lipids that creates a disordered nano-matrix, able to load higher amounts of lipophilic molecules than SLNs and avoiding leakage during storage [31-34].

The choice of the type and concentration of the nanoparticle lipid matrix is crucial since it can affect the physico-chemical aspects of SLNs and NLCs, the encapsulation parameters, as

well as the long-term stability of the formulation. Thus, in view of an industrial production, a preliminary formulation screening appears imperative [35,36].

The present investigation has been conducted to develop a nanoparticulate approach for counteracting skin pollution. In particular, a preformulation study was performed to select the type and composition of lipid nanoparticles suitable for encapsulation of TOC and RA. To assess the effect of antioxidant loaded in nanoparticles, a Western blot analysis has been performed to evaluate heme oxygenase expression on human skin explants treated with nanoparticles and exposed to CS.

Experimental

Reagents

The copolymer poly(ethylene oxide) (80)–poly(propylene oxide) (27) (poloxamer 188) was a gift from BASF ChemTrade GmbH (Burgbernheim, Germany). Miglyol 812 N, caprylic/capric triglycerides (miglyol) was a gift of Cremer Oleo Division (Witten, Germany). Glyceryl distearate (precirol ATO5, precirol), glyceryl dibehenate (compritol 888ATO, compritol) and mono-, di-, tri-glyceride esters of fatty acids (C_{10}–C_{18}) (suppocire AM, suppocire) were kind gifts of Gattefossè (Milan, Italy). Glyceryl tristearate (tristearin), α-tocopherol (TOC), retinoic acid (RA) and HPLC solvents were purchased from Sigma-Aldrich, Merck (Darmstadt, Germany).

Preparation of lipid nanoparticles

Lipid nanoparticles were prepared by a hot homogenization technique based on ultrasound treatment. In both cases the dispersing phase was an aqueous solution of poloxamer 188 (2.5% w/w) [37]. In the case of SLN the disperse phase was constituted of one solid lipid (i.e., tristearin, precirol, compritol or suppocire), while in the case of NLC, a mixture between one solid lipid and the liquid lipid caprylic/capric triglycerides (miglyol) (1:1 w/w ratio) was employed. In both cases the lipid phase was 5 or 10% by weight, with respect to the whole weight of the dispersion. The nanoparticle dispersion acronyms and compositions are reported in Table 1 and Table 2.

Firstly, an emulsion was obtained adding the poloxamer 188 aqueous phase (4.5/4.75 mL) heated at 80 °C to the molten lipid phase (250/500 mg), followed by mixing at 15000 rpm, at 80 °C for 1 min (IKA T25 digital ultraturrax). Secondly, the emulsion was subjected to ultrasound homogenization at 6.75 kHz for 15 min (Microson ultrasonic Cell Disruptor-XL Minisonix) and

Table 1: Composition of solid lipid nanoparticles (SLNs).

preparation	composition % (w/w)					
	lipid phase				water phase	
	tristearin	compritol	precirol	suppocire	poloxamer	water
SLN T5	5	–	–	–	2.37	92.63
SLN T10	10	–	–	–	2.25	87.75
SLN C5	–	5	–	–	2.37	92.63
SLN C10	–	10	–	–	2.25	87.75
SLN P5	–	–	5	–	2.37	92.63
SLN P10	–	–	10	–	2.25	87.75
SLN S5	–	–	–	5	2.37	92.63
SLN S10	–	–	–	10	2.25	87.75

Table 2: Composition of nanostructured lipid carriers (NLCs).

preparation	composition % (w/w)						
	lipid phase					water phase	
	tristearin	compritol	precirol	suppocire	miglyol	poloxamer	water
NLC T5	2.5	–	–	–	2.5	2.37	92.63
NLC T10	5.0	–	–	–	5.0	2.25	87.75
NLC C5	–	2.5	–	–	2.5	2.37	92.63
NLC C10	–	5.0	–	–	5.0	2.25	87.75
NLC P5	–	–	2.5	–	2.5	2.37	92.63
NLC P10	–	–	5.0	–	5.0	2.25	87.75
NLC S5	–	–	–	2.5	2.5	2.37	92.63
NLC S10	–	–	–	5.0	5.0	2.25	87.75

allowed to cool at 25 °C. Lipid nanoparticle dispersions were stored at room temperature. In the case of drug-loaded nanoparticles, TOC (0.4–0.8% w/w with respect to the whole dispersion; 8% w/w with respect to the lipid phase) or RA (0.02% w/w with respect to the whole dispersion; 0.4% w/w with respect to the lipid phase) were solubilized in caprylic/capric triglycerides (miglyol) and then added to the fused lipid phase before the emulsification step. The nanoparticle acronyms are reported in Table 3.

Photon correlation spectroscopy (PCS) analysis

Submicrometer particle analysis was performed using a Zetasizer Nano S90 device (Malvern Instruments, Malvern, England) equipped with a 5 mW helium neon laser with a wavelength output of 633 nm. The glassware was cleaned of dust by washing with detergent and rinsing twice with water for injections. The measurements were made in triplicate at 25 °C at an angle of 90°, and the data were interpreted using the "CONTIN" method [38].

Cryogenic transmission electron microscopy (cryo-TEM) analysis

The samples were vitrified as previously described [39]. The vitrified specimen was transferred to a Zeiss EM922 Omega transmission electron microscope for imaging using a cryoholder (CT3500, Gatan). The temperature of the sample was kept below −175 °C throughout the examination. The specimens were examined with doses of about 1000–2000 e/nm^2 at 200 kV. The images were digitally recorded by a CCD camera (Ultrascan 1000, Gatan) using an image processing system (GMS 1.9 software, Gatan). In addition, the size distribution of the nanoparticles was performed by measuring 1000 nanoparticles for each cryo-TEM image by the digital analyzer ImageJ 1.48v.

Small-angle X-ray scattering (SAXS) measurements

Small-angle X-ray scattering (SAXS) experiments were performed at the SAXS BM29 beamline of the European Synchrotron (ESRF) in Grenoble, France. NLC samples were filled in glass capillaries. The experiments were performed at 30 and 37 °C, both in the presence and absence of TOC and RA. The investigated Q-range ($Q = 4\pi \sin\theta/\lambda$, where 2θ is the scattering angle and λ is the X-ray wavelength) was from 0.01 to 0.5 Å^{-1}, the wavelength used was 0.99 Å. The sample exposure time was 160 s, which ensured enough statistical accuracy without degrading the samples by radiation. The Bragg peaks observed were indexed considering the possible symmetries commonly observed in lipid systems (lamellar, hexagonal or cubic) [40]. Accordingly, from the averaged spacing of the observed peaks the unit cell dimension of the phase was calculated.

Encapsulation efficiency and loading capacity of lipid nanoparticles

The encapsulation efficiency (EE) and loading capacity (LC) of TOC and RA in NLCs were determined as previously described [41]. A 0.5 mL aliquot of each NLC batch was loaded into a centrifugal filter (Microcon centrifugal filter unit YM-10 membrane, NMWCO 10 kDa, Sigma-Aldrich, St. Louis, MO, USA) and centrifuged (Spectrafuge™ 24D Digital Microcentrifuge, Woodbridge, NJ, USA) at 8,000 rpm for 20 min. The amount of drug was determined after dissolving the lipid phase with a known amount of methanol (1:10 v/v) for 2 h under stirring. The TOC and RA content was analyzed after filtration by high-performance liquid chromatography (HPLC) using a Knauer Eurospher II RP C18 column (Knauer, Germany) (15 × 0.4 cm) stainless steel packed with 5 µm particles, eluted at room temperature with different mobile phases. Samples of 50 µL were injected through the rheodyne injector system fitted with a 50 µL fixed loop and compared with standards of known

Table 3: Composition of antioxidant-containing NLCs.

preparation	composition % (w/w)								
	lipid phase							water phase	
	tristearin	compritol	precirol	suppocire	miglyol	TOC[a]	RA[b]	poloxamer	water
NLC T5-TOC	2.5	–	–	–	2.5	0.4	–	2.37	92.23
NLC T10-TOC	5.0	–	–	–	5.0	0.8	–	2.25	86.95
NLC C5-TOC	–	2.5	–	–	2.5	0.4	–	2.37	92.23
NLC C10-TOC	–	5.0	–	–	5.0	0.8	–	2.25	86.95
NLC P5-TOC	–	–	2.5	–	2.5	0.4	–	2.37	92.23
NLC P10-TOC	–	–	5.0	–	5.0	0.8	–	2.25	86.95
NLC S5-TOC	–	–	–	2.5	2.5	0.4	–	2.37	92.23
NLC S10-TOC	–	–	–	5.0	5.0	0.8	–	2.25	86.95
NLC T10-RA	5.0	–	–	–	4.98	–	0.02	2.25	87.75

[a]TOC: α-tocopherol; [b]RA: retinoic acid.

concentration. In the case of TOC, the mobile phase was methanol, and the flow rate was 1 mL/min at 295 nm, while for RA, acetonitrile/methanol/methylene chloride (70:15:15, v/v) was employed, with a flow rate of 1 mL/min at 325 nm. The analyses were conducted in triplicate. EE and LC were determined using Equation 1 and Equation 2

$$\mathrm{EE} = L/T \times 100 \quad (1)$$

$$\mathrm{LC} = L/T_{\text{lipid phase}} \times 100 \quad (2)$$

where L is the amount of drug effectively present within the nanoparticles, T stands for the total amount of drug initially added to the lipid phase and $T_{\text{lipid phase}}$ is the total weight of lipid phase in the formulation. Determinations were performed six times in independent experiments and the mean values ± standard deviations were calculated.

Stability studies

After production, the nanoparticles were stored in glass containers at 25 °C for 6 months [42]. To assess the physical and chemical stability, particle size analysis and TOC encapsulation efficiency were periodically evaluated by PCS and HPLC, respectively, as above reported.

Western blot analysis for HO-1 and HO-2 protein

Cytotoxicity determination

Experiments were carried out to assess the range of NLC T10-TOC, NLC C10-TOC, NLC P10-TOC and NLC S10-TOC concentrations that are nontoxic for cells. Briefly, human immortalized keratinocytes (HaCaT) were treated for 24 h with the different NLC formulations at various TOC concentrations, ranging from 25 to 200 μM. Cytotoxicity was evaluated by spectrophotometric quantification of the LDH released in culture medium, using a commercial kit (Sigma-Aldrich, Merck, Darmstadt, Germany), as previously described [43].

Human skin explant (HSE) culture

Skin explants were prepared from the superfluous skin of healthy adult donors (18–60 years old). Breast or abdominal tissue specimens were obtained from patients undergoing plastic surgery. Skin biopsies (12 mm punches) were cultured into standard 6-well plates in contact with culture medium at 37 °C in 5% CO_2 humidified air. The culture medium was Dulbecco's Modified Eagle Medium (DMEM) with 1% antibiotic-antimycotic solution (10,000 units penicillin, 10 mg streptomycin and 25 μg amphotericin B – Sigma-Aldrich, Germany) and 1% L-glutamine (Sigma-Aldrich, Germany) [43]. After 1 day in culture, the medium was changed and HSEs were topically treated with 50 μL of NLC T10 and NLC T10-TOC for 24 h.

Cigarette smoke (CS) exposure

After 24 h of treatment, the HSEs were exposed for 30 minutes to CS generated by burning one research cigarette (12 mg tar, 1.1 mg nicotine) using a vacuum pump, as previously described [44]. Control HSEs were exposed to filtered air. After exposure, the explants were incubated in fresh media at 37 °C in a humidified 5% CO_2 atmosphere for 24 h.

Protein extraction

Samples for Western blot analysis were washed in PBS and frozen in liquid nitrogen. The biopsies were extracted in ice-cold conditions using a tissue protein extraction reagent (T-PER buffer, Thermo Fisher Scientific, MA, USA) added consisting of protease and phosphatase inhibitor cocktails (Sigma, Milan, Italy), using a bead-based homogenizer at 12400 rpm at 4 °C for 15 min. The protein concentration was measured by the Bradford method (BioRad, CA, USA) [40].

Western blot analysis

The samples (25 μg protein) were loaded onto 10% sodium dodecyl sulfate polyacrylamide gel (SDS-PAGE) and then transferred onto nitrocellulose membranes. Blots were blocked in PBS containing 0.5% Tween 20 and 5% not-fat milk (BioRad). The membranes were incubated overnight at 4 °C with the appropriate primary antibody HO-1 (Abcam, Cambridge, UK). The membranes were then incubated with horseradish peroxidase conjugated secondary antibody for 1 h at RT, and the bound antibodies were detected in a chemiluminescent reaction (ECL, BioRad). Chemiluminescence was detected on a ChemiDoc imager (BioRad) [45]. The blots were reprobed with β-actin as the loading control. Images of the bands were digitized, and the densitometry of the bands was performed using ImageJ software [46].

Statistical analysis

For each of the variables tested, two-way analysis of variance (ANOVA) was used. A significant result was indicated by a p value <0.05. All the results are expressed as mean ± SD of 6 determinations for nanoparticle characterization experiments and 3 determinations obtained in 3 independent experiments for in vitro cultured cells tests.

Results and Discussion

Effect of lipid composition on nanoparticle macrostructure

In order to obtain a nanoparticulate system suitable for cutaneous administration of antioxidants, different lipid compositions have been considered, as reported in Table 1 and Table 2.

The selection of the lipid composition has been performed by choosing nottoxic, commercial lipids with similar chemical composition and different carbon chain lengths on the basis of our expertise concerning tristearin and caprylic/capric triglycerides (miglyol) [39]. Namely, SLNs were produced based on the use of solid di- or tri-glycerides, with chain lengths ranging between 18 and 21 carbon atoms, while for NLC production, the same solid lipids were employed in mixture (1:1 w/w) with the liquid caprylic/capric triglycerides (miglyol), characterized by C_8–C_{10} chains.

With regard to surfactant concentration, higher poloxamer amounts, namely 3 and 4% w/w with respect to the aqueous phase, have been tested. However, the increase of poloxamer led to foam formation during the preparation, which caused irregular and inhomogeneous formulations; thus 2.5% w/w of poloxamer was used.

The hot homogenization method followed by ultrasound [39] lead to production of milky and homogeneous dispersions. Immediately after cooling, in most cases, a small amount of coalesced lipid phase appeared on the surface of the dispersion. The weight of this agglomerate, spanning between 0 and 4.65% by weight with respect to the total amount of the lipid phase, was a function of the lipid composition. Indeed, both the amount and the type of lipid phase appear to influence the agglomerate formation. Particularly, the longer the lipid chain, the higher the agglomerate weight according to the following trend: compritol (2 C_{21} chains) > tristearin (3 C_{18} chains) > precirol (2 C_{18} chains) > suppocire (3 C_{10}–C_{18} chains). Specifically, in the latter case, the agglomerate was almost absent (Table 4). In addition, the extent of agglomeration was lower for NLC, probably due to the presence of the liquid lipid.

Table 4: Dimensional characteristics of SLNs or NLCs and the presence of agglomerates.

Preparation	Z-average, D_z (nm)	Polydispersity index	Agglomerate[a] (%)
SLN T5	148.6 ± 74.5	0.35 ± 0.11	2.86 ± 0.04
SLN T10	164.9 ± 9.4	0.33 ± 0.04	4.65 ± 0.03
SLN C5	244.5 ± 26.5	0.36 ± 0.01	3.43 ± 0.02
SLN C10	488.9 ± 25.3	0.32 ± 0.04	3.77 ± 0.04
SLN P5	245.5 ± 31.9	0.31 ± 0.03	2.48 ± 0.03
SLN P10	453.1 ± 9.3	0.39 ± 0.02	2.99 ± 0.04
SLN S5	220.9 ± 15.6	0.37 ± 0.06	1.13 ± 0.03
SLN S10	201.8 ± 82.1	0.39 ± 0.06	0.60 ± 0.04
NLC T5	122.6 ± 34.2	0.32 ± 0.07	2.14 ± 0.02
NLC T10	127.9 ± 29.1	0.29 ± 0.03	2.54 ± 0.01
NLC C5	160.2 ± 25.5	0.29 ± 0.03	3.15 ± 0.02
NLC C10	136.8 ± 51.5	0.24 ± 0.04	3.25 ± 0.01
NLC P5	148.1 ± 29.5	0.22 ± 0.10	1.51 ± 0.01
NLC P10	159.8 ± 33.7	0.30 ± 0.08	1.84 ± 0.02
NLC S5	131.3 ± 30.5	0.31 ± 0.05	0 ± 0.01
NLC S10	136.1 ± 13.5	0.29 ± 0.07	0 ± 0.01

[a]Loss of lipids (lipid phase) due to the partial coalescence of the lipid phase during the formation of the O/W emulsion. % refers to the weight of the lipid phase. Data represent the mean ± SD of 6 independent experiments.

Effect of lipid composition on nanoparticle size distribution

The SLN and NLC dimensions, measured by PCS and expressed by the Z-average, D_z, are reported in Figure 1 and Table 4. In the case of SLN with 5% lipid phase concentration, mean diameters were comprised between 148 and 245 nm, with some differences due to the lipid composition. The doubling of the lipid phase concentration, however, induced an increase of the mean diameter, especially in the case of SLN P10 and SLN C10, whose Z-average reached almost 500 nm. In the case of NLC, the lipid phase composition scarcely affected the mean diameter, ranging between 125 and 160 nm both for 5% and 10% of lipid phase. The polydispersity index was always below 0.39, with smaller values in the case of NLCs.

The Z-average mean diameters of SLNs and NLCs stored at 25 °C were measured after 3 months from production. In the case of SLNs, the mean diameter dramatically increased, as reported in Figure 1A and 1B, especially for SLN T10, SLN C10 and SLN P10, reaching values undetectable by PCS, where instead, the mean diameter of SLN S5 and SLN S10 did not improve. This behavior can be attributed to the lipid phase containing SLN that influences both agglomerate and the mean diameter of the nanoparticles. On the contrary, the NLCs maintained their mean diameters almost unvaried, irrespectively of the lipid phase type and concentration (Figure 1C and 1D).

In order to avoid agglomeration phenomena and to control the mean size, only NLCs have been considered for antioxidant loading.

Production and characterization of NLCs containing antioxidants

To produce antioxidant-containing NLCs, different amounts of TOC and RA were loaded in NLCs, as reported in Table 3. Particularly, since TOC is practically insoluble in water (logP 8.84), it was directly added to caprylic/capric triglycerides (miglyol) in order to improve its solubility (reaching 16 mg/mL) before addition of solid lipids [47]. The doubling of the lipid phase concentration enabled to doubling the amount of TOC loading. The macroscopic characteristic of NLCs containing TOC was milky and homogeneous, similar to the empty NLCs. Both the presence of agglomerates and the mean size of

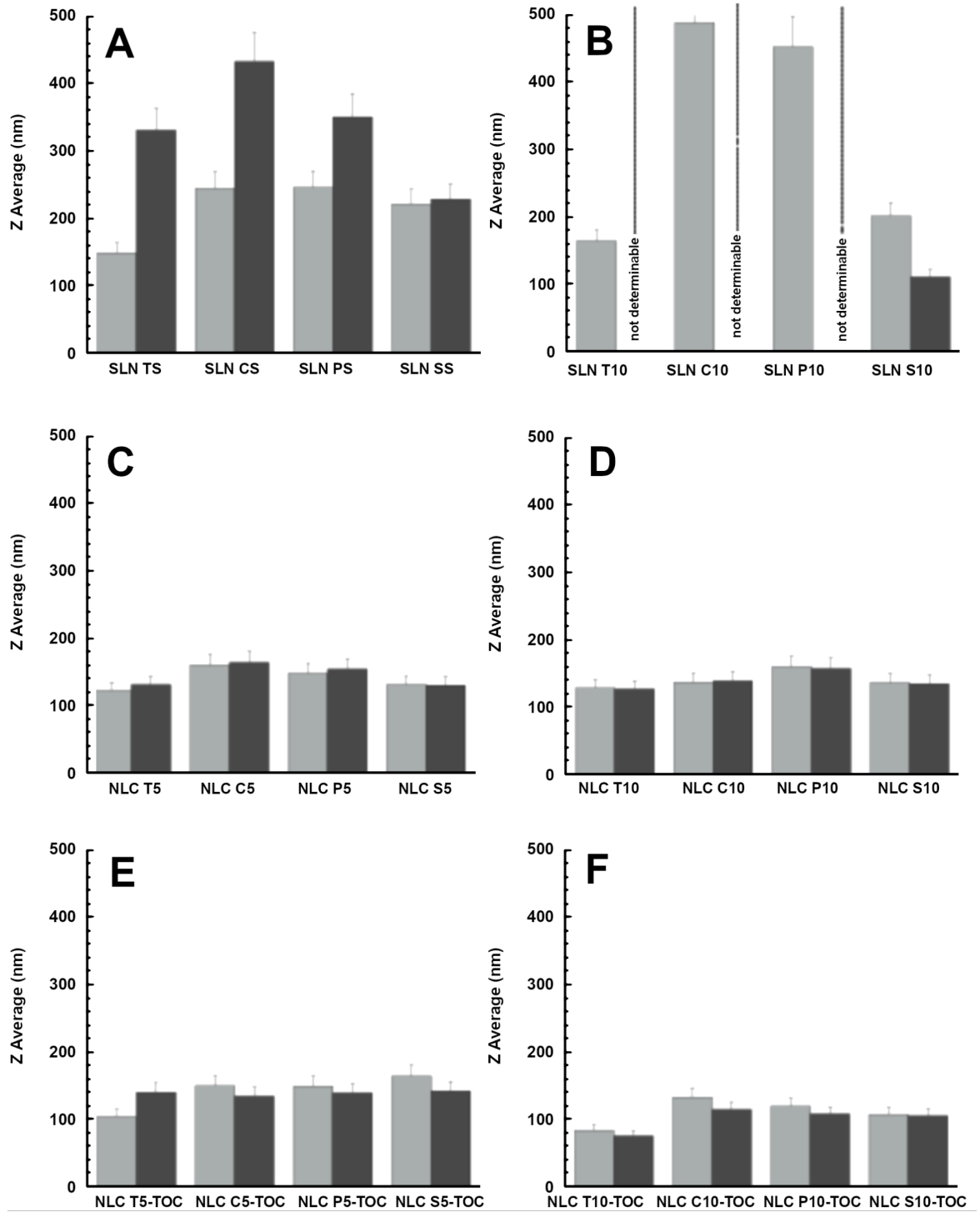

Figure 1: Variation of the Z-average mean diameters, D_z, of SLNs (A, B) and NLCs (C, D) produced in the absence of antioxidants and NLC loaded with TOC (E, F) evaluated at 1 (light grey) and 90 (grey) days after nanoparticle production. In the case of SLN T10, SLN C10 and SLN P10, mean diameters were not measurable by PCS 90 days after production.

NLCs containing TOC were lower with respect to their empty counterparts (Table 5). This trend suggest that TOC could contribute to stabilize the interface between the lipid and the aqueous phase, leading to smaller droplets and finally to smaller nanoparticles. The agglomerate presence was more evident in the case of compritol and absent in the case of suppocire, as in the case of empty NLCs, while mean dimensions were inversely proportional to the amount of lipid phase and TOC. As ob-

Table 5: Dimensional characteristics, agglomeration and encapsulation parameters of antioxidant-containing NLCs.

NLC preparation	Z-average, D_z (nm)	Polydispersity index	Agglomerate[a] (%)	Encapsulation efficiency[b]	Loading capacity[c]
NLC T5-TOC	104.5 ± 32.0	0.33 ± 0.11	1.22 ± 0.02	90.96 ± 1.3	7.27 ± 0.1
NLC T10-TOC	82.8 ± 10.7	0.36 ± 0.05	1.24 ± 0.01	90.69 ± 2.8	7.25 ± 0.2
NLC C5-TOC	149.4 ± 36.9	0.22 ± 0.03	2.25 ± 0.01	95.61 ± 1.5	7.64 ± 0.2
NLC C10-TOC	132.7 ± 51.3	0.34 ± 0.05	3.17 ± 0.02	79.15 ± 2.5	6.33 ± 0.1
NLC P5-TOC	149.5 ± 30.3	0.30 ± 0.02	1.11 ± 0.01	93.58 ± 1.7	7.48 ± 0.1
NLC P10-TOC	118.5 ± 31.9	0.30 ± 0.05	1.12 ± 0.02	90.99 ± 2.2	7.27 ± 0.2
NLC S5-TOC	164.6 ± 21.7	0.29 ± 0.06	0.00 ± 0.01	88.16 ± 1.3	7.05 ± 0.1
NLC S10-TOC	106.1 ± 24.2	0.29 ± 0.07	0.00 ± 0.01	60.72 ± 2.1	4.85 ± 0.1
NLC T10-RA	98.4 ± 20.2	0.27 ± 0.12	2.52 ± 0.01	67.24 ± 0.8	0.16 ± 0.0

[a]Loss of lipids (lipid phase) due to the partial coalescence of the lipid phase during the formation of the O/W emulsion. After cooling the coalesced lipid phase appeared as a small flake floating on the surface of the NLC dispersion. [b]Percentage (w/w) of drug in the whole dispersion with respect to the total amount used for the preparation. [c]Percentage (w/w) of drug within nanoparticles as compared to the amount of lipid used for the preparation. Data represent the mean ± S.D. of 6 independent experiments.

served in the case of the empty counterparts, Z-average mean diameters, D_z, of antioxidants containing NLC stored at 25 °C for 3 months were almost unvaried (Figure 1E and 1F). Particularly, NLC T10-TOC displayed the smallest mean diameter, even after 3 months.

Due to the encouraging results obtained using tristearin 10%, RA was loaded into NLC T10. Due to its poor water solubility (logP 6.3), as in the case of TOC, RA was added to caprylic/capric triglycerides (miglyol), improving its solubility to 4 mg/mL [48]. In the case of NLC T10-RA, despite the small mean diameter (98 nm), the agglomeration phenomenon was more noticeable as compared to NLC T10-TOC (Table 5).

The NLC morphology was investigated by cryo-TEM and a few images are reported in Figure 2. In general, the NLC shape appears discoid in the top view, or more electron-dense and rod-like in the edge-on view. In the case of tristearin-based NLCs, the shape was roundish, both for empty (Figure 2A) and antioxidant-loaded NLC T10 (Figure 2B and C). In the case of compritol (Figure 2D) and precirol (Figure 2E) based NLCs, ovoid and triangular structures were observed. At last, in the case of suppocire NLCs, besides the presence of some irregular structures (Figure 2F), spherical structures were detected (inset of Figure 2F), resembling vesicles rather than to solid particles.

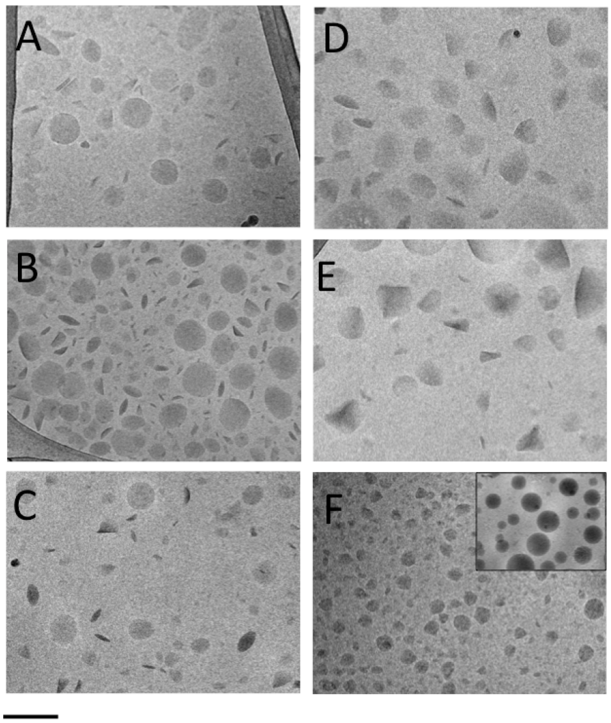

Figure 2: Cryo-TEM images of NLC T10 (A), NLC T10-TOC (B), NLC T10-RA (C), NLC C5-TOC (D), NLC P5-TOC (E), NLC S5-TOC (F). The scale bar below corresponds to 200 nm in panels A–E and 300 nm in panel F.

The inner morphology of the NLCs was further characterized by SAXS [39,40]. In particular, SAXS experiments were performed on NLC samples prepared by using tristearin or suppocire both in the presence and in the absence of TOC and RA. By way of illustration, Figure 3 shows the low-angle diffraction profiles obtained as a function of the lipid phase concentration from tristearin-based NLCs (top graph, A) and from suppocire-based NLCs (middle graph, B), both containing TOC. The presence of Bragg peaks in the NLC T5-TOC and NLC T10-TOC samples shows that the inner structure of the NLC at 30 °C depends on the used lipid: tristearin guarantees the presence of an ordered structural organization inside the NLC, while suppocire is not able to preserve such an organization. According to the cryo-TEM findings, vesicles rather than nanoparticles probably form in this condition.

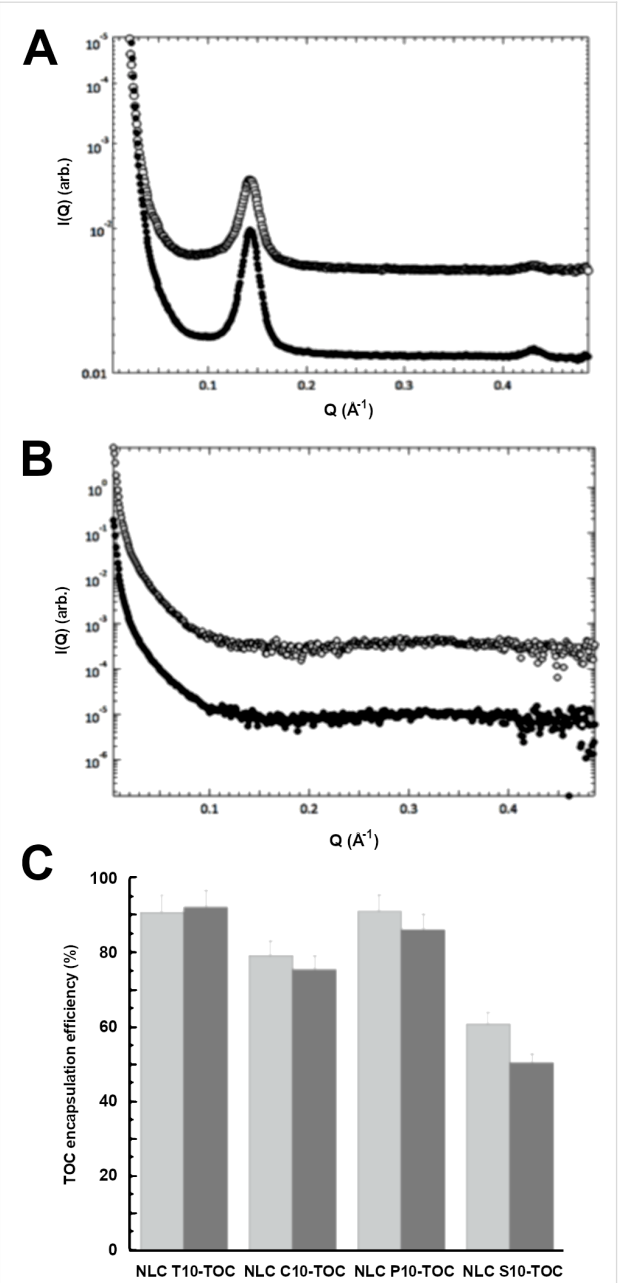

Figure 3: SAXS profiles observed for A: NLCT5-TOC (open symbol) and NLCT10-TOC (closed symbol), B: NLCS5-TOC (open symbol), and NLCS10-TOC (closed symbol). C: TOC encapsulation efficiency in the indicated NLC, evaluated at 1 (light grey) and 90 (grey) days after production.

The analysis of the position of the peaks observed in tristearin-based NLCs allowed the identification of the internal structural organization for NLC T5-TOC and NLC T10-TOC: because the spacing ratios scale as 1:2:3.., a lamellar organization was derived [34,35]. The corresponding unit cell dimension, which in a lamellar organization is the repeated distance between two lamellae, was 43.9 Å. It should be noted that similar results were obtained from empty tristearin-based NLCs: the packing of the lamellae in the nanoparticle inner region is not affected by the presence of the antioxidant. The scattering profiles obtained from NLC T5-RA and NLC T10-RA were very similar (data not shown), confirming the described behavior.

Encapsulation of antioxidants in NLCs

The influence of the NLC lipid composition on the capability to incorporate antioxidants was studied by evaluating the EE and LC. The values reported in Table 5 and Figure 3C evidenced that in the case of tristearin or precirol based NLCs, the EE of TOC was >90%, irrespective of the lipid phase concentration. In the case of NLC C10-TOC, both a decrease in the EE value and an increase in agglomeration were detected with respect to NLC C5-TOC, suggesting that the doubling of the lipid concentration promoted agglomeration of the lipid phase, partially avoiding TOC encapsulation within the nanoparticles. This hypothesis was corroborated by disaggregation and HPLC analysis of the lipid phase agglomerate, revealing the presence of 13% w/w TOC with respect to the total amount used for NLC production.

The lowest EE values were found in the case of NLC S10-TOC and NLC T10-RA. In the case of suppocire, TOC EE values decreased from 88 to 60% by doubling the lipid phase concentration, suggesting that the presence of vesicles instead of nanoparticles prevented high loading of the antioxidant within their structure.

Regarding NLC T10-RA, as for NLC C10-TOC, an amount of antioxidant (11%) was found within the agglomerate of the lipid phase, justifying the reason for the low EE value of RA. LC values of NLCs containing TOC were between 4.85 and 7.64%, whilst in the case of RA, the LC was only 0.16% due to the lower amount of RA employed for NLC production (0.05 mg/100 mg lipid phase, instead of 8 mg/100 mg lipid phase used in the case of TOC).

In order to detect the capability of NLC to control the encapsulation of antioxidants under storage, the EE values were evaluated for 90 days (Figure 3C). Particularly, NLCs containing 10% lipid phase were selected due to their marked dimensional stability.

The TOC EE values were almost unvaried in the case of NLC T10-TOC – they slightly decreased in the case of NLC C10-TOC and NLC P10-TOC, whilst the decrease was more evident in the case of NLC S10-TOC, passing from 60 to 48%. It can be hypothesized that the prevalence of vesicles in NLC S10-TOC, instead of more structured carriers, hindered the TOC encapsulation. Lastly, in the case of NLC T10-RA, RA encapsulation dramatically decreased –the EE value halved one month after

production (data not shown). Due to their poor stability, NLC T10-RA samples were not considered for further studies.

Cytotoxicity of NLCs containing TOC

As the produced formulations are intended for topical administration on the skin, experiments on human keratinocytes were conducted in order to test the cytotoxicity of NLC T10-TOC, NLC C10-TOC, NLC P10-TOC and NLC S10-TOC. The LDH release in the media was assessed 24 h after TOC treatment at the concentrations of 25, 50, 100 and 200 μM.

As shown in Figure 4, no NLC cytotoxicity was observed with respect to control cells and no significant difference among the different NLCs was noticed, confirming the biocompatibility of the components.

Due to the obtained results, NLC T10-TOC samples were selected for further ex vivo studies. Indeed, this kind of NLC displayed better physico-chemical properties with respect to NLC based on different lipid compositions, being able to longer maintain the size and the EE of TOC.

Antioxidant effect of NLCs containing TOC

Following the results obtained in the 2D cell model, the study of the protective effect of NLC T10-TOC was carried out on HSE.

CS contains many components able to elicit oxidative stress, which can induce the cytoprotective enzyme heme oxygenase (HO-1). An HO-1 increase promotes protection against inflammation and/or cell death induced by CS [49,50]. In order to

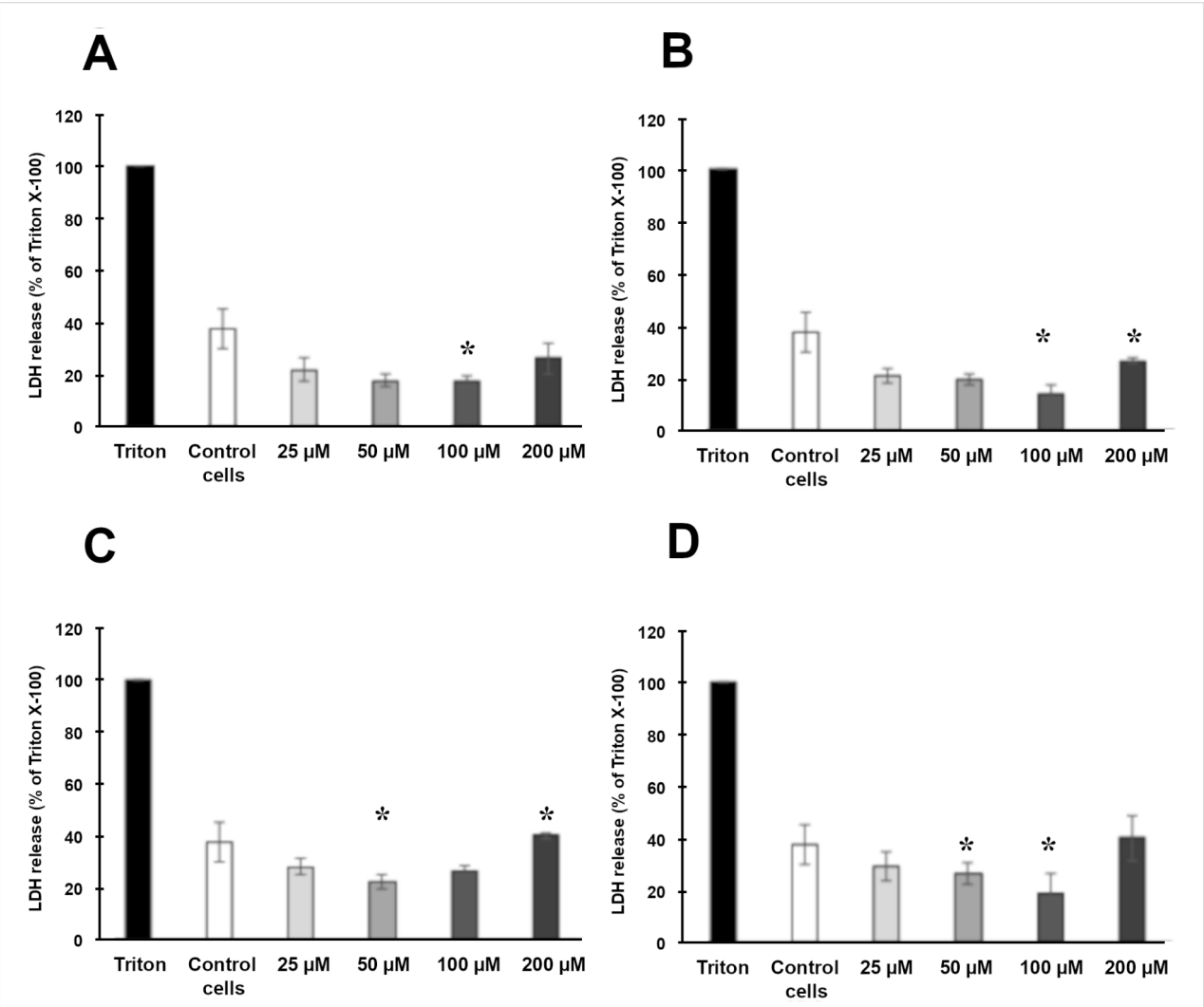

Figure 4: Cytotoxicity of NLC T10-TOC (A), NLC C10-TOC (B), NLC P10-TOC (C) and NLC S10-TOC (D) evaluated by LDH release from HaCaT cells in the media after 24 h of treatment. Data are expressed as percentage LDH release as compared to the maximum release of LDH from Triton-X100-treated cells. Data are given as mean ± SD, representative of three independent experiments with at least three technical replicates each time. * indicates statistically significant difference to untreated control cells (unpaired *t*-test, $p < 0.01$).

evaluate the effect of NLC T10-TOC in preventing damage caused by CS, the HO-1 expression was evaluated on HSE cultures exposed to CS or to air for 24 h. Namely HO-1 has been determined by Western blot analysis, quantified by densitometry and normalized to the beta-actin level for each sample (Figure 5A). The mean relative density ratios of three experiments are shown in Figure 5B. As depicted, the expression of the HO-1 protein level is significantly induced by the CS exposure because of the ability of this outdoor stressor to promote oxidative-related cellular modifications to the skin [39]. On the other hand, HO-1 levels in skin explants treated with NLC T10-TOC and exposed to CS were dramatically and significantly prevented (47% decrease, $p < 0.001$ vs control).

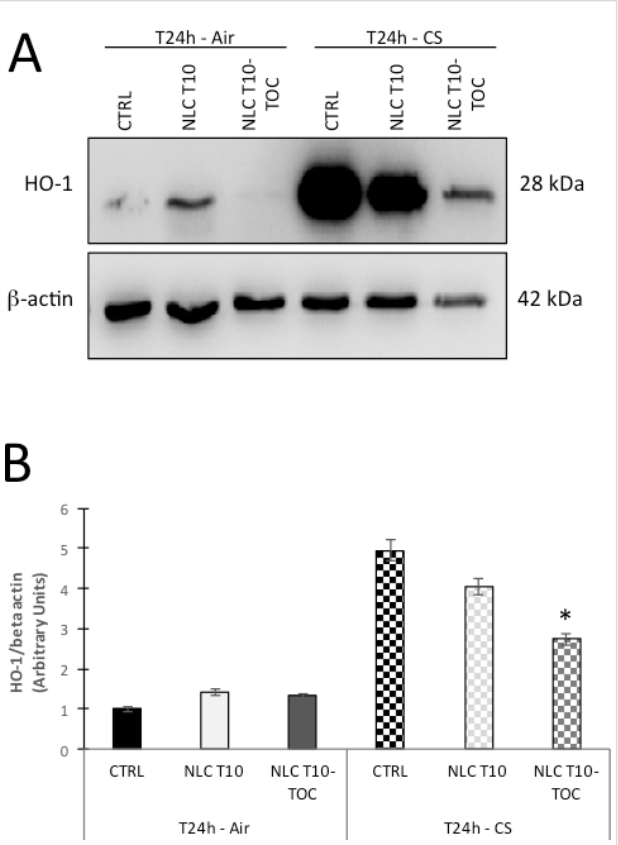

Figure 5: Effect of cigarette smoke (CS) on heme-oxygenase (HO-1) expression evaluated on human skin explants (HSE) treated with NLCT 10 or NLCT 10-TOC, exposed to air or CS for 30 min and harvested after 24 h. A) Representative Western blot analyses of HO-1 protein expression (with the respective β-actin controls). B) Mean expression of HO-1 as a ratio of β-actin. The results are shown as the mean of three experiments. * $p < 0.05$ with respect to the control.

These results suggest that NLC T10-TOC can effectively reduce the induction of cutaneous HO-1, which is a sensor of tissue stress, suggesting the ability of this topical application to prevent CS-induced skin damage. Further studies will be required to investigate the dose and type-dependent manner of action of TOC loaded in NLCs with respect to an unloaded TOC solution.

Conclusion

This work has underlined the importance of technological screening in the design of a nanoparticulate lipid dosage formulation. Notably, dimensional and morphological characterization of nanoparticles should be performed at different durations of time after production. This investigation has demonstrated that the type and concentration of the lipid phase affect the physico-chemical stability of nanoparticles. The NLC T10-TOC sample that was selected by the preformulation study deserved further in vitro and in vivo studies. Indeed, supplementary studies will be performed to investigate the activity of hydrophilic antioxidant molecules, such as ascorbic acid and *N*-acetyl-cysteine, loaded in NLCs and in comparison with conventional "non-nano" formulations. In addition, since some authors have demonstrated that CS induces depletion of some essential vitamins, such as TOC and RA [23], it should be interesting to evaluate the suitability of NLC T10-TOC as an oral antioxidant supplement.

Acknowledgements

This work was funded by "FIR 2018" of Ferrara University, Italy.

ORCID® iDs

Elisabetta Esposito - https://orcid.org/0000-0002-8416-3629
Maddalena Sguizzato - https://orcid.org/0000-0002-2100-2043
Markus Drechsler - https://orcid.org/0000-0001-7192-7821
Paolo Mariani - https://orcid.org/0000-0003-4293-1009
Federica Carducci - https://orcid.org/0000-0002-3985-7998
Rita Cortesi - https://orcid.org/0000-0002-1060-2676

References

1. Rembiesa, J.; Ruzgas, T.; Engblom, J.; Holefors, A. *Cosmetics* **2018,** *5,* 4–12. doi:10.3390/cosmetics5010004
2. Saha, S. P.; Bhalla, D. K.; Whayne, T. F.; Gairola, C. G. *Int. J. Angiol.* **2007,** *16,* 77–83. doi:10.1055/s-0031-1278254
3. Onor, I. O.; Stirling, D. L.; Williams, S. R.; Bediako, D.; Borghol, A.; Harris, M. B.; Darensburg, T. B.; Clay, S. D.; Okpechi, S. C.; Sarpong, D. F. *Int. J. Environ. Res. Public Health* **2017,** *14,* 1147. doi:10.3390/ijerph14101147
4. Kennedy, C.; Bastiaens, M. T.; Willemze, R.; Bouwes Bavinck, J. N.; Bajdik, C. D.; Westendorp, R. G. J. *J. Invest. Dermatol.* **2003,** *120,* 548–554. doi:10.1046/j.1523-1747.2003.12092.x
5. Silvano, A.; Nistri, S.; Calosi, L.; Romagnoli, P. *Ital. J. Anat. Embryol.* **2019,** *124,* 42–57.
6. Suehara, L. Y.; Simone, K.; Maia, M. *An. Bras. Dermatol.* **2006,** *81,* 34–39. doi:10.1590/s0365-05962006000100004
7. Hu, S. S.; Neff, L.; Agaku, I. T.; Cox, S.; Day, H. R.; Holder-Hayes, E.; King, B. A. *Morb. Mortal. Wkly. Rep.* **2016,** *65,* 685–691. doi:10.15585/mmwr.mm6527a1

8. Benowitz, N. L.; Hukkanen, J.; Jacob, P., III. Nicotine Chemistry, Metabolism, Kinetics and Biomarkers. In *Handbook of Experimental Pharmacology;* Barrett, J. E., Ed.; Springer Berlin: Berlin, Germany; pp 29–60. doi:10.1007/978-3-540-69248-5_2
9. Bruno, R. S.; Traber, M. G. *J. Nutr.* **2005,** *135,* 671–674. doi:10.1093/jn/135.4.671
10. Bruno, R. S.; Leonard, S. W.; Atkinson, J.; Montine, T. J.; Ramakrishnan, R.; Bray, T. M.; Traber, M. G. *Free Radical Biol. Med.* **2006,** *40,* 689–697. doi:10.1016/j.freeradbiomed.2005.10.051
11. Alberg, A. J. *Toxicology* **2002,** *180,* 121–137. doi:10.1016/s0300-483x(02)00386-4
12. Thomsen, S. F.; Sørensen, L. T. *Skin Therapy Lett.* **2010,** *15,* 4–7.
13. Handelman, G. J.; Packer, L.; Cross, C. E. *Am. J. Clin. Nutr.* **1996,** *63,* 559–565. doi:10.1093/ajcn/63.4.559
14. Dietrich, M.; Block, G.; Norkus, E. P.; Hudes, M.; Traber, M. G.; Cross, C. E.; Packer, L. *Am. J. Clin. Nutr.* **2003,** *77,* 160–166. doi:10.1093/ajcn/77.1.160
15. Mistry, N. *Cosmetics* **2017,** *4,* 57. doi:10.3390/cosmetics4040057
16. Wolf, G. *J. Nutr.* **2005,** *135,* 363–366. doi:10.1093/jn/135.3.363
17. Buettner, G. R. *Arch. Biochem. Biophys.* **1993,** *300,* 535–543. doi:10.1006/abbi.1993.1074
18. Chen, J.; Wei, N.; Lopez-Garcia, M.; Ambrose, D.; Lee, J.; Annelin, C.; Peterson, T. *Eur. J. Pharm. Biopharm.* **2017,** *117,* 286–291. doi:10.1016/j.ejpb.2017.04.008
19. Vaz, S.; Silva, R.; Amaral, M. H.; Martins, E.; Sousa Lobo, J. M.; Silva, A. C. *Colloids Surf., B* **2019,** *179,* 242–249. doi:10.1016/j.colsurfb.2019.03.036
20. Okuno, M.; Kojima, S.; Matsushima-Nishiwaki, R.; Tsurumi, H.; Muto, Y.; Friedman, S.; Moriwaki, H. *Curr. Cancer Drug Targets* **2004,** *4,* 285–298. doi:10.2174/1568009043333023
21. Ross-Innes, C. S.; Stark, R.; Holmes, K. A.; Schmidt, D.; Spyrou, C.; Russell, R.; Massie, C. E.; Vowler, S. L.; Eldridge, M.; Carroll, J. S. *Genes Dev.* **2010,** *24,* 171–182. doi:10.1101/gad.552910
22. Uray, I. P.; Dmitrovsky, E.; Brown, P. H. *Semin. Oncol.* **2016,** *43,* 49–64. doi:10.1053/j.seminoncol.2015.09.002
23. Xue, Y.; Harris, E.; Wang, W.; Baybutt, R. C. J. *J. Biomed. Sci. (London, U. K.)* **2015,** *22,* 84–92. doi:10.1186/s12929-015-0189-0
24. Andersen, F. A. *Int. J. Toxicol.* **2002,** *21,* 51–116. doi:10.1080/10915810290169819
25. MacGregor, J. L.; Maibach, H. I. *Exog. Dermatol.* **2002,** *1,* 68–73. doi:10.1159/000058335
26. Saez, V.; Souza, I. D. L.; Mansur, C. R. E. *Int. J. Cosmet. Sci.* **2018,** *40,* 103–116. doi:10.1111/ics.12452
27. Eiras, F.; Amaral, M. H.; Silva, R.; Martins, E.; Lobo, J. M. S.; Silva, A. C. *Int. J. Pharm.* **2017,** *519,* 373–380. doi:10.1016/j.ijpharm.2017.01.045
28. Castro, G. A.; Oréfice, R. L.; Vilela, J. M. C.; Andrade, M. S.; Ferreira, L. A. M. *J. Microencapsulation* **2007,** *24,* 395–407. doi:10.1080/02652040701288519
29. Kumar, S.; Randhawa, J. K. *Mater. Sci. Eng., C* **2013,** *33,* 1842–1852. doi:10.1016/j.msec.2013.01.037
30. Pardeike, J.; Hommoss, A.; Müller, R. H. *Int. J. Pharm.* **2009,** *366,* 170–184. doi:10.1016/j.ijpharm.2008.10.003
31. Üner, M.; Yener, G. *Int. J. Nanomed.* **2007,** *2,* 289–300.
32. Jores, K.; Mehnert, W.; Drechsler, M.; Bunjes, H.; Johann, C.; Mäder, K. *J. Controlled Release* **2004,** *95,* 217–227. doi:10.1016/j.jconrel.2003.11.012
33. Müller, R. H.; Mäder, K.; Gohla, S. *Eur. J. Pharm. Biopharm.* **2000,** *50,* 161–177. doi:10.1016/s0939-6411(00)00087-4
34. Jenning, V.; Thünemann, A. F.; Gohla, S. H. *Int. J. Pharm.* **2000,** *199,* 167–177. doi:10.1016/s0378-5173(00)00378-1
35. Dingler, A.; Gohla, S. *J. Microencapsulation* **2002,** *19,* 11–16. doi:10.1080/02652040010018056
36. Paliwal, R.; Babu, R. J.; Palakurthi, S. *AAPS PharmSciTech* **2014,** *15,* 1527–1534. doi:10.1208/s12249-014-0177-9
37. Esposito, E.; Drechsler, M.; Mariani, P.; Carducci, F.; Servadio, M.; Melancia, F.; Ratano, P.; Campolongo, P.; Trezza, V.; Cortesi, R.; Nastruzzi, C. *Biomed. Microdevices* **2017,** *19,* 44–58. doi:10.1007/s10544-017-0188-x
38. Pecora, R. *J. Nanopart. Res.* **2000,** *2,* 123–131. doi:10.1023/a:1010067107182
39. Esposito, E.; Fantin, M.; Marti, M.; Drechsler, M.; Paccamiccio, L.; Mariani, P.; Sivieri, E.; Lain, F.; Menegatti, E.; Morari, M.; Cortesi, R. *Pharm. Res.* **2008,** *25,* 1521–1530. doi:10.1007/s11095-007-9514-y
40. Kulkarni, C. V. *Nanoscale* **2012,** *4,* 5779–5791. doi:10.1039/c2nr31465g
41. Puglia, C.; Bonina, F.; Rizza, L.; Cortesi, R.; Merlotti, E.; Drechsler, M.; Mariani, P.; Contado, C.; Ravani, L.; Esposito, E. *J. Pharm. Sci.* **2010,** *99,* 2819–2829. doi:10.1002/jps.22028
42. Pugh, W. J. In *Aultons's Pharmaceutics-The design and manufacture of the medicines;* Aulton, M. E., Ed.; Churchil Livingstone Elsevier: London, United Kingdom, 2007; pp 99–107.
43. Esposito, E.; Sticozzi, C.; Ravani, L.; Drechsler, M.; Muresan, X. M.; Cervellati, F.; Cortesi, R.; Valacchi, G. *Exp. Dermatol.* **2015,** *24,* 449–454. doi:10.1111/exd.12696
44. Muresan, X. M.; Sticozzi, C.; Belmonte, G.; Savelli, V.; Evelson, P.; Valacchi, G. *Mech. Ageing Dev.* **2018,** *172,* 78–85. doi:10.1016/j.mad.2017.11.006
45. Muresan, X. M.; Sticozzi, C.; Belmonte, G.; Cervellati, F.; Ferrara, F.; Lila, M. A.; Valacchi, G. *Arch. Biochem. Biophys.* **2018,** *658,* 1–6. doi:10.1016/j.abb.2018.09.014
46. Valacchi, G.; Pecorelli, A.; Belmonte, G.; Pambianchi, E.; Cervellati, F.; Lynch, S.; Krol, Y.; Oresajo, C. *J. Invest. Dermatol.* **2017,** *137,* 1373–1375. doi:10.1016/j.jid.2017.01.034
47. *Virtual Computational Chemistry Laboratory,* ALOGPS 2.1; , http://www.vcclab.org/lab/alogps/.
48. NCBI homepage U.S.. National Library of Medicine National Center for Biotechnology Information: Bethesda, MA, U.S.A.https://pubchem.ncbi.nlm.nih.gov/compound/Retinoic-acid.
49. Abraham, N. G.; Kappas, A. *Pharmacol. Rev.* **2008,** *60,* 79–127. doi:10.1124/pr.107.07104
50. Atzori, L.; Caramori, G.; Lim, S.; Jazrawi, E.; Donnelly, L.; Adcock, I.; Barnes, P. J.; Chung, K. F. *Respir. Med.* **2004,** *98,* 530–535. doi:10.1016/j.rmed.2003.11.007

BEILSTEIN JOURNAL OF NANOTECHNOLOGY

Preservation of rutin nanosuspensions without the use of preservatives

Pascal L. Stahr and Cornelia M. Keck*§

Full Research Paper

Open Access

Address:
Department of Pharmaceutics and Biopharmaceutics, Philipps-Universität Marburg, Robert-Koch-Str. 4, 35037 Marburg, Germany

Email:
Cornelia M. Keck* - cornelia.keck@pharmazie.uni-marburg.de

* Corresponding author
§ Phone: +49(0)6421 2825885

Keywords:
nanocrystals; nanosuspension; no preservative; rutin; stability

Beilstein J. Nanotechnol. **2019,** *10,* 1902–1913.
doi:10.3762/bjnano.10.185

Received: 09 April 2019
Accepted: 27 August 2019
Published: 19 September 2019

This article is part of the thematic issue "Frontiers in pharmaceutical nanotechnology".

Guest Editor: M. G. Wacker

Abstract

Nanocrystals are used as universal approach to improve the bioactivity of poorly soluble active ingredients. They are produced by various techniques, typically yielding aqueous nanosuspensions, which are prone to microbial contamination. Preservation of nanocrystals is possible but might not always be feasible, as preservatives might interfere with other excipients in the formulations or with chemicals used in assays, cell cultures or animal models. Therefore, to enable an easier use of nanocrystals, preservative-free nanosuspensions would be a good alternative. In this study, rutin nanocrystals were frozen and stored for three months at −20 °C. The chemical, physical and microbial stability were monitored, and the results were compared to preserved nanosuspensions. The frozen nanosuspensions remained stable and possessed excellent stability over the whole time of storage, indicating that the freeze–thaw process is suitable for the production of preservative-free nanosuspensions with excellent long-term stability. The freeze–thaw process for nanosuspensions is a simple concept and is suggested as alternative, when preserved nanosuspensions cannot be used.

Introduction

Nanocrystals for pharmaceutical use were invented in the early 1990s [1-4]. They are composed of 100% substance, are stabilized with only small amounts of surfactants, and possess particle sizes below 1 µm. According to the Ostwald–Freundlich equation nanocrystals possess a higher curvature leading to an enhanced dissolution pressure and thus to an enhanced kinetic saturation solubility [5]. Due to their small size they possess an increased surface area, resulting in an increased dissolution rate expressed by the Noyes–Whitney equation. In addition, they also possess an increased adhesiveness and thus, represent a universal, powerful and well-known formulation principle to overcome poor aqueous solubility and poor bioavailability of class-II and class-VI active ingredients of the biopharmaceutics classification system (BCS) [6,7]. Nanocrystals are already used

in various pharmaceutical drug products for oral use. Examples are Rapamune® (Sirolimus, Wyeth), Emend® (Aprepitant, Merck), Tricor® (Fenofibrate, Abbott), Megace ES® (Megestrol, Par Pharm) or Triglide® (First Horizon Pharmaceuticals). In 2009 the first parenteral drug product, Invega Sustenna® (Paliperidone palmitate, Johnson & Johnson), was approved by the FDA. However, besides oral or parenteral administration, nanocrystals can also be used to improve the bioactivity of poorly soluble active ingredients via other routes of administration. Examples include pulmonal, ocular or dermal application [8-12].

Nanocrystals can be produced by different methods. Examples are precipitation, wet milling, high-pressure homogenization or combinations of these methods [1-4]. Regardless of the process used, all these methods will yield nanosuspensions, i.e., nanocrystals dispersed in a liquid. As liquid formulations are not always a convenient dosage form for the final drug product, in most cases nanosuspensions need to be formulated into other, more convenient, dosage forms. Depending on the route of administration this could be tablets, pellets, powders, gels or creams. However, prior to the formulation into final drug products, the aqueous nanosuspensions need to be stored, which certainly requires a sufficient stability of the nanosuspension. For this, besides chemical and physical stability, also the microbial stability needs to be considered.

One method to avoid microbial contamination of aqueous formulations during storage is the use of preservatives. In previous studies it was already found that preservatives can strongly impair the physical stability of the nanosuspensions. Reasons for this are changes of pH value or of the conductivity of the dispersion medium, or the adsorption of the preservatives onto the surface of the particles, which changes the charge of the particles (zeta potential) and forces agglomeration of the nanocrystals. To avoid instabilities of nanosuspensions only very hydrophilic and non-charged preservatives, which will not interact with the nanocrystals, should be used. Due to the above-mentioned reasons, only a few preservatives are available for the preservation of nanocrystals. Suitable preservatives for the preservation of nanocrystals include different alcohols, i.e., pentylene glycol or mixtures of phenoxyethanol and ethyl hexyl glycerol [13-15].

The limited number of preservatives and sometimes the incompatibility of these preservatives with other excipients in the final formulation are inconvenient for a successful formulation of nanosuspensions. Therefore, to enable a more convenient formulation of nanocrystals in the future, this work aimed at investigating an alternative method to maintain the microbial stability of nanosuspensions during storage.

Considering that bacterial growth strongly depends on the temperature, it was hypothesized that freezing of non-preserved nanosuspensions might prevent bacterial growth of the nanosuspensions during storage. However, the harsh conditions during freezing and thawing might also impair the physical stability of the nanocrystals and might cause agglomeration of the particles, which would then lead to a loss of the “nano properties”. Hence, in this case the method could not be exploited to preserve nanosuspensions without preservative.

To investigate whether the freeze–thaw method is suitable for the production of long-term stable non-preserved nanosuspensions with high microbial quality, previously developed nanosuspensions containing the flavonoid rutin as model substance and either Plantacare 2000 or Poloxamer 188 (PLX 188) as stabilizers were produced by high-pressure homogenization as described previously [16-19]. Each of the nanosuspensions obtained was allocated into two parts. One part was preserved, and the other part remained non-preserved. All formulations were stored at different temperatures for a period of three months and size, zeta potential, antioxidant capacity and the microbial quality were determined and monitored over this period of time (Figure 1).

Results and Discussion

Production and characterization of nanosuspensions

High-pressure homogenization yielded rutin nanosuspensions with a relatively broad size distribution, i.e., polydispersity indices (PdI values) above 0.3 and some larger particles with sizes above 4 µm (Table 1). Because of this, the nanosuspensions were expected to be prone to Ostwald ripening, i.e., particle growth during storage was expected. Limited physical stability of suspensions is advantageous if a study aims at investigating different stabilizing and destabilizing effects, because in comparison to highly physically stable formulations, destabilizing effects can be detected earlier during storage, making a discrimination between stabilizing and destabilizing effects clearer.

The suspension stabilized with PLX 188 yielded sizes of about 410 nm. Slightly larger nanocrystals with a slight agglomeration were obtained when Plantacare was used as stabilizer (Table 1 and Table 2). From this it was expected that non-preserved nanosuspensions stabilized with PLX 188 might possess a slightly better physical stability than the Plantacare-stabilized formulations. Upon the addition of the preservatives only very minor changes in size were observed for both formulations (Table 1) and for the Plantacare-stabilized formulation even a slight deagglomeration was determined (Table 2). Also the zeta potential values did not change significantly in both

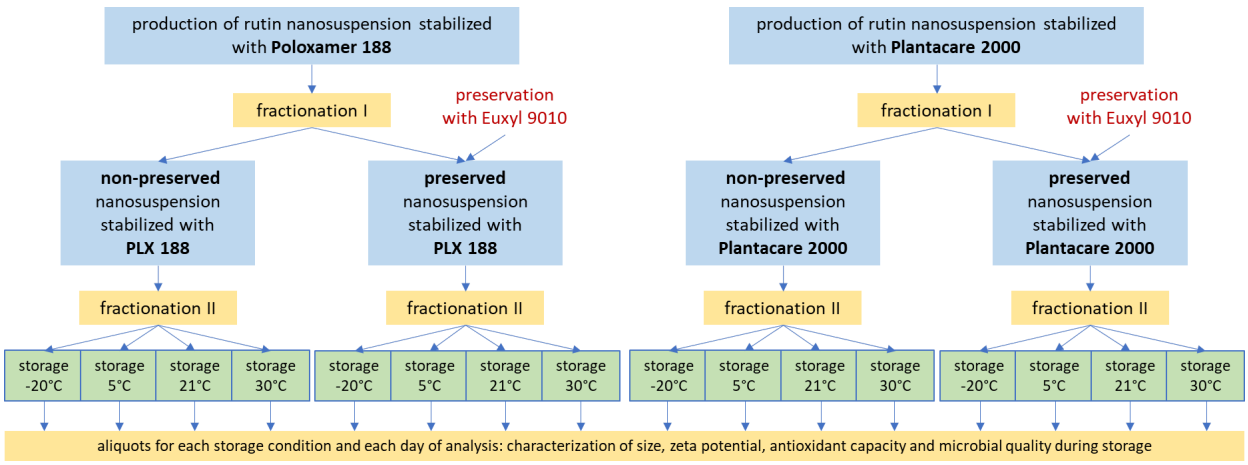

Figure 1: Scheme of the study. Rutin nanosuspensions with two different stabilizers were produced. The formulations were allocated, one aliquot was preserved, and the other part remained non-preserved. All formulations obtained were stored at different temperatures for three months. During this time changes in size, zeta potential, antioxidant capacity and microbial quality were monitored.

Table 1: Overview of results obtained from the characterization of the nanocrystals at the day of production.

stabilizer	preservative	DLS data		zeta potential [mV]		LD data [µm][a]	
		z-ave [nm]	PdI	in water	in medium	*d*(*v*)0.50	*d*(*v*)0.95
PLX 188	no preservative	408 ± 45	0.31 ± 0.08	−29.4 ± 2.9	−24.8 ± 2.6	1.3 ± 0.17	4.09 ± 0.15
	with preservative	412 ± 29	0.30 ± 0.05	−27.0 ± 7.8	−24.6 ± 3.0	1.3 ± 0.12	4.13 ± 0.15
Plantacare 2000	no preservative	436 ± 30	0.32 ± 0.06	−30.6 ± 4.0	−39.5 ± 2.7	1.2 ± 0.11	4.02 ± 0.11
	with preservative	447 ± 15	0.33 ± 0.06	−29.3 ± 2.7	−37.6 ± 3.3	1.2 ± 0.12	3.99 ± 0.11

[a]*d*(*v*): volumetric median diameter.

water and original dispersion medium (Table 1), again indicating no, or only a very limited, impairment of the stabilization mechanisms of the nanocrystals by the hydrophilic preservative [20].

Physical stability

The physical stability was assessed by size measurements over a period of three months of samples under all storage conditions. Increases in *d*(*v*) values, *z*-average, and polydispersity index (PdI) over time indicated instability. The laser diffractometry (LD) data and the dynamic light scattering (DLS) data obtained from this part of the study are shown in Figures 2–7.

For the non-preserved nanosuspensions, increasing storage temperatures reduced the physical stability of the non-preserved suspensions (Figure 2, Figure 3, Figure 6, Figure 7). Consequently, the least stable formulations were obtained when the formulations were stored at 30 °C. Reasons for this are the more pronounced particle growth due to Ostwald ripening at elevated temperatures and/or destabilization due to accelerated bacterial growth, which might excrete compounds that contribute to changes in pH value or conductivity in the medium or interact with the particles. Such changes should become visible in the zeta potential values. However, this was not the case in this study (Figure 8). Therefore, the observed destabilization at elevated temperatures of the non-preserved nanosuspensions might be more related to Ostwald ripening. The assumption is also underlined by the fact that the Poloxamer-stabilized formulations, which possessed a narrower size distribution, i.e., no agglomerates at the day of production (c.f. Table 2), were found to be more stable than the Plantacare-stabilized formulations with a broader size distribution due to a slight agglomeration of the nanocrystals at the day of production.

The trend for physical stability was different for the preserved nanosuspensions. The most stable formulations were obtained when the samples were stored at room temperature. Lower (except freezing) and higher temperatures reduced the stability (Figures 4–7). Reasons for this cannot be explained completely but might be due to the presence of the preservatives that were added to the samples at room temperature. Changes in tempera-

Table 2: Microscopic images of the nanosuspensions stabilized with Poloxamer 188 (left) and Plantacare 2000 (right) at the day of production. Magnification: 400-fold.

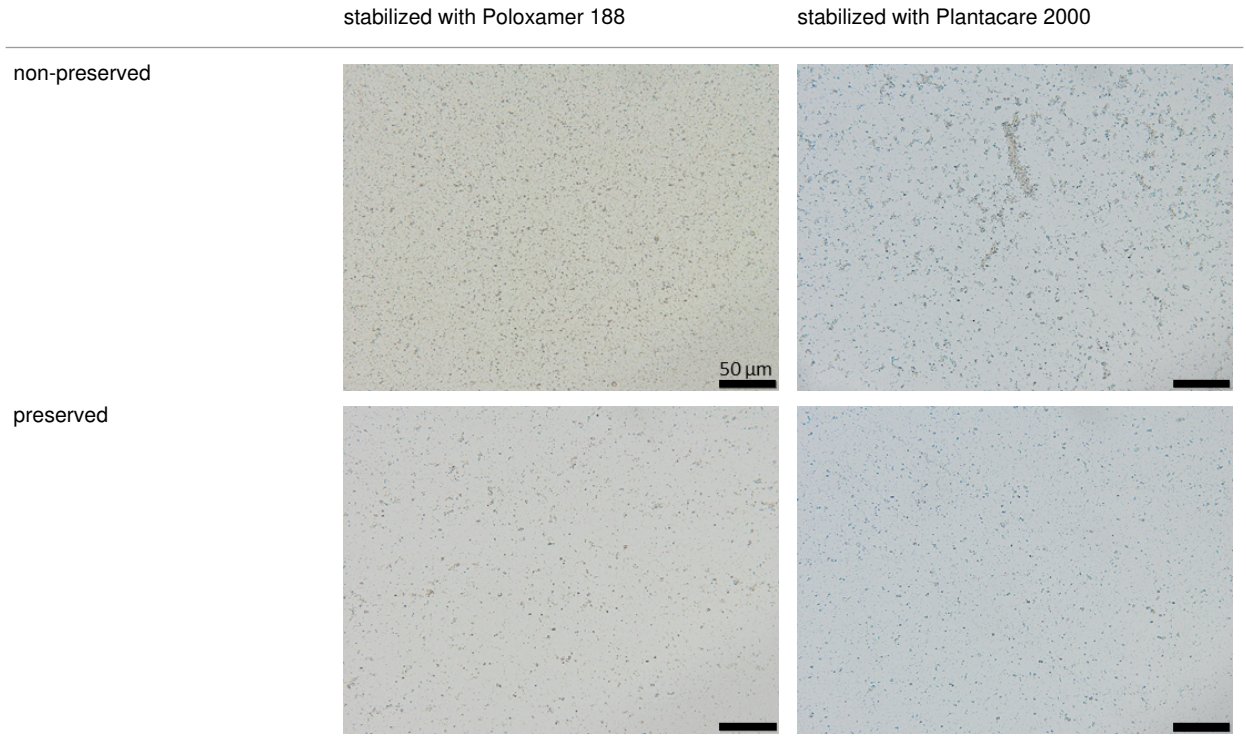

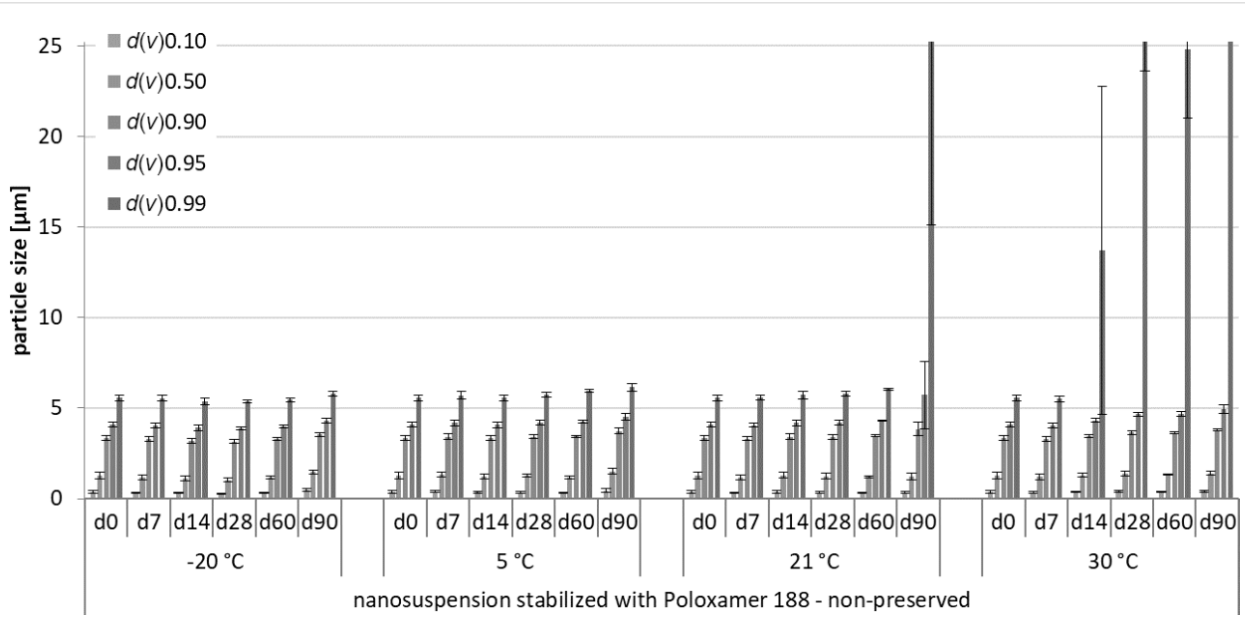

Figure 2: Physical stability during three months of storage at different storage temperatures for the non-preserved nanosuspensions stabilized with Poloxamer 188 (LD data).

ture might change the interaction between preservative and particles and thus the stability. More research is needed to understand these phenomena in detail.

Most interesting results were obtained for the samples that were stored in frozen state. Physically stable formulations, i.e., without pronounced changes in *z*-average, PdI and LD values, were

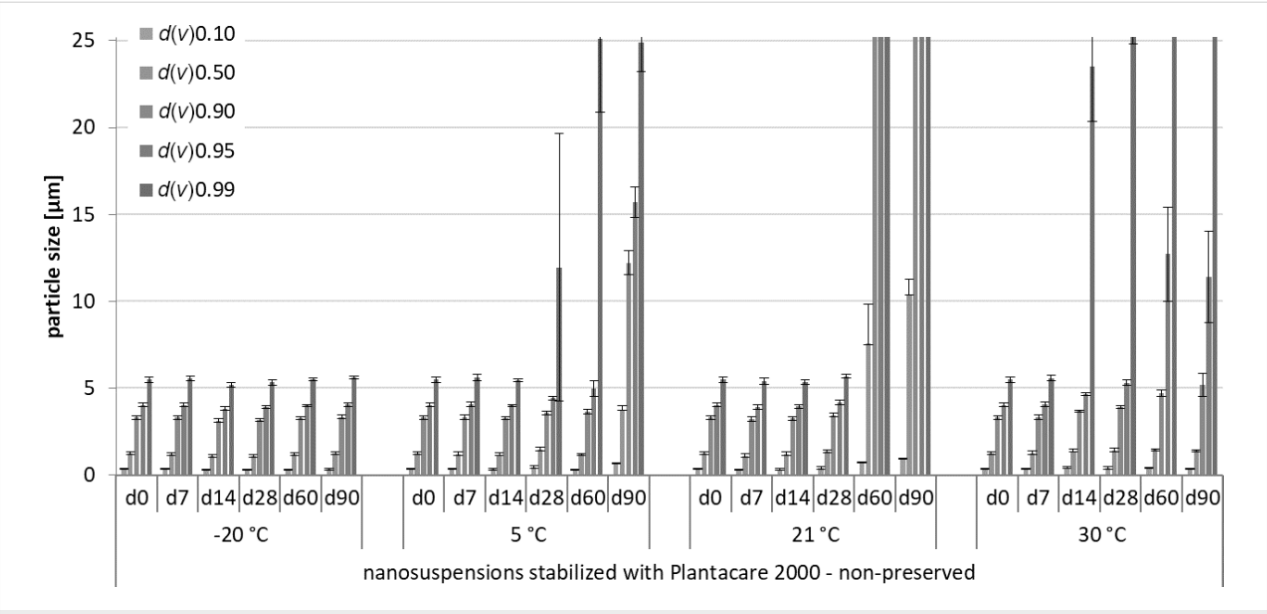

Figure 3: Physical stability during three months of storage at different storage temperatures for the non-preserved nanosuspensions stabilized with Plantacare 2000 (LD data).

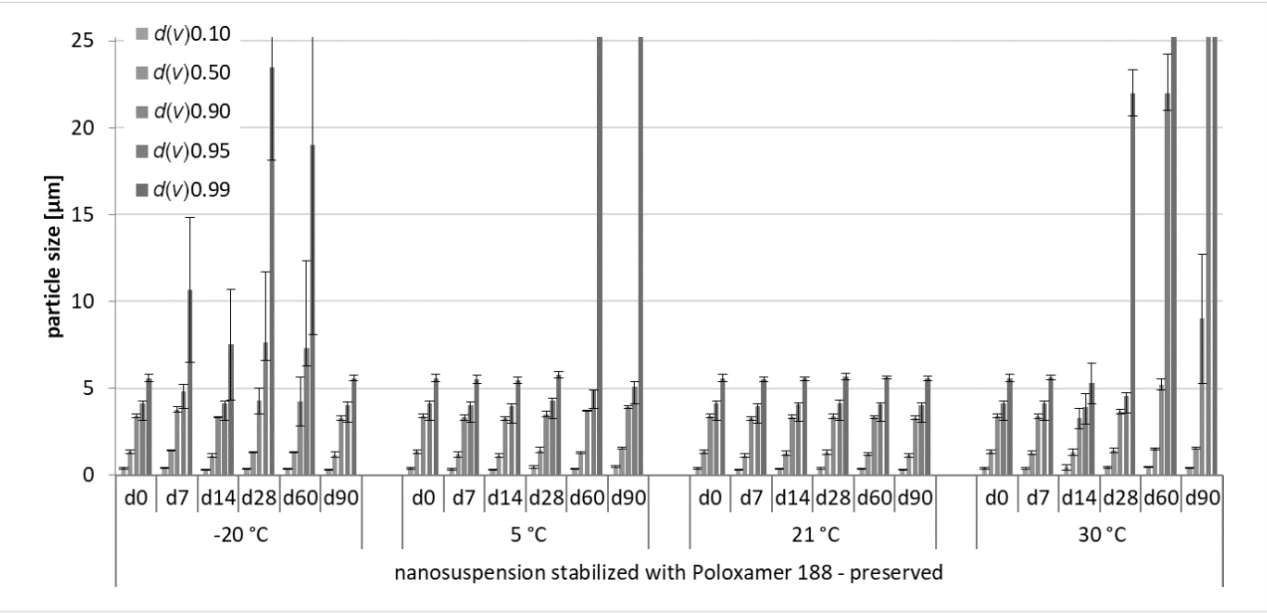

Figure 4: Physical stability during three months of storage at different storage temperatures for the preserved nanosuspensions stabilized with Poloxamer 188 (LD data).

obtained for the non-preserved suspensions when stored at −20 °C. These results were not expected, because in general it is assumed that freezing of colloidal formulations leads to changes in the stabilizing layer and the particle interactions, being the cause for agglomeration of the nanoparticles. Especially freezing of nanosuspensions that contain dissolved active ingredients in "supersaturation" is hazardous, because due to the reduction in temperature, re-crystallization of dissolved active ingredients can easily occur. Nevertheless, the data obtained from this study indicate that it is possible to freeze–thaw nanosuspensions with good steric and/or electrostatic stabilization, without impairing their physical stability. The later fact seems to be highly important, especially when looking at the data obtained for the frozen and preserved nanosuspensions. Here, it was found that preserved nanosuspensions that were stabilized with PLX 188 became unstable during the freeze–thaw process, whereas Plantacare-stabilized formulations remained stable.

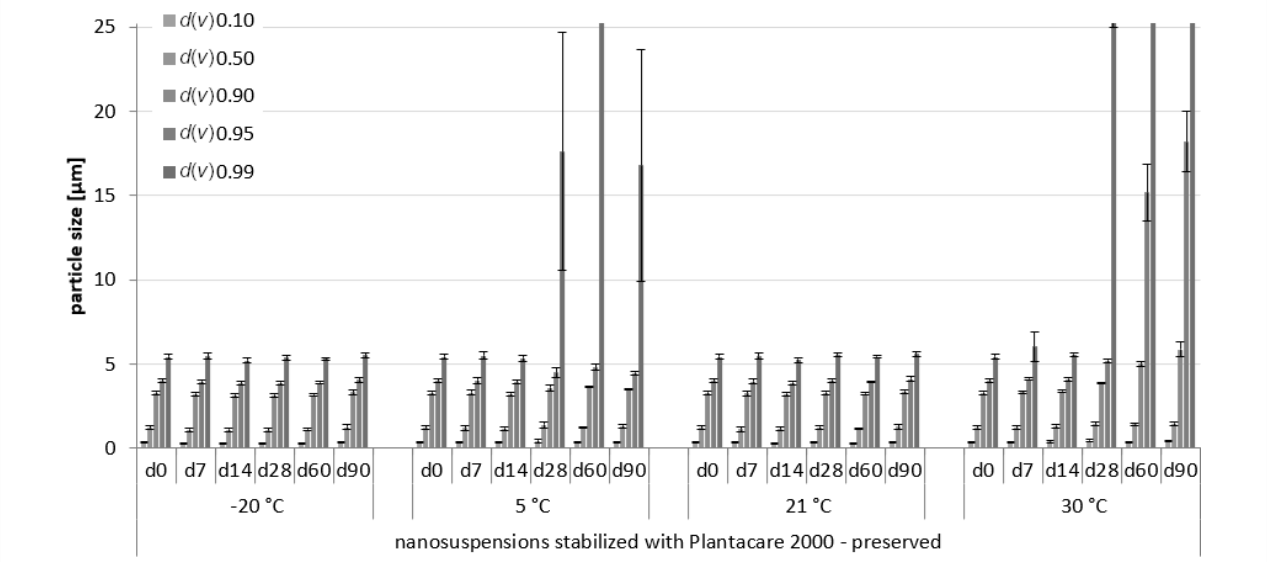

Figure 5: Physical stability during three months of storage at different storage temperatures for the preserved nanosuspensions stabilized with Plantacare 2000 (LD data).

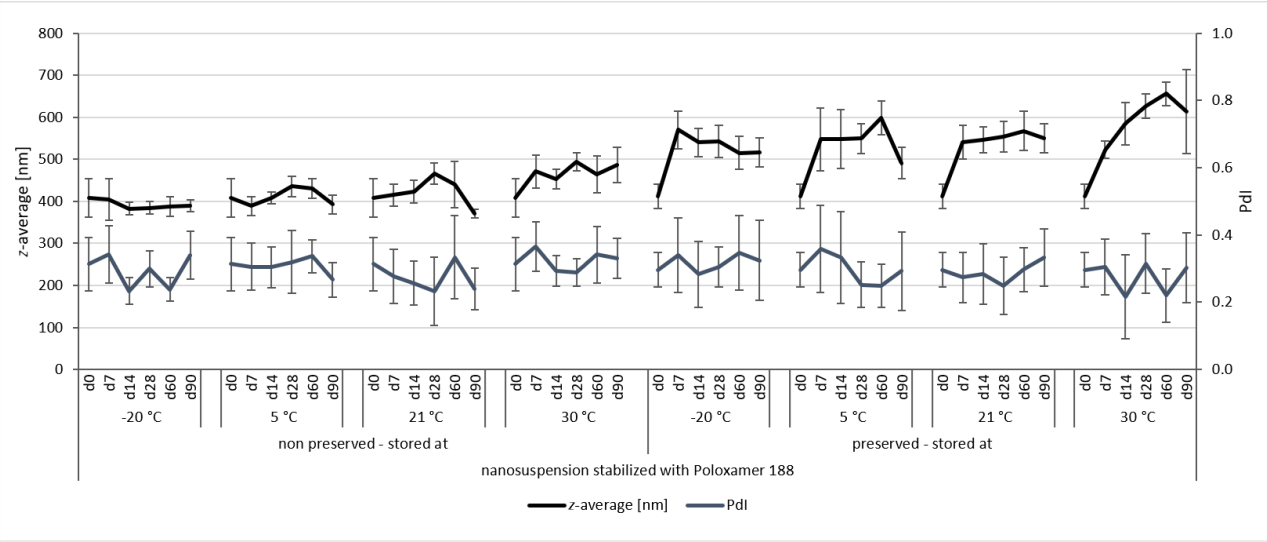

Figure 6: Physical stability during three months of storage at different storage temperatures for the nanosuspensions stabilized with Poloxamer 188 (DLS data).

Reasons for the differences might be the different stabilizers that interact differently with the preservative. Poloxamer 188 is a non-ionic surfactant, providing steric stabilization for the nanocrystals. In general, a thick surfactant layer that is indicated by a zeta potential (ZP) near zero should be obtained for good steric stabilization [21]. However, in our study ZP analysis revealed that the thickness of the layer is relatively low (ZP > 20 mV, cf. Table 1). Hence, steric stabilization of the formulation stabilized with PLX 188 is relatively poor. Upon the addition of the preservative to the formulations stabilized with PLX 188 a very limited decrease in ZP was detected when the suspensions were analysed in original dispersion medium (c.f. Table 1). This might indicate that small amounts of the non-charged preservative are adsorbed onto the surface of the nanocrystals where it might interact with the polymer layer. This interaction might cause a re-arrangement of the already thin stabilizing layer around the nanocrystals and might therefore explain the decreased stabilization efficacy of the poloxamer in the preserved formulations. The destabilizing effect of PLX 188 in combination with other excipients in nanocrystal formulations was also shown by a study of Beirowski and co-workers, who showed that some combinations of poloxamer and cryoprotectant were unsuitable for stabilizing nanocrystals during a freezing process [22].

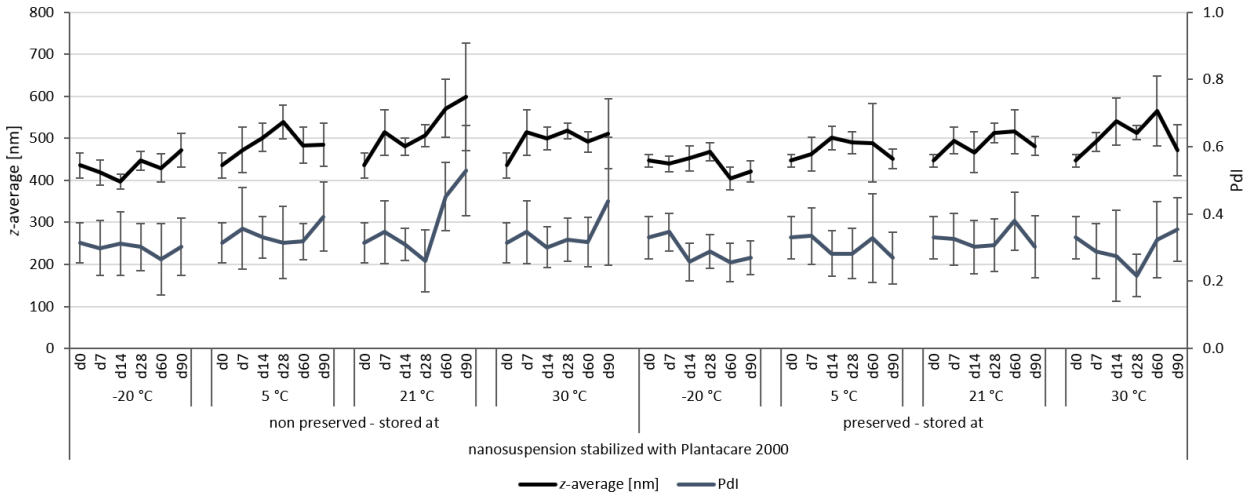

Figure 7: Physical stability during three months of storage at different storage temperatures for the nanosuspensions stabilized with Plantacare 2000 (DLS data).

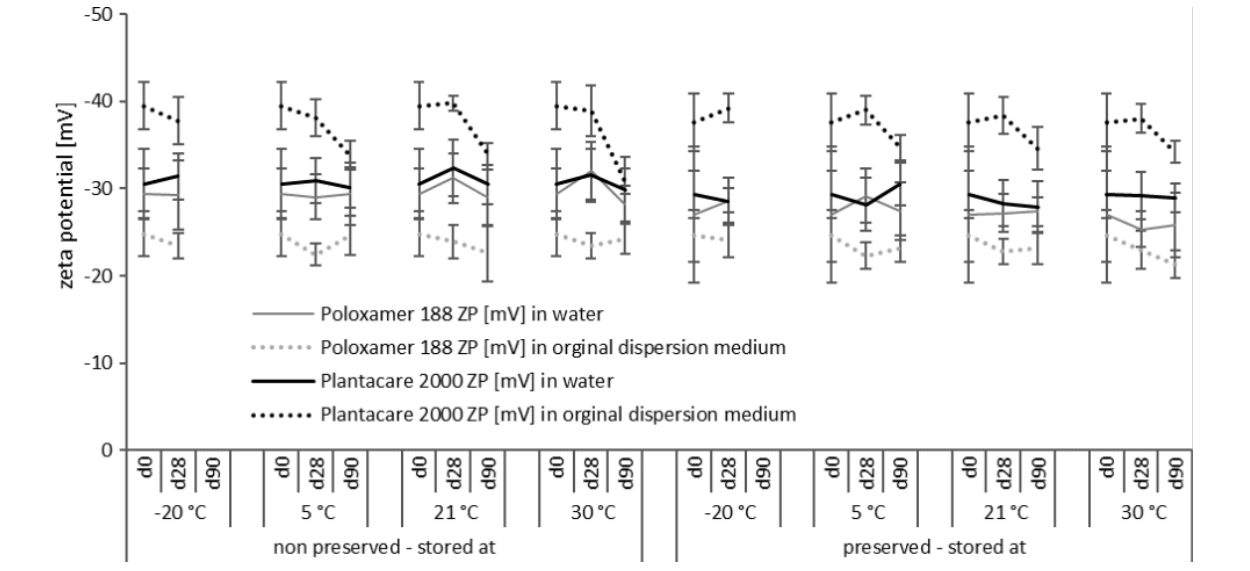

Figure 8: Determination of zeta potentials of the non-preserved and preserved rutin nanosuspensions during three months of storage at different storage temperatures.

In contrast to PLX 188, Plantacare, which is an alkyl polyglucoside, is mostly providing electrostatic stabilization. This can be seen by the differences in ZP analysed in water and original dispersion medium, respectively. The zeta potential is about −40 mV in original dispersion medium and is reduced to about −30 mV when analysed in water, because upon dilution with water surfactant is "washed off" from the particle surface, which results in less electrostatic stabilization of the particles. However, due to its chemical structure, Plantacare is also able to provide steric stabilization. This leads to an excellent stabilization capacity combining steric and electrostatic stabilization [23,24]. Upon addition of the preservative only very small differences in ZP values were detected for both, water and original dispersion medium (c.f. Table 1), indicating only very minor impairment of the preservative. In fact, Plantacare provides a very efficient stabilization mechanism, which is not significantly impaired by the addition of the preservative. This explains the slightly better physical stability than that of the preserved PLX-stabilized nanosuspensions.

Antioxidant capacity

The antioxidant capacity (AOC) was measured with the DPPH assay in which the IC_{50} value is determined. The IC_{50} value determines the amount of antioxidant needed to scavenge 50% of

the free radical. Consequently, the smaller the IC_{50} value the higher is the antioxidant capacity. In this study, the IC_{50} values for the different formulations did not change during storage, independent on preservative, storage time and storage temperature (Figure 9). Hence, all these parameters did not affect the AOC of the formulations. As the AOC is an indirect measure for the chemical stability, data indicate excellent chemical stability of all aliquots during storage. The data are in good agreement with a recent study by Müller et al. in which the authors could prove chemical stability of a rutin nanosuspension for more than nine years [25].

Microbial quality

The growth of bacteria and fungi was determined for all formulations after one, two and three months of storage. All preserved formulations showed excellent microbial quality. No fungi or bacteria were detected during the three months of storage (Figure 10). For the non-preserved nanosuspensions, data indicated that for all formulations the number of bacteria was fairly low upon the production with high-pressure homogenization, which is a well-described technique to reduce the number of bacteria in liquids [26]. The growth of microorganisms during storage was temperature-dependent and was also found to be slightly influenced by the type of stabilizer, i.e., a slightly lower and slower increase in microbial growth was found for the Plantacare-stabilized formulations (Figure 10 and Table 3). A possible reason for this observation could be the antimicrobial activity of the stabilizer Plantacare, which was already described in previous works by Jurado and co-workers [27,28].

Finally, it was found that for all formulations that were stored in frozen state at −20 °C no bacterial growth occurred. Hence, the

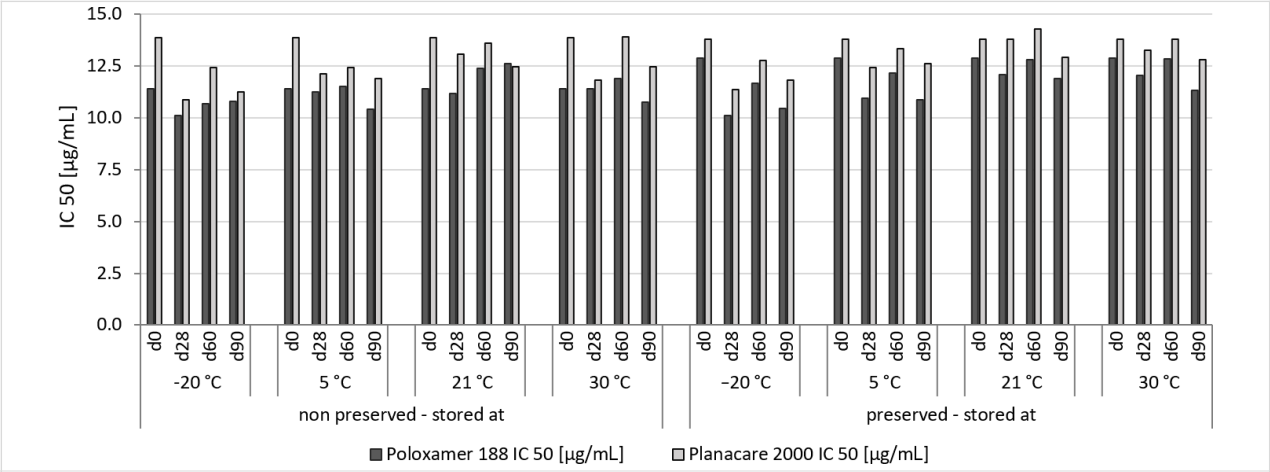

Figure 9: Antioxidant capacity, determined as IC_{50} value, of the rutin nanosuspensions during storage. No changes in IC_{50} values were determined during three months of storage, thus indicating good chemical stability of all rutin nanosuspensions.

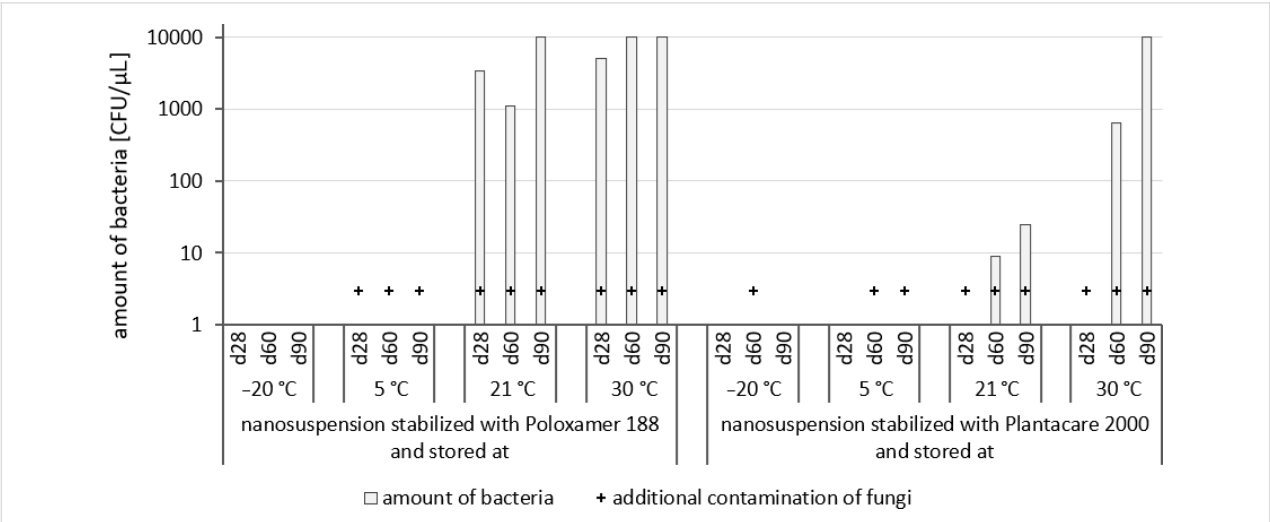

Figure 10: Determination of microbial activity (CFU) during three months of storage.

Table 3: Determination of microbial quality during three months of storage. P188: rutin nanosuspension stabilized with Poloxamer 188, PLC: rutin nanosuspension stabilized with Plantacare 2000, (+) = preserved with Euxyl 9010, (−) non-preserved.

	storage temperature			
	−20 °C	5 °C	21 °C	30 °C
d28 bacteria	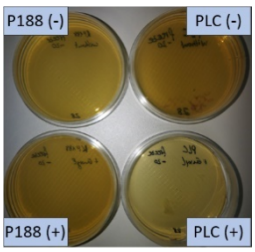	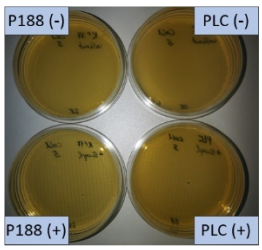	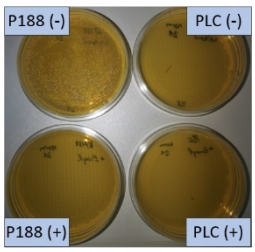	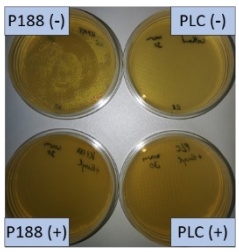
d28 fungi	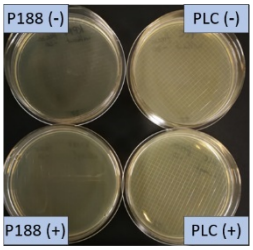	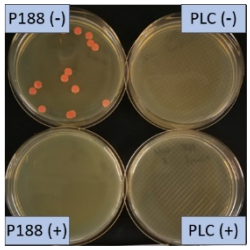	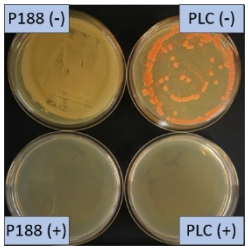	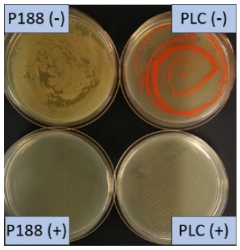
d60 bacteria	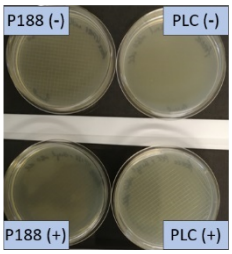	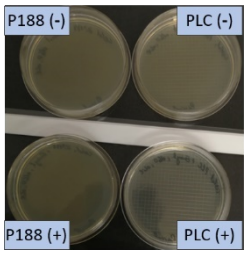	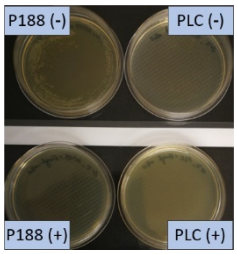	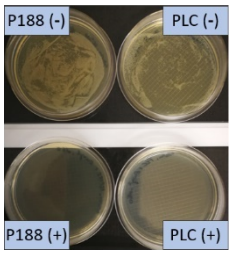
d60 fungi	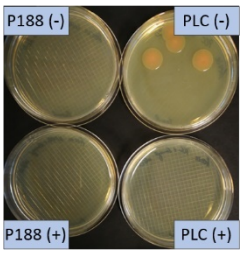	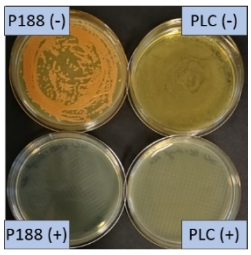	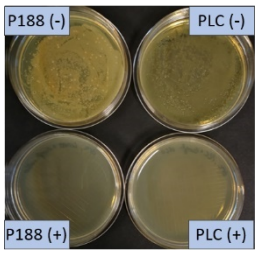	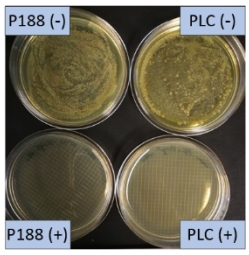
d90 bacteria	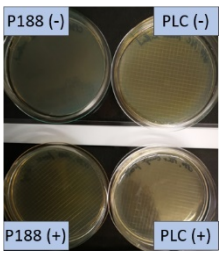	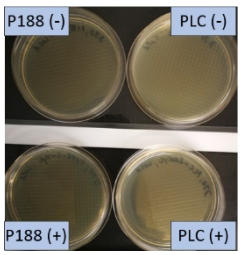	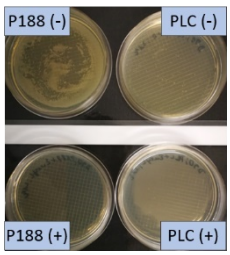	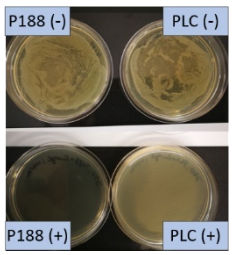
d90 fungi	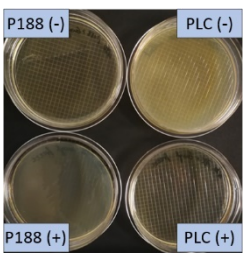	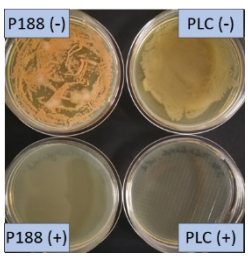	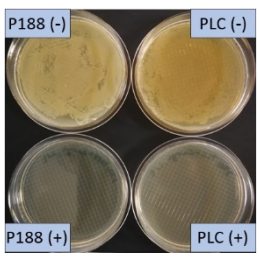	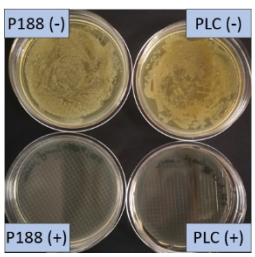

hypothesis, that storing nanosuspensions after production in frozen state might prevent bacterial growth during storage without the use of preservatives, could be confirmed by this set of data. The same trend was also observed for the growth of fungi. However, there was one exception, which was observed for the Plantacare-stabilized formulation at day 60 of storage. At this time point a slight contamination with fungi was observed for one aliquot (Figure 10 and Table 3). However, no contamination with fungi was observed at the next time point, i.e., after 90 days of storage. In fact, after three months of storage at −20 °C and upon thawing all non-preserved nanosuspensions were found to possess an excellent microbial quality, as no fungal and no bacterial growth was detected.

These findings so far are very promising and could enable a new concept to produce preservative-free nanosuspensions that can be stored over a longer period until further use or processing into final dosage forms. Preservative-free aqueous nanosuspensions would be a convenient formulation principle, because there will be no need to take possible interactions with preservatives and/or other excipients into consideration. Allergies of consumers and/or regulatory hurdles can also be circumvented with this concept.

The freeze–thaw concept is simple and can be exploited not only in industry but also in early drug development, where nanosuspensions are often used for early formulation of poorly soluble drug candidates. In this environment, the freeze–thaw concept could improve the predictability of screenings. At present, due to the lack of microbial stability, nanosuspensions need to be prepared shortly before the experiments, i.e., assays, cell culture or in vivo studies, are performed. Any repeating of the tests or continued tests will require the production of new suspensions, which might possess slightly different properties, which in turn might then cause differences in the (in vivo) data. By using thawed nanosuspensions from only one batch, these variations could be circumvented.

In conclusion, the freeze–thaw concept was shown to be a simple method to prevent microbial contamination during storage of aqueous rutin nanosuspensions. The new method is believed to enable new possibilities for the use of nanosuspensions and thus can be seen as a highly promising concept, not only in pharma, but also in food and cosmetics. Next steps should now investigate if the concept can also be exploited for other active ingredients and other stabilizers.

Conclusion

Preserved and non-preserved rutin nanosuspensions stabilized with different stabilizers were produced in this study and were stored for three months at different storage temperatures. During this time physical stability and microbial quality were monitored. In addition, the antioxidant capacity, as an indicator for the chemical stability, was assessed. All formulations were chemically stable over the whole time of observation. Physical stability was influenced by the type of surfactant, the preservative and the storage temperature. Preserved samples were only stable when stored at room temperature. Storage at higher or lower temperatures strongly impaired their physical stability. However, the microbial quality was excellent for all preserved nanosuspensions. Non-preserved samples possessed a better physical stability than the preserved nanosuspension. Proving again that preservatives impair the physical stability of nanosuspensions. Most interestingly, it was found that freezing did not alter the physical stability of the non-preserved suspensions. Hence, nanosuspensions could be frozen, stored up to three months at −20 °C and possessed unchanged particle sizes upon thawing. Storage at −20 °C also prevented bacterial growth of the non-preserved nanosuspensions, whereas storage at higher temperatures caused microbial contamination of the suspensions. The freeze–thaw concept was therefore found to be a suitable method to produce not only physically and chemically but also microbially stable rutin nanosuspensions. More research is now needed to investigate if the method can also be transferred to other nanosuspensions or nanosized formulations. All in all, the method seems to be a promising method to enable long time storage of aqueous nanosuspensions with excellent stability and without the use of preservatives. It can be used for improved formulation development of poorly soluble active ingredients in both lab scale and industrial scale.

Experimental

Materials

Rutin was purchased from Denk Ingredients GmbH (Germany). The stabilizers Poloxamer 188 (PLX 188, Kolliphor® P 188) and alkyl polyglucoside C8-C16 (Plantacare® 2000 UP) were kindly provided from BASF AG (Germany). The preservative was composed of 90% (w/w) 2-phenoxyethanol and 10% (w/w) of 1,2-propanediol as ready to use mixture (Euxyl® 9010) and was obtained from Schülke & Mayr GmbH (Germany). Purified water was obtained from a PURELAB Flex 2 (ELGA LabWater & Veolia, Germany). All other analytical chemicals were of analytical grade and used as received.

Methods

Production of nanosuspensions

Rutin nanosuspensions [16-19] were produced by high-pressure homogenization (HPH) using an EmulsiFlex-C50 (Avestin, Germany). For this, bulk suspensions containing 5% (w/w) rutin and 1% (w/w) surfactant were prepared. The pre-dispersions were homogenized with a high-speed stirrer (D-27, Miccra GmbH, Germany) at 24,000 rpm for 5 min in continu-

ous mode and were subsequently subjected to HPH (20 cycles at 1500 bar). During homogenization and between each cycle the suspensions were cooled to below 10 °C by using a cooling bath to avoid heating of the suspensions and subsequent agglomeration of the crystals [29].

Characterization of nanosuspensions

Determination of particle size and physical stability: Nanosuspensions were characterized regarding size by three different and independent methods. The hydrodynamic diameter and the polydispersity (*z*-average (*z*-ave) and PdI) were analysed by dynamic light scattering (DLS) with a Zetasizer Nano ZS (Malvern Panalytical GmbH, Germany). As DLS measurements, when used as stand-alone method for the characterization of submicron-sized particles, can be misleading because larger sized particles are not detected [30-33], light microscopy (Olympus BX53, equipped with an Olympus SC50 CMOS color camera, Japan) and laser diffraction (LD) were used as additional techniques to securely detect possible larger particles and agglomerates within the suspensions. By LD analysis the volumetric median diameters $d(v)0.1$, $d(v)0.5$, $d(v)0.9$, $d(v)0.95$ and $d(v)0.99$ were analysed with a Mastersizer 3000 (Malvern Panalytical GmbH, Germany). Particle diameters were calculated with Mie-theory by using 1.57 as real refractive index and 0.01 as imaginary refractive index.

The zeta potential (ZP) of the nanocrystals was determined in water (adjusted to a constant conductivity of 50 µS/cm) and in original dispersion media, i.e., surfactant solution, containing either 1% (w/w) PLX 188 or Plantacare 2000, respectively. Measurements were performed via laser-Doppler-anemometry (LDA) by using a Zetasizer Nano ZS (Malvern Panalytical GmbH, Germany), which determines the electrophoretic mobility (EM), which was then converted into the ZP by using the Helmholtz–Smoluchowski equation [21].

Determination of antioxidant capacity: The antioxidant capacity was assessed by calculating the IC_{50} value, which was determined by using the DPPH assay [34]. DPPH (1,1-diphenyl-2-picryl-hydrazyl, Sigma-Aldrich, Germany) is a free radical that can be reduced by antioxidants. Upon reduction the colour of the free radical changes and thus the amount of reduced DPPH can be accessed via UV–vis spectroscopy. For the determination of the IC_{50} values, 100 µL of the samples containing different concentrations of the nanocrystals (200, 100, 50, 25, 12.5, 6.25, 3.125 µg/mL) were added to 100 µL of a 0.3 mM methanolic solution of DPPH. After 30 min incubation time in the dark, the absorbance was measured by a UV–vis plate reader (Multiskan GO, Thermo scientific, Germany) at 517 nm. The inhibition activity (inhibition [%]) was calculated as

$$\text{inhibition}[\%] = \left(1 - {A_{\text{sample}}}/{A_0}\right) \cdot 100,$$

where A_{sample} is the absorbance of the sample and A_0 is the absorbance of the control (DPPH solution). The resulting linear function of inhibition against concentration was used to calculate the IC_{50} value (µg/mL). The IC_{50} value represents the concentration needed to scavenge 50% of the free radical. Rutin, which was used in this study as model drug, is a well-known antioxidant. Hence, if chemical degradation of the active ingredient occurs, changes in the IC_{50} value during storage can be observed [35]. As methanol is a good solvent for rutin, the addition of the nanocrystals to the methanolic DPPH solution led to a complete dissolution of the rutin nanocrystals. Hence, all rutin remaining in the formulations was dissolved during the test and thus the DPPH assay was used as a surrogate for the determination of the chemical stability.

Determination of microbial quality: To verify the biological stability, a simple agar plate test after Ph. Eur. 8 was used. The agar (Müller–Hinton agar, Sigma) was dispersed in water, autoclaved and directly poured into sterile petri dishes (60 mm in diameter) at 28, 60 and 90 days after preparation of the nanosuspensions and used immediately after cooling. Subsequently, 10 µL of the nanosuspension or a 1:100 dilution in water were distributed evenly over the entire surface by means of a cell spreader. For detection of existing bacteria, the agar plate containing the suspension or dilution was incubated for 24 h at 36 °C and 90% humidity. Fungal contamination was detected after 7 days at 25 °C storage by using undiluted nanosuspensions. For evaluation, the visible bacterial colonies were counted, or the presence of fungal growth was noted. With dense colonization, the number of colony forming units (CFU) was set to 10000 CFU/µL.

ORCID® iDs

Cornelia M. Keck - https://orcid.org/0000-0001-8888-2340

References

1. Auweter, H.; Bohn, H.; Heger, R.; Horn, D.; Siegel, B.; Siemensmeyer, K. Precipitated water-insoluble colorants in colloid disperse form. U.S. Patent 6,494,924B1, Dec 12, 2002.
2. List, M.; Sucker, H. Pharmaceutical colloidal hydrosols for injection. G.B. Patent 2,200,048, July 27, 1988.
3. Müller, R. H.; Becker, R.; Kruss, B.; Peters, K. Pharmaceutical nanosuspensions for medicament administration as systems with increased saturation solubility and rate of solution. U.S. Patent 5,858,410, Dec 1, 1999.
4. Liversidge, G. G.; Cundy, K. C.; Bishop, J. F.; Czekai, D. A. Surface modified drug nanoparticles. U.S. Patent 5,145,684, Sept 8, 1992.
5. Wu, W.; Nancollas, G. H. *J. Solution Chem.* **1998,** *27,* 521–531. doi:10.1023/a:1022678505433

6. Müller, R. H.; Gohla, S.; Keck, C. M. *Eur. J. Pharm. Biopharm.* **2011,** *78,* 1–9. doi:10.1016/j.ejpb.2011.01.007
7. Müller, R. H.; Keck, C. M. *Int. J. Pharm.* **2010,** *390,* 1–2. doi:10.1016/j.ijpharm.2010.02.005
8. Fan, M.; Geng, S.; Liu, Y.; Wang, J.; Wang, Y.; Zhong, J.; Yan, Z.; Yu, L. *Curr. Pharm. Des.* **2018,** *24,* 2416–2424. doi:10.2174/1381612824666180515154109
9. Patel, V.; Sharma, O. P.; Mehta, T. *Expert Opin. Drug Delivery* **2018,** *15,* 351–368. doi:10.1080/17425247.2018.1444025
10. Sharma, O. P.; Patel, V.; Mehta, T. *Drug Delivery Transl. Res.* **2016,** *6,* 399–413. doi:10.1007/s13346-016-0292-0
11. Keck, C. M.; Müller, R. H. *Eur. J. Pharm. Biopharm.* **2006,** *62,* 3–16. doi:10.1016/j.ejpb.2005.05.009
12. Agarwal, V.; Bajpai, M. *Recent Pat. Nanotechnol.* **2015,** *9,* 178–194. doi:10.2174/1872210510999151126112644
13. Al Shaal, L.; Mishra, P. R.; Müller, R. H.; Keck, C. M. *Pharmazie* **2014,** *69,* 173–182. doi:10.1691/ph.2014.3032
14. Kobierski, S.; Ofori-Kwakye, K.; Müller, R. H.; Keck, C. M. *Pharmazie* **2011,** *66,* 942–947. doi:10.1691/ph.2011.1038
15. Obeidat, W. M.; Schwabe, K.; Müller, R. H.; Keck, C. M. *Eur. J. Pharm. Biopharm.* **2010,** *76,* 56–67. doi:10.1016/j.ejpb.2010.05.001
16. Mauludin, R.; Müller, R. H.; Keck, C. M. *Int. J. Pharm.* **2009,** *370,* 202–209. doi:10.1016/j.ijpharm.2008.11.029
17. Mauludin, R.; Müller, R. H.; Keck, C. M. *Eur. J. Pharm. Sci.* **2009,** *36,* 502–510. doi:10.1016/j.ejps.2008.12.002
18. Scholz, P.; Arntjen, A.; Müller, R. H.; Keck, C. M. *Int. J. Pharm.* **2014,** *465,* 388–395. doi:10.1016/j.ijpharm.2014.02.026
19. Scholz, P.; Keck, C. M. *Int. J. Pharm.* **2015,** *482,* 27–37. doi:10.1016/j.ijpharm.2014.11.008
20. Al Shaal, L.; Müller, R. H.; Keck, C. M. *Pharmazie* **2010,** *65,* 86–92.
21. Müller, R. H. *Zetapotential und Partikeladung in der Laborpraxis;* Wissenschaftliche Verlagsgesellschaft: Suttgart, Germany, 1996.
22. Beirowski, J.; Inghelbrecht, S.; Arien, A.; Gieseler, H. *J. Pharm. Sci.* **2011,** *100,* 1958–1968. doi:10.1002/jps.22425
23. Kobierski, S.; Ofori-Kwakye, K.; Müller, R. H.; Keck, C. M. *Pharmazie* **2009,** *64,* 741–747. doi:10.1691/ph.2009.9097
24. Kovacevic, A.; Savic, S.; Vuleta, G.; Müller, R. H.; Keck, C. M. *Int. J. Pharm.* **2011,** *406,* 163–172. doi:10.1016/j.ijpharm.2010.12.036
25. Müller, R. H.; Hespeler, D.; Keck, C. M. *Euro Cosmetics* **2018,** *11,* 6–9.
26. Diels, A. M. J.; Michiels, C. W. *Crit. Rev. Microbiol.* **2006,** *32,* 201–216. doi:10.1080/10408410601023516
27. Jurado, E.; Fernández-Serrano, M.; Núñez Olea, J.; Lechuga, M.; Jiménez, J. L.; Ríos, F. *Bull. Environ. Contam. Toxicol.* **2012,** *88,* 290–295. doi:10.1007/s00128-011-0479-5
28. Jurado, E.; Fernández-Serrano, M.; Núñez-Olea, J.; Luzón, G.; Lechuga, M. *Water Sci. Technol.* **2009,** *59,* 2351–2358. doi:10.2166/wst.2009.266
29. Keck, C. M. Cyclosporine nanosuspensions: Optimised size characterisation & oral formulations. Ph.D. Thesis, Freie Universität Berlin, Berlin, Germany, 2006.
30. Gioria, S.; Caputo, F.; Urbán, P.; Maguire, C. M.; Bremer-Hoffmann, S.; Prina-Mello, A.; Calzolai, L.; Mehn, D. *Nanomedicine (London, U. K.)* **2018,** *13,* 539–554. doi:10.2217/nnm-2017-0338
31. Knoth, D.; Keck, C. M. *Phys. Status Solidi A* **2018,** *215,* 1700962. doi:10.1002/pssa.201700962
32. Keck, C. M.; Müller, R. H. *Int. J. Pharm.* **2008,** *355,* 150–163. doi:10.1016/j.ijpharm.2007.12.004
33. Keck, C. M. *Int. J. Pharm.* **2010,** *390,* 3–12. doi:10.1016/j.ijpharm.2009.08.042
34. Kedare, S. B.; Singh, R. P. *J. Food Sci. Technol.* **2011,** *48,* 412–422. doi:10.1007/s13197-011-0251-1
35. Klimczak, I.; Małecka, M.; Szlachta, M.; Gliszczyńska-Świgło, A. *J. Food Compos. Anal.* **2007,** *20,* 313–322. doi:10.1016/j.jfca.2006.02.012

License and Terms

BEILSTEIN JOURNAL OF NANOTECHNOLOGY

Incorporation of doxorubicin in different polymer nanoparticles and their anticancer activity

Sebastian Pieper[‡1], Hannah Onafuye[‡2], Dennis Mulac[1], Jindrich Cinatl Jr.[3], Mark N. Wass[2], Martin Michaelis[*2,§] and Klaus Langer[*1,¶]

Full Research Paper

Open Access

Address:
[1]Institute of Pharmaceutical Technology and Biopharmacy, University of Muenster, Corrensstraße 48, 48149 Muenster, Germany, [2]Industrial Biotechnology Centre and School of Biosciences, University of Kent, Canterbury CT2 7NJ, United Kingdom and [3]Institute for Medical Virology, University Hospital, Goethe-University, Paul Ehrlich-Straße 40, 60596 Frankfurt am Main, Germany

Email:
Martin Michaelis[*] - m.michaelis@kent.ac.uk; Klaus Langer[*] - k.langer@uni-muenster.de

* Corresponding author ‡ Equal contributors
§ Phone: +44 1227 / 82-7804, Fax: +44 1227 / 82-4034
¶ Phone: +49 251 8339860, Fax: +49 251 8339308

Keywords:
cancer; doxorubicin; drug release; nanoparticles; poly(lactic-*co*-glycolic acid) (PLGA)

Beilstein J. Nanotechnol. **2019,** *10,* 2062–2072.
doi:10.3762/bjnano.10.201

Received: 31 May 2019
Accepted: 02 October 2019
Published: 29 October 2019

This article is part of the thematic issue "Frontiers in pharmaceutical nanotechnology".

Guest Editor: M. G. Wacker

Abstract

Background: Nanoparticles are under investigation as carrier systems for anticancer drugs. The expression of efflux transporters such as the ATP-binding cassette (ABC) transporter ABCB1 is an important resistance mechanism in therapy-refractory cancer cells. Drug encapsulation into nanoparticles has been shown to bypass efflux-mediated drug resistance, but there are also conflicting results. To investigate whether easy-to-prepare nanoparticles made of well-tolerated polymers may circumvent transporter-mediated drug efflux, we prepared poly(lactic-*co*-glycolic acid) (PLGA), polylactic acid (PLA), and PEGylated PLGA (PLGA-PEG) nanoparticles loaded with the ABCB1 substrate doxorubicin by solvent displacement and emulsion diffusion approaches and assessed their anticancer efficiency in neuroblastoma cells, including ABCB1-expressing cell lines, in comparison to doxorubicin solution.

Results: The resulting nanoparticles covered a size range between 73 and 246 nm. PLGA-PEG nanoparticle preparation by solvent displacement led to the smallest nanoparticles. In PLGA nanoparticles, the drug load could be optimised using solvent displacement at pH 7 reaching 53 µg doxorubicin/mg nanoparticle. These PLGA nanoparticles displayed sustained doxorubicin release kinetics compared to the more burst-like kinetics of the other preparations. In neuroblastoma cells, doxorubicin-loaded PLGA-PEG nanoparticles (presumably due to their small size) and PLGA nanoparticles prepared by solvent displacement at pH 7 (presumably due to their high drug load and superior drug release kinetics) exerted the strongest anticancer effects. However, nanoparticle-encapsulated doxorubicin did not display increased efficacy in ABCB1-expressing cells relative to doxorubicin solution.

Conclusion: Doxorubicin-loaded nanoparticles made by different methods from different materials displayed substantial discrepancies in their anticancer activity at the cellular level. Optimised preparation methods resulted in PLGA nanoparticles characterised by increased drug load, controlled drug release, and high anticancer efficacy. The design of drug-loaded nanoparticles with optimised anticancer activity at the cellular level is an important step in the development of improved nanoparticle preparations for anticancer therapy. Further research is required to understand under which circumstances nanoparticles can be used to overcome efflux-mediated resistance in cancer cells.

Introduction

According to Globocan, there "were 14.1 million new cancer cases, 8.2 million cancer deaths and 32.6 million people living with cancer (within five years of diagnosis) in 2012 worldwide" [1]. Despite substantial improvements over recent decades, the prognosis for many cancer patients remains unacceptably poor. In particular, the outlook is grim for patients that are diagnosed with disseminated (metastatic) disease who cannot be successfully treated by local treatment (surgery, radiotherapy). These patients depend on systemic drug therapy. However, the therapeutic window is small, and anticancer therapies are typically associated with severe side-effects [2,3].

One strategy to develop more effective cancer therapies is to use nano-sized drug delivery systems that mediate a more specific tumour accumulation of transported drugs. Tumour targeting can be achieved via the enhanced permeability and retention (EPR) effect, which is the consequence of increased leakiness of the tumour vasculature and a lack of lymph drainage [4]. Nano-sized drug carrier systems can also prolong the circulation time of anticancer drugs, protect them from degradation, and sustain therapeutic drug concentrations due to prolonged/controlled drug release. In addition, nanoparticles can be used to administer poorly soluble agents, as demonstrated for nab-paclitaxel, a HSA nanoparticle-based paclitaxel preparation approved for the treatment of different forms of cancer [4-9].

Another important aspect of the efficacy of nanoparticles as delivery system for anticancer is their uptake and, in turn, the drug transport into cancer cells. Uptake mechanisms may differ between different types of nanoparticles, which may affect their effectiveness as carriers for anticancer drugs. Here, we prepared and directly compared the effects of doxorubicin-loaded polylactic acid (PLA) and poly(lactic-*co*-glycolic acid) (PLGA) nanoparticles in neuroblastoma cells. PLA and PLGA are well-known ingredients of FDA- and EMA-approved drugs for human use [10,11] and are easily degraded into their monomers, lactic acid and glycolic acid. Furthermore, a copolymer composed of polyethylene glycol (PEG) and PLGA (PLGA-PEG) was used for nanoparticle preparation. PEGylated ("stealth") nanoparticles display prolonged systemic circulation time, because they avoid agglomeration, opsonisation, and phagocytosis [12].

In previous studies PLA-, PLGA-, PLA-PEG-, and PLGA-PEG-based nanometre-sized drug carriers loaded with or covalently linked to doxorubicin have been prepared by methods including emulsion diffusion, solvent displacement, micelle formation, and film rehydration followed by pH-gradient method [13-19].

The expression of ATP-binding cassette (ABC) transporters such as ABCB1 (also known as MDR1 or P-glycoprotein/P-gp), which efflux a range of anticancer drugs, is an important drug resistance mechanism in cancer cells [20,21]. Different nano-sized drug carrier systems including PLA-, PLGA-, and PEG-based preparations have been reported to bypass the transporter-mediated efflux of anticancer drugs including doxorubicin [20,22-31]. However, there are also conflicting results from studies in which encapsulation of anticancer drugs into nanoparticles did not result in increased efficacy in ABCB1-expressing cancer cells relative to drug solution [19,32,33]. Hence, systematic studies are required to better understand the prospects and limitations of nanoparticles as carriers for anticancer drugs, in particular in the context of efflux-mediated resistance.

Since nanoparticles prepared by simple methods have the highest chance of clinical translation, doxorubicin was incorporated into nanoparticles prepared from PLA, PLGA, and PLGA-PEG by emulsion diffusion or solvent displacement approaches, two well-established and comparatively simple preparation methods. The resulting nanoparticles were compared by particle diameter, polydispersity index, zeta potential, drug load, and drug release behaviour. Preliminary results on the preparation of doxorubicin-loaded PLGA nanoparticles have been previously published [34]. Selected preparations were tested for anticancer efficacy in cancer cell lines, including cell lines that express ABCB1.

Results and Discussion

Influence of the preparation technique on particle diameter and polydispersity index

Nanoparticles based on poly(lactic-*co*-glycolic acid) (PLGA), a copolymer composed of polyethylene glycol (PEG) and PLGA (PLGA-PEG) and polylactic acid (PLA), respectively, were pre-

pared in the presence of doxorubicin by either emulsion diffusion or solvent displacement technique. The resulting particle diameters are presented in Figure 1.

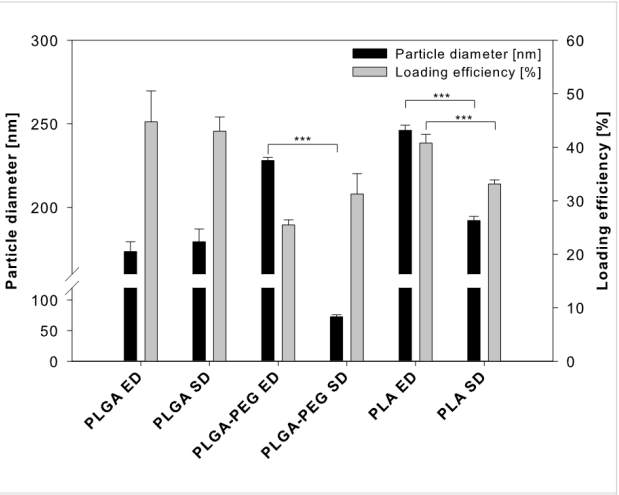

Figure 1: Resulting particle diameters and loading efficiencies for different nanoparticle formulations using emulsion diffusion (ED) or solvent displacement (SD) techniques (data expressed as means ± SD, $n \geq 3$).

Emulsion diffusion (173.5 ± 5.9 nm) and solvent displacement (179.4 ± 7.6 nm) resulted in PLGA nanoparticles with similar diameters. In contrast, solvent displacement resulted in PLGA-PEG nanoparticles of 72.6 ± 3.3 nm whereas emulsion diffusion resulted in PLGA-PEG nanoparticles of 222.6 ± 3.1 nm. In accordance, solvent displacement using the stabiliser PVA at concentrations between 2% and 4% (w/v) and controlled injection at mild stirring had previously been shown to produce PLGA-PEG nanoparticles with a diameter below 100 nm [35-37]. The hydrophilic PEG chains may sterically stabilise the nanoparticles by reducing PLGA aggregation during nanoparticle formation resulting in smaller particle diameters [38].

Emulsion diffusion resulted in PLA nanoparticles of 246.2 ± 2.9 nm and solvent displacement in PLA nanoparticles of 192.1 ± 2.5 nm. The detailed reason for this is not clear, but in the case of the emulsion diffusion technique the resulting particle size is mainly influenced by the droplet size during the initial emulsification step. In principle, PLA nanoparticles can be prepared at a range of sizes that is determined by parameters including the preparation method, the exact polymer used, and the encapsulated drug [39-42]. Optimisation is possible [39,42] but was not subject of this study focused on the comparison of different nanoparticle systems prepared by simple methods. Polydispersity indices smaller than 0.1 indicated a monodisperse size distribution for all nanoparticle preparations. Monodispersity and particle diameters were confirmed by scanning electron microscopy (SEM) images (Figure 2).

Influence of the preparation technique on loading efficiency and drug release

Loading efficiencies ranging from 25.5 ± 1.0% to 44.8 ± 5.8% of the applied doxorubicin were detected in the different nanoparticle preparations as shown in Figure 1, resulting in drug loads between 2.6 ± 0.2 µg doxorubicin/mg nanoparticle and 6.7 ± 0.3 µg doxorubicin/mg nanoparticle (Table 1).

Table 1: Nanoparticle (NP) yield and doxorubicin (Dox) drug load results for nanoparticles prepared by either emulsion diffusion (ED) or solvent displacement (SD) technique (data expressed as means ± SD, $n \geq 3$).

NP system	NP yield [mg NP/mL]	NP yield [%]	drug load [µg Dox/mg NP]
PLGA ED	3.3 ± 0.4	66.8 ± 7.2	6.7 ± 0.3
PLGA SD	8.5 ± 0.4	70.4 ± 3.0	5.1 ± 0.2
PLGA-PEG ED	4.2 ± 0.1	84.4 ± 1.8	3.0 ± 0.2
PLGA-PEG SD	7.6 ± 0.9	63.6 ± 7.4	4.1 ± 0.6
PLA ED	8.0 ± 1.0	79.6 ± 9.8	2.6 ± 0.2
PLA SD	5.3 ± 0.2	44.1 ± 1.8	6.3 ± 0.1

In the case of PLGA and PLGA-PEG nanoparticles, emulsion diffusion and solvent displacement resulted in nanoparticles with a similar drug load. In PLA nanoparticles, there was a substantial difference between the techniques (solvent displacement: 6.3 ± 0.1 µg doxorubicin/mg nanoparticle, emulsion diffusion: 2.6 ± 0.2 µg doxorubicin/mg nanoparticle) (Table 1). The reasons underlying this difference are not clear, but emulsion diffusion has been considered of limited efficacy for the encapsulation of hydrophilic drugs [43,44].

All nanoparticles displayed a similar drug release behaviour characterised by an initial burst release (Figure 3), which is in accordance to previous studies and may be caused by processes including the release of drug adsorbed to the nanoparticles and/or rapid drug diffusion through the particle matrix [15,39,45-47].

PEGylated polymers may result in a more porous particle structure, which is caused by aqueous channels created by PEG chains and anticipated to further increase the initial burst release [48]. However, the burst release was not increased substantially further using PLGA-PEG nanoparticles. A slight drop in the doxorubicin concentration was noticeable in the medium of the PLGA nanoparticles. This may be the consequence of doxorubicin adsorption to BSA [49], which was added to simulate the presence of plasma proteins, in combination with a slower post-burst doxorubicin release compared to the other nanoparticle systems. Such a burst release should be avoided, because it may result in drug release shortly after i.v. application before the

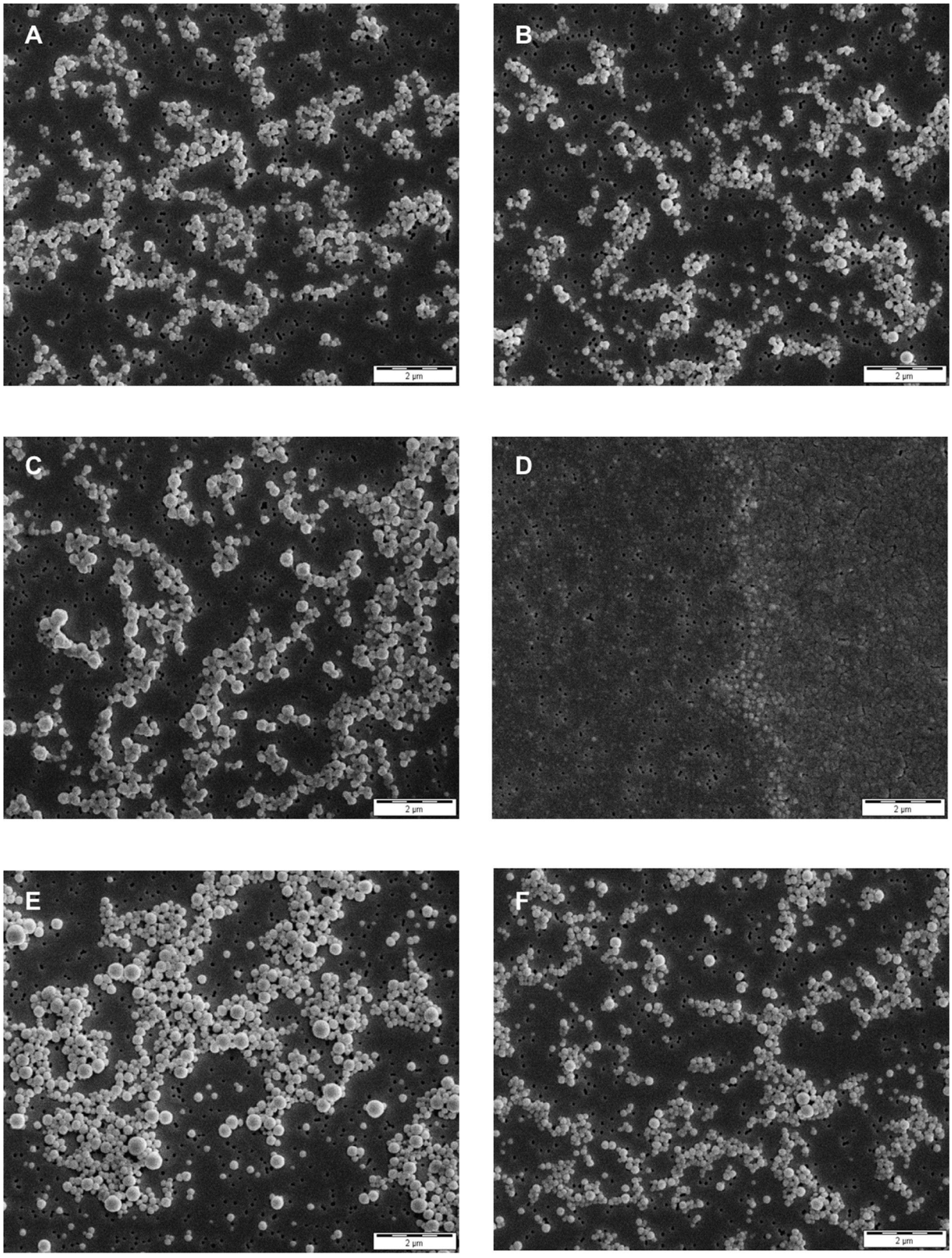

Figure 2: SEM images of nanoparticles using emulsion diffusion (ED) or solvent displacement (SD) preparation technique. (A) PLGA nanoparticles ED, (B) PLGA nanoparticles SD, (C) PLGA-PEG nanoparticles ED, (D) PLGA-PEG nanoparticles SD, (E) PLA nanoparticles ED, (F) PLA nanoparticles SD. Images were taken at 10,000× magnification.

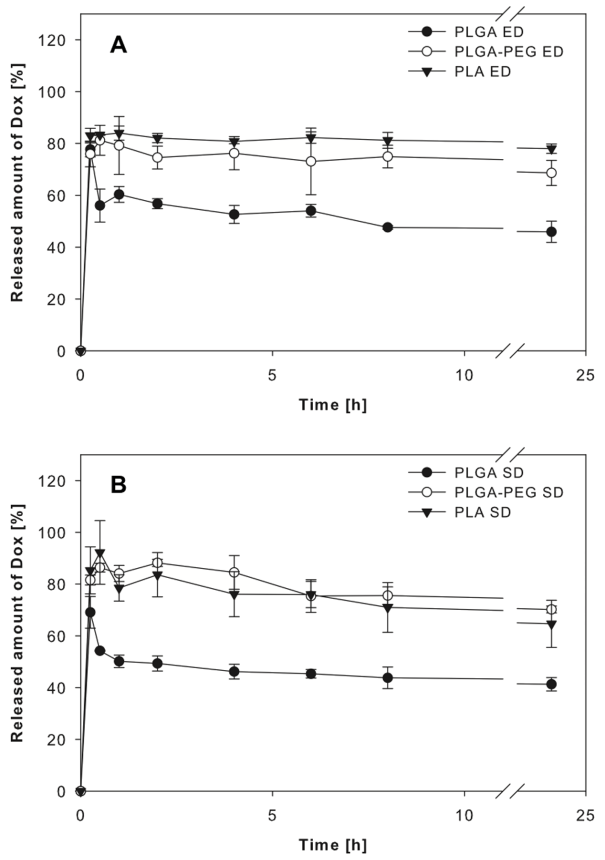

Figure 3: Doxorubicin (Dox) release profiles over 24 h for all nanoparticle systems using (A) emulsion diffusion (ED) or (B) solvent displacement (SD) preparation technique (data expressed as means ± SD, n = 3).

nanoparticles reach the desired site of drug action, e.g., the tumour tissue [50].

To optimise the loading efficiency and drug release kinetics of PLGA nanoparticles the pH value of the stabiliser solution used during nanoparticle preparation was increased to 7. At this pH value, doxorubicin exists in the more lipophilic deprotonated form [51]. The use of PVA solution at pH 7 had no influence on the nanoparticle characteristics such as particle diameter, PDI, and zeta potential (Table 2).

Table 2: Resulting particle diameter, polydispersity index (PDI), and zeta potential (ZP) for PLGA nanoparticles prepared by an unmodified PVA solution and a PVA solution adjusted to pH 7 (data expressed as means ± SD, n = 3).

PVA solution	diameter [nm]	PDI	ZP [mV]
without pH adjustment	177.9 ± 1.0	0.039 ± 0.031	−41.6 ± 2.0
pH 7	174.1 ± 2.8	0.057 ± 0.030	−43.8 ± 3.7

However, loading efficiency and drug load increased. The drug load raised from 6.7 ± 0.3 µg doxorubicin/mg nanoparticle (44.8 ± 5.8% loading efficiency) without pH adjustment to 7.9 ± 0.8 µg doxorubicin/mg nanoparticle (60.2 ± 3.8% loading efficiency) at pH 7. By increasing the amount of doxorubicin to 2 mg, the drug load of PLGA nanoparticles could be further enhanced (non-adjusted pH: 18.0 ± 3.2 µg doxorubicin/mg nanoparticle; pH 7: 31.6 ± 3.1 µg doxorubicin/mg nanoparticle, respectively) (Figure 4).

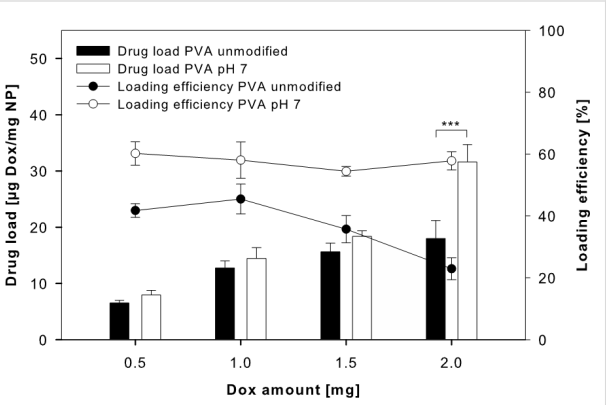

Figure 4: Doxorubicin (Dox) drug load and loading efficiency for PLGA nanoparticles (NPs) prepared using a PVA solution without pH adjustment and a PVA solution adjusted to pH 7 (data expressed as means ± SD, n = 3).

Different amounts of doxorubicin did not change the loading efficiency at pH 7. Using aqueous solutions instead of methanol, we increased the doxorubicin amount during preparation to 5 mg and 7.5 mg per 50 mg PLGA. While 5 mg resulted in an increase of the drug load to 52.5 ± 0.4 µg doxorubicin/mg nanoparticle, 7.5 mg doxorubicin did not result in a significant further increase (54.4 ± 3.4 µg doxorubicin/mg nanoparticle) (Figure 5A).

This was an improvement in drug load compared to a nanoparticle preparation in the presence of 2 mg doxorubicin. However, a further increase of doxorubicin resulted in unstable nanoparticle systems, as indicated by increasing particle diameter and polydispersity index (Figure 5B). The loading efficiency for PLGA nanoparticles prepared at pH 7 with 5 mg doxorubicin was higher than this for nanoparticles manufactured with 7.5 mg doxorubicin (50.6 ± 0.6% and 33.9 ± 0.5%, respectively). These loading efficiencies are in the range of those described for similar preparations, although higher drug loads have been described when using alternative PLGA-based formulations such as nanoparticles or micelles with doxorubicin covalently bound to the polymer, nanoparticles produced by nanoprecipitation, micelles based on multi-arm star-shaped PLGA–PEG block copolymers, or nanopolymersomes [14-18].

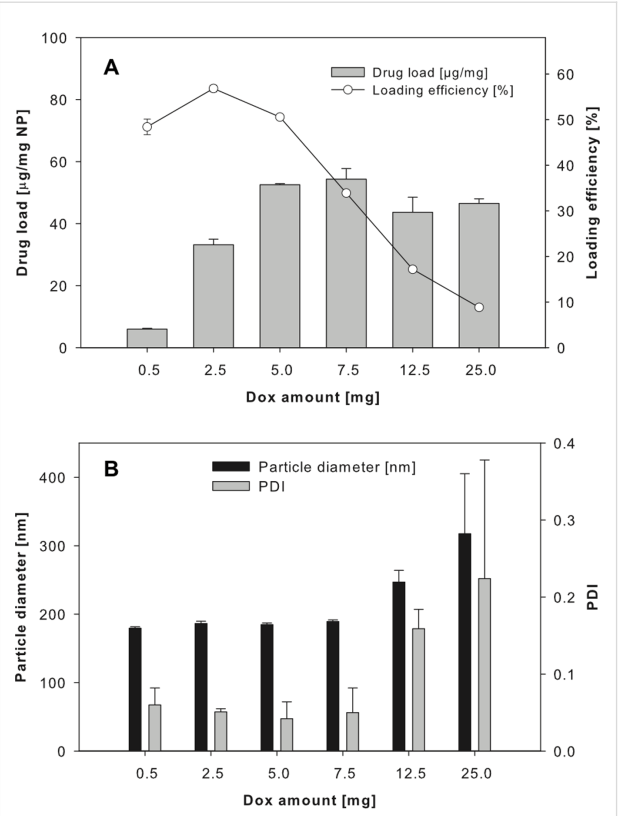

Figure 5: (A) Drug load and loading efficiencies as well as (B) particle diameter and PDI for different amounts of doxorubicin (Dox) used for the preparation of PLGA nanoparticles by emulsion diffusion technique (data expressed as means ± SD, n = 3).

In addition, PLGA nanoparticles prepared at pH 7 displayed a more controlled and sustained doxorubicin release than PLGA nanoparticles prepared without pH adjustment (Figure 6). Hence, PLGA nanoparticles prepared at pH 7 with 5 mg doxorubicin were selected for cell culture experiments.

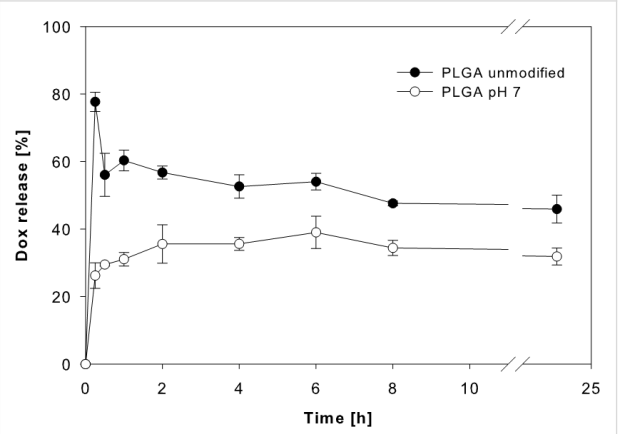

Figure 6: Release profiles of doxorubicin from PLGA nanoparticles prepared using an unmodified PVA solution and a PVA solution adjusted to pH 7 (data expressed as means ± SD, n = 3).

The different release kinetics from PLGA nanoparticles prepared at pH 7, may be attributed to the higher lipophilicity of doxorubicin at this pH value and, in turn, a stronger incorporation into the lipophilic PLGA nanoparticle matrix. This explanation is consistent with data showing that PLGA nanoparticle degradation is unlikely to occur in a 24 h timeframe [50,52]. More sustained release patterns have been shown to be achievable by alternative nanoparticle approaches based on PLGA such as nanoparticles or micelles with doxorubicin covalently bound to the polymer, nanoparticles produced by nanoprecipitation, micelles based on multi-arm star-shaped PLGA–PEG block copolymers, or nanopolymersomes [14-18].

Nanoparticle efficacy in cell culture

Finally, the effects of doxorubicin-loaded PLA nanoparticles prepared by solvent displacement (because they were smaller and the drug load was higher compared to those prepared by emulsion diffusion), PLGA nanoparticles prepared by solvent displacement at a non-adjusted pH value and at pH 7, and PLGA-PEG nanoparticles prepared by emulsion diffusion and solvent displacement were tested for their effects on the viability of the neuroblastoma cell line UKF-NB-3, its doxorubicin-adapted sub-line UKF-NB-3^{r}DOX^{20}, and its vincristine-resistant sub-line UKF-NB-3^{r}VCR^{1}. In all three cell lines, PLA nanoparticles, PLGA nanoparticles prepared by solvent displacement at a non-adjusted pH value, and PLGA-PEG nanoparticles prepared by emulsion diffusion displayed reduced efficacy compared to doxorubicin solution (Figure 7).

In contrast, PLGA nanoparticles prepared by solvent displacement at pH 7 and PLGA-PEG nanoparticles prepared by solvent displacement were similarly active as free doxorubicin (Figure 7). The corresponding empty nanoparticles did not affect cell viability in the tested concentrations.

The main difference between the doxorubicin-loaded PLGA-PEG nanoparticles prepared by solvent displacement and the other preparations is the size. It is the only preparation in which nanoparticles have a size clearly smaller than 100 nm (72.6 ± 3.3 nm, Figure 1). This might indicate that the cellular uptake of smaller nanoparticles is higher than that of larger nanoparticles, which is coherent with previous findings showing that cellular uptake of nanoparticles decreases with an increase of size [53]. PLGA nanoparticles prepared by solvent displacement at pH 7 displayed the highest drug load. Hence, their superior effects may be explained by an increased drug transport per nanoparticle into cancer cells.

Nano-sized drug carriers have been shown to bypass efflux-mediated drug resistance [25]. This included various nanoparticle and liposome formulations of the ABCB1 substrate doxoru-

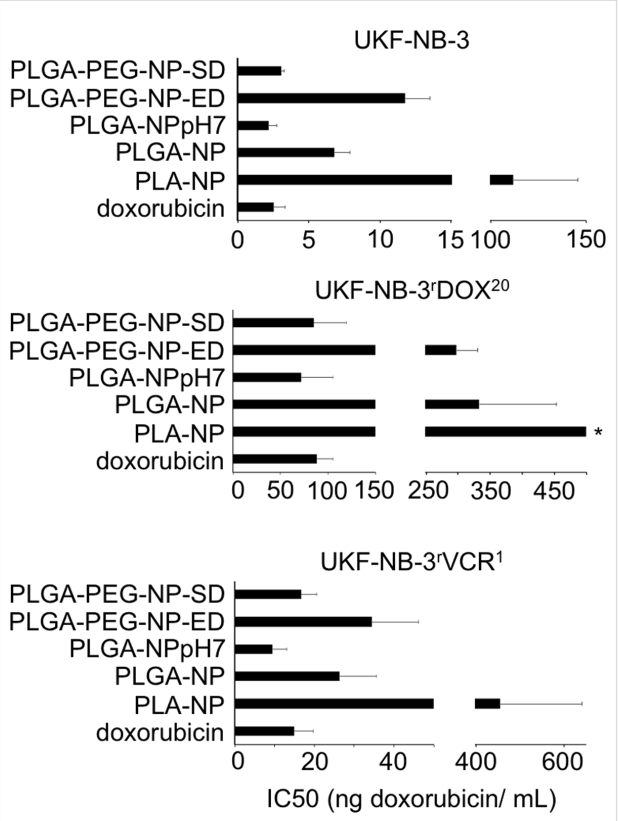

Figure 7: Doxorubicin concentrations that reduce neuroblastoma cell viability by 50% (IC50) when administered encapsulated into different nanoparticle preparations (PLA-NP, PLA nanoparticles prepared by solvent displacement; PLGA-NP, PLGA nanoparticles prepared by solvent displacement at a non-adjusted pH value; PLGA-NPpH7, PLGA nanoparticles prepared by solvent displacement at pH 7; PLGA-PEG-ED, PLGA-PEG nanoparticles prepared by emulsion diffusion; PLGA-PEG-SD, PLGA-PEG nanoparticles prepared by solvent displacement) compared to doxorubicin solution (doxorubicin). Unloaded nanoparticles did not affect cell viability in the tested concentration range. *IC50 > 500 ng/mL.

bicin that were shown to modify the cellular uptake and intracellular distribution of doxorubicin resulting in enhanced effects against ABCB1-expressing cancer cells, when compared to free doxorubicin in solution [26-31]. The doxorubicin-adapted UKF-NB-3 sub-line UKF-NB-3^{r}DOX^{20} is characterised by high ABCB1 expression [54]. In addition, the vincristine-resistant UKF-NB-3 sub-line UKF-NB-3^{r}VCR^{1} displays cross-resistance to doxorubicin and becomes sensitised to doxorubicin by the specific ABCB1 inhibitor zosuquidar (Figure 8). This indicates that drug resistance is at least in part mediated by ABCB1 in this cell line. However, free doxorubicin solution and doxorubicin bound to PLGA-PEG nanoparticles prepared by solvent displacement or PLGA nanoparticles prepared by solvent displacement at pH 7 displayed similar efficacy in UKF-NB-3^{r}DOX^{20} and UKF-NB-3^{r}VCR^{1} cells (Figure 7). Hence, these drug carrier systems are not able to overcome transporter-mediated drug resistance. One reason for this may be that the doxorubicin burst release kinetics observed for these nanoparticles do not enable a sufficient bypassing of transporter-mediated drug efflux. However, PLGA nanoparticles prepared by solvent displacement at pH 7 did not display improved efficacy in ABCB1-expressing cells despite improved drug release kinetics. Possibly, other PLGA-based preparations, which display more sustained drug release, such as nanoparticles or micelles with doxorubicin covalently bound to the polymer, nanoparticles produced by nanoprecipitation, micelles based on multi-arm star-shaped PLGA–PEG block copolymers, or nanopolymersomes [14-18] may overcome such limitations.

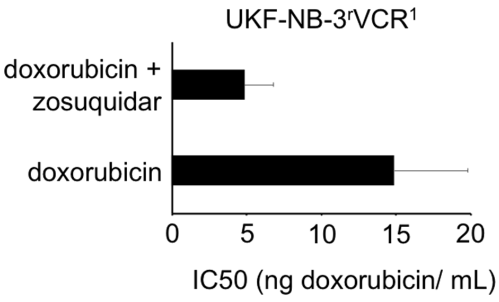

Figure 8: Doxorubicin concentrations that reduce UKF-NB-3^{r}VCR^{1} viability by 50% (IC50) in the absence or presence of the ABCB1 inhibitor zosuquidar (1 μM). Zosuquidar did not affect cell viability when administered alone.

Conclusion

In this study, we synthesised a range of doxorubicin-loaded PLA- and PLGA-based nanoparticle systems using emulsion diffusion and solvent displacement approaches. Our results show that particle size, loading efficiency, and drug release kinetics can be controlled by the production procedure. Testing of the nanoparticle preparations in the neuroblastoma cell line UKF-NB-3 and its sub-lines with acquired resistance to doxorubicin or vincristine indicated that smaller nanoparticles and a high drug load result in nanoparticle preparations that have a similar efficacy at the cellular level as doxorubicin solution. In particular, doxorubicin-loaded PLGA-PEG nanoparticles prepared by solvent displacement, which displayed the smallest diameter, and PLGA nanoparticles prepared by solvent displacement at pH 7, which displayed the highest drug load, exerted the most pronounced anticancer effects, which were comparable to doxorubicin solution. Since nanoparticle preparations are known to have the capacity to improve the in vivo activity of anticancer drugs by tumour targeting through the EPR effect, this is an important step in the development of improved nanoparticle preparations. However, the investigated nanoparticle preparations did not circumvent transporter-mediated drug efflux. Hence, more research is required to identify drug carrier systems that reliably bypass efflux-mediated drug resistance.

Experimental

Reagents

PLGA (Resomer® RG502H), PLA (Resomer® R203H), and PLGA-PEG (Resomer® RGP d 50155) were obtained from Evonik Industries AG (Essen, Germany). Ethyl acetate, dichloromethane, and methanol were purchased from VWR International GmbH (Darmstadt, Germany). Acetone, acetonitrile and dimethyl sulfoxide (DMSO) were obtained from Carl Roth GmbH (Karlsruhe, Germany). Poly(vinyl alcohol) (PVA, 30,000–70,000 Da), bovine serum albumin (BSA), HSA, and glutaraldehyde were obtained from Sigma-Aldrich Chemie GmbH (Karlsruhe, Germany). Dulbecco's Phosphate buffered saline (PBS) was purchased from Biochrom GmbH (Berlin, Germany). Doxorubicin was obtained from LGC Standards GmbH (Wesel, Germany). All chemicals were of analytical grade and used as received.

Nanoparticle preparation via emulsion diffusion

PLA and PLGA nanoparticles were prepared by a previously described emulsion diffusion technique [35,55]. PLA, PLGA, or PLGA-PEG were dissolved in organic solvents (Table 3) and 200 µL of a methanolic doxorubicin solution (2.5 mg/mL) was added.

This solution was then poured into 5 mL (1%, m/v) PVA solution and afterwards homogenized with an Ultra Turrax (IKA-Werke, Staufen, Germany) as indicated in Table 3. Subsequently this pre-emulsion was mixed with another 5 mL (1%, m/v) PVA solution. After stirring overnight, the resultant nanoparticles were purified three times by centrifugation at 21,000*g* for 15 min (Eppendorf Centrifuge 5430 R, Eppendorf, Hamburg, Germany) and re-dispersion in purified water.

After the final purification step, an aliquot of the nanoparticle suspension was centrifuged and the resulting pellet was dissolved in 1 mL DMSO in order to measure the entrapped amount of doxorubicin by HPLC (see below).

In order to increase the drug load for PLGA nanoparticles different volumes of the methanolic doxorubicin solution (2.5 mg/mL) were used corresponding to 1.0, 1.5, and 2.0 mg total doxorubicin. For a further increase in drug load different aqueous doxorubicin solutions (ranging from 10.0 to 50.0 mg/mL) were used to achieve total doxorubicin amounts of 0.5, 2.5, 5.0, 7.5, 12.5, and 25.0 mg. Here, the PLGA solution in ethyl acetate was homogenized with the aqueous doxorubicin solution and 5 mL (1%, m/v) PVA solution to achieve the pre-emulsion. In all experiments to increase the drug load the amount of the polymer was kept constant at 50 mg. To prepare doxorubicin-loaded nanoparticles at a defined pH value of 7, a PVA solution (1%, m/v) in phosphate buffer (15.6 mg/mL $NaH_2PO_4 \cdot 2H_2O$; pH adjusted to pH 7 with NaOH) was used.

Nanoparticle preparation via solvent displacement

Nanoparticle preparation via solvent displacement was performed modified after Murakami et al. [13] as previously described by Pieper and Langer [34]. 60 mg polymer were dissolved in 2 mL acetone and combined with 200 µL methanolic doxorubicin solution (2.5 mg/mL). This mixture was injected into 4 mL 2% (m/v) PVA solution to produce PLGA and PLGA-PEG nanoparticles or into 4 mL 1% (m/v) PVA solution to produce PLA nanoparticles. After stirring overnight at 550 rpm and evaporation of the organic solvent, PLA and PLGA nanoparticles were purified three times by centrifugation at 21,000 g for 15 min and re-dispersion in purified water. PLGA-PEG nanoparticles were purified three times by centrifugation at 30,000*g* for 60 min and re-dispersion in purified water.

Determination of particle size, size distribution and zeta potential

Average particle size and the polydispersity were measured by photon correlation spectroscopy (PCS) using a Malvern zetasizer nano (Malvern Instruments, Herrenberg, Germany). The resulting particle suspensions were diluted 1:100 with purified water and measured at a temperature of 22 °C using a backscattering angle of 173°. The zeta potential was determined with the same instrument and the same diluted nanoparticle suspension by laser Doppler microelectrophoresis.

Scanning electron microscopy (SEM)

For scanning electron microscopy (SEM), the particle suspensions were diluted with purified water to 0.25 mg/mL. The suspension was dripped on a filter (MF-Millipore™ membrane

Table 3: Preparation parameters for nanoparticles based on different polymers using emulsion diffusion technique.

polymer	amount of polymer	organic solvent	homogenisation
PLGA	50 mg	2.5 mL ethyl acetate	15,000 rpm for 5 min
PLA	100 mg	2.0 mL dicholoromethane	18,000 rpm for 15 min
PLGA-PEG	50 mg	2.5 mL ethyl acetate	15,000 rpm for 5 min

filter VSWP, 0.1 µm) and dried for 24 h in a desiccator. Afterwards, the membranes were sputtered with gold under argon atmosphere (SCD 040, BAL-TEC, Balzers, Liechtenstein). The SEM pictures were received at an accelerating voltage of 10,000 V and a working distance of 10 mm (CamScan CS4, Cambridge Scanning Company, Cambridge, UK).

Doxorubicin quantification via HPLC-UV

The amount of doxorubicin that had been incorporated into the nanoparticles was determined by HPLC-UV (HPLC 1200 series, Agilent Technologies GmbH, Böblingen, Germany) using a LiChroCART 250 × 4 mm LiChrospher 100 RP 18 column (Merck KGaA, Darmstadt, Germany). The mobile phase was a mixture of water and acetonitrile (70:30) containing 0.1% trifluoroacetic acid [56]. In order to obtain symmetric peaks a gradient was used. In the first 6 min the percentage of water was reduced from 70% to 50%. Subsequently within 2 min the amount of water was further decreased to 20% and then within another 2 min increased again to 70%. These conditions were hold for a final 5 min resulting in a total runtime of 15 min. While using a flow rate of 0.8 mL/min, an elution time for doxorubicin of t = 7.5 min was achieved. The detection of doxorubicin was performed at a wavelength of 485 nm [57].

In vitro drug release studies

To study drug release in vitro, a nanoparticle suspension of 1 mg nanoparticles in 1 mL of PBS containing 5% (m/v) bovine serum albumin (BSA) was shaken at 37 °C with 500 rpm. Nanoparticle suspensions were centrifuged (30,000g, 15 min) after 0, 0.5, 1, 2, 4, 6, 8, and 24 h, and an aliquot (250 µL) of the supernatant was diluted with 750 µL ethanol (96%, v/v) in order to precipitate BSA. After a second centrifugation step (30,000g, 10 min) the supernatant was analysed for the amount of released doxorubicin by HPLC as mentioned above. Additionally, the resulting pellet was dissolved in DMSO in order to calculate doxorubicin recovery.

Cell culture

The MYCN-amplified neuroblastoma cell line UKF-NB-3 was established from stage-4 neuroblastoma patients [54]. UKF-NB-3 sub-lines adapted to growth in the presence of doxorubicin 20 ng/mL (UKF-NB-3^{r}DOX^{20}) [54] or vincristine 1 ng/mL (UKF-NB-3^{r}VCR^{1}) were established by continuous exposure to step-wise increasing drug concentrations as previously described [54,58] and derived from the Resistant Cancer Cell Line (RCCL) collection (https://research.kent.ac.uk/ibc/the-resistant-cancer-cell-line-rccl-collection/).

All cells were propagated in Iscove's modified Dulbecco's medium (IMDM) supplemented with 10% foetal calf serum, 100 U/mL penicillin and 100 mg/mL streptomycin at 37 °C. The drug-adapted sub-lines were continuously cultured in the presence of the indicated drug concentrations. Cells were routinely tested for mycoplasma contamination and authenticated by short tandem repeat profiling.

Cell viability assay

Cell viability was determined by 3-(4,5-dimethylthiazol-2-yl)-2,5-diphenyltetrazolium bromide (MTT) assay modified after Mosmann [59], as previously described [55]. 2×10^4 cells suspended in 100 µL cell culture medium were plated per well in 96-well plates and incubated in the presence of various concentrations of drug or drug preparations for 120 h. Where indicated, the ABCB1 inhibitor zosuquidar was added at a fixed concentration of 1 µM. Then, 25 µL of MTT solution (1 mg/mL (w/v) in PBS) were added per well, and the plates were incubated at 37 °C for an additional 4 h. After this, cells were lysed using 200 µL of a buffer containing 20% (w/v) sodium dodecylsulfate and 50% (v/v) N,N-dimethylformamide (pH 4.7) at 37 °C for 4 h. Absorbance was determined at 570 nm for each well using a 96-well multiscanner. After subtracting of the background absorption, the results are expressed as percentage viability relative to untreated control cultures. Drug concentrations that inhibited cell viability by 50% (IC50) were determined using CalcuSyn (Biosoft, Cambridge, UK).

Statistical methods

All experiments of nanoparticle preparation and characterisation were performed at least three times. The results are shown as average value with standard deviation. Significance tests were conducted with Sigma Plot 12.5 (Systat Software GmbH, Erkrath, Germany), using a one-way ANOVA test with the Holm–Sidak post test. Significance levels were depicted as * for $p \leq 0.05$, ** for $p \leq 0.01$, and *** for $p \leq 0.001$.

ORCID® iDs

Hannah Onafuye - https://orcid.org/0000-0002-0307-1416
Mark N. Wass - https://orcid.org/0000-0001-5428-6479
Martin Michaelis - https://orcid.org/0000-0002-5710-5888
Klaus Langer - https://orcid.org/0000-0002-0203-7478

Preprint

A non-peer-reviewed version of this article has been previously published as a preprint https://doi.org/10.1101/403923

References

1. International Agency for Research on Cancer. http://globocan.iarc.fr/Pages/fact_sheets_cancer.aspx (accessed Sept 7, 2019).
2. Steeg, P. S. *Nat. Rev. Cancer* **2016,** *16,* 201–218. doi:10.1038/nrc.2016.25
3. Siegel, R. L.; Miller, K. D.; Jemal, A. *Ca-Cancer J. Clin.* **2018,** *68,* 7–30. doi:10.3322/caac.21442

4. Rodallec, A.; Benzekry, S.; Lacarelle, B.; Ciccolini, J.; Fanciullino, R. *Crit. Rev. Oncol. Hematol.* **2018,** *129,* 1–12. doi:10.1016/j.critrevonc.2018.06.008
5. Brufsky, A. *Exp. Hematol. Oncol.* **2017,** *6,* 7. doi:10.1186/s40164-017-0066-5
6. Mir, M.; Ahmed, N.; Rehman, A. U. *Colloids Surf., B* **2017,** *159,* 217–231. doi:10.1016/j.colsurfb.2017.07.038
7. Ricciardi, A.; Quijano, E.; Putman, R.; Saltzman, W.; Glazer, P. *Molecules* **2018,** *23,* 632. doi:10.3390/molecules23030632
8. Tan, Y. F.; Lao, L. L.; Xiong, G. M.; Venkatraman, S. *J. Controlled Release* **2018,** *284,* 39–48. doi:10.1016/j.jconrel.2018.06.014
9. Zhao, C.-Y.; Cheng, R.; Yang, Z.; Tian, Z.-M. *Molecules* **2018,** *23,* 826. doi:10.3390/molecules23040826
10. Tyler, B.; Gullotti, D.; Mangraviti, A.; Utsuki, T.; Brem, H. *Adv. Drug Delivery Rev.* **2016,** *107,* 163–175. doi:10.1016/j.addr.2016.06.018
11. Wischke, C.; Schwendeman, S. P. *Int. J. Pharm.* **2008,** *364,* 298–327. doi:10.1016/j.ijpharm.2008.04.042
12. Suk, J. S.; Xu, Q.; Kim, N.; Hanes, J.; Ensign, L. M. *Adv. Drug Delivery Rev.* **2016,** *99,* 28–51. doi:10.1016/j.addr.2015.09.012
13. Murakami, H.; Kobayashi, M.; Takeuchi, H.; Kawashima, Y. *Int. J. Pharm.* **1999,** *187,* 143–152. doi:10.1016/s0378-5173(99)00187-8
14. Yoo, H. S.; Park, T. G. *J. Controlled Release* **2001,** *70,* 63–70. doi:10.1016/s0168-3659(00)00340-0
15. Yoo, H. S.; Lee, K. H.; Oh, J. E.; Park, T. G. *J. Controlled Release* **2000,** *68,* 419–431. doi:10.1016/s0168-3659(00)00280-7
16. Betancourt, T.; Brown, B.; Brannon-Peppas, L. *Nanomedicine (London, U. K.)* **2007,** *2,* 219–232. doi:10.2217/17435889.2.2.219
17. Alibolandi, M.; Sadeghi, F.; Abnous, K.; Atyabi, F.; Ramezani, M.; Hadizadeh, F. *Eur. J. Pharm. Biopharm.* **2015,** *94,* 521–531. doi:10.1016/j.ejpb.2015.07.005
18. Ma, G.; Zhang, C.; Zhang, L.; Sun, H.; Song, C.; Wang, C.; Kong, D. *J. Mater. Sci.: Mater. Med.* **2016,** *27,* 17. doi:10.1007/s10856-015-5610-4
19. Tam, Y. T.; To, K. K. W.; Chow, A. H. L. *Colloids Surf., B* **2016,** *139,* 249–258. doi:10.1016/j.colsurfb.2015.12.026
20. Sosnik, A. *Adv. Drug Delivery Rev.* **2013,** *65,* 1828–1851. doi:10.1016/j.addr.2013.09.002
21. Robey, R. W.; Pluchino, K. M.; Hall, M. D.; Fojo, A. T.; Bates, S. E.; Gottesman, M. M. *Nat. Rev. Cancer* **2018,** *18,* 452–464. doi:10.1038/s41568-018-0005-8
22. Li, P.-Y.; Lai, P.-S.; Hung, W.-C.; Syu, W.-J. *Biomacromolecules* **2010,** *11,* 2576–2582. doi:10.1021/bm1005195
23. Mo, S.-M.; Oh, I.-J. *J. Nanosci. Nanotechnol.* **2011,** *11,* 1795–1798. doi:10.1166/jnn.2011.3406
24. Wang, J.; Li, L.; Wu, L.; Sun, B.; Du, Y.; Sun, J.; Wang, Y.; Fu, Q.; Zhang, P.; He, Z. *Eur. J. Pharm. Sci.* **2017,** *99,* 185–192. doi:10.1016/j.ejps.2016.12.014
25. Bar-Zeev, M.; Livney, Y. D.; Assaraf, Y. G. *Drug Resist. Updates* **2017,** *31,* 15–30. doi:10.1016/j.drup.2017.05.002
26. Bennis, S.; Chapey, C.; Robert, J.; Couvreur, P. *Eur. J. Cancer* **1994,** *30,* 89–93. doi:10.1016/s0959-8049(05)80025-5
27. Maiti, C.; Parida, S.; Kayal, S.; Maiti, S.; Mandal, M.; Dhara, D. *ACS Appl. Mater. Interfaces* **2018,** *10,* 5318–5330. doi:10.1021/acsami.7b18245
28. Oliveira, M. S.; Aryasomayajula, B.; Pattni, B.; Mussi, S. V.; Ferreira, L. A. M.; Torchilin, V. P. *Int. J. Pharm.* **2016,** *512,* 292–300. doi:10.1016/j.ijpharm.2016.08.049
29. Prados, J.; Melguizo, C.; Ortiz, R.; Velez, C.; J. Alvarez, P.; L. Arias, J.; A. Ruiz, M.; Gallardo, V.; Aranega, A. *Anti-Cancer Agents Med. Chem.* **2012,** *12,* 1058–1070. doi:10.2174/187152012803529646
30. Thierry, A. R.; Vigé, D.; Coughlin, S. S.; Belli, J. A.; Dritschilo, A.; Rahman, A. *FASEB J.* **1993,** *7,* 572–579. doi:10.1096/fasebj.7.6.8097173
31. Wong, H. L.; Bendayan, R.; Rauth, A. M.; Xue, H. Y.; Babakhanian, K.; Wu, X. Y. *J. Pharmacol. Exp. Ther.* **2006,** *317,* 1372–1381. doi:10.1124/jpet.106.101154
32. Chavanpatil, M. D.; Patil, Y.; Panyam, J. *Int. J. Pharm.* **2006,** *320,* 150–156. doi:10.1016/j.ijpharm.2006.03.045
33. Vallo, S.; Kõpp, R.; Michaelis, M.; Rothweiler, F.; Bartsch, G.; Brandt, M. P.; Gust, K. M.; Wezel, F.; Blaheta, R. A.; Haferkamp, A.; Cinatl, J., Jr. *Oncol. Lett.* **2017,** *13,* 4085–4092. doi:10.3892/ol.2017.5986
34. Pieper, S.; Langer, K. *Mater. Today: Proc.* **2017,** *4,* S188–S192. doi:10.1016/j.matpr.2017.09.185
35. Astete, C. E.; Sabliov, C. M. *J. Biomater. Sci., Polym. Ed.* **2006,** *17,* 247–289. doi:10.1163/156856206775997322
36. Kwon, H.-Y.; Lee, J.-Y.; Choi, S.-W.; Jang, Y.; Kim, J.-H. *Colloids Surf., A* **2001,** *182,* 123–130. doi:10.1016/s0927-7757(00)00825-6
37. Zhou, Z.; Badkas, A.; Stevenson, M.; Lee, J.-Y.; Leung, Y.-K. *Int. J. Pharm.* **2015,** *487,* 81–90. doi:10.1016/j.ijpharm.2015.03.081
38. Ameller, T.; Marsaud, V.; Legrand, P.; Gref, R.; Barratt, G.; Renoir, J.-M. *Pharm. Res.* **2003,** *20,* 1063–1070. doi:10.1023/a:1024418524688
39. Musumeci, T.; Ventura, C. A.; Giannone, I.; Ruozi, B.; Montenegro, L.; Pignatello, R.; Puglisi, G. *Int. J. Pharm.* **2006,** *325,* 172–179. doi:10.1016/j.ijpharm.2006.06.023
40. Altmeyer, C.; Karam, T. K.; Khalil, N. M.; Mainardes, R. M. *Mater. Sci. Eng., C* **2016,** *60,* 135–142. doi:10.1016/j.msec.2015.11.019
41. Dalmolin, L. F.; Khalil, N. M.; Mainardes, R. M. *Mater. Sci. Eng., C* **2016,** *62,* 1–8. doi:10.1016/j.msec.2016.01.031
42. Lee, B. K.; Yun, Y.; Park, K. *Adv. Drug Delivery Rev.* **2016,** *107,* 176–191. doi:10.1016/j.addr.2016.05.020
43. Delie, F.; Berton, M.; Allémann, E.; Gurny, R. *Int. J. Pharm.* **2001,** *214,* 25–30. doi:10.1016/s0378-5173(00)00627-x
44. Rao, J. P.; Geckeler, K. E. *Prog. Polym. Sci.* **2011,** *36,* 887–913. doi:10.1016/j.progpolymsci.2011.01.001
45. Corrigan, O. I.; Li, X. *Eur. J. Pharm. Sci.* **2009,** *37,* 477–485. doi:10.1016/j.ejps.2009.04.004
46. Danhier, F.; Lecouturier, N.; Vroman, B.; Jérôme, C.; Marchand-Brynaert, J.; Feron, O.; Préat, V. *J. Controlled Release* **2009,** *133,* 11–17. doi:10.1016/j.jconrel.2008.09.086
47. Faisant, N.; Akiki, J.; Siepmann, F.; Benoit, J. P.; Siepmann, J. *Int. J. Pharm.* **2006,** *314,* 189–197. doi:10.1016/j.ijpharm.2005.07.030
48. Ruan, G.; Feng, S.-S. *Biomaterials* **2003,** *24,* 5037–5044. doi:10.1016/s0142-9612(03)00419-8
49. Chassany, O.; Urien, S.; Claudepierre, P.; Bastian, G.; Tillement, J.-P. *Cancer Chemother. Pharmacol.* **1996,** *38,* 571–573. doi:10.1007/s002800050529
50. Danhier, F.; Ansorena, E.; Silva, J. M.; Coco, R.; Le Breton, A.; Préat, V. *J. Controlled Release* **2012,** *161,* 505–522. doi:10.1016/j.jconrel.2012.01.043

51. Tewes, F.; Munnier, E.; Antoon, B.; Ngaboni Okassa, L.; Cohen-Jonathan, S.; Marchais, H.; Douziech-Eyrolles, L.; Soucé, M.; Dubois, P.; Chourpa, I. *Eur. J. Pharm. Biopharm.* **2007,** *66,* 488–492. doi:10.1016/j.ejpb.2007.02.016
52. Li, S. *J. Biomed. Mater. Res.* **1999,** *48,* 342–353. doi:10.1002/(sici)1097-4636(1999)48:3<342::aid-jbm20>3.0.co;2-7
53. Salatin, S.; Maleki Dizaj, S.; Yari Khosroushahi, A. *Cell Biol. Int.* **2015,** *39,* 881–890. doi:10.1002/cbin.10459
54. Kotchetkov, R.; Driever, P. H.; Cinatl, J.; Michaelis, M.; Karaskova, J.; Blaheta, R.; Squire, J. A.; Von Deimling, A.; Moog, J.; Cinatl, J., Jr. *Int. J. Oncol.* **2005,** *27,* 1029–1037. doi:10.3892/ijo.27.4.1029
55. Michaelis, M.; Matousek, J.; Vogel, J.-U.; Slavik, T.; Langer, K.; Cinatl, J.; Kreuter, J.; Schwabe, D.; Cinatl, J. *Anti-Cancer Drugs* **2000,** *11,* 369–376. doi:10.1097/00001813-200006000-00007
56. Dreis, S.; Rothweiler, F.; Michaelis, M.; Cinatl, J., Jr.; Kreuter, J.; Langer, K. *Int. J. Pharm.* **2007,** *341,* 207–214. doi:10.1016/j.ijpharm.2007.03.036
57. Sanson, C.; Schatz, C.; Le Meins, J.-F.; Soum, A.; Thévenot, J.; Garanger, E.; Lecommandoux, S. *J. Controlled Release* **2010,** *147,* 428–435. doi:10.1016/j.jconrel.2010.07.123
58. Michaelis, M.; Rothweiler, F.; Barth, S.; Cinatl, J.; van Rikxoort, M.; Löschmann, N.; Voges, Y.; Breitling, R.; von Deimling, A.; Rödel, F.; Weber, K.; Fehse, B.; Mack, E.; Stiewe, T.; Doerr, H. W.; Speidel, D.; Cinatl, J. *Cell Death Dis.* **2011,** *2,* e243. doi:10.1038/cddis.2011.129
59. Mosmann, T. *J. Immunol. Methods* **1983,** *65,* 55–63. doi:10.1016/0022-1759(83)90303-4

License and Terms

BEILSTEIN JOURNAL OF NANOTECHNOLOGY

BergaCare SmartLipids: commercial lipophilic active concentrates for improved performance of dermal products

Florence Olechowski[1], Rainer H. Müller[2] and Sung Min Pyo[*2]

Review

Open Access

Address:
[1]Berg + Schmidt GmbH & Co. KG, An der Alster 81, 20099 Hamburg, Germany and [2]Freie Universität Berlin, Institute of Pharmacy, Pharmaceutics, Pharmaceutical Nanotechnology & NutriCosmetics, Kelchstr. 31, Berlin 12169, Germany

Email:
Sung Min Pyo[*] - pyo.sungmin@fu-berlin.de

* Corresponding author

Keywords:
chemical stabilization of active agents; controlled release; firm inclusion; nanostructured lipid carriers (NLCs); penetration enhancement; skin occlusion; SmartLipids; solid lipid nanoparticles (SLNs)

Beilstein J. Nanotechnol. **2019,** *10,* 2152–2162.
doi:10.3762/bjnano.10.208

Received: 08 May 2019
Accepted: 26 September 2019
Published: 04 November 2019

This article is part of the thematic issue "Frontiers in pharmaceutical nanotechnology".

Guest Editor: M. G. Wacker

Abstract

SmartLipids are the latest generation of dermal lipid nanoparticles with solid particle matrix. Their characteristic properties resulting from the “chaotic” and disordered particle matrix structure are reviewed. These properties are high loading and firm inclusion of active agents, physical stability of the particle matrix lipid modification (primarily α, β′), and related to these three properties the improved chemical stabilization of labile active agents. Exemplarily data for these effects are shown and underlying mechanisms are discussed. Further, general properties of lipid nanoparticles, which are also exhibited by the SmartLipids, are reviewed. These include the restauration of the protective lipid skin barrier (anti-pollution effect), penetration enhancement by occlusion (invisible patch effect) and the option to control the release of active agents for optimized biological effect and reduction of side effects (e.g., skin irritation through sensitizing active agents), which improves the skin tolerability. Regulatory aspects, such as submicron particle status, excipients, and certifications, are also discussed.

Introduction

To meet the increasing expectations and demands of consumers in personal care and cosmetics, as well of patients in medical care, dermal delivery systems are needed to improve the performance of dermal formulations. There are also requirements from the formulation manufacturer regarding perfected delivery systems. The primary requirements for an optimized carrier system are:

1. Sufficiently high loading capacity allowing for the utilization of low amounts of carrier, so as to not distinctly affect the properties of the formulation, e.g., skin feeling;
2. physical stability, i.e., firm inclusion of active agents and remaining integrity of the carriers in the final formulation during shelf life;

3. effective protection and stabilization of chemically labile active agents, e.g., retinol as a classical example;
4. restoration of the natural skin barrier (recently in focus in the framework of "anti-pollution" strategies);
5. penetration enhancement and increased bioavailability allowing for a reduced application frequency, enabling the use of active agents that could not be used before due to lack of penetration, e.g., certain antioxidants;
6. controlled and prolonged release in order to avoid too high concentrations on the skin that may cause irritancy (e.g., retinol and tretinoin);
7. composition preferentially of natural or naturally derived and modified raw materials that are ideally biodegradable and in conformity to ECOCERT/COSMOS (e.g., natural lipids or semisynthetic lipids derived from natural lipids).

Emulsions can only partially meet these requirements. For example, the protection of chemically lipophilic active agents is limited by the diffusional exchange with water. Controlled release is not possible due to the high diffusion coefficient, *D*, in oils of low viscosity (Einstein equation). Release typically takes place very fast within seconds or milliseconds [1]. The age of smart delivery systems for skin started with the introduction of liposomes to the cosmetic market in 1986 from the company Dior with the product Capture. Liposomes have several advantages for dermal delivery, e.g., adhesiveness to skin due to the small nanometric size, increase of skin moisture related leading to wrinkle reduction, and a stabilization of active agents to some extent.

In the following years attempts were made to come up with better delivery systems of the next generation. Looking back, these efforts were of limited or no success. For example, many expectations were raised with dermal microemulsions. However, the need of relatively high surfactant concentrations (skin irritating/damaging effects) and the often unpleasant application feeling did lead to a market failure. Polymeric nanoparticles, developed by P. P. Speiser for pharmaceutical purposes in the middle of the 1970s [2], found only limited use in consumer care/cosmetics. Problems are often the lack of regulatory status of many polymers used, expensive large-scale production and the lack of biodegradability (no "green" products possible, thus no certification after ECOCERT/COSMOS). There were also developments of various "somes", being derived from the liposomes and finding few applications (e.g., niosomes, ethosomes, transfersomes, pharmacosomes, herbosomes, colloidosomes, sphinosomes and cubosomes [3].

A step forward in 1991 was the development of a carrier made from solid lipids, the solid lipid nanoparticles (SLNs). They are derived from the emulsions by replacing the liquid lipid (oil) with a solid lipid and therefore are solid at body temperature. The second generation of these particles, the nanostructured lipid carriers (NLCs), made it to the cosmetic market in 2005 and are typically a mixture of one solid lipid and one liquid lipid [4], e.g., tristearin and caprylic/capric triglyceride, also being solid at body temperature.

In 2014 a new generation of carriers was developed, called SmartLipids [5,6]. They combine all the existing advantages of the previous particles made from solid lipids/lipid blends and add new key features. These are distinctly increased loading capacity and firm inclusion of the active agents, together with improved physical stability and increased chemical stabilization. This was achieved by creating a "chaotic" matrix structure by blending many different lipids, e.g., up to ten solid lipids, or mixture of solid and liquid lipids [7]. The structure of the SmartLipids and related key advantages are discussed. Briefly reviewed are the properties of SmartLipids originating from being solid lipid particles, i.e., possessing the same beneficial properties as abovementioned SLNs and NLCs. Industrial aspects such as regulatory issues and technical questions are covered regarding the production of marketable products in cosmetics and consumer care.

Review

What exactly are SmartLipids – definition

SLN were made from typically one solid lipid only. Such lipids can form highly ordered lipid crystalline structures (β modification), which leaves little space to accommodate active agents and limits its loading capacity. Sometimes expulsion of the active agent takes place during storage, when the lipid re-orders from α and/or β′ modification to primarily β modification. To overcome the loading limitation in NLCs, oil was admixed to the solid lipid, since liquid lipids (oils) exhibit higher solubilities for active agents compared to solid lipids. In NLCs, the solubilities of solid and liquid lipid are approximately additive, i.e., the solubility of active agents in the NLC particle blend is increased. However, the increase comes at the expense of an accelerated reordering during storage, as oils can accelerate the transition process to the β modification.

In the SmartLipids principle many structurally very different lipids (typically up to ten) are blended on purpose, being spatially incompatible due to differences in structure (mixture of mono-, di and triglycerides, or waxes) and length of the fatty acid chains. This was achieved by blending solid lipids only (e.g., with chains C14–C22), or by admixing limited amounts of oils (e.g., containing C8–C12 fatty acids). This leads to a lipid particle matrix structure being primarily or to a considerable extent in α modification with some β′ modification, having

many imperfections for an enhanced loading capacity of active agents (Figure 1). Due to the structural differences of the lipid molecules, reordering during storage to the highly ordered β modification is blocked or distinctly slowed down. Thus, no expulsion of active agents takes place leading to firm inclusion. The addition of oils increases the loading capacity further, but oil addition needs to be limited in order to prevent an accelerated reordering of the lipid matrix.

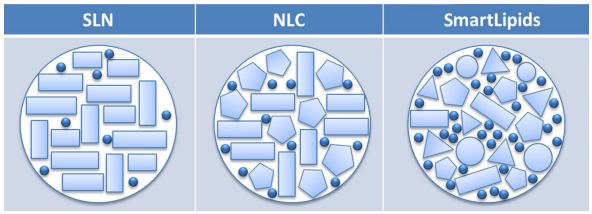

Figure 1: Simple representation of the structure of SmartLipids. The mixture of structurally very different solid and liquid lipids leads to a chaotic, less ordered structure (α, β′) with many imperfections, providing high loading capacity. The structure remains unchanged during storage leading to a firm inclusion of active agents with chemical stabilization and no expulsion of the active agents [10].

Some of the previously described NLC particles already represent the "SmartLipids principle". This is the case when the one solid lipid used in the mixture of one solid/one liquid lipid is a commercial lipid that is already a blend of multiple lipids, or when it is a priori a "wild mixture" of different structures, e.g., carnauba wax, mostly consisting of aliphatic esters (40.0 wt %), diesters of 4-hydroxy cinnamic acid (21.0 wt %), ω-hydroxy carboxylic acids (13.0 wt %) and fatty acid alcohols (12.0 wt %). The chain length of fatty acids and alcohols is mainly in the range of C26–C30 [8]. Another classical example of a commercial lipid blend is Cutina LM, which is composed of three pure lipids and three natural lipid mixtures (cetearyl alcohol, cetearyl glucoside, octyldodecanol, carnauba wax, candelilla wax, and beeswax). Different from the SmartLipids principle are, e.g., NLCs made from a relatively uniform solid lipid, e.g., tristearin (mainly C18 triglyceride) blended with caprylic/capric triglyceride [9].

Dermal application – main key features of SmartLipids

High loading capacity and firm inclusion of active agents

The unordered "chaotic" matrix state of SmartLipids provides enough defects to accommodate distinctly higher amounts of active agents compared to SLNs and NLCs. This can be seen regarding the maximum loading achieved for retinol and lidocaine (Figure 2). In this case the loading increases by a factor of about 15 and 3, respectively.

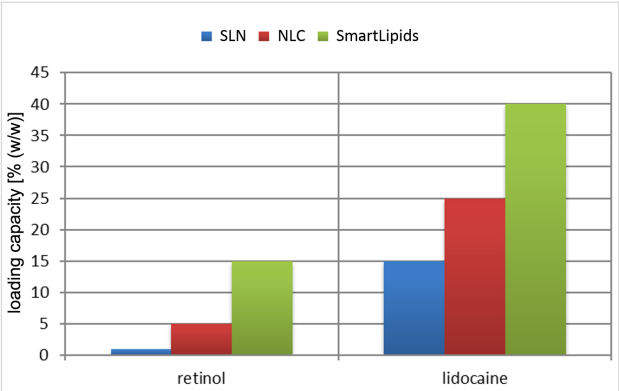

Figure 2: Maximum loading reported for SLNs, NLCs and SmartLipids for the dermal active agents retinol [11-13] (left) and lidocaine [14] (right).

The higher loading capacity ensures the firm inclusion of the active agent as well. In NLCs it was sometimes necessary to incorporate, e.g., 5% retinol (= maximum loading) to achieve the desired retinol concentration in the final product. At the maximum loading capacity, reordering could cause the expulsion of the active agent into the water phase (crystal formation). This is not the case in SmartLipids, since the maximum loading capacity is increased to 15. Even slight reordering will not lead to active expulsion when lower loadings than the maximum possible are employed. Of course, the degree of loading affects also the release (cf. section 3.4).

Physical stability in products

The aspects of physical stability in lipid particle dispersions during storage and in final products are (1) an unchanged crystalline structure of the particle matrix and (2) the quantitative proof of remaining existence/presence of particles. The created crystalline structure should primarily remain in the unordered state for firm inclusion of loaded active agents, which can be measured by combining differential scanning calorimetry (DSC) with X-ray diffraction. Ruick showed a fast transition from the α modification to the β modification when SLNs were produced with tristearin (Figure 3), while a SmartLipids mixture with eight solid lipids remained practically unchanged during one year of storage.

Carriers, especially fluid carriers such as liposomes, can reduce in number in a final product during shelf life. Liposomes have a tendency to fuse with the stabilizer layers of oil droplets in oil/water creams. For the best quality, the quantitative stability of the carriers is desirable. Especially, quantitative stability is required in case of pharmaceutical formulations. Quantitative analysis of, e.g., liposomes in final products is relatively difficult, but required in some countries from regulatory authorities. The difficulty of such analysis was tried to circumvent, e.g., by

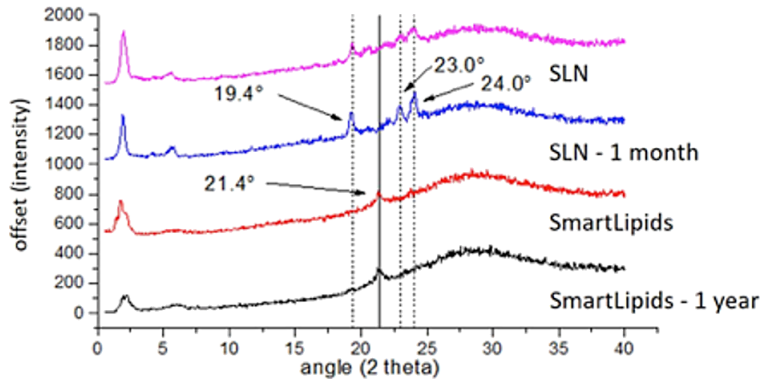

Figure 3: X-ray diffraction patterns of SLNs (pink curve) and SmartLipids mixture (red curve) determined directly after production and after one month (SLNs: blue curve) and one year (SmartLipids: black curve) storage at room temperature [5].

only specifying "lecithin" in the product, despite knowing that a main contribution of the product performance is coming from the existing liposomes formed by lecithin. In contrast, the quantitative proof of 100% existing lipid particles with solid particle matrix is very easy by measuring the melting enthalpy using differential scanning calorimetry (DSC). The melting enthalpy of a SmartLipids suspension can be determined before addition to the product, after addition to a gel or a cream and after storage. In case the particles dissolve, e.g., in an oil of a cream, the melting enthalpy will decrease. Thus, the physical stability of SmartLipids is easy to analyze and to prove.

Chemical stabilization of active agents

Classical fluid carriers such as nanoemulsion and liposomes have a limited ability to protect labile lipophilic active agents. Due to the partitioning coefficient, K, after Nernst, the lipophilic active agents are primarily enriched in the lipid phase and only to a small extent in the water phase. But there is a diffusional exchange between the oil and the water phase. The active agent diffuses from the oil into the water phase, the active agent is degraded in the water phase (e.g., hydrolyzed), the degraded active agent diffuses back into the oil phase and is replaced in the water phase by new non-degraded active agent from the oil. This is a kind of vicious circle (Figure 4, right). Due to the relatively low viscosity, η, of oil (70–100 mPa·s) and phospholipid bilayers (184 mPa·s [15]), this process takes place relatively fast. The diffusion coefficient D can be calculated using the Einstein equation:

$$D = \frac{k_B T}{6\pi\eta r},$$

with k_B being the Boltzmann constant and T being the absolute temperature. In contrast, the viscosity η in solid particles is very high, e.g., 653 mPa·s for solid paraffin. Thus, the abovementioned exchange is practically avoided or at least strongly minimized [16] (Figure 4).

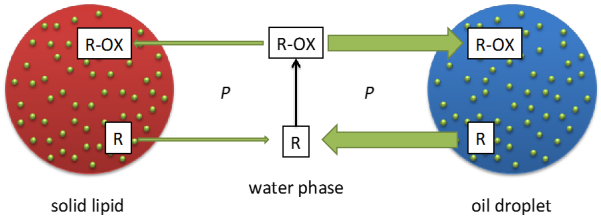

Figure 4: Fast degradation of lipophilic active agents (R) in fluid carriers (blue), such as oil/water emulsions or creams and liposomes, through fast exchange with the water phase (right) in comparison to a minimized exchange of active between a highly viscous solid carrier (red) and the water phase (left) (*P*: partitioning coefficient); modified with permission from [17], copyright 2017 Elsevier.

Retinol is a chemically highly labile molecule, and thus the efficient stabilization in dermal products is a challenge. Retinol was incorporated into various carrier systems, but only with limited increase in stability. Stabilities reported were 20% after ten days in liposomes [18], 40% after 24 h in a nanoemulsion [19], 50% after 24 h in zein colloidal particles [19] and 60% after one month in a nanoemulsion stabilized by silica [20]. A screening was performed in two SmartLipids mixtures. The solid particle matrix itself is protective for labile molecules as outlined above. Up to 86% retinol remained after six months of storage at room temperature (Figure 5, lower right). This stabilization is due to the solid character of the carrier matrix with limited exchange of active agent with the water phase, and the protection of the active agent inside the solid carrier matrix, e.g., against access of oxygen and light. To have an even better stabilized system, lipophilic anti-oxidants were added leading to about 85–95% retinol remaining at room temperature (Figure 5,

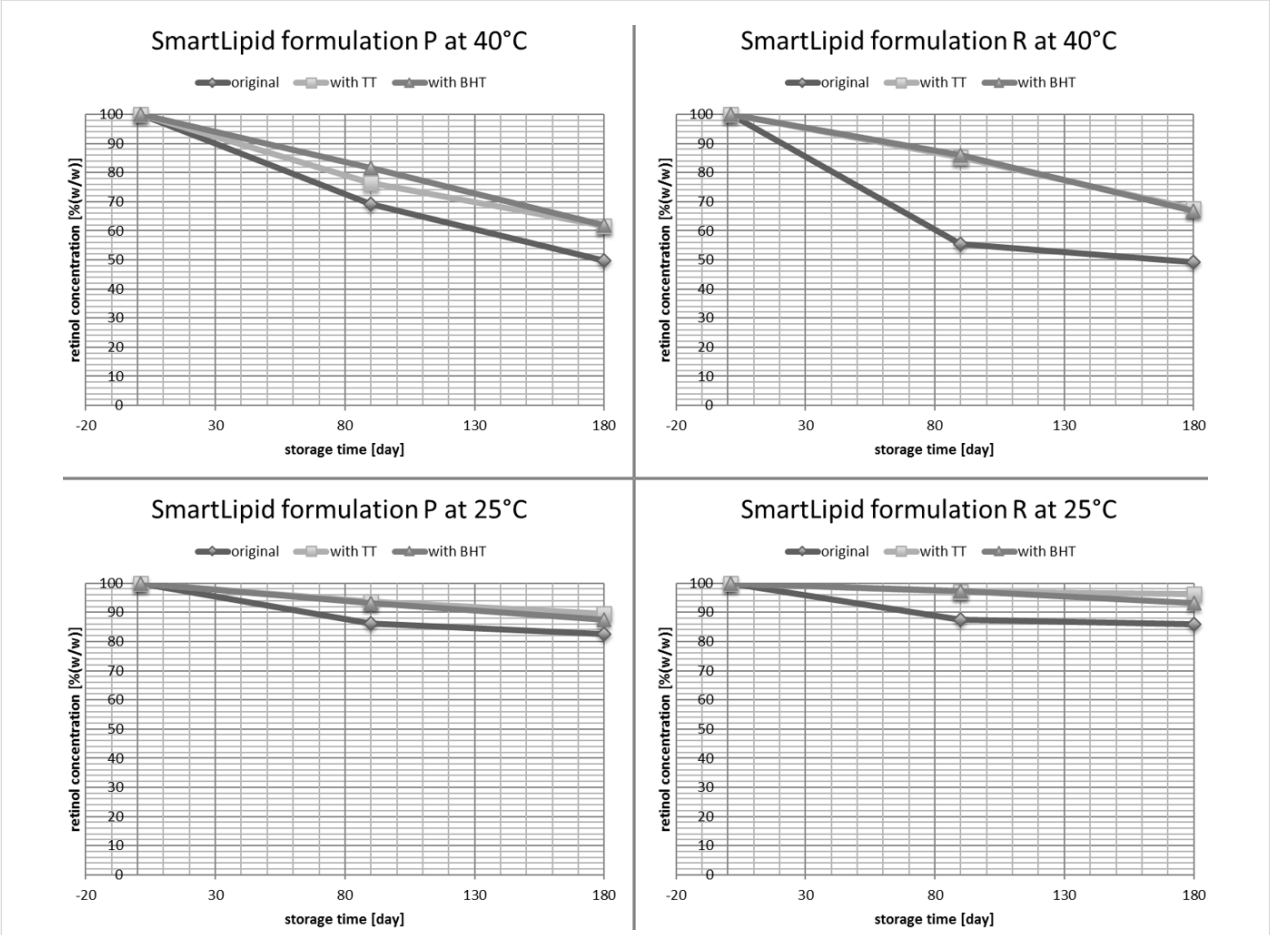

Figure 5: Storage study with retinol loaded SmartLipids particles over six months. Remaining retinol content in SmartLipids formulation P (left) and R (right) before and after incorporation of lipophilic antioxidants Tinogard TT and BHT at 40 °C (upper) and room temperature (25 °C, lower), [10].

lower row), and 65–70% at a stress temperature of 40 °C (Figure 5, upper row). More complex particle structures of SmartLipids lead to better incorporation and protection of active agents.

Size of SmartLipids submicrometer particles – legal aspects

By definition, nanoparticles possess a size in the nanometer range, i.e., from a few nanometers to below 1000 nm. Legally, after the EU cosmetic guideline [21], nanoparticles are only particles with a size below 100 nm, precisely a particle population with more than 50% of the particles below 100 nm based on the number distribution. Incorporating a nanoparticle material needs to be declared in the INCI nomenclature by the addition of "nano".

A typical mean size of SmartLipids particles is in the range of 200–400 nm, measured by laser light scattering, i.e., photon correlation spectroscopy (PCS). The calculated size is based on the intensity signal of the scattered laser light, which is used to calculate a so-called correlation function $g(\tau)$. The obtained mean diameter is the intensity-weighted so-called z-average (z-ave). The correlation function $g(\tau)$ can be converted to a size distribution by Fourier transformation. EU regulations require a measuring method that can cover the full size range of a particle population. The measuring range of PCS is roughly from about 3 nm to 6 µm. Suspensions of SmartLipids do not contain particles below 3 nm, and practically no, or only negligible contents of, particles larger than 6 µm. Thus, PCS is a suitable method to meet the EU requirements for SmartLipids products. The absence of particles above 6 µm could be proven by laser diffraction (Malvern Mastersizer 2000, Malvern, UK). In this case the volume distribution was taken, because it is more sensitive to show a few large particles than the number distribution.

To avoid the linguistic confusions: technically the particles are nanoparticles but at the same time are legally not nanoparticles. Those particle populations should be classified as "submicrometer particles". Submicrometer particles are in the size range be-

tween 100 nm and 1000 nm, nanoparticles are smaller than 100 nm. Hence, SmartLipids are submicrometer particles.

Industrial production of SmartLipids - standard & customized products

The production of SmartLipids is identical to that of SLNs and NLCs [22]. The lipid mixture is heated to approximately 5–10 °C above the melting point of the highest melting lipid, then the active agent is dissolved in the lipid melt and the melt containing the active agent is dispersed in a hot aqueous stabilizer solution (surfactant, polymer) of identical temperature by high-speed stirring to form a coarse emulsion. This pre-emulsion is then passed through a high-pressure homogenizer, and typically one or two homogenization cycles are applied. Homogenizers used are typically piston–gap homogenizers, e.g., the APV Gaulin 5.5. homogenizer with a production capacity of up to 150 L/h (medium scale) [7], and the GEA Niro Soavi homogenizer with production capacities of up to 10.000 L/h (large scale). The obtained hot nanoemulsion is cooled, the lipid blend re-crystallizes and forms solid lipid particles. The suspensions are preserved by standard preservatives (e.g., euxyl® PE 9010) or are alternatively prepared preservative-free by adding, e.g., pentylene glycol. Standard products are available on the market, while coenzyme Q10 and retinol are in preparation. Formulations with customer-specific active agents can also be prepared on an exclusive basis. Concentrates have a typical particle content of 10% or 20%. For the incorporation into cosmetic products, the dermal formulations are produced as normal, but with slightly reduced water content. At the end of the production, the SmartLipids concentrates are admixed under blending with a stirrer.

Dermal application – general features of lipid nanoparticles with solid particle matrix

Adhesion onto skin with increased residence time/ prolonged release

There are many properties that are identical for the several types of lipid nanoparticles – SLNs, NLCs and SmartLipids – because they only depend on physical characteristics (e.g., particle size or general adhesiveness of small particles) or chemical characteristics (e.g., nature of the particle material, in this case lipid). Thus, data published previously regarding these general features also apply to the newly developed SmartLipids particles.

It is well known that decreasing the particle size leads to a larger interaction area between particles and substrate and thereby the adhesiveness increases. The classical and often cited example from food industry is the different adhesiveness of crystalline sugar and icing sugar onto bakery products. Large crystals tend to fall off, whereas icing sugar forms sticky layers on bakery products. Thus, all nanoparticles, e.g., as reported for liposomes [23,24], have an increased adhesiveness to skin. In a recent study it could be shown that the adhesiveness of solid lipid particle suspensions to human skin is superior to fluid nanoemulsion droplets. Both, similar in size, were labeled with Nile red and applied in a square onto the inner forearm. The presence of applied particles was detected using an UV lamp with a wavelength of 365 nm (Figure 6, left). Then the forearms were washed under flowing water and rubbed with the thumb. Most of the nanoemulsion was washed off, whereas the lipid particles mostly remained on the skin (Figure 6, right). This increased adhesiveness and related residence time on the skin promotes a prolonged release of active agents, especially when sweating occurs with subsequent tissue wiping by the consumer or when skin areas are covered with clothes.

Restauration of the natural skin barrier and anti-pollution effect

Due to unhealthy skin conditions or general stress by environmental factors, the natural skin barrier (lipid film on the stratum corneum) can be damaged, i.e., thinned or even partially lost (bare patches). This has negative effects on the cells below and could lead to a higher transepidermal water loss (TEWL). In addition, the skin is more exposed to environmental stress, ranging from UV/IR radiation to pollution from the air, e.g.,

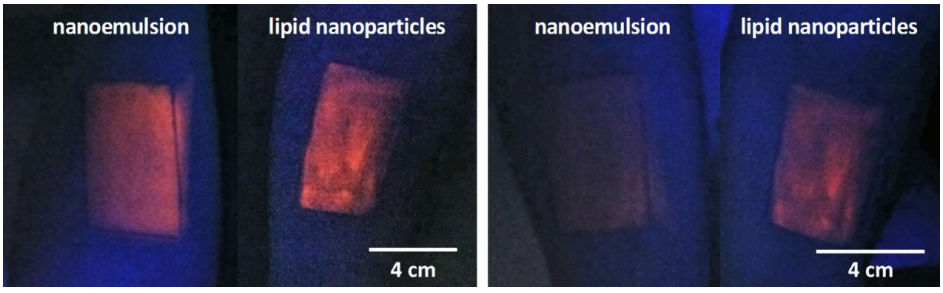

Figure 6: Left: Nile red-labeled lipid nanoparticle suspension (right arm) and nanoemulsion (left arm) applied to human forearm directly after application. Right: **B**oth arms after washing under flowing water with rubbing. The lipid nanoparticles are highly adhesive and mostly remain on the skin (right arm).

particulate matter. Especially in the last two years, skin care products/cosmetics with "anti-pollution" effect are a key topic. Cosmetic formulations can reduce the adsorption of particulate matter onto the skin and minimize related negative skin effects. Thus, the effective restauration of the skin barrier is an important feature of lipid nanoparticles [25], and a long residence time of the particles on the skin even under mechanical stress is beneficial to fight pollution factors.

The lipid particles adhere onto the skin as any nanosized particle does and form a film. This film formation can be followed by measuring the dielectric constant of the skin, using a Corneometer® (Courage + Khazaka Electronic GmbH, Germany) [26]. The probe determines the dielectric constant, *D*, of the skin through a condenser in the probe. An insulator medium in the condenser reduces the measured *D* value. For example, *D* is 0 for a complete insulator (vacuum), about 5 for lipids and organic liquids, and 80 for pure water. The reading is given in arbitrary units. If the skin moisture increases through the application of a cosmetic cream, the obtained *D* value increases. However, if an insulator material is between the probe and the skin (i.e., a lipid film), the *D* value decreases (Figure 7, lower row). This was shown in [27,28]. Applying a lipid particle film to the skin led to the formation of a lipid layer thicker than the normal barrier, resulting in *D* values below the *D* values of the normal lipid film on skin (Figure 7, upper row). The thickness of the created lipid film by applying lipid particle suspensions is controlled by the particle concentration in the suspension. The formation of a film can also be concluded by measuring the decrease in transepidermal water loss (TEWL) after application of the lipid particles in a formulation.

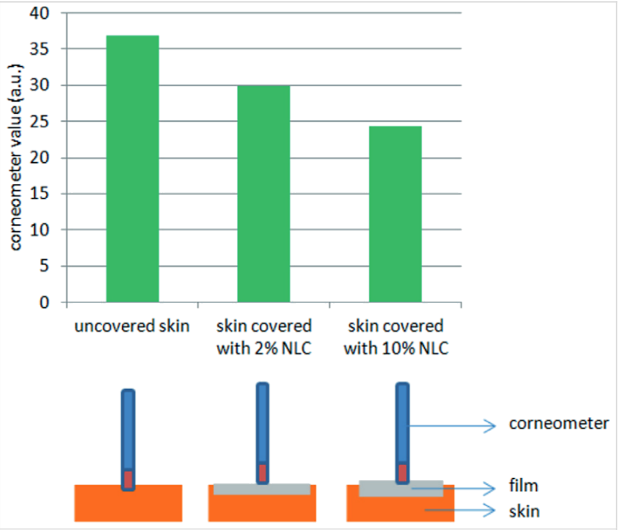

Figure 7: Determination of the relative film thickness by measuring the dielectric constant *D* on skin. Probe readings of untreated skin and skin with applied increasing concentration of lipid particle suspension; reproduced with permission from [27], copyright 2013 Euro Cosmetics.

Following this model, any lipid particle can be used to repair the stratum corneum film, independent on its lipid composition and loaded active agent, as it was the case in [27,28]. Restauration of the natural lipid barrier is thus a beneficial effect generated already by unloaded SmartLipids on the skin. Also, ceramides can be used to produce SmartLipids, albeit primarily for the higher priced cosmetic sector.

Increased penetration and bioavailability

Occlusion increases the dermal penetration of many active agents. Occlusion leads to increased moisture content of the skin as well as increased percutaneous absorption of most active agents [29,30]. A simple but efficient way to obtain occlusion in the hospital is to cover a cream-treated skin area with a plastic foil. Pharmaceutical transdermal patches benefit also from the occlusion effect of their polymer films, promoting penetration. However, such patches are of no or limited use for facial cosmetics. A compromise is to apply cosmetic masks for a limited time, requiring consumer patience and compliance to the regular treatment. In contrast, lipid particle formulations are described in the literature as "invisible patch" [27]. After being applied to the skin, they show controlled occlusive and delivery effects comparable to patches (or some masks) but are "invisible" and thus create their effect up to 24 h. Increased penetration of active agents due to occlusion is extensively described in the literature [29].

To show the ability of SmartLipids to provide efficient skin penetration, a particle suspension was prepared containing 0.2% curcumin. Curcumin has many positive effects on the skin [31,32] and is at the same time fluorescent, allowing for a good and easy detection in the skin by fluorescence microscopy. The suspension was applied to pig ear skin in a covered Franz cell, incubated for 24 h and then skin slices were investigated by normal light and fluorescence microscopy (Figure 8, left column). Figure 8 (upper row) shows the fluorescence microscopy images. The lower row shows overlays of fluorescence and light microscopy images, allowing to locate the fluorescence in the epidermis. For comparison, a tenfold higher concentrated 2% curcumin suspension is shown in Figure 8 (middle column). The curcumin remains as a thick fluorescent layer on top of the stratum corneum, showing practically no fluorescence inside the epidermis. Finally, a curcumin containing marketed product from the US is shown, according to HPLC analysis containing 0.0001% curcumin in dissolved form, corresponding to its maximum solubility. Only negligible fluorescence in the skin was detectable (Figure 8, right column). This shows that SmartLipids are an enabling technology to provide efficient skin penetration even for such problematic, poorly soluble active agents such as curcumin. This increased bioavailability in the skin enables real skin effects.

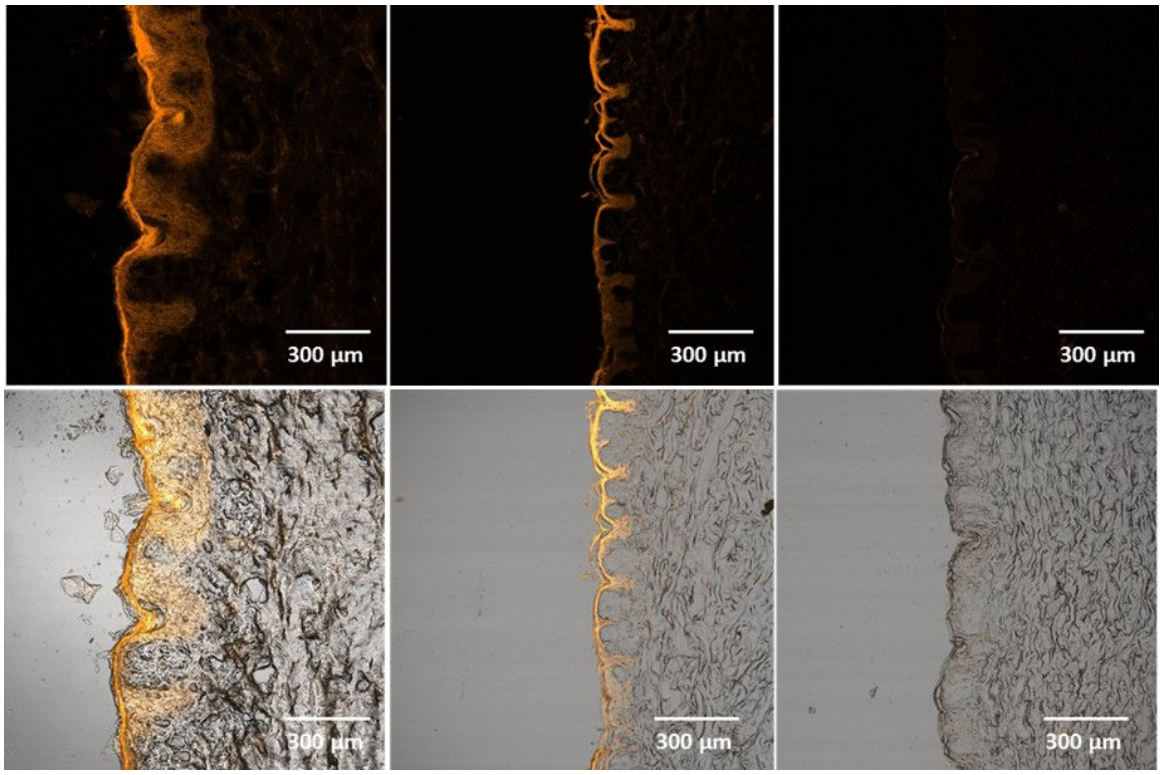

Figure 8: Penetration of curcumin into pig ear skin, vertical pig ear slices, fluorescence microscopy images (upper row) and overlay of fluorescence and light microscopy images (lower row); after application of 0.2% curcumin suspension in SmartLipids (left column), 2.0% curcumin micrometer-size crystal suspension (middle) and a commercial curcumin containing gel product (right). Incubation time was 24 h. Both laser strength (35%) and fluorescence detector gain (720 V) were kept constant during all measurements.

This study based on curcumin fluorescence was a qualitative study as the fluourescence intensity was not measured quantitatively. However, strong fluorescence (SmartLipids), limited fluorescence (suspension) and practically no fluorescence (marketed product) show clear differences. The comparison with the marketed product was meant to show that there is an urgent need for improved dermal curcumin formulations. It should be kept in mind, that both the SmartLipids and the micrometer-crystal formulation contained a mixture of non-dissolved curcumin and curcumin dissolved in the outer phase of the dermal formulation. The non-dissolved curcumin acts as a depot to replace the curcumin in the formulation penetrating the skin. This is the way, how the formulations work, and the SmartLipids work better.

Controlled and prolonged release

Optimized performance of active agents might depend strongly on the rate of their release from the carrier. Desirable release might be fast, prolonged/sustained or should be as slow as possible (even to no release at all). That means, a carrier system should provide the ability to control the release of active agents. A prolonged release is desirable in many formulations, e.g., in anti-aging compounds such as retinol. A controlled release is also desirable for active agents having a skin irritation potential, because concentrations that are too high and promote irritation need to be avoided. It was shown for tretinoin, that incorporation into lipid particles avoided skin irritation [33]. Little or no release is ideal for molecular sunscreens for UV protection, which should not penetrate into but remain on the skin, ideally inside the carrier, to generate their protective effect. At best, they should remain inside the lipid particle, since it was shown that there is a synergistic effect of the particle matrix on the molecular sunscreen increasing its protective efficiency [34]. This allows the reduction of molecular sunscreen concentration in a product.

The release can be controlled by the localization of the active agent inside the solid lipid particle matrix. Without going into technical details, the localization of the active agent can be modified by the composition of the lipid particle matrix, concentration of active agent and production parameters. A very fast release is generated, when the active agent is primarily located in the outer shell of the particles (enriched shell model), a prolonged release when the active is evenly distributed throughout the whole carrier matrix (solid solution model), and a very slow/strongly delayed release when the active is mainly located

in the core (enriched core model) (Figure 9). For example, a very fast and complete release within minutes was shown for cyclosporine (Figure 10, upper row) [35], and an extremely prolonged release of only 37.1% of prednisolone after 5 weeks was achieved with solid lipid nanoparticles (Figure 10, lower row) [36] The distinctly reduced side effects of tretinoin re-

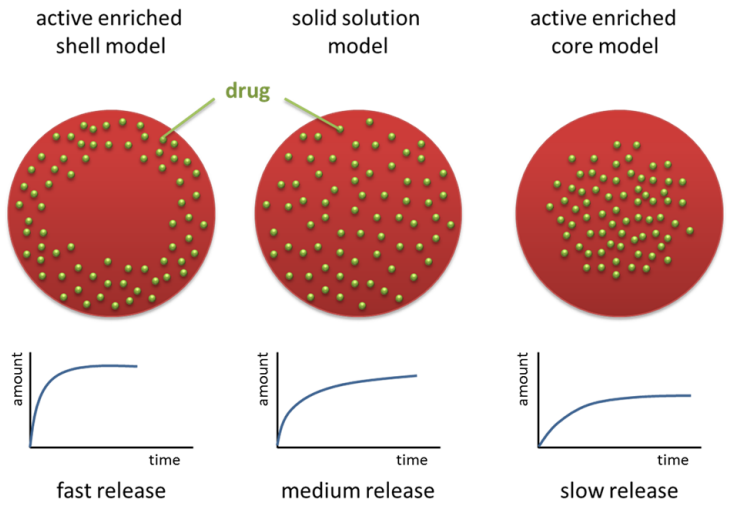

Figure 9: Models of cosmetic active agents or drugs (green) incorporated into lipid nanoparticles, from left to right: enriched shell model (fast release), solid solution model (prolonged release) and enriched core model (very slow release); reproduced with permission from [17], copyright 2017 Elsevier.

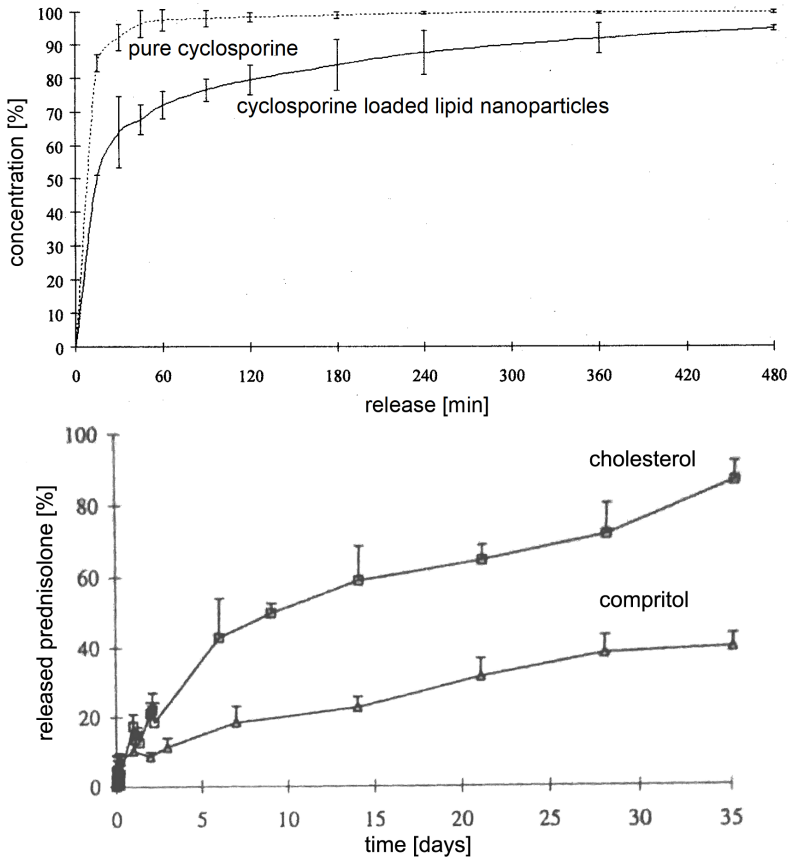

Figure 10: Examples of release profiles from lipid nanoparticles: very fast release of cyclosporine within minutes (upper row, after [35]), and the other extreme of very slow release of prednisolone over 35 days (lower row, after [36], explainable by enriched shell and enriched core model, respectively.

leased from lipid nanoparticles can be explained by a controlled release, avoiding high peak concentrations of free tretinoin on the skin.

In dermal sunscreen formulations, the lipophilic sunscreens are normally dissolved in the oil phase of oil/water emulsions. Due to the liquid state of the oil droplets, the evenly and molecularly dispersed sunscreen within the droplets can be released quickly and penetrate into the skin. The release of oxybenzone from an emulsion and SLNs was compared in an in vitro Franz cell model. The release from emulsions was two times faster (Figure 11) [37]. The distinctly slower release from the lipid nanoparticles shows their potential of reducing undesired side effects by large amounts of sunscreen penetrating into the skin.

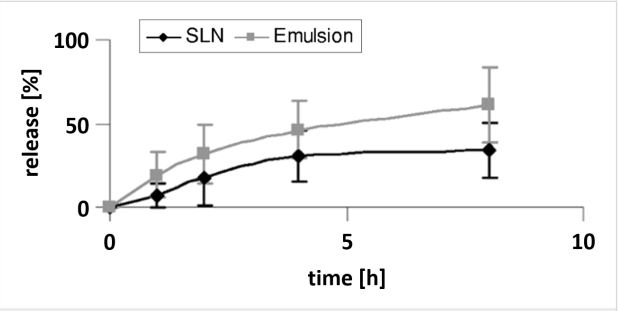

Figure 11: In vitro release of the sunscreen oxybenzone from a nanoemulsion (grey) and from a SLN suspension (black) measured in Franz diffusion cells, after [37].

Conclusion

The lipid nanoparticle history started in 1991 with SLNs, the second generation of NLCs entered the cosmetic market just 14 years later in 2005, much faster than the liposomes did (they needed about 20 years from invention to cosmetic market in 1986). With the "SmartLipids concept" a mature industrial delivery system is available since 2016. The outstanding feature is the number of delivery advantages combined in one single system. Specific to SmartLipids are:

1. High loading capacity,
2. firm inclusion of active agents,
3. physical stability of the carrier in the final formulation (and easy to prove) and thus
4. improved chemical stabilization of active agents.

General features of all lipid nanoparticles are the restauration of the natural protective lipid barrier, and penetration enhancement with increased dermal bioavailability and controlled/optimized release.

Even if a different carrier system is superior in one or two properties, the sum of the combined delivery advantages in SmartLipids outweighs this in most cases. On top, to meet upcoming consumer expectations, conformity to ECOCERT/COSMOS can be provided and the particles are not nanosized but submicrometer carriers. Contract manufacturing on industrial scale under GMP is available, also for customized formulations. Thus, the basis for broad use in cosmetics and consumer care products is given.

ORCID® iDs

Florence Olechowski - https://orcid.org/0000-0002-3906-2001

References

1. Washington, C.; Evans, K. *J. Controlled Release* **1995,** *33,* 383–390. doi:10.1016/0168-3659(94)00110-g
2. Birrenbach, G.; Speiser, P. P. *J. Pharm. Sci.* **1976,** *65,* 1763–1766. doi:10.1002/jps.2600651217
3. Bansal, S.; Kashyap, C. P.; Aggarwal, G.; Harikumar, S. L. *Int. J. Res. Pharm. Chem.* **2012,** *2,* 704–713.
4. Das, S.; Ng, W. K.; Tan, R. B. H. *Eur. J. Pharm. Sci.* **2012,** *47,* 139–151. doi:10.1016/j.ejps.2012.05.010
5. Müller, R. H.; Ruick, R.; Keck, C. M. smartLipids® — the next generation of lipid nanoparticles by optimized design of particle matrix. In *Proceedings of the Annual Meeting of German Pharmaceutical Society,* Frankfurt, Sept 24–26, 2014; .
6. Müller, R. H.; Ruick, R.; Keck, C. M. smartLipids® — the new generation of lipid nanoparticles after SLN and NLC. In *Proceedings of the Annual Meeting of American Association of Pharmaceutical Scientists,* San Diego, CA, U.S.A., Nov 2–6, 2014; .
7. Müller, R. H.; Olechowski, F.; Köpke, D.; Pyo, S. M. SmartLipids — The Third Generation of Solid Submicron Lipid Particles for Dermal Delivery of Actives. In *Nanocosmetics – From Ideas to Products;* Cornier, J.; Keck, C. M.; van de Voorde, M., Eds.; Springer International Publishing: Cham, Switzerland, 2019; pp 141–159. doi:10.1007/978-3-030-16573-4_7
8. Wolfmeier, U.; Schmidt, H.; Heinrichs, F.-L.; Michalczyk, G.; Payer, W.; Dietsche, W.; Boehlke, K.; Hohner, G.; Wildgruber, J. Waxes. *Ullmann's Encyclopedia of Industrial Chemistry;* Wiley-VCH Verlag GmbH & Co. KGaA: Weinheim, Germany, 2000. doi:10.1002/14356007.a28_103
9. Ruick, R. SmartLipids – die neue Generation der Lipidnanopartikel nach SLN und NLC. Ph.D. Thesis, Freie Universität Berlin, Berlin, Germany, 2016.
10. Pyo, S. M. Nanocrystals & lipid nanoparticles for optimized delivery of active agents. Ph.D. Thesis, Freie Universität Berlin, Berlin, Germany, 2016.
11. Ding, Y.; Pyo, S. M.; Müller, R. H. *Pharmazie* **2017,** *72,* 728–735. doi:10.1691/ph.2017.7016
12. Jee, J.-P.; Lim, S.-J.; Park, J.-S.; Kim, C.-K. *Eur. J. Pharm. Biopharm.* **2006,** *63,* 134–139. doi:10.1016/j.ejpb.2005.12.007
13. Jenning, V. Lipid-Nanopartikel (SLN) als Trägersystem für die dermale Applilkation von Retinol. Ph.D. Thesis, Freie Universität Berlin, Berlin, Germany, 1999.
14. Pyo, S. M.; Schubert, V.; Zölfl, S.; Tauber, M.; Müller, R. H. Production of highly loaded lidocaine NLC (nanostructured lipid carriers) for laser pre-treatment. In *Proceedings of the Polish-German Symposium on Pharmaceutical Sciences: Retrospects, Insights and Prospects,* Kiel, Germany, May 26–27, 2015; .

15. Diederichs, J. E.; Müller, R. H. *Arch. Pharm. (Weinheim, Ger.)* **1991,** *324,* 607.
16. Olechowski, F.; Pyo, S. M.; Müller, R. H. BergaCare SmartLipids retinol — novel optimized formulation for dermal retinol. In *Proceedings of the Annual Meeting of American Association of Pharmaceutical Scientists,* San Diego, CA, U.S.A., Nov 2–6, 2017; .
17. Pyo, S.-M.; Müller, R. H.; Keck, C. M. Encapsulation by nanostructured lipid carriers. In *Nanoencapsulation Technologies for the Food and Nutraceutical Industries;* Jafari, S., Ed.; Elsevier: Amsterdam, Netherlands, 2017; Vol. 1, pp 114–137. doi:10.1016/b978-0-12-809436-5.00004-5
18. Ko, S.; Lee, S.-C. *Afr. J. Biotechnol.* **2010,** *9,* 6158–6161. doi:10.5897/ajb10.917
19. Pan, Y.; Tikekar, R. V.; Wang, M. S.; Avena-Bustillos, R. J.; Nitin, N. *Food Hydrocolloids* **2015,** *43,* 82–90. doi:10.1016/j.foodhyd.2014.05.002
20. Zhao, Y.; Guan, Y.; Pan, Y.; Nitin, N.; Tikekar, R. V. *Food Res. Int.* **2015,** *74,* 269–274. doi:10.1016/j.foodres.2015.05.008
21. Regulation (EC) No 1223/2009 of the European Parliament and of the Council of 30 November 2009 on Cosmetic Products. https://eur-lex.europa.eu/legal-content/EN/TXT/HTML/?uri=CELEX:32009R1223&from=DE (accessed Sept 26, 2019).
22. Jenning, V.; Lippacher, A.; Gohla, S. H. *J. Microencapsulation* **2002,** *19,* 1–10. doi:10.1080/713817583
23. Nastruzzi, C.; Esposito, E.; Menegatti, E.; Walde, P. *J. Appl. Cosmetol.* **1993,** *11,* 77–91.
24. Touitou, E.; Junginger, H. E.; Weiner, N. D.; Nagai, T.; Mezei, M. *J. Pharm. Sci.* **1994,** *83,* 1189–1203. doi:10.1002/jps.2600830902
25. Müller, R. H.; Staufenbiel, S.; Keck, C. M. *Household Pers. Care Today* **2014,** *9* (2), 18–25.
26. Courage, W. Courage, W. Hardware and measuring principle: corneometer. In *Bioengineering and the skin: water and stratum corneum;* Elsner, P.; Berardesca, E.; Maibach, H. I., Eds.; CRC Press: Boca Raton, FL, U.S.A., 1994; pp 171–175.
27. Müller, R. H.; Sinambela, P.; Keck, C. M. *Euro Cosmet.* **2013,** *6,* 20–22.
28. Müller, R. H.; Alexiev, U.; Sinambela, P.; Keck, C. M. Nanostructured Lipid Carriers (NLC): The Second Generation of Solid Lipid Nanoparticles. In *Percutaneous Penetration Enhancers Chemical Methods in Penetration Enhancement – Nanocarriers;* Dragicevic, N.; Maibach, H. I., Eds.; Springer Berlin: Berlin, Germany, 2016; pp 161–185. doi:10.1007/978-3-662-47862-2_11
29. Zhai, H.; Maibach, H. I. *Skin Pharmacol. Appl. Skin Physiol.* **2001,** *14,* 1–10. doi:10.1159/000056328
30. Rahimpour, Y.; Hamishehkar, H. *Expert Opin. Drug Delivery* **2012,** *9,* 443–455. doi:10.1517/17425247.2012.666968
31. Thangapazham, R. L.; Sharma, A.; Maheshwari, R. K. Beneficial role of curcumin in skin diseases. In *The Molecular Targets and Therapeutic Uses of Curcumin in Health and Disease;* Aggarwal, B. B.; Surh, Y. J.; Shishodia, S., Eds.; Advances in Experimental Medicine and Biology, Vol. 595; Springer: Boston, MA, U.S.A., 2007; pp 343–357. doi:10.1007/978-0-387-46401-5_15
32. Phan, T.-T.; See, P.; Lee, S.-T.; Chan, S.-Y. *J. Trauma: Inj., Infect., Crit. Care* **2001,** *51,* 927–931. doi:10.1097/00005373-200111000-00017
33. Lai, F.; Pireddu, R.; Corrias, F.; Fadda, A. M.; Valenti, D.; Pini, E.; Sinico, C. *Int. J. Pharm.* **2013,** *458,* 104–109. doi:10.1016/j.ijpharm.2013.10.007
34. Müller, R. H.; Wissing, S.; Mäder, K. UV radiation reflecting or absorbing agents, protecting against harmful UV radiation and reinforcing the natural skin barrier. U.S. Patent US6814959, Nov 11, 2004.
35. Runge, S. A. Solid lipid nanoparticles (SLN®) as colloidal bioactive carriers for the oral administration of ciclosporin A. Ph.D. Thesis, Freie Universität Berlin, Berlin, Germany, 1998.
36. zur Mühlen, A.; Schwarz, C.; Mehnert, W. *Eur. J. Pharm. Biopharm.* **1998,** *45,* 149–155. doi:10.1016/s0939-6411(97)00150-1
37. Wissing, S. A.; Müller, R. H. *J. Controlled Release* **2002,** *81,* 225–233. doi:10.1016/s0168-3659(02)00056-1

License and Terms

BEILSTEIN JOURNAL OF NANOTECHNOLOGY

Microfluidics as tool to prepare size-tunable PLGA nanoparticles with high curcumin encapsulation for efficient mucus penetration

Nashrawan Lababidi[1], Valentin Sigal[1], Aljoscha Koenneke[1], Konrad Schwarzkopf[2], Andreas Manz[3] and Marc Schneider[*1,§]

Full Research Paper

Open Access

Address:
[1]Department of Pharmacy, Biopharmaceutics and Pharmaceutical Technology, Saarland University, 66123 Saarbrücken, Germany, [2]Department of Anaesthesia and Intensive Care, Klinikum Saarbrücken, Winterberg, 66119 Saarbrücken, Germany and [3]KIST Europe, 66123 Saarbrücken, Germany

Email:
Marc Schneider[*] - Marc.Schneider@uni-saarland.de

* Corresponding author
§ Phone: +49 (0)681 302-2438

Keywords:
curcumin; human pulmonary mucus; microfluidics; muco-penetrating nanoparticles; nanomedicine; permeability; PLGA nanoparticles

Beilstein J. Nanotechnol. **2019,** *10,* 2280–2293.
doi:10.3762/bjnano.10.220

Received: 25 June 2019
Accepted: 24 October 2019
Published: 19 November 2019

This article is part of the thematic issue "Frontiers in pharmaceutical nanotechnology".

Guest Editor: M. G. Wacker

Abstract

Great challenges still remain to develop drug carriers able to penetrate biological barriers (such as the dense mucus in cystic fibrosis) and for the treatment of bacteria residing in biofilms, embedded in mucus. Drug carrier systems such as nanoparticles (NPs) require proper surface chemistry and small size to ensure their permeability through the hydrogel-like systems. We have employed a microfluidic system to fabricate poly(lactic-*co*-glycolic acid) (PLGA) nanoparticles coated with a muco-penetrating stabilizer (Pluronic), with a tunable hydrodynamic diameter ranging from 40 nm to 160 nm. The size dependence was evaluated by varying different parameters during preparation, namely polymer concentration, stabilizer concentration, solvent nature, the width of the focus mixing channel, flow rate ratio and total flow rate. Furthermore, the influence of the length of the focus mixing channel on the size was evaluated in order to better understand the nucleation–growth mechanism. Surprisingly, the channel length was revealed to have no effect on particle size for the chosen settings. In addition, curcumin was loaded (EE% of ≈68%) very efficiently into the nanoparticles. Finally, the permeability of muco-penetrating PLGA NPs through pulmonary human mucus was assessed; small NPs with a diameter of less than 100 nm showed fast permeation, underlining the potential of microfluidics for such pharmaceutical applications.

Introduction

In the last decades, the application of nanotechnology in medicine has gained significant attention, especially in the biomedical field for vaccine delivery [1,2], in anticancer therapies [3,4], as well as for gene delivery [5,6]. Owing to the unique physicochemical properties of nanoparticles, the nanoparticle surface can be specifically modified to meet the needs of the desired application [7,8]. Such surface modifications can also be applied to protect drug carriers from being inactivated by avoiding interaction with mucus [9-11]. Nanoparticles (NPs) have shown a tremendous effect in terms of facilitating the diffusion of drugs through biological barriers, for example, through thick mucus in cystic fibrosis [10,12-16]. Notably, only NPs with size less than 200 nm have the ability to permeate easily through mucus without being immobilized by the natural size-filtering mechanism [10,17-19]. Furthermore, modifying the surface chemistry of NPs is beneficial for avoiding the interaction/filtering mechanisms such as H-bond interaction and electrostatic interactions [15,17,20-24]. Moreover, NPs as a carrier system have shown the ability to protect the loaded drug from inactivation, reduce unwanted side effects and enhance the efficacy of the active pharmaceutical ingredient (API) due to improved solubility and bioavailability [25]. As penetrating particulate systems also raise the question of toxicity, biocompatible systems such as poly(lactide-*co*-glycolide) (PLGA) (a very benign material) are considered to be well-suited. PLGA NPs have been extensively studied in the pharmaceutical field, relying on PLGA's biodegradability and the fact that it is FDA approved for some products [26,27]. Many different methods have been established to prepare PLGA NPs, such as double emulsion and nanoprecipitation [28,29]. Among many other techniques, nanoprecipitation was adopted very quickly to prepare sub-micrometer particles, because it is a simple and straightforward technique, without the involvement of any chemical additives, and also does not require harsh formulation parameters, such as high energy input or mechanical shear stress (e.g., by sonification) [30,31]. Nonetheless, the preparation of sub-micrometer NPs in a conventional “bench-top” nanoprecipitation method still faces several critical challenges, such as the lack of reproducibility, which restricts it from being widely adopted in the pharmaceutical industry [32,33]. This issue is mainly attributed to the poor control of the mixing time in many approaches. This problem holds true especially for the preparation of NPs of size less than 200 nm, which are preferred with respect to their biological penetration potential. Improved control with respect to the mixing time can be achieved by utilizing impinging jets or microfluidic systems, as they allow to control the mixing time on the order of milliseconds instead of minutes [34,35]. The mixing time was proven to be the major factor that influences the size and monodispersity of colloidal particles [36]. The mixing time can be tuned by adjusting the flow rate of the solvents or channel geometry. Additionally, fast mixing (as in microfluidics) has shown a variety of advantages over conventional methods (bench-top) regarding the physicochemical and encapsulation properties of the nanoparticles [36]. A LabSmith system (LabSmith, Inc., Livermore, USA) was used for the manufacture of PLGA NPs using the nanoprecipitation method. This system offers stable conditions to produce monodisperse particles of small size. At the same time, it offers the possibility to vary some additional factors during preparation, such as channel diameter and channel length [37]. For the successful permeation of the particles through mucus, small particles are required. To ensure proper treatment, it is necessary to reach the target dose; therefore, a high drug loading into the NP carrier is necessary to compensate for their small size in order to reach the target dose. In this study, the encapsulation of a lipophilic model drug (curcumin, a nonsteroidal naturally anti-inflammatory drug) was assessed by comparing different preparation approaches, such as bench-top preparations with different injection procedures. The choice of an anti-inflammatory drug for potential loading into PLGA NPs was made to address strong and continuous inflammatory responses which could have an impact in, for example, cystic fibrosis treatment [38]. The potential for application in cystic fibrosis treatment was highlighted monitoring the penetration of the particles through human pulmonary mucus.

Results and Discussion

Influence of different parameters on the NP size

Smaller nanoparticles (NPs) are known to have a better diffusion through mucus, whereby they can evade the natural size-filtration mechanism [10,14,39]. Furthermore, the surface chemistry of NPs plays a crucial role in facilitating their penetration through mucus [9]. In this context, we have used microfluidics to produce size-tunable PLGA NPs coated with a muco-penetrating stabilizer (Pluronic F68). Relevant factors influencing the NP size were examined, such as flow rate ratio, PLGA concentration, solvent type, diameter of the mixing channel, and stabilizer concentration. Furthermore, as our system allows us to cut different lengths of mixing channels, the impact of the length of the mixing channel on the nucleation–growth mechanism of the nanoprecipitation process was evaluated, which is an underestimated aspect of current microfluidic research.

Effect of flow rate ratio and total flow speed

The flow rate ratio was calculated as

$$\text{Flow rate ratio} = \frac{\text{flow rate of organic phase}}{\text{flow rate of aqueous phase}} \quad (1)$$

We varied the flow rate ratio (FRR) of the organic phase to the aqueous phase from 0.05–1 and the flow speed of the aqueous phase was set to a fixed value ranging from 10 to 100 µL/min while adapting the organic phase volume accordingly. At a flow rate ratio of 0.05, a substantial reduction of the NP size from ≈150 to 70 nm was obtained (Figure 1).

The reduction in the NP size is attributed to the rapid and efficient mixing process as described in literature [36]. Further, the Ostwald ripening phenomena could be avoided at short mixing times [40]. Additionally, for FRRs above 0.2 (by adjusting only the flow rate of the organic phase) larger NPs were obtained. This implies that an increase in the width of the focus point of the organic phase occurred as a result of the higher FRR as illustrated in Figure 2 [41]. For this reason, a longer time was required for the diffusive material to be mixed. Another scenario was proposed by Wang et al. [42], who suggested that the increase in NP size at higher FRR is related to the use of larger amounts of solvent causing swelling of the NPs. Afterwards, the influence of increasing the flow speed was studied when using higher flow speeds of the aqueous phase (but adjusting the same FRR) on the size of the NPs. The aqueous phase flow was set to 10, 50 or 100 µL/min while keeping the flow of the organic phase constant at 10 µL/min. It was observed that an increase in the flow speed of the aqueous phase from 10–100 µL/min led to a reduction in the mean diameter of the NPs from 150 to 70 nm at a flow ratio of 0.05 (Figure 1). This evidence points to the fact that most likely the polymer concentration decreases by increasing the aqueous phase flow rate, thus small NPs were obtained. Another reason could be that the rate of the NP growth decreased as well [43,44]. Markedly, the tendency of NP aggregation decreased at a higher flow of the aqueous phase due to the large volume of the

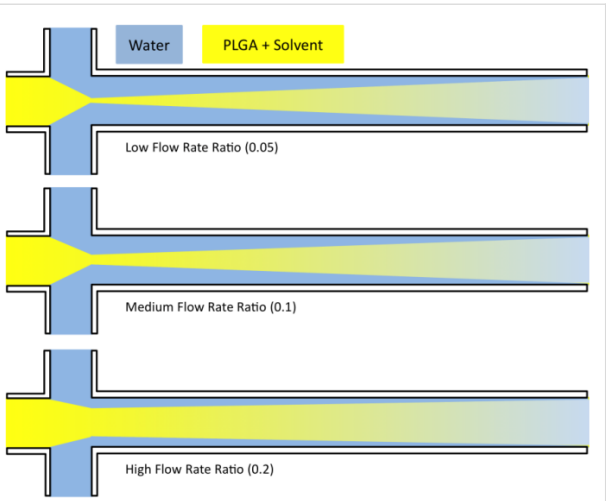

Figure 2: Illustration the impact of increasing the flow rate ratio on the mixing pattern and the geometry of the flowing solvents. The increasing mixing time at higher ratios could lead to larger particle sizes.

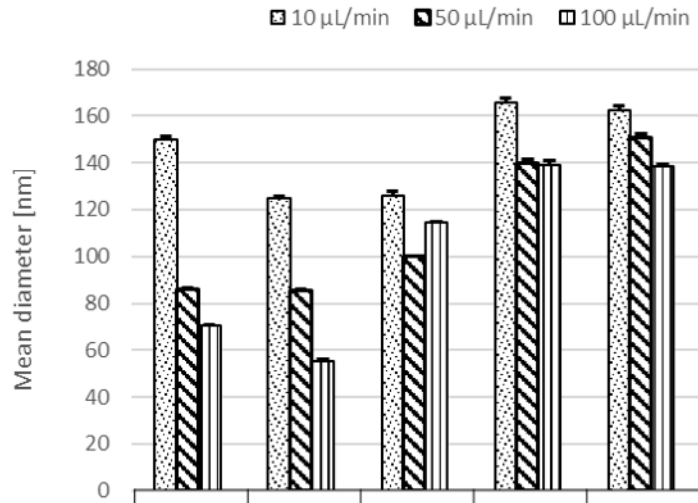

PDI	0.05	0.1	0.2	0.4	0.6	0.8	1
10 µL/min	0.100 ±0.025	0.098 ±0.04	0.107 ±0.016	0.054 ±0.014	0.024 ±0.018	0.031 ±0.009	0.064 ±0.022
50 µL/min	0.143 ±0.004	0.12 ±0.007	0.048 ±0.010	0.040 ±0.032	0.033 ±0.023	0.081 ±0.010	0.082 ±0.003
100 µL/min	0.142 ±0.022	0.197 ±0.006	0.089 ±0.009	0.05 ±0.017	0.077 ±0.004	0.083 ±0.018	0.085 ±0.013

Figure 1: The effect of the flow rate ratio (0.05–1.0) and flow speed of the aqueous phase (10–100 µL/min) on NP size and size distribution.

aqueous phase, which prevents particle interaction (this was indicated by PDI (polydispersity index, respreswenting the size distribution) values always being <0.1 for all particles prepared by microfluidics). Moreover, the particles are easier to redisperse and are more stable within the aqueous suspension.

Effect of polymer concentration

The nanoprecipitation mechanism is predicted to be primarily ruled by the Marangoni effect where the concentration gradient and the concentration of the polymer play a role in influencing the colloidal properties [45]. For this purpose, the influence of the polymer concentration (PLGA) on the NP mean diameter was tested. It can be observed that by varying the polymer concentration (PLGA) from 1 mg/mL up to 10 mg/mL the particle size increased from 65 nm up to 150 nm for a FRR of 0.05. The same behavior was found for all other flow rate ratios investigated (Figure 3).

This effect is most likely related to the increasing viscosity of the organic phase, which led to impeded diffusivity of the organic phase into the aqueous phase, and thus to a longer mixing time. Also, it appears that a large number of nuclei are formed and the high concentration of polymer per unit volume promotes particle growth, therefore larger particles were obtained [43]. Using a PLGA concentration of >10 mg/mL resulted in clogging of the mixing channel due to agglomeration. For concentrations less than 1 mg/mL, we were not able to produce monodisperse PLGA NPs; several peaks ranging from 20 nm up to 100 nm were observed in DLS (data not shown). This was supported by a large PDI (>0.7), indicating a polydisperse sample [44]. Furthermore, the presence of very small particles could originate from micelle formation from the stabilizer present, as previously discussed in literature [42].

Effect of the diameter of the focus channel

Besides the flow rate, flow rate ratio and polymer concentration, the channel geometry is an important factor impacting on the NP size. This holds true especially for the width of the focus channel in which NP formation takes place. Literature has demonstrated that the key factor to control the NP properties is the mixing time (τ^{mix}), which is directly connected to the channel dimensions. The mixing time depends on the geometry as described by [36]:

$$\tau^{mix} \sim \frac{w_f^2}{4D} = \frac{w^2}{9D\left(1+\frac{1}{FRR}\right)^2} \quad (2)$$

where D is the diffusivity of the used solvent, w_f is the width of the focus channel, w is the width of the other channels, and FRR is the flow rate ratio of the organic phase to the aqueous

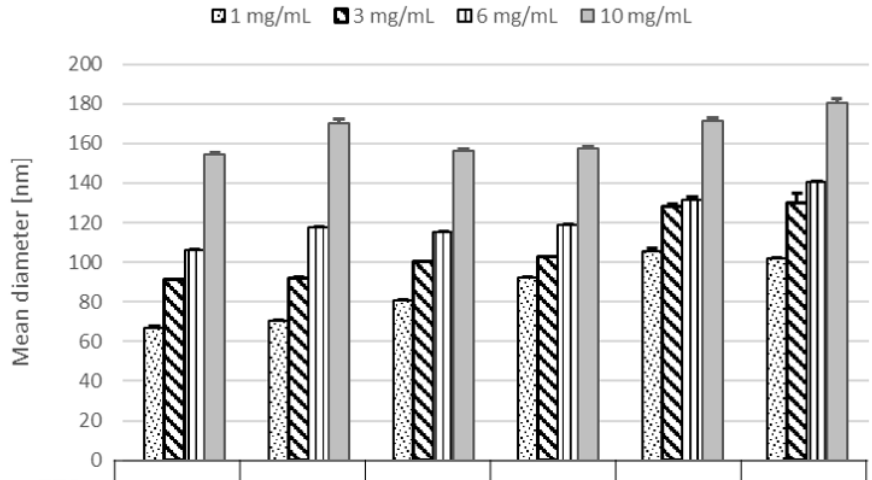

PDI	0.05	0.1	0.2	0.4	0.5	0.6
1 mg/mL	0.231 ±0.004	0.070 ±0.011	0.078 ±0.011	0.054 ±0.020	0.091 ±0.008	0.075 ±0.015
3 mg/mL	0.095 ±0.007	0.154 ±0.007	0.106 ±0.013	0.094 ±0.010	0.069 ±0.012	0.063 ±0.013
6 mg/mL	0.098 ±0.010	0.100 ±0.006	0.138 ±0.008	0.140 ±0.013	0.128 ±0.014	0.122 ±0.006
10 mg/mL	0.102 ±0.015	0.146 ±0.004	0.141 ±0.022	0.106 ±0.019	0.033 ±0.032	0.069 ±0.025

Figure 3: Effect of different PLGA concentrations (1–10 mg/mL) on NP size and PDI at different flow rate ratios.

phase. According to this equation, modulating the width of the focus channel w_f will modulate the flow rate of the organic phase to the aqueous phase. As the focus channels in our microfluidic system can be varied from 20 µm up to 300 µm, we could elucidate the influence of the channel width on the nanoparticle properties. In Figure 4 it can be seen that the NP size was reduced from 120 to 70 nm as a result of modulating the width of the mixing channel from 280 to 100 µm at a 0.05 flow rate ratio due to shortened mixing times. This effect can be clearly seen for the slowest FRR. For larger FRR values, the effect between channel sizes of 180 and 280 µm is no longer evident as the effect of mixing time on particle size has less influence (this behavior is similar to that of a batch reactor [46]). Due to the reduction of the channel diameter, the mixing time was minimized to a FRR of 0.05 (0.27 ms) in contrast to τ^{mix} = 2.19 ms at a FRR of 0.6. Additionally, a focus channel of 50 µm was tested, but this, unfortunately, resulted in a multimodal size distribution of NPs, which is most likely due to the non-stable flow pattern (turbulent flow instead of laminar flow).

Effect of stabilizer concentration

Additionally, to aid the successfully permeation of the NPs through mucus without being trapped, the PLGA NPs can be coated with a muco-inert stabilizer. Using the appropriate stabilizing molecules could reduce the interaction with mucus, and at the same time, foster stability of the colloidal system, thus minimizing NP agglomeration and nucleation growth [40]. Pluronic F68 was proven to be a muco-inert material [11,47] and was therefore chosen as a stabilizer. The addition of Pluronic F68 (1%) resulted in a slight decrease of the NP diameter to ≈70 nm at 0.05 flow rate ratio in comparison to the stabilizer-free (water) NPs with a 90 nm particle diameter (Figure 5).

These observations are consistent with previously presented results with respect to the presence or absence of stabilizers [48]. The slight effect on the size might be due to an increased viscosity of the aqueous phase and thus a prolonged mixing time. Also, the small particle size at low concentrations of Pluronic F68 might be due to the dominating effect of the surface tension over the change in viscosity [49].

The viscosity of low concentrated Pluronic F68 solutions might not be strong enough to play a crucial role in influencing the NP size, although it might aid in stabilizing the surface and to avoid nuclei growth. These results were in accordance with results from the conventional methods indicating a more stable system using stabilizers (data not shown). Overall the size differences are very small and the stability of the colloidal system is im-

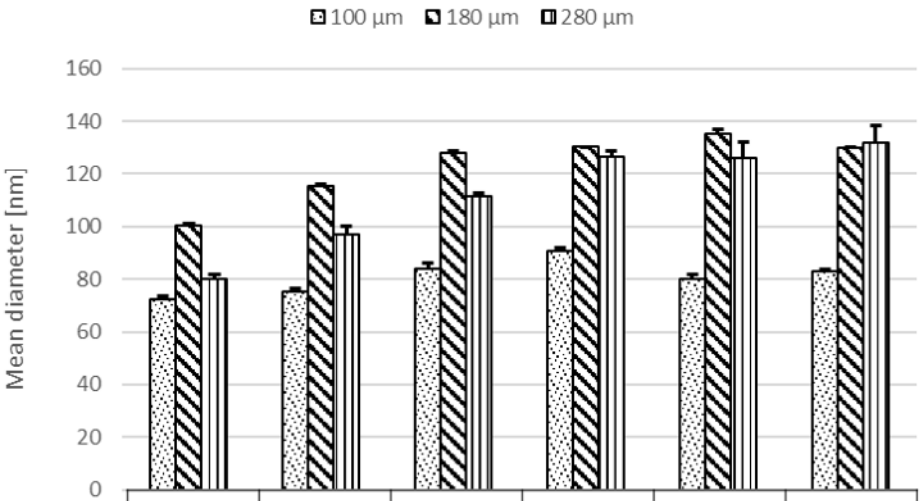

PDI	0.05	0.1	0.2	0.4	0.5	0.6
100 µm	0.142 ±0.025	0.098 ±0.006	0.116 ±0.010	0.163 ±0.014	0.182 ±0.015	0.179 ±0.010
180 µm	0.063 ±0.012	0.062 ±0.022	0.069 ±0.016	0.073 ±0.004	0.109 ±0.011	0.104 ±0.012
280 µm	0.134 ±0.038	0.084 ±0.018	0.043 ±0.005	0.057 ±0.011	0.057 ±0.017	0.036 ±0.033

Figure 4: Effect of adjusting the diameter of the focusing channel (100 µm, 180 µm and 280 µm) on NP size and size distribution at different flow rate ratios.

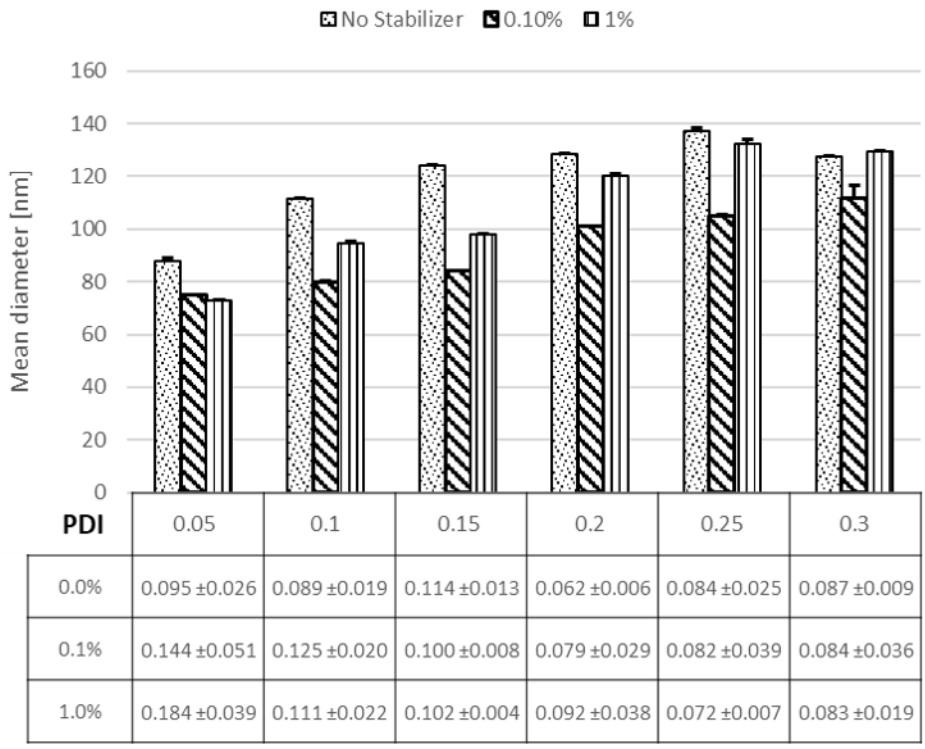

PDI	0.05	0.1	0.15	0.2	0.25	0.3
0.0%	0.095 ±0.026	0.089 ±0.019	0.114 ±0.013	0.062 ±0.006	0.084 ±0.025	0.087 ±0.009
0.1%	0.144 ±0.051	0.125 ±0.020	0.100 ±0.008	0.079 ±0.029	0.082 ±0.039	0.084 ±0.036
1.0%	0.184 ±0.039	0.111 ±0.022	0.102 ±0.004	0.092 ±0.038	0.072 ±0.007	0.083 ±0.019

Figure 5: Effect of stabilizer concentration (0.1% and 1% of F68) on NP size and size distribution compared to NPs without stabilizer.

proved with higher stabilizer concentrations. Therefore, 1% Pluronic F68 might be the most suitable system.

Effect of solvent nature and solvent mixture

Drug solubility relies fundamentally on the solvent used. Therefore, assessing the influence of the nature of the solvent on the colloidal properties of our drug carrier would be meaningful. Different solvents were used to elaborate their impact on NP size namely, dimethyl sulfoxide (DMSO), acetonitrile and acetone. We observe no correlation between the viscosity of the used solvent and the final NP size but the Hildebrand solubility parameter (Table 1) correlates with the formation of small NPs [50].

When DMSO was used as solvent, the NP size was reduced from 120 to 40 nm at a 0.05 flow rate ratio in comparison to acetone and acetonitrile (ACN), as can be seen in Figure 6. This data illustrates that the nature of the organic phase plays a decisive role in controlling the diffusion of the organic phase to the aqueous phase, which induces as well a change in the mixing time [50,51].

Effect of the length of the focus mixing channel

Attempts have been made to explain the mechanisms of nanoprecipitation in order to have better control over the kinetics of the colloid formation. To the best of our knowledge, no comprehensive study has presented relevant experimental evidence enabling more insight into the nanoprecipitation mechanism. Our microfluidic system has a unique feature allowing us to select different mixing channel lengths. The impact of the length of the mixing channel was investigated, using 1 cm, 3 cm and 5 cm long mixing channels. Figure 7 shows that the length of the mixing channel has no impact on particle size in our

Table 1: Properties and miscibility of organic solvents with water according to the Hildebrand solubility parameter.

	M_w [g/mol]	Density [g/cm^3]	Molar volume [cm^3/mol]	Heat of evaporation [J/mol]	Hildebrand solubility parameter [MPa$^{1/2}$]
acetonitrile	41.05	0.786	52.23	33225	24.28
DMSO	78.13	1.1	71.03	52900	26.65
water	18.01	1	18.01	44000	48.03
acetone	58.08	0.784	74.08	31300	19.74

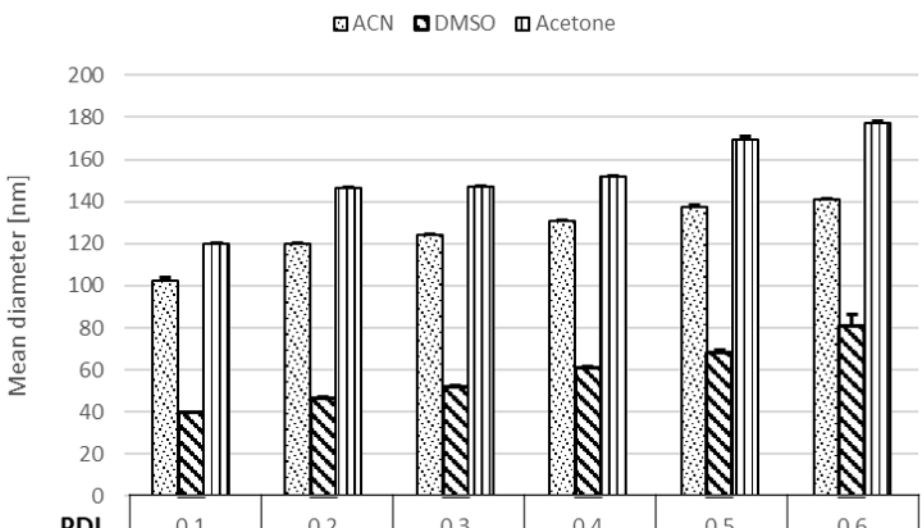

PDI	0.1	0.2	0.3	0.4	0.5	0.6
ACN	0.130 ±0.070	0.097 ±0.036	0.084 ±0.009	0.089 ±0.011	0.089 ±0.012	0.074 ±0.023
DMSO	0.217 ±0.069	0.186 ±0.039	0.192 ±0.026	0.186 ±0.020	0.193 ±0.028	0.185 ±0.063
Acetone	0.133 ±0.039	0.166 ±0.032	0.065 ±0.045	0.221 ±0.154	0.154 ±0.092	0.083 ±0.046

Figure 6: Effect of solvent nature (acetonitrile (ACN), dimethyl sulfoxide (DMSO) and acetone) on NP size and PDI at different flow rate ratios.

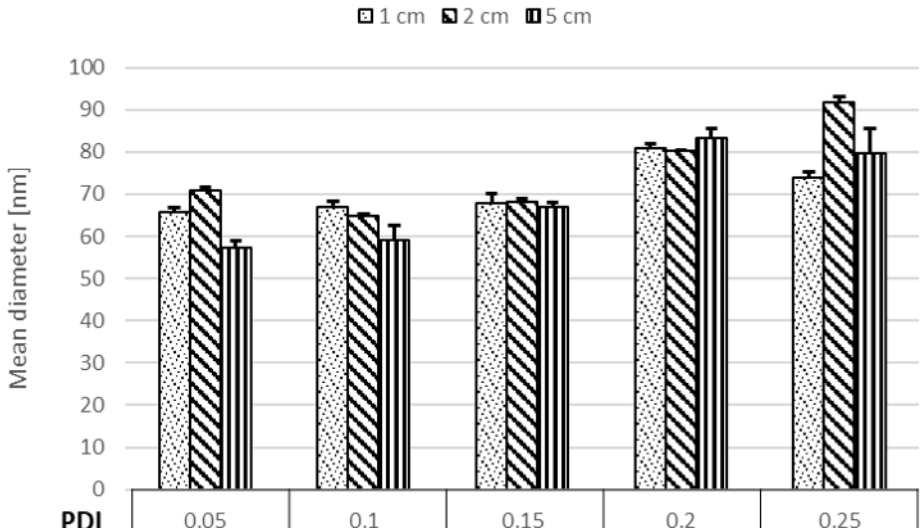

PDI	0.05	0.1	0.15	0.2	0.25
1 cm	0.079 ±0.005	0.150 ±0.008	0.162 ±0.010	0.131 ±0.029	0.134 ±0.009
2 cm	0.163 ±0.008	0.120 ±0.017	0.157 ±0.005	0.167 ±0.009	0.148 ±0.011
5 cm	0.158 ±0.002	0.125 ±0.016	0.140 ±0.007	0.142 ±0.004	0.133 ±0.012

Figure 7: Effect of using different mixing channel lengths (1 cm, 2 cm and 5 cm) on the NP size and size distribution.

setup, suggesting that possible effects occur at shorter distances after the mixing point.

It can be seen at the 0.05 flow rate ratio that for all channel lengths the NP diameter was between 50–60 nm. Also for the other flow rate ratios, no influence of the channel length could be observed (Figure 7); only for the highest flow rate ratio, a difference between the different channel lengths could be observed. According to literature, nanoprecipitation is more linked to nucleation and growth, which consists of three stages: nucleation, growth, and aggregation, as illustrated in Figure 8 [52].

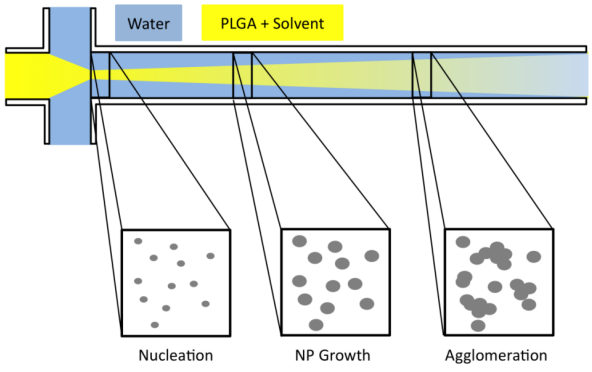

Figure 8: Illustration of nucleation and growth mechanism of nanoprecipitation along the focus mixing channel in a microfluidic system.

Based on the theoretical description of the mechanism, the particle formation is dependent on the time available for growth and agglomeration. Aggregation is assumed to happen after the initial formation and it is assumed to depend on the length of the mixing channel [36]. Therefore, adjusting the length of the mixing channel to only allow for nuclei formation should hinder NP growth, thus ensuring that only the nuclei (small NPs) would be collected.

Overall, the separation of the three stages could be meaningful to understand their respective influence on the colloidal size. We can conclude that on a length scale of >1 cm, the process is already completed.

Encapsulation of curcumin into PLGA NPs using different techniques

Finally, after evaluating the parameters which are relevant to have an influence on the colloidal properties, the incorporation of the drug into the nanocarrier was addressed. The goal was to compare the encapsulation efficiency of curcumin into PLGA NPs while using different approaches (microfluidics, injected by hand (bulk) or using a syringe pump (conventional)). As can be seen from Figure 9, loading curcumin in PLGA NPs using

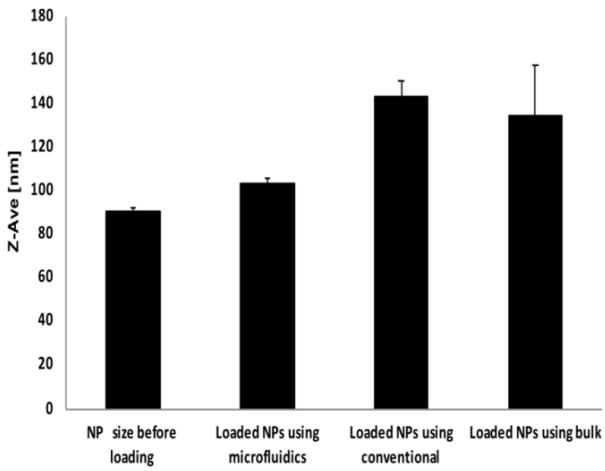

Figure 9: Comparison of the NP size after encapsulation using different approaches, namely the microfluidic system and two benchtop procedures.

microfluidics resulted in an increase in particle size from 90 nm up to 100 nm.

In contrast, by loading the PLGA NPs using injection by hand (bulk) or using a syringe pump (conventional), larger sizes were found of up to 145 nm. Thus, microfluidics is an optimal method for producing small, loaded nanoparticles with a good reproducibility and small variability in size. This is most likely due to the ability of microfluidics to mix solutions under laminar flow conditions, ensuring controlled precipitation and short mixing times. Moreover, the microfluidic approach revealed a higher encapsulation of the lipophilic curcumin into PLGA. Using microfluidics, ≈67.15% of the curcumin was encapsulated while the average encapsulation was around ≈50% for the conventional approach (syringe pump) and 30% for hand-injection (bulk) approach (Figure 10), due to the lack of

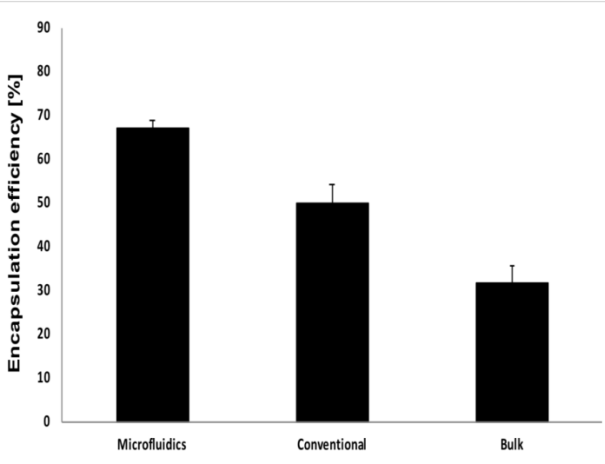

Figure 10: Encapsulation efficiency of curcumin using the different approaches.

laminar flow conditions and longer mixing time. Higher encapsulation was previously reported for other drugs [36], but for curcumin, no other reports are available to our knowledge.

Nanoparticle interaction with mucin

The stability of NPs within biological fluids is an essential factor with respect to their potential biological effects [53]. This holds especially true for the interaction of the particles with mucus. To estimate this, a mucin solution was chosen as a simple model for assessing the interaction of different types of surfactant-coated PLGA NPs with mucin [46,47]. The interaction with mucin as a major component for mucus is reflected in size changes and aggregation of the particles. PLGA NPs stabilized with Pluronic F68 or Pluronic 10500 showed no strong interaction with mucin from 0 to 180 min (Figure 11) as no change of size was determined. However, the size distribution for F68-coated particles increased from 0.035 to 0.5. For Pluronic 10500 stabilized particles, the increase was less pronounced, but still observable. In contrast, other types of Pluronic (9400, 3100 and 6400) have directly shown aggregation (from t_{start} = 0 min) as obvious from the increase in size (mean diameter up to 400 nm). A considerable shift in PDI from 0.026 to 0.5 was also noticed. The findings could be correlated with the amount of PEG in the polymers, which is more than 50% for Pluronic F68 and Pluronic 10500.

A considerable increase in size and size distribution would hamper the ability of the particles to serve as efficient drug delivery systems. Thus, all stabilizers that do not prohibit agglomeration are not suitable for our application. To investigate if the increase in PDI has a negative influence of the mucus penetration, the diffusion of Pluronic F68 stabilized particles with different sizes was analyzed.

Permeability of NPs through human pulmonary mucus

The interaction of NPs with mucin is a crude estimate for the interaction with mucus. Besides a specific surface chemistry with a tendency to avoid the interaction with mucins, NPs smaller than the pore size of mucus [54] need to be applied to

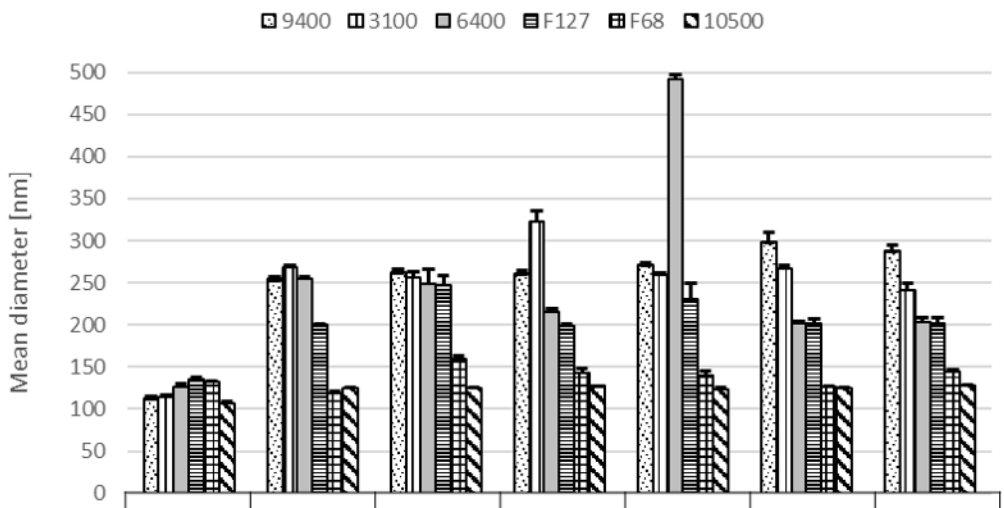

PDI	No Mucin	0	10	20	60	120	180
9400	0.074 ±0.007	0.514 ±0.005	0.521 ±0.037	0.526 ±0.037	0.547 ±0.015	0.471 ±0.089	0.498 ±0.030
3100	0.127 ±0.039	0.463 ±0.031	0.484 ±0.005	0.529 ±0.023	0.477 ±0.008	0.501 ±0.011	0.489 ±0.030
6400	0.032 ±0.023	0.495 ±0.005	0.581 ±0.023	0.510 ±0.027	0.555 ±0.016	0.512 ±0.007	0.507 ±0.007
F127	0.045 ±0.003	0.451 ±0.004	0.498 ±0.018	0.453 ±0.014	0.482 ±0.012	0.453 ±0.018	0.436 ±0.022
F68	0.034 ±0.020	0.433 ±0.017	0.522 ±0.116	0.536 ±0.120	0.468 ±0.070	0.437 ±0.021	0.413 ±0.018
10500	0.064 ±0.006	0.232 ±0.008	0.226 ±0.005	0.233 ±0.007	0.230 ±0.004	0.221 ±0.006	0.238 ±0.012

Figure 11: Size and size distribution of nanoparticles stabilized with different types of Pluronic before and after their distribution and interaction with mucin.

avoid the size-filtering mechanism [5,10]. A confocal laser scanning microscopy (CLSM)-based set up was used to study the penetration of NPs through pulmonary human mucus [39]. Different sized PLGA NPs (60 nm, 120 nm and 400 nm) were synthesized using microfluidics (fluorescently labelled). NPs in aqueous suspension were added on top of a thin layer of human pulmonary mucus. Then, the penetration kinetics was analyzed by scanning a defined volume at a fixed distance from the objective at different time points.

As illustrated in Figure 12, stabilizer-coated 60 nm PLGA NPs permeated through the human mucus directly when applied.

Penetration was observed up to 1 h after application. In contrast to the 60 nm particles, the 120 nm NPs reached the detection volume only after 30 min, whereas 400 nm particles were hardly observed in the respective volume, indicating no or at least a very slow penetration compared to the two other particle sizes. As all particles were stabilized with Pluronic F68, the stabilizer does not have an influence in this experiment. The only parameter varied was the nanoparticle size, playing a key role for the penetration behavior [10].

Conclusion

The ability of microfluidics to precisely mix reagents with short mixing times under laminar flow conditions allowed for the generation of monodisperse PLGA NPs of tunable size. Upon varying different factors during the preparation, the results showed that the most dominating influence on the NP size was governed by controlling the mixing time. Furthermore, we could show that the formation of particles is not influenced by a particle growth mechanism due to the diffusion in the mixing channel after a certain channel length (longer mixing times). In addition, the small particles produced in microfluidics were perfectly suited to diffuse through pulmonary mucus as a biological barrier without being immobilized. NPs of approximately 60 nm in diameter have demonstrated improved penetration through pulmonary human mucus in contrast to larger particles of 120 nm and 400 nm diameter. The latter could not reach the observation volume within 1 h, which was attributed to the size-filtering effect. This highly controllable preparation of small particles using microfluidics in combination with a specific muco-inert surface chemistry led to a promising drug delivery system with enhanced mucus penetration. Moreover, a high absolute curcumin encapsulation efficiency of ≈67.15% was obtained using microfluidics. Furthermore, the encapsulation was clearly improved in comparison with conventional bench-top nanoprecipitation methods.

Materials and methods

Materials

Porcine mucin, curcumin, rhodamine B (for covalent labelling of PLGA), dichlormethane, dicyclohexylcarbodiimide, 4-(dimethylamino)pyridine and acetonitrile (ACN) were purchased from Sigma-Aldrich (Steinheim, Germany) and poly(lactic-*co*-glycolic acid) (PLGA) (Resomer RG 503 H, 50:50 ratio, average M_w = 24,000–38,000 Da) was obtained from Evonik Industries (Darmstadt, Germany). Amphiphilic block copolymer Poloxamer (Pluronic F68, F127, 9400, 6200, 3100, 10500 and 6400) was a kind gift from BASF SE (Ludwigshafen, Germany). Pulmonary human mucus was collected by the endotracheal tube method after informed consent from patients (Winterberg Hospital, Saarbrücken, Germany). AlexaFluor-WGA (wheat germ agglutinin) was purchased from Invitrogen (Oregon, USA). All materials employed in the preparation of nanoparticles were of HPLC grade.

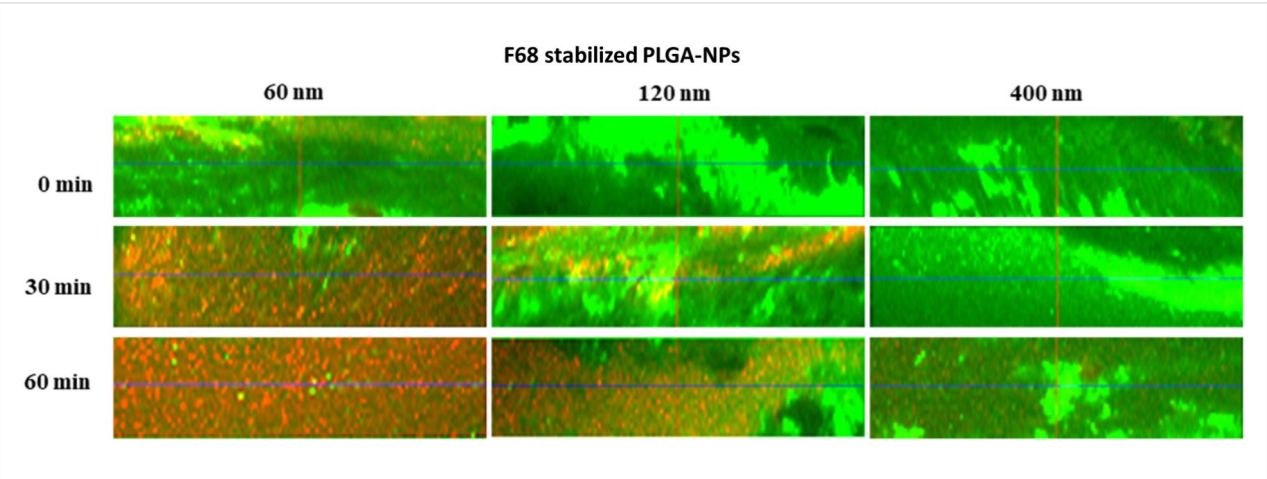

Figure 12: *xz*-micrographs taken in confocal laser scanning microscopy study of the penetration of differently sized F68-stabilized PLGA NPs. Fluorescently labelled (red fluorescence) 60, 120 and 400 nm NPs were imaged along 40 µm of pulmonary human mucus at predetermined time intervals. The mucus was stained with wheat germ agglutinin (green fluorescence).

Fluorescence labelling of PLGA

In a first step 1.1 equiv of rhodamine B was dissolved in dried dichloromethane (DCM) and activated with 1.5 equiv of dicyclohexylcarbodiimide (DCC, Scheme 1). This solution was stirred at room temperature. Subsequently, a solution with 1 equiv of PLGA and 0.1 equiv of 4-(dimethylamino)pyridine (DMAP), also in dried DCM, were added. The reaction was carried out at room temperature for 24 h. It was quenched by the addition of 1 mL of water. The organic solvent was removed with a rotational evaporator, and the remaining water was discarded. An overview of the concentration of the different components is given in Table 2. The indicated volume of solvents was used for synthesis with 600 mg PLGA and should be adjusted accordingly for other quantities.

Table 2: Overview of the concentration of the different components used for labelling.

	M [g/mol]	equiv	*n* [µmol]
PLGA RG 502 H	7000–17000	1.0	50
rhodamine B	479.01	1.1	55
DCC	206.33	1.5	75
DMAP	122.17	0.1	5

For the purification step, the polymer was dissolved in 20 mL of acetone and precipitated by adding the same volume of ethanol. The phases were separated by centrifugation at 20,000*g* for 20 min. The colored supernatant was removed and the polymer was obtained as a pink residue. The purification step was repeated for five cycles. After the last centrifugation, the polymer was dried under vacuum.

Synthesis of PLGA nanoparticles in a microfluidics system

A microfluidic system was assembled using a cross-channel microreactor design, connected via glass capillaries (180 µm ID and 300 OD, Labsmith, Livermore, USA). Monodispersed PLGA NPs coated with Pluronic F68 on the surface were synthesized as illustrated in Figure 13.

In brief, the stock solution of stabilizer containing Pluronic F68 (0.1%) was dissolved in water and injected into the side channels of the microfluidic reactor using a syringe pump (Harvard Apparatus PHD 2000 Syringe, Holliston, USA). In parallel, the organic phase containing 3 mg of PLGA in 1 mL ACN was pumped into the middle channel using another syringe pump (Multi Programmable Syringe Pump, Sarasota, USA). The flow rate ratios (FRR) of the two phases were varied from (0.05 up 1). The two liquids were brought together in the mixing channel and the PLGA started to precipitate and form NPs. The PLGA NP sample was collected from the outlet of the channel. Then the PLGA NP suspension was left overnight under stirring to

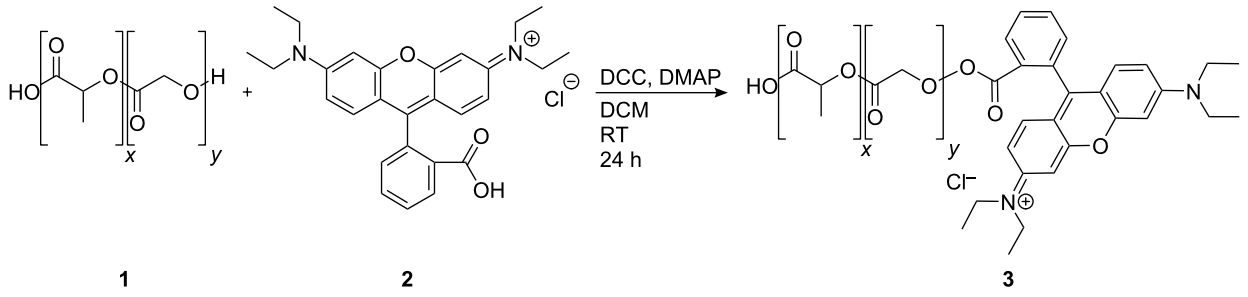

Scheme 1: Sketch of the reaction scheme for PLGA labelling with rhodamine B. The carboxy group of the fluorescence dye (**2**) is activated with DCC in water-free DCM and reacts with the terminal alcohol group of PLGA (**1**) under DMAP catalysis to the functionalized polymer (**3**).

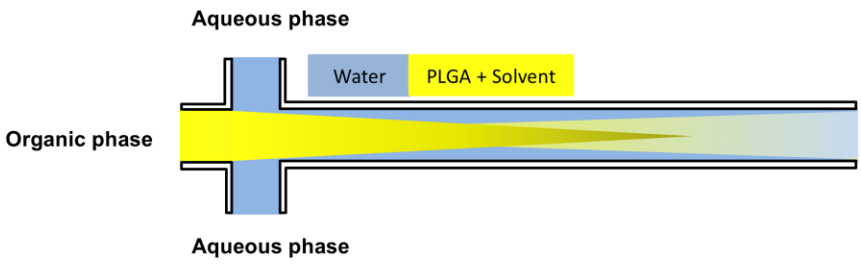

Figure 13: Design and flow pattern of the microfluidic system.

evaporate the organic solvent. Finally, the PLGA NP suspension was washed twice using centrifugation (30 min at 10,000*g* at 4 °C) and redispersed with Milli-Q water to remove excess stabilizer. The experiments were conducted under the same conditions in triplicate for all formulations.

Characterization of colloidal PLGA NPs

Measurement of size distribution

The colloidal properties of PLGA NPs such as size and size distribution (via the polydispersity index, PDI) were measured utilizing a Zetasizer Nano ZS90 (Malvern Instruments, Malvern, UK) instrument. All measurements were performed after a dilution step to adjust the particle concentration at least in triplicate under the same conditions.

In vitro assessment the interaction of NPs with mucin as a simple model

Mucin (1%) was dissolved in water containing 1% NaCl and left overnight under stirring at room temperature to form a kind of artificial mucus (AM). The sample was stored in the refrigerator (4 °C) until use. The AM was incubated with the suspension of PLGA NPs that were stabilized with different types of Pluronic (F68, F127, 9400, 6200, 3100,10500 and 6400) with different block lengths and thus different HLB values in a 1:1 volume ratio at ambient conditions for predefined time intervals. Afterwards, the nano-suspension was centrifuged at 5000*g* for 10 min to separate the NPs from mucin prior to analysis. As a reference, the PLGA NPs before incubation were measured. The properties of the NPs after incubation with AM were measured using DLS to determine whether the NP size increased as a response to strong interactions with AM or if it remain unchanged.

The permeability of size-tunable muco-penetrating PLGA NPs through pulmonary human mucus

The permeation of rhodamine B labelled, F68-stabilized PLGA NPs (preparation with 0.1% Pluronic F68) was confirmed by 3D time lapse imaging utilizing confocal laser scanning microscopy (LSM710, Zeiss, Jena, Germany). Each 40 µL of pulmonary human mucus without air bubbles was labelled with 1 µL of AlexaFluor-wheat germ agglutinin. Afterwards, the stained mucus was placed in an imaging chamber made by nail polish on a cover slip resulting in an equally thick mucus layer [55]. At time zero, PLGA NPs were added on top of the mucus and z-stacks within the mucus sample were obtained at constant distance from the bottom of the slide. The permeability of PLGA NPs through mucus was tracked by the change in the fluorescence signal. This approach allowed us to study the size-dependent permeation of PLGA NP through pulmonary human mucus. One day before the experiments, frozen native pulmonary human mucus samples were left to thaw in the refrigerator at 4 °C. Rhodamine B labelled PLGA NPs of 60, 140 and 400 nm diameter were dispersed in Milli-Q water at 0.1% w/v. 5 µL of the nano-suspension was added on top of the mucus. Then, the time-dependent vertical penetration was observed by a 40×/1.1 objective at 37 °C utilizing humidified and temperature-controlled air in an incubation chamber (Zeiss, Jena, Germany) in order to avoid drying. The labelled pulmonary mucus was detected with λ_{ex} = 488 nm at a detection wavelength between 467−554 nm. PLGA NPs were excited at λ_{ex} = 561 nm and the signal was collected between 624–707 nm. The permeability of NPs within mucus was assessed from 0 min up to 1 h after their application. All experiments were made in triplicate.

Evaluation of drug encapsulation efficiency using different NP preparation approaches

To evaluate the encapsulation efficiency of curcumin (EE-Cur) into PLGA NPs, the influence of using different techniques was investigated. The EE-Cur after adding the organic phase into the aqueous phase by hand, by using a syringe pump or by using the microfluidic system was compared. In brief, a 9:1 ratio of PLGA to curcumin with a final concentration of 3 mg/mL was dissolved in 1 mL of ACN. Then, the organic phase was precipitated in an aqueous phase containing 0.1% Pluronic F68 as stabilizer. First, to prepare a conventional nanoprecipitation, a plastic syringe was used to inject the organic phase containing (PLGA curcumin) mixture into the aqueous phase by hand (bulk). In parallel to this, the second approach was carried out using a syringe pump (Harvard Apparatus PHD 2000 Syringe, Holliston, USA) with a flow rate setting of 0.1, while in the third approach, an organic phase flow of 20 µL/min and an aqueous phase flow of 200 µL/min were used in a microfluidic setup. The resulting flow rate ratio of 0.1 was used as a standard for NP preparation. All experiments were carried out at least in triplicate.

Determination of the encapsulation efficiency of curcumin

For analyzing the EE-Cur, 3 mg of the prepared nanoparticles (PLGA NPs) was dissolved in 2 mL of acetonitrile. 200 µL of each solution was then transferred to a solvent-resistant plate reader plate. The plate was placed in a Tecan plate reader (Tecan, Männedorf, Switzerland) and analyzed using an excitation wavelength of 460 nm and an emission wavelength of 515 nm. A calibration curve for curcumin was prepared using ACN as the solvent. Using the calibration curve, the amount of curcumin inside the sample solution was determined as [Drug encapsulated]. The stock solution for NP preparation contained 0.1 mg of curcumin for each 0.9 mg of PLGA NPs in 10 mL of acetonitrile and was defined as [Drug used]. With this and the analyzed amount of curcumin in the sample solution, the encap-

sulation efficiency (EE%) can be determined using following formula:

$$\mathrm{EE\%} = \frac{[\text{Drug encapsulated}]}{[\text{Drug used}]} * 100\%. \quad (3)$$

ORCID® iDs

Aljoscha Koenneke - https://orcid.org/0000-0002-1181-7206
Andreas Manz - https://orcid.org/0000-0001-9712-711X
Marc Schneider - https://orcid.org/0000-0002-9260-7357

References

1. Zhao, L.; Seth, A.; Wibowo, N.; Zhao, C.-X.; Mitter, N.; Yu, C.; Middelberg, A. P. J. *Vaccine* **2014,** *32,* 327–337. doi:10.1016/j.vaccine.2013.11.069
2. Singh, M.; Chakrapani, A.; O'Hagan, D. *Expert Rev. Vaccines* **2007,** *6,* 797–808. doi:10.1586/14760584.6.5.797
3. Davis, M. E.; Chen, Z.; Shin, D. M. *Nat. Rev. Drug Discovery* **2008,** *7,* 771–782. doi:10.1038/nrd2614
4. Wong, H. L.; Bendayan, R.; Rauth, A. M.; Li, Y.; Wu, X. Y. *Adv. Drug Delivery Rev.* **2007,** *59,* 491–504. doi:10.1016/j.addr.2007.04.008
5. Lai, S. K.; Wang, Y.-Y.; Hanes, J. *Adv. Drug Delivery Rev.* **2009,** *61,* 158–171. doi:10.1016/j.addr.2008.11.002
6. Lu, K.-Y.; Li, R.; Hsu, C.-H.; Lin, C.-W.; Chou, S.-C.; Tsai, M.-L.; Mi, F.-L. *Carbohydr. Polym.* **2017,** *165,* 410–420. doi:10.1016/j.carbpol.2017.02.065
7. Niemeyer, C. M. *Angew. Chem., Int. Ed.* **2001,** *40,* 4128–4158. doi:10.1002/1521-3773(20011119)40:22<4128::aid-anie4128>3.0.co;2-s
8. Forrest, M. L.; Kwon, G. S. *Clinical developments in drug delivery nanotechnology;* Elsevier: Amsterdam, Netherlands, 2008; pp 861–862. doi:10.1016/j.addr.2008.02.013
9. Mura, S.; Hillaireau, H.; Nicolas, J.; Kerdine-Römer, S.; Le Droumaguet, B.; Delomènie, C.; Nicolas, V.; Pallardy, M.; Tsapis, N.; Fattal, E. *Biomacromolecules* **2011,** *12,* 4136–4143. doi:10.1021/bm201226x
10. Lai, S. K.; O'Hanlon, D. E.; Harrold, S.; Man, S. T.; Wang, Y.-Y.; Cone, R.; Hanes, J. *Proc. Natl. Acad. Sci. U. S. A.* **2007,** *104,* 1482–1487. doi:10.1073/pnas.0608611104
11. Yang, M.; Lai, S. K.; Wang, Y.-Y.; Zhong, W.; Happe, C.; Zhang, M.; Fu, J.; Hanes, J. *Angew. Chem., Int. Ed.* **2011,** *50,* 2597–2600. doi:10.1002/anie.201006849
12. Nafee, N.; Husari, A.; Maurer, C. K.; Lu, C.; de Rossi, C.; Steinbach, A.; Hartmann, R. W.; Lehr, C.-M.; Schneider, M. *J. Controlled Release* **2014,** *192,* 131–140. doi:10.1016/j.jconrel.2014.06.055
13. Craparo, E. F.; Porsio, B.; Sardo, C.; Giammona, G.; Cavallaro, G. *Biomacromolecules* **2016,** *17,* 767–777. doi:10.1021/acs.biomac.5b01480
14. Forier, K.; Messiaen, A.-S.; Raemdonck, K.; Deschout, H.; Rejman, J.; De Baets, F.; Nelis, H.; De Smedt, S. C.; Demeester, J.; Coenye, T.; Braeckmans, K. *Nanomedicine (London, U. K.)* **2013,** *8,* 935–949. doi:10.2217/nnm.12.129
15. Leal, J.; Smyth, H. D. C.; Ghosh, D. *Int. J. Pharm.* **2017,** *532,* 555–572. doi:10.1016/j.ijpharm.2017.09.018
16. Santos, R. S.; Figueiredo, C.; Azevedo, N. F.; Braeckmans, K.; De Smedt, S. C. *Adv. Drug Delivery Rev.* **2018,** *136–137,* 28–48. doi:10.1016/j.addr.2017.12.010
17. Tang, B. C.; Dawson, M.; Lai, S. K.; Wang, Y.-Y.; Suk, J. S.; Yang, M.; Zeitlin, P.; Boyle, M. P.; Fu, J.; Hanes, J. *Proc. Natl. Acad. Sci. U. S. A.* **2009,** *106,* 19268–19273. doi:10.1073/pnas.0905998106
18. Murgia, X.; Pawelzyk, P.; Schaefer, U. F.; Wagner, C.; Willenbacher, N.; Lehr, C.-M. *Biomacromolecules* **2016,** *17,* 1536–1542. doi:10.1021/acs.biomac.6b00164
19. Lieleg, O.; Ribbeck, K. *Trends Cell Biol.* **2011,** *21,* 543–551. doi:10.1016/j.tcb.2011.06.002
20. Witten, J.; Samad, T.; Ribbeck, K. *Curr. Opin. Biotechnol.* **2018,** *52,* 124–133. doi:10.1016/j.copbio.2018.03.010
21. Osman, G.; Rodriguez, J.; Chan, S. Y.; Chisholm, J.; Duncan, G.; Kim, N.; Tatler, A. L.; Shakesheff, K. M.; Hanes, J.; Suk, J. S.; Dixon, J. E. *J. Controlled Release* **2018,** *285,* 35–45. doi:10.1016/j.jconrel.2018.07.001
22. Griesser, J.; Hetényi, G.; Federer, C.; Steinbring, C.; Ellemunter, H.; Niedermayr, K.; Bernkop-Schnürch, A. *Int. J. Pharm.* **2019,** *557,* 124–134. doi:10.1016/j.ijpharm.2018.12.048
23. Murgia, X.; Loretz, B.; Hartwig, O.; Hittinger, M.; Lehr, C.-M. *Adv. Drug Delivery Rev.* **2018,** *124,* 82–97. doi:10.1016/j.addr.2017.10.009
24. Netsomboon, K.; Bernkop-Schnürch, A. *Eur. J. Pharm. Biopharm.* **2016,** *98,* 76–89. doi:10.1016/j.ejpb.2015.11.003
25. Tureli, N.; Tureli, A. E.; Schneider, M. *Drug Delivery Lett.* **2014,** *4,* 193–207. doi:10.2174/2210303104666140222002101
26. Anderson, J. M.; Shive, M. S. *Adv. Drug Delivery Rev.* **1997,** *28,* 5–24. doi:10.1016/s0169-409x(97)00048-3
27. Parveen, S.; Misra, R.; Sahoo, S. K. *Nanomedicine (N. Y., NY, U. S.)* **2012,** *8,* 147–166. doi:10.1016/j.nano.2011.05.016
28. Zambaux, M.; Bonneaux, F.; Gref, R.; Maincent, P.; Dellacherie, E.; Alonso, M.; Labrude, P.; Vigneron, C. *J. Controlled Release* **1998,** *50,* 31–40. doi:10.1016/s0168-3659(97)00106-5
29. Cherian, A. K.; Rana, A. C.; Jain, S. K. *Drug Dev. Ind. Pharm.* **2000,** *26,* 459–463. doi:10.1081/ddc-100101255
30. Barichello, J. M.; Morishita, M.; Takayama, K.; Nagai, T. *Drug Dev. Ind. Pharm.* **1999,** *25,* 471–476. doi:10.1081/ddc-100102197
31. Govender, T.; Stolnik, S.; Garnett, M. C.; Illum, L.; Davis, S. S. *J. Controlled Release* **1999,** *57,* 171–185. doi:10.1016/s0168-3659(98)00116-3
32. Whitesides, G. M. *Nature* **2006,** *442,* 368–373. doi:10.1038/nature05058
33. Schiller, S.; Hanefeld, A.; Schneider, M.; Lehr, C.-M. *Pharm. Res.* **2015,** *32,* 2995–3006. doi:10.1007/s11095-015-1681-7
34. Günday Türeli, N.; Türeli, A. E.; Schneider, M. *Int. J. Pharm.* **2016,** *515,* 343–351. doi:10.1016/j.ijpharm.2016.10.025
35. Ding, S.; Anton, N.; Vandamme, T. F.; Serra, C. A. *Expert Opin. Drug Delivery* **2016,** *13,* 1447–1460. doi:10.1080/17425247.2016.1193151
36. Karnik, R.; Gu, F.; Basto, P.; Cannizzaro, C.; Dean, L.; Kyei-Manu, W.; Langer, R.; Farokhzad, O. C. *Nano Lett.* **2008,** *8,* 2906–2912. doi:10.1021/nl801736q
37. Valencia, P. M.; Farokhzad, O. C.; Karnik, R.; Langer, R. *Nat. Nanotechnol.* **2012,** *7,* 623–629. doi:10.1038/nnano.2012.168
38. Jurenka, J. S. *Altern. Med. Rev.* **2009,** *14,* 141–153.
39. Nafee, N.; Forier, K.; Braeckmans, K.; Schneider, M. *Eur. J. Pharm. Biopharm.* **2018,** *124,* 125–137. doi:10.1016/j.ejpb.2017.12.017

40. Rabinow, B. E. *Nat. Rev. Drug Discovery* **2004,** *3,* 785–796. doi:10.1038/nrd1494
41. Liu, K.; Zhu, Z.; Wang, X.; Gonçalves, D.; Zhang, B.; Hierlemann, A.; Hunziker, P. *Nanoscale* **2015,** *7,* 16983–16993. doi:10.1039/c5nr03543k
42. Wang, R. K.; Chen, W.-C.; Campos, D. K.; Ziegler, K. J. *J. Am. Chem. Soc.* **2008,** *130,* 16330–16337. doi:10.1021/ja806586v
43. D'Addio, S. M.; Prud'homme, R. K. *Adv. Drug Delivery Rev.* **2011,** *63,* 417–426. doi:10.1016/j.addr.2011.04.005
44. Capretto, L.; Cheng, W.; Carugo, D.; Katsamenis, O. L.; Hill, M.; Zhang, X. *Nanotechnology* **2012,** *23,* 375602. doi:10.1088/0957-4484/23/37/375602
45. Fessi, H.; Puisieux, F.; Devissaguet, J. P.; Ammoury, N.; Benita, S. *Int. J. Pharm.* **1989,** *55,* R1–R4. doi:10.1016/0378-5173(89)90281-0
46. Watanabe, S.; Ohsaki, S.; Fukuta, A.; Hanafusa, T.; Takada, K.; Tanaka, H.; Maki, T.; Mae, K.; Miyahara, M. T. *Adv. Powder Technol.* **2017,** *28,* 3104–3110. doi:10.1016/j.apt.2017.09.005
47. Ensign, L. M.; Lai, S. K.; Wang, Y.-Y.; Yang, M.; Mert, O.; Hanes, J.; Cone, R. *Biomacromolecules* **2014,** *15,* 4403–4409. doi:10.1021/bm501419z
48. Nikoubashman, A.; Lee, V. E.; Sosa, C.; Prud'homme, R. K.; Priestley, R. D.; Panagiotopoulos, A. Z. *ACS Nano* **2016,** *10,* 1425–1433. doi:10.1021/acsnano.5b06890
49. Liu, D.; Cito, S.; Zhang, Y.; Wang, C.-F.; Sikanen, T. M.; Santos, H. A. *Adv. Mater. (Weinheim, Ger.)* **2015,** *27,* 2298–2304. doi:10.1002/adma.201405408
50. de Oliveira, A. M.; Jäger, E.; Jäger, A.; Stepánek, P.; Giacomelli, F. C. *Colloids Surf., A* **2013,** *436,* 1092–1102. doi:10.1016/j.colsurfa.2013.08.056
51. Khan, S. A.; Schneider, M. *Macromol. Biosci.* **2014,** *14,* 1627–1638. doi:10.1002/mabi.201400214
52. Markwalter, C. E.; Pagels, R. F.; Wilson, B. K.; Ristroph, K. D.; Prud'homme, R. K. *J. Visualized Exp.* **2019,** No. 143, No. e58757. doi:10.3791/58757
53. Nafee, N.; Schneider, M.; Schaefer, U. F.; Lehr, C.-M. *Int. J. Pharm.* **2009,** *381,* 130–139. doi:10.1016/j.ijpharm.2009.04.049
54. Gross, A.; Torge, A.; Schaefer, U. F.; Schneider, M.; Lehr, C.-M.; Wagner, C. *J. Mech. Behav. Biomed. Mater.* **2017,** *71,* 216–222. doi:10.1016/j.jmbbm.2017.03.009
55. Schneider, M.; Barozzi, S.; Testa, I.; Faretta, M.; Diaspro, A. *Biophys. J.* **2005,** *89,* 1346–1352. doi:10.1529/biophysj.104.054502

License and Terms

BEILSTEIN JOURNAL OF NANOTECHNOLOGY

Design of a nanostructured mucoadhesive system containing curcumin for buccal application: from physicochemical to biological aspects

Sabrina Barbosa de Souza Ferreira[1], Gustavo Braga[2], Évelin Lemos Oliveira[2], Jéssica Bassi da Silva[1], Hélen Cássia Rosseto[1], Lidiane Vizioli de Castro Hoshino[3], Mauro Luciano Baesso[3], Wilker Caetano[2], Craig Murdoch[4], Helen Elizabeth Colley[4] and Marcos Luciano Bruschi[*1]

Full Research Paper

Open Access

Address:
[1]Laboratory of Research and Development of Drug Delivery Systems, Postgraduate Program in Pharmaceutical Sciences, Department of Pharmacy, State University of Maringa, Maringa, Brazil, [2]Department of Chemistry, State University of Maringa, Maringa, Brazil, [3]Department of Physics, State University of Maringa, Maringa, Brazil and [4]The School of Clinical Dentistry, The University of Sheffield, Sheffield, UK

Email:
Marcos Luciano Bruschi[*] - mlbruschi@uem.br

* Corresponding author

Keywords:
curcumin; mucoadhesion; oral squamous cell carcinoma; permeation; poloxamer 407

Beilstein J. Nanotechnol. **2019,** *10,* 2304–2328.
doi:10.3762/bjnano.10.222

Received: 30 April 2019
Accepted: 23 October 2019
Published: 25 November 2019

This article is part of the thematic issue "Frontiers in pharmaceutical nanotechnology".

Guest Editor: M. G. Wacker

Abstract

Mucoadhesive nanostructured systems comprising poloxamer 407 and Carbopol 974P® have already demonstrated good mucoadhesion, as well as improved mechanical and rheological properties. Curcumin displays excellent biological activity, mainly in oral squamous cancer; however, its physicochemical characteristics hinder its application. Therefore, the aim of this study was to develop nanostructured formulations containing curcumin for oral cancer therapy. The photophysical interactions between curcumin and the formulations were elucidated by incorporation kinetics and location studies. They revealed that the drug was quickly incorporated and located in the hydrophobic portion of nanometer-sized polymeric micelles. Moreover, the systems displayed plastic behavior with rheopexy characteristics at 37 °C, viscoelastic properties and a gelation temperature of 36 °C, which ensures increased retention after application in the oral cavity. The mucoadhesion results confirmed the previous findings with the nanostructured systems showing a residence time of 20 min in porcine oral mucosa under flow system conditions. Curcumin was released after 8 h and could permeate through the porcine oral mucosa. Cytotoxicity testing revealed that the formulations were selective to cancer cells over healthy cells. Therefore, these systems could improve the physicochemical characteristics of curcumin by providing improved release and permeation, while selectivity targeting cancer cells.

Introduction

The development of nanostructured systems containing poloxamer 407 (P407) and Carbopol 974P® (C974P) have previously been shown to have rheological and mechanical characteristics beneficial for pharmaceutical and biomedical use [1]. P407 is a non-ionic block copolymer with polypropylene oxide (PPO) and polyethylene oxide (PEO) segments, which can display thermoresponsive properties forming nanometer-sized micelles, hydrogels and lyotropic liquid crystals [2,3]. The increase of temperature can promote the self-assembly from unimers to micelles, with large endothermic heat. In this sense, PPO-groups dehydrate in a hydrophobic core with a surrounding hydrated shell. Higher concentrations of P407 are used (15% to 20%, w/w) as colloidal gelling systems in a cubic hexagonal core with ordered structure, which enable the solubilization of hydrophilic and hydrophobic drugs [4-9]. Moreover, C974P is an acrylic-acid derivative, highly cross-linked, hydrophilic, and displays mucoadhesive properties [1]. In this sense, an increase in temperature promotes the nanometer-sized assembly into three-dimensional micelles with a hydrophobic core of PPO and a hydrophilic shell of PEO that can interact by hydrogen bonds with the hydrophilic acrylic-acid derivative polymer. This results in a binary polymeric system with good viscoelasticity, mucoadhesion, softness and flow properties [1,10,11]. Therefore, different combinations and the characterization of their different functionalities have been reported in the literature [1-3]. These nanostructured systems with mucoadhesive and thermoresponsive properties could provide new properties, including biocompatibility, improved mechanical characteristics tailored for the specific application, in addition to new release mechanisms and improved permeability [9,12-14].

The delivery through the mucosa via buccal administration has shown several advantages as a drug delivery target site. The ease of accessibility for administration and removal, more permeable than skin and containing a rich blood flow and avoidance of first-pass effects, makes this route useful for systemic or local applications [15]. However, the dynamic physiological properties of the oral cavity, such as the variable salivary flow due to different types of stimulation, during mastication, speech and swallowing, could hinder the development of drug delivery systems for this route [15,16]. In order to avoid these drawbacks, nanostructured systems with mucoadhesive polymers, such as acrylic-acid derivatives, have been investigated due to some important characteristics. They can provide intimate contact between the dosage form and tissue, which could guarantee high drug flux through the absorbing tissue to subsequently increase drug permeation and bioavailability [14,15]. In addition, the incorporation of thermoresponsive materials, like P407, could facilitate the administration and preparation of these formulations [10,17].

Head and neck cancer is the sixth most common malignancy worldwide and the prognosis is poor, with a five-year survival of less than 54% and accounting for around 300,000 deaths and more than 550,000 new cases each year worldwide [18,19]. Oral squamous cell carcinoma (OSCC), the primary cause of this cancer type, has been associated with many risk factors, mainly related to excessive intake of alcoholic beverages, tobacco use, high exposure to UV radiation, immunosuppression and age. These risk factors are involved in the transformation of healthy oral mucosal cells (called keratinocytes) to premalignant dysplastic lesions, which can develop to OSCC. Although these lesions can develop in different regions of the oral cavity, including the lip, buccal mucosa, and hard and soft palate, they are most commonly found on the tongue and floor of the mouth [18,20-24]. Despite the advances in conventional methods (chemotherapy, radiotherapy and surgery), the prognosis of OSCC has not improved. In addition, many adverse effects and complications have been reported with current treatment strategies including, facial disfigurement, loss of speech, mastication and swallowing and even in the mildest cases oral mucositis and candidiasis, which drastically reduce the life quality of the patient [21,25]. Early diagnosis by a dentist or physician ensures early treatment to avoid metastatic spread [26-28].

Curcuminoids, derived from curcuma root (*Curcuma longa*), have been used for many centuries in Asian countries as a spice and coloring agent, but also as a medicine [29]. This group of yellow polyphenols are composed of curcumin (CUR), demetoxycurcumin and bis-demetoxycurcumin, which represent 77%, 17% and 3% of the content of the dried extract from curcuma root, respectively [30,31]. CUR has shown anti-inflammatory, antirheumatic and antioxidant activities and it has been used in hepatic and other chronic diseases including diabetes [32]. Recently, the activity of CUR as an anticancer drug has been evidenced and shown to act on a variety of molecular targets that regulate the proliferation and apoptosis, decrease the expression of NF-κB and increase insulin-like growth factor-binding protein 5 (IGFBP-5) and cytochrome P450, family 1, member A1 (CYP1A1) [32-34]. Moreover, CUR can be useful as adjuvant in cancer treatment, after surgical procedure, or in combination with chemotherapy [35-41]. Despite its broad therapeutic potential, CUR has limited stability to light and pH, as well as poor solubility. CUR is also susceptible to degradation due to the formation of phenylate anions and high production of CUR radicals, since this polyphenol has demonstrated high lipophilicity (log P 3.29) and low solubility in aqueous solutions and under alkaline conditions (pH > 7) [30,31,42]. These physicochemical characteristics hinder the bioavailability and therapeutic efficacy of this drug. Consequently, there is a need

to associate CUR with carriers to ensure the delivery to the target site and thereby protect the drug from degradation, increase the solubility and provide controlled release as well as permeation, while maintaining biological activity [31,43-45].

To our knowledge, systems containing P407 and C974P have not been investigated to carry CUR and therefore the aim of this study was to develop nanostructured systems containing P407, C974P and CUR to target OSCC. Once developed, we investigated the behavior of the drug in the formulations for their chemical, rheological, mechanical and mucoadhesive characteristics. We also measured the in vitro drug release profile, permeation and the cytotoxic potential of these systems.

Results and Discussion

Interaction studies of curcumin in mucoadhesive nanostructured systems

As CUR is highly hydrophobic, unstable and susceptible to degradation by light and pH [31], the interaction of CUR formulations was studied by photophysical methods. The aim was to understand the interaction between this hydrophobic drug with the hydrophobic core of the three-dimensional structure of P407-micelles.

Investigation of CUR interaction with the system

In order to improve the understanding of these interactions between CUR and the formulations, stability assays using photophysical studies were performed to provide information about the interactions of CUR with the polymer blends under different conditions, including the cool storage temperature in refrigerator (10 °C), administration temperature of the formulation to the patient (25 °C), body temperature (37 °C) and over body temperature (45 °C) at pH 7, but also at pH 5 and 10 at 37 °C [46]. The formulations composed of P407, C974P and CUR showed pH 5 during the preparation and before the pH adjustment step, due to the acidic properties of the mucoadhesive polymers [47]. Furthermore, the stability by photophysical studies of polymer blends containing 0.01% (w/w) P407, 1.6×10^{-4}% (w/w) C974P and 1.8×10^{-5} mol/L CUR were spectroscopically evaluated using an emission slit of 5–10 nm. The spectra are displayed in Figure 1. The systems showed a higher emission intensity and larger widths at pH 7, due to the thermal energy employed for CUR encapsulation during the rotary evaporation.

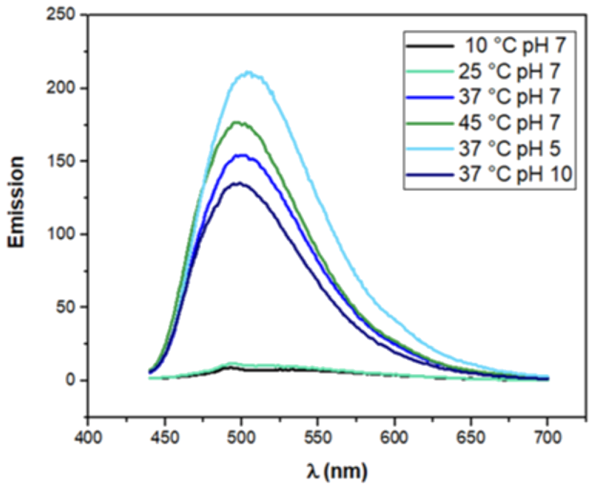

Figure 1: Emission spectra of systems containing 0.01% (w/w) P407, 1.6×10^{-4}% (w/w) C974P and 1.8×10^{-5} mol/L CUR at 10 °C, 25 °C, 37 °C, 45 °C in pH 7, 37 °C in pH 5 and pH 10, obtained with an emission slit of 5–10 nm.

Moreover, the emission intensity of the formulations was lower at pH 10 in comparison to pH 7 at 37 °C. These results could be explained by new chemical species from pKa that do not appear in the emission spectra due to the excitation wavelength of 422 nm (CUR maximum absorption).

Anisotropy of fluorescence (r) was also investigated for the samples with maximum peak spectral emission (Table 1).

Anisotropy is considered a powerful technique to investigate the molecular dynamics of fluorescent solutes, such as CUR. During the fluorescence analysis, the molecules are excited by linearly polarized light, and they absorb and emit the fluorescence in a polarized way. If the emission is highly polarized (approximately or equal to one), the molecules will not rotate between absorption and emission, which would suggest that they are associated with macromolecules. Therefore, the emission of polarization is described as anisotropy [48,49]. Furthermore, this measurement can be used to characterize specific or nonspecific linking as it is dependent on the fraction of fluorescent solute interacting with macromolecules or on the rigidity of the formed complex [48]. Anisotropy values close to zero are related to depolarized emission and intense molecule rotation [49].

Table 1: Anisotropy (r) of formulation containing poloxamer 407 (P407), Carbopol 974P(C974P) and curcumin (CUR) under different conditions of pH and temperature.

Formulation	r			
	37 °C (pH 5)	37 °C (pH 7)	45 °C (pH 7)	37 °C (pH 10)
P407/C974P/ CUR	0.2104	0.2517	0.2881	0.2863

Furthermore, the temperature changes were more remarkable than the variation in pH, with the systems investigated at 45 °C displaying higher anisotropy values in comparison to those evaluated at 37 °C.

Incorporation kinetics

Incorporation kinetics were evaluated by observing the fluorescence emission properties of CUR in order to evaluate if the spectra obtained from the thermal analysis were influenced by the end time of the sample preparation. The time required for CUR incorporation into the polymeric micelles was also determined. Moreover, this analysis allows for the understanding of diffusion and interaction of CUR at a micellar interface. The analyses were carried out in a fluorescence spectrometer with emission and excitation slits of 5–10 nm at 25 °C, once the polymeric micelles were formed, to ensure higher specificity of the results [4]. This evaluation simulates the incorporation of CUR into polymeric systems by the second method of preparation, since the binary polymeric system was prepared and then CUR was incorporated, without pH adjustment at pH 5. On the other hand, by the first method of preparation, the incorporation of CUR was performed during the evaporation of ethanol in the rotary evaporator. Therefore, the incorporation kinetic profile was carried out at 25 and 37 °C, for simulation of the temperature of CUR incorporation by the second and the first preparation method, respectively. Furthermore, the analysis at 37 °C results in the condition where P407 micelles are well-structured. The profiles and kinetic adjustments of CUR incorporation into the polymeric systems is shown in Figure 2.

In general, the effect of temperature did not change the pattern of CUR incorporation. The emission intensity displayed an initial peak with further decrease and maintained emission until the end of the analysis, which hampered the generation of a kinetic pattern for first or second order in both analyzed temperatures. These mechanisms would improve the understanding of the involved mechanisms of this interaction. Kinetic studies of CUR and P407 were carried out by Braga [50], and the initial peak was not observed. Thus, the existence of this initial peak (pattern I) is suggested to occur due to the reorganization of the nanostructured system when CUR is quickly incorporated, as well as the presence of C974P in the micelle structure and subsequent redistribution of CUR in the micellar interface in order to ensure the same concentration of the molecule in the polymeric micelles. Moreover, CUR is incorporated from a highly concentrated medium (ethanolic stock solution) to a low concentrated medium (binary polymeric systems), where a partitioning process take place in a dynamic exchange between CUR molecules incorporated in the micelle and those dissolved in the ethanol until the equilibrium is achieved with decrease in the emission intensity [51]. Two distinct stages (pattern II and III) after pattern I could be observed due to the stabilization of these micellar systems, where CUR becomes aggregated with lower emission intensity.

The temperature was found to influence the velocity of CUR incorporation. This micellar system at 25 °C showed fast incorporation in different locations, at around 1 min, due to the facilitated accessibility of CUR in the monomeric aggregates of P407 and C974P. In addition, lower intensity emission peaks could be observed for these systems at 25 °C, since at lower temperatures PPO groups are hydrated and display weak hydrophobic interactions [6]. On the other hand, the systems evaluated at 37 °C demonstrated slower incorporation, around 60 min, due

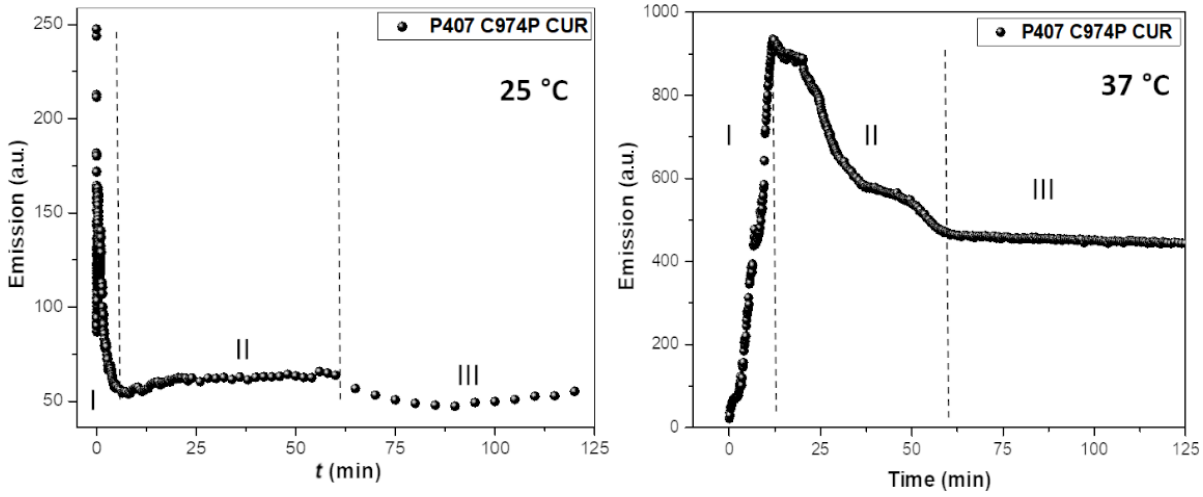

Figure 2: Incorporation kinetic profiles of systems containing poloxamer 407 (P407), Carbopol 974P (C974P) and curcumin (CUR) obtained at 25 °C and 37 °C.

to the structuring of the micelles to promote a steric hindrance as well as higher emission intensity that promotes increased hydrophobicity of PPO blocks with higher affinity with CUR.

CUR localization by fluorescence quenching

The localization of CUR in the polymeric systems was performed by fluorescence quenching, using iodide as a hydro-soluble suppressor [2,52-54]. The studies were performed at 25 °C (room and administration temperature) and 37 °C (body temperature). Using this assay, it is possible to evaluate the location of CUR in the polymeric system during drug release and to determine the location of encapsulated drugs. If the drug is located in an external location, it forms a complex with iodide, and consequently, the intensity of the spectra decreases [52]. The fluorescence quenching studies were carried out with formulations composed of 0.02% (w/w) P407, 3.2×10^{-4}% (w/w) C974P and 3.6×10^{-5} mol/L CUR prepared by solid dispersion and stored at 25 °C (Figure 3). Considering the high concentration of water, this analysis was not influenced by the viscosity of the formulations. Moreover, the system was constantly agitated with a magnetic stir bar.

In the spectra shown in Figure 3, it was evident that formulations evaluated at 37 °C showed a higher spectral intensity in comparison to studies performed at 25 °C. These results can be explained by the structure of thermoresponsive systems in response to an increase in temperature. Moreover, for the formulations evaluated at 25 °C, a decrease in emission was observed during iodide addition, which demonstrates the higher accessibility of the hydro-soluble suppressor, and consequently, higher collisions with CUR [52,54,55]. However, the spectra of the systems evaluated at 37 °C exhibited overlapping peaks, which demonstrates that CUR is not accessible to complex with the hydro-soluble suppressor. This suggests that the CUR is localized in the micelle core at 37 °C, which results in a slower release from the nanostructured system.

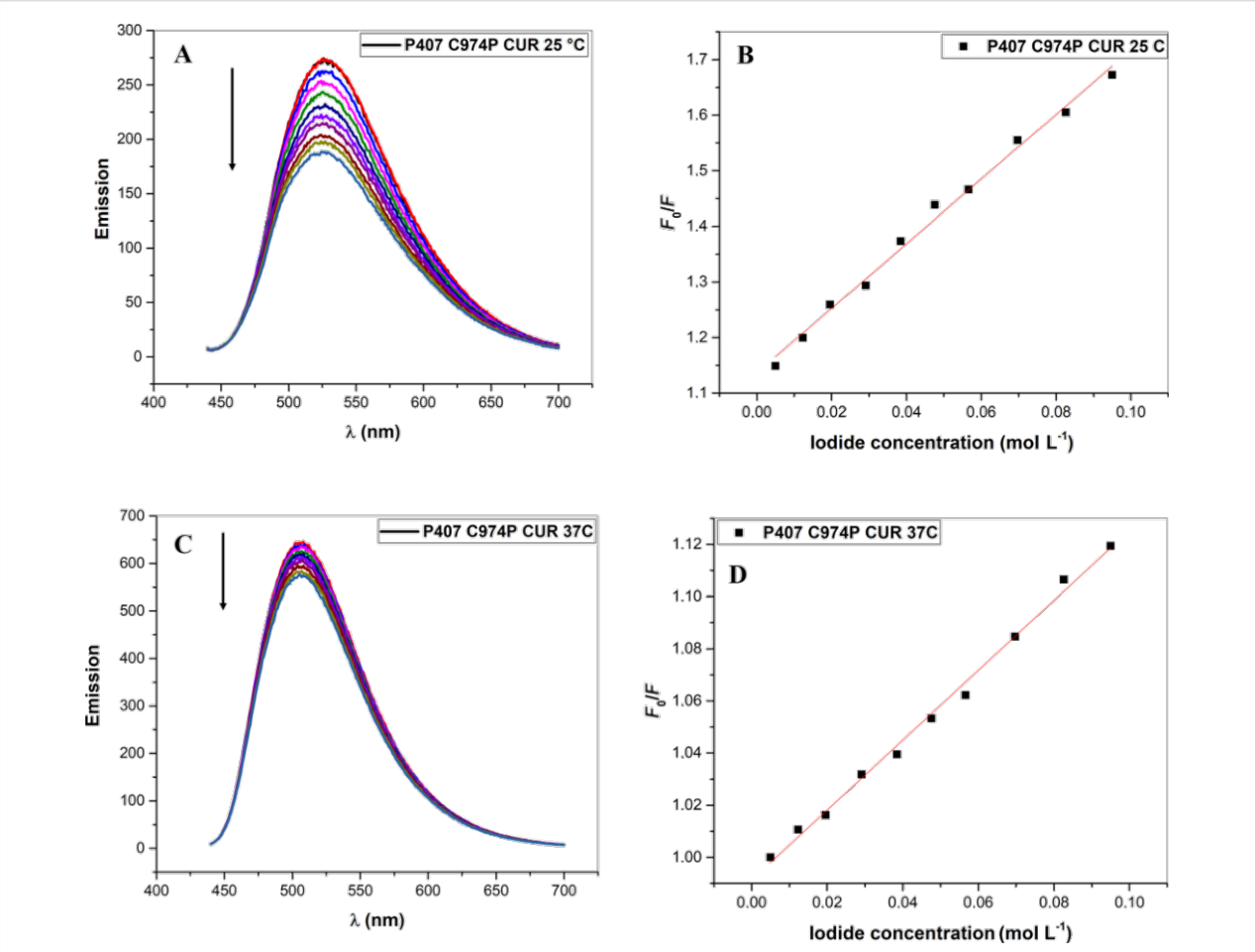

Figure 3: Fluorescence emission spectra and K_{sv} determination by Equation 3 of CUR (3.6×10^{-5} mol/L) at 25 °C (A and B) and 37 °C (C and D) for P407 (0.2%, w/w) and C974P (3.2×10^{-4}%, w/w); λ_{exc} = 422 nm with a 5–10 nm slit width. The spectral variation of CUR with I^- concentration as determined by fluorescence emission at 25 °C (B) and 37 °C (D). The arrows in (A) and (C) indicate the fluorescence suppression direction of CUR with I^- concentration.

High Stern–Volmer constant (K_{sv}) values are correlated with the CUR being externally located, with accessibility for complexation with iodide. Conversely, low K_{sv} values suggest an internal location, and consequently, no accessibility to the suppressor molecule. The system evaluated at 37 °C displayed lower K_{sv} values (K_{sv} = 1.3403 mol/L), whereas formulations evaluated at 25 °C showed higher K_{sv} values (K_{sv} = 5.8090 mol/L).

In this context, systems containing C974P displayed spectroscopic characteristics that favored further studies, as they presented lower K_{sv} values, indicating internal location of CUR in P407-micelles as well as higher anisotropy values. This result suggested that the viscosity of the microenvironment helped to obtain stronger interactions. In addition, the system stored at 25 °C also showed interesting results, in that they did not show any visible sign of CUR precipitates after 15 days of storage (Figure S1 in Supporting Information File 1), indicating that CUR was in an internal location.

Morphological analysis by scanning electron microscopy

The morphological characteristics of the preparations with and without CUR were evaluated by scanning electron microscopy (SEM) (Figure 4). Micrographs of formulations containing P407 and C974P revealed polymeric fragments with heterogeneous, but well defined, structures. This was probably due to the presence and movement of water that was removed due to the freeze-drying process. Besides, the portion of the microstructures or microchannels exhibiting exposed breakage (Figure 4B) were probably due to the interaction between P407 and C974P.

SEM micrographs of preparation containing CUR showed the presence of more irregular structures and channels without defined orientation. These data can be explained by the preparation method since the samples were frozen at −20 °C, where restructuring of the polymer can be observed. Moreover, the negative charge of C974P and CUR hindered the exploration of the structure at higher magnification due to the interaction of these components and the microscopic filaments.

Morphological analysis by transmission electron microscopy

The nanostructured organization of the polymeric systems is evidenced in Figure 5. In the absence of CUR, the micelles (Figure 5A and 5B) are represented by the white spherical shapes of approximately 20 nm in diameter. Some authors have performed transmission electron microscopy (TEM) of P407-systems and showed smaller micelles (≈10 nm) with higher homogeneity [56-58].

These differences in the micelle size could be due to the presence of C974P and interactions between PEO segments of P407 and hydroxyls of C974P.

Moreover, the TEM images of the nanostructured systems containing CUR have been obtained at 37 °C (Figure 5C and 5D).

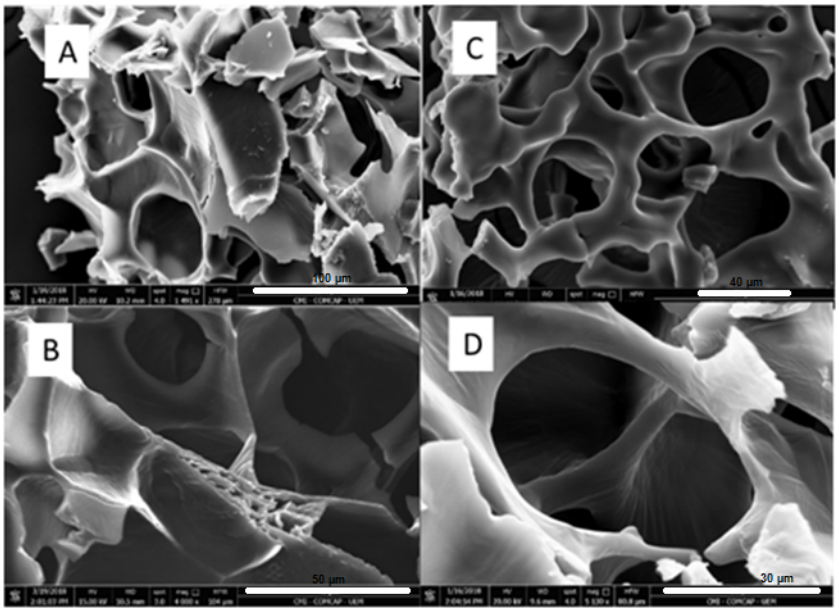

Figure 4: SEM micrographs of systems containing 15% (w/w) P407, 0.25% (w/w) C974P: without CUR original magnification ×1500 (A, scale bar = 100 µm) and ×4000 (B, scale bar = 40 µm); containing CUR original magnification ×1800 (C, scale bar = 50 µm) and ×5000 (D, scale bar = 30 µm).

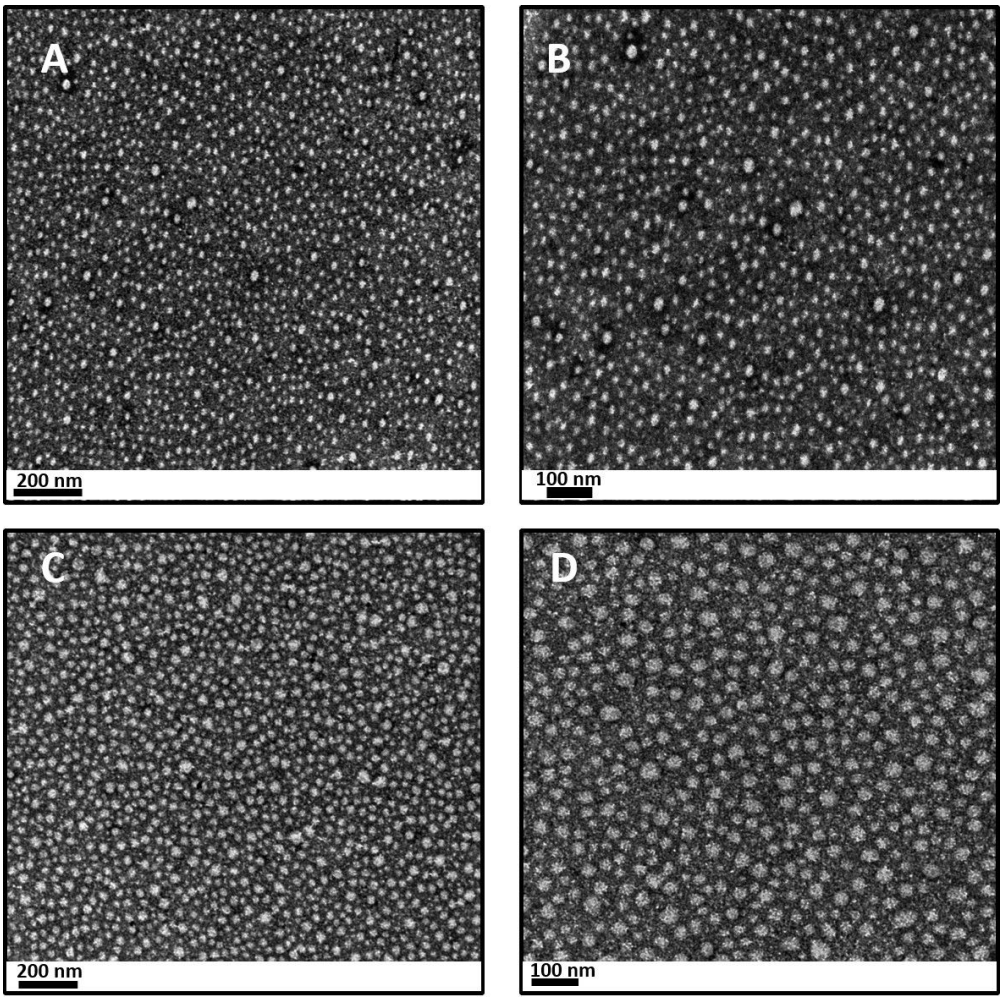

Figure 5: TEM images of nanostructured systems at 37 °C demonstrating the individual micellar organization: (A) and (B) represent the nanostructured systems in the absence of CUR, scale bar equals to 200 and 100 nm, respectively. (C) and (D) represent the nanostructured systems containing CUR, scale bar equals to 200 and 100 nm, respectively.

Considering that CUR is found in the hydrophobic PPO core, as demonstrated in the localization studies, it was observed to have better homogenization of the size and shape of the micelles in comparison to the systems without the drug. Additionally, the micelles were larger (≈40 nm), probably due to the interaction of PPO and CUR. In this sense, the presence of CUR promoted a better structuring of the system.

Micelle size analysis

The micelle size, polydispersity index (PDI) and D90% of the nanostructured systems with and without CUR were determined by dynamic light scattering (DLS) and the results are displayed in Table 2.

The polymer concentration should be low enough to circumvent multiple scattering in DLS measurements [56]. Thus, the systems were diluted in two different concentrations, 0.3% and 1.5% (w/w), in relationship to the amount of P407 in the formulations. It was observed that the system is quite dynamic. Thus, the most diluted system (0.3%, w/w) showed a significantly higher micelle size and PDI ($p < 0.05$), probably due to the presence of water, which can enable higher hydration of the polymeric chains. The presence of CUR significantly reduced the PDI ($p < 0.05$) for the system diluted at 0.3% (w/w) P407 at both temperatures, and at 37 °C for the system diluted at 1.5% (w/w) P407. Moreover, the presence of CUR did not change the PDI for the different P407 dilutions (0.3 and 1.5%, w/w) at 37 °C. The presence of CUR decreased the micelle size (D) in the 0.3% (w/w) P407 dilution at 25 °C, but significantly increased D for all other conditions of ($p < 0.05$). Thus, the increase in the P407 concentration results in nanometer-sized micelles with a lower PDI. In addition, the presence of CUR increases the micelle size and also results in a low PDI. The TEM results and particle size when diluted to 0.3% (w/w) P407 were

Table 2: Micelle size (*D*), polydispersion index (PDI) and micelle size distribution (D10%, D50% and D90%) of the nanostructured systems with and without CUR, evaluated at 25 °C and 37 °C[a].

System dilution (%, w/w)[b]	Analysis	Temperature			
		25 °C		37 °C	
		P407/C974P	P407/C974P/CUR	P407/C974P	P407/C974P/CUR
0.3	*D* (nm)	26.87 ± 5.37	12.83 ± 0.12	14.50 ± 6.32	19.23 ± 0.06
	PDI	1.04 ± 0.04	0.39 ± 0.02	0.24 ± 0.02	0.23 ± 0.01
	D10% (nm)	21.70 ± 0.00	10.77 ± 0.06	10.97 ± 0.31	15.50 ± 0.17
	D50% (nm)	21.87 ± 0.70	11.77 ± 0.06	13.23 ± 0.76	18.17 ± 0.12
	D90% (nm)	25.57 ± 3.39	15.47 ± 0.15	18.20 ± 1.21	22.30 ± 0.10
1.5	*D* (nm)	5.10 ± 0.17	15.90 ± 1.31	13.50 ± 0.35	11.33 ± 0.64
	PDI	0.29 ± 0.01	0.17 ± 0.00	0.14 ± 0.02	0.19 ± 0.01
	D10% (nm)	3.73 ± 0.15	11.53 ± 1.06	9.83 ± 0.21	8.37 ± 0.42
	D50% (nm)	4.57 ± 0.21	14.00 ± 1.28	12.13 ± 0.38	10.20 ± 0.44
	D90% (nm)	6.30 ± 0.26	20.20 ± 1.67	17.03 ± 0.47	14.50 ± 0.53

[a]Results represents the average of at least three replicate analyses. [b]In relationship to P407 amount in the formulation.

similar (but not the same) due to water removal during the sample preparation for TEM analysis [56]. Therefore, the results showed the nanometer-sized structuring of the systems.

Rheology

The flow properties of binary polymeric systems containing 15% (w/w) P407, 0.25% (w/w) C974P, 0.08% (w/w) CUR were evaluated at 25 and 37 °C (Figure 6).

The nonlinear behavior to shear stress due to the shear rate (non-Newtonian), resulting in structural changes, was maintained even after the incorporation of CUR in the polymer blends. Moreover, the addition of CUR in binary polymeric systems did not lead to a change in flow rheological profiles at 25 °C, whereas a slight decrease of shear stress was observed for systems evaluated at 37 °C. In this way, CUR did not change the structuring of the system. Conversely, the increase in temperature leads to an increase in shear stress due to the thermoresponsive properties of the preparations.

Low hysteresis areas and different yield values could be observed in a prominent way at 37 °C, in comparison to systems investigated at 25 °C. Consequently, these systems showed shear thinning behavior flow, which is considered to be a desirable characteristic for pharmaceutical semi-solid formulations in order to facilitate clinical administration in a uniform way over the mucous tissue of the buccal cavity. Subsequently, it can recover the rheological properties that these systems presented before the shear stress application [10,59,60].

The effect of the presence of CUR and the increase in temperature were statistically evaluated by the consistency index (*K*), flow behavior index (*n*) and yield value. These indexes were calculated by the rheological models, Ostwald de Waele, Casson and Herschel–Bulkley. In order to verify the rheological model that could properly fit the *K* and *n* value, *R* or X^2 were calculated and it was observed that *R* values were closer to 1, according to Herschel–Bulkley theory (Table 3).

The presence of CUR did not lead to any significant differences ($p = 0.6875$) in the consistency index (*K*) of the preparations, and the formulations kept the same resistance to deformation [11], confirming that CUR is located in the core of the polymeric micelle (as shown by the localization analysis) and therefore did not alter the interactions between P407 and C974P in order to change the viscosity. Otherwise, the increase in temperature led to the significant increase of *K* ($p = 0.000210$) due to the thermoresponsive properties of P407 [4].

The formulations with and without CUR showed shear thinning behavior due to *n* values lower than 1 (Table 2). The positive yield values demonstrated that these systems are plastic [9]. Thus, the increase in temperature significantly decreased the *n* values ($p < 0.05$), whereas the presence of CUR had no significant influence on the *n* values ($p = 0.138912$).

The yield value and hysteresis area results are shown in Table 2. The yield value demonstrates the ability of the formulations to withstand a significant shear stress without flow, and then after the weakening of the structure, the ability to start to flow [61]. Both an increase in temperature and incorporation of CUR led to significant differences ($p < 0.05$) in the yield value. The significant increase in yield value with an increase in temperature and subsequent micelle structuring can be explained by

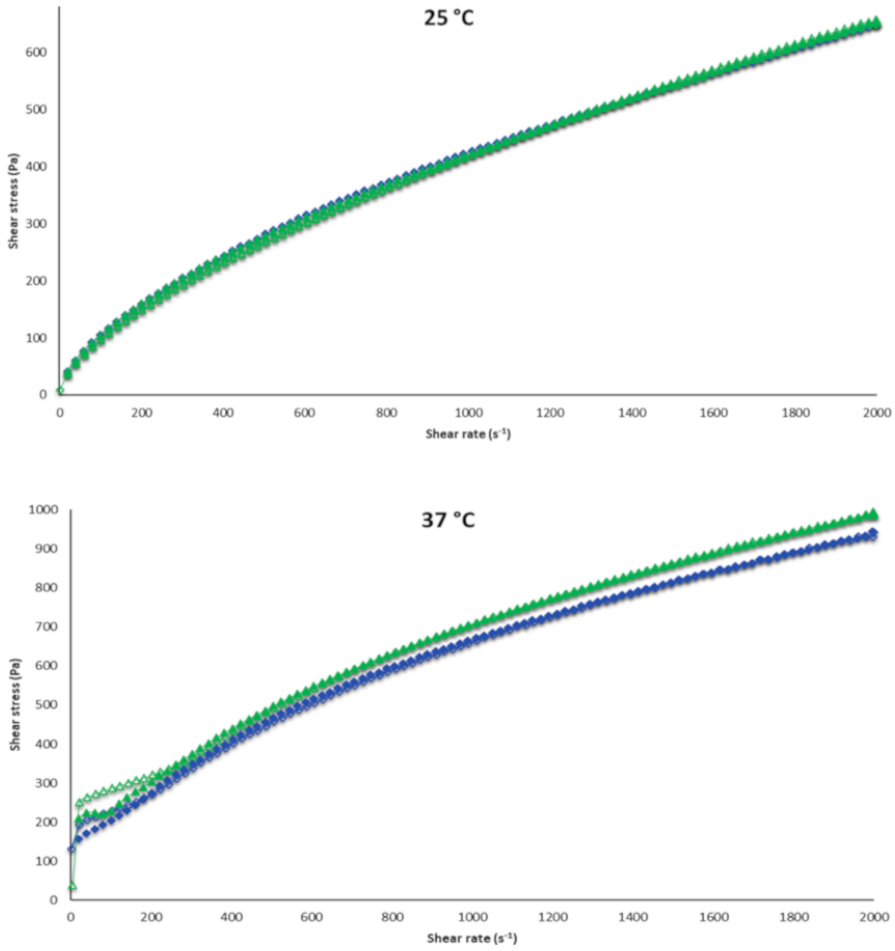

Figure 6: Flow rheograms of formulations containing 15% (w/w) P407, 0.25% (w/w) C974P (Δ - green) and 15% (w/w) P407, 0.25% (w/w) C974P and 0.08% (w/w) CUR (◊ - blue). The closed symbols represent up-curve and open symbols represent down-curve. Error bars have been omitted for clarity, and each rheogram represents the average of at least three replicates with variation coefficient 10%.

Table 3: Consistency index (*K*), flow behavior index (*n*), yield value and hysteresis area at 25 and 37 °C for systems containing P407, C974P with and without CUR.

Rheological properties	Temperature (°C)	P407/C974P/CUR (%, w/w) (15/0.25/0)	P407/C974P/CUR (%, w/w) (15/0.25/0.08)
K (Pa·s)^{n} [a]	25	5.4027 ± 0.2110	6.1910 ± 0.6374
	37	15.8867 ± 0.7379	15.4367 ± 0.8164
n (dimensionless)[a]	25	0.6311 ± 0.0058	0.6094 ± 0.0130
	37	0.5371 ± 0.0030	0.5395 ± 0.0068
Yield value (Pa)[a]	25	7.7960 ± 0.4634	2.2065 ± 0.8565
	37	48.6033 ± 3.0647	26.4000 ± 0.5200
Hysteresis area (Pa/s)[a,b]	25	7036.80 ± 2423.70	14381.16 ± 3607.37
	37	−17520.00 ± 8553.99	−26805.00 ± 2725.00

[a]Each number represents the mean of at least three replicates; [b]Positive number represents rheopexy and negative numbers represent thixotropy.

the transition from liquid to gel. However, the increase of CUR led to a significant decrease in the yield value, probably due to the higher exposure of the hydrophilic portion to water [62,63].

The hysteresis area of the formulations was investigated by RheoWin 4.10.0000 software (Haake®). The formulations displayed thixotropic behavior at 25 °C, which provides resistance to breakage in addition to higher structural flexibility,

which is due to the lower viscosity after the application of shear stress [64,65]. Conversely, the formulations exhibited a significant decrease ($p < 0.05$) in the hysteresis area at 37 °C (Tukey). Thus, both formulations (with and without CUR) demonstrated rheopetic behavior due to the higher influence of P407 in the structuring of the system at 37 °C. This behavior is considered important in order to increase the retention of preparations in the buccal cavity [59,60]. Moreover, the presence of CUR significantly decreased the hysteresis area ($p < 0.05$) at 37 °C. These systems displayed rheopexy at 37 °C, which are negative values. In this sense, the decrease in the hysteresis area means that the systems showed higher rheopexy areas. The presence of CUR resulted in an increase in the micelle size and homogeneity, as evidenced by TEM and the size analysis. Thus, an improved organization and higher resistance to the stress and shear rate applied were observed. This higher resistance to the flow explains the higher rheopexy of the systems containing CUR, mainly at 37 °C.

The effects of the presence of CUR and the change in temperature on the viscoelastic properties (G', G", η' and tan δ) of the systems was also evaluated (Figure 7).

An increase in frequency for both the elastic and viscous modulus was observed (Figure 6A and 6B). A decrease in the dynamic viscosity and loss tangent were observed with increasing frequency (Figure 6C and 6D). The exception is for the loss tangent of the CUR systems evaluated at 25 °C, which remain constant at the majority of the frequencies. Moreover, the increase in temperature led to the increase of G', G", η' and a decrease in tan δ for formulations with and without CUR. This behavior has already been previously observed for systems containing P407 and other acrylic acid derivatives [9,11], as well as polymer blends containing P407 and C974P or PCB [1,10].

Regarding the effect of the presence of CUR at 25 °C, an increase of G', G" and η' and a decrease of tan δ was observed for most frequencies. Hence, these changes provided better structuring and elasticity at 25 °C. However, polymer blends containing CUR investigated at 37 °C displayed lower G', G" and η' with an absence of significant changes for tan δ. These results could be explained by the difficult micelle structuring of P407 and jellified three-dimensional chains.

Furthermore, both preparations exhibited viscoelastic behavior, except for the polymer blends containing P407 and C974P without CUR at 25 °C. In these formulations, the G' values exceeded G" and the loss tangent was smaller than 1 for the viscoelastic preparations. Thus, the viscoelasticity is favorable to oscillatory movements performed at 25 °C, occurring during transport and storage of formulations [9].

The gelation temperature, $T_{sol–gel}$, of the formulations with and without CUR was investigated as well. The systems displayed lower G' values at low temperatures; however, high G" values were observed as the temperature was increased. Even with

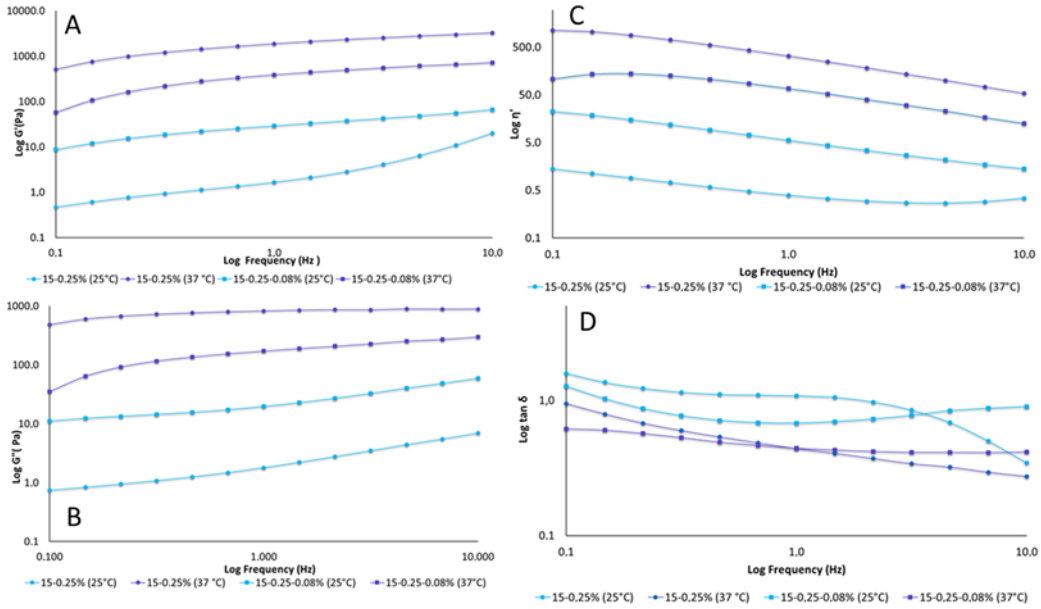

Figure 7: (A) Elastic modulus, G' (Pa), (B) viscous modulus, G" (Pa), (C) dynamic viscosity, η' (Pa), and (D) tan δ of the formulations containing P407 (15%, w/w) and C974P (0.25%, w/w) with and without CUR (0.08%, w/w) evaluated at 25 and 37 °C. Each point represents the average of at least three replicates with a variation coefficient lower than 10%.

the incorporation of CUR, the dynamic viscosity increased significantly due to the increase in temperature and gelation temperature [59,66]. The presence of CUR significantly increased ($p < 0.05$) the gelation temperature of the preparations from 36.03 ± 0.06 °C in systems without CUR (15/0.25) to 36.94 ± 0.12 °C in systems with CUR (15/0.25/0.08). Consequently, the structuring of the jellified three-dimensional chain is explained by the difficulty of the externalization of the hydrophilic portion (i.e., ethylene oxide (EO)) of micelles to interact with water and initiate the interaction between EO and C974P-hydroxil [43]. Despite the significant increase in the gelation temperature of the formulations containing CUR, the $T_{sol–gel}$ is considered suitable (between 25 and 37 °C).

Texture profile analysis

The mechanical properties of the preparations with and without CUR were evaluated by texture profile analysis (TPA). The information about the physical structure of gels obtained by TPA are useful for the development of nanostructured mucoadhesive systems related to the preparation, packaging, administration and structuring from development until the application and performance evaluation at the application site. In this way, the formulations should be resistant to the forces applied by the environment. This is also true for saliva, which can also be considered as a natural protection in the organism against impurities exposed to the mucosa and can hinder the retention of such systems and thereby impair the clinical efficacy [65-67].

Hardness, compressibility, adhesiveness, elasticity and cohesiveness results for the formulations with or without CUR at 25 and 37 °C are given in Figure 8. In addition, the effects of the presence of CUR and the increase in temperature were statistically evaluated for each parameter.

Hardness is an indicator of the ability to remove the formulation from the packaging material and its subsequent spreadability on the mucous tissue in a uniform layer to avoid any discomfort to the patient. Conversely, compressibility expresses the application of the formulation in the buccal cavity. Low compressibility and hardness values are desirable in order to

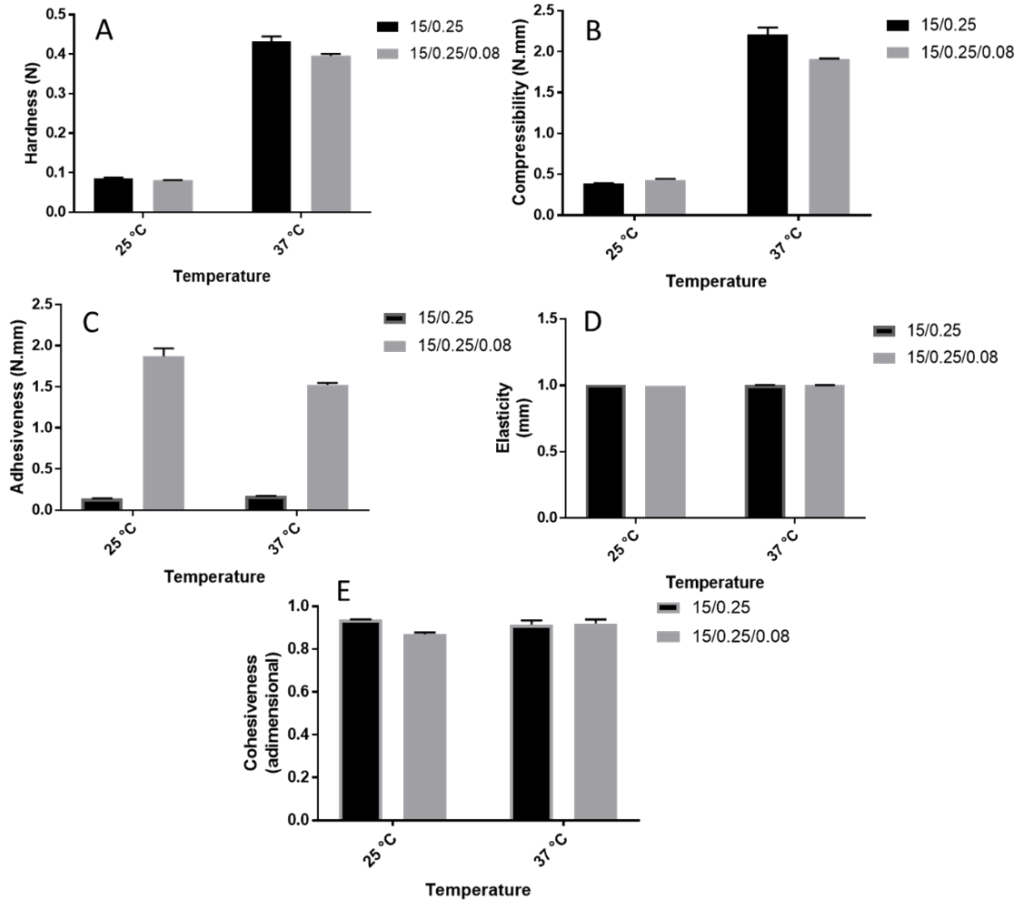

Figure 8: Textural properties of the systems containing P407, C974P and CUR, investigated at 25 and 37 °C: (A) hardness, (B) compressibility, (C) adhesiveness, (D) elasticity and (E) cohesiveness. Each value represents at least three replicates.

facilitate the removal of the preparation from the packaging material and administration in the buccal cavity and topically applied over the mucosa [66-68]. However, formulations should display enough resistance to avoid the product flowing from the packaging material and application site [10]. Adhesiveness, considered as the required work necessary to overcome the attraction forces between the sample surface and the polycarbonate probe surface, is a desirable parameter for mucoadhesive preparations aimed at buccal applications. In this sense, a higher adhesion could implicate higher retention, and consequently, higher clinical efficacy of preparations for buccal drug [67,68].

The incorporation of CUR significantly decreased ($p < 0.05$) the hardness and compressibility, which is a desirable characteristic to facilitate application of the formulation in the buccal cavity. This behavior has been observed previously for polymer blends containing P407 and other acrylic acid derivative with a similar cross-linking degree as C974P to carry hypericin [69]. In this study, the polymeric micelle relaxation due to the hydrophobic drug could explain this behavior and be related to the low yield values in the flow rheology analysis. On the other hand, CUR did not significantly ($p = 0.06597$) influence the adhesiveness values of different preparations. This phenomenon has been observed for other polymer blends containing hydrophobic drugs [7] since the mucoadhesive properties are obtained by the interaction between the hydrophilic portion of the polymeric micelles and mucosa [70].

It was also observed that an increase in temperature significantly ($p < 0.05$) increased hardness, compressibility and adhesiveness due to the thermoreversilibity of the material, which favors the structuring of the systems, as previously observed in the flow rheology with higher consistency index numbers. These higher values are desirable for a higher adhesion to the buccal cavity, leading to longer contact time. These results confirm that the system is mucoadhesive but also warrant further mucoadhesion investigations [11,59,71].

The gel ability to flow and return to the initial state is defined as elasticity [9]. In addition, cohesiveness is related to the restructuration and molecular interactions after subsequent shear stress during the application of the system [67,72]. The incorporation of CUR did not significantly influence ($p < 0.05$) the elasticity and cohesiveness, which could be explained by the influence by hydrogen bonds and water mobility in the sample. As elucidated in location studies, CUR is a hydrophobic molecule that is located in the core of polymeric micelles and thus it should not influence this parameter [9]. Regarding the temperature effect (at 25 and 37 °C), the preparations demonstrated elasticity and cohesiveness values significantly lower ($p < 0.05$) at 37 °C.

Syringeability

The work required to expel the formulation from a syringe (syringeability) at 25 °C was investigated by a texture analyzer. This test was performed in order to simulate extrusion of the formulation from the packaging material and during the administration over a lesion in the buccal cavity [59]. The effect of CUR incorporation in this system was evaluated, and despite the fact that the formulation containing CUR displayed a lower syringeability (32.6383 ± 2.1814 N·mm), it was not significantly lower ($p > 0.05$) than the syringeability of preparations without CUR (34.0390 ± 1.3390 N·mm). Thus, CUR incorporation did not influence the syringeability of the formulations and the results indicated the ability to administer the system [59].

Mucoadhesive properties

In vitro evaluation of mucoadhesive strength by detachment force

The mucoadhesive characteristics of preparations with and without CUR were evaluated by detachment force using a partially hydrated mucin disc as substrate [59,70]. According to this method, it is possible to obtain a graph with the force required to separate two surfaces with time and the maximum required force to separate the formulation from the mucin disc (mucoadhesive force). In addition, the adhesion work values were calculated.

The incorporation of CUR in mucoadhesive thermoresponsive systems led to a significant increase ($p < 0.05$) for both the mucoadhesive force from 0.2109 ± 0.0054 N without CUR to 0.2175 ± 0.0016 N with CUR and increase in the adhesion work from 0.6890 ± 0.0377 N·mm without CUR to 0.7667 ± 0.0475 N·mm with it incorporated. However, these results were not observed for adhesiveness, which could provide evidence of adhesion. This parameter evaluates the interaction between the formulation and polycarbonate probe, where this lower specificity explains this result. Conversely, the detachment force method relates the interaction of C974P-hydroxyls and the mucin chain. This is provided by the nanostructuring of polymer blends at body temperature, and hence, a P407 micelle structure with a hydrophobic nucleus and hydrophilic shell, which interacts with a mucoadhesive polymer in the external portion of polymeric micelles [10]. Moreover, these results are clinically relevant since the formulations containing CUR would display a longer residence time than the systems in the absence of this drug. Hence, the formulation should demonstrate the intimate contact with the oral mucosa, for prolonged periods, which could provide the concentration of the drug close to the cancer lesions with higher bioavailability [73].

The calculation of mucoadhesive force and adhesion work has already been discussed by other authors [70] since mucoadhe-

sive force is the most commonly used parameter to describe mucoadhesion. However, adhesion work seems to be influenced by the elasticity and plasticity of the investigated systems. It is suggested in the literature as the most suitable term for the evaluation of the detachment force since it can better detect the differences in mucoadhesive ability [74], as was observed for the formulations with and without CUR. Moreover, the work calculation (if converted to units of Joule) reflects the necessary energy to separate two surfaces. Thus, the significant increase of adhesion work correlates with higher interaction between the mucin surface and the preparations containing CUR.

Ex vivo mucoadhesive properties by falling liquid

Besides the detachment force, the determination of the mucoadhesive properties of nanostructured systems could also be explored by liquid falling experiments [30,74,75]. This method is related to the ability of systems stay adhered to surface mucosa with the falling liquid (PBS buffer) at 4 mL/min during 20 min. Higher flow resistance evidences strong adhesive interactions between preparations and mucosa. The amount of adhered gel is calculated in an indirect method. Thus the formulation eluted with buffer in a beaker containing Tween 80 and the drug in the formulation was quantified by chromatographic methods. Consequently, it was evaluated only for the CUR systems. The retention of the systems without CUR have already been evaluated by a similar method, where the formulations were marked with FITC-dextran and the retention was investigated by fluorescence microscopy [70]. The cumulative formulation percentage adhered versus time is displayed in Figure 9.

The time buffer elution effect as a function of time over the sample was statistically investigated and it was verified to significantly decrease ($p < 0.05$) the gel retention with time. Besides, the high variability observed is due to the irregularities of the mucosa surface. Thus, the formulation has already been eluted completely after 5 min. Even if the methodology used to evaluate the retention of the formulations without CUR was different [70], it is possible to compare the results, since the PBS flow rate used was the same (4 mL/min). In this sense, the tests carried out by Bassi da Silva and collaborators [70] demonstrated that the systems were eluted completely after 5 mL elution, which corresponds to 1 min 15 s. In this sense, the systems containing CUR demonstrated improved retention in comparison with the systems without CUR. This result agrees with the mechanical and rheological characteristics observed. One of the replicate images is showed in Figure 9B.

In vitro drug release profile

During the development of drug delivery systems for buccal application, in vitro drug release is highly important and is considered a prerequisite for absorption as it contributes to the rate and extension of drug bioavailability in the body [76]. Moreover, these investigations can distinguish between different systems containing the same drug, the same formulations after aging, and process changes during the preparation process [17,72].

CUR release profiles were obtained by the continuous monitoring of drug release over time. The key factors which could affect CUR release are release media volume, temperature and agitation or flow and cellulose acetate membrane [77]. Thus, in vitro drug release of CUR from the mucoadhesive nanostructured systems was carried out with controlled temperature and agitation in order to simulate conditions in the buccal cavity without regard to other physiological aspects (pH, salt concentration, enzymes and mouth movements during swallowing and

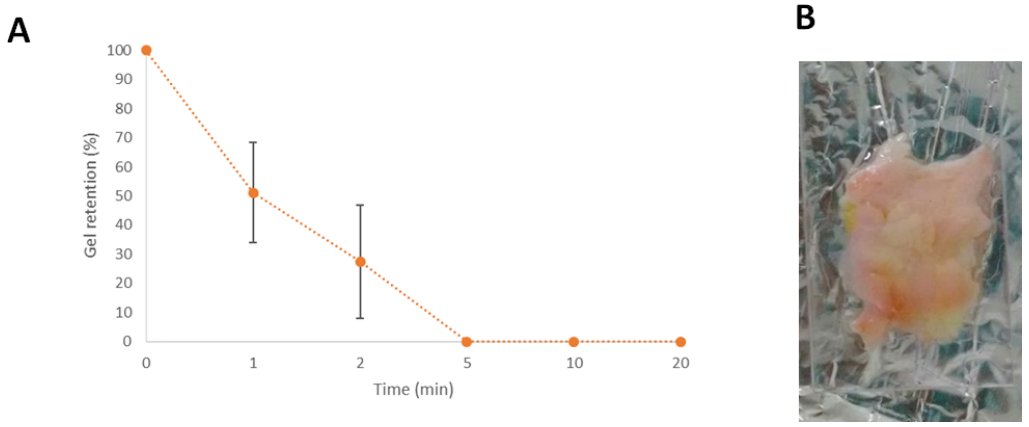

Figure 9: (A) Cumulative retention profile of a polymeric system containing poloxamer 407, Carbopol 974P® and curcumin retained in a mucous layer versus time. (B) Oral porcine mucosa after the end of the test.

speaking). These initial tests are important to verify if the drug could be released from the drug delivery system and how the applied technology influences the availability of the drug.

Another aspect to be considered for the in vitro drug release analysis is the choice of release medium. For hydrophobic drugs, sometimes it is necessary to add surfactants that can provide the sink condition. In this study, Tween 80 was used as a surfactant, as previously used in other in vitro CUR drug release investigations [30,78]. Tween 80 can interfere with the structure and rheological properties of the peripheral area of the gel. However, this situation is similar to in vivo conditions, where other substances with surfactant properties can be present in buccal environment [59,79].

The complete release of CUR (100%) occurred after approximately 8 h (Figure 10), making it suitable for buccal applications. The general equation (Equation 7) described for polymeric systems [80] was used to evaluate the release mechanism of CUR. Here, the release exponent (n), which determines if the drug release mechanism is Fickian (Case I) or non-Fickian (transport Case II, anomalous or super case II) revealed an n value of 0.6517. The nanostructured systems displayed anomalous release kinetics, hence, the polymeric chains were slowly reorganized, whereas CUR diffused by time-dependent anomalous effects. The solvent diffusion velocity displayed similar relaxation of the polymeric chains [77].

Ex vivo permeation of curcumin in porcine oral mucosa

Permeation studies are considered fundamental to determine the viability of oral mucosa as a targeting site for drug delivery [81,82]. These studies can be performed ex vivo, in vitro or in vivo and are dependent of the drug physicochemical characteristics and its behavior when incorporated in drug delivery systems and biological target tissue. The buccal cavity presents significant differences in permeability due to the composition and thickening of the mucosa [81,82].

Different animal species display varying thickness and keratinization patterns with porcine oral mucosa the most commonly employed for ex vivo testing due to the physiological similarities with human tissue, ethical considerations and low cost [81-83].

Permeation assay using a Franz cell is a quantitative technique where the amount of drug in the receptor medium is measured according to its physicochemical characteristics, for example, by chromatography or spectrophotometry. Thus, the permeation kinetic profile and the amount of retained drug in the mucosa can be measured. Considering the local application, it is advantageous for the drug to slowly permeate the mucosa without reaching blood vessels and systemic circulation [8].

The cumulative permeation percentage was calculated after each time point in porcine oral mucosa. However, even after 24 hours no drug in the receptor compartment was detected suggesting that the amount of CUR was below the detection limit for the chromatographic method used.

The retention of CUR in porcine oral mucosa was 6.99 ± 0.49% (or 47.67 ± 3.33 μg/cm^3), which demonstrates that the drug was retained in the mucosa but did not reach the blood flow. These results were influenced by the absence of the water in the donor acceptor. This condition promoted the relation with permeation by the PAS technique. These results were favorable for local application over the initial stages (Stage 0 – carcinoma in situ, Stage I – less than 2 cm tumor and Stage II – more than 2 and less than 4 cm tumor) after surgical procedure. Additionally, localized and initial tumors enable the choice of less aggressive

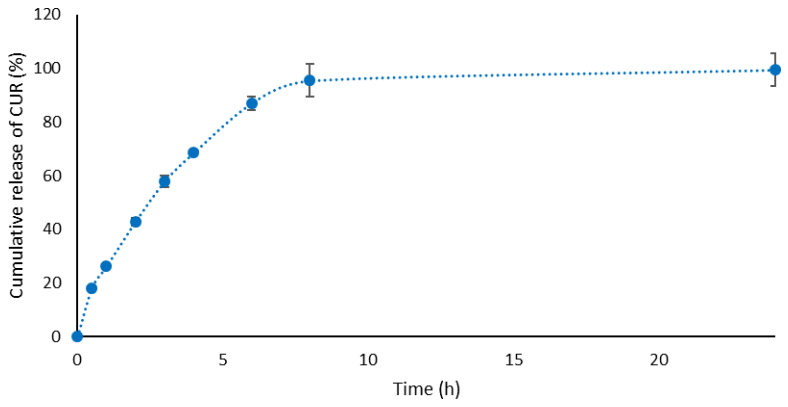

Figure 10: Release profile of CUR from a mucoadhesive nanostructured system containing 15% (w/w) P407, 0.25% (w/w) C974P and 0.08% (w/w) CUR.

treatments, such as the administration of nanostructured CUR [26,27]. According to Sannomiya and Furukawa [84], the surgical procedure is indicated for buccal squamous cells in initial stages, achieving tissue without tumor margin. For more advanced tumors, the use of chemotherapy and radiotherapy adjuvants is recommended [84].

Photoacoustic spectroscopy is useful in the investigation of permeation and distribution of substances in biological tissues in vitro, ex vivo and in vivo. This technique is based on the determination of optical spectral absorption by a photoacoustic signal created by the interaction of matter with radiation of a known wavelength [7,85]. Besides, the relatively low cost, non-destructible manner, and ability to detect low amounts of sample are interesting for investigation of opaque samples [7]. Moreover, this is a qualitative technique that determines if a drug can permeate or not and, if so, the depth of tissue that can be permeated. The permeation of CUR from polymer blends containing P407 and C974P® were performed in porcine mucosa by photoacoustic spectroscopy and the photoacoustic spectra of the formulations, tissues and permeation of CUR are shown in Figure 11.

The optical absorption spectra of CUR and formulations are presented in Figure 11A. A Gaussian adjustment was performed in order to decompose the spectra into its components. It can be observed that the drug exhibits an intense band that varies from 250 to 700 nm, with peaks around 250, 315, 427, 515 and 659 nm. The main absorption band of CUR is located at 427 nm and is due to the aromatic rings of hydroxyl groups and ether [86]. The polymer blend 15/0.25 demonstrated a large band that varies from 250 to 350 nm, with peaks at 250 to 295 nm. On the other hand, the blend 15/0.25/0.08 displays variation from 250 to 500 nm with peaks at 250, 295, 315, 359 and 427 nm. In this sense, the detection of these characteristic bands in the mucosa is indicative of the presence of the drug.

Regarding the photoacoustic spectra of porcine oral mucosa (Figure 11B), all samples displayed a band at 415 nm related to the blood vessels. Figure 9C exhibits that CUR from formulations could permeate the mucosa. Moreover, the thermal diffusion length (μ_s) was 31 µm on both sides of the oral mucosa. Thus, CUR permeated the total sample thickness (818 µm).

In this sense, the results of the PAS and Franz cell technique are complementary, since PAS can elucidate if the drug could permeate and the former is able to quantify the concentration of drug that went through the receptor vessel and was retained in the mucosa.

Drug and formulation cytotoxicity

The cytotoxicity potential of the drug and formulations with and without CUR were investigated on squamous carcinoma cells (FaDu and Cal27) and normal oral immortalized keratinocytes (FNB6). The three cell lines were exposed to a wide range of drug concentrations (0, 2.5, 5, 10, 20, 40, 80, 120 and 240 µM) for 24 h. Moreover, another range of drug concentrations (2000, 1500, 1000, 500, 300, 100, 20, 10 µM) was utilized for the formulations. After this period, cell viability was indirectly determined by MTT metabolic assay (Figure 12).

The viability of Cal27 was significantly decreased ($p < 0.05$) by the presence of the formulations, regardless of the presence of CUR. This cytotoxic effect was not observed in the FaDu and FNB6 cells. The cytotoxic effect of the formulations could be explained by the presence of P407, a known surfactant. The incorporation of CUR into nanostructured systems caused a sig-

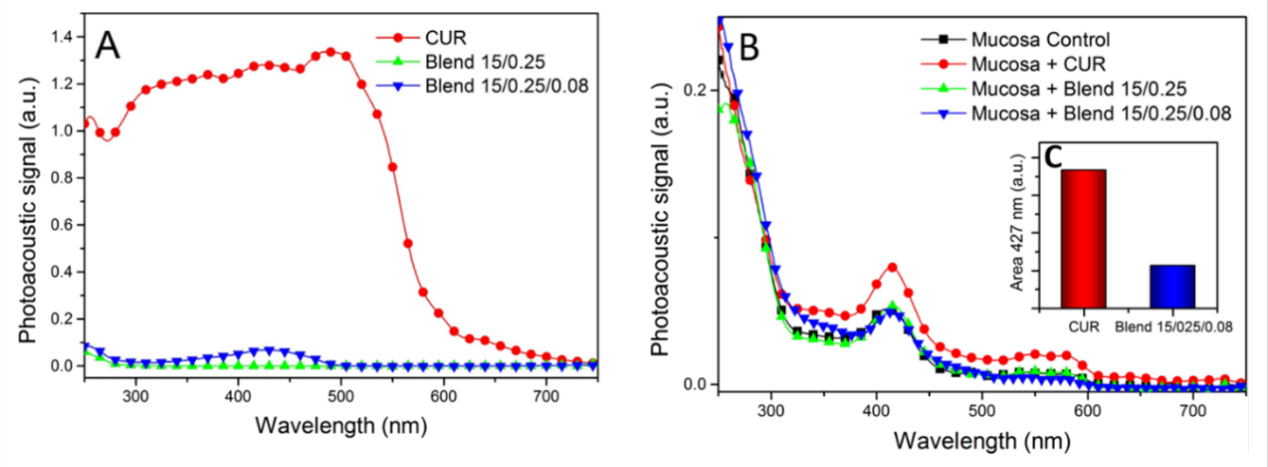

Figure 11: Optical absorption spectra obtained from PAS with (A) CUR and polymeric systems with and without CUR, (B) permeation of CUR through mucosa and (C) area of behavior of permeation of absorption band in 427 nm in mucosa.

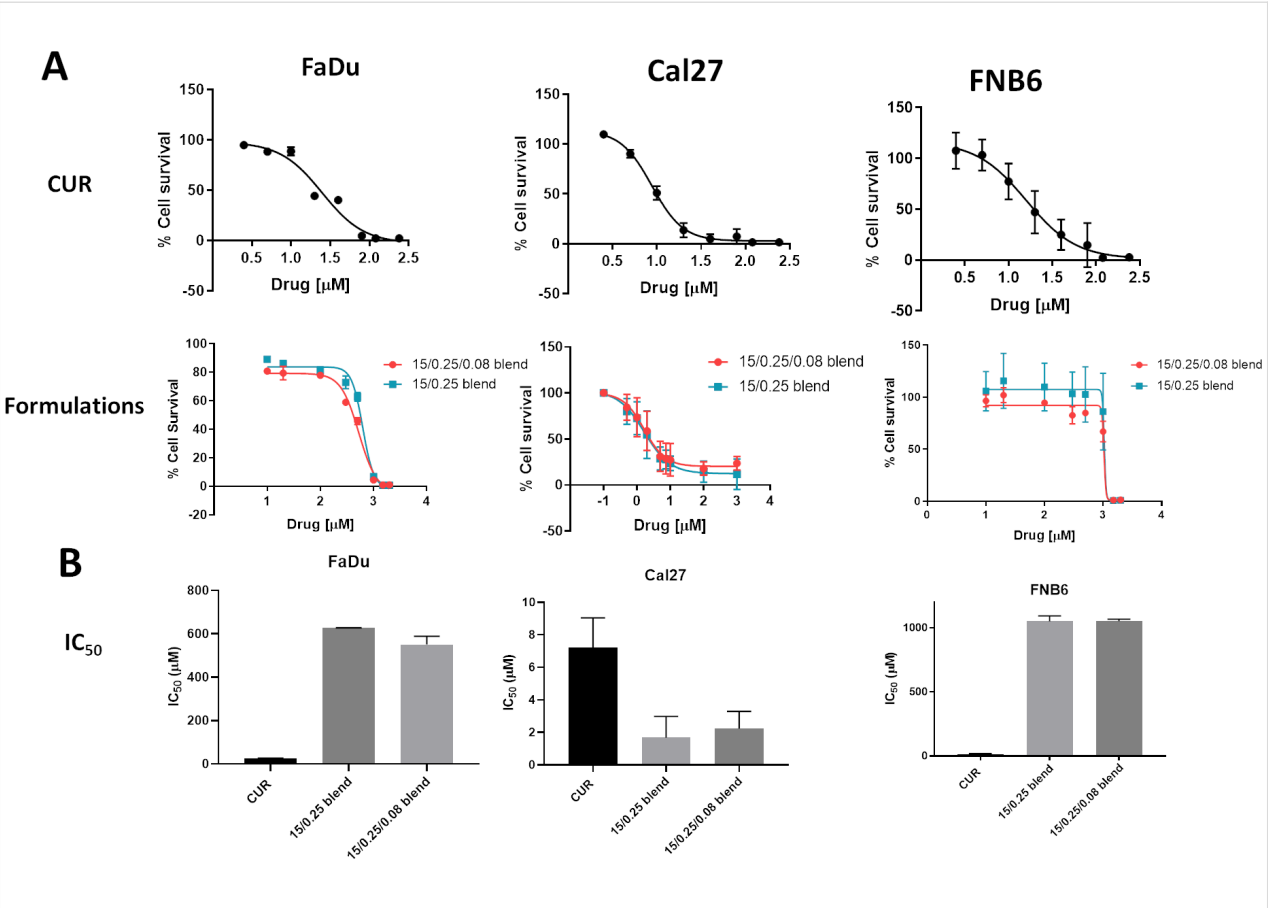

Figure 12: Cytotoxicity of formulations: (A) cell survival curves of drug and formulations, (B) IC_{50} comparisons of drug and formulations for two SCC (FaDu and Cal27) and one normal oral (FNB6) cell lines. Each IC_{50} value and percent cell survival represent average ± SEM (n = 3). CUR dispersed in DMSO aqueous solution exhibited cytotoxicity on all three cell types with average IC_{50} of 24.90 ± 2.30, 7.205 ± 1.831, 15.916 ± 3.440 μM, for FaDu, Cal27 and FNB6, respectively. The possible DMSO interference on methodology was investigated (Supporting Information File 1, Figure S2).

nificant ($p < 0.05$) increase in the IC_{50} values for both FaDu and FNB6 compared to Cal27.

This behavior indicated that CUR could be released and permeate before it could kill the cells. Moreover, the presence of CUR significantly decreased the IC_{50} due to its cytotoxicity properties [87]. The formulations were diluted in order to maintain the viability of the cells. Therefore, CUR is released into the medium that has a large amount of organic molecules and low water activity to disperse the drug. However, each cell line was cultivated in a different type of medium, DMEM, RPMI and Green's medium for Cal27, FaDu and FNB6, respectively. These different media could explain the results. The Cal27 viability was quite similar when treated with the drug and with the formulations, thus the same drug concentration is likely available. The slow drug release, ex vivo retention of CUR in the mucosa and the cytotoxic results suggest that these formulations would not be effective in primary therapy. However, it could be very useful after surgical procedure in order to kill the remaining cells.

Conclusion

The physicochemical, mechanical, pharmaceutical and biological properties of mucoadhesive nanostructured systems containing CUR were explored in this study. The photophysical interactions, CUR incorporation kinetics and the location of drug in the micelles were elucidated. The pharmaceutical aspects, including rheology, mechanical properties, CUR release and permeation using two complementary methods were also investigated. Moreover, the biological characterization involved investigation of the cytotoxicity in tumor and healthy cell lines. The formulations prepared from solid dispersions stored at 25 °C containing P407, C974P and CUR displayed viscoelastic properties, plastic behavior with rheopexy at body temperature (which provides better retention), and increased mucoadhesive force due to the presence of CUR. CUR tends to be located in the core of the micelles; consequently, the drug displayed slow and complete release after 8 h but did not permeate the porcine oral mucosa. The cytotoxicity studies revealed the increase in the cytotoxic effects for some tumor cell lines (Cal 27) when incorporated into the formulation but decreased cytotoxic effects

in healthy cells. Therefore, the nanostructured system demonstrated promising results due to the selectivity towards cancer cells in a monolayer cell culture in addition to exhibiting excellent physicochemical properties. Hence, further activity studies should be performed in tissue-engineered and in vivo models in order to test the performance of these systems in a more complex environment.

Experimental

Materials

Curcumin (>98% purity), poloxamer 407 and mucin from porcine stomach type II were purchased from Sigma-Aldrich (St. Louis, MO, USA). Carbopol 974P® was kindly donated by Lubrizol (São Paulo, SP, Brazil). Curcumin C3 complex® was received from Sabinsa® (West Windsor, USA) and triethanolamine, used as a neutralizing agent, was purchased from Galena (Campinas, SP, Brazil). Potassium iodide was purchased from Biotec (São Paulo, SP, Brazil), sodium chloride was purchased from Nuclear (Diadema, SP, Brazil) and polyssorbate 80 (Tween 80®) came from Synth® (Diadema, SP, Brazil).

Dulbecco's Modified Eagle's Medium high glucose (DMEM), fetal bovine serum (FBS), L-glutamine, penicillin, streptomycin and trypsin were purchased from Sigma-Aldrich (St. Louis, MO, USA).

Preparation of formulations

C974P (0.25%, w/w) was dispersed in purified water using a mechanical stirrer until complete dispersion. P407 (15%, w/w) was added to this mixture and the preparation was stored at 4 °C to ensure the complete wetting of the compounds. After 12 h, the formulations were stirred to provide the complete mixture of the two polymers. The final preparation was neutralized with triethanolamine, centrifuged at 3000 rpm to remove air bubbles, and stored at 4 °C for at least 24 h before further analysis [1,10,11]. Regarding the nanostructured systems containing curcumin, 15% (w/w) P407 was dispersed in ethanol and 0.08% (w/w) curcumin was added to the mixture and homogenized until complete mixture. The ethanol was eliminated using a rotary evaporator at 60 °C. When a thin film was obtained, the preparation was stored in a desiccator for 24 h. Afterwards, the thin film was added to the dispersion containing a mucoadhesive polymer (C974P), which was previously prepared. The system was stirred and finally the pH was adjusted to 7.0 using triethanolamine.

The nanostructured system containing CUR was also prepared by a second method (direct addition of CUR after preparation of binary polymeric system). Firstly, 0.25% of C974P was added to purified water and agitated until complete dispersion. Subsequently, 15% P407 was added to this mixture and stored in the refrigerator for 12 h. Afterwards, the mixture was agitated, CUR (0.08%, w/w) was added and the system pH was adjusted to 7 with triethanolamine.

Interaction studies of curcumin in mucoadhesive nanostructured systems

Interaction evaluation by photophysical studies

The interaction between CUR and the polymer blend was evaluated by fluorescence spectrophotometry, where the formulations were diluted in water and the final concentration of the components were 1.8×10^{-5} mol/L curcumin, 0.01% (w/w) P407 and 0.0001675% (w/w) C974P. The behavior of the formulations was monitored regarding the increase of temperature and pH changes in the fluorescence emission spectra and anisotropy values obtained by the fluorescence spectrophotometer (Varian Agilent Technologies®). The anisotropy (r) was automatically calculated by the software Eclipse ADL Program Selector, according to the Equation 1:

$$r = \frac{I_{VV} - GI_{VH}}{I_{VV} + 2GI_{VH}} \quad (1)$$

where I_{VH} and I_{VV} represent the intensity measured by the excitation of the vertically aligned polarizer and the horizontally aligned polarizer, respectively. G is the instrumental correction factor of the ratio of the sensitivities for vertically and horizontally polarized light [48,88,89].

The excitation wavelength was 422 nm with emission wavelength 440 to 700 nm and the emission slit was set to 5–10 nm. All the systems were evaluated at 10 (below the critical micellar temperature), 25, 37 and 45 °C (above the critical micellar temperature) at pH 7. In addition, the systems containing P407 and CUR were evaluated at pH 7 and 10 at a temperature of 37 °C. At the same time, the binary polymeric systems were monitored in pH 5, 7 and 10 at 37 °C. All the measurements were performed after thermal equilibrium was achieved [46,90,91].

Studies of curcumin incorporation kinetics

In order to simulate the mechanism of incorporation of curcumin and the required time for the drug to reach the core of the polymeric micelles, the incorporation kinetic profile was determined using the CUR addition sequence based on the second method of preparation. In a quartz cuvette, 22 µL of CUR stock solution (4.8×10^{-3} mol/L) was added to the P407 and C974P polymeric dispersion without pH adjustment, totaling 3 mL. The final concentration was 3.6×10^{-5} mol/L CUR, 0.02% (w/w) P407 and 0.0032% (w/w) C974P. The kinetic profile was evaluated at 25 °C and 37 °C, over 125 min by monitoring the fluorescence emission spectra, where the excitation wavelength was 422 nm and the emission slit was set to 5–10 nm [92].

Localization of curcumin in nanostructured systems

The relative location of curcumin in the polymer blends containing P407, C974P and CUR prepared by solid dispersion stored at 25 °C and 5 °C was performed using iodide (I^-) as a hydrophilic suppressor. Firstly, 133 µL of gel containing CUR and purified water were added to a 100 mL volumetric flask. Subsequently, increasing aliquots of KI (1 mol/L) were added in a solution containing polymeric micelles of CUR (3.6×10^{-5} mol/L), 0.02% (w/w) P407, and 0.0032% (w/w) C974P. The spectral emission profile from 440 to 700 nm was monitored after each iodide addition using an excitation wavelength of 422 nm and in most cases the emission slit was set to 5–10 nm. The Stern–Volmer (K_{sv}) constant was obtained at 25 and 37 °C by Equation 2:

$$\frac{F_0}{F} = 1 + K_{sv} \cdot \left[I^- \right] \quad (2)$$

where the emission values in the presence and absence of a suppressor are represented by F_0 and F, respectively, and the concentration of iodide in the solution is given by $[I^-]$ [91,93,94]. The dilution effect promoted by the addition of each hydrophilic suppressor aliquot was corrected for each spectral emission profile.

Morphological analysis by scanning electron microscopy

The morphological characteristics of formulations in the presence and absence of curcumin were evaluated by an electron scanning microscope (Quanta FEI, Thermo®, Oregon, USA). Approximately 2 g of the formulation was freeze-dried and a sample of material was placed on double-sided tape, and the sample was coated with colloidal gold under argon atmosphere.

Morphological analysis by transmittance electron microscopy

The morphology of the formulations was also determined using a JOEL JEM 1400 transmission electron microscope (Peabody, MA, USA). 0.2 mL of the nanostructured material was diluted in a 10 mL volumetric flask and placed on a formvar/Carbon 200 mesh, copper grid (Ted Tella, Redding, CA, USA). This set was negatively stained with 2% (w/v) uranyl acetate solution for observation [57,95,96]. The samples were prepared at 37 °C.

Micelle size analysis

The hydrodynamic diameter (D), polydispersity index (PDI) and size distribution of 10%, 50% and 90% (D10%, D50% and D90%) of micelles of the nanostructured systems was carried out by dynamic light scattering (DLS) analysis using a NanoPlus Particle Size Analyzer (Particulate Systems, Norcross, GA, USA). The formulation samples were diluted 50 and 10 times to provide P407 concentrations of 0.3% and 1.5% (w/w), respectively. The measurements were performed at 25 °C and 37 °C with at least three replicates.

Rheometry

The rheological analysis of the formulations was determined using a controlled stress rheometer (MARSII, Haake Thermo Fisher Scientific Inc., Newington, Germany) at 25 °C and 37 ± 0.1 °C with a geometry employing a parallel steel cone-plate (35 mm diameter, separated by a fixed distance of 0.052 mm, where the cone angle is 2°), as shown in Figure 13.

The samples were carefully placed in the device, and it was allowed to equilibrate for at least 1 min before analysis to ensure the minimized shearing of the sample.

Continuous shear flow rheology

In flow mode, the downward and upward curves were obtained over shear rates from 0 to 2000 s^{-1}, increasing over a period of 150 s, retained at the high limit during 10 s, and then decreasing over a period of 150 s. The flow properties were determined from at least five replicates and the upward flow curves were modelled using the power-law fluid (or the Ostwald–de Waele) relationship (Equation 3) [28,31,47]:

$$\tau = K\dot{\gamma}^n \quad (3)$$

where τ is shear stress (Pa), K is the consistency index [(Pa·s)^n], $\dot{\gamma}$ is shear rate (s^{-1}), and n is the flow behavior index (dimensionless).

The yield stress was evaluated by the rheological models of Casson (Equation 4) and Herschel–Bulkley (Equation 5) [97]:

$$\tau = \sqrt[n]{\left(\tau_0^n + \left(\dot{\gamma}\eta_p \right) \right)^n} \quad (4)$$

$$\tau = \tau_0 + K\dot{\gamma}^n \quad (5)$$

where τ_o is yield stress (Pa) and η_p is the Casson plastic viscosity. Moreover, the hysteresis area was calculated by the software RheoWin 4.10.0000 (Haake®).

Oscillatory rheology

In oscillatory mode, the linear viscoelastic region (LVR) was determined for each binary polymeric system. Subsequently, the frequency sweep analysis was performed from 0.1 to 10.0 Hz at 25 and 37 °C. The viscoelastic properties of the preparations, storage modulus (G'), loss modulus (G"), dynamic viscosity

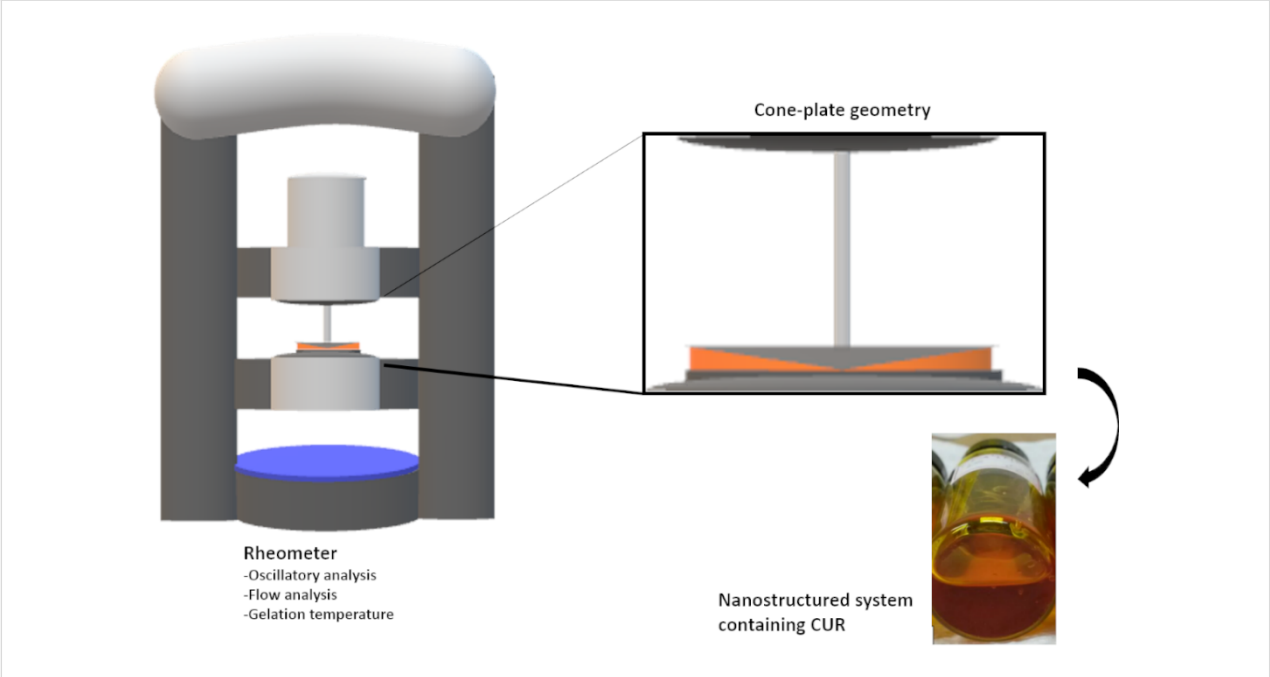

Figure 13: Schematic presentation of the rheological analysis setup utilized for continuous shear (flow) and oscillatory rheometry analysis of the formulations.

(η') and the loss tangent (tan δ) were calculated using the software RheoWin 4.10.0000 (Haake®). The analyses were performed at least in five replicate samples [27,28,98,99].

Sol–gel transition temperature

In oscillatory mode with a controlled temperature ramp, the sol–gel transition temperature ($T_{sol–gel}$) of the formulations was investigated as well. The LVR of each system was performed at 5 °C and 60 °C. Afterwards, over a range of 5–60 °C, the temperature sweep analysis was performed at a defined frequency (1.0 Hz) with a heating rate of 10 °C/min with controlled stress. The viscoelastic properties, G', G", η' and tan δ were calculated using the software RheoWin 4.10.0000 (Haake®) with at least five replicate samples in each case. $T_{sol–gel}$ is defined as the temperature at which G' was halfway between the values for solution and gel and was calculated for all preparations where η' increased with the significant increase of temperature [47,49-51].

Texture profile analysis

The texture profile analysis (TPA) of preparations with and without CUR was carried out using a texture profile analyzer TA-XTplus (Stable Micro Systems®, Surrey, UK) at 25 and 37 °C, in TPA mode, for at least three replicates [59]. A 13 g formulation was compressed at a depth of 15 mm, two times, by an analytical probe of polycarbonate (10 mm diameter) at a speed of 2 mm/s and with 15 s between the first and the beginning of the second compression. The resultant force versus distance plot provided the texture parameters, hardness, compressibility, adhesiveness, elasticity and cohesiveness [59].

Mucoadhesive properties

In vitro evaluation of mucoadhesive strength by detachment force

The mucoadhesive properties of the formulations (with and without CUR) were investigated using a texture analyser (TA-XTplus, Stable Micro Systems®) in tension mode at 37 °C, repeated at least three times. Firstly, the mucin disc was prepared by the compression of crude mucin, hydrated in mucin solution 5% (w/w) for 30 s and fixed in the TPA probe. The excess liquid was gently removed with absorbent paper. The samples were placed behind the analytical probe, which was lowered until both surfaces were in contact. Subsequently, a force of 0.1 N was applied for 30 s in order to ensure the intimate contact between the mucin disc and sample. Afterwards, the probe was raised at speed of 1.0 mm/s and the force required to detach the mucin disc from the formulations was determined from the plot of force versus time.

Ex vivo analysis of mucoadhesive properties by falling liquid method

The mucoadhesive properties of the formulations were also investigated by an ex vivo methodology using porcine oral mucosa on a flow through method. Porcine oral mucosa was taken from the cheek of young, white and freshly slaughtered pigs from a slaughterhouse authorized for human consumption

by the Brazilian Agriculture Ministry. After the oral mucosa was excised with scissors and a surgical scalpel, the samples were stored at −18 °C in a PBS solution and defrosted at room temperature on the experimental day (48 hours after the oral mucosa preparation) [30].

Inside a temperature-controlled chamber (37 °C), the oral mucosa samples were placed on the test channel behind a syringe-pump system, where phosphate sodium buffer was dropped over the mucosal samples (flow of 4 mL/min) (Figure 14). 100 µL of the formulation was placed over the oral mucosa and kept warm, in order to allow the adhesion between the mucosa and formulation. After 5 min, PBS was flowed over the set for 20 min. The samples of the elution liquid were collected after 1, 2, 5, 10, 15 and 20 min, with 1% (v/v) Tween 80 to allow the complete dispersion of CUR. The samples were diluted with methanol (1:2) and analyzed by the HPLC method. 20 µL of the sample was injected into a Shimadzu LC CBM 20 system (Tokyo, Japan) equipped with a UV–vis detector (SPD 20 A) and manual injector (7725i). A C18 reversed phase column (5 µm × 4.6 mm × 250 mm, Luna PFP, Phenomenex®, Torrance, USA) was used as a stationary phase and the mobile phase was acetonitrile and acetic acid solution (1.5%, v/v) in a gradient elution. The flow was adjusted to 1.0 mL/min and the peak area was detected at 425 nm. The amount of formulation removed from the surface of the substrate was calculated and deducted from the total, providing the retention data. The analysis was performed in triplicate using new oral mucosa for each experimental essay [10,52,53].

Syringeability determination

The formulation resistance to compression inside a syringe was determined by the syringeability work. The investigations were performed in a texture analyzer (TA-XTplus) in compression mode [100]. In order to avoid the entrapment of air, the formulations were carefully packed in 1 mL plastic syringes at 30 mm. Each syringe was vertically fixed in the texture meter and pressed at 2.0 mm·s^{-1}, to a depth of 30 mm, until initial contact with the syringe plunger was made. The analysis was performed at 25 °C with at least three replicates [47,55]. During the compression of the plunger, a graph of force versus distance was derived and the work demonstrates the resistance of the compression of syringe content.

In vitro drug release

The kinetics of the release of curcumin from the binary polymeric system was carried out using double-wall glass beaker with water bath temperature control at 37 ± 0.5 °C. 1.0 g polymeric system was placed on the bottom of the vessel at 37 °C to ensure the complete gelation of the formulation. Subsequently, 16 mL of the release media (Tween 80 aqueous solution; 1%, v/v) was carefully added in the recipient to obtain sink conditions and kept under constant agitation (Figure 15) [11,56,101]. 500 µL aliquots of samples were collected and replaced with the same volume of fresh medium at fixed time intervals, 0.5 h, 1 h, 2 h, 3 h, 4 h, 6 h, 8 h and 24 h. These samples were diluted with methanol (1:2), filtered with PTFE membranes and quantified by the HPLC method, as previously described [30]. The release profiles were calculated by plotting the amount released versus time. These release profiles were fitted with the Korsmeyer–Peppas equation (Equation 6), which describes the drug release from matrix polymeric systems [102]:

$$F = k \cdot t^n \quad (6)$$

where F represents the fraction of the drug released, t is the time released, k is the combined kinetic constant of structural and geometric characteristics of the apparatus and n is the release exponent, which reveals the drug release mechanism.

Ex vivo analysis of curcumin permeation in oral mucosa

Mucosa permeation by Franz cells

The permeation was investigated using porcine oral mucosa obtained as previously described in the section on ex vivo analysis of mucoadhesive properties by falling liquid method. Firstly,

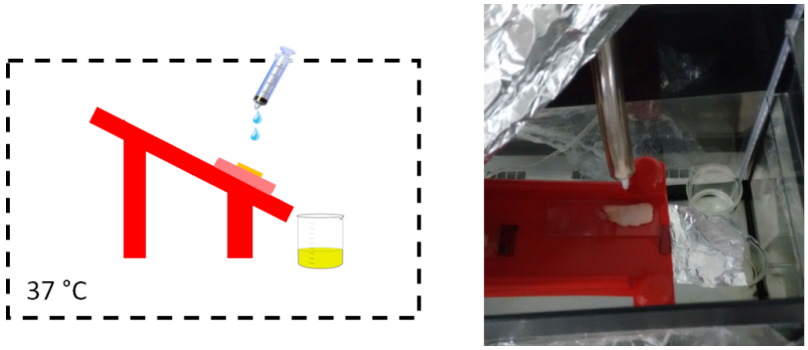

Figure 14: Schematic presentation of the setup utilized for ex vivo liquid falling mucoadhesion tests.

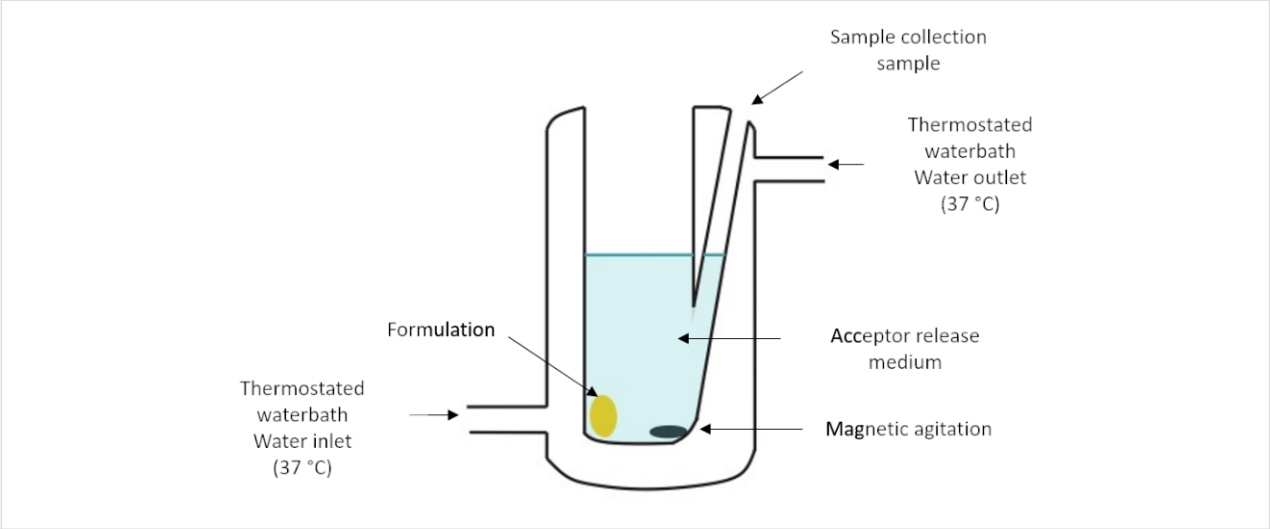

Figure 15: Schematic presentation of the modified Franz's cell used for the in vitro curcumin release measurements from the nanostructured system.

the tissues were defrosted at room temperature, then cut and placed between the donor and receptor compartment of the Franz cell. The receptor media, composed of 1% (v/v) Tween 80 in PBS buffer (pH 7.4), which provided the solublization of CUR, was placed in the receptor compartment. This system was maintained at 37 °C at constant stirring. 1 mL of the formulation was placed homogeneously over the mucosa in the donor compartment. The temperature of the formulation was maintained at 37 °C by thermal exchange between the tissue and the formulation and also the temperature control provided by the equipment [103,104]. Afterwards, 500 µL of the receptor medium was collected and replaced by fresh medium to ensure sink condition at 0.5 h, 1 h, 2 h, 3 h, 4 h, 6 h, 8 h and 24 h. The samples were diluted in methanol (1:2), filtered in PTFE and quantified by the HPLC method. At least three replicates were performed [56,61].

For the retention of CUR in the tissue, the porcine mucosa was taken from the recipient. The tissue was cut into small pieces and placed in a 5 mL volumetric flask with methanol and sonicated for 15 min. Subsequently, the 5 mL volumetric flask was completed, filtered with PTFE and quantified using the HPLC method. The analysis was performed for at least three samples.

Mucosal permeation by photoacoustic spectroscopy

The permeation of curcumin from the mucoadhesive thermoresponsive systems, performed in porcine oral mucosa, was investigated by photoacoustic spectroscopy. The oral mucosa was taken from porcine cheek as described previously. Firstly, 30 µg of the formulation was homogeneously placed over a 1 cm^3 surface of the oral mucosa. After 30 min, the sample was evaluated by photoacoustic spectroscopy. This essay was performed on home-built experimental equipment composed of a 1000 W Xenon arc lamp (Oriel, model 68820) as the light source with a nominal power of 800 W. The light was diffracted when passing through the 3.16 mm input and output slits of the monochromator (Oriel, model 77250) and then modulated at 13 Hz with a mechanical chopper (Stanford Research Systems, model SR 540) and then focused on the sample. Band-pass filters were used to eliminate higher order diffraction. The sample was placed inside the photoacoustic cell and sealed with a transparent quartz window (diameter of 8 mm and thickness of 2 mm). The photoacoustic signal generated by pressure changes resulting from the periodic heating of the sample was collected by a capacitive microphone (Brüel and Klaer, model 2669). A lock-in amplifier by EG&G Instruments, model 5110, was used. The thermal diffusion length (µs) was used to calculate the depth of tissue that contributed to the photoacoustic signal:

$$\mu_s = \sqrt{\frac{D}{\mu f}} \tag{7}$$

where D is the sample thermal diffusivity ($cm^{-2}{\cdot}s^{-1}$) and f is the light modulation frequency (Hz). Considering the thermal diffusivity of mucosa equal to skin, due to the similarity overall in terms of molecule distribution and histological architecture [105], $D = 4.1 \times 10^{-4}$ $cm^2{\cdot}s^{-1}$ [106,107] and f =13 Hz. Consequently, μ_s was 31 µm for oral mucosa and the total sample thickness was constant around 818 µm.

The photoacoustic signal was interpreted from the band absorption spectra, since the final photoacoustic signal is proportional to the sample absorption coefficient [107]. All spectra were normalized with a sample of carbon black in order to correct the source emission intensity in each wavelength [108].

Moreover, the spectra of at least three porcine oral mucosa were obtained by placing the tissue inside the photoacoustic cell and illuminating the side to be measured; then the tissue was turned upside down to illuminate the opposite side [56,60].

Cell culture

The cell lines FaDu (LGC Promochem, Middlesex, UK), originally isolated from a hypopharyngeal tumor and Cal27 (ATCC, Manassas, VA, USA, CRL-2095) from tongue squamous cell carcinoma (ECACC, Health Protection Agency Culture Collections, Salisbury, UK) were used in this study. FaDu cells were cultured in RPMI-1640, whereas Cal27 was cultured in Dulbecco's modified Eagle's (DMEM) medium high glucose. Both media were supplemented with 10% (v/v) fetal bovine serum (FBS), 2 mM L-glutamine, 100 UI/mL penicillin and 100 µg/mL streptomycin. The immortalized cell line FNB6 (a kind gift from Professor Keith Hunter), originally isolated from normal oral keratinocytes, were cultured in adenine enriched medium; DMEM and Ham's F12 medium in a 3:1 (v/v) supplemented with 10% (v/v) FBS, 0.1 mM cholera toxin, 10 ng/mL epidermal growing factor, 0.4 µg/mL hydrocortisone, 0.18 mM adenine, 5 mg/mL transferrin, 2 mM L-glutamine, 0.2 mM triiodothyronine, 0.625 mg/mL amphotericin B, 100 UI/mL penicillin and 100 µg/mL streptomycin. All cells were incubated at 37 °C in a 5% CO_2 humidified atmosphere and sub-cultivated using trypsin-EDTA when 80% confluence was reached.

Cytotoxicity and biological activity evaluation

The in vitro cytotoxicity of preparations with and without CUR, as well as the drug alone, were carried out on FNB6, Cal27 and FaDu cells using an MTT assay as previously described [85]. Briefly, 2×10^5 cells were seeded in each well of a 96-well plate before addition of the formulations with and without CUR with increased polymeric content (2000, 1500, 1000, 500, 300, 100, 20, 10 µM CUR) and free CUR (240,120, 80, 40, 20, 10, 5 and 2.5 µM). After 24 h, the media with CUR and/or the formulations was aspirated, the cells were washed three times with PBS and more 200 µL media was added to each well and the cells were incubated for a further 24 h. Monolayer cultures were incubated for 1 h at 37 °C with 0.5 mg/mL MTT solution, after which the solution removed and acidified isopropanol was added to remove the blue formazan crystals. The optical density was measured at 570 nm with a 630 nm reference correction.

Statistical analysis

The effect of CUR presence and temperature in micelle size analysis, consistency index (K), flow index (n), yield value, hysteresis area and texture profile analysis parameters (hardness, compressibility, adhesiveness, elasticity and cohesiveness) were statistically compared using two-way ANOVA. On the other hand, the effect of the presence of CUR on the mucoadhesive strength, softness and syringeability were statistically evaluated by one-way ANOVA. Moreover, the effect of the drug and formulation on cell viability was evaluated by two-way ANOVA. Student t-test was used to determine the influence of temperature on dynamic viscosity of the formulations. All the cases of ANOVA post hoc comparison of individual groups were carried out using Tukey. For all cases, $p < 0.05$ was accepted as significant [23,28,31].

Supporting Information

Supporting Information File 1

The results of the evaluation of the storage temperature of the formulations and the investigation on the DMSO interference in the CUR cytotoxicity studies.
[https://www.beilstein-journals.org/bjnano/content/supplementary/2190-4286-10-222-S1.pdf]

Acknowledgements

The authors are grateful to CAPES (nº 88881.188732/2018-01-PDSE program) [grant number – 001] (*Coordenação de Aperfeiçoamento de Pessoal de Nível Superior*/Coordination for the Improvement of Higher Education of Brazil), CNPq (*Conselho Nacional de Desenvolvimento Científico e Tecnológico*/National Counsel of Technological and Scientific Development of Brazil), FINEP (*Financiadora de Estudos e Projetos*/Financier of Studies and Projects of Brazil), State University of Maringa, The University of Sheffield, and Dr. Sebastian Spain (Department of Chemistry - The University of Sheffield) for their support during this project.

ORCID® iDs

Sabrina Barbosa de Souza Ferreira - https://orcid.org/0000-0001-8364-0449
Gustavo Braga - https://orcid.org/0000-0001-6383-2152
Évelin Lemos Oliveira - https://orcid.org/0000-0002-8208-0950
Jéssica Bassi da Silva - https://orcid.org/0000-0003-0586-7802
Hélen Cássia Rosseto - https://orcid.org/0000-0002-5331-157X
Lidiane Vizioli de Castro Hoshino - https://orcid.org/0000-0002-5118-5370
Mauro Luciano Baesso - https://orcid.org/0000-0001-6017-2582
Wilker Caetano - https://orcid.org/0000-0002-9402-8324
Craig Murdoch - https://orcid.org/0000-0001-9724-122X
Helen Elizabeth Colley - https://orcid.org/0000-0003-0053-7468
Marcos Luciano Bruschi - https://orcid.org/0000-0002-4838-5742

References

1. De Souza Ferreira, S. B.; Da Silva, J. B.; Volpato Junqueira, M.; Belincanta Borghi-Pangoni, F.; Guttierres Gomes, R.; Luciano Bruschi, M. *J. Mech. Behav. Biomed. Mater.* **2017,** *74,* 142–153. doi:10.1016/j.jmbbm.2017.05.040

2. Bodratti, A.; Alexandridis, P. *J. Funct. Biomater.* **2018,** *9,* 11. doi:10.3390/jfb9010011
3. Alexandridis, P.; Holzwarth, J. F.; Hatton, T. A. *Macromolecules* **1994,** *27,* 2414–2425. doi:10.1021/ma00087a009
4. Dumortier, G.; Grossiord, J. L.; Agnely, F.; Chaumeil, J. C. *Pharm. Res.* **2006,** *23,* 2709–2728. doi:10.1007/s11095-006-9104-4
5. Campanholi, K. d. S. S.; Braga, G.; da Silva, J. B.; da Rocha, N. L.; de Francisco, L. M. B.; de Oliveira, É. L.; Bruschi, M. L.; de Castro-Hoshino, L. V.; Sato, F.; Hioka, N.; Caetano, W. *Langmuir* **2018,** *34,* 8230–8244. doi:10.1021/acs.langmuir.8b00658
6. Wanka, G.; Hoffman, H.; Ulbricht, W. *Macromolecules* **1994,** *27,* 4145–4159. doi:10.30906/0869-2092-2018-81-10-8-14
7. Borghi-Pangoni, F. B.; Junqueira, M. V.; de Souza Ferreira, S. B.; Silva, L. L.; Rabello, B. R.; de Castro, L. V.; Baesso, M. L.; Diniz, A.; Caetano, W.; Bruschi, M. L. *Photodiagn. Photodyn. Ther.* **2017,** *19,* 284–297. doi:10.1016/j.pdpdt.2017.06.016
8. Junqueira, M. V.; Borghi-Pangoni, F. B.; Ferreira, S. B. S.; Rabello, B. R.; Hioka, N.; Bruschi, M. L. *Langmuir* **2016,** *32,* 19–27. doi:10.1021/acs.langmuir.5b02039
9. De Souza Ferreira, S. B.; Moço, T. D.; Borghi-Pangoni, F. B.; Junqueira, M. V.; Bruschi, M. L. *J. Mech. Behav. Biomed. Mater.* **2016,** *55,* 164–178. doi:10.1016/j.jmbbm.2015.10.026
10. De Souza Ferreira, S. B.; Da Silva, J. B.; Borghi-Pangoni, F. B.; Junqueira, M. V.; Bruschi, M. L. *J. Mech. Behav. Biomed. Mater.* **2017,** *68,* 265–275. doi:10.1016/j.jmbbm.2017.02.016
11. Jones, D. S.; Bruschi, M. L.; de Freitas, O.; Gremião, M. P. D.; Lara, E. H. G.; Andrews, G. P. *Int. J. Pharm.* **2009,** *372,* 49–58. doi:10.1016/j.ijpharm.2009.01.006
12. Lefnaoui, S.; Moulai-Mostefa, N. *Colloids Surf., A* **2014,** *458,* 117–125. doi:10.1016/j.colsurfa.2014.01.007
13. Liu, J.; Lin, S.; Li, L.; Liu, E. *Int. J. Pharm.* **2005,** *298,* 117–125. doi:10.1016/j.ijpharm.2005.04.006
14. Mayol, L.; Quaglia, F.; Borzacchiello, A.; Ambrosio, L.; Rotonda, M. I. L. *Eur. J. Pharm. Biopharm.* **2008,** *70,* 199–206. doi:10.1016/j.ejpb.2008.04.025
15. Bruschi, M. L.; de Freitas, O. *Drug Dev. Ind. Pharm.* **2005,** *31,* 293–310. doi:10.1081/ddc-52073
16. Fonseca-Santos, B.; Chorilli, M. *Mater. Sci. Eng., C* **2018,** *86,* 129–143. doi:10.1016/j.msec.2017.12.022
17. Bruschi, M. L.; Lara, E. H. G.; Martins, C. H. G.; Vinholis, A. H. C.; Casemiro, L. A.; Panzeri, H.; Gremião, M. P. D. *Drug Dev. Ind. Pharm.* **2006,** *32,* 229–238. doi:10.1080/03639040500466312
18. Brener, S.; Jeunon, F.; Barbosa, A.; Grandinetti, H. *Rev. Bras. Cancerol.* **2007,** *53,* 63–69.
19. World Health Organization. Locally advanced squamous carcinoma of the head and neck. *2014 Review of Cancer Medicines on the WHO List of Essential Medicines;* World Health Organization: Geneva, Switzerland, 2014; pp 1–8.
20. Colley, H. E.; Hearnden, V.; Jones, A. V.; Weinreb, P. H.; Violette, S. M.; MacNeil, S.; Thornhill, M. H.; Murdoch, C. *Br. J. Cancer* **2011,** *105,* 1582–1592. doi:10.1038/bjc.2011.403
21. Graciano, T. B.; Coutinho, T. S.; Cressoni, C. B.; Freitas, C. d. P.; Pierre, M. B. R.; de Lima Pereira, S. A.; Shimano, M. M.; Cristina da Cunha Frange, R.; Garcia, M. T. J. *Photodiagn. Photodyn. Ther.* **2015,** *12,* 98–107. doi:10.1016/j.pdpdt.2014.11.003
22. Hsu, F.-C.; Huang, T.-T.; Chiou, W.-Y.; Lee, C.-C.; Lee, M.-S.; Hsiao, S.-H.; Lin, H.-Y.; Su, Y.-C.; Hung, S.-K. *Tzu Chi Med. J.* **2010,** *22,* 96–102. doi:10.1016/s1016-3190(10)60048-1
23. Longo, J. P. F.; Lozzi, S. P.; Azevedo, R. B. *RGO, Rev. Gaucha Odontol.* **2011,** *59,* 51–57.
24. Ettinger, K. S.; Ganry, L.; Fernandes, R. P. *Oral Maxillofac. Surg. Clin. North Am.* **2019,** *31,* 13–29. doi:10.1016/j.coms.2018.08.002
25. Kuriakose, M. A.; Sharan, R. *Oral Maxillofac. Surg. Clin. North Am.* **2006,** *18,* 493–511. doi:10.1016/j.coms.2006.06.003
26. Del Corso, G.; Villa, A.; Tarsitano, A.; Gohel, A. *Cancer Cell Microenviron.* **2016,** *3,* e1332.
27. Rethman, M. P.; Carpenter, W.; Cohen, E. E. W.; Epstein, J.; Evans, C. A.; Flaitz, C. M.; Graham, F. J.; Hujoel, P. P.; Kalmar, J. R.; Koch, W. M.; Lambert, P. M.; Lingen, M. W.; Oettmeier, B. W., Jr.; Patton, L. L.; Perkins, D.; Reid, B. C.; Sciubba, J. J.; Tomar, S. L.; Wyatt, A. D., Jr.; Aravamudhan, K.; Frantsve-Hawley, J.; Cleveland, J. L.; Meyer, D. M. *J. Am. Dent. Assoc., JADA* **2010,** *141,* 509–520. doi:10.14219/jada.archive.2010.0223
28. *Cancer Facts and Figures 2017;* America Cancer Society: Atlanta, U.S.A., 2017.
29. Vasimalai, N.; Vilas-Boas, V.; Gallo, J.; Cerqueira, M. d. F.; Menéndez-Miranda, M.; Costa-Fernández, J. M.; Diéguez, L.; Espiña, B.; Fernández-Argüelles, M. T. *Beilstein J. Nanotechnol.* **2018,** *9,* 530–544. doi:10.3762/bjnano.9.51
30. Oliveira, M. B.; da Silva, J. B.; Montanha, M. C.; Kimura, E.; Diniz, A.; Bruschi, M. L. *Curr. Drug Delivery* **2018,** *15,* 1112–1122. doi:10.2174/1567201815666180503121043
31. de Souza Ferreira, S. B.; Bruschi, M. L. *Ther. Delivery* **2019,** *10,* 83–86. doi:10.4155/tde-2018-0075
32. Mazzarino, L.; Loch-Neckel, G.; Bubniak, L. D. S.; Mazzucco, S.; Santos-Silva, M. C.; Borsali, R.; Lemos-Senna, E. *J. Nanosci. Nanotechnol.* **2015,** *15,* 781–791. doi:10.1166/jnn.2015.9189
33. Sharma, C.; Kaur, J.; Shishodia, S.; Aggarwal, B. B.; Ralhan, R. *Toxicology* **2006,** *228,* 1–15. doi:10.1016/j.tox.2006.07.027
34. Zlotogorski, A.; Dayan, A.; Dayan, D.; Chaushu, G.; Salo, T.; Vered, M. *Oral Oncol.* **2013,** *49,* 187–191. doi:10.1016/j.oraloncology.2012.09.015
35. Batra, H.; Pawar, S.; Bahl, D. *Pharmacol. Res.* **2019,** *139,* 91–105. doi:10.1016/j.phrs.2018.11.005
36. Esposito, T.; Lucariello, A.; Hay, E.; Contieri, M.; Tammaro, P.; Varriale, B.; Guerra, G.; De Luca, A.; Perna, A. *Chem.-Biol. Interact.* **2019,** *305,* 112–118. doi:10.1016/j.cbi.2019.03.031
37. Fratantonio, D.; Molonia, M. S.; Bashllari, R.; Muscarà, C.; Ferlazzo, G.; Costa, G.; Saija, A.; Cimino, F.; Speciale, A. *Phytomedicine* **2019,** *55,* 23–30. doi:10.1016/j.phymed.2018.08.009
38. Negrette-Guzmán, M. *Eur. J. Pharmacol.* **2019,** *859,* 172513. doi:10.1016/j.ejphar.2019.172513
39. Singh, S. P.; Alvi, S. B.; Pemmaraju, D. B.; Singh, A. D.; Manda, S. V.; Srivastava, R.; Rengan, A. K. *Int. J. Biol. Macromol.* **2018,** *110,* 375–382. doi:10.1016/j.ijbiomac.2017.11.163
40. Varshosaz, J.; Jajanian-Najafabadi, A.; Soleymani, A.; Khajavinia, A. *Polym. Test.* **2018,** *65,* 217–230. doi:10.1016/j.polymertesting.2017.11.020
41. Yue, G. G.-L.; Kwok, H.-F.; Lee, J. K.-M.; Jiang, L.; Wong, E. C.-W.; Gao, S.; Wong, H.-L.; Li, L.; Chan, K.-M.; Leung, P.-C.; Fung, K.-P.; Zuo, Z.; Lau, C. B.-S. *Pharmacol. Res.* **2016,** *111,* 43–57. doi:10.1016/j.phrs.2016.05.025
42. Lestari, M. L. A. D.; Indrayanto, G. Curcumin. In *Profiles of Drug Substances, Excipients and Related Methodology;* Britain, H. G., Ed.; Elsevier: Amsterdam, Netherlands, 2014; Vol. 39, pp 113–204. doi:10.1016/b978-0-12-800173-8.00003-9

43. Samanta, S.; Roccatano, D. *J. Phys. Chem. B* **2013,** *117,* 3250–3257. doi:10.1021/jp309476u
44. Sun, Y.; Du, L.; Liu, Y.; Li, X.; Li, M.; Jin, Y.; Qian, X. *Int. J. Pharm.* **2014,** *469,* 31–39. doi:10.1016/j.ijpharm.2014.04.039
45. Zhao, L.; Du, J.; Duan, Y.; Zang, Y.; Zhang, H.; Yang, C.; Cao, F.; Zhai, G. *Colloids Surf., B* **2012,** *97,* 101–108. doi:10.1016/j.colsurfb.2012.04.017
46. Morais, F. A. P. Estudos Das Propriedades Físico-Químicas Da Hipericina Encapsulada Em Vesículas Lipossomais Unilamelares de DPPC Visando Aplicações Em Terapia Fotodinâmica. Ph.D. Thesis, Universidade Estadual de Maringá, 2016.
47. Carvalho, F. C.; Bruschi, M. L.; Evangelista, R. C.; Gremião, M. P. D. *Braz. J. Pharm. Sci.* **2010,** *46,* 1–17. doi:10.1590/s1984-82502010000100002
48. Pallicer, J. M.; Krämer, S. D. *J. Pharm. Biomed. Anal.* **2012,** *71,* 219–227. doi:10.1016/j.jpba.2012.08.009
49. Lakowicz, J. R., Ed. *Principles of Fluorescence Spectroscopy;* Springer US: Boston, MA, U.S.A., 2006. doi:10.1007/978-0-387-46312-4
50. Braga, G. Estudos Cinéticos e Termodinâmicos de Sistemas Poliméricos Para Aplicação Em Terapia Fotodinâmica Em Terapia Fotodinâmica. Ph.D. Thesis, State University of Maringá, 2018.
51. Kabanov, A. V.; Batrakova, E. V.; Alakhov, V. Y. *J. Controlled Release* **2002,** *82,* 189–212. doi:10.1016/s0168-3659(02)00009-3
52. de Morais, F. A. P.; Gonçalves, R. S.; Vilsinski, B. H.; de Oliveira, É. L.; Rocha, N. L.; Hioka, N.; Caetano, W. *J. Photochem. Photobiol., B* **2019,** *190,* 118–127. doi:10.1016/j.jphotobiol.2018.11.019
53. Grimm, B.; Porra, R. J.; Rüdiger, W.; Scheer, H. *Chlorophylls and Bacteriochlrophylls: Biochemistry, Biophysics, Functios and Applications;* Springer: Dordrecht, Netherlands, 2006. doi:10.1007/1-4020-4516-6
54. Estevão, B. M.; Pellosi, D. S.; de Freitas, C. F.; Vanzin, D.; Franciscato, D. S.; Caetano, W.; Hioka, N. *J. Photochem. Photobiol., A* **2014,** *287,* 30–39. doi:10.1016/j.jphotochem.2014.04.015
55. Pellosi, D. S.; Estevão, B. M.; Semensato, J.; Severino, D.; Baptista, M. S.; Politi, M. J.; Hioka, N.; Caetano, W. *J. Photochem. Photobiol., A* **2012,** *247,* 8–15. doi:10.1016/j.jphotochem.2012.07.009
56. Pragatheeswaran, A. M.; Chen, S. B. *Langmuir* **2013,** *29,* 9694–9701. doi:10.1021/la401639g
57. Antonino, R. S. C. M. Q.; Nascimento, T. L.; de Oliveira Junior, E. R.; Souza, L. G.; Batista, A. C.; Lima, E. M. *J. Controlled Release* **2019,** *303,* 12–23. doi:10.1016/j.jconrel.2019.04.011
58. Lam, Y.-M.; Grigorieff, N.; Goldbeck-Wood, G. *Phys. Chem. Chem. Phys.* **1999,** *1,* 3331–3334. doi:10.1039/a902369k
59. Bruschi, M. L.; Jones, D. S.; Panzeri, H.; Gremião, M. P. D.; de Freitas, O.; Lara, E. H. G. *J. Pharm. Sci.* **2007,** *96,* 2074–2089. doi:10.1002/jps.20843
60. Fabri, F. V.; Cupertino, R. R.; Hidalgo, M. M.; Monteiro Weffort de Oliveira, R. M.; Bruschi, M. L. *Drug Dev. Ind. Pharm.* **2011,** *37,* 1446–1454. doi:10.3109/03639045.2011.584387
61. Curran, S. J.; Hayes, R. E.; Afacan, A.; Williams, M. C.; Tanguy, P. A. *J. Food Sci.* **2002,** *67,* 176–180. doi:10.1111/j.1365-2621.2002.tb11379.x
62. Schoenwald, R. D.; Ward, R. L.; DeSantis, L. M.; Roehrs, R. E. *J. Pharm. Sci.* **1978,** *67,* 1280–1283. doi:10.1002/jps.2600670923
63. Almeida, H.; Amaral, M. H.; Lobão, P.; Sousa Lobo, J. M. *Expert Opin. Drug Delivery* **2013,** *10,* 1223–1237. doi:10.1517/17425247.2013.796360
64. Lee, C. H.; Moturi, V.; Lee, Y. *J. Controlled Release* **2009,** *136,* 88–98. doi:10.1016/j.jconrel.2009.02.013
65. Carvalho, F. C.; Calixto, G.; Hatakeyama, I. N.; Luz, G. M.; Gremião, M. P. D.; Chorilli, M. *Drug Dev. Ind. Pharm.* **2013,** *39,* 1750–1757. doi:10.3109/03639045.2012.734510
66. Baloglu, E.; Karavana, S. Y.; Senyigit, Z. A.; Guneri, T. *Pharm. Dev. Technol.* **2011,** *16,* 627–636. doi:10.3109/10837450.2010.508074
67. Tuğcu-Demiröz, F.; Acartürk, F.; Erdoğan, D. *Int. J. Pharm.* **2013,** *457,* 25–39. doi:10.1016/j.ijpharm.2013.09.003
68. Gratieri, T.; Gelfuso, G. M.; Rocha, E. M.; Sarmento, V. H.; de Freitas, O.; Lopez, R. F. V. *Eur. J. Pharm. Biopharm.* **2010,** *75,* 186–193. doi:10.1016/j.ejpb.2010.02.011
69. Borghi-Pangoni, F. B.; Junqueira, M. V.; de Souza Ferreira, S. B.; Silva, L. L.; Rabello, B. R.; de Castro, L. V.; Baesso, M. L.; Diniz, A.; Caetano, W.; Bruschi, M. L. *Photodiagn. Photodyn. Ther.* **2017,** *19,* 284–297. doi:10.1016/j.pdpdt.2017.06.016
70. da Silva, J. B.; Khutoryanskiy, V. V.; Bruschi, M. L.; Cook, M. T. *Int. J. Pharm.* **2017,** *528,* 586–594. doi:10.1016/j.ijpharm.2017.06.025
71. Andrews, G. P.; Gorman, S. P.; Jones, D. S. *Biomaterials* **2005,** *26,* 571–580. doi:10.1016/j.biomaterials.2004.02.062
72. De Araújo Pereira, R. R.; Godoy, J. S. R.; Svidzinski, T. I. S.; Bruschi, M. L. *J. Pharm. Sci.* **2013,** *102,* 1222–1234. doi:10.1002/jps.23451
73. Bruschi, M. L.; de Francisco, L. M. B.; S. de Toledo, L. d. A.; B. Borghi, F. *Recent Pat. Drug Delivery Formulation* **2015,** *9,* 79–87. doi:10.2174/1872211308666141122220459
74. Bassi da Silva, J.; Ferreira, S. B. d. S.; de Freitas, O.; Bruschi, M. L. *Drug Dev. Ind. Pharm.* **2017,** *43,* 1053–1070. doi:10.1080/03639045.2017.1294600
75. Madsen, K. D.; Sander, C.; Baldursdottir, S.; Pedersen, A. M. L.; Jacobsen, J. *Int. J. Pharm.* **2013,** *448,* 373–381. doi:10.1016/j.ijpharm.2013.03.031
76. Bruschi, M. L.; Borghi-Pangoni, F. B.; Junqueira, M. V.; de Souza Ferreira, S. B. Nanostructured Therapeutic Systems with Bioadhesive and Thermoresponsive Properties. In *Nanostructures for Novel Therapy;* Ficai, D.; Grumezescu, A. M., Eds.; Micro and Nano Technologies; Elsevier: Amsterdam, Netherlands, 2017; pp 313–342. doi:10.1016/b978-0-323-46142-9.00012-8
77. Mathematical Models of Drug Release. In *Strategies to Modify the Drug Release from Pharmaceutical Systems;* Bruschi, M. L., Ed.; Woodhead Publishing: Sawston, United Kingdom, 2015; Vol. 1, pp 63–86. doi:10.1016/b978-0-08-100092-2.00005-9
78. Jug, M.; Hafner, A.; Lovric, J.; Kregar, M. L.; Pepíc, I.; Vaníc, Z.; Cetina-Cizmek, B.; Filipovic-Grcic, J. *J. Pharm. Biomed. Anal.* **2017,** 1–17.
79. Nakamoto, R. Y. *J. Prosthet. Dent.* **1979,** *42,* 539–542. doi:10.1016/0022-3913(79)90249-x
80. Korsmeyer, R. W.; Gurny, R.; Doelker, E.; Buri, P.; Peppas, N. A. *Int. J. Pharm.* **1983,** *15,* 25–35. doi:10.1016/0378-5173(83)90064-9
81. Patel, V. F.; Liu, F.; Brown, M. B. *J. Controlled Release* **2012,** *161,* 746–756. doi:10.1016/j.jconrel.2012.05.026
82. Said, Z. Analysis of Corticosteroid Drug Delivery Using Tissue-Engineered Oral Mucosa for The Treatment of Inflammatory Mucosal Diseases. Ph.D. Thesis, University of Sheffield, Sheffield, United Kingdom, 2018.

83. Marxen, E.; Axelsen, M. C.; Pedersen, A. M. L.; Jacobsen, J. *Int. J. Pharm.* **2016,** *511,* 599–605. doi:10.1016/j.ijpharm.2016.07.014
84. Sannomiya, E.; Furukawa, S. *Rev. Bras. Odontol.* **2000,** *57,* 336–338.
85. Berbicz, F.; Nogueira, A. C.; Neto, A. M.; Natali, M. R. M.; Baesso, M. L.; Matioli, G. *Eur. J. Pharm. Biopharm.* **2011,** *79,* 449–457. doi:10.1016/j.ejpb.2011.03.026
86. Crivello, J. V.; Bulut, U. *J. Polym. Sci., Part A: Polym. Chem.* **2005,** *43,* 5217–5231. doi:10.1002/pola.21017
87. de Campos, P. S.; Matte, B. F.; Diel, L. F.; Jesus, L. H.; Bernardi, L.; Alves, A. M.; Rados, P. V.; Lamers, M. L. *Phytother. Res.* **2017,** *31,* 1433–1440. doi:10.1002/ptr.5872
88. Calori, I. R.; Pellosi, D. S.; Vanzin, D.; Cesar, G. B.; Pereira, P. C. S.; Politi, M. J.; Hioka, N.; Caetano, W. *J. Braz. Chem. Soc.* **2016,** *27,* 1938–1948. doi:10.5935/0103-5053.20160079
89. Mondal, S.; Ghosh, S. *J. Photochem. Photobiol., B* **2012,** *115,* 9–15. doi:10.1016/j.jphotobiol.2012.06.004
90. Braga, G. *Propriedades Físico Químicas Do Fenotiazínico Azul de Ortotoluidina Em Sistemas Homogêneos e Copolímericos de P-123 e F-127;* Universidade Estadual de Maringá, 2014.
91. Gerola, A. P.; de Morais, F. A. P.; Costa, P. F. A.; Kimura, E.; Caetano, W.; Hioka, N. *Spectrochim. Acta, Part A* **2017,** *173,* 213–221. doi:10.1016/j.saa.2016.09.019
92. Gerola, A. P.; Silva, D. C.; Jesus, S.; Carvalho, R. A.; Rubira, A. F.; Muniz, E. C.; Borges, O.; Valente, A. J. M. *RSC Adv.* **2015,** *5,* 94519–94533. doi:10.1039/c5ra14331d
93. Wenceslau, A. C.; Ferreira, G. L. Q. C.; Hioka, N.; Caetano, W. *J. Porphyrins Phthalocyanines* **2015,** *19,* 1168–1176. doi:10.1142/s1088424615500996
94. Pereira, C. I. D. *Estudo Das Propriedades Físico-Químicas Da Molecula de Curcumina Frente a Sistemas Organizados Biomiméticos (Sistemas Micelares);* Universidade Estadual de Maringá, 2015.
95. de Freitas, C. F.; Pellosi, D. S.; Estevão, B. M.; Calori, I. R.; Tsubone, T. M.; Politi, M. J.; Caetano, W.; Hioka, N. *Photochem. Photobiol.* **2016,** *92,* 790–799. doi:10.1111/php.12645
96. de Alcântara Sica de Toledo, L.; Rosseto, H. C.; dos Santos, R. S.; Spizzo, F.; Del Bianco, L.; Montanha, M. C.; Esposito, E.; Kimura, E.; Bonfim-Mendonça, P. d. S.; Svidzinski, T. I. E.; Cortesi, R.; Bruschi, M. L. *AAPS PharmSciTech* **2018,** *19,* 3258–3271. doi:10.1208/s12249-018-1163-4
97. Hemphill, T.; Campos, W.; Pilehvari, A. *Oil Gas J.* **1993,** *91,* 45–50.
98. Andrews, G. P.; Jones, D. S. *Biomacromolecules* **2006,** *7,* 899–906. doi:10.1021/bm050620y
99. Edsman, K.; Carlfors, J.; Petersson, R. *Eur. J. Pharm. Sci.* **1998,** *6,* 105–112. doi:10.1016/s0928-0987(97)00075-4
100. Jones, D. S.; Woolfson, A. D.; Djokic, J. *J. Appl. Polym. Sci.* **1996,** *61,* 2229–2234. doi:10.1002/(sici)1097-4628(19960919)61:12<2229::aid-app24>3.3.co;2-8
101. Borghi-Pangoni, F. B.; Junqueira, M. V.; de Souza Ferreira, S. B.; Silva, L. L.; Rabello, B. R.; Caetano, W.; Diniz, A.; Bruschi, M. L. *Pharm. Res.* **2016,** *33,* 776–791. doi:10.1007/s11095-015-1826-8
102. Zhang, Y.; Huo, M.; Zhou, J.; Zou, A.; Li, W.; Yao, C.; Xie, S. *AAPS J.* **2010,** *12,* 263–271. doi:10.1208/s12248-010-9185-1
103. Pierre, M. B. R.; Lopez, R. F. V.; Bentley, M. V. L. B. *Braz. J. Pharm. Sci.* **2009,** *45,* 109–116. doi:10.1590/s1984-82502009000100013
104. Rossetti, F. C.; Lopes, L. B.; Carollo, A. R. H.; Thomazini, J. A.; Tedesco, A. C.; Bentley, M. V. L. B. *J. Controlled Release* **2011,** *155,* 400–408. doi:10.1016/j.jconrel.2011.06.034
105. Giovannacci, I.; Magnoni, C.; Vescovi, P.; Painelli, A.; Tarentini, E.; Meleti, M. *Arch. Oral Biol.* **2019,** *105,* 89–98. doi:10.1016/j.archoralbio.2019.07.001
106. Brown, S. M.; Baesso, M. L.; Shen, J.; Snook, R. D. *Anal. Chim. Acta* **1993,** *282,* 711–719. doi:10.1016/0003-2670(93)80136-9
107. Rosencwaig, A. *Annu. Rev. Biophys. Bioeng.* **1980,** *9,* 31–54. doi:10.1146/annurev.bb.09.060180.000335
108. Ames, F. Q.; Sato, F.; de Castro, L. V.; de Arruda, L. L. M.; da Rocha, B. A.; Cuman, R. K. N.; Baesso, M. L.; Bersani-Amado, C. A. *J. Biomed. Opt.* **2017,** *22,* 055003. doi:10.1117/1.jbo.22.5.055003

License and Terms

BEILSTEIN JOURNAL OF NANOTECHNOLOGY

Internalization mechanisms of cell-penetrating peptides

Ivana Ruseska and Andreas Zimmer*

Review

Open Access

Address:
Institute of Pharmaceutical Sciences, Department of Pharmaceutical Technology and Biopharmacy, University of Graz, 8010 Graz, Austria

Email:
Andreas Zimmer* - andreas.zimmer@uni-graz.at

* Corresponding author

Keywords:
cell-penetrating peptides; direct translocation; drug delivery; endocytosis; internalization

Beilstein J. Nanotechnol. **2020,** *11,* 101–123.
doi:10.3762/bjnano.11.10

Received: 26 June 2019
Accepted: 18 December 2019
Published: 09 January 2020

This article is part of the thematic issue "Frontiers in pharmaceutical nanotechnology".

Guest Editor: M. G. Wacker

Abstract

In today's modern era of medicine, macromolecular compounds such as proteins, peptides and nucleic acids are dethroning small molecules as leading therapeutics. Given their immense potential, they are highly sought after. However, their application is limited mostly due to their poor in vivo stability, limited cellular uptake and insufficient target specificity. Cell-penetrating peptides (CPPs) represent a major breakthrough for the transport of macromolecules. They have been shown to successfully deliver proteins, peptides, siRNAs and pDNA in different cell types. In general, CPPs are basic peptides with a positive charge at physiological pH. They are able to translocate membranes and gain entry to the cell interior. Nevertheless, the mechanism they use to enter cells still remains an unsolved piece of the puzzle. Endocytosis and direct penetration have been suggested as the two major mechanisms used for internalization, however, it is not all black and white in the nanoworld. Studies have shown that several CPPs are able to induce and shift between different uptake mechanisms depending on their concentration, cargo or the cell line used. This review will focus on the major internalization pathways CPPs exploit, their characteristics and regulation, as well as some of the factors that influence the cellular uptake mechanism.

Introduction

The cell membrane is a semipermeable barrier, serving as a protective layer for the cells. It is an essential organelle for cell survival and function. As a barrier, it only allows the transport of compounds with small molecular size, which can be transported using channels and specific carriers [1,2]. Macromolecules, however, are unable to use these modes of entry [2].

The production of novel therapeutic molecules, which do not adhere to the "canonical" rules defining what a drug molecule should be like, has been accelerated these days. One part of this new group are proteins, peptides and nucleic acids, all developed with one thing in mind – bypassing the limitations of conventional therapeutics [3]. The novelty of these macromo-

lecular compounds lies in their ability to target specific molecules and biological pathways, and thus, modulate molecular activities in a positive or negative manner [4]. The outstanding possibilities offered by the use of such molecules (proteins, peptides and nucleic acids) in the diagnostics and treatment of a number of diseases render them exceptionally attractive. Nonetheless, there are some obstacles that need to be overcome, such as the limited cellular uptake and low target specificity of these molecules. In order to do so, we are in great need for new delivery and administration strategies.

Thus far, a plethora of cellular translocation techniques have been developed – either using biophysical methods (such as microinjection, electroporation and magnetofection), biochemical methods (for example, the use of amphipathic detergents) and viral vectors [5]. However, no matter how effective, these methods have shown to cause cytotoxic effects, and when it comes to viral vectors, a high probability of viral gene insertion into the host genome exists [6]. Therefore, the delivery strategy for macromolecules is still left as an unanswered question. In the best case scenario, an efficient delivery system would provide enzymatic protection and stability for the drug, an improved distribution and target specificity, as well as a lack of toxicity [3].

Cell-penetrating peptides as drug delivery systems

Having in mind the attention they have gained, cell-penetrating peptides (CPPs) have become a current hotspot in medical research [7]. Compared to the other translocation techniques mentioned, CPPs are capable of entering the cells in a noninvasive manner, they do not destroy the integrity of the cellular membranes and are considered highly efficient and safe. Thus, they provide new avenues for research and applications in life sciences [8]. In general, CPPs can be defined as diverse peptides with a maximal length of 30 amino acids. They are characterized by a high content of basic amino acids and an overall positive charge. CPPs are known to have a high rate of permeation into cells and are able to cross membranes of different cell types, while showing low cytotoxicity and no immunological response [6].

This class of peptides was first introduced in the late 1980s, with the discovery of the TAT peptide, encoded by the human immunodeficiency virus type 1 (HIV-1) by Frankel et al. [9], who showed that the TAT peptide could enter cells and translocate into the nucleus. The following decade unfolded with the discovery of the neuronal cell internalization of penetratin, the first ever CPP. Penetratin was derived from the third helix of the homeodomain of *Drosophila antennapedia*. This discovery was closely followed by the development of two peptides used for the noncovalent delivery of proteins and peptides, MPG and Pep-1 [10]. Today, we have a myriad of CPPs and databases which allow one to browse existing CPPs based on chemical modifications, category, cargo or peptide lengths [6].

Classification of cell penetrating peptides

CPPs are currently classified in several ways, depending on their individual properties. Table 1 presents a short overview of some of the most commonly used CPPs, listing their amino acid sequence and properties. In this review, only a short outlook of their classification will be given. For more detailed information about the classification of CPPs, reviews are listed in references [5,7,11].

Based on the interaction between the CPP and the therapeutic agent, two main classes of peptides can be distinguished. The first class includes CPPs which form a covalent conjugate with the cargo by chemical cross-linking or by cloning, followed by the expression of a CPP fusion protein. Such interactions have been seen in several CPPs such as TAT derivatives, penetratin or polyarginines [10]. It seems that covalent modification is most suitable for charge-neutral oligonucleotides such as peptide nucleic acids (PNAs) and phosphorodiamidate morpholino oligonucleotides (PMOs) [3,12]. Concerning charged molecules such as siRNA or miRNA, the covalent

Table 1: Overview of some the most commonly used CPPs describing their sequence, class and charge.

Name	Amino acid sequence	CPP class	Charge	Ref.
TAT	YGRKKRRQRRR	cationic	8	[9]
penetratin	RQIKIWFQNRRMK WKK	cationic	7	[24]
R9	RRRRRRRRR	cationic	9	[67]
MPG	GALFLGWLGAAGSTMGAPKKKRKV	amphipathic	24	[31]
Pep-1	KETWWETWWTEWSQPKKRKV	amphipathic	2	[30]
transportan-10	AGYLLGKINLKALAALAKKIL-amide	amphipathic	4	[5]
PepFect6	stearyl-AGYLLGK(ε-TMQ)INLKALAALAKKIL	amphipathic	10	[20]
Bac7	RRIRPRPPRLPRPRPRPLPFPRPG	proline-rich	9	[7]

conjugation leads to restricted biological activity, most likely due to the steric hindrance caused by the covalently-linked CPP, which is an obstacle for the incorporation of siRNA/miRNA into the RISC complex. Because of this, the siRNA/miRNA molecule cannot be loaded into the complex and manifest its effect [13].

Regarding covalent strategies of cargo-attachment, there is a great promise in biorthogonal chemistry, which allows for the design of efficient conjugation reactions even in a complex biological environment [14-16]. Provided that a cleavable covalent bond is achieved, the charged molecule could be released in the cytoplasm and exert its effect. Thus, a bond such as the disulfide one, could be the Holy Grail in covalent CPP-siRNA/miRNA delivery [17]. It has been reported that CPP-siRNA conjugates have reduced transient and stable expression of reporter transgenes in a number of mammalian cell lines [18]. In this case, thiol-containing siRNAs were synthesized and conjugated to penetratin or transportan by a reducible disulfide bond, and there was no change in the structure or activity of the siRNA molecule. Another report for a successful disulfide link between the TAT peptide and siRNA comes from Chiu and co-workers [19]. The stable complex was able to achieve the localization of the siRNA in specific cytoplasmic compartments in the perinuclear region. Andaloussi et al. also developed a stable CPP-siRNA system, derived from transportan-10, containing a proton-acceptor moiety and a stearyl group (for lipophilic interaction), called PepFect6. This system has shown to promote siRNA delivery to difficult-to-transfect cells [20].

The second class within this classification scheme is formed by CPPs which noncovalently complex their cargo. They occur mostly as amphipathic peptides, consisting of a hydrophilic and a hydrophobic domain. Pep-1 and MPG are amphipathic peptides which are reported to form stable, noncovalent complexes with cargo molecules through electrostatic interaction. Pep-1 has successfully been used to deliver small peptides and proteins into cells, while MPG has shown to efficiently deliver small interfering RNA (siRNA) into cultured cell lines [3,10].

The interplay between hydrophilic and hydrophobic amino acids in the sequence of CPPs as well as their length give rise to the second type of classification. According to these properties, CPPs can be regarded as primary or secondary amphipathic or nonamphipathic peptides. Primary amphipathic peptides contain typically more than 20 amino acids and have sequentially hydrophilic and hydrophobic amino acids in their primary structure [5,21]. This group includes MPG, penetratin, CADY, pVec, and other peptides. Secondary amphipathic peptides commonly have less than 20 amino acids in their sequence and are able to take their α-helix or β-sheet conformation after interaction with phospholipid membranes [5]. Secondary α-helical CPPs have a highly hydrophobic patch on one face, whereas the other face can be cationic, anionic or polar. Amphipathic β-sheet CPPs are based on one hydrophobic and one hydrophilic stretch of amino acids exposed to the solvent. A class of secondary amphipathic CPPs are the proline-rich peptides [7]. Nonamphipathic peptides are rather short peptides, such as HIV-TAT, which have a high content of positively charged amino acids such as arginine or lysine. Studies suggest that at least eight positive charges are necessary for efficient uptake to occur [7].

Cellular uptake of CPPs

Over 30 years of the discovery of CPPs have passed, and their internalization mechanism remains yet to be deciphered. Although their uptake has been reported in a wide variety of cell types and in combination with different cargoes, the exact entry path still remains a question. It is of crucial importance for the overall safety and efficacy assessment that the internalization behavior of CPPs is evaluated. Furthermore, knowledge of the uptake mechanism can be essential for the development of CPP-delivery systems with cell-specificity and low toxicity.

The complexity in resolving this matter arises from the intrinsic properties of the peptides, such as their charge distribution and length. These characteristics allow them to interact with numerous cell surface molecules, which can influence the choice of an entrance path in a great manner [7]. The above mentioned factors, just a few out of many, guide the internalization paths of CPPs to two major routes: endocytosis (active or energy-dependent uptake) and membrane translocation (direct/passive or energy-independent uptake). Overall, the type of uptake which will be selected mainly depends on the physicochemical properties of the peptide and the cargo as well as the concentration applied, in combination with the structural properties of the plasma membrane. As an example, nowadays it is well established that at physiological conditions and low peptide concentration endocytosis prevails, while when a peptide is applied at higher amounts, it translocates the plasma membrane directly. A deviation from this rule is penetratin, which at low concentration passes the membrane in an energy-independent manner, while at higher concentration, it switches to endocytosis [22]. Thus, the challenge which remains, from a therapeutic point of view, is to recognize and point out the uptake route which produces a relevant biological response.

Despite the deciphering of the uptake mechanism of CPPs being a work in progress, it is still not a scheme which should be build up from scratch. A “core” consensus exists, according to which the initial step toward CPPs’ uptake is the interaction with cell

surface proteoglycans, via electrostatic forces. Additionally, interactions with several membrane proteins have been described as well [7]. The following parts will focus on the major internalization paths CPPs exploit, as well as the parameters which have a major impact on the selection of uptake mechanism. Furthermore, the recent advances in the knowledge of the uptake mechanisms used by the most prominent CPPs are discussed. Figure 1 gives an overview of the active and passive uptake mechanisms CPPs use to enter cells.

Review

Direct translocation through the cell membrane

The direct translocation of CPPs through the cell membrane as an energy-independent mechanism and an alternative to endocytosis was suggested after internalization of CPPs was observed at low temperature [23]. As a process which requires no energy, direct translocation is regarded as a single-step process including mechanisms involving the formation of inverted micelles, pores and the 'carpet' model [21]. This process can be tested under specific experimental conditions – low temperature, energy depletion and the use of endocytic inhibitors for instance. In general, direct translocation requires the interaction of positively charged CPPs with negatively charged components of the cellular membrane such as the phospholipid bilayer, which then leads to the CPP entrance [6]. Furthermore, direct translocation requires permanent or temporary destabilization of the membrane for internalization to occur. It is generally accepted that direct translocation occurs at high CPP concentration and is most probable for primary amphipathic CPPs such as transportan analogues and MPG [1].

Inverted micelle formation

Direct translocation via the formation of inverted micelles was initially reported for penetratin as a mechanism involved at the early stages of cellular uptake [24]. Penetratin is a protein transduction domain derived from the homeoprotein Antennapeadia. It is one of the first peptides described that was able to successfully carry active molecules into cells and is one of the most studied CPPs thus far [25].

The first step in the internalization process is the formation of electrostatic interaction between the peptide and the cellular membrane, which affects the lipid supramolecular organization. This process may lead to changes in the membrane curvature [26]. Such membrane curvatures or invaginations can lead to the formation of inverted micelles that entrap the peptide. The hydrophilic environment inside the inverted micelle allows

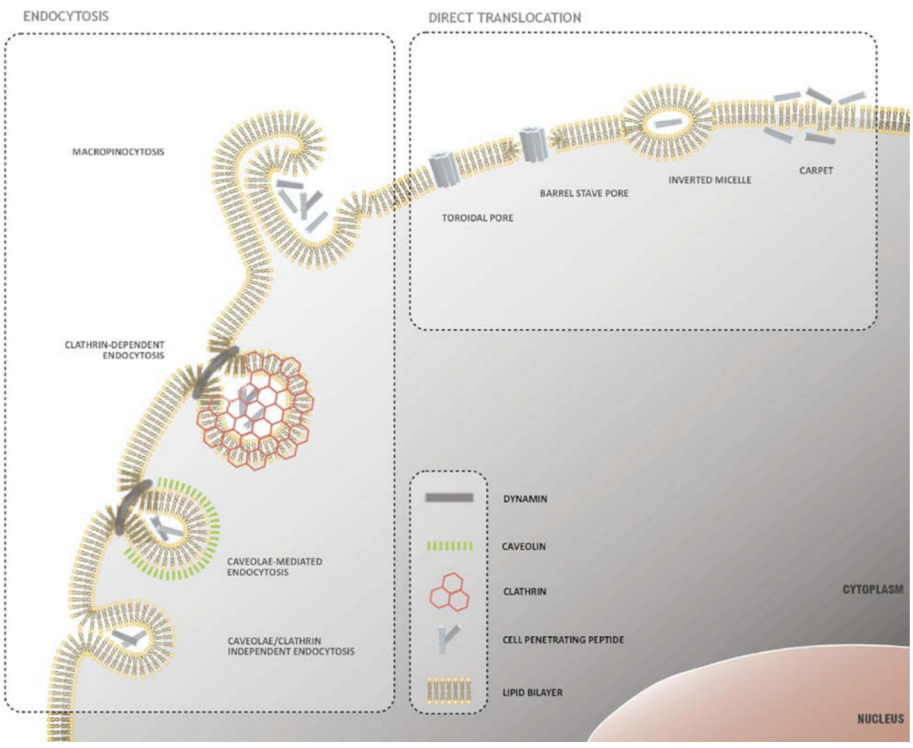

Figure 1: Mechanisms of CPP uptake. Two main mechanisms have been proposed: direct translocation through the cellular membrane, which requires no energy, and endocytosis, an energy-dependent process. Reprinted from [23], copyright Trabulo et al., 2010. CC-BY 3.0 (https://creativecommons.org/licenses/by/3.0/).

accumulation of the peptide and is favorable for the transport of hydrophilic compounds conjugated to the peptide. Subsequently, the micelle is destabilized and the peptide–cargo complex is released in the cytoplasm. However, recent data suggest that penetratin internalization occurs via direct translocation or endocytosis depending on the penetratin concentration.

Direct translocation via pore formation

In analogy to the inverted micelle formation model, the membrane perturbation observed during internalization of peptides led to the proposition of alternative uptake mechanisms. Direct translocation via pore formation includes two different models, the 'barrel-stave' model and the 'toroidal' model.

The 'barrel-stave' model is characteristic of amphipathic α-helical peptides. These peptides form bundles after interacting with the cellular membrane, which have channels in their centers. The pore is formed by the inwardly facing hydrophilic surfaces and the interaction between the outwardly facing hydrophobic residues with the lipid membrane [27].

On the other hand, the 'toroidal' model applies for peptides which are able to form α-helices when they come in touch with cellular membranes. According to this model, the interaction between the positive side chains of the peptide and the phosphate groups leads to the accumulation of the peptide on the outer leaflet of the membrane [28]. The peptides then cause bending of the lipid monolayer into the interior, forming a hydrophilic gap in the membrane, in which phospholipid heads and peptides are found.

The transient pore formation models are in general proposed as mechanisms used by primary amphipathic peptides [1]. The Pep-family of peptides belongs to the group of primary amphipathic peptides. The leader peptide, Pep-1, is a short peptide which efficiently promotes the delivery and cellular localization of a variety of peptides, proteins and antibodies in a broad spectrum of cell lines. It has a length of 21 amino acids and consists of three domains, each conferring a specific function: (i) a hydrophobic, tryptophan-rich sequence required for the interaction with macromolecules and cell-membrane targeting, (ii) a hydrophilic sequence, rich in lysine, derived from the nuclear localization sequence (NLS) of SV-40 large T antigen, necessary for improving the solubility and the intracellular localization of the peptide and (iii) a spacer domain, which improves the flexibility. It has been reported by Deshayes et al. [29] that the internalization of Pep-1 occurs via transient pore formation depending on the formation of α-helices.

Pep-1 internalization has been claimed to be independent of the endosomal pathway, which results in limited degradation of the peptide and its cargo inside the cells as well as rapid release of the cargo as soon as the cell membrane has been crossed. It was demonstrated that the free form of Pep-1 interacts strongly with the lipid components in the membrane, leading to a conformational change – the peptide tends to form α-helices. The conformational transitions have been confirmed by CD, NMR and FTIR data. The helical structure that Pep-1 obtains when interacting with the cell membrane favors its insertion into the membrane by forming a transient, transmembrane pore-like structure. Helical folding has also been observed for Pep-1/cargo complexes, suggesting that the cargo does not affect the peptide uptake process [30]. Membrane perturbation as an internalization mechanism has also been proposed for the MPG-family of amphipathic peptides (Figure 2) [3,17,31].

MPG carriers are amphipathic peptides able to form stable complexes with antisense oligonucleotides, plasmid DNA, siRNA

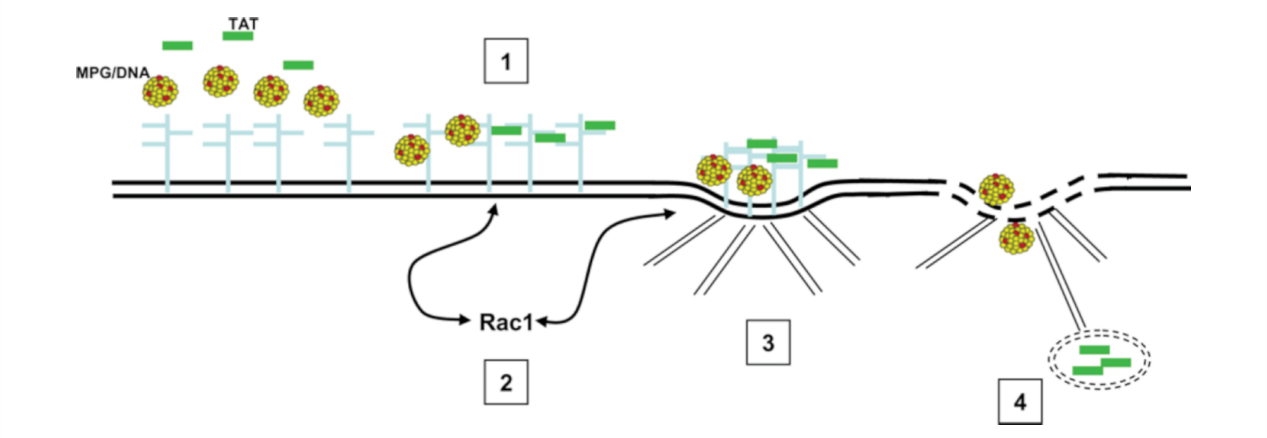

Figure 2: Model for the initial step of cellular uptake of MPG or MPG/cargo complexes. (1) Binding of MPG or MPG/cargo to the extracellular matrix via the proteoglycan platform; (2) clustering of glycosaminoglycans (GAGs), which in turn activates the Rac1 GTPase; (3) actin network remodeling; (4) increase of membrane fluidity, promoting MPG uptake. Reprinted with permission from [32], copyright 2007 The Royal Society of Chemistry.

and peptides, which improve their stability and cellular uptake. MPG bears three domains: (i) a hydrophobic domain derived from the fusion domain of HIV-1 gp41, (ii) a lysine-rich nuclear localization sequence (NLS) derived from SV-40 large T antigen with five positive charges and (iii) a spacer sequence. Studies performed at low temperature with several inhibitors present, which interfere with the endosomal pathway, have suggested that the uptake of MPG and MPG-cargo complexes does not involve endocytosis. Most likely, MPG internalization is associated with the ability of the peptide to interact with lipids and induce membrane destabilization rather than with active uptake [32].

Studies on the conformational states of MPG and its ability to interact with phospholipids demonstrate that MPG undergoes a transition from unordered into a folded state upon interaction with lipids. What is interesting here is that the new conformational state of MPG is a β-sheet, which differs from the helices that Pep-1 forms, although the two peptides have only slight differences in their structure. Furthermore, MPG folds into β-sheets upon interaction with its cargo, an action that leads to a more pronounced β-sheet folding induced by the phospholipids. This new conformational state eases the formation of transient pore-like structures in the membrane, which leads to the translocation of the MPG/cargo complexes [33].

MPG also shows an inherent ability to induce membrane permeability, whether associated with cargo or not. This process might be due to the actin remodeling allowed by the GTPase Rac 1, a regulatory molecule activated by electrostatic interaction between MPG and GAGs in the extracellular matrix. The two aforementioned actions might constitute the 'onset' of the internalization mechanism and have a part in the impact of MPG on membrane fluidity and permeability [32].

Carpet model

The 'carpet' model describing the direct penetration of some peptides was proposed in 1992 by Pouny and co-workers [34]. According to this model, the positively charged segments of the peptide lie parallel to the membrane surface and are bound to the acidic phospholipid headgroups. The peptides self-associate in a 'carpet'-like manner. It is postulated that the hydrophobic sites are embedded in the lipid region of the membrane, while the hydrophilic parts orient towards the hydrophilic region, which in turn causes structural reorganization and internalization of the CPP. Since the hydrophobic interaction is necessary for this model, it seems unlikely that it is being used for the internalization of strongly cationic peptides such as TAT. According to this, it is logical that this mechanism was first proposed for dermaseptin, which is an antimicrobial, amphipathic peptide. Electrostatic interaction is essential for the binding between the CPP and the membrane. Achieving a high local concentration at the membrane's surface is also a key factor for inducing membrane penetration by this model [35].

An alternative to the 'carpet' model is the 'membrane-thinning' effect, which was first proposed for maganin. Maganin is an amphipathic peptide, composed of 23 residues, which exhibits a broad-spectrum of antimicrobial activity. This model is characterized by a 'carpet' formation followed by a perturbation resulting from the interaction of the negatively charged lipids in the outer leaflet in the membrane and the cationic groups of the CPP. This causes a lateral rearrangement of the negative charges and a thinning of the membrane. The aggregation of the CPPs at the membrane surface provokes a reduction of the local surface tension and allows for intercalation of the CPP within the membrane. After the internalization of the peptide, the membrane reseals [36,37].

Direct translocation mechanisms used by arginine-rich peptides

The debate regarding the internalization of cationic, arginine-rich peptides, has been long going, and still, the exact mechanism remains to be understood. Initial studies indicated a direct translocation across the cellular membrane that bypassed endocytosis and the involvement of specific receptors. Indeed, cationic CPPs were shown to traverse membranes at low temperature and in the presence of metabolic or endocytic inhibitors. However, in 2003, Richard et al. [38] showed that the results obtained might be a misconception due to the use of fixed cells. They postulated that the fixatives could change the intracellular distribution of the peptides. Additionally, it was shown that flow cytometry (a method frequently used for internalization studies) could not distinguish between peptides that are bound to the membrane and those inside the cell. What is more, experiments using living cells showed that the majority of the CPPs is associated with the outer leaflet of the cell membrane. This evidence led to the conclusion that an energy-dependent process is the major route for the internalization of CPPs.

Nonetheless, novel studies on living cells show that the uptake of arginine-rich peptides could be a combination of both direct translocation and endocytosis. What supports this hypothesis is the mixture of punctate and diffuse staining observed using confocal microscopy [39,40]. It is assumed that the punctate staining indicates endocytic uptake, while the diffuse staining is correlated with direct translocation. The switch between different uptake mechanisms might be concentration-dependent. It has been shown that at low concentration, arginine-rich CPPs are mainly endocytosed, whereas rapid cytoplasmic entry occurred at higher concentration [41]. The latter is associated

with the accumulation of the peptide at certain membrane areas called nucleation zones [42]. New findings of these type could further broaden what is already a very wide horizon in the field of CPP research – their internalization mechanism.

The first mechanism explaining the direct penetration of arginine-rich peptides exploits the importance of guanidine groups. This concept was first proposed by Sakai et al. [43], who showed that oligo-arginines could be partitioned into lipid phases from the aqueous phase in the presence of phosphatidylglycerol, a behavior of arginine often referred to as "arginine magic". The guanidine group found on arginine has proven to form bidentate hydrogen bonds and electrostatic interaction with sulfate, phosphate and carboxylate moieties, all of which can be found on cell surface components. It is thought that the formation of these hydrophobic counterion complexes promotes the accumulation of CPPs on the cell surface and leads to their internalization. However, upon membrane translocation, the peptide backbone has to cross the lipid core. It is assumed that there is hydrophobic interaction between the less hydrophilic peptide backbone and the lipid core involved in this process. The aforementioned translocation processes have been observed for octa-arginine (R8) and the HIV TAT peptide [44].

Studies conducted on the internalization of dodeca-arginine (R12) in HeLa cells, however, suggest a different uptake behavior. Hirose et al. [45] suggest the formation of "particle-like" structures during the interaction and uptake of poly-arginines. The "particles" form simultaneously and have a diameter of 1–3 μm. It is suggested that both membrane components and R12 are involved in the formation of these "particles". Furthermore, their formation as well as the peptide uptake occur at low temperature (4 °C) in the first 10–20 min of incubation. The authors suggest that the membrane-peptide particle-like structures lead to membrane inversion, which they proved by detecting phosphatidylserine on the cell surface using annexin V. The formation of particle-like aggregates was also reported by Ziegler et al. [46], who investigated the uptake of fluorescently labeled HIV TAT in fibroblasts.

The third mechanism used by the arginine-rich peptides to directly cross the cellular membranes involves the formation of pores. A theoretical model using molecular dynamics simulations was proposed for the translocation of the TAT peptide, which explains the relevance of peptide–phosphate interaction during the pore formation [47]. This theoretical model was later proven experimentally in osteosarcoma and human smooth muscle cells [48]. According to the proposed model, when a concentration threshold is achieved on one of the membrane leaflets, the TAT peptides are attracted to the phosphate groups on the other leaflet. The peptides act cooperatively to facilitate translocation. As a higher TAT concentration is reached, phosphate groups from neighboring phospholipids are drawn to the peptide due to the opposite electrical charge. This process divides the membrane into regions rich in TAT and phosphate groups and into uncharged regions and leads to membrane thinning. TAT forms "complexes" with the phospholipids, due to the interaction between the arginine and lysine side chains with the negatively charged phosphate groups, which then start penetrating the membrane. Simultaneously, water molecules penetrate and solvate the charged groups. With time, the effect of the water molecules results in a transient water pore. Carrying along the attached phospholipids, TAT moves smoothly onto the pore walls and crosses the membrane [47]. Pore formation and translocation can be achieved only after a certain number of peptides is introduced to the membrane surface [49]. A theoretical model for membrane translocation by the formation of water pores has been suggested for hexa-arginine as well [50].

Endocytosis as an active pathway for CPP uptake

The transport of essential small molecules such as amino acids, sugars and ions occurs through the action of integral membrane protein pumps and channels. Macromolecules, however, require a different machinery in order to traverse the cellular membrane, which usually needs energy. Endocytosis is the active process in which macromolecules are carried into the cell in vesicles or vacuoles pinched-off of the plasma membrane and involves two distinct steps: endocytic uptake followed by endosomal escape [51].

Endocytosis is a complex process composed of more than one mechanism and is generally divided into two categories: phagocytosis and pinocytosis. Phagocytosis involves the uptake of large particles and is restricted to specialized cells (macrophages, monocytes and neutrophils). Pinocytosis, on the other hand, involves the uptake of fluids and solutes and occurs in all cells. At least four different mechanisms have been described for pinocytosis: macropinocytosis, clathrin-mediated endocytosis (CME), caveolae-mediated endocytosis (CvME) and clathrin- and caveolae-independent endocytosis (Figure 3) [52].

All of the endocytic mechanisms described depend on distinct components and mechanisms. To some extent, the choice of pathway can be determined by the cell types and their state of differentiation. However, when it comes to the internalization of nanocarriers such as CPPs, their physicochemical properties and surface reactivates are also important [54].

It is now generally recognized that CPPs at low concentration, and when conjugated to cargo, are taken up by cells in an energy-dependent manner. Endocytosis as a mechanism for the

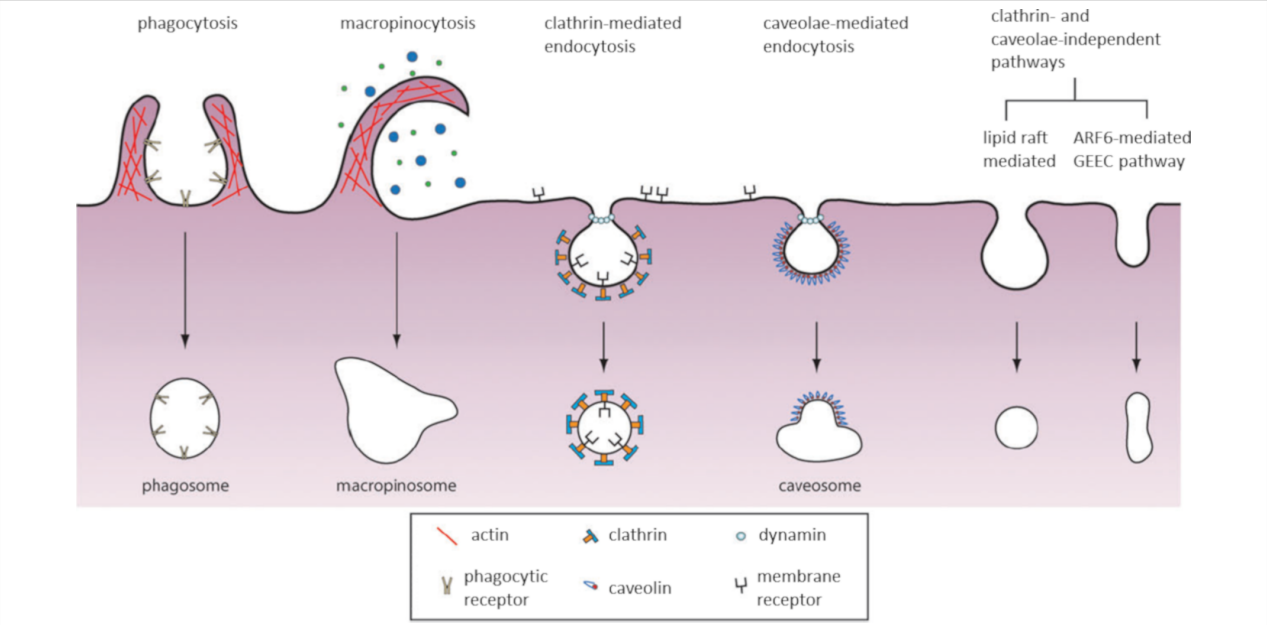

Figure 3: Mechanisms of endocytic entry into the cell. Reprinted with permission from [53], copyright 2011 The Royal Society of Chemistry.

transport of CPPs across cellular membranes was suggested in 2003, after Richard et al. [38] pointed to the possible errors in the results describing direct translocation due to the experimental methods used. Since this initial report, studies which described the active transport of CPPs emerged. Most of the older studies conducted on this matter as well as more recent ones suggest macropinocytosis as the main entry path for CPPs into cells [55-59]. Table 2 summarizes the endocytic mechanisms used by each CPP conjugate mentioned in the following text.

Macropinocytosis as an entry mechanism

Macropinocytosis is a rapid, lipid raft-dependent and receptor-independent form of endocytosis [60]. It is a process accompanying the membrane ruffling induced in many cell types upon stimulation by growth factors or other signals. Macropinocytosis involves an actin-driven membrane protrusion that results in an increase in fluid-phase uptake [61]. These protrusions do not 'envelop' a ligand-coated particle, but instead they collapse onto and fuse with the plasma membrane to generate large endocytic vesicles called macropinosomes [52].

Although macropinocytosis was initially thought to be a nonregulated process, it is now known that this uptake process is a highly organized one. Macropinocytosis consists of quite a few signaling events which involve the remodeling of the cytoskeleton. Most of the macropinocytosis regulators belong to the group of kinases (such as Src, PI3) and GTPases (Rho family, Ras family, Rab proteins), which trigger the actin-driven formation of membrane protrusions [62-64].

Table 2: Summary of the endocytic mechanisms used by CPP–cargo conjugates.

Macropinocytosis	Clathrin-mediated endocytosis (CME)	Caveolae-mediated endocytosis (CvME)	Clathrin- and caveolae-independent endocytosis
TAT-protein conjugates [60]	unconjugated TAT [83]	TAT-protein conjugates [92,93]	p18 and p28 azurin fragments [98,99]
poly-arginines [65-67]	MPG/siRNA conjugate [84,85]	proline-rich CPPs [94]	transportan [95]
NickFect51 [77]	NickFect51-cargo conjugates [77]	transportan-10-protein conjugates [95]	low molecular weight protamine (LMWP)/siRNA conjugate [104]
	octa-arginine (R8) [44]	PepFect14/DNA conjugate [97]	
		p18 and p28 azurin fragments [98,99]	
		CVP1 [100]	

As mentioned above, macropinocytosis normally occurs in response to stimulation by growth factors such as the macrophage colony-stimulating factor-1 (CSF-1), the epidermal growth factor (EGF) and the platelet-derived growth factor or tumor-promoting factors [63]. However, this mechanism provides an effective path for drug delivery. It has been described as the pathway used to deliver arginine-rich CPPs such as octa-arginine and TAT peptides into cells.

Kaplan et al. investigated the internalization of the TAT peptide in living cells [56]. The active uptake of TAT was established after experiments were conducted at low temperature, at which all molecular movement in the cell membrane is essentially arrested. After exposing the cells to β-cyclodextrin (which depletes cell surface associated cholesterol) and macropinocytosis-specific inhibitors (such as cytochalasin D, an inhibitor of F-actin or EIPA, an inhibitor or the Na^+/H^+ exchange), a dose-dependent reduction of the internalized peptide was observed, which led to the conclusion that TAT transduction into cells occurs by lipid raft mediated endocytosis. Similar results regarding the internalization mechanism of TAT-protein conjugates were reported by Wadia and co-workers [60].

Macropinocytosis has also been suggested as the active uptake process used by other cationic, arginine-rich peptides. Studies conveyed on the internalization of octa-arginine (R8) peptide in HeLa cells showed that the uptake was significantly suppressed by the macropinocytosis inhibitors EIPA and cytochalasin D. In accordance with these results, it was also observed that octa-arginine treatment caused significant rearrangement of the actin cytoskeleton, a process that seems to be crucial for macropinocytosis [55]. Nona-arginine (R9), dodeca-arginine (R12) as well as Flock-House-Virus-derived peptide, also lead to cell internalization via macropinocytosis [65-67]. Furthermore, it is possible that dodeca-arginine acts as a potential target for CXCR4, which is a chemokine receptor that induces macropinocytosis [66].

Recently, a great amount of effort has been put into deciphering the interaction of CPPs with the extracellular matrix as well as with membrane components, which cause the actin rearrangement and lead to the internalization of peptides. The role of glycosaminoglycans in the initial contacts of CPPs and cells and in the initiation of internalization has been a part of several reviews so far [3,27,28,68,69].

The extensive research done on arginine-rich peptides, especially octa-arginine (R8) by Nakase et al. [55], sheds some light on the interaction that leads to macropinocytosis. Their initial studies showed that oligo-arginines as well as TAT provoke actin rearrangement in the initial moments of interaction with cell membranes. The ruffling which was caused by the peptides was similar to the one caused by the interaction of VEGF and its receptor, VEGFR. This led to the suggestion that there are sequence similarities between the basic, arginine-rich domains in CPPs and the growth factors that are known to provoke macropinocytosis. Further research focusing on the importance of the membrane-associated proteoglycans heparan sulfate proteoglycan (HSPG) showed that HSPG was necessary for the uptake of R8, and even more interestingly, it was essential for the uptake of TAT. The observed difference might be due to the higher positive charge of R8 that allows the peptide to interact with more proteoglycans rather than just HSPG. This would suggest that HSPG might be a primary receptor for the cellular uptake of some cationic peptides [61,70].

Syndecans, single transmembrane domain proteins which act as co-receptors for G protein-coupled receptors, have also been proposed to have part in the initiation of macropinocytosis. After the interaction with extracellular ligands, multimerization of syndecans is thought to occur, which in turn induces actin polymerization. Arginine-rich peptides have shown to have this effect on the cellular signal transduction via syndecan multimerization. Multimerization of syndecan-4 was observed in the presence of R8, followed by an increase in the internalized amount of the peptide [71,72]. All of the aforementioned interactions lead to the internalization of arginine-rich peptides by the activation of Rac protein.

On the other hand, Pang et al. [73] propose a different set of interactions that could induce the macropinocytosis of CPPs. In this case, the research group investigated the uptake of TAT-peptide functionalized nanoparticles and they proposed the CendR (C-end-rule) pathway as a possible mechanism that activates macropinocytosis. This route involves the NRP1, a transmembrane protein and a co-receptor of various ligands, and it has several structural requirements for the peptide: it should have C-terminal arginine with a free α-carboxyl group and the natural L-conformation. It is thought that the binding of TAT to NRP1 could induce macropinocytosis independent of HSPG. However, it seems that NRP1 and HSPG work simultaneously in the induction of the active uptake of CPPs. Furthermore, the interaction with this protein might be specific for CPPs conjugated to nanoparticles and perhaps macromolecules.

Since the membrane-bound proteoglycans have been associated with the activation of membrane ruffling and macropinocytosis, it seems logical to conclude that their interaction with arginine-rich peptides will induce the aforementioned path. However, more evidence is needed in order to state that proteoglycans act as receptors for macropinocytosis. Tanaka et al. [66] demonstrated that the uptake of dodeka-arginine (R12) can be medi-

ated by the CXCR4 chemokine receptor. This conclusion is supported by the inhibition of R12 internalization by a CXCR4 knockdown as well as the colocalization of R12 and CXCR4 observed by LSCM in macropinosomes in cells. R8 and TAT did not activate the CXCR4-mediated uptake, which might explain why there is a higher cellular uptake efficiency of R12 over these peptides. Further findings on the internalization of R8 suggest lanthionine synthetase component C-like protein 1 (LanCL1) as a possible receptor that could provoke R8 macropinocytosis. LanCL1 is considered a cytosolic, peripheral membrane protein, which was found to stimulate R8 uptake in HeLa cells. The exact biological function of the protein is not yet clearly defined. Therefore, further studies are needed to address in detail the contribution of LanCL1 in the promotion of R8 uptake [74].

Scavenger receptors are a family of cell surface glycoproteins first recognized to bind modified low-density lipoproteins (LDL) such as acetylated and oxidized LDLs. These receptors have been reported to mediate the translocation of negatively charged CPP/cargo complexes through cellular membranes [75]. Scavenger receptors are known to bind promiscuously to polyanionic ligands and were shown to be involved in multiple endocytic pathways (macropinocytosis, CME, and caveolae-dependent endocytosis). In several papers, it has been demonstrated that the scavenger receptors class A3 and 5 (SCARA3 and SCARA5) are at least partially responsible for the uptake of CPPs [76]. Arukuusk et al. [77] have reported the involvement of SCARA3 and SCARA5 in the uptake of the anionic CPP NickFect51, a stearylated transportan 10 (TP10) analog, via macropinocytosis.

Clathrin-mediated endocytosis (CME)

The advanced understanding of the molecular mechanisms governing clathrin-mediated endocytosis (CME) makes this uptake mechanism the best-characterized type of endocytosis thus far. CME is a receptor-dependent, clathrin-mediated and dynamin-required process [78]. Clathrin-mediated endocytosis occurs in all mammalian cells and supports the continuous uptake of essential nutrients such as LDL particles, which carry cholesterol to cells and bind to the LDL receptor (LDLR), and iron-laden transferrin (Tfn) that binds to Tfn receptors (TfnR) [52]. It is a crucial process throughout the life of an organism, as it is responsible for the uptake of transmembrane receptors and transporters, for remodeling the plasma membrane composition in response to environmental changes and for regulating cell surface signaling.

Clathrin-mediated endocytosis can be generally described as a process involving the strong binding of a ligand to a specific cell surface receptor, resulting in the assembly of clathrins in a polyhedral lattice on the cytosolic surface of the cell membrane. This process is followed by the invagination of the clathrin-coated membrane surface towards the cytoplasm and formation of a coated pit that adopts the shape of a spherical membrane structure with a diameter of 100–150 nm. Shallow pits undergo progressive invagination into dome-like shapes, which are connected to the plasma membrane by a funnel-like rim. Further invagination leads to the formation of a spherical bud, and the rim transforms into an hourglass-like membrane neck. Eventually, the neck undergoes fission [79]. For this step, dynamin, a kind of GTPase, is required. In subsequent steps, the released clathrin-coated vesicles (CCVs) are rapidly uncoated and delivered to early endosomes, which mature to late endosomes. Late endosomes then deliver their cargo to lysosomes, organelles characterized by a very low pH value, which is usually the last step in this uptake process [39,78]. Clathrin-mediated endocytosis has been proposed as another mechanism that arginine-rich CPPs use for their uptake.

Clathrin-mediated endocytosis as a highly organized process: Early studies on clathrin-mediated endocytosis focused on nutrient receptors which are constitutively internalized (such as the TfnR and LDLR). This led to CME being understood as a constitutive process. In their review on the regulation of CME, Mettlen et al. [80] compare this viewpoint on CME with the circulation of buses according to a set timetable irrespective of the number and destinations of passengers. This analogy is quite correct, having in mind that CCVs were thought to form at a fixed rate, independent of the cargo. Nowadays, data show that CME is a highly regulated and cargo-driven process.

CME can be divided into five stages: (i) initiation of endocytic events, (ii) cargo loading, (iii) membrane bending, (iv) vesicle scission and (v) disassembly of the coat. Each of the stages mentioned is highly orchestrated by a series of molecular interactions [80].

The initiation phase, the first step in this biochemical pathway, is the focal point for regulation. It defines the site where the endocytic vesicle will be formed and is likely the key stage for regulating the frequency of endocytic events. The so-called hot spots for vesicle formation are usually zones in the plasma membrane enriched with phosphatidylinositol 4,5-biphosphate ($PI(4,5)P_2$) which interacts with adaptor proteins. However, local differences in the concentration of cargo could also provoke recruitment and clustering of adaptor proteins. The pioneer molecules which initiate the formation of the CCV are adaptor proteins, working together with scaffold proteins. The most important adaptor protein is adaptor protein 2 (AP2) complex, which binds to $PI(4,5)P_2$ and then recruits scaffold pro-

teins to the plasma membrane. Due to allosterically regulated AP2 conformational changes caused by the $PI(4,5)P_2$ and cargo binding, as well the scaffold proteins, AP2 triggers clathrin assembly [80,81].

The second step in CME is called "cargo loading". Basically, it involves the binding of clathrin-coat components to the cytosolic regions of the transmembrane cargo molecules. This drives the clustering of all cargo molecules to one region of the membrane, where the clathrin-coated vesicle will be formed. Oftentimes this point in CME has been referred to as "cargo checkpoint", meaning that if a certain threshold of cargo molecules is not reached, the process of vesicle budding will be either delayed or aborted [82].

Membrane bending is the following step in CME. Several endocytic modules contribute to the formation of a membrane curvature: the coat, the actin filaments, and the scission proteins. Clathrin is the coat-component that has a part in the membrane bending process. When it binds to the adaptor protein complex on the plasma membrane, clathrin rapidly assembles into icosahedral cages. It is thought that the polymerization of clathrin could be responsible for the membrane curvature. The actin cytoskeleton also contributes to membrane bending during CME. There is evidence that rapid actin polymerization occurs in the region surrounding the coat and the base of the growing membrane invagination. After vesicle scission, actin filaments depolymerize in seconds [79,82].

Vesicle scission is the process where the CCV is separated from the donor membrane. This step is catalyzed by the large GTPase dynamin. First, dynamin assembles into tight oligomers, allowing constriction of the membrane neck. After GTP hydrolysis, dynamin oligomers further constrict in the presence of GTP. The constricted state of the membrane causes spontaneous transitions to a hemi-fission and then to a fission state [82]. Recent evidence also suggests that dynamin is necessary in the initial steps of vesicle formation [80].

The disassembly of the coat is the process in which the new vesicle is released to fuse with an early endosome. In addition, the endocytic machinery proteins are also released so that they can be reused for another endocytic event. This process is promoted by an ATPase activity, which leads to clathrin and dynamin depolymerization. Dephosphorylation of $PI(4,5)P_2$ to phosphoinositol 4-phosphate also mediates the coat disassembly [80,82].

Clathrin-mediated endocytosis and CPPs: A common trait of all CPPs is their ability to switch between different uptake mechanisms depending on multiple exogenous factors. Clathrin-mediated endocytosis has been described as one mechanism CPPs can use to traverse cell membranes. Thus far, it has been reported as a pathway used by the TAT peptide, oligoarginines as well as by anionic CPPs.

After denoting endocytosis as an uptake mechanism for CPPs, the work of Richard et al. [83] continued to focus on the specific endocytic paths used by the peptides. In 2005 they suggested that the uptake of full-size TAT peptides in HeLa cells occurs through clathrin-mediated endocytosis. Their findings were supported by the use of specific CME inhibitors, which led to a decrease in the uptake of the peptide. After uptake, TAT was targeted to acidic compartments in the cytoplasm, which is in accordance with the CME flow. They speculated that the interaction between TAT and heparan sulfates plays a significant part in the internalization, although these receptors are not a prerequisite for TAT entry. However, this implies only for unconjugated TAT, as it has been demonstrated that there is an alternative uptake pathway for TAT in the presence of conjugated cargo. Around the same time, it was reported that MPGα/siRNA complexes were also taken up by CME, although earlier MPG had shown to enter cells in an energy-independent manner [84,85]. MPGα is a derivative of the original MPG peptide. It is possible that the type of attached cargo influences the chosen uptake pathway, since it was shown that CME inhibitors decreased the amount of MPGα/siRNA complexes inside cells.

More than a decade later, the deciphering of endocytic mechanisms involved in CPP uptake as well as the exact receptors used still continues. Recent findings suggest the involvement of a few receptor types in the internalization of CPPs, which prefer CME over other uptake mechanisms.

Kawaguchi et al. [86] have recently reported that syndecan-4, one of the heparan sulfate proteoglycans, is an endogenous membrane-associated receptor for the cellular uptake of R8 peptide via clathrin-mediated endocytosis. RNA interference-mediated knockdown experiments in combination with pharmacological inhibitors support their results. These results contradict the former findings of the group, which stated that syndecans were involved in the uptake of R8 via macropinocytosis. However, there is a possibility for syndecans to have multiple roles in the uptake of CPPs [44].

Indeed, there is a chance that binding to heparan sulfates could provoke several endosomal pathways. Heparan sulfates can be conjugated to a variety of proteins with different spatial distributions such as the cell-surface associated syndecans and glypicans, which further determines the biological outcome of the ligand binding. Syndecans are transmembrane proteins, where-

as glypicans are associated with the plasma membrane via a glycosylphosphatidylinositol (GPI) anchor. As a consequence of this contrast, syndecans and glypicans may be preferentially sorted to clathrin-coated and caveolin/lipid raft plasma membrane domains, respectively. Uptake of glypican-bound ligands may proceed primarily through caveolin-dependent endocytosis. This might indicate a possible role for syndecans in clathrin-mediated endocytosis [87].

As an interesting contrast to the common cationic CPPs, Arukuusk et al. [88] suggest negatively charged CPPs as oligonucleotide carriers. The CPPs are not inherently anionic, but confer a negative charge after they are complexed with a nucleic acid in cell culture media. The group has already demonstrated that the uptake of these anionic particles is mediated by the scavenger receptors SCARA3 and SCARA5 [75]. This is logical, since their negative charge would not let them interact with negatively charged components of the plasma membrane, which is the first step in the internalization of nanoparticles in cells, so there must be a receptor involved. Their results have shown that one of their CPP/cargo complexes, the NickFect1 stearylated transportan 10 (TP10) analog, crosses the membrane using clathrin-mediated endocytosis. However, this cannot be regarded as the one and absolute pathway this complex uses, since scavenger receptors are known to be involved in multiple endocytic pathways. Furthermore, this endocytic path may not be used by the peptide alone, and may be the result of cargo attachment to the peptide [77].

Caveolae-mediated endocytosis (CvME)

Caveolae are flask-shaped invaginations in the cellular membrane, which have a diameter of about 50–100 nm. They were described for the first time in the early 1950s, as present in many cell types [89]. Caveolae were assumed to be mediators in the transport of serum proteins to tissues across the endothelium of blood vessels. Nowadays, caveolae are known to encircle cholesterol and sphingolipid-rich domains of the plasma membrane, in which a number of signaling molecules may be located [52]. Since they are highly hydrophobic and rich in cholesterol and sphingolipids, some authors often refer to caveolae as lipid rafts [89,90]. Caveolae have been implicated in numerous functions, having important roles in cell signaling, lipid regulation and endocytosis [91].

The most famous ligand for this pathway seems to be albumin. The binding to its receptor, gp60, provokes internalization of the protein. In addition, there is a growing number of receptors, other than the gp60, which are known to induce caveolae-mediated uptake. These receptors are involved in the uptake of ligands such as folic acid, alkaline phosphatase, and pathogens as ganglioside-bound cholera toxin, SV40 virus, polyoma virus, HIV virus. Using caveolae-dependent endocytosis, pathogens can escape the endosomolytic intracellular path.

Caveolae on the plasma membrane: The shape and structural organization of caveolae are conferred by members of the caveolin gene family, caveolin-1, -2 and -3 (Cav-1, -2 and -3). Cav-1 and -2 are rather ubiquitous, being highly co-expressed in fibroblasts, adipocytes, endothelial cells and pneumocytes. Cav-3 is expressed independently and is limited to the skeletal musculature and cardiac myocytes. Cav-1 seems to be the one giving shape to the caveole. It is a small integral membrane protein, whose hydrophobic amino acids are inserted into the inner leaflet of the membrane bilayer in a hairpin-like form. The cytosolic region functions as a scaffolding domain and has been implicated in cholesterol and sphingolipid-rich membrane domain binding [52,89,91]. Cav-1 was shown to be highly immobile at the plasma membrane. Therefore, it seems that this protein stabilizes the plasma membrane association of the invaginations, postponing their dynamin-dependent budding and detachment, regulating the constitutive endocytosis. This could also mean that the uptake can be opened by some specific signaling events. If so, ligand internalization via caveolae-dependent endocytosis may be signal mediated in cells expressing Cav-1 [90]. Cav-2 has also been suggested as necessary for the formation of deep plasma membrane-attached caveolae.

Further studies on caveolae-dependent endocytosis have made it clear that caveolae formation requires proteins other than caveolins. The second group of proteins needed is named cavins. In contrast to caveolins, cavins are peripheral membrane proteins which bind molecular components of the caveolar domain facing the cytosol. Recently, a crucial role in caveolae formation has been attributed to PTRF (polymerase I and transcript release factor), also known as cavin-1. In the last steps of caveolae biogenesis, PTRF is recruited to the plasma membrane and it most likely operates as a coat protein for caveolae. Binding of cavin-1 to the domain containing oligomerized caveolins, cholesterol and phosphatidylserine stabilizes the membrane curvature to produce the classical flask-shaped caveolae [89,91].

Two other components which are essential for the caveolae formation are the actin cytoskeleton as well as cholesterol. The actin cross-linking protein filamin is one of the proteins identified as a ligand for Cav-1 and it is thought that PTRF may serve as a direct connection between the caveolae and the cytoskeleton [89].

Caveolae internalization and trafficking: Electron microscopy data show that caveolae are tightly connected to the actin filaments, which suggest a role for the cytoskeleton in caveolae-

dependent endocytosis. The internalization of caveolae is facilitated by the disruption/reorganization of the cytoskeleton. Local disassembly of the cortical actin network is essential to initiate inward transport of caveolae along microtubules, which serve as transporting tracks. These observations show a dual role for actin in caveolar internalization: one is to keep the organization of caveolae and maintain their immobility at the plasma membrane, and the other is to promote vesicle budding and release from the membrane [91].

Another factor that regulates caveolae budding is the activity of kinases and phosphatases. Cav-1 and -2 are known to be substrates for Src, a tyrosine kinase which phosphorylates the scaffolding domain of both proteins. The simultaneous phosphorylation might equally be important in regulating caveolae budding and pinching off from the cellular membrane. On the contrary, phosphatases seem to inhibit caveolar endocytosis. PP1 and PP2 (protein phosphatases) activity contributes to the dephosphorylation of Cav-1 and -2 [89,90].

Caveolae endocytosis relies heavily on dynamin, a multidomain GTPase, shown to interact directly with Cav-1. Ligand binding disrupts the local actin cytoskeleton and promotes dynamin II recruitment to the site of internalization. Dynamin oligomerization and subsequent GTP hydrolysis result in the formation of a collar, which constricts the neck of caveolae and results in release from the membrane [91].

The question left after membrane release is whether the internalized caveolae can fuse with endosomes and follow the classical endocytic pathway or there is an alternative pathway involving different cellular compartments. Studies on caveolar internalization have shown that this path is always accompanied by the appearance of grape-like caveolar complexes, which are termed caveosomes. These are pH neutral multi-caveolar structures with a heterogeneous morphology, presumably distinct from the classical endocytic organelles. The future fate of these structures is not entirely clear. Viruses are known to use this pathway to avoid lysosomal degradation. However, other data show that ligands such as the cholera toxin internalized by caveolae can be driven to the classical endocytic organelles [89].

Caveolae-mediated endocytosis and CPPs: The first report that caveolae-mediated endocytosis can take part in the uptake of CPPs comes from Fittipladi and co-workers [92]. Their main focus was the internalization of TAT fusion proteins. This observation is a contrast to the aforementioned possible TAT uptake pathways – macropinocytosis and clathrin-mediated endocytosis. However, in this case the specific uptake path might depend mostly on the cargo attached to the peptide. The research group came to this conclusion after investigating the uptake of TAT fusion proteins in fixed cells as well as in real time using living cells. After using methyl-β-cyclodextrin, they observed an impairment of endocytosis. Furthermore, there was no co-localization observed with transferrin, a common agent used to trace clathrin-mediated endocytosis, while the peptide conjugates clearly co-localized with cholera toxin, a marker for caveolae-mediated endocytosis. In addition, the uptake process seemed to occur slowly, which is incompatible with the fast dynamics described for CME. This might be due to Cav-1, which stabilizes the caveosomes on the cell membrane, and thus, slows down the uptake process [92,93].

It was postulated that this process occurs due to the interaction of the peptide complex with heparan sulfate chains of HSPG. However, based on this idea, one may wonder how the interaction of TAT and HSPG can lead to both CME and CvME. Indeed, the preferred uptake road mainly depends on the association with the proteins conjugated to heparan sulfates (syndecans and glypicans). Glypicans have been shown to prefer CvME for ligand uptake [87]. Fusing the TAT peptide with a protein could favor binding to glypicans, and thus, the uptake via CvME.

Caveolae-mediated endocytosis has also been observed in the uptake of proline-rich CPPs [94]. Proline-rich peptides are a chemically and structurally diverse family of cell-penetrating vectors characterized by the presence of pyrrolidine rings from prolines. The amphipathic group of proline-rich peptides has been particularly effective, demonstrating efficient cellular uptake and no cytotoxicity. Investigations of the uptake pathway of these peptides have shown that their internalization is energy-dependent and they mostly co-localize with cholera toxin. This leads to the conclusion that caveolae-mediated endocytosis is mainly involved in amphipathic, proline-rich CPPs uptake. Furthermore, the uptake is thought to be provoked by the interaction between the CPPs and glycosaminoglycans in the extracellular matrix [94].

Säälik and co-workers [95] have reported that transportan and transportan-10 (TP10) mediate protein delivery using caveolae-mediated endocytosis. Studying the uptake mechanism, the group showed that internalization was impaired by cholesterol depletion and Cav-1 downregulation. Co-localization with markers for caveosomes was also observed. This led to the conclusion that CvME might be one of the paths involved in transportan–cargo complex uptake. However, other mechanisms might have a part as well. What is interesting here is that in both cases, with TAT fusion proteins and transportan–protein complexes, caveolae-mediated uptake seems to be the preferred pathway. This is probably a result of the increase in

size due to cargo linkage to the CPP, which is in accordance with the size-dependency of the internalization mechanism. Conjugates larger in size are usually taken up by CvME, while the free peptides might use a different path [96].

Stearylated-transportan analogues were also reported to enter cells via CvME [97]. PepFect14 (PF14) complexes with plasmid DNA (pDNA) were detected in endocytic vesicles close to the plasma membrane. The vesicles were mostly of caveolar origin, clearly distinguishable from clathrin-coated structures. The group describes them as grape-like groups or rosettes. Within 1 h of incubation, PF14/pDNA complexes were found in multivesicular bodies. It is postulated that in this case, CvME is provoked by the interaction of PF14/pDNA complexes with scavenger receptors, since their uptake was significantly decreased after SCARA knockdown.

The following report for CvME involvement in CPP uptake comes from a group working on azurin. Azurin is a 128 amino acid-long copper containing redox protein. As a class, redox proteins are not normally classified as CPPs. However, the amphipathic azurin fragments p18 and p28 containing 54 to 67 amino acids have the α-helical structure of azurin. These fragments represent the protein transduction domains of azurin and are reported to have cell cycle inhibitory and antiangiogenic effects [98,99]. Studying the uptake of these fragments, the group observed that both peptides did not enter cells if cholesterol was depleted, and they highly co-localized with Cav-1 in the first 30 min of incubation. This indicates that, at least in part, internalization was caveolae-mediated.

More recently, the N-terminus of VP1 from chicken anemia virus (CAV), designated as CVP1, was shown to act as CPP and efficiently deliver exogenous molecules through caveolae-mediated endocytosis [100]. While employing several endocytic inhibitors, methylated β-cyclodextrin significantly reduced the uptake of CVP1, which implies caveolae-mediated endocytosis as a possible internalization mechanism. The peptide has shown to be more efficient than TAT in delivering cargo molecules.

Clathrin- and caveolae-independent endocytosis

The plasma membrane is the spot of origin for complex endocytic pathways, and we are beginning to get a deeper understanding about the way these pathways are regulated. Having defined a substantial number of molecules involved in CME and CvME, other portals for entry into the cells remain obscure. One such pathway involved specifically in the uptake of lipids and fluids may be clathrin- and caveolae-independent [101].

Nowadays, it is accepted that lipids and lipid–protein interaction have a crucial role in the functional compartmentalization of the plasma membrane into microdomains. The term ‘lipid rafts’ has been used to define these lipid domains, formed by the interaction of sterols and sphingolipids. Lipid rafts are small structures, 40–50 nm in diameter, that diffuse freely on the cell surface. The partitioning of certain macromolecules into lipid rafts eases their internalization via endocytic pathway which is clathrin- and caveolae-independent. Even though caveolae are considered a lipid raft subtype and are sometimes classified as identical structures, it is now well established that endocytosis occurs even in cells devoid of caveolae. This conclusion is supported by the fast kinetics of the independent pathway, knowing that due to Cav-1 caveolae-mediated endocytosis is a slow process. This process was best characterized for cytokine receptors on lymphocytes, glycosylphosphatidylinositol anchored proteins (GPI-AP) and viruses [52,101,102].

Although the mechanisms that govern clathrin- and caveolae-independent endocytosis are still poorly understood, it is known that these coat-free pathways can be dynamin-dependent or -independent. For example, it has been shown that this fluid-phase uptake can occur in the presence of a dynamin mutant form, where the canonical endocytic pathways are blocked [52].

The most famous representative for the dynamin-dependent pathway is the interleukine-2 receptor (IL-2R). Studies confirm that IL-2R subunits associate with lipid raft domains, and dynamin regulates the budding and pinching off from the membrane, while the actin-based machinery facilitates the entry [52]. On the other side, endocytosis in the absence of identifiable coats and a particular pinching machinery posed multiple problems. Recent evidence suggests that, in the absence of a specific coat, lipid accumulation could initiate membrane deformation by physically making the membrane bud and form a vesicle. Endocytosis of GPI-AP does not involve any detectable coat nor is it dynamin-dependent. The GPI-anchor was required for internalization via a pathway sensitive to cholesterol depletion. Immediately after internalization, GPI-AP were seen in labile tubular structures. These structures are termed GEECs (GPI-enriched endosomal compartments). This pathway has been shown to be highly actin-dependent [101,103].

Another dynamin-independent path is the ARF-associated pathway, which is thought to be used by the SV40 virus [102]. This pathway is only one of the mechanisms the virus uses to enter cells, since it is known that infection happens via CvME as well. Studies using the virus have shown that the pathway is cholesterol-dependent, involving coat-free endocytic vesicles with a neutral pH and fast uptake kinetics.

Flotillins appear to outline another, dynamin- and coat-independent pathway, which has been used by GPI-anchored CD59 in

HeLa cells. Flotillin 1 and 2 seem to induce membrane invaginations in a dose-dependent manner. Furthermore, phosphorylation by tyrosine kinases seems to activate endocytosis via this pathway. However, some studies suggest that flotillins might be involved also in dynamin-dependent pathways, serving as adaptor proteins for specific cargo.

CPPs internalized via clathrin- and caveolae-independent endocytosis: Concerning CPPs, clathrin- and caveolae-independent endocytosis has only been reported in a few cases so far. Azurin and its fragments p18 and p28, which were mentioned earlier as peptides using CvME to enter cells, might also use a caveolae-independent pathway. It is postulated that this process occurs in parallel with CvME [98]. Another case is the internalization of transportan and transportan-10. Although both of the peptides have shown to enter cells via caveosomes, another uptake process is also possible. Flotillins were thought to be involved in the clathrin- and caveolae-independent uptake of transportans [95]. The most recent report of a CPP using this mechanism of internalization comes from Ye and co-workers [104]. The group used low molecular weight protamine (LMWP) as siRNA carrier. It was noted that LMWP/siRNA complexes entered cells in spite of the presence of inhibitors for all the major endocytic pathways as well as GTPase inhibitors. This led to the conclusion that the uptake of the complex might be clathrin- and caveolae-independent and also dynamin-independent, as suggested by the fraction of internalized complexes in the presence of a GTPase inhibitor.

Release from endosomes

CPPs have proven to be molecules able to hijack or induce one or more endocytic mechanisms. As a result, CPP/cargo complexes tend to accumulate inside endocytic organelles, which more often than not, is not the preferred site of action. However, many reports have now established that CPP/cargo complexes can escape from endocytic organelles and reach the cytosolic space. Therefore, CPPs appear to promote the release of molecules trapped in endocytic vesicles, which is essential for intracellular delivery. As is known, molecules which remain within endosomes cannot display their biological activity. In addition, these molecules are subjected to degradation by acidic pH or hydrolases, as they travel from early endosomes to late endosomes, and finally, are fused with lysosomes [105].

Mechanisms of endosomal escape and strategies to improve it: The release from endosomes seems to be a limiting step in the endocytic uptake of CPPs – it determines the efficiency with which a cargo reaches the cytosol. Thus, understanding the mechanisms that underline this process is of great importance. A great part of the challenge in understanding how CPPs escape endosomes lies in the frequent poor efficiency of endosomal release of these systems. This does not pose a problem for cargos which require a small number of copies to elicit a response, however, ones which require a larger number of copies often fail to show biological effects.

Several mechanisms for endosomal escape have been proposed so far. One possible mechanism is based on the ability of CPPs to induce membrane disruption. Positively charged CPPs are thought to interact with negatively charged phospholipids in the endosomal membrane [105]. This interaction would result in the formation of a membrane pore and leakage, which would ease the release of CPPs. TAT has been shown to induce leakage of endosomes after interacting with negatively charged phospholipids in the endosomal membrane [106]. Another possible mechanism for escape is the formation of ionic pairs between CPPs and negatively charged membrane lipids, which would then partition across the endosomal membrane [107]. This mechanism has been proposed for oligo-arginines [108]. In the following, some of the most common strategies used to improve endosomal release are discussed. Figure 4 gives a representation of these mechanisms.

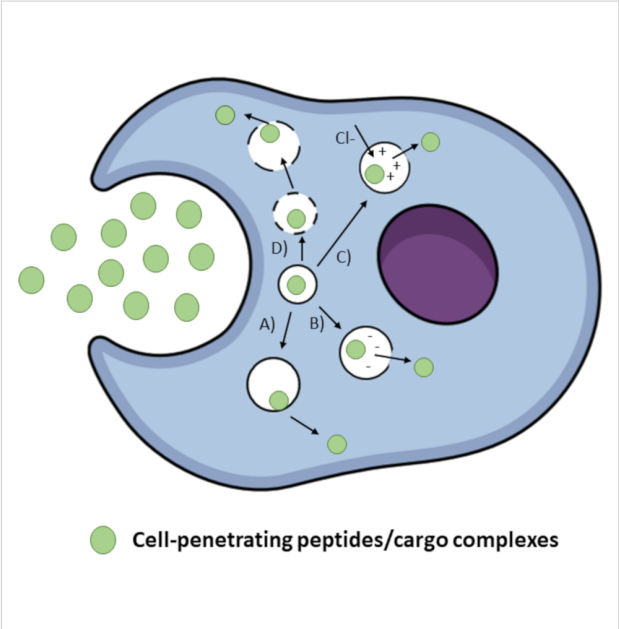

Figure 4: Most commonly used strategies for improving the endosomal release of CPPs. A) Fusogenic lipids, B) pH-sensitive membrane disruptive peptides, C) 'Proton sponge' effect, D) Endosomolytic agents such as chloroquine.

Strategies to improve endosomal release of CPPs:

1. Use of fusogenic lipids: Fusogenic lipids have been suggested as a tool to improve the endosomal release of CPPs. The inclusion of a neutral helper lipid such as dioleoylphosphatidylethanolamine (DOPE), is known to greatly enhance the release and activity of the cargo molecule. For instance, DOPE incor-

poration in lipoplexes or TAT-pDNA complexes showed a vast improvement in transfection efficacy.

The mechanism by which DOPE is thought to mediate endosomal release is the following. At lower pH levels, which are found in endosomes, DOPE shifts its phase from lamellar to an inverted hexagonal phase. The inverted hexagonal phase supports the fusion of the nanocarrier and the endosomal membrane, which finally destabilizes the membrane to release the nanocarrier into the cytosol (Figure 4) [107].

2. Membrane-disruptive peptides: What would be a better way of overcoming the endosomal trap than mimicking nature's mechanisms such as those that viruses use? This can be easily done by conjugating a viral fusion sequence to a nanocarrier. For this purpose, a commonly used peptide is the HA2 peptide. It is a pH-sensitive fusogenic peptide derived from the hemagglutinin protein of influenza virus. The HA2 peptide has an α-helix structure at its N-terminus capable of insertion into membranes. Under the acidic pH conditions in endosomes, a conformational change exposes the α-helix structure, which then fuses with the endosomal membrane and is followed by the release of the virus in the cytosol [23,107]. This method has been used to improve the endosomal release of TAT complexes with proteins, as well as for transportan–peptide nucleic acid (PNA) complexes [60,109].

3. The 'proton sponge' effect: The 'proton sponge' effect, in which the buffering capacity of an agent is used to increase osmotic pressure within endosomes leading to their swelling, rupture and release of contents, has been investigated as another strategy to improve the endosomal release of CPPs. One of the commonly used agents in this case is histidine. At acidic conditions in the endosomes, the imidazole group in histidine is protonated, which results in osmotic swelling and rupture of the endosome [110]. This strategy has been successfully employed to enhance the gene expression of a TAT/pDNA complex [111]. Another way to exploit the proton sponge effect is to use membrane disruptive polymers such as polyethylenimine (PEI). Upon protonation, PEI provokes the rupture of endosomes. PEI has been combined with a TAT/pDNA complex and has improved its cytosolic delivery [107].

4. Use of endosomolytic agents: The most famous representative of endosomolytic agents is chloroquine, a weak base that can enter cells and accumulate in endosomes and lysosomes after being protonated. At low concentration, chloroquine can inhibit endosome acidification and thus, prevent its maturation. At high concentration, it can cause endosomal swelling and rupture. Wadia and co-workers [60] reported that chloroquine enhanced the nuclear delivery of TAT fusion proteins. This method has also improved the delivery of siRNA complexed with MPGα [23,84].

5. Photochemical Internalization: Photosensitizers that can accumulate in the endosomes have been used to achieve endosomal release. These compounds are able to localize in cell membranes and are taken up by endocytosis, where they again localize in the endosomal membrane. Upon irradiation with light of a specific wavelength, these molecules are able to produce reactive oxygen species (ROS). These ROS will damage and rupture endosomal membranes, causing the release of the endosomal cargo [105].

Factors affecting the cellular uptake mechanism

The internalization mechanism of CPPs still remains a matter of debate. In spite of many similarities between different CPPs, their uptake mechanisms may vary considerably. This leads to contradictory observations, mostly because there is a great number of factors that affect the cellular uptake and translocation mechanism. In general, the factors that determine the uptake routes of cell penetrating peptides can be divided into two major groups: i) the physicochemical properties, concentration of peptide and its cargo and ii) the properties of the plasma membrane, its lipid and protein composition.

Contradictory results regarding the internalization mechanism of CPPs often arise due to differences in experimental conditions. The fist important factor is the CPP concentration. In many cases, it has been shown that the applied concentration greatly affects the uptake pathway. Another factor is the net charge of the peptides, especially the positive charges coming from arginine residues. Most of the CPPs are rich in arginine residues, and arginine (in particular, its guanidinium group) is more favorable than lysine for the delivery and the uptake of CPP. Amphipathicity is another factor known to influence uptake. Primary and secondary amphipathic peptides can directly penetrate through the cell membrane at low concentration, while nonamphipathic CPPs use endocytosis [1]. The temperature at which the experiment is conducted can also influence the internalization mechanism. Fretz et al. [41] have observed the temperature dependence of R8 translocation across plasma membranes. They have found that at 4 °C diffuse signals from the fluorescently labeled peptide are more prominent in the cytoplasm, which is usually an indicator for a direct translocation across the membrane. However, at 37 °C, both diffuse and punctate signals were observed, pointing to a possible activation of an endocytic mechanism at higher temperature. Cargo molecules attached to CPPs can also greatly influence the uptake path. The roles of cargo, concentration and cell lines will be further discussed below.

Role of cargo molecules

The cargo conjugated to the CPP is often a very important parameter of internalization. Tünnemann et al. [112] compared the uptake of TAT conjugated to peptides and globular proteins in living cells. They found that the size of cargo fused to TAT had a great influence on the uptake mechanism. The larger complexes containing proteins were seen inside vesicular structures, while the TAT-peptide conjugates were diffusely distributed throughout the cell. This indicates that the size of the cargo, which naturally influences the size of the overall complex, leads to a different uptake mechanism. The smaller the size, the greater is the chance that the complex will be taken up by direct translocation. At larger dimensions, however, endocytosis prevails. This is similar to the case of the uptake mechanism of unconjugated TAT compared to TAT fused to a cargo, where the presence of a cargo molecule decides between two different endocytosis mechanisms [83,93]. Unconjugated TAT prefers CME to enter cells, while its conjugated counterpart is more likely to use CvME.

The uptake of other arginine-rich peptides is also a subject of cargo influence. Maiolo et al. [113] investigated the effects of cargo molecules on the uptake of R7 and R7W (R7 conjugated to a tryptophan residue). The peptides alone showed diffuse signals in the cytoplasm of the cells used. However, after fusion to cargo peptides, there was a significant reduction in the diffuse signal and a small increase in the punctate signal coming from endocytic vesicles.

Role of concentration

The concentration of the CPP is a supreme factor, since it can trigger different uptake pathways. It is believed that endocytosis usually occurs at low peptide concentration, and it switches to direct penetration when the concentration is higher. While investigating the role of temperature in the uptake of R8, Fretz et al. [41] also tested the dependence on the concentration. When lower peptide concentration was used, vesicular labeling was observed in the cytoplasm indicating endocytic uptake. At higher concentration, vesicular and diffuse labeling were present, indicating that endocytosis and direct penetration might occur simultaneously. This was later confirmed by another research group, which observed a similar behavior of the peptide dependent on the concentration [114]. R9 and TAT have also been tested for concentration-dependent uptake [67,114]. These peptides also show predominantly vesicular signals at lower concentration and extensive cytosolic labeling at higher concentration. However, in this case the situation becomes more complicated, because at low concentration (<5 μM) endocytic inhibitors had only a slight effect on the uptake of R9 and TAT, while at higher concentration clathrin inhibitors seem to strongly influence the uptake. Indeed, it was observed that the peptides are, to some extent, taken up by vesicular structures at higher concentration, in addition to the fast, nonendocytic uptake via nucleation zones [67]. As this results suggest, the effect of the CPP concentration on the uptake mechanism can be much more complicated than initially thought.

In contrast, penetratin seems to work differently. For this peptide, it has been shown that direct penetration occurs at low concentration. The switch to endocytosis occurs when the concentration is increased [26].

Role of the cell type

The cell lines used in experiments for CPP internalization also have a huge impact on the mechanism of uptake. In particular, the properties of the plasma membrane and the extracellular matrix structure can play a major role in CPP uptake. It is known that the first contact during internalization forms between the positively charged CPPs and the negatively charged GAGs from the extracellular matrix.

Hällbrink et al. [115] investigated how the peptide-to-cell ratio influenced the cellular uptake into Chinese hamster ovary (CHO) cells. To be more specific, they wanted to see how the uptake changes if the number of peptides, instead of the concentration, is increased at a constant cell number. Furthermore, they observed the impact of cell number and confluence on the uptake. What they have shown is that doubling the incubation volume at a fixed number of cells increased the intracellular peptide concentration more efficiently than doubling of the external peptide concentration. Moreover, applying a fixed peptide concentration to different cell densities revealed a decrease of the uptake at higher confluence. This could be caused by the different membrane composition or the different endocytosis behavior of the growing cells. Another possibility is that access to the membrane decreases as confluence increases. These results are an interesting example of how experimental factors in cell culture can influence the uptake efficiency.

Mueller et al. [116] did a profound investigation of the uptake of 22 different CPPs in four different cell lines. They used Cos-7, HEK293, HeLa and MDCK as representative cell lines and studied the internalization of some of the most prominent CPPs such as penetratin, TAT, transportan, Pep-1, MPG, MAP, R7 and R9. The results led to the categorization of CPPs into three groups according to their behavior, showing high (penetratin, transportan, MAP), medium (TAT, Pep-1, MPG) and low cellular uptake. What is interesting here is that the results show cell-dependent uptake for some of the peptides. For example, MPG was preferentially taken up by Cos-7 cells, fibroblast-like cells

derived from monkey kidney tissue. This could be due to the fact that MPG has a NLS derived from SV-40 large T antigen, the virus which was used for obtaining the Cos-7 cell line [117,118]. Penetratin was the favorite for HeLa cells, while transportan entered all cell lines with similar efficiency. The effect of endocytosis inhibitors was also shown to be cell-dependent, thus implicating different uptake mechanisms in different cell lines. For example, TAT showed mostly vesicular distribution in all cell types. However, a more diffuse signal, as well as cytoplasmic and nucleic localization was found for HeLa and MDCK cells.

Cell-dependent uptake was also observed for R7 and R7W [113]. Their uptake was investigated using the two different cell lines A431 and U2OS. Endocytic uptake was shown to be more prevalent in A431 than in U2Os cells as measured by the vesicular distribution of the peptides.

It is generally accepted that the first contact that leads to CPP internalization is between the positively charged peptides and the negatively charged GAGs from the extracellular matrix. In this case, heparan sulfate proteoglycans have been given the prominent role of inducing membrane translocation of several CPPs. Although all tissues express proteoglycans, the level of expression is determined by the state of differentiation and growth of the cell, and specific HPSG isoforms are known to be differentially expressed in different cell types [119]. The influence of different HSPG isoforms has yet to be investigated in detail. However, it is known that the uptake of some CPPs depends highly on the presence of these proteoglycans. It has been reported several times that the interaction with HSPGs is essential for the uptake of TAT [83,120]. Proteoglycan-binding has been observed to be important for the internalization of R8 and R9 as well [70,121].

Recently, a study investigated the influence of cell lines on the uptake of a CPP with a potential anticancer activity [122]. The CPP is sC18, a peptide derived from the C-terminal domain of the antimicrobial peptide CAP18. Its uptake was investigated in HeLa, PC-3, HCT-15 and MCF-7 as cancer cell lines, and HEK293 as a noncancer cell line. Interestingly, in all cancer cell lines, a diffuse fluorescent signal next to a punctate distribution was observed in the cytoplasm as well as nuclear accumulation. However, in the noncancer cell line just a punctate distribution was seen, and hardly any peptide in the nucleus was observed.

Role of membrane properties

A substantial amount of knowledge has been obtained about the permeability properties of CPPs since they were first discovered. Despite the information about their cell penetration mechanism being sometimes confusing and contradictive, we are familiar with their properties (such as physicochemical properties and concentration) which influence their uptake. However, less is known about the influence of the plasma membrane properties on the uptake. The number of studies on this topic is rather narrow, however, information about the impact of plasma membrane composition and how it changes and adapts is available from studies using poly-arginines [123].

Crosio et al. studied the influence of the membrane properties on the uptake of lysine- and cysteine-modified nona-arginine (KR9C) by utilizing anionic membranes with different fluidity and rigidity (a saturated membrane composed of DOPG/DPPC, an unsaturated membrane composed of DOPG/DOPC or a mixture of DOPC with cholesterol). They found that the peptide adsorbs on the polar regions of all membranes and this leads to the reduction of the anionic membrane charge. The peptide was able to get inserted into both DOPG/DOPC and DOPG/DPPC layers, however, when it came to the monolayers containing cholesterol, its insertion was impaired. This led to the conclusion that cholesterol molecules located in the cell membrane can hinder the uptake of poly-arginines.

The most likely explanation for the insertion of the peptide into the lipid layer is the ability of poly-arginines to recruit negatively charged phospholipid heads and thus decrease the surface pressure of the membrane. The peptide also increased the conductivity of both saturated and unsaturated layers and caused membrane deformations. The membrane deformations are thought to be caused by the charge neutralization, which can lead to a decrease in bending rigidity. A similar behavior was described for the TAT peptide by Herce et al., discussed in more detail in a previous section (Direct translocation mechanisms used by arginine-rich peptides), where the incorporation of water into the membrane together with the peptide as well as membrane thinning have been mentioned [47,48,123].

In vivo application of CPPs

CPPs demonstrated to be highly efficient in cargo delivery in vitro, being able to mediate the uptake of different cargo molecules in a number of cell lines. However, their success as delivery systems in vivo has been limited, mostly due to in vivo stability issues (they are susceptible to proteolytic degradation), immunogenicity or toxicity due to the lack of specificity [7,124,125]. Up to now, a number of in vivo studies have been done, in which CPPs such as TAT or penetratin have been tested for their cytotoxic and immunogenic potential [3]. The outcome so far shows that CPPs exert low cytotoxicity and no immune response. This gives the promise that, in some cases, these results can be translated to humans [126].

A CPP called PepFect6, which is based on covalently modified TP10 by the introduction of a proton-accepting moiety to facilitate endosomal escape and stearylation for an improved serum stability, was tested for its toxicity and immunogenicity in mice, following systemic administration. The in vivo studies showed that the peptide was mainly distributed in the liver, in the lung or in the kidney, with no associated toxicity and a negligible immune response. Furthermore, more than 60% gene silencing has been observed by using this peptide (PepFect6 was used as a carrier for the HPRT1 house-keeping gene siRNA) [20,124].

Another example of a successful application of a CPP in vivo is given by Toro and co-workers [127,128]. In this case, the TAT protein was used as a protein transduction domain, and it was conjugated to purine nucleoside phosphorylase (PNP), an intracellular enzyme crucial for purine degradation. The toxic and immunogenic effects as well as the effects on the biological activity of the cargo were observed in mice. Defects in PNP activity are known to result in metabolic abnormalities and fatal T cell immunodeficiency. The conjugation of the enzyme to TAT had positive effects on the retention and the distribution of PNP, as well as on the immunogenicity. The TAT-fusion prevented the enzyme from being excreted, while the nonfused PNP was undetectable in blood and tissues only after several hours after administration. Furthermore, TAT-PNP maintained its biological activity and an increase in T cell number was observed, besides an increase in the titer of antibodies against TAT-PNP.

In vivo studies have also been conveyed on Duchenne muscular dystrophy (DMD), a deadly neuromuscular pathology caused by the absence of the dystrophin protein and characterized by a progressive weakness of skeletal muscles. Here, penetratin was used as a CPP conjugated to a NF-κB peptide inhibitor, since NF-κB is known to be a possible target for therapeutic intervention. Mice were treated intraperitoneally and showed an improvement in motor performance. CPPs can also be used in the development of delivery systems for cancer treatment, since oftentimes traditional chemotherapy lacks specificity. For such purpose, the amphipathic peptide MPG has been utilized as a carrier for a siRNA molecule targeting cyclin B1 (a mitosis-regulating protein with altered expression in various forms of cancer). The complexes were functionalized with a cholesterol moiety, in order to be more suitable for systemic administration. After intravenous administration, a significant reduction in the tumor size was observed [126].

An attractive approach in the use of CPPs would be to circumvent the parenteral method of administration and find another less invasive but effective mode of drug delivery system application. Schiroli et al. [129] have reported the use of a peptide for ocular delivery (POD) with cell penetrating properties, known to diffuse into the corneal layers. The peptide was noncovalently complexed to a siRNA molecule, and the knockdown of luciferase reported gene expression in the corneal epithelium was evaluated. After topical administration of the complex, a 30% reduction in the expression was observed, with no inflammatory or toxic effects.

Worth mentioning is an in vivo study done by Ghatnekar et al., who studied the effect of antennapedia cell internalization sequence linked to the C-terminus of connexin43, called ACT1, in wound healing. Mouse and pig models of skin wound healing were used, and wounds were assessed for structural and functional markers of inflammation, scaring and healing. It was shown that the ACT1 peptide promotes regenerative healing and decreases inflammation [130]. As a topically applied peptide, ACT1 also showed promising results in a phase II trial [131]. For further reading on the preclinical and clinical application of CPPs, a great overview is given in a review by Guidotti and colleagues [126].

Conclusion

CPPs present a major breakthrough as delivery systems for macromolecules. CPPs are capable of entering the body in a noninvasive manner, they do not destroy the integrity of cellular membranes, and are considered highly efficient and safe. Thus far, they have been used to safely deliver molecules such as peptides, proteins and nucleic acids that are generally difficult to deliver due to some of their inherent properties. Therefore, they provide new horizons for research and application in medical sciences.

The uptake of CPPs has been reported in a wide variety of cell types and in combination with different cargo molecules. However, the exact mechanism CPPs use to traverse cell membranes still seems like an unsolvable riddle. As it is stated above, CPPs use different mechanisms to enter cells. In general, the mechanisms can be divided into two broad groups: endocytosis and direct penetration. Nevertheless, there is not even one CPP that strictly falls into one of the two categories. In the literature, it is described that many CPPs use different uptake pathways depending on their structure, net charge, concentration, type of cargo, cell lines used, temperature at which uptake studies were conducted and incubation times. The high variability in these factors between different laboratories leads to controversial results regarding the internalization mechanism, so at some points, this obstacle seems very hard to overcome. Undoubtedly, by further investigating the influence of each parameter and by the standardization of the recent experimental methods, more light will be shed on the mechanisms CPPs use

to enter cells. Or, to freely quote Richard Feynman – "There's plenty of room at the bottom".

ORCID® iDs

Andreas Zimmer - https://orcid.org/0000-0003-3127-287X

References

1. Madani, F.; Lindberg, S.; Langel, Ü.; Futaki, S.; Gräslund, A. *J. Biophys.* **2011,** 1–10. doi:10.1155/2011/414729
2. Guo, Z.; Peng, H.; Kang, J.; Sun, D. *Biomed. Rep.* **2016,** *4,* 528–534. doi:10.3892/br.2016.639
3. Heitz, F.; Morris, M. C.; Divita, G. *Br. J. Pharmacol.* **2009,** *157,* 195–206. doi:10.1111/j.1476-5381.2009.00057.x
4. Lönn, P.; Dowdy, S. F. *Expert Opin. Drug Delivery* **2015,** *12,* 1627–1636. doi:10.1517/17425247.2015.1046431
5. Reissmann, S. *J. Pept. Sci.* **2014,** *20,* 760–784. doi:10.1002/psc.2672
6. Silva, S.; Almeida, A. J.; Vale, N. *Biomolecules* **2019,** *9,* 22. doi:10.3390/biom9010022
7. Wang, F.; Wang, Y.; Zhang, X.; Zhang, W.; Guo, S.; Jin, F. *J. Controlled Release* **2014,** *174,* 126–136. doi:10.1016/j.jconrel.2013.11.020
8. Zhang, D.; Wang, J.; Xu, D. *J. Controlled Release* **2016,** *229,* 130–139. doi:10.1016/j.jconrel.2016.03.020
9. Frankel, A. D.; Pabo, C. O. *Cell* **1988,** *55,* 1189–1193. doi:10.1016/0092-8674(88)90263-2
10. Munyendo, W. L.; Lv, H.; Benza-Ingoula, H.; Baraza, L. D.; Zhou, J. *Biomolecules* **2012,** *2,* 187–202. doi:10.3390/biom2020187
11. Deshayes, S.; Morris, M. C.; Divita, G.; Heitz, F. *Cell. Mol. Life Sci.* **2005,** *62,* 1839–1849. doi:10.1007/s00018-005-5109-0
12. McClorey, G.; Banerjee, S. *Biomedicines* **2018,** *6,* 1–15. doi:10.3390/biomedicines6020051
13. Tai, W.; Gao, X. *Adv. Drug Delivery Rev.* **2017,** *110-111,* 157–168. doi:10.1016/j.addr.2016.08.004
14. Devaraj, N. K. *ACS Cent. Sci.* **2018,** *4,* 952–959. doi:10.1021/acscentsci.8b00251
15. Field, L. D.; Delehanty, J. B.; Chen, Y.; Medintz, I. L. *Acc. Chem. Res.* **2015,** *48,* 1380–1390. doi:10.1021/ar500449v
16. Sapsford, K. E.; Tyner, K. M.; Dair, B. J.; Deschamps, J. R.; Medintz, I. L. *Anal. Chem. (Washington, DC, U. S.)* **2011,** *83,* 4453–4488. doi:10.1021/ac200853a
17. Meade, B. R.; Dowdy, S. F. *Adv. Drug Delivery Rev.* **2008,** *60,* 530–536. doi:10.1016/j.addr.2007.10.004
18. Muratovska, A.; Eccles, M. R. *FEBS Lett.* **2004,** *558,* 63–68. doi:10.1016/s0014-5793(03)01505-9
19. Chiu, Y.-L.; Ali, A.; Chu, C.-y.; Cao, H.; Rana, T. M. *Chem. Biol.* **2004,** *11,* 1165–1175. doi:10.1016/j.chembiol.2004.06.006
20. EL Andaloussi, S.; Lehto, T.; Mäger, I.; Rosenthal-Aizman, K.; Oprea, I. I.; Simonson, O. E.; Sork, H.; Ezzat, K.; Copolovici, D. M.; Kurrikoff, K.; Viola, J. R.; Zaghloul, E. M.; Sillard, R.; Johansson, H. J.; Said Hassane, F.; Guterstam, P.; Suhorutšenko, J.; Moreno, P. M. D.; Oskolkov, N.; Hälldin, J.; Tedebark, U.; Metspalu, A.; Lebleu, B.; Lehtiö, J.; Smith, C. I. E.; Langel, Ü. *Nucleic Acids Res.* **2011,** *39,* 3972–3987. doi:10.1093/nar/gkq1299
21. Ruczynski, J.; Wierzbicki, P. M.; Kogut-Wierzbicka, M.; Mucha, P.; Siedlecka-Kroplewska, K.; Rekowski, P. *Folia Histochem. Cytobiol.* **2014,** *52,* 257–269. doi:10.5603/fhc.a2014.0034
22. Pae, J.; Säälik, P.; Liivamägi, L.; Lubenets, D.; Arukuusk, P.; Langel, Ü.; Pooga, M. *J. Controlled Release* **2014,** *192,* 103–113. doi:10.1016/j.jconrel.2014.07.002
23. Trabulo, S.; Cardoso, A. L.; Mano, M.; De Lima, M. C. P. *Pharmaceuticals* **2010,** *3,* 961–993. doi:10.3390/ph3040961
24. Derossi, D.; Chassaing, G.; Prochiantz, A. *Trends Cell Biol.* **1998,** *8,* 84–87. doi:10.1016/s0962-8924(98)80017-2
25. Maniti, O.; Alves, I.; Trugnan, G.; Ayala-Sanmartin, J. *PLoS One* **2010,** *5,* e15819. doi:10.1371/journal.pone.0015819
26. Alves, I. D.; Jiao, C.-Y.; Aubry, S.; Aussedat, B.; Burlina, F.; Chassaing, G.; Sagan, S. *Biochim. Biophys. Acta, Biomembr.* **2010,** *1798,* 2231–2239. doi:10.1016/j.bbamem.2010.02.009
27. Copolovici, D. M.; Langel, K.; Eriste, E.; Langel, Ü. *ACS Nano* **2014,** *8,* 1972–1994. doi:10.1021/nn4057269
28. Bechara, C.; Sagan, S. *FEBS Lett.* **2013,** *587,* 1693–1702. doi:10.1016/j.febslet.2013.04.031
29. Deshayes, S.; Morris, M. C.; Divita, G.; Heitz, F. *Biochim. Biophys. Acta, Biomembr.* **2006,** *1758,* 328–335. doi:10.1016/j.bbamem.2005.10.004
30. Deshayes, S.; Heitz, A.; Morris, M. C.; Charnet, P.; Divita, G.; Heitz, F. *Biochemistry* **2004,** *43,* 1449–1457. doi:10.1021/bi035682s
31. Simeoni, F.; Morris, M. C.; Heitz, F.; Divita, G. *Nucleic Acids Res.* **2003,** *31,* 2717–2724. doi:10.1093/nar/gkg385
32. Gerbal-Chaloin, S.; Gondeau, C.; Aldrian-Herrada, G.; Heitz, F.; Gauthier-Rouvière, C.; Divita, G. *Biol. Cell* **2007,** *99,* 223–238. doi:10.1042/bc20060123
33. Deshayes, S.; Gerbal-Chaloin, S.; Morris, M. C.; Aldrian-Herrada, G.; Charnet, P.; Divita, G.; Heitz, F. *Biochim. Biophys. Acta, Biomembr.* **2004,** *1667,* 141–147. doi:10.1016/j.bbamem.2004.09.010
34. Pouny, Y.; Rapaport, D.; Mor, A.; Nicolas, P.; Shai, Y. *Biochemistry* **1992,** *31,* 12416–12423. doi:10.1021/bi00164a017
35. Mudhakir, D.; Harashima, H. *AAPS J.* **2009,** *11,* 65–77. doi:10.1208/s12248-009-9080-9
36. Ludtke, S.; He, K.; Huang, H. *Biochemistry* **1995,** *34,* 16764–16769. doi:10.1021/bi00051a026
37. Shin, M. C.; Zhang, J.; Min, K. A.; Lee, K.; Byun, Y.; David, A. E.; He, H.; Yang, V. C. *J. Biomed. Mater. Res., Part A* **2014,** *102,* 575–587. doi:10.1002/jbm.a.34859
38. Richard, J. P.; Melikov, K.; Vives, E.; Ramos, C.; Verbeure, B.; Gait, M. J.; Chernomordik, L. V.; Lebleu, B. *J. Biol. Chem.* **2003,** *278,* 585–590. doi:10.1074/jbc.m209548200
39. Schmidt, N.; Mishra, A.; Lai, G. H.; Wong, G. C. L. *FEBS Lett.* **2010,** *584,* 1806–1813. doi:10.1016/j.febslet.2009.11.046
40. Ter-Avetisyan, G.; Tünnemann, G.; Nowak, D.; Nitschke, M.; Herrmann, A.; Drab, M.; Cardoso, M. C. *J. Biol. Chem.* **2009,** *284,* 3370–3378. doi:10.1074/jbc.m805550200
41. Fretz, M. M.; Penning, N. A.; Al-Taei, S.; Futaki, S.; Takeuchi, T.; Nakase, I.; Storm, G.; Jones, A. T. *Biochem. J.* **2007,** *403,* 335–342. doi:10.1042/bj20061808
42. Wallbrecher, R.; Ackels, T.; Olea, R. A.; Klein, M. J.; Caillon, L.; Schiller, J.; Bovée-Geurts, P. H.; van Kuppevelt, T. H.; Ulrich, A. S.; Spehr, M.; Adjobo-Hermans, M. J. W.; Brock, R. *J. Controlled Release* **2017,** *256,* 68–78. doi:10.1016/j.jconrel.2017.04.013
43. Sakai, N.; Futaki, S.; Matile, S. *Soft Matter* **2006,** *2,* 636–641. doi:10.1039/b606955j
44. Futaki, S.; Nakase, I. *Acc. Chem. Res.* **2017,** *50,* 2449–2456. doi:10.1021/acs.accounts.7b00221
45. Hirose, H.; Takeuchi, T.; Osakada, H.; Pujals, S.; Katayama, S.; Nakase, I.; Kobayashi, S.; Haraguchi, T.; Futaki, S. *Mol. Ther.* **2012,** *20,* 984–993. doi:10.1038/mt.2011.313
46. Ziegler, A.; Nervi, P.; Dürrenberger, M.; Seelig, J. *Biochemistry* **2005,** *44,* 138–148. doi:10.1021/bi0491604

47. Herce, H. D.; Garcia, A. E. *Proc. Natl. Acad. Sci. U. S. A.* **2007,** *104,* 20805–20810. doi:10.1073/pnas.0706574105
48. Herce, H. D.; Garcia, A. E.; Litt, J.; Kane, R. S.; Martin, P.; Enrique, N.; Rebolledo, A.; Milesi, V. *Biophys. J.* **2009,** *97,* 1917–1925. doi:10.1016/j.bpj.2009.05.066
49. Li, Z.-l.; Ding, H.-m.; Ma, Y.-q. *Soft Matter* **2013,** *9,* 1281–1286. doi:10.1039/c2sm26519b
50. Hu, J.-m.; Tian, W.-d.; Ma, Y.-q. *Macromol. Theory Simul.* **2015,** *24,* 399–406. doi:10.1002/mats.201500023
51. Zhao, F.; Zhao, Y.; Liu, Y.; Chang, X.; Chen, C.; Zhao, Y. *Small* **2011,** *7,* 1322–1337. doi:10.1002/smll.201100001
52. Conner, S. D.; Schmid, S. L. *Nature* **2003,** *422,* 37–44. doi:10.1038/nature01451
53. Chou, L. Y. T.; Ming, K.; Chan, W. C. W. *Chem. Soc. Rev.* **2011,** *40,* 233–245. doi:10.1039/c0cs00003e
54. Nel, A. E.; Mädler, L.; Velegol, D.; Xia, T.; Hoek, E. M. V.; Somasundaran, P.; Klaessig, F.; Castranova, V.; Thompson, M. *Nat. Mater.* **2009,** *8,* 543–557. doi:10.1038/nmat2442
55. Nakase, I.; Niwa, M.; Takeuchi, T.; Sonomura, K.; Kawabata, N.; Koike, Y.; Takehashi, M.; Tanaka, S.; Ueda, K.; Simpson, J. C.; Jones, A. T.; Sugiura, Y.; Futaki, S. *Mol. Ther.* **2004,** *10,* 1011–1022. doi:10.1016/j.ymthe.2004.08.010
56. Kaplan, I. M.; Wadia, J. S.; Dowdy, S. F. *J. Controlled Release* **2005,** *102,* 247–253. doi:10.1016/j.jconrel.2004.10.018
57. Yesylevskyy, S.; Marrink, S.-J.; Mark, A. E. *Biophys. J.* **2009,** *97,* 40–49. doi:10.1016/j.bpj.2009.03.059
58. Nakase, I.; Akita, H.; Kogure, K.; Gräslund, A.; Langel, Ü.; Harashima, H.; Futaki, S. *Acc. Chem. Res.* **2012,** *45,* 1132–1139. doi:10.1021/ar200256e
59. Farkhani, S. M.; Johari-ahar, M.; Zakeri-Milani, P.; Shahbazi Mojarrad, J.; Valizadeh, H. *Artif. Cells, Nanomed., Biotechnol.* **2015,** 1–5. doi:10.3109/21691401.2015.1031906
60. Wadia, J. S.; Stan, R. V.; Dowdy, S. F. *Nat. Med.* **2004,** *10,* 310–315. doi:10.1038/nm996
61. Futaki, S.; Nakase, I.; Tadokoro, A.; Takeuchi, T.; Jones, A. T. *Biochem. Soc. Trans.* **2007,** *35,* 784–787. doi:10.1042/bst0350784
62. Jones, A. T. *J. Cell. Mol. Med.* **2007,** *11,* 670–684. doi:10.1111/j.1582-4934.2007.00062.x
63. Lim, J. P.; Gleeson, P. A. *Immunol. Cell Biol.* **2011,** *89,* 836–843. doi:10.1038/icb.2011.20
64. Swanson, J. A.; Watts, C. *Trends Cell Biol.* **1995,** *5,* 424–428. doi:10.1016/s0962-8924(00)89101-1
65. Nakase, I.; Hirose, H.; Tanaka, G.; Tadokoro, A.; Kobayashi, S.; Takeuchi, T.; Futaki, S. *Mol. Ther.* **2009,** *17,* 1868–1876. doi:10.1038/mt.2009.192
66. Tanaka, G.; Nakase, I.; Fukuda, Y.; Masuda, R.; Oishi, S.; Shimura, K.; Kawaguchi, Y.; Takatani-Nakase, T.; Langel, Ü.; Gräslund, A.; Okawa, K.; Matsuoka, M.; Fujii, N.; Hatanaka, Y.; Futaki, S. *Chem. Biol.* **2012,** *19,* 1437–1446. doi:10.1016/j.chembiol.2012.09.011
67. Duchardt, F.; Fotin-Mleczek, M.; Schwarz, H.; Fischer, R.; Brock, R. *Traffic* **2007,** *8,* 848–866. doi:10.1111/j.1600-0854.2007.00572.x
68. Walrant, A.; Cardon, S.; Burlina, F.; Sagan, S. *Acc. Chem. Res.* **2017,** *50,* 2968–2975. doi:10.1021/acs.accounts.7b00455
69. Boisguérin, P.; Deshayes, S.; Gait, M. J.; O'Donovan, L.; Godfrey, C.; Betts, C. A.; Wood, M. J. A.; Lebleu, B. *Adv. Drug Delivery Rev.* **2015,** *87,* 52–67. doi:10.1016/j.addr.2015.02.008
70. Nakase, I.; Tadokoro, A.; Kawabata, N.; Takeuchi, T.; Katoh, H.; Hiramoto, K.; Negishi, M.; Nomizu, M.; Sugiura, Y.; Futaki, S. *Biochemistry* **2007,** *46,* 492–501. doi:10.1021/bi0612824
71. Nakase, I.; Noguchi, K.; Aoki, A.; Takatani-nakase, T.; Fujii, I.; Futaki, S. *Sci. Rep.* **2017,** *7,* 1–12. doi:10.1038/s41598-017-02014-6
72. Nakase, I.; Osaki, K.; Tanaka, G.; Utani, A.; Futaki, S. *Biochem. Biophys. Res. Commun.* **2014,** *446,* 857–862. doi:10.1016/j.bbrc.2014.03.018
73. Pang, H.-B.; Braun, G. B.; Ruoslahti, E. *Sci. Adv.* **2015,** *1,* e1500821. doi:10.1126/sciadv.1500821
74. Kawaguchi, Y.; Tanaka, G.; Nakase, I.; Imanishi, M.; Chiba, J.; Hatanaka, Y.; Futaki, S. *Bioorg. Med. Chem. Lett.* **2013,** *23,* 3738–3740. doi:10.1016/j.bmcl.2013.05.008
75. Ezzat, K.; Helmfors, H.; Tudoran, O.; Juks, C.; Lindberg, S.; Padari, K.; El-Andaloussi, S.; Pooga, M.; Langel, Ü. *FASEB J.* **2012,** *26,* 1172–1180. doi:10.1096/fj.11-191536
76. Helmfors, H.; Lindberg, S.; Langel, Ü. SCARA Involvement in the Uptake of Nanoparticles Formed by Cell-Penetrating Peptides. *Methods in Molecular Biology;* Springer New York: New York, NY, U.S.A., 2015; pp 163–174. doi:10.1007/978-1-4939-2806-4_11
77. Arukuusk, P.; Pärnaste, L.; Margus, H.; Eriksson, N. K. J.; Vasconcelos, L.; Padari, K.; Pooga, M.; Langel, Ü. *Bioconjugate Chem.* **2013,** *24,* 1721–1732. doi:10.1021/bc4002757
78. Xiang, S.; Tong, H.; Shi, Q.; Fernandes, J. C.; Jin, T.; Dai, K.; Zhang, X. *J. Controlled Release* **2012,** *158,* 371–378. doi:10.1016/j.jconrel.2011.09.093
79. Haucke, V.; Kozlov, M. M. *J. Cell Sci.* **2018,** *131,* 1–10. doi:10.1242/jcs.216812
80. Mettlen, M.; Chen, P.-H.; Srinivasan, S.; Danuser, G.; Schmid, S. L. *Annu. Rev. Biochem.* **2018,** *87,* 871–896. doi:10.1146/annurev-biochem-062917-012644
81. Smith, S. M.; Baker, M.; Halebian, M.; Smith, C. J. *Front. Mol. Biosci.* **2017,** *4,* 1–11. doi:10.3389/fmolb.2017.00072
82. Kaksonen, M.; Roux, A. *Nat. Rev. Mol. Cell Biol.* **2018,** *19,* 313–326. doi:10.1038/nrm.2017.132
83. Richard, J. P.; Melikov, K.; Brooks, H.; Prevot, P.; Lebleu, B.; Chernomordik, L. V. *J. Biol. Chem.* **2005,** *280,* 15300–15306. doi:10.1074/jbc.m401604200
84. Veldhoen, S.; Laufer, S. D.; Trampe, A.; Restle, T. *Nucleic Acids Res.* **2006,** *34,* 6561–6573. doi:10.1093/nar/gkl941
85. Laufer, S. D.; Detzer, A.; Sczakiel, G.; Restle, T. Selected Strategies for the Delivery of siRNA In Vitro and In Vivo. *RNA Technologies and Their Applications;* Springer Berlin: Berlin, Germany, 2010; pp 29–58. doi:10.1007/978-3-642-12168-5_2
86. Kawaguchi, Y.; Takeuchi, T.; Kuwata, K.; Chiba, J.; Hatanaka, Y.; Nakase, I.; Futaki, S. *Bioconjugate Chem.* **2016,** *27,* 1119–1130. doi:10.1021/acs.bioconjchem.6b00082
87. Christianson, H. C.; Belting, M. *Matrix Biol.* **2014,** *35,* 51–55. doi:10.1016/j.matbio.2013.10.004
88. Arukuusk, P.; Pärnaste, L.; Oskolkov, N.; Copolovici, D.-M.; Margus, H.; Padari, K.; Möll, K.; Maslovskaja, J.; Tegova, R.; Kivi, G.; Tover, A.; Pooga, M.; Ustav, M.; Langel, Ü. *Biochim. Biophys. Acta, Biomembr.* **2013,** *1828,* 1365–1373. doi:10.1016/j.bbamem.2013.01.011
89. Kiss, A. L.; Botos, E. *J. Cell. Mol. Med.* **2009,** *13,* 1228–1237. doi:10.1111/j.1582-4934.2009.00754.x
90. Nabi, I. R.; Le, P. U. *J. Cell Biol.* **2003,** *161,* 673–677. doi:10.1083/jcb.200302028

91. Branza-Nichita, N.; Macovei, A.; Lazar, C. Caveolae-Dependent Endocytosis in Viral Infection. *Molecular Regulation of Endocytosis;* InTech, 2012. doi:10.5772/48538
92. Fittipaldi, A.; Ferrari, A.; Zoppé, M.; Arcangeli, C.; Pellegrini, V.; Beltram, F.; Giacca, M. *J. Biol. Chem.* **2003,** *278,* 34141–34149. doi:10.1074/jbc.m303045200
93. Ferrari, A.; Pellegrini, V.; Arcangeli, C.; Fittipaldi, A.; Giacca, M.; Beltram, F. *Mol. Ther.* **2003,** *8,* 284–294. doi:10.1016/s1525-0016(03)00122-9
94. Pujals, S.; Giralt, E. *Adv. Drug Delivery Rev.* **2008,** *60,* 473–484. doi:10.1016/j.addr.2007.09.012
95. Säälik, P.; Padari, K.; Niinep, A.; Lorents, A.; Hansen, M.; Jokitalo, E.; Langel, Ü.; Pooga, M. *Bioconjugate Chem.* **2009,** *20,* 877–887. doi:10.1021/bc800416f
96. Rejman, J.; Oberle, V.; Zuhorn, I. S.; Hoekstra, D. *Biochem. J.* **2004,** *377,* 159–169. doi:10.1042/bj20031253
97. Veiman, K.-L.; Mäger, I.; Ezzat, K.; Margus, H.; Lehto, T.; Langel, K.; Kurrikoff, K.; Arukuusk, P.; Suhorutšenko, J.; Padari, K.; Pooga, M.; Lehto, T.; Langel, Ü. *Mol. Pharmaceutics* **2013,** *10,* 199–210. doi:10.1021/mp3003557
98. Taylor, B. N.; Mehta, R. R.; Yamada, T.; Lekmine, F.; Christov, K.; Chakrabarty, A. M.; Green, A.; Bratescu, L.; Shilkaitis, A.; Beattie, C. W.; Das Gupta, T. K. *Cancer Res.* **2009,** *69,* 537–546. doi:10.1158/0008-5472.can-08-2932
99. Mehta, R. R.; Yamada, T.; Taylor, B. N.; Christov, K.; King, M. L.; Majumdar, D.; Lekmine, F.; Tiruppathi, C.; Shilkaitis, A.; Bratescu, L.; Green, A.; Beattie, C. W.; Das Gupta, T. K. *Angiogenesis* **2011,** *14,* 355–369. doi:10.1007/s10456-011-9220-6
100. Hu, G.; Zheng, W.; Li, A.; Mu, Y.; Shi, M.; Li, T.; Zou, H.; Shao, H.; Qin, A.; Ye, J. *Vet. Res.* **2018,** *49,* 1–9. doi:10.1186/s13567-018-0513-2
101. Kirkham, M.; Parton, R. G. *Biochim. Biophys. Acta, Mol. Cell Res.* **2005,** *1745,* 273–286. doi:10.1016/j.bbamcr.2005.06.002
102. Damm, E.-M.; Pelkmans, L.; Kartenbeck, J.; Mezzacasa, A.; Kurzchalia, T.; Helenius, A. *J. Cell Biol.* **2005,** *168,* 477–488. doi:10.1083/jcb.200407113
103. Hemalatha, A.; Mayor, S. *F1000Research* **2019,** *8,* 138. doi:10.12688/f1000research.16549.1
104. Ye, J.; Pei, X.; Cui, H.; Yu, Z.; Lee, H.; Wang, J.; Wang, X.; Sun, L.; He, H.; Yang, V. C. *J. Ind. Eng. Chem. (Amsterdam, Neth.)* **2018,** *63,* 103–111. doi:10.1016/j.jiec.2018.02.005
105. Erazo-Oliveras, A.; Muthukrishnan, N.; Baker, R.; Wang, T.-Y.; Pellois, J.-P. *Pharmaceuticals* **2012,** *5,* 1177–1209. doi:10.3390/ph5111177
106. Yang, S.-T.; Zaitseva, E.; Chernomordik, L. V.; Melikov, K. *Biophys. J.* **2010,** *99,* 2525–2533. doi:10.1016/j.bpj.2010.08.029
107. El-Sayed, A.; Futaki, S.; Harashima, H. *AAPS J.* **2009,** *11,* 13–22. doi:10.1208/s12248-008-9071-2
108. Tünnemann, G.; Ter-Avetisyan, G.; Martin, R. M.; Stöckl, M.; Herrmann, A.; Cardoso, M. C. *J. Pept. Sci.* **2008,** *14,* 469–476. doi:10.1002/psc.968
109. El-Andaloussi, S.; Johansson, H. J.; Lundberg, P.; Langel, Ü. *J. Gene Med.* **2006,** *8,* 1262–1273. doi:10.1002/jgm.950
110. Beloor, J.; Zeller, S.; Choi, C. S.; Lee, S.-K.; Kumar, P. *Ther. Delivery* **2015,** *6,* 491–507. doi:10.4155/tde.15.2
111. Lo, S. L.; Wang, S. *Biomaterials* **2008,** *29,* 2408–2414. doi:10.1016/j.biomaterials.2008.01.031
112. Tünnemann, G.; Martin, R. M.; Haupt, S.; Patsch, C.; Edenhofer, F.; Cardoso, M. C. *FASEB J.* **2006,** *20,* 1775–1784. doi:10.1096/fj.05-5523com
113. Maiolo, J. R.; Ferrer, M.; Ottinger, E. A. *Biochim. Biophys. Acta, Biomembr.* **2005,** *1712,* 161–172. doi:10.1016/j.bbamem.2005.04.010
114. Jones, A. T.; Sayers, E. J. *J. Controlled Release* **2012,** *161,* 582–591. doi:10.1016/j.jconrel.2012.04.003
115. Hällbrink, M.; Oehlke, J.; Papsdorf, G.; Bienert, M. *Biochim. Biophys. Acta, Biomembr.* **2004,** *1667,* 222–228. doi:10.1016/j.bbamem.2004.10.009
116. Mueller, J.; Kretzschmar, I.; Volkmer, R.; Boisguerin, P. *Bioconjugate Chem.* **2008,** *19,* 2363–2374. doi:10.1021/bc800194e
117. Aruffo, A. Transient Expression of Proteins Using COS Cells. *Current Protocols in Molecular Biology;* John Wiley & Sons, Inc.: Hoboken, NJ, U.S.A., 2002. doi:10.1002/0471142727.mb1612s60
118. Gluzman, Y. *Cell* **1981,** *23,* 175–182. doi:10.1016/0092-8674(81)90282-8
119. Jones, S. W.; Christison, R.; Bundell, K.; Voyce, C. J.; Brockbank, S. M. V.; Newham, P.; Lindsay, M. A. *Br. J. Pharmacol.* **2005,** *145,* 1093–1102. doi:10.1038/sj.bjp.0706279
120. Tyagi, M.; Rusnati, M.; Presta, M.; Giacca, M. *J. Biol. Chem.* **2001,** *276,* 3254–3261. doi:10.1074/jbc.m006701200
121. Walrant, A.; Correia, I.; Jiao, C.-Y.; Lequin, O.; Bent, E. H.; Goasdoué, N.; Lacombe, C.; Chassaing, G.; Sagan, S.; Alves, I. D. *Biochim. Biophys. Acta, Biomembr.* **2011,** *1808,* 382–393. doi:10.1016/j.bbamem.2010.09.009
122. Gronewold, A.; Horn, M.; Ranđelović, I.; Tóvári, J.; Muñoz Vázquez, S.; Schomäcker, K.; Neundorf, I. *ChemMedChem* **2017,** *12,* 42–49. doi:10.1002/cmdc.201600498
123. Crosio, M. A.; Via, M. A.; Cámara, C. I.; Mangiarotti, A.; Del Pópolo, M. G.; Wilke, N. *Biomolecules* **2019,** *9,* 625. doi:10.3390/biom9100625
124. Suhorutsenko, J.; Oskolkov, N.; Arukuusk, P.; Kurrikoff, K.; Eriste, E.; Copolovici, D.-M.; Langel, Ü. *Bioconjugate Chem.* **2011,** *22,* 2255–2262. doi:10.1021/bc200293d
125. Habault, J.; Poyet, J.-L. *Molecules* **2019,** *24,* 927. doi:10.3390/molecules24050927
126. Guidotti, G.; Brambilla, L.; Rossi, D. *Trends Pharmacol. Sci.* **2017,** *38,* 406–424. doi:10.1016/j.tips.2017.01.003
127. Toro, A.; Paiva, M.; Ackerley, C.; Grunebaum, E. *Cell. Immunol.* **2006,** *240,* 107–115. doi:10.1016/j.cellimm.2006.07.003
128. Toro, A.; Grunebaum, E. *J. Clin. Invest.* **2006,** *116,* 2717–2726. doi:10.1172/jci25052
129. Schiroli, D.; Gómara, M. J.; Maurizi, E.; Atkinson, S. D.; Mairs, L.; Christie, K. A.; Cobice, D. F.; McCrudden, C. M.; Nesbit, M. A.; Haro, I.; Moore, T. *Mol. Ther.–Nucleic Acids* **2019,** *17,* 891–906. doi:10.1016/j.omtn.2019.07.017
130. Ghatnekar, G. S.; O'Quinn, M. P.; Jourdan, L. J.; Gurjarpadhye, A. A.; Draughn, R. L.; Gourdie, R. G. *Regener. Med.* **2009,** *4,* 205–223. doi:10.2217/17460751.4.2.205
131. Ghatnekar, G. S.; Grek, C. L.; Armstrong, D. G.; Desai, S. C.; Gourdie, R. G. *J. Invest. Dermatol.* **2015,** *135,* 289–298. doi:10.1038/jid.2014.318

BEILSTEIN JOURNAL OF NANOTECHNOLOGY

Phase inversion-based nanoemulsions of medium chain triglyceride as potential drug delivery system for parenteral applications

Eike Folker Busmann, Dailén García Martínez, Henrike Lucas and Karsten Mäder*

Full Research Paper

Open Access

Address:
Institute of Pharmacy, Martin Luther University Halle-Wittenberg, Halle (Saale), Germany

Email:
Karsten Mäder* - karsten.maeder@pharmazie.uni-halle.de

* Corresponding author

Keywords:
cellular toxicity; isotonicity; nanoemulsion; phase inversion; solvent free; surface properties

Beilstein J. Nanotechnol. **2020,** *11,* 213–224.
doi:10.3762/bjnano.11.16

Received: 30 June 2019
Accepted: 05 December 2019
Published: 17 January 2020

This article is part of the thematic issue "Frontiers in pharmaceutical nanotechnology".

Guest Editor: M. G. Wacker

Abstract

Lipid nanoemulsions are attractive drug delivery systems for lipophilic drugs. To produce nanoemulsions with droplets of very small diameter (<100 nm), we investigated thermotropic phase transitions as an alternative to the standard procedure of high-pressure homogenization. Employing shock dilution with ice-cold water during the phase inversion gives the opportunity to produce nanoemulsions without any use of potentially toxic organic solvents. The systematic investigation of the relation of the three involved components surfactant, aqueous phase and lipid phase showed that depending on the ratio of surfactant to lipid the emulsions contained particles of diameters between 16 and 175 nm with narrow polydispersity index distributions and uncharged surfaces. Nanoemulsions with particles of 50 and 100 nm in diameter showed very little toxicity to fibroblast cells in vitro. An unusual, exponential-like nonlinear increase in osmolality was observed with increasing concentration of the nonionic surfactant Kolliphor HS 15. The experimental results indicate, that nanoemulsions with particles of small and tunable size can be easily formed without homogenization by thermal cycling.

Introduction

Nanoscaled drug delivery systems such as solid lipid or polymeric nanoparticles, nanocapsules, liquid nanoemulsions, liposomes and micelles can be used to carry poorly water soluble ingredients of pharmaceuticals for parenteral applications [1-3]. Thereby, the physical entrapment of the active ingredients into the core of the nanoparticles gives the possibility to solubilize and protect the sensitive drugs or contrast agents [2,4,5]. Their pharmacokinetics, including the distribution from the blood stream into the tissue, depend mainly on the size and shape, the surface composition, the charge as well as the flexibility of the

nanoparticles [6-9]. Shock dilution with ice-cold water during phase inversion of the emulsion gives the opportunity to produce nanocapsules without the use of any potentially toxic organic solvent at low energy cost [10,11]. The choice and the amount of the surfactant show different effects on the final product. For example, these factors influence the feasibility of forming stable nanostructures, they affect the phase inversion zone, the in vitro cellular toxicity and the above mentioned particle and surface properties [3,4,12].

There are marketed drug products with significant hyperosmolality up to 2000 mOsmol/kg [13]. However, parenteral products should aim at isotonicity to reduce the risk of possible crenation (shriveling) or hemolysis of the red blood cells as well as significant pain at the site of injection or even phlebitis [13,14]. Therefore, a balance of increasing osmolality and the concentration of the dissolved educts needs to be considered to achieve isotonic nanoemulsions ensuring a painless intravenous application. The osmolality $O(c)$ increases usually linearly with the solute concentration c, depending on the osmotic coefficient ϕ, the number of ions or particles n and the molecular weight M [15]:

$$O(c) = \frac{\phi n}{M} \cdot c \qquad (1)$$

However, the osmolality of many surfactants approaches a plateau above the critical micelle concentration. The formation of a separate micellar phase leads to a constant monomer concentration, therefore to a thermodynamically constrained system with a constant chemical potential and hence a constant osmotic pressure [16].

The aim of this study was to investigate the phase inversion-based production of a lipid nanocarrier without using phospholipids. Thus, instead of solid shelled nanocapsules, flexible nanoemulsions should be formed. Therefore, we systematically investigated the impact of the sodium chloride concentration on the phase inversion and the influence of the three involved components surfactant, aqueous phase and lipid phase on the formation of stable isotonic nanoemulsions. Furthermore, the relation of the particle composition, the particle size and the in vitro toxicity to fibroblasts was investigated.

Results and Discussion

Influence of the salinity on the phase inversion and the formation of nanoemulsions

To investigate the influence of the salinity of the aqueous phase on the incipient phase inversion and hence on the point of forming stable but nonisotonic nanoemulsions, the conductivity of a medium chain triglyceride (MCT)/Kolliphor® HS 15/NaCl solution (20:20:60) was measured as shown in Figure 1. Increasing the salinity of the aqueous phase resulted in a significant decrease of the temperature at the incipient phase inversion from 81.5 °C at 0.4 wt % NaCl concentration to 65.4 °C at 5 wt % NaCl concentration. The particles in the nanoemulsion had an average diameter (z_{ave}) of 56–59 nm and a remarkably narrow polydispersity index (PDI) distribution of 0.03–0.06.

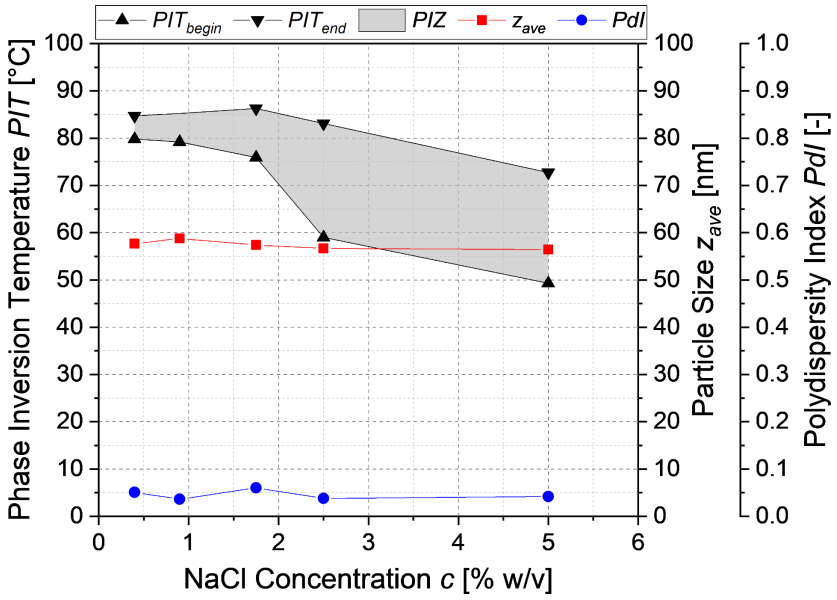

Figure 1: Influence of the salinity of the aqueous phase on the phase inverson zone (PIZ) for the nanoemulsions at a composition of MCT/Kolliphor/NaCl solution (20:20:60) along with the nanoparticle diameter and the PDI of the resulting nanoemulsion.

The salinity did not have a significant influence on the particle diameter and the PDI of the nanoemulsion formed by shock dilution.

Figure 2 shows the particle diameters and the PDIs of different nanoemulsions prepared using 1.75 wt % and 5 wt % NaCl solutions. Nanoemulsions were successfully formed using solutions of the compositions indicated by the colored zones. The solutions corresponding to the grey zones did not yield any stable nanoemulsions because they (1) resulted in creaming and/or coalescence directly after the shock dilution, or (2) the phase inversion temperature was higher than the boiling point of the aqueous phase. For solutions of higher salinity the area in which nanoemulsions were formed is enlarged, because the

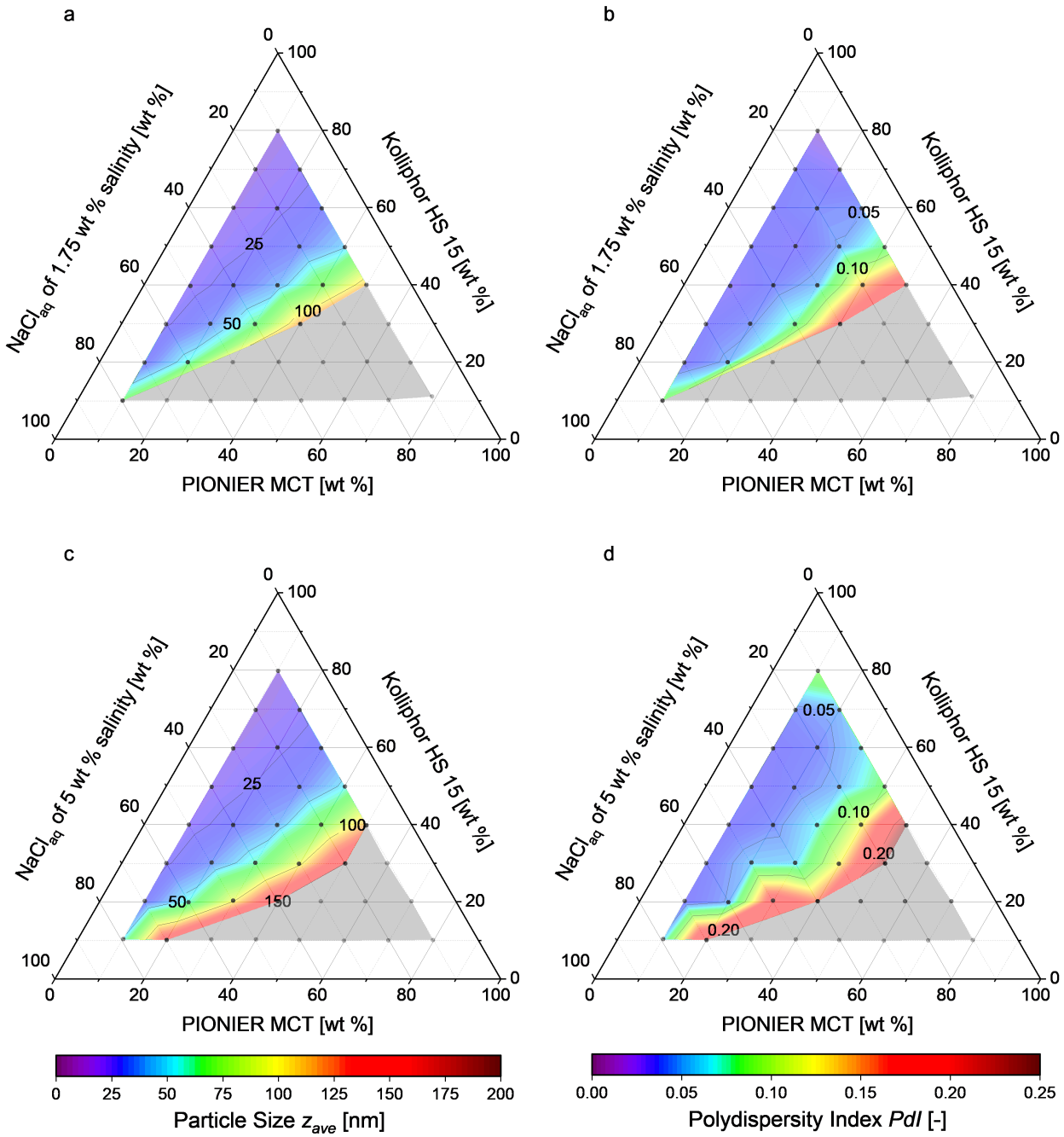

Figure 2: Ternary phase diagrams giving the particle diameter and the PDI of the nonisotonic nanoemulsions produced in (a, b) 1.75 wt % and (c, d) 5 wt % NaCl aqueous solution. Each dot represents the composition of the solution prepared for shock dilution. Formation of stable nanoemulsions occurs in the colored zone. Creaming coalescence or no phase inversion were observed in the grey zone.

phase inversion temperature lies further below the boiling point of the aqueous phase. This facilitated producing stable nanoemulsions with particles of 16–150 nm in diameter with narrow PDI distributions of 0.02–0.23. Increasing the mass share of the surfactant Kolliphor HS 15 led to smaller particles and narrower PDI distributions.

Influence of the nonionic surfactant Kolliphor HS 15 on the osmolality

The osmolality is an important parameter of the toxicity of parenteral dosage forms. The ideal osmolality values of an aqueous sodium chloride solution according to Ph. Eur. 2.2.35 and the experimentally determined osmolality of aqueous Kolliphor HS 15 are shown in Figure 3.

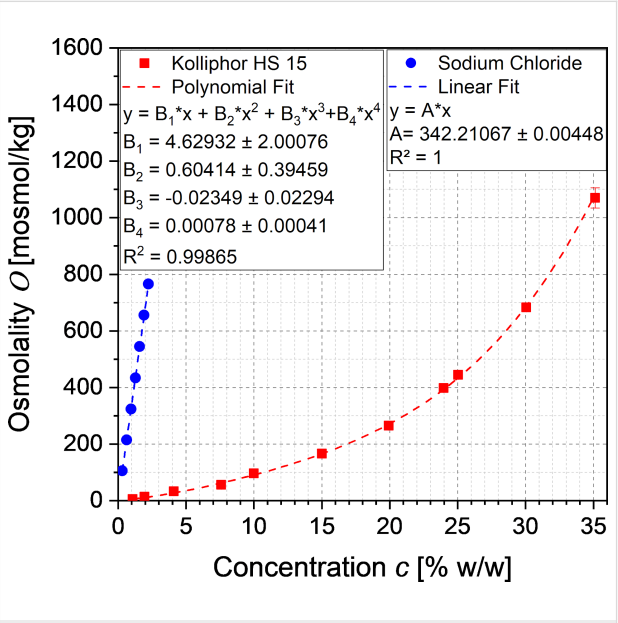

Figure 3: Ideal osmolality of aqueous sodium chloride solutions after Ph. Eur. 2.2.35 and experimental osmolality of aqueous dissolved Kolliphor HS 15, fitted according to Equation 1 and Equation 2.

The linearly increasing osmolality of the aqueous solution of sodium chloride was fitted with the linear van't Hoff law (Equation 1) at a coefficient of determination of 100%, and the reciprocal slope A was used for the term

$$\frac{M_{\mathrm{NaCl}}}{\phi_{\mathrm{NaCl}} n_{\mathrm{NaCl}}}$$

(see Equation 8) for the calculation of the salinity of isotonic nanoemulsions.

With increasing the concentration of the nonionic surfactant Kolliphor HS 15 the osmolality of the aqueous solution increased unexpectedly exponential-like instead of approaching the expected plateau above the critical micelle concentration. Intense literature research revealed only a single publication by Viegas and Henry [15] describing such a phenomenon for strongly interacting nonionic surfactants. The osmolality of solutions of such surfactants increases nonlinearly with the solute concentration due to increasing polymer–solvent hydrogen bonding at low temperatures, which prevents the flow of solvent molecules in the solution and thus affects osmosis. This phenomenon is described by a modified polynomial van't Hoff equation of 4th degree introduced by Huggins and Flory with the association or interacting constants $b1$, $b2$ and $b3$:

$$O(c) = \frac{\phi n}{M} \cdot c + \frac{\phi n b_1}{M} \cdot c^2 + \frac{\phi n b_2}{M} \cdot c^3 + \frac{\phi n b_3}{M} \cdot c^4 \qquad (2)$$

The experimental data corresponded well to the modified polynomial van't Hoff equation of 4th degree with a coefficient of determination of 99.865%. Thus, the equation was used for the calculation of the osmolality $O_{\mathrm{Kol}}(c_{\mathrm{Kol,p}})$.

Preparation of isotonic nanoemulsions

Given an osmolality of whole blood of 302 ± 5 mOsmol/kg and of blood plasma of 291 ± 4 mOsmol/kg [17], it was decided to produce nanoemulsions with a target osmolality of 300 mOsmol/kg. The necessary salinity of the aqueous phase for shock dilution was calculated according to Equations 8 to 11 for a product MCT mass share $x_{\mathrm{MCT,p}}$ of 8 wt %, which resulted in solutions of varying NaCl concentration (see Figure S1 in Supporting Information File 1).

Using this equation system for the production of isotonic nanoemulsions led to high salinities of up to 25 wt % in the aqueous phase before shock dilution. Increasing the salinity of the aqueous phase decreased the phase inversion temperature. In ternary phase diagrams, this decrease of the phase inversion temperature enlarged the area in which stable nanoemulsions were formed compared to the nonisotonic nanoemulsions produced in aqueous solutions of 1.75 wt % and 5 wt % NaCl concentration, as shown in Figure 4.

Nanoemulsions with particles of 16–175 nm in diameter were formed with narrow PDI distributions of 0.02–0.25, as illustrated in Figure 4a and Figure 4b. All nanoemulsions were stable over one month at room temperature. The sizes of the particles within the nanoemulsions depended only on the ratio of Kolliphor HS 15 to MCT. The dependence depicted in Figure 5 agrees well with a Holliday fit yielding a coefficient of determination of 98.86%. The increase of the concentration of the surfactant Kolliphor HS 15 and hence the increase of the ratio of Kolliphor HS 15 to MCT resulted in a prompt decrease of the particle diameter. The constant limit is reached at ratios above three.

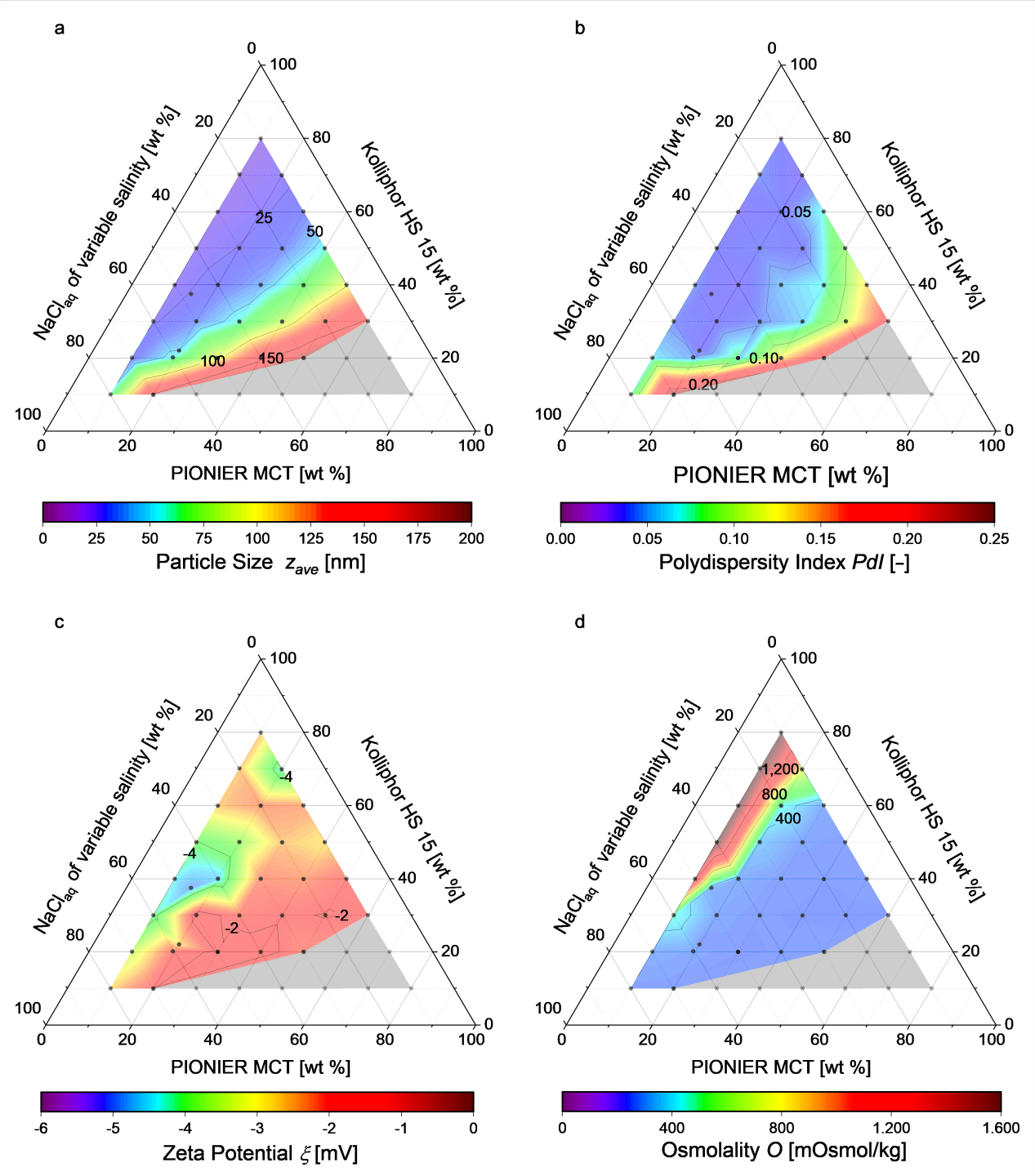

Figure 4: Ternary phase diagrams showing (a) the resulting particle diameter, (b) the PDI, (c) the zeta potential and (d) the osmolality. Each dot represents a certain solution composition. The formation of stable nanoemulsions occurs in the colored zone, while creaming coalescence or no phase inversion were observed in the grey zone.

The zeta potential of all nanoemulsions shown in Figure 4c was slightly negative between −1.6 and −4.6 mV, measured in 0.1× PBS at physiological pH 7.4. Thus, the composition of the nanoemulsion had no clear influence on the surface charge. Furthermore, isotonicity was nearly achieved for the formulations in the blue zone of Figure 4d. Formulations shown in the green, yellow and red zones resulted in hypertonicity although they were prepared in an NaCl free aqueous phase (compare Figure S1 in Supporting Information File 1) due to a final Kolliphor HS 15 concentration above 21 wt %. In these zones,

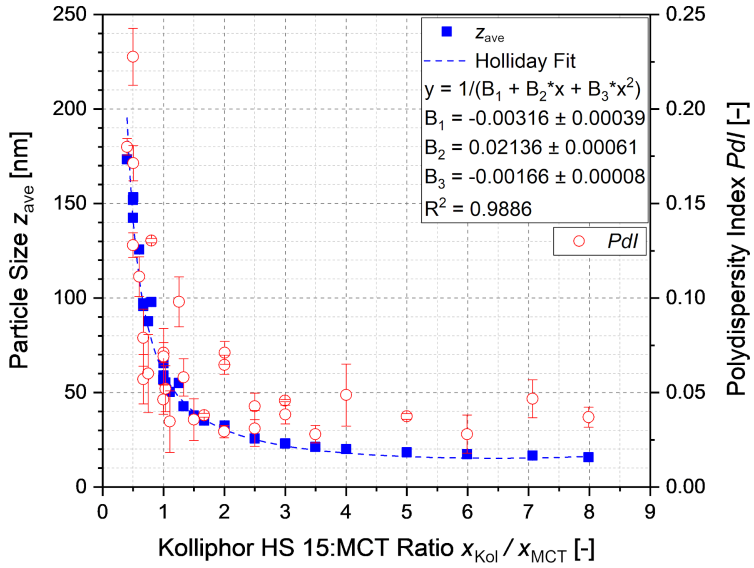

Figure 5: Particle diameters and PDI of the nanoemulsions depending on the Kolliphor HS 15:MCT ratio.

isotonicity may be achieved by producing nanoemulsions using a larger amount of aqueous solution for the shock dilution, which would also lead to a smaller MCT mass share in the product nanoemulsion.

Stability of the isotonic nanoemulsions

To investigate the stability of the nanoemulsions, four emulsions with particles of approximately 25 (NE25), 50 (NE50), 100 (NE100) and 150 nm (NE150) in diameter were chosen. Their composition and the final particle diameters observed in nine independently produced batches are listed in Table 1. Four selected nanoemulsions were stored at 5 ± 3 °C, room temperature (RT) and 40 ± 2 °C according to the ICH Guidelines Q1A. The impact of the storage conditions on the particle diameter is illustrated in Figure 6. With the exception of emulsion NE25, all nanoemulsions were stable over the course of eight weeks at the three storage conditions. Only NE25 underwent creaming and coalescence at 40 °C resulting in a significant increase of the particle diameter up to 146 nm and a high PDI of 0.35 within 8 weeks of storage. Hence, it is strongly recommended to store the nanoemulsions with particles of very small size at chilled conditions.

Cellular toxicity of the isotonic nanoemulsions

The cellular toxicity of the nanoemulsions NE25, NE50 and NE100 as well as the aqueous Kolliphor HS 15 solution to normal human dermal fibroblasts (NHDF) and mouse embryonic fibroblasts (3T3) was investigated. The impact of the nanoemulsions and the surfactant solution on the cell viability of the two cell lines after 4 and 24 h is illustrated in Figure 7. The viability of the cells treated with the different nanoemulsions is depicted as a function of the concentration of the surfactant Kolliphor HS 15. The resulting graphs indicate a similar behavior of all three nanoemulsions and the aqueous Kolliphor HS 15 solution, namely a decrease of the cell viability at a certain concentration c_{Kol}. The 3T3 cells responded more sensitively to the nanoemulsions and the pure surfactant solution. Furthermore, the long incubation time of 24 h led to cell toxicity at slightly lower concentrations for both cell lines. For com-

Table 1: Composition of the nanoemulsions NE25, NE50, NE100 and NE150 after shock dilution along with the particle diameters and PDI values of nine independently produced batches, c_{NaCl} describes the salinity of the aqueous phase of the final product.

	NE25	NE50	NE100	NE150
MCT [wt %]	8	8	8	8
Kolliphor HS 15 [wt %]	20	8.8	5.33	4
NaCl solution [wt %]	72	83.2	86.67	88
at c_{NaCl} [wt %]	0.084	0.654	0.763	0.798
particle diameter [nm]	26.2 ± 0.3	51.4 ± 0.7	99.4 ± 2.3	145.9 ± 4.7
polydispersity index [–]	0.046 ± 0.014	0.038 ± 0.006	0.092 ± 0.021	0.251 ± 0.091

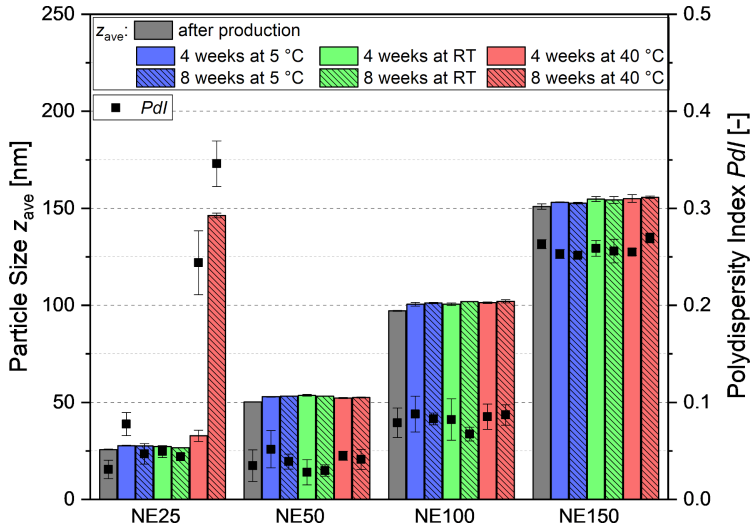

Figure 6: Long-term stability of four selected nanoemulsions with particles of approximately 25 (NE25), 50 (NE50), 100 (NE100) and 150 nm (NE150) in diameter at the recommended storage conditions according to the ICH guidelines Q1A of 5 ± 3 °C, room temperature (RT) and 40 ± 2 °C.

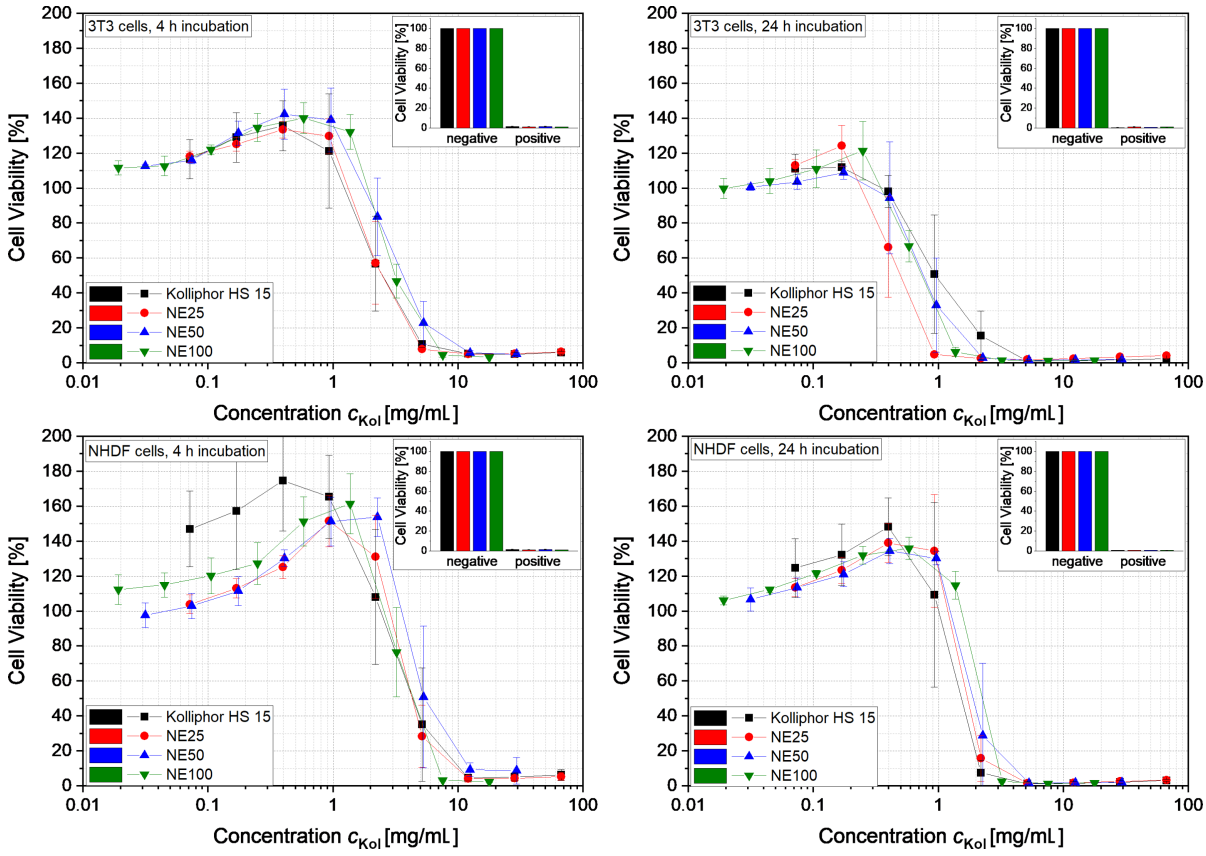

Figure 7: Viability of the cells of lines 3T3 and NHDF as a function of the Kolliphor HS 15 concentration c_{Kol} in the nanoemulsions NE25, NE50 and NE100 as well as the aqueous Kolliphor HS 15 solution (n = 3).

parison, for the current nanoemulsions, the cell viability began to decrease at values of the Kolliphor HS 15 concentration about 5 to 10 times higher than observed for a similar system with nanocapsules containing phospholipids as shells and Solutol HS 15 (also called Kolliphor HS 15) as surfactant which were tested on HaCaT cells [4]. At a concentration slightly

lower than the inhibiting Kolliphor HS 15 concentration, an increased cell viability was observed, which might be caused by a stimulated metabolism of the cells.

Table 2 lists the mean inhibitory concentration (IC_{50}) of Kolliphor HS 15 in an aqueous solution of Kolliphor HS 15 (second column) and the IC_{50} values of Kolliphor HS 15 in the nanoemulsions NE25, NE50 and NE100 (third, fourth and fifth column). The values in brackets refer to the concentration of MCT + Kolliphor HS15 in the nanoemulsions NE25, NE50 and NE100. The corresponding cell viability graphs are shown in Figure S2 in Supporting Information File 1. The IC_{50} values of Kolliphor HS 15 in the different nanoemulsions and the pure surfactant solution were similar for the different cell lines and incubation times employed. Thus, mainly the surfactant Kolliphor HS 15 inhibited cell viability at high concentration, since all remaining components are considered nontoxic. The IC_{50} values of the nanoemulsions (MCT + Kolliphor HS15) increased slightly with increasing particle diameter due to the lower Kolliphor HS 15 concentration in the nanoemulsions containing larger nanoparticles.

Figure 8 shows the morphology of the 3T3 and NHDF cells incubated for 24 h in a nontoxic solution with a concentration of

Table 2: Mean inhibitory concentration (IC_{50} in mg/mL) of Kolliphor HS 15 in an aqueous solution of Kolliphor HS 15 and IC_{50} of Kolliphor HS 15 in the nanoemulsions NE25, NE50 and NE100. The values in brackets refer to the concentration of MCT + Kolliphor HS15 in NE25, NE50 and NE100.

IC_{50} in mg/mL of:	Kolliphor HS 15	NE25	NE50	NE100
3T3, 4 h incubation	2.7 ± 0.9	2.6 ± 0.8 (3.6 ± 1.1)	3.8 ± 0.9 (7.3 ± 1.7)	3.3 ± 0.5 (8.2 ± 1.2)
NHDF, 4 h incubation	4.9 ± 2.2	4.5 ± 0.6 (6.3 ± 0.8)	6.2 ± 2.5 (11.9 ± 4.8)	4.6 ± 0.9 (11.5 ± 2.2)
3T3, 24 h incubation	1.2 ± 0.5	0.5 ± 0.2 (0.7 ± 0.2)	0.8 ± 0.3 (1.6 ± 0.6)	0.8 ± 0.1 (2.0 ± 0.2)
NHDF, 24 h incubation	1.5 ± 0.4	1.8 ± 0.2 (2.5 ± 0.3)	2.3 ± 0.9 (4.4 ± 1.7)	2.4 ± 0.1 (6.1 ± 0.2)

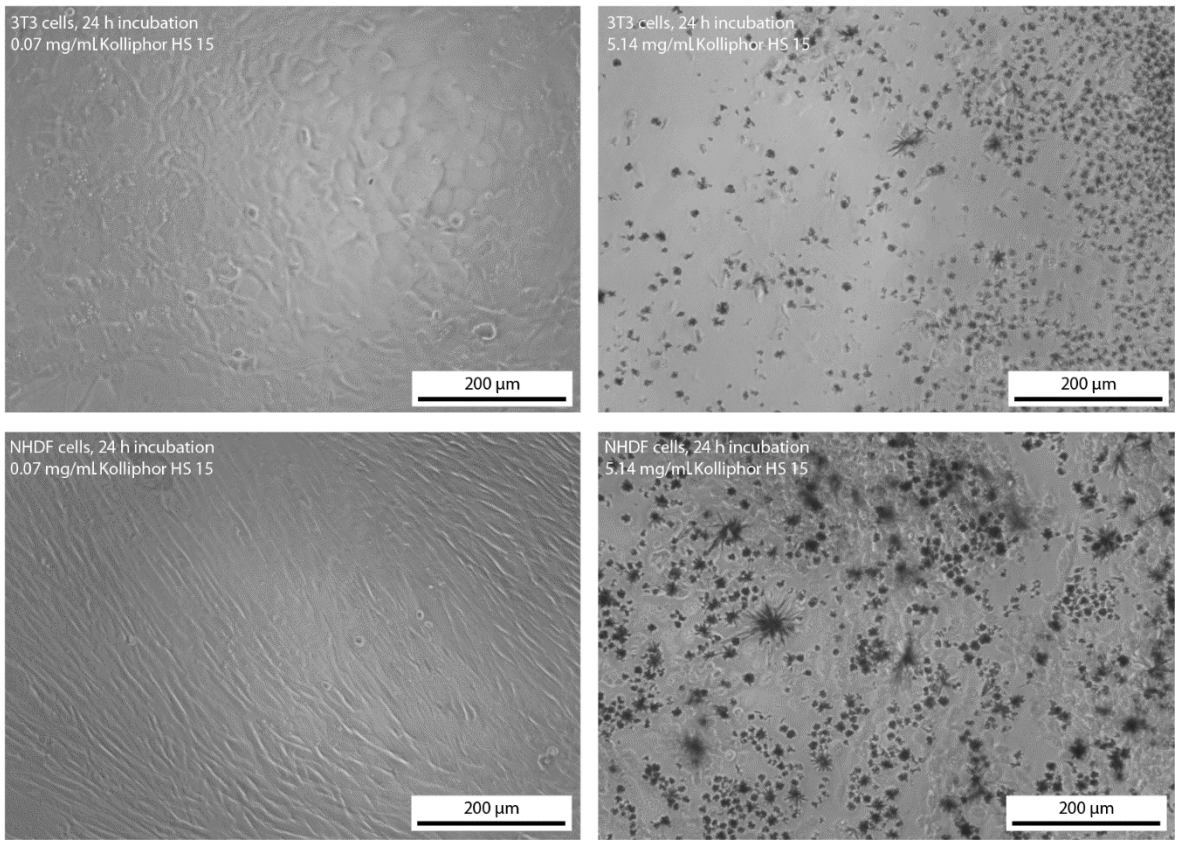

Figure 8: Morphology of the 3T3 and NHDF cells after 24 h incubation ion solutions with a concentration of the surfactant Kolliphor HS 15 of 0.07 and 5.14 mg/mL.

Kolliphor HS 15 of 0.07 mg/mL and a highly toxic solution with a concentration of Kolliphor HS 15 of 5.14 mg/mL. The microscopic pictures confirm the toxicity of the surfactant Kolliphor HS 15 at high concentration. The cells did not show any change in their morphology when dissolved in solutions of low surfactant concentration. However, the cells showed a shriveled morphology at high surfactant concentration. Furthermore, the formation of crystals was observed, which might consist of poorly water soluble 12-hydroxystearic acid as a metabolic degradation product of Kolliphor HS 15 at toxic and high surfactant concentration. 12-Hydroxystearic acid is known to form needle like structures. The formation of these crystals of 12-hydroxystearic acid might have caused the cell death in vitro for both cell lines. We assume, that the formation of 12-hydroxystearic acid-based precipitates is unlikely to occur in vivo because of the different transport and metabolic conditions.

Conclusion

The experimental results indicate that nanoemulsions with small particles of tunable size can be easily formed without homogenization by thermal cycling. Solutions of the nonionic surfactant Kolliphor HS 15 showed a nonlinear increase of osmolality with increasing Kolliphor HS 15 concentration, which corresponds well to the modified polynomial van't Hoff equation of 4th degree introduced by Huggins and Flory. This led to the hypertonicity of solutions with Kolliphor HS 15 concentration higher than 21 wt %. Considering this effect when calculating the salinity of the aqueous phase, stable isotonic and phospholipid-free MCT nanoemulsions were successfully produced with particles of tunable diameters between 16 to 175 nm and narrow PDI distributions depending on their lipid:surfactant ratio. Using a nonionic surfactant resulted in an uncharged surface of the emulsion droplets. The nanoemulsion with small particles of 25 nm in diameter showed an slightly increased cytotoxicity in comparison to the barely toxic nanoemulsions with particles of 50 and 100 nm in diameter. This effect is mainly caused by the very high amount of Kolliphor HS 15 in the nanoemulsion with the smallest particles. By choosing nanoemulsions with particles larger than 50 nm in diameter or by dilution of the nanoemulsions containing smaller particles with ice-cold water, very high surfactant concentrations could be avoided and the resulting MCT nanoemulsions might be suitable as potential drug delivery systems for intravenous applications. The presented phase inversion-based process offers a suitable alternative to the production of nanoemulsions based on high pressure homogenization. Particularly, nanoemulsions of particles with diameters smaller than 100 nm can be produced with remarkably narrow PDI distributions while reducing the demand of equipment, the process expenditure as well as the production volume.

Experimental

Materials

PIONIER MCT (medium chain triglyceride) was provided by Hansen & Rosenthal KG (Hamburg, Germany). Kolliphor HS 15 (macrogol 15 hydroxystearate) was provided by BASF SE (Ludwigshafen, Germany). Sodium chloride was purchased from Grüssing GmbH (Filsum, Germany), the components for the cell culture medium Dulbecco's Modified Eagle Medium – high glucose (DMEM), fetal calf serum (FCS), penicillin-streptomycin, L-glutamine solution and sodium pyruvate solution as well as the fluorescent dye resazurin sodium salt were purchased from Sigma-Aldrich Chemie GmbH (Germany, Steinheim). The near infrared fluorescent dye DiR was purchased from Invitrogen/Thermo Fisher Scientific Inc. (Carlsbad, USA). 0.2 µm sterile filtered water was used in all experiments and analytics and was double distilled.

Preparation of nanoemulsions

All nanoemulsions were prepared by a modified phase inversion-based process, which was initially developed by Heurtault et al. [10]. For the encapsulation of the fluorescent dye DiR as a potential label for noninvasive optical in vivo imaging, the solvent ethanol was evaporated from the dye stock solution and the remaining DiR was dissolved in MCT at a concentration of 0.3 mg/g. Kolliphor HS 15, which was molten at 50 °C, and MCT were dispersed in aqueous NaCl solution under magnetic stirring at ≈750 rpm. The emulsion was heated to 99 °C undergoing a phase inversion from an o/w to a w/o emulsion. The emulsion then was cooled back into its phase inversion zone, in which the mixtures turned transparent, and shock diluted with ice-cold water, as shown in Figure 9.

The amount of the respective educts was calculated with the following equations. The mass of MCT m_{MCT} is the product of its desired mass share $x_{MCT,p}$ in the nanoemulsion after shock dilution, which was set to 8 wt % in this study, and the desired total amount of the nanoemulsion m_{tot}:

$$m_{MCT} = m_{tot} \cdot x_{MCT,p} \tag{3}$$

The product of m_{MCT} and the desired ratio of the mass share of Kolliphor HS 15 $x_{Kol,0}$ and MCT $x_{MCT,0}$ results in the mass of Kolliphor HS 15 m_{Kol}:

$$m_{Kol} = m_{MCT} \cdot \frac{x_{Kol,0}}{x_{MCT,0}} = m_{tot} \cdot x_{MCT,p} \cdot \frac{x_{Kol,0}}{x_{MCT,0}} \tag{4}$$

The mass of the aqueous NaCl solution $m_{NaCl–Sol}$ is calculated by multiplying m_{MCT} and the ratio of $x_{Kol,0}$ and the mass share of the NaCl solution $x_{NaCl,0}$:

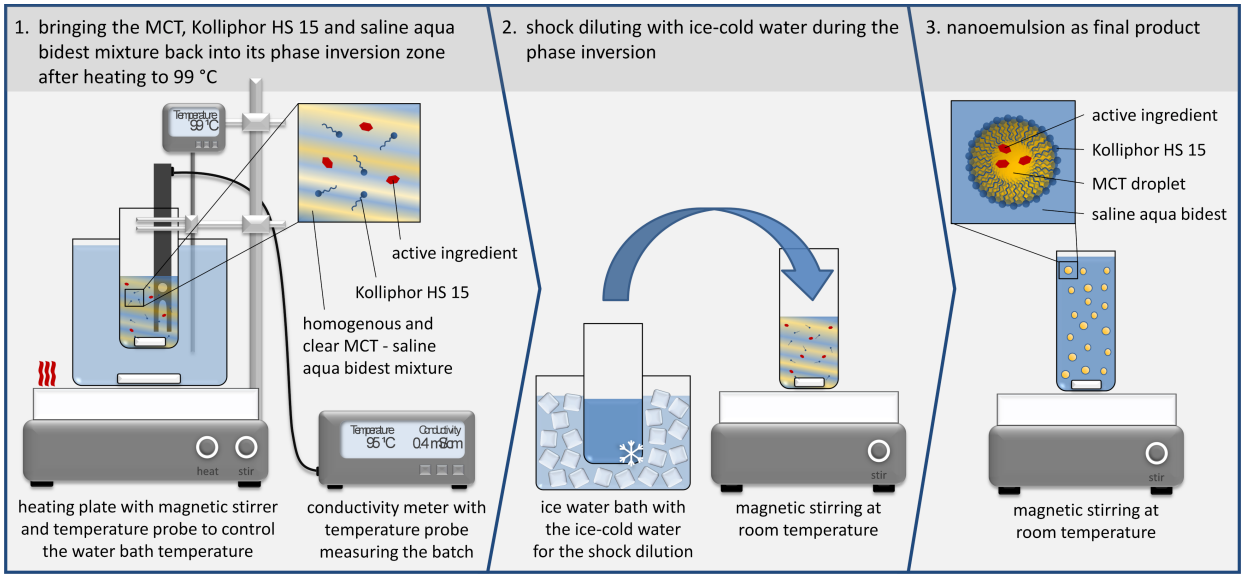

Figure 9: Scheme of the experimental set-up and the method of phase inversion-based production of the nanoemulsions.

$$m_{\text{NaCl–Sol}} = m_{\text{MCT}} \cdot \frac{x_{\text{NaCl–Sol},0}}{x_{\text{MCT},0}} = m_{\text{tot}} \cdot x_{\text{MCT,p}} \cdot \frac{1 - x_{\text{MCT},0} - x_{\text{Kol},0}}{x_{\text{MCT},0}} \quad (5)$$

The mass of the ice-cold water $m_{\text{ice water}}$ for shock dilution is the difference between the desired total mass of the nanoemulsion and the components calculated beforehand:

$$m_{\text{ice water}} = m_{\text{tot}} - m_{\text{MCT}} - m_{\text{Kol}} - m_{\text{NaCl–Sol}} = m_{\text{tot}} - m_{\text{tot}} \cdot x_{\text{MCT,p}} \cdot \left(1 + \frac{x_{\text{Kol},0}}{x_{\text{MCT},0}} + \frac{1 - x_{\text{MCT},0} - x_{\text{Kol},0}}{x_{\text{MCT},0}}\right) \quad (6)$$

To achieve isotonic nanoemulsions after shock dilution, the targeted osmolality of the saline aqueous phase $O_{\text{NaCl–Sol,p}}(c_{\text{NaCl,p}})$ is calculated as the difference of the osmolality of blood O_{blood} and the osmolality of the dissolved Kolliphor HS 15 $O_{\text{Kol,p}}(c_{\text{Kol,p}})$:

$$O_{\text{NaCl–Sol,p}}\left(c_{\text{NaCl,p}}\right) = O_{\text{blood}} - O_{\text{Kol,p}}\left(c_{\text{Kol,p}}\right) \quad (7)$$

Combining Equation 7 with Equation 1 and Equation 2 leads to the necessary sodium chloride concentration $c_{\text{NaCl,p}}$ to achieve the osmolality of blood and hence isotonicity:

$$c_{\text{NaCl,p}} = \left(O_{\text{blood}} - O_{\text{Kol}}\left(c_{\text{Kol,p}}\right)\right) \cdot \frac{M_{\text{NaCl}}}{\phi_{\text{NaCl}} n_{\text{NaCl}}} \quad (8)$$

Here, the concentration of Kolliphor HS 15 equals its mass share in the final product and is calculated by multiplying $x_{\text{MCT,p}}$ and the desired ratio of $x_{\text{Kol},0}$ and $x_{\text{MCT},0}$:

$$c_{\text{Kol,p}} = x_{\text{Kol,p}} = x_{\text{MCT,p}} \cdot \frac{x_{\text{Kol},0}}{x_{\text{MCT},0}} \quad (9)$$

Finally, the sodium chloride concentration $c_{\text{NaCl},0}$ before shock dilution is calculated by:

$$c_{\text{NaCl},0} = c_{\text{NaCl,p}} \cdot \frac{m_{\text{NaCl–Sol}} + m_{\text{ice water}}}{m_{\text{NaCl–Sol}}} \quad (10)$$

In case the calculated sodium chloride concentration exceeded 25 wt %, $c_{\text{NaCl},0}$ was set to 25 wt % and the residual salt was added to the ice-cold water at the following concentration:

$$c_{\text{NaCl,ice water}} = \frac{\left(m_{\text{NaCl–Sol}} + m_{\text{ice water}}\right) \cdot c_{\text{NaCl,p}}}{m_{\text{ice water}}} - \frac{m_{\text{NaCl–Sol}} \cdot c_{\text{NaCl},0}}{m_{\text{ice water}}} \quad (11)$$

Characterization of the phase inversion

The temperature of the phase inversion from an o/w to a w/o emulsion was determined by measuring the significant conduc-

tivity decrease during the heating process with the Mettler Toledo S230 SevenCompact conductivity meter.

Characterization of the osmolality

The osmolality was determined in triplicate with the KNAUER Semi-Mikro Osmometer. The osmolality of the sodium chloride solution (according to Ph. Eur. 2.2.35) was fitted linearly, and the experimentally determined osmolality of the aqueous solutions of Kolliphor HS 15 with different concentration were fitted with a polynomial function of 4th degree using the program Origin 2018G both with the intersection of the *y*-axis fixed at 0.

Particle size and zeta potential measurement

Particle diameters and zeta potentials were determined with the Malvern Instruments Zetasizer Nano ZS. To determine the particle diameters, the samples were diluted 1:100 in water and three measurements of 15 runs were conducted at 25 °C in the backscattering mode. The zeta potential was determined in triplicate with samples diluted 1:10 in 0.1× PBS with pH 7.4 at 25 °C with 10 to 50 runs per measurement.

Investigation of the stability

The samples were stored at 5 ± 3 °C, room temperature and at 40 ± 2 °C according to the storage conditions of the ICH guidelines Q1A.

Toxicity on NHDF and 3T3 cells

Approximately 20,000 NHDF cells and 10,000 3T3 cells were seeded in 96 well plates and grown for 24 h at 37 °C and 5% CO_2 in 100 µL of the corresponding cell culture media shown in Table 3. After adding 50 µL aseptic and 0.2 µm of the sterile, filtered and differently diluted nanoemulsions, the cells were incubated for 4 or 24 h. The cell viability was determined by a resazurin reduction assay. Therefore, 30 µL of a 0.15 mg/mL resazurin solution was added and the mixture was incubated for 2 h. Then, the fluorescence intensity was determines with the Cytation™ 5 imaging reader (BioTek Instruments) using the RFP 531(excitation)/593(emission) filter set. The cell viability was expressed as a percentage of the negative controls (untreated cells) after subtraction of the blank. All experiments were conducted in triplicate. The mean inhibitory concentration IC_{50} was determined by linear interpolation.

Table 3: Composition of the cell culture media.

compounds in vol %	3T3 cell medium	NHDF cell medium
DMEM	86.80	87.63
FCS	9.55	9.64
penicillin-streptomycin	0.95	0.96
L-glutamine solution	1.75	1.77
sodium pyruvat solution	0.95	–

Supporting Information

Supporting Information File 1

Additional figures.
[https://www.beilstein-journals.org/bjnano/content/supplementary/2190-4286-11-16-S1.pdf]

ORCID® iDs

Henrike Lucas - https://orcid.org/0000-0002-2494-5303
Karsten Mäder - https://orcid.org/0000-0003-1613-6976

References

1. Medina, J.; Salvadó, A.; del Pozo, A. *Int. J. Pharm.* **2001,** *216,* 1–8. doi:10.1016/s0378-5173(00)00664-5
2. Weiss, V. M.; Naolou, T.; Hause, G.; Kuntsche, J.; Kressler, J.; Mäder, K. *J. Controlled Release* **2012,** *158,* 156–164. doi:10.1016/j.jconrel.2011.09.077
3. Lefebvre, G.; Riou, J.; Bastiat, G.; Roger, E.; Frombach, K.; Gimel, J.-C.; Saulnier, P.; Calvignac, B. *Int. J. Pharm.* **2017,** *534,* 220–228. doi:10.1016/j.ijpharm.2017.10.017
4. Maupas, C.; Moulari, B.; Béduneau, A.; Lamprecht, A.; Pellequer, Y. *Int. J. Pharm.* **2011,** *411,* 136–141. doi:10.1016/j.ijpharm.2011.03.056
5. Harun, S.; Amin Nordin, S.; Abd Gani, S. S.; Shamsuddin, A. F.; Basri, M.; Bin Basri, H. *Int. J. Nanomed.* **2018,** *Volume 13,* 2571–2584. doi:10.2147/ijn.s151788
6. Schädlich, A.; Hoffmann, S.; Mueller, T.; Caysa, H.; Rose, C.; Göpferich, A.; Li, J.; Kuntsche, J.; Mäder, K. *J. Controlled Release* **2012,** *160,* 105–112. doi:10.1016/j.jconrel.2012.02.012
7. Hirsjärvi, S.; Sancey, L.; Dufort, S.; Belloche, C.; Vanpouille-Box, C.; Garcion, E.; Coll, J.-L.; Hindré, F.; Benoît, J.-P. *Int. J. Pharm.* **2013,** *453,* 594–600. doi:10.1016/j.ijpharm.2013.05.057
8. Hirsjärvi, S.; Dufort, S.; Gravier, J.; Texier, I.; Yan, Q.; Bibette, J.; Sancey, L.; Josserand, V.; Passirani, C.; Benoît, J.-P.; Coll, J.-L. *Nanomedicine (N. Y., NY, U. S.)* **2013,** *9,* 375–387. doi:10.1016/j.nano.2012.08.005
9. Lainé, A.-L.; Gravier, J.; Henry, M.; Sancey, L.; Béjaud, J.; Pancani, E.; Wiber, M.; Texier, I.; Coll, J.-L.; Benoît, J.-P.; Passirani, C. *J. Controlled Release* **2014,** *188,* 1–8. doi:10.1016/j.jconrel.2014.05.042
10. Heurtault, B.; Saulnier, P.; Pech, B.; Proust, J.-E.; Benoît, J.-P. *Pharm. Res.* **2002,** *19,* 875–880. doi:10.1023/a:1016121319668
11. Friberg, S. E.; Corkery, R. W.; Blute, I. A. *J. Chem. Eng. Data* **2011,** *56,* 4282–4290. doi:10.1021/je101179s
12. Heurtault, B.; Saulnier, P.; Pech, B.; Venier-Julienne, M.-C. C.; Proust, J.-E. E.; Phan-Tan-Luu, R.; Benoît, J.-P. *Eur. J. Pharm. Sci.* **2003,** *18,* 55–61. doi:10.1016/s0928-0987(02)00241-5
13. Roethlisberger, D.; Mahler, H.-C.; Altenburger, U.; Pappenberger, A. *J. Pharm. Sci.* **2016,** *106,* 446–456. doi:10.1016/j.xphs.2016.09.034
14. Stranz, M.; Kastango, E. S. *Int. J. Pharm. Compd.* **2002,** *6,* 216–220.
15. Viegas, T. X.; Henry, R. L. *Int. J. Pharm.* **1998,** *160,* 157–162. doi:10.1016/s0378-5173(97)00316-5

16. Gadelha, G.; Nawaz, M. S.; Hankins, N. P.; Khan, S. J.; Wang, R.; Tang, C. Y. *Desalination* **2014,** *354,* 97–106. doi:10.1016/j.desal.2014.09.009
17. Cheuvront, S. N.; Kenefick, R. W.; Heavens, K. R.; Spitz, M. G. *J. Clin. Lab. Anal.* **2014,** *28,* 368–373. doi:10.1002/jcla.21695

License and Terms

BEILSTEIN JOURNAL OF NANOTECHNOLOGY

Key for crossing the BBB with nanoparticles: the rational design

Sonia M. Lombardo[1,2], Marc Schneider[2], Akif E. Türeli[1] and Nazende Günday Türeli[*1]

Review

Open Access

Address:
[1]MyBiotech GmbH; Industriestraße 1B, 66802 Überherrn, Germany and [2]Department of Pharmacy, Biopharmaceutics and Pharmaceutical Technology, Saarland University, Campus C4 1, 66123 Saarbrücken, Germany

Email:
Nazende Günday Türeli[*] - n.guenday-tuereli@mybiotech.de

* Corresponding author

Keywords:
gold nanoparticles (AuNPs); blood–brain barrier (BBB); drug delivery; liposomes; nanomedicine; polymeric nanoparticles; solid lipid nanoparticles; superparamagnetic iron oxide nanoparticles (SPIONs)

Beilstein J. Nanotechnol. **2020,** *11,* 866–883.
doi:10.3762/bjnano.11.72

Received: 08 February 2020
Accepted: 08 May 2020
Published: 04 June 2020

This article is part of the thematic issue "Frontiers in pharmaceutical nanotechnology".

Guest Editor: M. G. Wacker

Abstract

Central nervous system diseases are a heavy burden on society and health care systems. Hence, the delivery of drugs to the brain has gained more and more interest. The brain is protected by the blood–brain barrier (BBB), a selective barrier formed by the endothelial cells of the cerebral microvessels, which at the same time acts as a bottleneck for drug delivery by preventing the vast majority of drugs to reach the brain. To overcome this obstacle, drugs can be loaded inside nanoparticles that can carry the drug through the BBB. However, not all particles are able to cross the BBB and a multitude of factors needs to be taken into account when developing a carrier system for this purpose. Depending on the chosen pathway to cross the BBB, nanoparticle material, size and surface properties such as functionalization and charge should be tailored to fit the specific route of BBB crossing.

Introduction

Neurological disorders and brain diseases are real burdens for modern societies and healthcare systems. According to the World Health Organization (WHO), in 2000, brain diseases such as Alzheimer's disease and other dementias ranked 14th among the causes of death worldwide with approximately 0.8 million deceased [1]. This number more than doubled in the last few years. In 2016, these diseases were responsible for 2.0 million deceased, ranking Alzheimer's disease 5th. Furthermore, according to the WHO, in 2016 stroke was still the second most frequent cause of death worldwide with approximately 5.8 million deceased. These tremendous numbers will continue to grow due to an aging population, with the rise of life expectancy worldwide. Moreover, there is still a large number of unmet medical needs concerning the treatment of most central nervous system (CNS) diseases, as it is the case for stroke where treatments are limited to brain reperfusion. No

treatments are available to recover the brain areas damaged by ischemia [2].

One of the main limitations for the treatment of neurological disorders is the difficulty to deliver drugs to the brain. The brain is surrounded by the blood–brain barrier (BBB), a selective barrier formed by the endothelial cells of the cerebral microvessels [3,4]. The surface of the microvessels is the largest interface for blood–brain exchange with an average of 12 to 18 m^2 in adults [5]. The BBB is responsible for maintaining the brain homeostasis by regulating ion and nutrient transport as well as protecting the brain against neurotoxic molecules [6]. To fulfill its function, the BBB has a unique anatomy. The brain endothelial cells are joined by tight junctions and do not present fenestrations [5-8]. The endothelial cells are surrounded firstly by a discontinuous layer of pericytes and secondly by the basal lamina, adjacent to the astrocyte feet (Figure 1). Unfortunately, most drugs cannot pass the BBB through physiological pathways due to the extreme selectivity of the barrier. This restricts systemic therapeutic treatments for most CNS diseases.

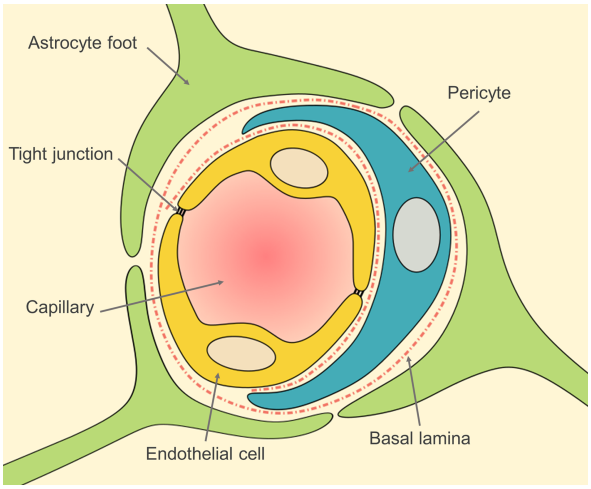

Figure 1: Blood–brain barrier anatomy. Inspired by [5].

Different strategies have been suggested to deliver drugs to the brain (Figure 2). First, drugs can be delivered to the brain by local delivery. Local delivery consists of directly delivering the drug to the brain by injection via a catheter or with the help of a convection-enhanced delivery system. Biodegradable polymer implants can also be used for sustained release of the drug [9,10]. These procedures require surgery and are therefore highly invasive. They are mostly used to treat glioblastomas or other brain tumors. Another way to reach the brain by

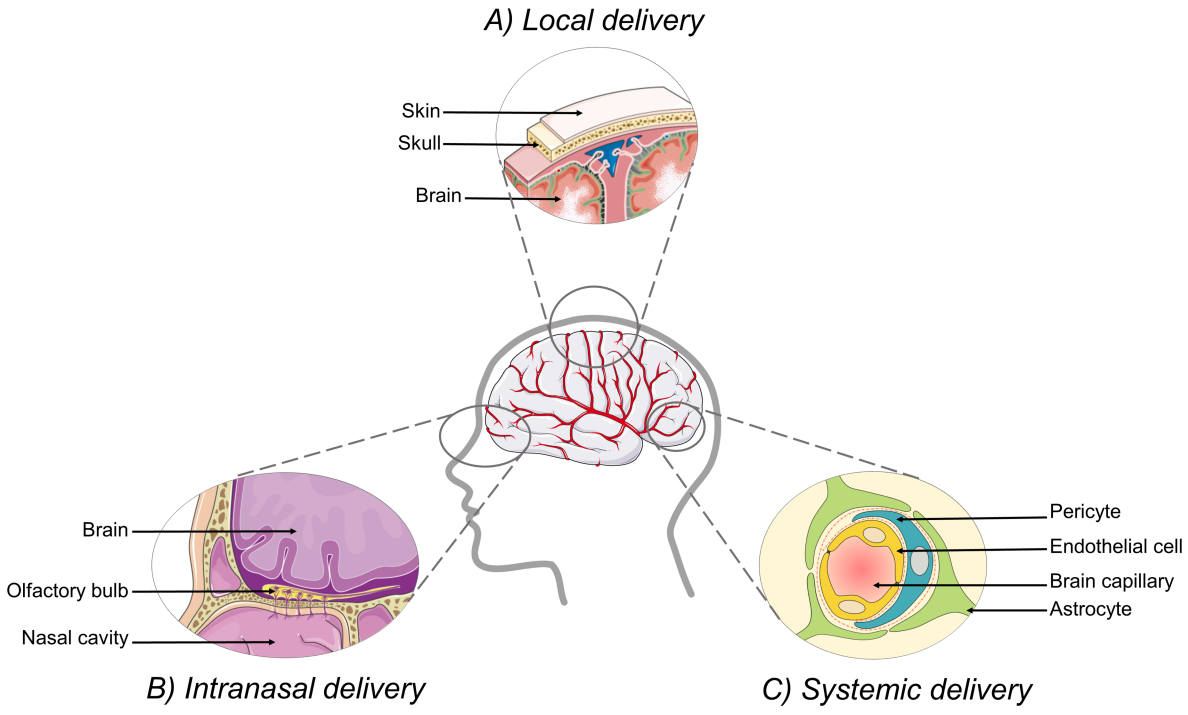

Figure 2: Brain delivery routes. A) Local delivery. Drugs can reach the brain by direct injection through the meninges. B) Intranasal delivery. Drugs can be transported to the brain via the olfactory bulb, located at the top of the nasal cavity. C) Systemic delivery. Drugs can reach the brain by crossing the blood–brain barrier (BBB) around the brain capillaries. Made using cliparts from Servier Medical Art by Servier, https://smart.servier.com/. Original cliparts are licensed under a Creative Commons Attribution 3.0 Unported License, https://creativecommons.org/licenses/by/3.0/.

bypassing the BBB is the intranasal route. After reaching the nasal cavity, a drug loaded inside nanocarriers can be transported along the olfactory bulb (olfactory pathway) and the trigeminal nerve (trigeminal pathway) directly to the CNS [11-13]. This innovative route has attracted lots of attention in the last few years and seems promising [14-16]. However, the intranasal route has drawbacks such as a high variability of the delivered dose depending on the state of the nasal mucosa [9,17]. Therefore, despite the difficulty of crossing the BBB, the most popular and well-studied delivery route remains the systemic pathway. One of the classic approaches to increase the ability of drugs to cross the BBB is to modify the molecular structure of the drugs or to use prodrugs. One example of a prodrug is levodopa, a prodrug of dopamine used for the treatment of Parkinson's disease. However, these options are not always possible depending on the structure of the molecule. Another possibility to increase drug delivery through the BBB is to increase the permeability of the BBB by reversible disruption, either by the use of osmotic agents such as hyperosmolar mannitol injection [18] or physical methods such as ultrasound [19,20]. However, as the BBB is one of the main protection mechanism of the brain against neurotoxins, disrupting it might lead to significant damage to the brain [21].

Finally, an innovative way to solve the permeation problem is to load drugs inside nanoparticles. According to the European Commission, nanomaterials are materials that contain at least 50% of particles in a size range of 1 to 100 nm [22]. More generally, nanoparticles are considered as solid colloidal particles with a size between 1 and 1000 nm [23]. They can be produced from a variety of different materials including polymers, lipids or inorganic materials such gold or iron oxide [21]. The first reported nanoparticles able to pass the BBB were poly(butyl cyanoacrylate) (PBCA) nanoparticles developed by Kreuter et al. in 1995. They enabled the successful delivery of the antinociceptive peptide dalargin in vivo [24]. Since then, numerous nanoparticle systems have been studied and optimized for brain delivery of small molecules and peptides [25]. Most of them are polymeric nanoparticles prepared with PBCA and polymers from the poly(ethylene) family such as poly(lactic acid) (PLA) and poly(lactic-*co*-glycolic acid) (PLGA) [25,26]. Liposomes and other lipidic nanoparticles have also been reported as able to pass the BBB [27], as well as protein-based nanoparticles (e.g., human serum albumin) [28], gold nanoparticles [29] and superparamagnetic iron oxide nanoparticles [30].

This review aims to summarize (i) the different pathways to cross the BBB, (ii) the strategies that can be employed to increase nanoparticle BBB permeation without disrupting the BBB, as well as (iii) the different nanoparticle types that can be used for drug delivery across the BBB.

Review

Crossing the BBB

Figure 3 describes multiple pathways to cross the BBB.

Paracellular pathway and passive transmembrane diffusion

The tight junctions between the endothelial cells severely limit the paracellular pathway of hydrophilic molecules. Therefore, most molecules have to go through the transcellular pathway to cross the BBB. However, only small lipophilic molecules, with a molecular weight lower than 400 Da and less than eight hydrogen bonds, or small gas molecules (such as CO_2 or O_2) can freely diffuse through the BBB by transmembrane diffusion [4]. Furthermore, the BBB endothelial cells have a low degree of pinocytic activity, which again restrains the transport of molecules to the brain [3,8,31].

Transport proteins: carrier-mediated transport and efflux proteins

To assure the transport to the brain of specific molecules such as nutrients or amino acids, transport proteins are present on the luminal and basolateral side of the endothelial cells. For instance, GLUT-1, large neutral amino acid transporters (LAT), nucleoside transporters and also organic cation and anion transporters have all been reported to play an important role for sustaining the high metabolic needs of the brain [31-33]. Their substrates can therefore cross the BBB through carrier-mediated transport. These carriers are size- and stereo-selective [34].

ATP-driven drug efflux pumps (ATP-binding cassette (ABC) transporters) also contribute to maintaining the brain homeostasis by excreting possible neurotoxic substances. Active pharmaceutical ingredients (API) can also be substrates of these efflux proteins and therefore be excreted by them. Among the efflux proteins present in the BBB, the most extensively described are P-glycoproteins (P-gp or ABCB1, MDR1 gene product), breast cancer resistance proteins (BCRP/ABCG2) and the multidrug resistance-associated proteins (MRP1, 2, 4 and 5, ABCC) [31,35-38]. With their ability to transport a large variety of compounds, these efflux proteins cause a significant problem for drug delivery.

Receptor-mediated transcytosis

Endogenous molecules that do not have a specific transporter can also reach the brain through receptor-mediated transcytosis (RMT). It has been shown that RMT activity in brain endothelial cells is reduced compared to peripheral endothelial cells [39]. However, this pathway remains one of the most promising for drug delivery through the BBB. Transcytosis includes three steps: endocytosis, intracellular vesicular trafficking and exocytosis [40]. Indeed, molecules bind to their receptors on the

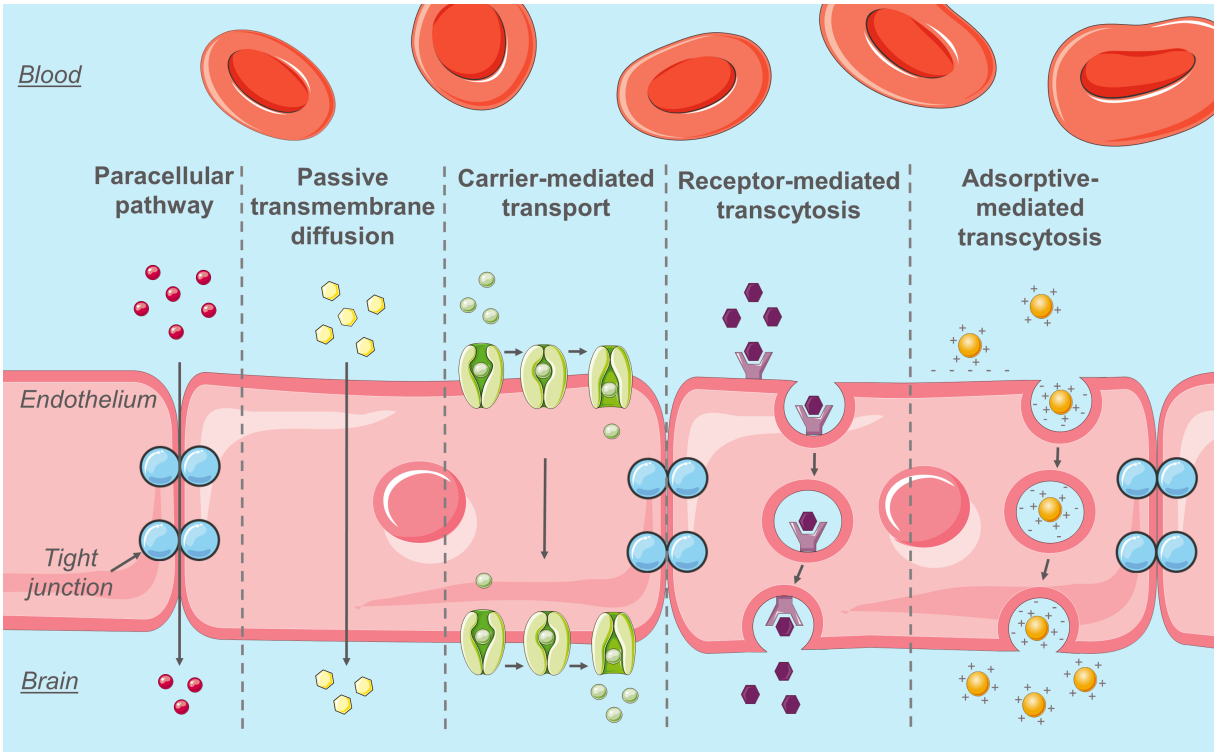

Figure 3: Physiological pathways through the BBB. Inspired by [3]. Made using cliparts from Servier Medical Art by Servier, https://smart.servier.com/. Original cliparts are licensed under a Creative Commons Attribution 3.0 Unported License, https://creativecommons.org/licenses/by/3.0/.

luminal side of the endothelial cells and endocytosis is initiated. The receptor–ligand complex is invaginated, which leads to the formation of intracellular transport vesicles. The vesicles are then sorted and the ones sorted for exocytosis cross the cell to release the ligand to its basolateral side. The receptor is then recycled [41]. Some of the receptors found on the luminal side of the BBB are transferrin receptor (TfR), insulin and insulin-like growth factor receptor, low-density lipoprotein receptor (LDLR), low-density lipoprotein receptor-related protein 1 and 2 (LRP1 and LRP2), scavenger receptor class B type I (SR-B1), leptin receptor and lactoferrin receptor [34,41]. More recently, nicotinic acetylcholine receptors (nAChRS) and diphtheria toxin receptor have also been described [34,42]. However, some receptors usually found on peripheral endothelial cells are not expressed, e.g., the albumin receptor [40,43].

Three major categories of endocytic vesicles have been identified and described in the brain endothelial cells: clathrin-coated pits, caveolae and macropinocytosis vesicles. Clathrin-coated pits are involved in most of the internalization processes mediated by receptors such as TfR or insulin receptors [39,40]. After endocytosis, the vesicles converge in the early endosome network, which functions as an intracellular sorting station. From there, cargo can be transported via sorting tubules to the basolateral side of the cells for exocytosis. Cargo can also stay in the early endosomes, which can mature in late endosomes and multi-vesicular bodies. Multi-vesicular bodies can either shuttle their cargo for exocytosis or fusion with lysosomes, where cargo degradation can occur. However, the cargo can avoid this fate by being shuttled back from the lysosomes to the Golgi apparatus and early endosomes by retrograde transport [39]. The intracellular pathway taken by the vesicles depends on the receptor, on the internalization pathway (clathrin-mediated or caveolae) and also on the type of ligand binding to the receptors [39]. Furthermore, it has been shown that bEND3 cells (mouse brain microvascular cell line) had less nanoparticles colocalized to the Golgi apparatus and lysosomes than C6 cells (rat glioma cell line), suggesting that intracellular vesicles could avoid lysosomes in brain endothelial cells [43,44]. Finally, the exocytosis process has not been described very well. It is still unclear if the tubules and multi-vesicular bodies merge directly with the basolateral membrane or if they release their cargo in basolateral endosomes that subsequently merge with the basolateral membrane. However, it has been shown that brain endothelial cells generate microvesicles that are released toward the brain [43].

Adsorptive-mediated transcytosis

Finally, another potential physiological way to cross the BBB is through adsorptive-mediated transcytosis (AMT). Whereas

RMT needs an interaction between a ligand and a receptor, AMT is a non-specific pathway. Therefore, the binding affinity of AMT is low, but its binding ability is high, leading to similar transcytosis efficiency as RMT [45,46]. AMT occurs through electrostatic interaction between a positively charged molecule, protein or peptide and the negatively charged luminal membrane of the brain endothelial cells. This process depends on energy, time and concentration and lasts for a few minutes. It is thus relatively slow compared to carrier-mediated transport [47,48]. The endocytotic process of AMT is mostly mediated by caveolae [40].

Strategies to enhance nanoparticle BBB permeation

To increase their BBB permeation ability, most nanoparticles are designed to be able to cross the BBB through transcytosis. To reach this goal, their surfaces have to be modified, either non-covalently with a coating or covalently by functionalization.

Coating with surfactants

Coating nanoparticles with a surfactant was the first method used to enhance their BBB permeation ability. The first reported nanoparticle system able to cross the BBB in vivo was developed by Kreuter and co-workers [24]. In their study, PBCA nanoparticles coated with polysorbate 80 (PS80) were able to successfully deliver dalargin, an antinociceptive peptide unable to cross the BBB by itself. A significant increase of analgesia was measured, showing that PS80-coated PBCA nanoparticles were able to deliver dalargin through the BBB to the brain. Following this discovery, different surfactants were tested to coat PBCA nanoparticles [49]. Dalargin-loaded PBCA nanoparticles were coated with polysorbate 20, 40, 60 and 80, poloxamer 184, 188, 388, 407 and 908, Brij® 35 and Cremophors® EZ and RH. Only PBCA nanoparticles coated with polysorbates showed a significant analgesic effect, and the highest effect was obtained for PS80-coated nanoparticles. Further studies showed that PS80 did not cause any toxic effects and did not disrupt the BBB at the dose used [50]. At the same time, Lück published in his thesis that apolipoprotein E (ApoE) was adsorbed on the surface of nanoparticles coated with polysorbate 20, 40, 60 or 80 after their incubation in human plasma [51]. However, ApoE was not adsorbed on uncoated nanoparticles or nanoparticles coated with poloxamer 338 and 407, Cremophor® EL or Cremophor® RH40. Building on this work and to study the mechanism behind the transcytosis of PBCA nanoparticles, dalargin-loaded PBCA nanoparticles were coated with apolipoproteins A-II, B, C-II, E and J with or without precoating with PS80 [52] and the antinociceptive effect of dalargin on mice was measured. A significant increase of the antinociceptive effect was observed for nanoparticles coated with apolipoproteins B (ApoB) and E without precoating with PS80, showing that these apolipoproteins increased the BBB crossing of PBCA nanoparticles. Interestingly, the antinociceptive effect of dalargin was even more pronounced for PBCA nanoparticles precoated with PS80 and overcoated with ApoB and ApoE. In the same study, loperamide-loaded PBCA nanoparticles coated with PS80 were injected to ApoE-deficient and control mice. An antinociceptive effect of loperamide could only be observed in control mice, showing that apolipoproteins were involved in the BBB crossing mechanism of PS80-coated PBCA nanoparticles. Thus, it was concluded that PS80-coated nanoparticles could adsorb apolipoproteins selectively in the blood and cross the BBB through RMT by interacting with LDL receptors present on the luminal side of brain endothelial cells.

In another study by Kreuter's team, PBCA nanoparticles loaded with doxorubicin and coated with either PS80 or poloxamer 188 (P188) could increase the survival of rats implanted with intracranial glioblastoma [53]. Interestingly, P188 coating was also able to increase the BBB permeation ability of PBCA nanoparticles. However, in their first study, P188-coated dalargin-loaded PBCA nanoparticles were not able to increase significantly the antinociceptive effect of dalargin [49]. Thus, it was proposed that the binding of doxorubicin led to an alteration of the nanoparticle surface properties that allowed ApoE and B to be bound. It was then concluded that the BBB permeation ability of nanoparticles was not only dependent of the surfactant coating but also of the nature of the nanoparticle core composition, not only of the polymer, but also of the API [54].

The ability of surfactants to interact with apolipoproteins was confirmed in another study by Petri et al., where the efficacy of PBCA nanoparticles loaded with doxorubicin and coated with either PS80 or P188 for the treatment of rat intracranial glioblastoma was investigated [55]. The results showed that the antitumor effect of doxorubicin-loaded PBCA nanoparticles was significantly enhanced when they were coated with either PS80 or P188. The plasma proteins adsorbed on coated PBCA nanoparticles were investigated by 2D PAGE and the results showed that a considerable amount of apolipoproteins A-I (Apo A-I) were adsorbed on PS80- and P188-coated nanoparticles. No significant differences of the amount of adsorbed apolipoproteins between PS80- and P188-coated nanoparticles could be observed.

Similar results were observed for PLGA nanoparticles stabilized with PS80 or P188. PLGA nanoparticles loaded with either loperamide or doxorubicin were coated with PS80 or P188 and tested in vivo in rodents [56]. In both cases, P188-coated PLGA nanoparticles showed a higher efficacy than

PS80-coated nanoparticles, but both formulations were able to cross the BBB and deliver their cargo. On the other hand, in another study, coumarin-6-loaded PLGA nanoparticles coated with either chitosan or PS80 showed a better crossing ability than P188-coated nanoparticles [57]. This result seems to be in accordance with the suggestion from Kreuter et al. that the core of the nanoparticles could influence the surface properties of the nanoparticles and therefore their ability to bind with apolipoproteins in the blood [54]. PS80 coating was also successful for PLA-*b*-PEG nanoparticles [58] but failed for PLA nanoparticles [59]. PLGA-PEG-PLGA nanoparticles loaded with loperamide and coated with either PS80 or P188 were compared [60]. Both formulations could cross the BBB but P188 seemed to permeate to a higher degree than PS80.

In conclusion, PS80 is nowadays the gold standard for increasing the BBB crossing of polymeric particles as it was shown to be able to increase the apolipoprotein–nanoparticle interaction for a wide range of polymers without any toxicity to the BBB. However, alternatives, such as P188, exist. Furthermore, the efficacy of the coating is also influenced by the composition of the nanoparticle core, i.e., the polymer and API in use.

Surface functionalization

To be able to cross the BBB by RMT, nanoparticle surfaces can be functionalized with specific ligands. This approach has been well studied and a multitude of different ligands has been tested. Some of the recent advances for this approach are summarized in Table 1.

As described above, coating nanoparticles with apolipoproteins allows nanoparticles to cross the BBB by interacting with LDL receptor-related protein (LRP1) for ApoB and ApoE [115] and with SR-BI for Apo A-I [116]. In the same way, conjugating

Table 1: Summary of surface functionalization strategies for improved BBB crossing of nanoparticles.[a]

target	functionalization	nanoparticle	size (nm)	zeta potential (mV)	ref.
scavenger receptor class B type 1 (SR-BI)	apolipoprotein A-I	HSA	250–270	–23 to –36	[61]
			225	–35	[62]
		proticles	120–150	10 to 20	[63]
LDL receptor-related protein (LRP1)	apolipoprotein B and E	HSA	220–240	–37 to –40	[62]
			340 ± 8.6	N.A.	[64]
		SLNs	<200	–13	[65]
			119.7 ± 2.5	–54.3 ± 2.1	[66]
	modified apolipoprotein E peptide	liposomes	123 ± 3	–15.2 ± 1.1	[67]
	angiopep-2	PEG-PCL	<100	–3.28 ± 0.75	[68]
		SLNs	111.4	–16.4	[69]
		AuNPs	39.96 ± 0.57	–19.38 ± 0.58	[70]
		AuNRs	118.5	–10.5	[71]
transferrin receptor	transferrin	PLGA	88.8 ± 27.5	–32.5 ± 8.2	[72]
		SLNs	126.4 ± 2.96	3.7 ± 0.5	[73]
		HSA	183 ± 10	–28 ± 8	[74]
		MSN-PLGA	150	–18.1 ± 0.5	[75]
transferrin receptor	transferrin	liposomes	100	30.2	[76]
			124.5 ± 6.4	–5.19 ± 0.45	[77]
		AuNPs	41	N.A.	[78]
		AuNRs	46.7 × 13.7	N.A.	[79]
	anti-transferrin receptor antibody (OX26)	PEG-chitosan	200	18.23 ± 4.06	[80]
		PLGA	166 ± 2	–13 ± 1	[81]
		HSA	168 ± 5	–28 ± 6	[74]
		chitosan	235.7 ± 10.2	22.88 ± 1.78	[82]
		PLA-PEG	121.8 ± 9.9	18.1 ± 1.3	[83]
		liposomes	117 ± 2	N.A.	[84]
			153 ± 11	–7.5 ± 1.2	[85]
	THR peptide	AuNPs	13 ± 1.7	–41 ± 2	[86]

Table 1: Summary of surface functionalization strategies for improved BBB crossing of nanoparticles.[a] (continued)

lactoferrin receptor	lactoferrin	PEG-PLGA	90	–24	[87]
			109	N.M	[88]
		procationic liposomes	123–129	–4.3 to –20.2	[89]
		NLC	99.7–103.8	–5.80 to –17.90	[90]
opioid receptor	glycopeptide g7	PLGA	200–300	–8 to –12	[91]
			183 ± 12	16.9 ± 0.4	[92]
			162–211	–6.1 to –15.2	[93]
			195 ± 12	–13.7 ± 0.8	[94]
insulin receptor	insulin	HSA	190 ± 19	–36 ± 6	[28]
		AuNPs	20	N.A.	[95]
	anti-insulin receptor antibody (29B4)	HSA	157 ± 11	–36 ± 4	[28]
receptor for advanced glycation end products	CLPFFD peptide	AuNPs	12 ± 1.7	N.A.	[96]
		AuNRs	50 × 10	25	[97]
diphtheria receptor	CRM197	PLGA	219 ± 11	–14.2 ± 0.5	[94]
thiamine transporter	thiamine	SLNs	67 ± 8.2	N.A.	[98]
glutathione transporter	glutathione	liposomes	95	–8.3	[99]
			127	N.A.	[100]
phage-display technique	TGN peptide	PEG-PLGA	151	–19.59	[101]
	Tet-1 peptide	PLGA	150–200	–20 to –30	[102]
rabies virus target	RVG29	chitosan–pluronic NC	63 ± 32	12.1 ± 0.8	[103]
		HSA	89.3 ± 1.9	–33 ± 0.9	[104]
		AuNRs	117.7 × 50.3	14.2 ± 2.5	[105]
cell-penetrating peptide	TAT	PLA	157 ± 8.9	2.4 ± 0.3	[106]
		liposomes	124.5 ± 6.4	–5.19 ± 0.45	[77]
		AuNPs	21.4 ± 0.9	N.A.	[107]
	penetratin	PEG-PLA	100	–4.42	[108]
	SynB	PEG-GS	194.6 ± 6.4	31.8 ± 3.1	[109]
adsorptive-mediated transport	cationic bovine serum albumin (CBSA)	PEG-PLA	82.1 ± 4.0	–12.19 ± 1.21	[110]
			329 ± 44	–19	[111]
		liposomes	90–165	N.A.	[112]
		SLNs	94.5 ± 1.5	10.3 ± 0.6	[113]
	trimethylated chitosan	PLGA	136.8–146.7	17.7 to 21.0	[114]

[a]AuNPs = gold nanospheres, AuNRs = gold nanorods, GS = gelatin–siloxane, HSA = human serum albumin, MSNs = magnetic silica nanoparticles, NC = nanocarrier, NLC = nanostructured lipid carrier, N.A. = not available, PEG = polyethylene glycol, PLA = poly(lactic acid), PLGA = poly(lactic-*co*-glycolic acid), PCL = polycaprolactone, SLNs = solid lipid nanoparticles.

nanoparticles with angiopep-2, a ligand of LRP1, also enables BBB crossing. Another extensively studied RMT pathway is through transferrin and lactoferrin receptors by conjugating nanoparticles with their respective ligands, transferrin and lactoferrin [72-74,87,88]. However, these nanoparticles have to face competition with the endogenous ligands of these receptors. This problem can be avoided by using antibodies against transferrin receptors, i.e., OX26, which bind to another binding site of the receptor [74,80-83]. However, it has been shown that OX26 is mostly associated with brain capillaries through the brain parenchyma [117]. It was then hypothesized that the high affinity of the antibody for the TfR might prevent its release from the abluminal surface of brain endothelial cells. The detection of OX26 in the cerebrospinal fluid (CSF) and in neurons only in areas of close proximity to the ventricular system also suggest that OX26 might reach the brain through the blood–CSF barrier [118]. Furthermore, some studies have shown that anti-TfR antibodies with high affinity/avidity for the receptor could be sorted toward lysosomal degradation after endocytosis, whereas antibodies with lower affinity/avidity

were sorted for transcytosis [119,120]. To the best of our knowledge, the exact intracellular pathway taken by OX26 inside the brain endothelial cells has not been described well yet. Its high affinity for the TfR receptor might induce its entry into lysosomes inside the cells. However, the high number of papers reporting the ability of nanoparticles conjugated with OX26 to reach the brain seems to indicate either that it is not the case, and/or that OX26 is able to shunt the BBB through the blood–CSF barrier.

Other receptors have also been studied such as the opioid, insulin and diphteria receptors or the receptor for advanced glycation end products (RAGE) [28,91-94,96]. It is also possible to cross the BBB by targeting active transporters such as the thiamine or glutathione transporters [98-100].

Some more advanced techniques have also been developed to find new targeting peptides for the BBB, such as the phage-display technique. This technique is an effective method for isolating novel peptides with specific binding properties. DNA sequences are inserted into bacteriophage genes, resulting in the expression of the encoded proteins on their surface. Biopanning is then used to isolate and amplify phages displaying peptides able to interact with the proteins or cell lines of interest [121]. The results of this technique are entirely dependent on the library of DNA sequences used and attention should be given to select tissue-specific peptides [122]. Among others, two interesting peptides have been identified using this technique: TGN and Tet-1. TGN was identified through in vivo phage display [123]. Mice were injected with a library of phages and phages recovered in the brain were amplified, leading to the identification of TGN peptide as an interesting BBB targeting peptide. Tet-1 was identified through its affinity for the trisialoganglioside (GT1b) receptor, the main neuronal target of tetanus toxin [121]. Tet-1 can interact specifically with motor neurons and is capable of retrograde delivery to the neuronal cells [102]. Thus, conjugating nanoparticles with Tet-1 allows them to shunt the BBB by reaching the brain through retrograde axonal transport.

A short peptide derived from rabies virus glycoprotein (RVG), RVG-29, has also been used to increase brain delivery of nanoparticles [103,104]. RVG-29 interacts specifically with the nicotinic acetylcholine receptor (AchR) on neuronal cells [124]. The exact pathway through which RVG-29 reaches the CNS is not fully understood. One hypothesis could be that RVG-29 reaches the CNS by following the rabies virus pathway, i.e., through retrograde axonal transport from motor neuronal cells. It is also believed that RVG-29 could increase BBB crossing through AMT by increasing the positive charge on the nanoparticle surface [125].

Another investigated way to increase BBB permeation is to use cell-penetrating peptides (CPPs). These peptides usually contain between five and 40 amino acids, including a large amount of basic amino-acid residues, resulting in an overall net positive charge [108,126]. CPPs are able to enhance membrane penetration and cell internalization of their conjugated cargo in a large variety of cells, through pathways not always well known [126,127]. In the case of BBB crossing, their positive charge might induce their transcytosis through the AMT pathway. Multiple CPPs have been used to deliver nanoparticles to the brain such as the HIV-1 trans-activating transcriptor (TAT) [77,106,107], penetratin [108] or SynB [109].

Finally, conjugating nanoparticles with positively charged polymers or proteins such as chitosan or cationic bovine serum albumin (CBSA) allows them to cross the BBB by AMT, as described above [110-112,114]. PEG-PLA nanoparticles were labeled with coumarin-6 and conjugated with either CBSA or BSA in a study by Lu and co-workers [110]. Transcytosis assays were performed on a co-culture BBB in vitro model and showed that CBSA-nanoparticles had an apparent permeability (Pe) seven times higher than that of BSA-nanoparticles. Furthermore, a leaching study of coumarin-6 was performed at pH 4.0 and 7.4 and showed that less than 1% of the dye was released from the nanoparticles after 80 h. Thus, coumarin-6 was an accurate probe for the nanoparticle detection. It was therefore possible to conclude that the fluorescence detected in the abluminal compartment during the transcytosis assay was due to the probe inside the nanoparticles, and not due to free coumarin-6. Hence, it seems that CBSA-conjugated nanoparticles are indeed uptaken by the cells and transported to the abluminal side. They do not just adhere on the surface of endothelial cells and release their cargo. However, AMT is a non-specific pathway. Using this route to reach the brain may lead to more adverse effects than RMT as nanoparticles may also accumulate in other organs [128,129].

Influence of size and zeta potential

It has been shown that surface functionalization or surface coating are the most important determinants for BBB crossing. For functionalized nanoparticles, size seems to have little impact and nanoparticles in a large size range (from 12 to 340 nm) have been found to cross the BBB (Table 1). Gao and Jiang studied the influence of the size of methotrexate-loaded PS80-coated PBCA nanoparticles on their ability to cross the BBB in vivo [130]. Nanoparticles with sizes from 70 to 345 nm were studied. Between 170 and 345 nm, no impact of nanoparticle size on the brain delivery of methotrexate could be observed. Only 70 nm nanoparticles showed a slight increase in brain delivery. It has been proven that endocytosis is a size-de-

pendent process and that smaller nanoparticles under 100 nm can be endocytosed more easily by cells [131-133]. Moreover, it has been shown that gold nanoparticles under 15 nm were able to cross the BBB without any functionalization, probably through the transmembrane or the paracellular pathway, whereas gold particles bigger than 50 nm were not found in the brain [134-136]. Thus, very small particles may cross the BBB more easily.

Furthermore, after successfully crossing the BBB, size can have an impact on the diffusion of the nanoparticles through the brain extracellular space (ECS). The ECS is a well-connected foam-like structure formed from the interstitial space between neural cells [137,138]. The ECS possesses a large diversity of dimensions down to 40 nm, and up to 700 nm in local expansions also known as “dead spaces" [137,139]. Thus, small nanoparticles can diffuse further in the ECS and therefore deliver their cargo to the brain more efficiently, whereas bigger particles might get stuck in the narrowest parts of the ECS. However, according to Begley’s brain superhighways theory, nanoparticles could be able to diffuse in the brain tissue through the cytoplasm of astrocytes [140]. The long processes of astrocytes can form cytoplasmic bridges in the brain tissue from the BBB to neurons and to the blood–CSF barrier. It was shown that the aquaporines-4 expressed at the end feet of astrocytes allow for the uptake of water and its solutes from the ECS into their cytoplasms. Water can then be released globally into the brain extracellular fluid. Nanoparticles could follow a similar pathway. They could be endocytosed by the astrocytes at their end feet and then diffuse through their cytoplasms in the brain tissue. Nanoparticles could then diffuse faster and with less size restrictions than through the tortuous ECS.

As already described above, the zeta potential can also have an impact on the BBB crossing ability of nanoparticles. Nanoparticles expressing positive charges on their surface can cross the BBB through AMT. However, positively charged nanoparticles have a faster plasma clearance rate, which lowers their residence time in brain microvessels and therefore their brain delivery is reduced [133]. Furthermore, attention should be given to the toxicity of cationic nanoparticles, as they may alter cell membranes during adsorption. For instance, cationic gold nanoparticles have been shown to be 27 times more cytotoxic than their negative counterparts, due to the disruption of the cell membranes [141-143].

Pegylation

Pegylation of nanoparticles increases their circulation time by granting them “stealth” properties, thus increasing their residence time in brain microvessels and their brain delivery [144]. Pegylation alone does not allow nanoparticles to cross the BBB, as it has been shown in multiple studies [87,123,145,146]. However, coating nanoparticles with PEG allows them to better diffuse through the ECS [147]. Indeed, an important constituent of the ECS is the extracellular matrix, constituted of proteoglycans, hyaluronan and small proteins that can interact with nanoparticles and drastically hinder their diffusion [137]. By densely coating 40 nm and 100 nm fluorescent polystyrene nanoparticles with PEG, the nanoparticles were able to diffuse through the brain ECS of live mice, thanks to PEG limiting the adhesive interactions between the ECS and the nanoparticles, whereas the uncoated nanoparticles were stuck in the tissue [147]. Interestingly, neither pristine nor pegylated 200 nm nanoparticles could penetrate the brain tissue due to steric hindrance, confirming the importance of nanoparticle size for ECS diffusion described above. Thus, nanoparticles larger than 200 nm are able to cross the BBB but are unable to move on forward and diffuse through the ECS.

Nanoparticles for drug delivery through the BBB

Polymeric nanoparticles

Polymeric nanoparticles are the most extensively studied nanoparticle system for brain delivery. They can be produced from synthetic or natural polymers. Polymeric particles can cross the BBB when coated with surfactants, as described above, or after surface functionalization, as can be seen in Table 1. To be used for brain delivery, the polymeric nanoparticles need to be biodegradable and biocompatible, thus limiting the choice of polymers. As already discussed above, PBCA nanoparticles were the first nanoparticles shown able to cross the BBB [24]. Soon after, PLA and PLGA nanoparticles demonstrated the same abilities [56]. For example, PLGA nanoparticles loaded with loperamide and functionalized with glycopeptide g7 or with a mutated form of diphtheria toxin (CRM197) have been shown to significantly increase the analgesic effect of loperamide in mice [94]. Furthermore, it was shown that CRM197 allowed the carrier system to cross the BBB by RMT as well as by up-regulation of caveolin-1-mediated transport. Investigation on g7-NPs and CRM197-NP tropisms revealed that both formulations reached all brain areas without impacting the BBB integrity and accumulated in interneurons. Both PBCA and PLA/PLGA polymers are biodegradable and biocompatible polymers. However, PLA and PLGA exhibit some advantages over PBCA. They are FDA-approved and have a slower degradation rate than PBCA, allowing for a more sustained delivery [148,149]. Furthermore, a formulation of PLGA nanoparticles loaded with doxorubicin (NanoBB-1-Dox) has been investigated in a phase-I clinical trial for the treatment of glioblastoma multiforme through systemic chemotherapy [150]. Following the good tolerance of the treatment, NanoBB-1-Dox will be investigated in a phase-II study, which might prove the ability of

PLGA nanoparticles to cross the BBB in humans. Some other polymers have also been used to develop nanoparticles for brain delivery such as polycaprolactone (PCL) [68] or chitosan [80,82] but to a lesser extent than PBCA and PLA/PLGA nanoparticles. For instance, enhanced accumulation in an in vivo intracranial glioma mice model of PEG-PCL nanoparticles functionalized with angiopep-2 could be observed by real-time fluorescence imaging [68]. Nanoparticles could be observed in the glioma bed and infiltrating margin, showing that nanoparticles functionalized with angiopep-2 could exhibit dual-targeting abilities. Firstly, angiopep-2 allowed the nanoparticles to cross the BBB through RMT by recognition of LRP1 on the BBB and, secondly, angiopep-2 increased the accumulation of nanoparticles in glioma cells thanks to recognition of the LRP1 on the glioma cells surface.

Lipid-based nanoparticles

Liposomes: Liposomes are well-known and well-studied nanocarrier systems. They are composed of a lipid bilayer surrounding a hydrophilic core. Liposomes can thus be loaded with a wide variety of hydrophilic and lipophilic cargos [151]. Some liposome formulations have already received marketing authorizations, such as Ambisome®, Doxil®, Myocet® or more recently Onivyde™. However, no liposomal formulations have received approval for clinical use for the treatment of CNS diseases, although some clinical trials are currently ongoing. A phase-I trial of anti-EGFR-immunoliposomes loaded with doxorubicin, still recruiting, might provide soon clinical information on the ratio between the concentration of doxorubicin in the cerebro-spinal fluid and in the peripheral blood after intravenous administration [152].

Liposomes can cross the BBB through RMT. Positively charged liposomes can also reach the brain through AMT [151]. As shown in Table 1, liposomes have already been conjugated with a variety of ligands such as transferrin [76], lactoferrin [89], anti-transferrin receptor antibody [84,85], glutathione [99,100] or CBSA [112]. In a study by Chen et al. the efficacy of the BBB targeting ligands angiopep-2, T7 and peptide-22, which are specific ligands of, respectively, LRP1, transferrin receptor and LDLR were compared. Liposomes were conjugated with each ligand and their cellular uptake by brain capillary endothelial cells (BCECs) was tested [153]. It was shown that the cellular uptake of liposomes functionalized with peptide-22 was significantly higher than that of liposomes conjugated with angiopep-2 or T7. A dual-crossing glioma targeting liposomal drug delivery system was then developed by conjugating peptide-22 and c(RGDfK), a ligand of integrin $\alpha_v\beta_3$ that showed ability to target glioma cells, to liposomes loaded with doxorubicin. This formulation was tested in vivo on an intracranial glioma-bearing mouse model. The nanocarrier system was able to cross the BBB and to accumulate in glioma cells, thus improving the cytotoxicity effect of doxorubicin.

To cross the BBB and to target glioma cells, liposomes have also been conjugated with cell-penetrating peptides. For example, in a study by Liu et al., a novel dual receptor recognizing the cell-penetrating peptide R8-dGR, which could bind to both integrin $\alpha_v\beta_3$ and neuropilin-I receptors, was used to functionalize liposomes [154]. This formulation was tested in vitro and in vivo on intracranial glioma-bearing mice. The R8-dGR-conjugated liposomes could cross the bEnd.3 (murine brain endothelial cells) monolayer in vitro and exhibited a significantly higher accumulation in the brain than non-conjugated liposomes, showing the ability of this carrier system to cross the BBB. It was also shown that these particles could accumulate in the glioma cells and significantly increase the survival time of mice when loaded with paclitaxel. Thus, this formulation could be a promising drug delivery system for antitumor therapy.

Solid lipid nanoparticles: Solid lipid nanoparticles (SLNs) are particles with a solid lipid core at room and body temperature [27]. SLNs can be prepared with biocompatible lipids, thus leading to low cytotoxicity [155]. Furthermore, SLNs can be prepared using a cost-effective high-pressure homogenization method. This method avoids the use of organic solvents and can be used at large scale, making SLNs interesting for the pharmaceutical industry [156].

Interestingly, plain and stealth SLNs have been shown to cross the BBB, without any functionalization [157-160]. However, stealth SLNs showed better brain delivery of doxorubicin than pristine SLNs. This effect was even more pronounced in SLNs coated with increasing amounts of stealth agents, due to their longer blood circulation time [158]. These experiments showed that no specific targeting molecules or coatings are necessary for SLNs to cross the BBB. These nanoparticles are inherently able to cross the BBB through a pathway that has not been well investigated.

However, it is also possible to increase the amount of drug delivered to the brain by coating and conjugating SLNs. Coating SLNs with PS80 has been proven to be successful for the brain delivery of curcumin [161]. Studies have shown that PS80 allows ApoE adsorption on SLNs in the same way as for PBCA and PLGA nanoparticles [162].

Surface functionalization of SLNs has also been vastly used to improve their brain delivery. For example, SLNs functionalized with ApoE [65,66], angiopep-2 [69], transferrin [73], thiamine [98] and CBSA [113] have shown increased delivery of their

cargos to the brain compared to the molecules alone. For instance, in a study by Dal Magro et al., the brain bioavailability in mice of SLNs functionalized with an ApoE-derived peptide was studied depending on the administration route of the nanoparticles. The nanoparticles were administered either by the intraperitoneal, the intravenous or the intratracheal route [66]. Using in vivo fluorescence molecular tomography revealed that the SLNs could be observed in the brain after intravenous and intratracheal administration, showing their ability to cross the BBB. Furthermore, a superior retention of the nanoparticles in the brain was noticed after intratracheal administration compared to the intravenous and the intraperitoneal route, without inducing any acute inflammatory reaction in the lungs. The mechanism behind this increased brain confinement are not well understood. However, the authors concluded that pulmonary administration seemed to be a feasible strategy for brain delivery.

Interestingly, in a study by Peira et al., SLNs have been successfully loaded with superparamagnetic iron oxide and were able to cross the BBB [163]. Thus, SLNs could be potentially used as carriers for CNS MRI contrast agents.

Nanostructured lipid carriers: Although most of the reported applications of nanostructured lipid carriers (NLCs) for brain delivery are using the intranasal pathway [164-167], some studies have shown that NLC are also able to deliver drugs to the brain through the BBB. NLC are lipid-based particles composed of a liquid lipid phase inside a solid lipid phase [27]. The liquid lipid phase allows for a better solubilization of APIs and thus for a higher drug loading capacity than that of SLNs [168].

NLCs loaded with itraconazole prepared with PS80 were able to almost double the itraconazole concentration in the brain compared to the drug alone [169]. In another study, arginine–glycine–aspartic acid peptide (RGD)-modified NLCs were used for the delivery of temozolomide (TMZ) and their efficacy was tested on a glioblastoma multiforme mouse model. The RGD-TMZ/NLCs displayed high antitumor efficacy in vivo, with an inhibition of the tumor four times higher than that of the drug alone [170]. Moreover, in a study by Tsai et al., baicalein was loaded inside NLCs prepared with poloxamer 188. The NLCs revealed 7.5- and 4.7-fold higher baicalein accumulations in the cerebral cortex and brainstem, respectively, compared to the aqueous solution [171]. It is also possible to increase the BBB targeting ability of NLCs by adsorbing lactoferrin at their surface [90]. In a study by Meng et al., results have shown that lactoferrin-modified NLCs were able to accumulate in the brain more than twice as much as pristine NLCs in an Alzheimer's disease rat model [90].

Thus, even if the BBB permeation potential of NLCs has only been studied to a small extent [172], it seems that this nanoparticle system might be promising for brain delivery through the systemic pathway.

Inorganic nanoparticles

Gold nanoparticles: Gold nanoparticles are inorganic particles the shape (spheres, shells, rods) and size of which can be tailored depending on the synthesis process [173]. Most studies on the brain delivery of gold nanoparticles used gold nanospheres (AuNPs). AuNPs are composed of a gold core and covalently or non-covalently attached surface ligands. AuNPs have many very interesting properties. They can be easily synthetized and coated or conjugated to carry various cargos, from small molecules to proteins and nucleic acids [174]. Furthermore, AuNPs show low immunogenicity and toxicity due to their inert core [78]. Finally, AuNPs could be used as X-ray contrast agent if their concentration in the brain is sufficiently high to allow for their detection, making them potential carriers for theranostic treatments [174].

It has been shown that the organ distribution of gold nanoparticles depends on the size of the particles. In multiple in vivo studies on rodents, low amounts of AuNPs of 10–15 nm were able to cross the BBB and reach the brain. However, the vast majority of the administered dose was found in the liver and in the blood [134-136]. Moreover, the amount of gold found in the brain was dependent on the AuNP dose, showing no sign of saturation at the doses tested. This suggests that the AuNPs might cross the BBB through a non-saturable pathway such as passive transmembrane diffusion or the paracellular pathway [175]. Of course, depending on the surface ligands of the AuNPs, the pathway taken might differ. Hydrophilic ligands might hinder the transmembrane diffusion of the particles. Surface modifications with specific ligands such as transferrin [78], THR peptide (a transferrin receptor ligand) [86], angiopep-2 [70], insulin [95] and CLPFFD peptide, a peptide derived from β-amyloids able to interact with RAGE [96], have been shown to increase the BBB delivery of AuNPs by allowing them to cross the BBB through RMT. Moreover, AuNPs have been extensively used to reach brain tumors. Due to their small size, AuNPs can diffuse more easily through the disrupted BBB of the brain tumor vasculature, making them a useful carrier for drugs or imaging agents. The use of targeting ligands, such as angiopep-2, TAT or EGF, allows their accumulation to be increased in these specific areas [70,78,107,176].

Although to a lower extent, gold nanorods (AuNRs) have also been used for brain delivery. AuNRs, like AuNPs, exhibit an optical feature called surface plasmon resonance, which allows them to strongly absorb light in the infrared region [177,178].

The advantage of AuNRs over AuNPs is that their aspect ratio (length divided by width) allows for the adjustment of the absorption wavelength in the near infrared (NIR) region (650–1350 nm), thus exploiting the so-called optical window. Light in this wavelength range can penetrate more deeply into the human body thanks to the low absorption by tissue and blood, making these nanoparticles interesting for theranostic treatments [177,179,180]. By excitation of surface plasmon oscillations, local heating can be generated, making these particles interesting for tumor treatment by photothermal therapy [178]. Furthermore, nanorods can be internalized more easily by cells as their increased surface allows them to interact more easily with receptors on the cell membranes [181]. AuNRs have been functionalized to increase their BBB delivery of angiopep-2 [71], RVG29 [105], CLPFFD [97] or transferrin [79]. In a study by Praça et al., AuNPs and AuNRs were functionalized with different amounts of transferrin and tested in vitro on a BBB model and in vivo on mice after intravenous administration [79]. In vitro and in vivo results showed that AuNPs and AuNRs with a medium density of transferrin had the highest transport efficiency across the BBB, due to their lower avidity for the transferrin receptor. The latter allowed them to more easily escape the endosomes to reach the cytosol, thus avoiding the lysosomal pathway. In vivo studies confirmed the ability of functionalized AuNPs and AuNRs to cross the BBB as both formulations were found in the brain of mice in larger quantity than the bare formulations. Interestingly, AuNRs accumulated in the subventricular zone (SVZ), a neurogenic niche, while AuNPs were mostly found in non-neurogenic regions. Disruption of the BBB by NIR light irradiation of AuNRs increased the AuNRs ability to accumulate in the SVZ, making this formulation interesting for targeting neural stem cells.

Superparamagnetic iron oxide nanoparticles: Superparamagnetic iron oxide nanoparticles (SPIONs) are based on magnetite (Fe_3O_4) or maghemite (γ-Fe_2O_3) molecules encapsulated in polysaccharides, synthetic polymers or monomer coatings and have a size range from 1 to 100 nm [21,182]. SPIONs possess interesting magnetic properties and some formulations have already been approved as MRI contrast agents for imaging of the liver by the Food and Drug Administration (FDA) [183]. However, these formulations are no longer available because of concerns about toxicity and fatal anaphylactic reactions. Nowadays, ferumoxytol is the only SPION formulation approved by the FDA for human use, under the commercial name Feraheme®. Although its indication is for the treatment of iron deficiency in patients with renal failure, it is also clinically used for MRI of adrenal glands and kidneys [183,184]. As they are composed of iron, a normal component of the human body, SPIONs are believed to have low toxicity and high biocompatibility. SPIONs are metabolized in the lysosomes into a soluble non-superparamagnetic form or iron. Then, iron ions join the iron pool in the blood and can be incorporated by erythrocytes as part of hemoglobin [21,183]. However, the concern about serious anaphylactic reactions, the cause of which is not well understood, seriously restrains their use in clinical treatments. In 2015, the FDA released a “Boxed Warning”, the strongest type of warning, regarding the serious risks following the use of Feraheme. Feraheme can still be used following strict instructions to limit the risk and is under close surveillance by the FDA. Thus, even if SPIONs could be potential tools for imaging the brain and more especially for imaging brain tumors, this issue should be thoroughly investigated.

Similar to AuNPs, SPIONs smaller than 50 nm are able to cross the disrupted BBB around brain tumors or in diseases such as Alzheimer’s or ischemic stroke [185]. Using targeting ligands such as EGF, cetuximab (an anti-EGFR antibody), or anti-Aβ peptide antibodies, their accumulation in these areas can be increased [30,186,187]. For example, in a study by Shevtsov et al., SPIONs conjugated with EGF were tested as contrast agent in an intracranial rat glioma model [30]. Functionalized SPIONs were able to cross the tumor BBB and to accumulate in the tumor and demonstrated high magnetic resonance contrast potential, confirming the ability of functionalized SPIONs to act as a diagnostic agent for intracranial glioma.

Conclusion

Crossing the BBB remains one of the most challenging tasks for drug delivery to the brain. Different physiological pathways can be employed for crossing the BBB including receptor-mediated transcytosis or adsorptive-mediated transcytosis. To reach this goal, a multitude of nanocarrier systems, such as polymeric, lipid-based or inorganic nanoparticles, have been developed and shown able to cross the BBB owing to their tailored surface properties. In numerous studies, the physical coating of nanoparticles with surfactants and the chemical functionalization with specific ligands have been proven to be successful strategies to enhance the BBB crossing through RMT or AMT. Size and charge of the nanoparticles are also aspects that can influence their penetration into the brain. Smaller nanoparticles are able to cross the BBB more easily and to diffuse better through the brain. However, bigger nanoparticles, if correctly functionalized, are also able to cross the BBB, although to a slightly lower extent. Thus, key to increase the amount of drug delivered to the brain is finding the optimal particle size. Larger particles can be loaded with larger amounts of drugs but will reach the brain in lower concentrations, smaller nanoparticles cannot contain large amounts of API but will reach the brain in higher concentrations. By rationally designing nanoparticle systems, the crossing of the BBB in preclinical studies has been successfully demonstrated repeatedly. However, very few clinical data

are available on the efficacy of these strategies in the human body. More efforts should now be taken to accelerate the translation of these results into clinical stages, for instance, by focusing on the behavior of the nanoparticles in human blood and investigating the protein corona forming around them, by investigating the particle–cell interactions or by looking for biomimetic solutions.

Acknowledgements

Figure 2 was made using cliparts "Brain arteries" (https://smart.servier.com/smart_image/brain-circulation/), "Meningitis" (https://smart.servier.com/smart_image/meningitis-2/) and "Nasal cavity" (https://smart.servier.com/smart_image/nasal-cavity/) from Servier Medical Art by Servier. Figure 3 was made using cliparts "Erythrocyte" (https://smart.servier.com/smart_image/erythrocyte-2/), "Tight junctions" (https://smart.servier.com/smart_image/tissue-jonction-10/), "Endothelium" (https://smart.servier.com/smart_image/endothelium-2/) and the "Receptors and channels" collection (https://smart.servier.com/category/cellular-biology/receptors-and-channels/) from Servier Medical Art by Servier. Original cliparts are licensed under a Creative Commons Attribution 3.0 Unported License, https://creativecommons.org/licenses/by/3.0/.

Funding

This review has been written as part of the NANOSTEM project, a Marie Skłodowska-Curie Innovative Training Network (ITN). This project has received funding from the European Union's Horizon 2020 research and innovation programme under grant agreement No 764958.

ORCID® iDs

Sonia M. Lombardo - https://orcid.org/0000-0002-8538-5012
Marc Schneider - https://orcid.org/0000-0002-9260-7357
Nazende Günday Türeli - https://orcid.org/0000-0002-6310-4785

References

1. World Health Organization. The top 10 causes of death. https://www.who.int/news-room/fact-sheets/detail/the-top-10-causes-of-death (accessed Feb 22, 2019).
2. Rajkovic, O.; Potjewyd, G.; Pinteaux, E. *Front. Neurol.* **2018,** *9,* No. 734. doi:10.3389/fneur.2018.00734
3. Abbott, N. J.; Rönnbäck, L.; Hansson, E. *Nat. Rev. Neurosci.* **2006,** *7,* 41–53. doi:10.1038/nrn1824
4. Sweeney, M. D.; Sagare, A. P.; Zlokovic, B. V. *Nat. Rev. Neurol.* **2018,** *14,* 133–150. doi:10.1038/nrneurol.2017.188
5. Abbott, N. J.; Patabendige, A. A. K.; Dolman, D. E. M.; Yusof, S. R.; Begley, D. J. *Neurobiol. Dis.* **2010,** *37,* 13–25. doi:10.1016/j.nbd.2009.07.030
6. Hawkins, B. T.; Davis, T. P. *Pharmacol. Rev.* **2005,** *57,* 173–185. doi:10.1124/pr.57.2.4
7. Saraiva, C.; Praça, C.; Ferreira, R.; Santos, T.; Ferreira, L.; Bernardino, L. *J. Controlled Release* **2016,** *235,* 34–47. doi:10.1016/j.jconrel.2016.05.044
8. Ballabh, P.; Braun, A.; Nedergaard, M. *Neurobiol. Dis.* **2004,** *16,* 1–13. doi:10.1016/j.nbd.2003.12.016
9. Patel, M. M.; Goyal, B. R.; Bhadada, S. V.; Bhatt, J. S.; Amin, A. F. *CNS Drugs* **2009,** *23,* 35–58. doi:10.2165/0023210-200923010-00003
10. Chaichana, K. L.; Pinheiro, L.; Brem, H. *Ther. Delivery* **2015,** *6,* 353–369. doi:10.4155/tde.14.114
11. Mistry, A.; Stolnik, S.; Illum, L. *Int. J. Pharm.* **2009,** *379,* 146–157. doi:10.1016/j.ijpharm.2009.06.019
12. Bourganis, V.; Kammona, O.; Alexopoulos, A.; Kiparissides, C. *Eur. J. Pharm. Biopharm.* **2018,** *128,* 337–362. doi:10.1016/j.ejpb.2018.05.009
13. Gänger, S.; Schindowski, K. *Pharmaceutics* **2018,** *10,* 116. doi:10.3390/pharmaceutics10030116
14. Erdő, F.; Bors, L. A.; Farkas, D.; Bajza, Á.; Gizurarson, S. *Brain Res. Bull.* **2018,** *143,* 155–170. doi:10.1016/j.brainresbull.2018.10.009
15. Agrawal, M.; Saraf, S.; Saraf, S.; Antimisiaris, S. G.; Chougule, M. B.; Shoyele, S. A.; Alexander, A. *J. Controlled Release* **2018,** *281,* 139–177. doi:10.1016/j.jconrel.2018.05.011
16. Pires, P. C.; Santos, A. O. *J. Controlled Release* **2018,** *270,* 89–100. doi:10.1016/j.jconrel.2017.11.047
17. Lochhead, J. J.; Thorne, R. G. *Adv. Drug Delivery Rev.* **2012,** *64,* 614–628. doi:10.1016/j.addr.2011.11.002
18. Blanchette, M.; Fortin, D. Blood-Brain Barrier Disruption in the Treatment of Brain Tumors. In *The Blood-Brain and Other Neural Barriers: Reviews and Protocols;* Nag, S., Ed.; Methods in Molecular Biology; Humana Press: Totowa, NJ, USA, 2011; pp 447–463. doi:10.1007/978-1-60761-938-3_23
19. Etame, A. B.; Diaz, R. J.; O'Reilly, M. A.; Smith, C. A.; Mainprize, T. G.; Hynynen, K.; Rutka, J. T. *Nanomedicine (N. Y., NY, U. S.)* **2012,** *8,* 1133–1142. doi:10.1016/j.nano.2012.02.003
20. Bing, K. F.; Howles, G. P.; Qi, Y.; Palmeri, M. L.; Nightingale, K. R. *Ultrasound Med. Biol.* **2009,** *35,* 1298–1308. doi:10.1016/j.ultrasmedbio.2009.03.012
21. Posadas, I.; Monteagudo, S.; Ceña, V. *Nanomedicine (London, U. K.)* **2016,** *11,* 833–849. doi:10.2217/nnm.16.15
22. European Commission. Definition - Nanomaterials. http://ec.europa.eu/environment/chemicals/nanotech/faq/definition_en.htm (accessed Nov 11, 2018).
23. Fattal, E.; Vauthier, C. *Drug Delivery: Nanoparticles; Encyclopedia of Pharmaceutical Technology*, Vol. 2; James Swarbrick: New York, NY, USA, 2007; p 1183.
24. Kreuter, J.; Alyautdin, R. N.; Kharkevich, D. A.; Ivanov, A. A. *Brain Res.* **1995,** *674,* 171–174. doi:10.1016/0006-8993(95)00023-j
25. Kreuter, J. *Adv. Drug Delivery Rev.* **2014,** *71,* 2–14. doi:10.1016/j.addr.2013.08.008
26. Andrieux, K.; Couvreur, P. *Wiley Interdiscip. Rev.: Nanomed. Nanobiotechnol.* **2009,** *1,* 463–474. doi:10.1002/wnan.5
27. Tapeinos, C.; Battaglini, M.; Ciofani, G. *J. Controlled Release* **2017,** *264,* 306–332. doi:10.1016/j.jconrel.2017.08.033
28. Ulbrich, K.; Knobloch, T.; Kreuter, J. *J. Drug Targeting* **2011,** *19,* 125–132. doi:10.3109/10611861003734001
29. Aghaie, T.; Jazayeri, M. H.; Manian, M.; Khani, L.; Erfani, M.; Rezayi, M.; Ferns, G. A.; Avan, A. *J. Cell. Biochem.* **2019,** *120,* 2749–2755. doi:10.1002/jcb.27415

30. Shevtsov, M. A.; Nikolaev, B. P.; Yakovleva, L. Y.; Marchenko, Y. Y.; Dobrodumov, A. V.; Mikhrina, A. L.; Martynova, M. G.; Bystrova, O. A.; Yakovenko, I. V.; Ischenko, A. M. *Int. J. Nanomed.* **2014,** *9,* 273–287. doi:10.2147/ijn.s55118
31. Sanchez-Covarrubias, L.; Slosky, L. M.; Thompson, B. J.; Davis, T. P.; Ronaldson, P. T. *Curr. Pharm. Des.* **2014,** *20,* 1422–1449. doi:10.2174/13816128113199990463
32. Banks, W. A.; Owen, J. B.; Erickson, M. A. *Pharmacol. Ther.* **2012,** *136,* 82–93. doi:10.1016/j.pharmthera.2012.07.006
33. Boado, R. J.; Li, J. Y.; Nagaya, M.; Zhang, C.; Pardridge, W. M. *Proc. Natl. Acad. Sci. U. S. A.* **1999,** *96,* 12079–12084. doi:10.1073/pnas.96.21.12079
34. Zhang, Z.; Zhan, C. Receptor-Mediated Transportation through BBB. In *Brain Targeted Drug Delivery System;* Gao, H.; Gao, X., Eds.; Academic Press, 2019; pp 105–128. doi:10.1016/b978-0-12-814001-7.00005-6
35. Kim, R. B. *Drug Metab. Rev.* **2002,** *34,* 47–54. doi:10.1081/dmr-120001389
36. Mahringer, A.; Ott, M.; Reimold, I.; Reichel, V.; Fricker, G. *Curr. Pharm. Des.* **2011,** *17,* 2762–2770. doi:10.2174/138161211797440221
37. Miller, D. S. *Trends Pharmacol. Sci.* **2010,** *31,* 246–254. doi:10.1016/j.tips.2010.03.003
38. Chen, R.; Zhao, X.; Hu, K. Efflux Pump Inhibition to Enhance Brain Targeting Delivery. In *Brain Targeted Drug Delivery System;* Gao, H.; Gao, X., Eds.; Academic Press, 2019; pp 185–196. doi:10.1016/b978-0-12-814001-7.00008-1
39. Villaseñor, R.; Lampe, J.; Schwaninger, M.; Collin, L. *Cell. Mol. Life Sci.* **2019,** *76,* 1081–1092. doi:10.1007/s00018-018-2982-x
40. Pulgar, V. *Front. Neurosci.* **2019,** *12,* No. 1019. doi:10.3389/fnins.2018.01019
41. Jones, A. R.; Shusta, E. V. *Pharm. Res.* **2007,** *24,* 1759–1771. doi:10.1007/s11095-007-9379-0
42. Lajoie, J. M.; Shusta, E. V. *Annu. Rev. Pharmacol. Toxicol.* **2015,** *55,* 613–631. doi:10.1146/annurev-pharmtox-010814-124852
43. Preston, J. E.; Joan Abbott, N.; Begley, D. J. Transcytosis of Macromolecules at the Blood–Brain Barrier. In *Advances in Pharmacology;* Davis, T. P., Ed.; Pharmacology of the Blood Brain Barrier: Targeting CNS Disorders, Vol. 71; Academic Press, 2014; pp 147–163. doi:10.1016/bs.apha.2014.06.001
44. Gao, H.; Yang, Z.; Zhang, S.; Pang, Z.; Jiang, X. *J. Drug Targeting* **2014,** *22,* 450–459. doi:10.3109/1061186x.2014.886038
45. Hervé, F.; Ghinea, N.; Scherrmann, J.-M. *AAPS J.* **2008,** *10,* 455–472. doi:10.1208/s12248-008-9055-2
46. Lu, W. *Curr. Pharm. Biotechnol.* **2012,** *13,* 2340–2348. doi:10.2174/138920112803341851
47. Zhu, X.; Jin, K.; Huang, Y.; Pang, Z. Brain Drug Delivery by Adsorption-Mediated Transcytosis. In *Brain Targeted Drug Delivery System;* Gao, H.; Gao, X., Eds.; Academic Press, 2019; pp 159–183. doi:10.1016/b978-0-12-814001-7.00007-x
48. Bickel, U.; Yoshikawa, T.; Pardridge, W. M. *Adv. Drug Delivery Rev.* **2001,** *46,* 247–279. doi:10.1016/s0169-409x(00)00139-3
49. Kreuter, J.; Petrov, V. E.; Kharkevich, D. A.; Alyautdin, R. N. *J. Controlled Release* **1997,** *49,* 81–87. doi:10.1016/s0168-3659(97)00061-8
50. Kreuter, J.; Ramge, P.; Petrov, V.; Hamm, S.; Gelperina, S. E.; Engelhardt, B.; Alyautdin, R.; von Briesen, H.; Begley, D. J. *Pharm. Res.* **2003,** *20,* 409–416. doi:10.1023/a:1022604120952
51. Lück, M. Plasmaproteinadsorption Als Möglicher Schlüsselfaktor Für Eine Kontrollierte Arzneistoffapplikation Mit Partikulären Trägern. Ph.D. Thesis, Freie Universität Berlin, Berlin, Germany, 1997.
52. Kreuter, J.; Shamenkov, D.; Petrov, V.; Ramge, P.; Cychutek, K.; Koch-Brandt, C.; Alyautdin, R. *J. Drug Targeting* **2002,** *10,* 317–325. doi:10.1080/10611860290031877
53. Ambruosi, A.; Gelperina, S.; Khalansky, A.; Tanski, S.; Theisen, A.; Kreuter, J. *J. Microencapsulation* **2006,** *23,* 582–592. doi:10.1080/02652040600788080
54. Kreuter, J. *J. Nanosci. Nanotechnol.* **2004,** *4,* 484–488. doi:10.1166/jnn.2003.077
55. Petri, B.; Bootz, A.; Khalansky, A.; Hekmatara, T.; Müller, R.; Uhl, R.; Kreuter, J.; Gelperina, S. *J. Controlled Release* **2007,** *117,* 51–58. doi:10.1016/j.jconrel.2006.10.015
56. Gelperina, S.; Maksimenko, O.; Khalansky, A.; Vanchugova, L.; Shipulo, E.; Abbasova, K.; Berdiev, R.; Wohlfart, S.; Chepurnova, N.; Kreuter, J. *Eur. J. Pharm. Biopharm.* **2010,** *74,* 157–163. doi:10.1016/j.ejpb.2009.09.003
57. Tahara, K.; Miyazaki, Y.; Kawashima, Y.; Kreuter, J.; Yamamoto, H. *Eur. J. Pharm. Biopharm.* **2011,** *77,* 84–88. doi:10.1016/j.ejpb.2010.11.002
58. Ren, T.; Xu, N.; Cao, C.; Yuan, W.; Yu, X.; Chen, J.; Ren, J. *J. Biomater. Sci., Polym. Ed.* **2009,** *20,* 1369–1380. doi:10.1163/092050609x12457418779185
59. Raudszus, B.; Partikel, K.; Mulac, D.; Langer, K. *Mater. Today: Proc.* **2017,** *4,* S193–S199. doi:10.1016/j.matpr.2017.09.186
60. Chen, Y.-C.; Hsieh, W.-Y.; Lee, W.-F.; Zeng, D.-T. *J. Biomater. Appl.* **2013,** *27,* 909–922. doi:10.1177/0885328211429495
61. Zensi, A.; Begley, D.; Pontikis, C.; Legros, C.; Mihoreanu, L.; Büchel, C.; Kreuter, J. *J. Drug Targeting* **2010,** *18,* 842–848. doi:10.3109/1061186x.2010.513712
62. Kreuter, J.; Hekmatara, T.; Dreis, S.; Vogel, T.; Gelperina, S.; Langer, K. *J. Controlled Release* **2007,** *118,* 54–58. doi:10.1016/j.jconrel.2006.12.012
63. Kratzer, I.; Wernig, K.; Panzenboeck, U.; Bernhart, E.; Reicher, H.; Wronski, R.; Windisch, M.; Hammer, A.; Malle, E.; Zimmer, A.; Sattler, W. *J. Controlled Release* **2007,** *117,* 301–311. doi:10.1016/j.jconrel.2006.11.020
64. Michaelis, K.; Hoffmann, M. M.; Dreis, S.; Herbert, E.; Alyautdin, R. N.; Michaelis, M.; Kreuter, J.; Langer, K. *J. Pharmacol. Exp. Ther.* **2006,** *317,* 1246–1253. doi:10.1124/jpet.105.097139
65. Neves, A. R.; Queiroz, J. F.; Reis, S. *J. Nanobiotechnol.* **2016,** *14,* 27. doi:10.1186/s12951-016-0177-x
66. Dal Magro, R.; Ornaghi, F.; Cambianica, I.; Beretta, S.; Re, F.; Musicanti, C.; Rigolio, R.; Donzelli, E.; Canta, A.; Ballarini, E.; Cavaletti, G.; Gasco, P.; Sancini, G. *J. Controlled Release* **2017,** *249,* 103–110. doi:10.1016/j.jconrel.2017.01.039
67. Bana, L.; Minniti, S.; Salvati, E.; Sesana, S.; Zambelli, V.; Cagnotto, A.; Orlando, A.; Cazzaniga, E.; Zwart, R.; Scheper, W.; Masserini, M.; Re, F. *Nanomedicine (N. Y., NY, U. S.)* **2014,** *10,* 1583–1590. doi:10.1016/j.nano.2013.12.001
68. Xin, H.; Jiang, X.; Gu, J.; Sha, X.; Chen, L.; Law, K.; Chen, Y.; Wang, X.; Jiang, Y.; Fang, X. *Biomaterials* **2011,** *32,* 4293–4305. doi:10.1016/j.biomaterials.2011.02.044
69. Kadari, A.; Pooja, D.; Gora, R. H.; Gudem, S.; Kolapalli, V. R. M.; Kulhari, H.; Sistla, R. *Eur. J. Pharm. Biopharm.* **2018,** *132,* 168–179. doi:10.1016/j.ejpb.2018.09.012

70. Ruan, S.; Yuan, M.; Zhang, L.; Hu, G.; Chen, J.; Cun, X.; Zhang, Q.; Yang, Y.; He, Q.; Gao, H. *Biomaterials* **2015,** *37,* 425–435. doi:10.1016/j.biomaterials.2014.10.007
71. Velasco-Aguirre, C.; Morales-Zavala, F.; Salas-Huenuleo, E.; Gallardo-Toledo, E.; Andonie, O.; Muñoz, L.; Rojas, X.; Acosta, G.; Sánchez-Navarro, M.; Giralt, E.; Araya, E.; Albericio, F.; Kogan, M. J. *Nanomedicine (London, U. K.)* **2017,** *12,* 2503–2517. doi:10.2217/nnm-2017-0181
72. Chang, J.; Paillard, A.; Passirani, C.; Morille, M.; Benoit, J.-P.; Betbeder, D.; Garcion, E. *Pharm. Res.* **2012,** *29,* 1495–1505. doi:10.1007/s11095-011-0624-1
73. Gupta, Y.; Jain, A.; Jain, S. K. *J. Pharm. Pharmacol.* **2007,** *59,* 935–940. doi:10.1211/jpp.59.7.0004
74. Ulbrich, K.; Hekmatara, T.; Herbert, E.; Kreuter, J. *Eur. J. Pharm. Biopharm.* **2009,** *71,* 251–256. doi:10.1016/j.ejpb.2008.08.021
75. Cui, Y.; Xu, Q.; Chow, P. K.-H.; Wang, D.; Wang, C.-H. *Biomaterials* **2013,** *34,* 8511–8520. doi:10.1016/j.biomaterials.2013.07.075
76. Zhao, H.; Bao, X.-j.; Wang, R.-z.; Li, G.-l.; Gao, J.; Ma, S.-h.; Wei, J.-j.; Feng, M.; Zhao, Y.-j.; Ma, W.-b.; Yang, Y.; Li, Y.-n.; Kong, Y.-g. *Hum. Gene Ther.* **2011,** *22,* 207–215. doi:10.1089/hum.2010.111
77. Chen, X.; Yuan, M.; Zhang, Q.; Ting Yang, Y.; Gao, H.; He, Q. *Curr. Pharm. Biotechnol.* **2016,** *17,* 636–650. doi:10.2174/1389201017666160401144440
78. Dixit, S.; Novak, T.; Miller, K.; Zhu, Y.; Kenney, M. E.; Broome, A.-M. *Nanoscale* **2015,** *7,* 1782–1790. doi:10.1039/c4nr04853a
79. Praça, C.; Rai, A.; Santos, T.; Cristovão, A. C.; Pinho, S. L.; Cecchelli, R.; Dehouck, M.-P.; Bernardino, L.; Ferreira, L. S. *J. Controlled Release* **2018,** *284,* 57–72. doi:10.1016/j.jconrel.2018.06.013
80. Aktaş, Y.; Yemisci, M.; Andrieux, K.; Gürsoy, R. N.; Alonso, M. J.; Fernandez-Megia, E.; Novoa-Carballal, R.; Quiñoá, E.; Riguera, R.; Sargon, M. F.; Çelik, H. H.; Demir, A. S.; Hıncal, A. A.; Dalkara, T.; Çapan, Y.; Couvreur, P. *Bioconjugate Chem.* **2005,** *16,* 1503–1511. doi:10.1021/bc050217o
81. Loureiro, J. A.; Gomes, B.; Fricker, G.; Coelho, M. A. N.; Rocha, S.; Pereira, M. C. *Colloids Surf., B* **2016,** *145,* 8–13. doi:10.1016/j.colsurfb.2016.04.041
82. Gu, J.; Al-Bayati, K.; Ho, E. A. *Drug Delivery Transl. Res.* **2017,** *7,* 497–506. doi:10.1007/s13346-017-0368-5
83. Tang, X.; Liang, Y.; Zhu, Y.; Xie, C.; Yao, A.; Chen, L.; Jiang, Q.; Liu, T.; Wang, X.; Qian, Y.; Wei, J.; Ni, W.; Dai, J.; Jiang, Z.; Hou, W. *Int. J. Nanomed.* **2015,** *10,* 6227–6241. doi:10.2147/ijn.s84656
84. Xia, C.-F.; Boado, R. J.; Zhang, Y.; Chu, C.; Pardridge, W. M. *J. Gene Med.* **2008,** *10,* 306–315. doi:10.1002/jgm.1152
85. Mourtas, S.; Lazar, A. N.; Markoutsa, E.; Duyckaerts, C.; Antimisiaris, S. G. *Eur. J. Med. Chem.* **2014,** *80,* 175–183. doi:10.1016/j.ejmech.2014.04.050
86. Prades, R.; Guerrero, S.; Araya, E.; Molina, C.; Salas, E.; Zurita, E.; Selva, J.; Egea, G.; López-Iglesias, C.; Teixidó, M.; Kogan, M. J.; Giralt, E. *Biomaterials* **2012,** *33,* 7194–7205. doi:10.1016/j.biomaterials.2012.06.063
87. Hu, K.; Shi, Y.; Jiang, W.; Han, J.; Huang, S.; Jiang, X. *Int. J. Pharm.* **2011,** *415,* 273–283. doi:10.1016/j.ijpharm.2011.05.062
88. Hu, K.; Li, J.; Shen, Y.; Lu, W.; Gao, X.; Zhang, Q.; Jiang, X. *J. Controlled Release* **2009,** *134,* 55–61. doi:10.1016/j.jconrel.2008.10.016
89. Chen, H.; Tang, L.; Qin, Y.; Yin, Y.; Tang, J.; Tang, W.; Sun, X.; Zhang, Z.; Liu, J.; He, Q. *Eur. J. Pharm. Sci.* **2010,** *40,* 94–102. doi:10.1016/j.ejps.2010.03.007
90. Meng, F.; Asghar, S.; Gao, S.; Su, Z.; Song, J.; Huo, M.; Meng, W.; Ping, Q.; Xiao, Y. *Colloids Surf., B* **2015,** *134,* 88–97. doi:10.1016/j.colsurfb.2015.06.025
91. Valenza, M.; Chen, J. Y.; Di Paolo, E.; Ruozi, B.; Belletti, D.; Ferrari Bardile, C.; Leoni, V.; Caccia, C.; Brilli, E.; Di Donato, S.; Boido, M. M.; Vercelli, A.; Vandelli, M. A.; Forni, F.; Cepeda, C.; Levine, M. S.; Tosi, G.; Cattaneo, E. *EMBO Mol. Med.* **2015,** *7,* 1547–1564. doi:10.15252/emmm.201505413
92. Tosi, G.; Vergoni, A. V.; Ruozi, B.; Bondioli, L.; Badiali, L.; Rivasi, F.; Costantino, L.; Forni, F.; Vandelli, M. A. *J. Controlled Release* **2010,** *145,* 49–57. doi:10.1016/j.jconrel.2010.03.008
93. Costantino, L.; Gandolfi, F.; Tosi, G.; Rivasi, F.; Vandelli, M. A.; Forni, F. *J. Controlled Release* **2005,** *108,* 84–96. doi:10.1016/j.jconrel.2005.07.013
94. Tosi, G.; Vilella, A.; Veratti, P.; Belletti, D.; Pederzoli, F.; Ruozi, B.; Vandelli, M. A.; Zoli, M.; Forni, F. *Mol. Pharmaceutics* **2015,** *12,* 3672–3684. doi:10.1021/acs.molpharmaceut.5b00446
95. Shilo, M.; Motiei, M.; Hana, P.; Popovtzer, R. *Nanoscale* **2014,** *6,* 2146–2152. doi:10.1039/c3nr04878k
96. Guerrero, S.; Araya, E.; Fiedler, J. L.; Arias, J. I.; Adura, C.; Albericio, F.; Giralt, E.; Arias, J. L.; Fernández, M. S.; Kogan, M. J. *Nanomedicine (London, U. K.)* **2010,** *5,* 897–913. doi:10.2217/nnm.10.74
97. Vio, V.; Riveros, A. L.; Tapia-Bustos, A.; Lespay-Rebolledo, C.; Perez-Lobos, R.; Muñoz, L.; Pismante, P.; Morales, P.; Araya, E.; Hassan, N.; Herrera-Marschitz, M.; Kogan, M. J. *Int. J. Nanomed.* **2018,** *13,* 6839–6854. doi:10.2147/ijn.s175076
98. Lockman, P. R.; Oyewumi, M. O.; Koziara, J. M.; Roder, K. E.; Mumper, R. J.; Allen, D. D. *J. Controlled Release* **2003,** *93,* 271–282. doi:10.1016/j.jconrel.2003.08.006
99. Gaillard, P. J.; Appeldoorn, C. C. M.; Dorland, R.; van Kregten, J.; Manca, F.; Vugts, D. J.; Windhorst, B.; van Dongen, G. A. M. S.; de Vries, H. E.; Maussang, D.; van Tellingen, O. *PLoS One* **2014,** *9,* e82331. doi:10.1371/journal.pone.0082331
100. Lindqvist, A.; Rip, J.; Gaillard, P. J.; Björkman, S.; Hammarlund-Udenaes, M. *Mol. Pharmaceutics* **2013,** *10,* 1533–1541. doi:10.1021/mp300272a
101. Li, J.; Zhang, C.; Li, J.; Fan, L.; Jiang, X.; Chen, J.; Pang, Z.; Zhang, Q. *Pharm. Res.* **2013,** *30,* 1813–1823. doi:10.1007/s11095-013-1025-4
102. Mathew, A.; Fukuda, T.; Nagaoka, Y.; Hasumura, T.; Morimoto, H.; Yoshida, Y.; Maekawa, T.; Venugopal, K.; Kumar, D. S. *PLoS One* **2012,** *7,* e32616. doi:10.1371/journal.pone.0032616
103. Kim, J.-Y.; Choi, W. I.; Kim, Y. H.; Tae, G. *Biomaterials* **2013,** *34,* 1170–1178. doi:10.1016/j.biomaterials.2012.09.047
104. Chen, W.; Zhan, C.; Gu, B.; Meng, Q.; Wang, H.; Lu, W.; Hou, H. *J. Drug Targeting* **2011,** *19,* 228–234. doi:10.3109/1061186x.2010.492523
105. Lee, C.; Hwang, H. S.; Lee, S.; Kim, B.; Kim, J. O.; Oh, K. T.; Lee, E. S.; Choi, H.-G.; Youn, Y. S. *Adv. Mater. (Weinheim, Ger.)* **2017,** *29,* 1605563. doi:10.1002/adma.201605563
106. Rao, K. S.; Reddy, M. K.; Horning, J. L.; Labhasetwar, V. *Biomaterials* **2008,** *29,* 4429–4438. doi:10.1016/j.biomaterials.2008.08.004

107. Cheng, Y.; Dai, Q.; Morshed, R. A.; Fan, X.; Wegscheid, M. L.; Wainwright, D. A.; Han, Y.; Zhang, L.; Auffinger, B.; Tobias, A. L.; Rincón, E.; Thaci, B.; Ahmed, A. U.; Warnke, P. C.; He, C.; Lesniak, M. S. *Small* **2014,** *10,* 5137–5150. doi:10.1002/smll.201400654
108. Xia, H.; Gao, X.; Gu, G.; Liu, Z.; Hu, Q.; Tu, Y.; Song, Q.; Yao, L.; Pang, Z.; Jiang, X.; Chen, J.; Chen, H. *Int. J. Pharm.* **2012,** *436,* 840–850. doi:10.1016/j.ijpharm.2012.07.029
109. Tian, X.; Wei, F.; Wang, T.-x.; Wang, P.; Lin, X.; Wang, J.; Wang, D.; Ren, L. *Int. J. Nanomed.* **2012,** *7,* 1031–1041. doi:10.2147/ijn.s26541
110. Lu, W.; Tan, Y.-Z.; Hu, K.-L.; Jiang, X.-G. *Int. J. Pharm.* **2005,** *295,* 247–260. doi:10.1016/j.ijpharm.2005.01.043
111. Parikh, T.; Bommana, M. M.; Squillante, E., III. *Eur. J. Pharm. Biopharm.* **2010,** *74,* 442–450. doi:10.1016/j.ejpb.2009.11.001
112. Thöle, M.; Nobmann, S.; Huwyler, J.; Bartmann, A.; Fricker, G. *J. Drug Targeting* **2002,** *10,* 337–344. doi:10.1080/10611860290031840
113. Agarwal, A.; Majumder, S.; Agrawal, H.; Majumdar, S.; Agrawal, G. P. *Curr. Nanosci.* **2011,** *7,* 71–80. doi:10.2174/157341311794480291
114. Wang, Z. H.; Wang, Z. Y.; Sun, C. S.; Wang, C. Y.; Jiang, T. Y.; Wang, S. L. *Biomaterials* **2010,** *31,* 908–915. doi:10.1016/j.biomaterials.2009.09.104
115. Wagner, S.; Zensi, A.; Wien, S. L.; Tschickardt, S. E.; Maier, W.; Vogel, T.; Worek, F.; Pietrzik, C. U.; Kreuter, J.; von Briesen, H. *PLoS One* **2012,** *7,* e32568. doi:10.1371/journal.pone.0032568
116. Panzenboeck, U.; Balazs, Z.; Sovic, A.; Hrzenjak, A.; Levak-Frank, S.; Wintersperger, A.; Malle, E.; Sattler, W. *J. Biol. Chem.* **2002,** *277,* 42781–42789. doi:10.1074/jbc.m207601200
117. Moos, T.; Morgan, E. H. *J. Neurochem.* **2001,** *79,* 119–129. doi:10.1046/j.1471-4159.2001.00541.x
118. Paterson, J.; Webster, C. I. *Drug Discovery Today: Technol.* **2016,** *20,* 49–52. doi:10.1016/j.ddtec.2016.07.009
119. Niewoehner, J.; Bohrmann, B.; Collin, L.; Urich, E.; Sade, H.; Maier, P.; Rueger, P.; Stracke, J. O.; Lau, W.; Tissot, A. C.; Loetscher, H.; Ghosh, A.; Freskgård, P.-O. *Neuron* **2014,** *81,* 49–60. doi:10.1016/j.neuron.2013.10.061
120. Bien-Ly, N.; Yu, Y. J.; Bumbaca, D.; Elstrott, J.; Boswell, C. A.; Zhang, Y.; Luk, W.; Lu, Y.; Dennis, M. S.; Weimer, R. M.; Chung, I.; Watts, R. J. *J. Exp. Med.* **2014,** *211,* 233–244. doi:10.1084/jem.20131660
121. Liu, J. K.; Teng, Q.; Garrity-Moses, M.; Federici, T.; Tanase, D.; Imperiale, M. J.; Boulis, N. M. *Neurobiol. Dis.* **2005,** *19,* 407–418. doi:10.1016/j.nbd.2005.01.022
122. Bazan, J.; Całkosiński, I.; Gamian, A. *Hum. Vaccines Immunother.* **2012,** *8,* 1817–1828. doi:10.4161/hv.21703
123. Li, J.; Feng, L.; Fan, L.; Zha, Y.; Guo, L.; Zhang, Q.; Chen, J.; Pang, Z.; Wang, Y.; Jiang, X.; Yang, V. C.; Wen, L. *Biomaterials* **2011,** *32,* 4943–4950. doi:10.1016/j.biomaterials.2011.03.031
124. Kumar, P.; Wu, H.; McBride, J. L.; Jung, K.-E.; Hee Kim, M.; Davidson, B. L.; Kyung Lee, S.; Shankar, P.; Manjunath, N. *Nature* **2007,** *448,* 39–43. doi:10.1038/nature05901
125. Oswald, M.; Geissler, S.; Goepferich, A. *Mol. Pharmaceutics* **2017,** *14,* 2177–2196. doi:10.1021/acs.molpharmaceut.7b00158
126. Silva, S.; Almeida, A. J.; Vale, N. *Biomolecules* **2019,** *9,* 22. doi:10.3390/biom9010022
127. Farkhani, S. M.; Valizadeh, A.; Karami, H.; Mohammadi, S.; Sohrabi, N.; Badrzadeh, F. *Peptides* **2014,** *57,* 78–94. doi:10.1016/j.peptides.2014.04.015
128. Goulatis, L. I.; Shusta, E. V. *Curr. Opin. Struct. Biol.* **2017,** *45,* 109–115. doi:10.1016/j.sbi.2016.12.005
129. Chen, Y.; Liu, L. *Adv. Drug Delivery Rev.* **2012,** *64,* 640–665. doi:10.1016/j.addr.2011.11.010
130. Gao, K.; Jiang, X. *Int. J. Pharm.* **2006,** *310,* 213–219. doi:10.1016/j.ijpharm.2005.11.040
131. Oh, N.; Park, J.-H. *Int. J. Nanomed.* **2014,** *9* (Suppl. 1), 51–63. doi:10.2147/ijn.s26592
132. Zhang, S.; Li, J.; Lykotrafitis, G.; Bao, G.; Suresh, S. *Adv. Mater. (Weinheim, Ger.)* **2009,** *21,* 419–424. doi:10.1002/adma.200801393
133. Jo, D. H.; Kim, J. H.; Lee, T. G.; Kim, J. H. *Nanomedicine (N. Y., NY, U. S.)* **2015,** *11,* 1603–1611. doi:10.1016/j.nano.2015.04.015
134. De Jong, W. H.; Hagens, W. I.; Krystek, P.; Burger, M. C.; Sips, A. J. A. M.; Geertsma, R. E. *Biomaterials* **2008,** *29,* 1912–1919. doi:10.1016/j.biomaterials.2007.12.037
135. Sonavane, G.; Tomoda, K.; Makino, K. *Colloids Surf., B* **2008,** *66,* 274–280. doi:10.1016/j.colsurfb.2008.07.004
136. Khlebtsov, N.; Dykman, L. *Chem. Soc. Rev.* **2011,** *40,* 1647–1671. doi:10.1039/c0cs00018c
137. Nicholson, C.; Hrabětová, S. *Biophys. J.* **2017,** *113,* 2133–2142. doi:10.1016/j.bpj.2017.06.052
138. Syková, E.; Nicholson, C. *Physiol. Rev.* **2008,** *88,* 1277–1340. doi:10.1152/physrev.00027.2007
139. Godin, A. G.; Varela, J. A.; Gao, Z.; Danné, N.; Dupuis, J. P.; Lounis, B.; Groc, L.; Cognet, L. *Nat. Nanotechnol.* **2017,** *12,* 238–243. doi:10.1038/nnano.2016.248
140. Begley, D. J. *Sci. Transl. Med.* **2012,** *4,* 147fs29. doi:10.1126/scitranslmed.3004611
141. Lin, J.; Zhang, H.; Chen, Z.; Zheng, Y. *ACS Nano* **2010,** *4,* 5421–5429. doi:10.1021/nn1010792
142. Goodman, C. M.; McCusker, C. D.; Yilmaz, T.; Rotello, V. M. *Bioconjugate Chem.* **2004,** *15,* 897–900. doi:10.1021/bc049951i
143. Lin, J.-Q.; Zheng, Y.-G.; Zhang, H.-W.; Chen, Z. *Langmuir* **2011,** *27,* 8323–8332. doi:10.1021/la201086u
144. Suk, J. S.; Xu, Q.; Kim, N.; Hanes, J.; Ensign, L. M. *Adv. Drug Delivery Rev.* **2016,** *99,* 28–51. doi:10.1016/j.addr.2015.09.012
145. Liu, Z.; Gao, X.; Kang, T.; Jiang, M.; Miao, D.; Gu, G.; Hu, Q.; Song, Q.; Yao, L.; Tu, Y.; Chen, H.; Jiang, X.; Chen, J. *Bioconjugate Chem.* **2013,** *24,* 997–1007. doi:10.1021/bc400055h
146. Guo, J.; Gao, X.; Su, L.; Xia, H.; Gu, G.; Pang, Z.; Jiang, X.; Yao, L.; Chen, J.; Chen, H. *Biomaterials* **2011,** *32,* 8010–8020. doi:10.1016/j.biomaterials.2011.07.004
147. Nance, E. A.; Woodworth, G. F.; Sailor, K. A.; Shih, T.-Y.; Xu, Q.; Swaminathan, G.; Xiang, D.; Eberhart, C.; Hanes, J. *Sci. Transl. Med.* **2012,** *4,* 149ra119. doi:10.1126/scitranslmed.3003594
148. Sulheim, E.; Baghirov, H.; von Haartman, E.; Bøe, A.; Åslund, A. K. O.; Mørch, Y.; de Lange Davies, C. *J. Nanobiotechnol.* **2016,** *14,* 1. doi:10.1186/s12951-015-0156-7
149. Makadia, H. K.; Siegel, S. J. *Polymers (Basel, Switz.)* **2011,** *3,* 1377–1397. doi:10.3390/polym3031377
150. Filon, O.; Krivorotko, P.; Kobyakov, G.; Razjivina, V.; Maximenko, O.; Gelperina, S.; Kreuter, J. *J. Clin. Oncol.* **2017,** *35,* e13537. doi:10.1200/jco.2017.35.15_suppl.e13537
151. Vieira, D. B.; Gamarra, L. F. *Int. J. Nanomed.* **2016,** *11,* 5381–5414. doi:10.2147/ijn.s117210

152. Doxorubicin-loaded Anti-EGFR-immunoliposomes (C225-ILs-dox) in High-grade Gliomas - Full Text View - ClinicalTrials.gov. https://clinicaltrials.gov/ct2/show/NCT03603379 (accessed Feb 4, 2020).
153. Chen, C.; Duan, Z.; Yuan, Y.; Li, R.; Pang, L.; Liang, J.; Xu, X.; Wang, J. *ACS Appl. Mater. Interfaces* **2017,** *9,* 5864–5873. doi:10.1021/acsami.6b15831
154. Liu, Y.; Mei, L.; Xu, C.; Yu, Q.; Shi, K.; Zhang, L.; Wang, Y.; Zhang, Q.; Gao, H.; Zhang, Z.; He, Q. *Theranostics* **2016,** *6,* 177–191. doi:10.7150/thno.13532
155. Cacciatore, I.; Ciulla, M.; Fornasari, E.; Marinelli, L.; Di Stefano, A. *Expert Opin. Drug Delivery* **2016,** *13,* 1121–1131. doi:10.1080/17425247.2016.1178237
156. Patel, M.; Souto, E. B.; Singh, K. K. *Expert Opin. Drug Delivery* **2013,** *10,* 889–905. doi:10.1517/17425247.2013.784742
157. Fundarò, A.; Cavalli, R.; Bargoni, A.; Vighetto, D.; Zara, G. P.; Gasco, M. R. *Pharmacol. Res.* **2000,** *42,* 337–343. doi:10.1006/phrs.2000.0695
158. Zara, G. P.; Cavalli, R.; Bargoni, A.; Fundarò, A.; Vighetto, D.; Gasco, M. R. *J. Drug Targeting* **2002,** *10,* 327–335. doi:10.1080/10611860290031868
159. Zara, G. P.; Bargoni, A.; Cavalli, R.; Fundarò, A.; Vighetto, D.; Gasco, M. R. *J. Pharm. Sci.* **2002,** *91,* 1324–1333. doi:10.1002/jps.10129
160. Bargoni, A.; Cavalli, R.; Zara, G. P.; Fundarò, A.; Caputo, O.; Gasco, M. R. *Pharmacol. Res.* **2001,** *43,* 497–502. doi:10.1006/phrs.2001.0813
161. Kakkar, V.; Mishra, A. K.; Chuttani, K.; Kaur, I. P. *Int. J. Pharm.* **2013,** *448,* 354–359. doi:10.1016/j.ijpharm.2013.03.046
162. Göppert, T. M.; Müller, R. H. *J. Drug Targeting* **2005,** *13,* 179–187. doi:10.1080/10611860500071292
163. Peira, E.; Marzola, P.; Podio, V.; Aime, S.; Sbarbati, A.; Gasco, M. R. *J. Drug Targeting* **2003,** *11,* 19–24. doi:10.1080/1061186031000086108
164. Jain, K.; Sood, S.; Gowthamarajan, K. *Drug Delivery* **2015,** *22,* 940–954. doi:10.3109/10717544.2014.885999
165. Gartziandia, O.; Herran, E.; Pedraz, J. L.; Carro, E.; Igartua, M.; Hernandez, R. M. *Colloids Surf., B* **2015,** *134,* 304–313. doi:10.1016/j.colsurfb.2015.06.054
166. Alam, M. I.; Baboota, S.; Ahuja, A.; Ali, M.; Ali, J.; Sahni, J. K.; Bhatnagar, A. *Int. J. Pharm.* **2014,** *470,* 99–106. doi:10.1016/j.ijpharm.2014.05.004
167. Wavikar, P. R.; Vavia, P. R. *J. Liposome Res.* **2015,** *25,* 141–149. doi:10.3109/08982104.2014.954129
168. Attama, A. A. *Recent Pat. Drug Delivery Formulation* **2011,** *5,* 178–187. doi:10.2174/187221111797200524
169. Lim, W. M.; Rajinikanth, P. S.; Mallikarjun, C.; Kang, Y. B. *Int. J. Nanomed.* **2014,** *9,* 2117–2126. doi:10.2147/ijn.s57565
170. Song, S.; Mao, G.; Du, J.; Zhu, X. *Drug Delivery* **2016,** *23,* 1404–1408. doi:10.3109/10717544.2015.1064186
171. Tsai, M.-J.; Wu, P.-C.; Huang, Y.-B.; Chang, J.-S.; Lin, C.-L.; Tsai, Y.-H.; Fang, J.-Y. *Int. J. Pharm.* **2012,** *423,* 461–470. doi:10.1016/j.ijpharm.2011.12.009
172. Khosa, A.; Reddi, S.; Saha, R. N. *Biomed. Pharmacother.* **2018,** *103,* 598–613. doi:10.1016/j.biopha.2018.04.055
173. Zhang, X. *Cell Biochem. Biophys.* **2015,** *72,* 771–775. doi:10.1007/s12013-015-0529-4
174. Male, D.; Gromnicova, R.; McQuaid, C. Gold Nanoparticles for Imaging and Drug Transport to the CNS. In *International Review of Neurobiology;* Al-Jamal, K. T., Ed.; Nanotechnology and the Brain, Vol. 130; Academic Press, 2016; pp 155–198. doi:10.1016/bs.irn.2016.05.003
175. Lasagna-Reeves, C.; Gonzalez-Romero, D.; Barria, M. A.; Olmedo, I.; Clos, A.; Sadagopa Ramanujam, V. M.; Urayama, A.; Vergara, L.; Kogan, M. J.; Soto, C. *Biochem. Biophys. Res. Commun.* **2010,** *393,* 649–655. doi:10.1016/j.bbrc.2010.02.046
176. Cheng, Y.; Meyers, J. D.; Agnes, R. S.; Doane, T. L.; Kenney, M. E.; Broome, A.-M.; Burda, C.; Basilion, J. P. *Small* **2011,** *7,* 2301–2306. doi:10.1002/smll.201100628
177. Burrows, N. D.; Lin, W.; Hinman, J. G.; Dennison, J. M.; Vartanian, A. M.; Abadeer, N. S.; Grzincic, E. M.; Jacob, L. M.; Li, J.; Murphy, C. J. *Langmuir* **2016,** *32,* 9905–9921. doi:10.1021/acs.langmuir.6b02706
178. Niidome, T.; Yamagata, M.; Okamoto, Y.; Akiyama, Y.; Takahashi, H.; Kawano, T.; Katayama, Y.; Niidome, Y. *J. Controlled Release* **2006,** *114,* 343–347. doi:10.1016/j.jconrel.2006.06.017
179. An, L.; Wang, Y.; Tian, Q.; Yang, S. *Materials* **2017,** *10,* 1372. doi:10.3390/ma10121372
180. Parab, H. J.; Chen, H. M.; Lai, T.-C.; Huang, J. H.; Chen, P. H.; Liu, R.-S.; Hsiao, M.; Chen, C.-H.; Tsai, D.-P.; Hwu, Y.-K. *J. Phys. Chem. C* **2009,** *113,* 7574–7578. doi:10.1021/jp9000169
181. Kolhar, P.; Anselmo, A. C.; Gupta, V.; Pant, K.; Prabhakarpandian, B.; Ruoslahti, E.; Mitragotri, S. *Proc. Natl. Acad. Sci. U. S. A.* **2013,** *110,* 10753–10758. doi:10.1073/pnas.1308345110
182. Laurent, S.; Forge, D.; Port, M.; Roch, A.; Robic, C.; Vander Elst, L.; Muller, R. N. *Chem. Rev.* **2008,** *108,* 2064–2110. doi:10.1021/cr068445e
183. Thakor, A. S.; Jokerst, J. V.; Ghanouni, P.; Campbell, J. L.; Mittra, E.; Gambhir, S. S. *J. Nucl. Med.* **2016,** *57,* 1833–1837. doi:10.2967/jnumed.116.181362
184. Neuwelt, A.; Sidhu, N.; Hu, C.-A. A.; Mlady, G.; Eberhardt, S. C.; Sillerud, L. O. *AJR, Am. J. Roentgenol.* **2015,** *204,* W302–W313. doi:10.2214/ajr.14.12733
185. Liu, D.-F.; Qian, C.; An, Y.-L.; Chang, D.; Ju, S.-H.; Teng, G.-J. *Nanoscale* **2014,** *6,* 15161–15167. doi:10.1039/c4nr03942d
186. Kaluzova, M.; Bouras, A.; Machaidze, R.; Hadjipanayis, C. G. *Oncotarget* **2015,** *6,* 8788–8806. doi:10.18632/oncotarget.3554
187. Sillerud, L. O.; Solberg, N. O.; Chamberlain, R.; Orlando, R. A.; Heidrich, J. E.; Brown, D. C.; Brady, C. I.; Vander Jagt, T. A.; Garwood, M.; Vander Jagt, D. L. *J. Alzheimer's Dis.* **2013,** *34,* 349–365. doi:10.3233/jad-121171